

AD A 054205

AGARD-LS-93

20060313020

AGARD-LS-93

AGARD

ADVISORY GROUP FOR AEROSPACE RESEARCH & DEVELOPMENT

7 RUE ANCELLE 92200 NEUILLY SUR SEINE FRANCE

DDC FILE COPY

AGARD LECTURE SERIES No. 93

Recent Advances in Radio and Optical Propagation for Modern Communications, Navigation and Detection Systems

BEST AVAILABLE COPY

DISTRIBUTION STATEMENT A

Approved for public release;
Distribution Unlimited

NORTH ATLANTIC TREATY ORGANIZATION



DISTRIBUTION AND AVAILABILITY
ON BACK COVER

RECEIVED
MAY 23 1978
SULLIVAN
A

1

14

AGARD-LS-93

NORTH ATLANTIC TREATY ORGANIZATION
ADVISORY GROUP FOR AEROSPACE RESEARCH AND DEVELOPMENT
(ORGANISATION DU TRAITE DE L'ATLANTIQUE NORD)

7

AGARD Lecture Series, No. 93

61

RECENT ADVANCES IN RADIO AND OPTICAL
PROPAGATION FOR MODERN COMMUNICATIONS,
NAVIGATION AND DETECTION SYSTEMS.

11

1 Apr 78

10 274p.

Best Available Copy

DISTRIBUTION STATEMENT A
Approved for public release;
Distribution Unlimited

DDC
RECEIVED
MAY 23 1978
REGISTERED
A

The material in this publication was assembled to support a Lecture Series under the sponsorship of the Electromagnetic Wave Propagation Panel and the Consultant and Exchange Programme of AGARD, presented on 8-9 May 1978 in Oslo, Norway, 11-12 May 1978 in London, England and 15-16 May 1978 in Rome, Italy.

400 043

LB

THE MISSION OF AGARD

The mission of AGARD is to bring together the leading personalities of the NATO nations in the fields of science and technology relating to aerospace for the following purposes:

Exchanging of scientific and technical information;

Continuously stimulating advances in the aerospace sciences relevant to strengthening the common defence posture;

Improving the co-operation among member nations in aerospace research and development;

Providing scientific and technical advice and assistance to the North Atlantic Military Committee in the field of aerospace research and development;

Rendering scientific and technical assistance, as requested, to other NATO bodies and to member nations in connection with research and development problems in the aerospace field;

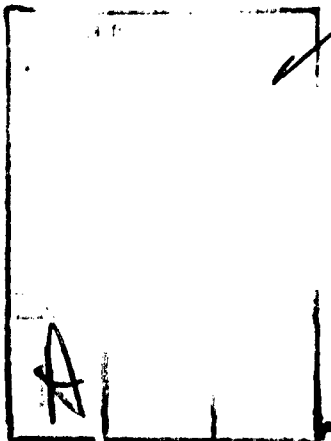
Providing assistance to member nations for the purpose of increasing their scientific and technical potential;

Recommending effective ways for the member nations to use their research and development capabilities for the common benefit of the NATO community.

The highest authority within AGARD is the National Delegates Board consisting of officially appointed senior representatives from each member nation. The mission of AGARD is carried out through the Panels which are composed of experts appointed by the National Delegates, the Consultant and Exchange Program and the Aerospace Applications Studies Program. The results of AGARD work are reported to the member nations and the NATO Authorities through the AGARD series of publications of which this is one.

Participation in AGARD activities is by invitation only and is normally limited to citizens of the NATO nations.

A large part of the content of this publication has been reproduced directly from material supplied by AGARD or the authors; the remainder has been set by Technical Editing and Reproduction Ltd.



Published April 1978

Copyright © AGARD 1978
All Rights Reserved

ISBN 92-835-1280-4



Printed by Technical Editing and Reproduction Ltd
Harford House, 7-9 Charlotte St, London, W1P 1HD

PREFACE

This Lecture Series No.93 was sponsored by the Electromagnetic Wave Propagation Panel of AGARD and was implemented by the Consultant and Exchange Programme. The aim of this Lecture Series was to introduce engineers and system designers to new studies in the field of radio wave and optical propagation. With new requirements of greater data rates in communication and detection being developed, the limits of the medium through which the energy is propagated must be considered.

Ionospheric limitations and tropospheric effects which contribute to radio wave propagation problems were introduced, as well as the problems of coherent propagation and image reconstruction, incoherent propagation, and remote sensing, in optical systems. Propagation problems associated with modern systems were investigated, including those relative to laser transmission, such as transmission-radiation difficulties, blooming and LIDAR. Incoherent optical propagation was discussed, with emphasis on scintillations, absorption, refraction and scattering loss. The effects of atmospheric properties, surface signatures and the sea on infra-red, ultra-violet, and microwave remote sensing were presented. Radio wave scintillation effects on tracking and methods of communication through the aurora and the equatorial irregularities also were presented, leading logically into a description of the need for forecasting and prediction of the ionospheric parameters, and discussion of development of techniques to accomplish that prediction.

The Lecture Series included examination of low frequency radio wave propagation, analyses of LF navigation system errors and problems and new LF systems. The field of range and position error correction in navigation and positioning systems were discussed and included radar and navigation correction techniques. HF transmission was presented, including backscatter and forward scatter HF radars, developments in ray tracing, and channel selection topics.

This Lecture Series concluded with techniques applicable to artificial modification of propagation media, with both high power and chemical release methods being presented.

This ambitious Lecture Series summarized several symposia and specialists meetings, provided expert condensation of the material and described the need for additional effort as well as the latest progress in the field.

LIST OF SPEAKERS

Lecture Series Director: Dr J.Aarons
Department of the Air Force
Air Force Geophysics Laboratory
Hanscom Air Force Base
Massachusetts 01731
USA

Dr M.Bertolotti
Institute of Physics
Faculty of Engineering
Rome University
Rome
Italy

Dr K.Davies
NOAA
Boulder
Colorado 80302
USA

Dr D.T.Gjessing
Royal Norwegian Council for
Scientific and Industrial Research
P.O.Box 25
N-2007 Kjeller
Norway

Dr D.H.Höhn
Forschungsinstitut für Optik
Forschungsgesellschaft für Angewandte
Naturwissenschaften e.V. (FGAN)
FfO Schloss Kressbach
D-7400 Tübingen 1
Germany

Dr T.B.Jones
Department of Physics
University of Leicester
University Road
Leicester LE1 7RH
England

Dr G.E.Peckham
Department of Physics
Heriot Watt University
Edinburgh
Scotland

CONTENTS

	Page
PREFACE	iii
LIST OF SPEAKERS	iv
	Reference
INTRODUCTION TO OPTICAL PROBLEMS OF SYSTEMS by D.H.Höhn	1
PHYSICS OF INCOHERENT OPTICAL PROPAGATION by D.H.Höhn	2
PROPAGATION PROBLEMS RELATIVE TO LASER TRANSMISSION by M.Bertolotti	3
INTRODUCTION TO RADIO-WAVE PROPAGATION EFFECTS ON SYSTEMS by J.Aarons	4
HIGH FREQUENCY RADIO-WAVE PROPAGATION IN THE IONOSPHERE by T.B.Jones	5
FORECASTING AND PREDICTION OF IONOSPHERIC PARAMETERS by K.Davies	6
IONOSPHERIC EFFECTS ON SATELLITE NAVIGATION AND AIR TRAFFIC CONTROL SYSTEMS by J.A.Klobuchar	7
IONOSPHERIC SCINTILLATIONS – AN INTRODUCTION by J.Aarons	8
ARTIFICIAL MODIFICATION OF THE IONOSPHERE by K.Davies	9
THE PROPAGATION OF LOW AND VERY LOW FREQUENCY RADIO-WAVES by T.B.Jones	10
REMOTE SENSING by G.E.Peckham	11
TARGET DETECTION AND IDENTIFICATION METHODS BASED ON RADIO- AND OPTICAL WAVES by D.T.Gjessing	12
BIBLIOGRAPHY	B

INTRODUCTION TO OPTICAL PROBLEMS OF SYSTEMS

by
Dieter H. Hahn
Forschungsinstitut für Optik der FGAN
Schloss Kressbach, D7400 Tübingen 1
F.R. Germany

SUMMARY

The effects of atmospheric optical propagation on modern optical/optronic systems, as used for communications, navigation and detection are discussed in general. With respect to the different types of systems (passive-active, imaging-non imaging, coherent-incoherent) basic environmental effects, especially related to propagation are summarized, as affecting the general incoherent background, target (i.e. the scene) and propagation medium (i.e. the atmosphere), offering the apparent information to the optical/optronic system, and the observer. These effects are related to the relevant atmospheric constituents. So, propagation is introduced as a part of optronic system analysis, as necessary for armament development and asking for further research on atmospheric propagation. Meteorological aspects, e.g. the probability of certain propagation conditions or forecasting problems, are identified as essential for armament development and especially for the effective application of systems during military missions.

1. ATMOSPHERIC OPTICS AND METEOROLOGY AS RELEVANT TO OPTICAL/OPTRONICAL SYSTEMS

For communication, navigation and detection optical and optronic systems usually have to operate through the atmosphere, aside from underwater and space missions, that will not be discussed within this context. But other military applications of such systems, like optical tracking, guidance and control of targets and weapons, including optical counter measures and possible laser weapons, will be mentioned here in general also.

The term "optical system" is standing for human vision and classical (to avoid the term "passive", sometimes used for it) vision aids like telescopes without inherent radiation amplification and/or wavelength conversion, e.g. for infrared vision. The term "optronic system" is used for devices that include amplification and/or wavelength conversion, and that may be sensitive not only to intensity but also to phase and polarization. Photographic cameras, forming a class by itself, are not treated explicitly, they may be covered by the term optical system. Optronic systems are e.g. image intensifier/converter systems, low light level television devices, gated viewing systems, thermal imagers, laser range finders and designators, tracker and seeker heads, laser communication links, as well as medium and high power lasers for jamming and weapon types of applications. They all suffer from environmental limitations, that may be classified as

- propagation effects, and
- scene characteristics.

In the latter case inherent characteristics, like reflectivity, are resulting together with environmental effects, like ambient irradiation, temperature and modifications of reflectivity by rain, in initial target and background characteristics. Both classes of environmental effects are not at all independent of each other but strongly coupled.

As mentioned before generally, environmental effects are limiting optical/optronic systems. Sometimes, however, they may even form the physical basis of a system. So, laser warning devices are based on atmospheric scattering if they should not only detect laser beams directly touching the device. Systems detecting and measuring atmospheric effects, like LIDARs, will not be discussed in this context, even if they are of military interest to allow remote sensing of essential atmospheric parameters, e.g. cross wind (see lecture 4.).

With respect to operational applications natural and battlefield environmental features have to be studied together, to evaluate system limitations. In any case electromagnetic radiation (in this context visual and ir) has to propagate through the atmosphere, that means through a mixture of different

- molecules,
- aerosols, and
- hydrometeors,

variable in space and time. The relevant atmospheric optical propagation effects caused by these constituents are

- refraction,
 - absorption,
 - scattering,
 - turbulence effects, and
 - nonlinear effects.
- Path radiance

has to be included, even if it is dependent on irradiation of the propagation path as well as on scattering and absorption for wavelengths up to about 3 μm . For longer wavelengths $\lambda > 3 \mu\text{m}$ thermal emission of the atmosphere is causing a thermal path radiance. It adds to the optical signal, resulting in a contrast degradation of an image, e.g. vision through fog. With respect to photon noise it is equivalent to an increase in noise. Path radiance is strongly related to scene characteristics, for $\lambda < 3 \mu\text{m}$ by generally the same ambient irradiation, for $\lambda > 3 \mu\text{m}$ through air temperature affecting the thermal characteristics of background and targets without inherent heat sources, aside from cloud cover and other environmental features.

These general statements hold for a wavelength range from about 0.3 μm up to about 15 μm , covering the area of optical/optronic systems, but may be extended up to mm-waves. So they are applicable also for the area

of sub-mm-waves, where optical/optronic techniques together with hf-techniques and suitable lasers may result in new devices during the near future, and for mm-waves, where interesting systems are already existing.

For a given set of atmospheric constituents the physical processes of interaction, e.g. absorption, may be studied experimentally and theoretically including the system relevant optical effects. This usually is called the field of atmospheric optics, covering the whole wavelength range from about $0.3 \mu\text{m}$ up to about mm. Theory including optronic and information processing aspects allows for modelling of systems and description of their limitations, e.g. maximum recognition range of a certain thermal imager against tanks among other vehicles, as a function of the propagation conditions. The variability of atmospheric constituents in time and space, and of the meteorological parameters, e.g. temperature and pressure, has to be taken into account for this type of system analysis. This variability is determined by meteorology, that offers probabilities for the occurrence of individual weather conditions and forecasting capabilities. For a given time (natural irradiation!) they result in a certain environmental situation, as relevant for optical/optronic systems, sometimes simply called "optical weather".

Aside from a physical understanding of atmospheric optical effects and their modelling sometimes physicists and engineers are not fully aware as necessary of the probability of certain propagation effects. So they may be over or underestimated. Armament has to be based on system analysis including environmental effects and their probability under natural and battlefield conditions. But the effective use of military optical/optronic systems during a mission in addition is dependent on forecasting possibilities of the "optical weather". Based on the available systems and the present threat only they allow to determine the most effective measures and counter measures.

If the statement can be made, that it is available a very good knowledge on the physical processes involved, aside from some nonlinear effects, and a good, but not sufficient knowledge on the constituents (e.g. ir aerosol properties), it has to be mentioned that for significant meteorological statistics of relevant optical effects still results of current projects are necessary (e.g. Project OPAQUE, NATO AC/243 (Panel IV/RSG.8): [1]). But systematic studies of optical effects at the battlefield and better forecasting techniques are up to future projects, aside from promising results of projects at several NATO countries, entering this area, e.g. project BAVOS at U.K. and several projects at the U.S.A. [2].

2. OPTICAL/OPTRONICAL SYSTEMS AND RELEVANT PROPAGATION EFFECTS

Table 1 compiles main examples of systems introduced or today under development for military applications. "Passive" indicates that only ambient radiation sources are used, either natural or man made, but not controlled as part of the system under consideration. For examples see Table 1 itself and Fig.1. "Active" systems include a radiation source, today usually a laser, being part of the system and possibly controlled by an operator/observer. They may be subdivided into coherent and incoherent systems up to the coherence status of the source (e.g. resulting in speckled images), and the application of coherent detection techniques (e.g. laser and optical heterodyning, sensitive to phase fluctuations caused by atmospheric turbulence).

The distinction between "imaging" and "non imaging" systems seems to be straight forward, but it has to be mentioned that there is some overlapping, e.g. with respect to 1-dimensional systems, like line scanners, or tracker and seeker heads, using special modulation techniques or some detectors to collect 2-dimensional information of the target and its location, but not offering an image for visual inspection. "Purely transmitting" systems, i.e. usually lasers together with suitable optics, e.g. adaptive optics for high power laser weapons, are mentioned as a class by itself, because propagation of medium and high power radiation suffers from additional effects on low power radiation by thermally induced and non-linear interactions, like blooming or self-defocussing or even self-focussing. To allow for pointing and tracking of such a laser system certainly other means are necessary unless the beam is acting as part of an active tracker system simultaneously. The tasks mentioned are only essential examples rather than a complete listing.

The column environmental effects/parameters summarizes the physical effects and the describing parameters with respect to system performance and limitations. To avoid a larger table this approach could not be strictly systematic. Scene, source and in general also device parameters are included.

In Fig.1 some systems in operation are shown. Especially also the interrelation of them is indicated, but only for demonstration and not at all with respect to their application based on an operational situation or concept. Fig.2 tries to relate Table 1 schematically to the basic concepts of passive and active systems, and may be used by the reader without further comments to relate special propagation effects, as presented during this lecture series, to the types of systems mentioned.

3. ATMOSPHERIC CONSTITUENTS AND RELATED OPTICAL EFFECTS

This section is devoted to a short compilation of atmospheric constituents and their contributions to the optical effects mentioned already in section 1 and 2.

Table 2 summarizes the most essential molecules and presents information on aerosols (suspended solid or liquid particles with diameters between about 10^{-3} and $50 \mu\text{m}$, or larger, e.g. dust particles) and hydrometeors (rain, hail, snow, cloud and fog droplets or particles resp. with diameters from about $50 \mu\text{m}$ up to some mm, or cm in case of hail). Separated for the visual range, say up to about $0.7 \mu\text{m}$, and the ir range $0.7 \mu\text{m} < \lambda < 15 \mu\text{m}$ their main contribution to scattering and absorption is indicated. Strong effects are marked. Scattering is classified into Rayleigh, Mie and geometrical scattering, equivalent to scattering by particles very much smaller, comparable, or very much larger than the wavelength under consideration, resulting in different types of scattering functions, as discussed in further lectures.

Optically relevant atmospheric turbulence, in this context simply called "atmospheric turbulence", resulting in fluctuations of the index of refraction and strongly affecting the propagation of electromagnetic radiation will

later be discussed in detail (lecture 3). It is not included in Table 2, because the index of refraction is no constituent of the atmosphere.

Additional constituents, e.g. as produced by battlefield activities, can be classified into molecules, aerosols or hydrometeors and added to a table like Table 2. Dust particles may be handled formally as aerosols. Certainly the effects are dependent on the local meteorological situation that usually will be changed also by battlefield activities (e.g. increase of temperature and additional wind caused by battlefield fires, increasing turbulence). Aside from this rather complicated problem and the determination of diameters and chemical composition of the typical battlefield constituents, their overall inhomogeneous distribution and their inherent inhomogeneity and time dependence have to be studied in detail for different ambient weather conditions and battlefield situations.

With respect to the natural constituents the index of refraction of aerosols at ir wavelengths is still not known with an accuracy necessary for system analysis and forecasting. Similar arguments hold for hydrometeor effects on optical propagation. So, aside from fine structures of absorption, aerosol and hydrometeor parameters, including their meteorology, are the most critical items of today's defence oriented atmospheric optical research, but also civilian applications are asking for further results of this type, because optronic systems there will also be more and more used within the near future. For sub-mm and mm wave systems hydrometeors are of high importance also, because at these wavelengths scattering by molecules is negligible, and also aerosol scattering is no longer very essential, if not very long paths are to be considered. Hydrometeor size distributions are important, because scattering by them has to be handled as Mie scattering with respect to these long wavelengths.

The optical effects of atmospheric turbulence were studied in detail since lasers are available, starting from earlier astronomically oriented results. So, much information is available. But, e.g. for coherent systems there is still much need for further research on phase fluctuations caused by atmospheric turbulence. Turbulence effects under battlefield conditions are asking for much experimental and theoretical work, because they are limiting the effectiveness of systems like designators and active trackers, that seems to be of very high importance for the next generation of guided weapons.

Another problem range, not mentioned explicitly before, is formed by the propagation effects along slant paths. They can be mathematically treated, but only if relevant height profiles of meteorological/optical parameters are available. Fig.3 shows some essential features of the height structure of the atmosphere. The rather inhomogeneous area up to about 12 km asks aside from meteorological routine sounding and forecasting for remote sensing measures, to allow short time forecasting as necessary for military missions, usually implying air support. For details see lecture 4. In addition experimental research is still necessary to check slant path models, for e.g. transmission like LOWTRAN, and especially for turbulence effects.

4. CONCLUSION

Within this introductory lecture it was tried to summarize the degradation of optical information by atmospheric effects. Signal levels are decreased by absorption and scattering, path radiance is added to the signals, decreasing the contrast. Both effects are increasing noise. Turbulence is producing an atmospheric modulation transfer function resulting in an image degradation, and fluctuations of intensity, phase and other beam parameters, limiting the application of laser beams. So, system analysis and development have to study these effects to optimize the system under consideration with respect to its meteorological range of application, including optical effects under battlefield conditions. Finally only based on forecasting the "optical weather" during military missions such systems can be used with a maximum of effectiveness. The same holds for decisions on the most effective counter measures against optical/optronic systems.

REFERENCES

- [1] Proposal for a Measurement Programme on Optical (and Infrared) Atmospheric Quantities in Europe (OPAQUE), 1975, NATO AC/243 (Panel III/RSG.3) D/17, and Instrumentation for the Common Project OPAQUE, 1975, addendum to this document; now performed by NATO AC/243 (Panel IV/RSG.8) and presented in documents of this group.
- [2] A.R.Downs, A Review of Atmospheric Transmission Information in the Optical and Microwave Spectral Regions, 1976, USA Ballistic Research Laboratories, Memorandum Report No.2710.

With respect to this introduction it does not seem to be meaningful to refer to more literature, but it has to be mentioned that it is based on the cooperation with my colleagues at the FFO, and especially also with colleagues of other NATO countries engaged in the work of NATO AC/243 (Panel IV), and its RSGs, especially RSG.7 (on imaging devices...) and RSG.8 (on atmospheric transmission, performing the project OPAQUE).

system				environmental effects/parameters
type	device (main examples)	mil. task (essential examples)		
passive	imaging	human eye (+ telescope) (photographic camera) image intensifier/converter low light level television thermal imager (line scanner)	reconnaissance trucker seeker driver sight	scene : amb. irradiance/reflectivity emission atm. : absorption, scattering, turbulence refraction emission (device : assessment figures (+ special, optically relevant battlefield effects)
	none imaging	photometer radiometer	(trucker) (seeker) laser warning device	
active	imaging	s. above pass. im. + source, e.g. spotlight + ... gated viewing laser added thermal imager	hum. spotlight vision act. driver sight reconnaissance act. tracker act. seeker	(source : assessment figures atm. : absorption, scattering, turbulence (refraction, emission) scene : irradiance/reflectivity atm. : absorption, scattering, turbulence (refraction, emission) (device : assessment figures (+ special, optically relevant battlefield effects)
		photom., radiom. + laser scanner	reconnaissance act. tracker act. seeker	
	none imaging	(eye), photom., radiom. + source	comm. link laser range finder and loc. laser marker and design. LADAR opt. IFF	
purely transm.	laser + optics (if pointed by other means)	dazzling, jamming weapon	(source : assessment figures atm. : absorption, scattering, turbulence non linear interaction (refraction) (target : irradiance	

Table 1: Main optical/optronical systems, their essential tasks, and the most relevant environmental effects/parameters.

atm. constituents	conc.	main optical effects	
		visual	ir
<u>molecules</u> ($\sim 10^{-4} \mu\text{m}$)	<u>vol. %</u>		
nitrogen N_2	78.1	Rayleigh sca.	-
oxygen O_2	21.0	Rayleigh sca.	-
argon A	1.0	(Rayleigh sca.)	-
carbon dioxide CO_2	3×10^{-2}	-	abs.
neon Ne	1.8×10^{-3}	-	-
helium He	5.2×10^{-4}	-	-
methane CH_4	1.4×10^{-4}	-	abs.
crypton Kr	1.1×10^{-4}	-	-
nitrous oxide N_2O	5×10^{-5}	-	abs.
hydrogen H_2	5×10^{-5}	-	-
xenon Xe	8.6×10^{-6}	-	-
water vapor H_2O	0.1×1.0	-	abs.
ozone, near gr. O_3	$0 - 10^{-5}$	(abs.)	(abs.)
ozone layer 25 km O_3	10^{-4}		
<u>aerosols</u> ($10^{-3} - 50 \mu\text{m}$)	$\frac{\text{cm}^{-3}}{50 - 10^5}$	Mie. sca. (abs.)	Rayleigh/Mie sca. abs.
<u>hydrometeors</u> ($50 \mu\text{m} - \text{mm} - \text{cm?}$)	not gen.appl. (inhom!)	geom. sca. abs.	(Mie)/geom.sca. abs.

Table 2: Main optically relevant constituents of the atmosphere, diameter range, concentration (constant mixing ratio up to about 90 km for N_2 till Xe), and main optical effects for visual and ir radiation up to about $15 \mu\text{m}$. (partly from M.L. Votsia, Atmospheric Optical Environment, 1972, R & D Techn. Report ECOM-7023).

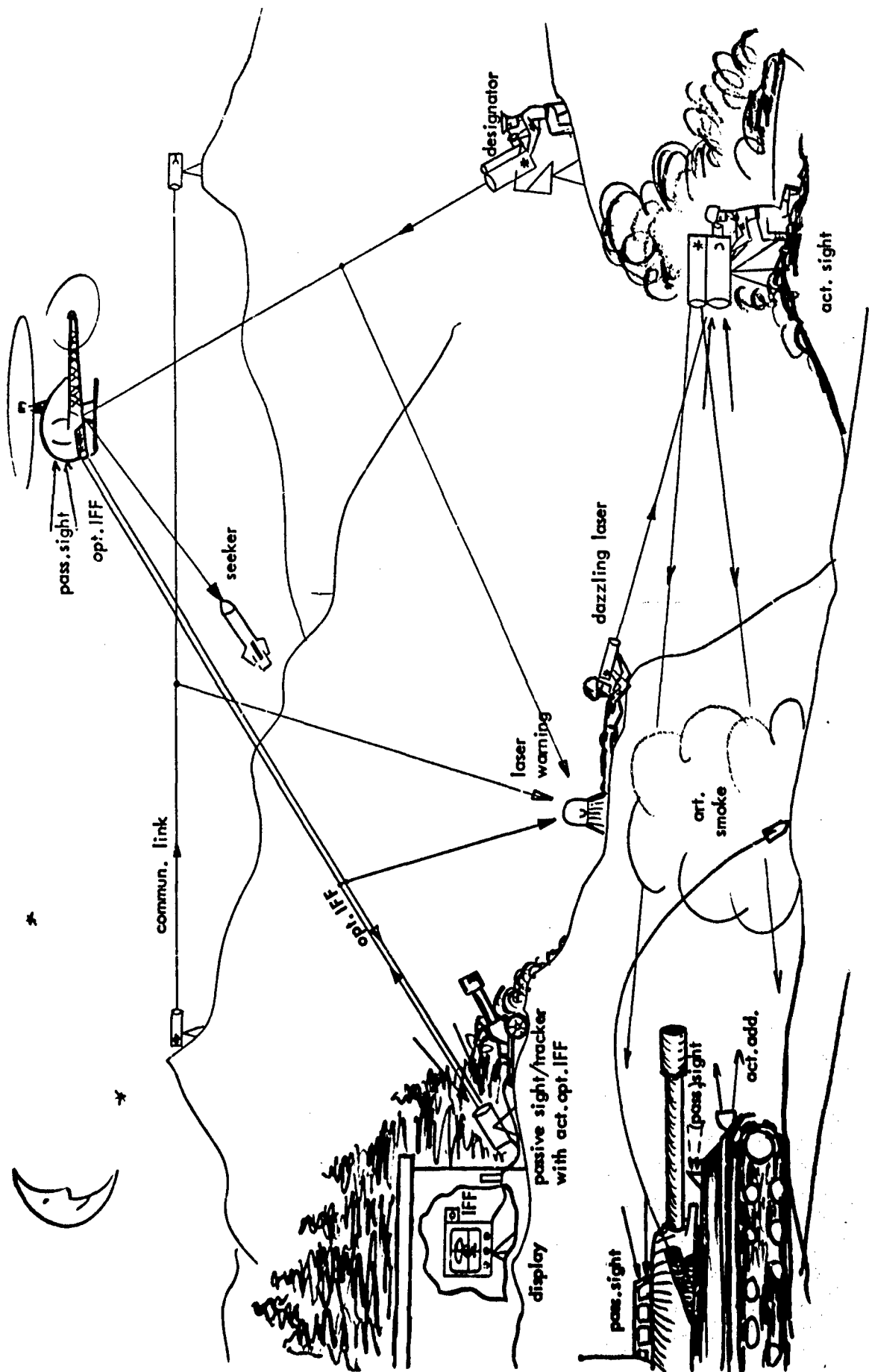


Fig. 5: Several examples for military optical systems in operation, schematically.

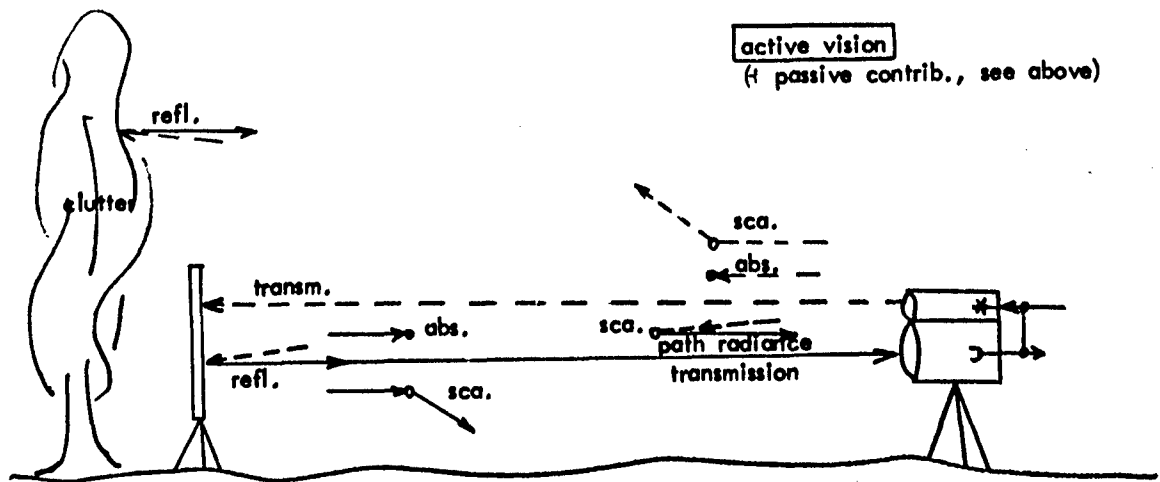
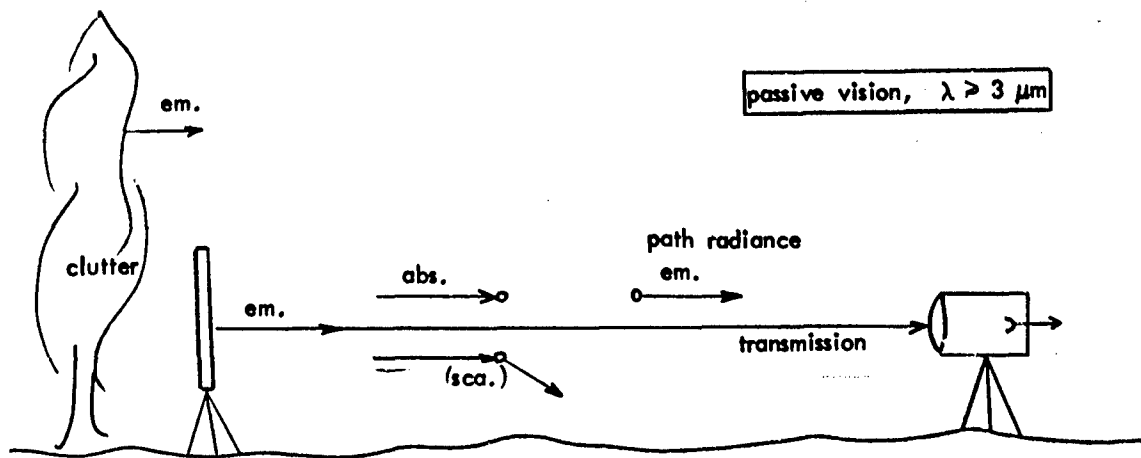
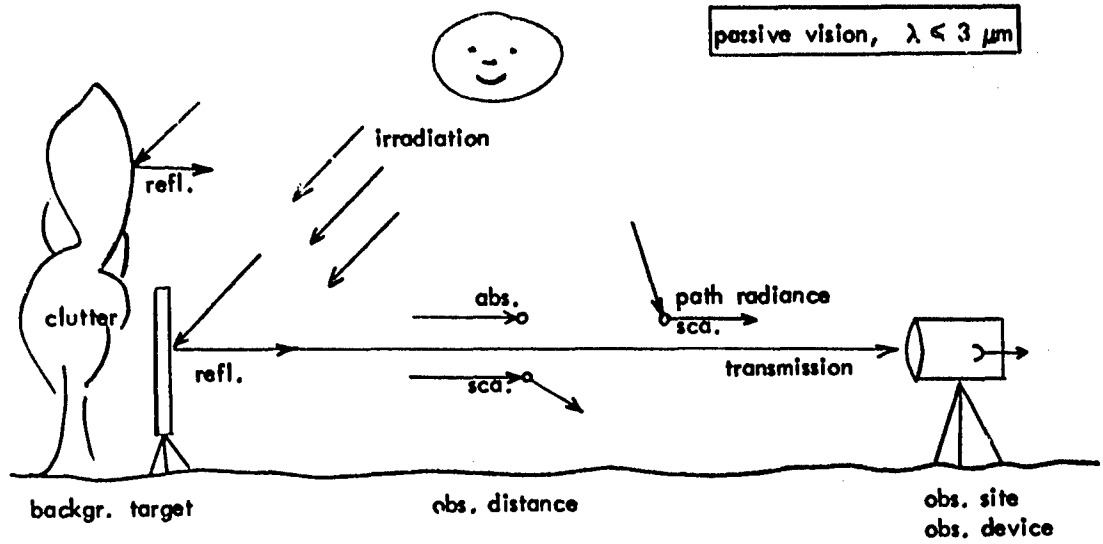


Fig.2:

Atmospheric effects, as relevant to passive optronical systems for $\lambda < 3 \mu\text{m}$ (path radiance mainly produced by scattering) and $\lambda > 3 \mu\text{m}$ (path radiance mainly produced by atmospheric emission: thermal vision), and for active systems (---: active irradiation; passive contributions have to be added, dependent on $\lambda \lesssim 3 \mu\text{m}$).
 (partly from D.H.Höfn, Atmospheric Vision $0.35 \mu\text{m} < \lambda < 14 \mu\text{m}$, Appl.Opt. 1975, Vol.14, page 404; for details see lecture 2).

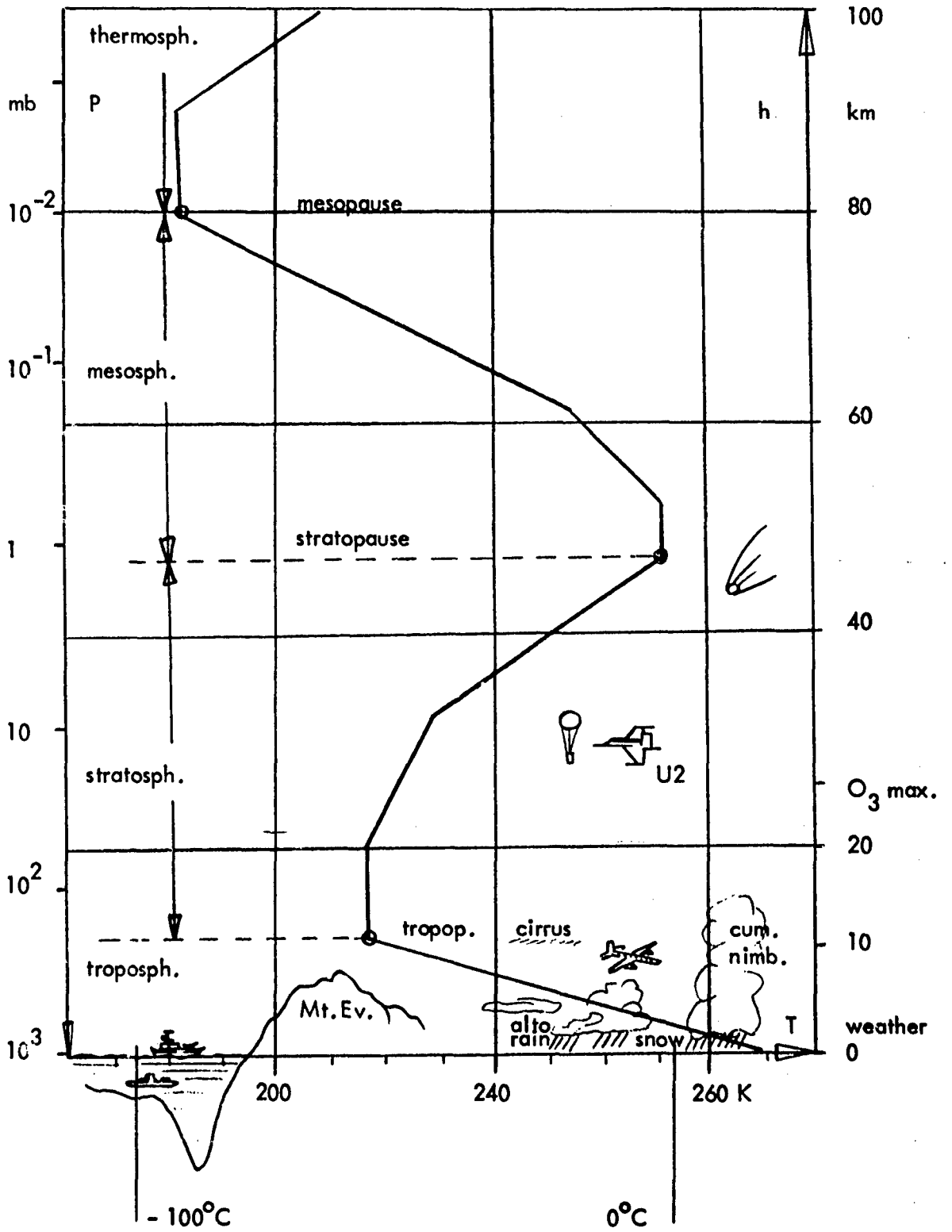


Fig.3: Temperature-altitude profile to 100 km for U.S. standard atmosphere 1962 and indications of the "weather area". (partly after ECOM-7023, see Table 2).

PHYSICS OF INCOHERENT OPTICAL PROPAGATION

by

Dieter H. Höhn

Forschungsinstitut für Optik der FGAN

Schloss Kressbach, D 7400 Tübingen

F.R.Germany

SUMMARY

Atmospheric optical effects are discussed as relevant to optical/optronic systems, i.e. atmospheric refraction (only in general) and transmission. The basic relations for atmospheric absorption and scattering are presented. Effects of atmospheric molecules, aerosols and hydrometeors are described for the wavelength range $0.3 \mu\text{m}$ to $15 \mu\text{m}$. Optical effects of atmospheric turbulence (see lecture 3) and high power laser propagation are not included. - With respect to atmospheric vision the general vision formula is presented together with remarks on atmospheric path radiance and on perception range modelling. This includes the definition of visual range V_N , and maximum perception range R_{max} , e.g. with respect to thermal vision through the atmosphere. - Finally the current project OPAQUE is mentioned as an example for the collection of data on atmospheric optical and infra-red effects as relevant to the performance of optical/optronic systems and forecasting of the "optical weather".

CONTENT

1. INTRODUCTION
2. ATMOSPHERIC OPTICAL EFFECTS
 - 2.1 Atmospheric Refraction
 - 2.2 Atmospheric Transmission
 - 2.3 Atmospheric Absorption and Scattering
 - 2.4 Molecular (2.4.1), Aerosol (2.4.2), and Hydrometeor (2.4.3) Effects
 - 2.5 Transmission Computer Code LOWTRAN
3. ATMOSPHERIC VISION
 - 3.1 General Vision Formula and Perception Criteria
 - 3.2 Atmospheric Path Radiance
 - 3.3 Perception Range Modelling Concepts
4. MEASUREMENT PROJECT OPAQUE
5. CONCLUSIONS

REFERENCES

1. INTRODUCTION

As discussed in general in lecture 1 atmospheric optical ($0.3 \mu\text{m} < \lambda < 15 \mu\text{m}$) effects are usually limiting the performance of optical/optronic systems. Several examples, including the indication of the main atmospheric effects with respect to different types of systems were also presented there. This lecture 2 is devoted to a geophysical discussion of the essential atmospheric optical effects, aside from those, produced by atmospheric turbulence (lecture 3) and those related to high power laser propagation, e.g. [1,2]. The intention is to present them in a way, that their interrelation is evident. So, the main emphasis is neither the presentation of numerical material, directly applicable to the analysis of special systems and their atmospheric limitations, nor that of an extended bibliography. It will be

tried to present the basic relations and to identify the large variety of atmospheric optical propagation effects. This may lead to a physical and meteorological understanding, necessary to decide in each system oriented study firstly on all relevant environmental effects, limiting the system. Only afterwards detailed calculations may be performed. Areas of current research or those, asking for future activities, will be mentioned within each section.

Detailed equations for numerical analysis may be easily found in relevant text-books, hand-books, review-reports and proceedings on atmospheric optics, including mostly tables and graphs, e.g. [1,3-11, 14, 21]. Current papers on problem areas, mentioned in the following, also may be easily found by a quick look through the yearly subject index of relevant journals, e.g. [12], and especially the report series of the research establishments within NATO, devoted to atmospheric optics. Most of the cooperative effort in this area is established by, and reported to NATO AC/243 (Panel IV): On Optics and Far-Infra-Red; this Panel and its RSGs are also publishing relevant papers, e.g. Ref.[1] of lecture 1.

2. ATMOSPHERIC OPTICAL EFFECTS

2.1 Atmospheric Refraction

The index of refraction $n = c/v$, with $c =$ velocity of propagation in a vacuum and v in air, is numerically described by the refractive modulus

$$N = (n - 1) \cdot 10^6 = \frac{77.6 P}{T} + \frac{0.584 P}{T \lambda^2} \quad (- 0.06 P_{wv}), \quad (1)$$

with $P =$ atmospheric pressure and $P_{wv} =$ partial pressure of water vapour in mb, $T =$ air temperature in K, and $\lambda =$ wavelength in μm , for wavelengths including the 8 to 14 μm band. If pressure and/or temperature, i.e. the index of refraction n , are changing spatially in a systematic way, a beam is refracted. This effect is called atmospheric refraction. Typical time constants of temporal variations of atmospheric refraction are starting with minutes. Statistical fluctuations of n , as caused by atmospheric turbulence, result in fluctuations of optical parameters including beam direction, and will be discussed in lecture 3. n is decreasing with increasing temperature and wavelength, and with decreasing pressure, e.g. with increasing altitude, see Eq.(1) and Fig.3 of lecture 1. Its dependency on wavelength is small, as demonstrated by Table 1:

λ	0.3	0.7	4	10	μm
N	292	276	273	273	

Table 1: Wavelength dependency of $N = (n - 1) \cdot 10^6$ at 15°C, 1013.25 mb (and dry air $P_{wv} = 0$).

Looking upwards under normal atmospheric conditions, see Fig.3 of lecture 1, atmospheric refraction results in an apparent lifting of the target, increasing with increasing zenith distance (zero for zenith vision) and target distance. To offer an idea of the magnitudes involved from the visible throughout the infra-red including thermal vision, mean values for nearly horizontal vision (terrestrial refraction $\tilde{\alpha}$) as a function of the target distance R , and for slant vision (astronomical refraction $\tilde{\gamma}$), i.e. the observation of extraterrestrial or quasi-extraterrestrial objects as a function of zenith distance z are presented in Table 2:

R	1	4	8	12	20	km
$\tilde{\alpha}$	2	8	17	25	42	arc.sec.
	10	40	85	125	210	μ rad

z	90	89	85	60	10	0	arc.degr.
$\tilde{\gamma}$	35	24	9.8	1.7	0.2	0	arc.min.
	10	7.0	2.8	0.5	0.06	0	mrad

Table 2: Typical terrestrial refraction $\tilde{\alpha}$ as a function of target distance R, and astronomical refraction $\tilde{\gamma}$ as a function of zenith distance z, i.e. apparent lifting of the target for upward and horizontal vision.

This effect is equivalent to a lifting and simultaneously broadening of the horizon, resulting in trans-horizon vision. Under anomalous (negative) refraction targets as well as the horizon are lowered, the latter simultaneously is narrowed. In the case of looking downward the inverse effects are to be observed. The occurrence of special atmospheric layers result in phenomena like mirages, fata morgana, etc.

Variations of atmospheric refraction result e.g. in laser beam wandering, preferably vertically, with time constants of about minutes around sunrise and sunset. At distances up to about 10 km dispersion effects for wavelengths from the visible up to about 15 μ m are usually negligible. Under usual middle European conditions over some km beam wandering of mrad is typical. The same holds for the apparent line of sight of imaging devices.

But dispersion effects are essential if optical and infra-red means are used together with sub-mm and hf systems. For longer wavelengths the wavelength dependency is decreasing further, but the influence of water vapour is increasing drastically. For sub-mm and mm waves, say in general 20 μ m up to about 1 cm, further research seems to be necessary. Beyond $\lambda = 1$ cm the following relation holds, that is demonstrating this statement, if compared with Eq. (1):

$$N = (n - 1) \cdot 10^6 = \frac{77.6 P}{T} + \frac{370\,000 P_{\text{wv}}}{T^2} \quad (2)$$

For formulae and numerical values used here, and further details, see e.g. [5, 10]. These short comments on atmospheric refraction should have shown that also for thermal systems it may have to be taken into account, especially if they are used for applications related to guidance and control, or navigation. For the wavelength range $20 \mu\text{m} < \lambda < 1$ cm further research seems to be necessary to establish a reliable water vapour term as a function of λ .

2.2 Atmospheric Transmission

The atmospheric spectral transmission $\tau_\lambda(R)$ for the wavelength λ along the range R of a parallel beam is given by

$$\tau_\lambda(R) = \Phi_\lambda(R) / \Phi_{\lambda,0} < 1. \quad (3)$$

$\Phi_{\lambda,0}$ is the spectral radiant flux (in $\text{W}\mu\text{m}^{-1}$) under consideration at $R = 0$, $\Phi_\lambda(R)$ that at R. The differential attenuation along the length dx establishing this transmission can be described by

$$d\Phi_\lambda = -\sigma_\lambda \Phi_\lambda dx . \quad (4)$$

Integration offers for a homogeneous medium ($\sigma_\lambda = \text{const.}$):

$$\tau_\lambda(R) = \Phi_\lambda(R) / \Phi_{\lambda,0} = \exp -\sigma_\lambda R . \quad (5)$$

Eq. (5) is the wellknown exponential extinction law, sometimes called Bouguer's, Lambert's or Beer's Law. σ_λ , usually given in km^{-1} , is the spectral extinction coefficient. It is additive with respect to different, independent attenuation mechanisms and constituents:

$$\sigma_\lambda = \alpha_\lambda + \beta_\lambda , \quad (6)$$

$$= \sigma_{\lambda M} + \sigma_{\lambda A} + \sigma_{\lambda H} . \quad (7)$$

Eq. (6) selects for absorption (α) and scattering (β), see section 2.3, Eq. (7) for different atmospheric constituents, i.e. molecules (M), aerosols (A) and hydrometeors (H), see section 2.4.

For inhomogeneous distributions of absorbing and scattering atmospheric constituents the transmission $\tau_\lambda(R)$ may be calculated by integration along the path R . The distribution of the local extinction coefficient has to be known either actually, e.g. by in situ or remote sensing methods, or at least by a model applicable to the actual meteorological situation:

$$\begin{aligned} \tau_\lambda(R) &= \exp - \int_0^R \sigma_\lambda(x) dx , \\ &= \exp - \sigma_{\lambda,0} \overline{R}_\lambda , \\ &= \exp - \overline{\sigma}_\lambda R . \end{aligned} \quad (8)$$

Eq. (8) presents the usual definitions, suitable to describe inhomogeneous transmission. \overline{R}_λ is the equivalent transmission path at $R = 0$ with $\sigma_{\lambda,0}$ there, often used for slant path transmission. The mean extinction coefficient $\overline{\sigma}_\lambda$ can be applied to statistically inhomogeneous paths, e.g. to long path transmission problems.

Transmission τ is given usually as a number (< 1) or in percent ($< 100\%$). For longer wavelengths often decibels (db) are used. Because $10 \log_{10}(\Phi_0/\Phi) = \text{db}$, it follows $\sigma \approx 0.23 \text{ db}$ with σ in km^{-1} , or $\text{db/km} = 4.34\sigma$ and $\tau = 10^{-0.1\text{db}}$.

The relations presented as Eq. (3) to (8) are applicable to monochromatic radiation, e.g. laser radiation, only. In addition they can certainly be used for polychromatic radiation, if σ_λ is independent of wavelength with respect to the accuracy necessary for a certain analysis. But in general an integration is necessary to calculate broad band transmission values as used for thermal vision (e.g. 3-5 and 8-13 μm):

$$\tau_{\lambda, \Delta\lambda}(R) = \frac{\Delta\lambda \int \Phi_{\lambda,0} [\exp -\sigma_\lambda R] d\lambda}{\Delta\lambda \int \Phi_{\lambda,0} d\lambda} , \quad (9)$$

$$= \frac{\Delta\lambda \int \Phi_{\lambda,0} [\exp - \int_0^R \sigma_\lambda(x) dx] d\lambda}{\Delta\lambda \int \Phi_{\lambda,0} d\lambda} , \quad (10)$$

for homogeneous and inhomogeneous conditions resp. For system analysis instead of $\Delta\lambda$, describing a rectangular wavelength band only, the spectral responsivity \mathcal{R}_λ of the receiver has to be included as another factor in the integral. The integrals are equivalent to broad band radiant fluxes, given in W.

If an average extinction coefficient $\overline{\sigma_\lambda, \Delta\lambda}$ for the wavelength band under consideration is used to calculate the transmission by Eq.(5), i.e. the exponential law, instead of Eq.(9), i.e. the correct integration, the calculated transmission values for short ranges would be higher than the actual ones. That for long ranges would be lower. Physically this results simply because at the beginning of the transmission range the radiation at wavelengths with high σ_λ is attenuated much more than that with low σ_λ . Therefore the spectral content of the radiation is changing along the transmission range, so that wavelengths with low σ_λ are dominating more and more. These results for long range transmission in an overall extinction law flatter than an exponential one.

For wavelength bands comparable with atmospheric windows, see section 2.4.1 and 2.5 (Fig.2 and 3), the extinction coefficient for the dominating wavelengths after transmission ranges between some 100 m and 1 km is more or less wavelength independent. Therefore the exponential extinction law can be used for long range window transmission, including a correction term, as a good approximation. This is very helpful for system analysis because of the simple handling of exponential relations and these ranges $R > 1$ km, quite comparable with operational ranges sensitive to atmospheric limitations.

2.3 Atmospheric Absorption and Scattering

With respect to absorption, it may be mentioned only, that it is defined as the transfer of radiant energy to other kinds of energy, caused by interaction between radiation and matter. The absorption coefficient α , as introduced by Eq.(6) is related to the complex index of refraction $m = n - ix$, suitable to describe absorbing matter, by

$$\alpha = \frac{R_a}{R} \frac{4\pi x}{\lambda}, \quad (11)$$

with R_a = interaction pathlength, R = macroscopical transmission range. Absorption was indicated in Fig.2 of lecture 1 by $\rightarrow\infty$. Absorption effects of atmospheric constituents will be discussed in section 2.4.

More general comments are necessary on scattering, i.e. within this context: the deflection of radiation from its original direction, if striking a surface or propagating through a medium. It is described by the volume scattering function

$$\beta(\varphi) = \frac{dI(\varphi)}{E dV}, \quad (12)$$

given in $\text{sr}^{-1} \text{m}^{-1}$ with $I(\varphi)$ = radiant intensity in Wsr^{-1} for a certain angle φ with respect to the original direction, E = irradiance in Wm^{-2} of the volume element dV in m^3 , see Fig.1. The scattering coefficient β , covering all losses by scattering, follows by integration:

$$\beta = 2\pi \int_0^{180} \beta(\varphi) \sin \varphi d\varphi, \quad (13)$$

if unpolarized radiation is assumed, i.e. if rotational symmetry is present. $\beta(\varphi)$, given in $\text{sr}^{-1} \text{m}^{-1}$, normalized to β , given in m^{-1} (or km^{-1}), is called the relative scattering function, given in sr^{-1} :

$$\beta'(\varphi) = \beta(\varphi) / \beta . \quad (14)$$

It allows easily to discuss the three most relevant scattering processes in the atmosphere.

If the diameter d of the scattering particle is much smaller than the wavelength λ , say $d \leq 0.2 \lambda$, a symmetrical scattering function exists with $\beta'(\varphi) \sim (1 + \cos^2 \varphi)$. Rotational symmetry with respect to the direction of incidence is present, if no oriented scattering particles have to be assumed within the atmosphere. If no wavelength dependency of n has to be taken into account, the scattering coefficient β is proportional to λ^{-4} . This is the area of Rayleigh scattering, see Fig.1 and section 2.4.1.

For diameters d comparable with the wavelength, say $0.2 \lambda \leq d \leq 5\lambda$, forward scattering is increasing more and more with increasing diameters d , see Fig.1. Because of diffraction effects β_λ is fluctuating with λ for a given d , see Fig.4 (before it becomes constant for $\lambda \ll d$). This is the area of Mie scattering, where all scattering quantities are very sensitive to variations of d , and especially also to the size distribution of particles in the realistic case of ensembles of particles, different in size and complex index of refraction m , as present in the atmosphere. Scattering and absorption no longer can be separated, because $m = n - ik$ is describing absorption by k , see Eq.(11), as well as scattering by n itself. Mie's scattering theory covers Rayleigh scattering for small λ as well as geometrical scattering for large λ , also, because it is based strictly on electromagnetic wave theory. Usually spherical particles can be assumed in the context of atmospheric scattering, so that no additional problems are entering the calculations with respect to the relevant boundary conditions, as for non spherical particles, especially irregular particles like snow. For some more details see section 2.4.2.

Large particles, say $d > 5 \lambda$, are scattering mostly by reflection and internal refraction. Forward scattering is the most dominant process, only some minor secondary maxima are present for other directions, see Fig.1. The extinction coefficient is wavelength independent, if the wavelength dependency of n is negligible, see section 2.1. Absorption and scattering may be separated. In section 2.4.3 an example will be discussed.

For details on theory and the available computer codes, as well as for more sophisticated effects (e.g. none spherical particles, polarisation effects) the relevant text-books may be used. In the following the different atmospheric constituents will be discussed with respect to their contributions to these transmission effects at different wavelength bands, as already indicated in lecture 1, Table 2.

2.4 Molecular, Aerosol and Hydrometeor Effects

2.4.1 Molecular Effects

For all wavelengths, considered here: $\lambda > 0.3 \mu\text{m}$, it holds the relation $d \ll \lambda$ because of $d \sim 10^{-4} \mu\text{m}$ for molecules. Therefore molecular scattering can be handled always as Rayleigh scattering with

$$\beta_{\lambda M} = \frac{32 \pi^3}{N} \cdot \frac{(n-1)^2}{\lambda^4} , \quad (15)$$

where N = molecular concentration (about $2.7 \cdot 10^{19} \text{cm}^{-3}$ at sea level). In the case of clear air at sea level

there follows the spectral Rayleigh scattering coefficient $\beta_{\lambda M} = 1.16 \cdot 10^{-2} \text{ km}^{-1}$, $8 \cdot 10^{-8} \text{ km}^{-1}$ and 10^{-15} km^{-1} for the wavelengths $\lambda = 0.55 \mu\text{m}$, $10.6 \mu\text{m}$ and 1 mm resp. In the visible range, where molecular absorption usually can be neglected, molecular scattering determines the maximum visual range V_{NR} , the so called Rayleigh visibility:

$$V_{NR} = \frac{3.912}{\sigma} = 337 \text{ km} , \quad (16)$$

as defined in section 3.3 by Eq.(28) and equivalent to a transmission of 0.02 along this range.

Molecular absorption, especially essential in the infra-red range, is highly wavelength dependent because of the line structure originated by atmospheric gaseous constituents, see Table 2 of lecture 1. Fig.2 demonstrates this by offering a schematical low resolution transmission spectrum of the atmosphere, together with an indication of the absorbing atmospheric gaseous constituents. The atmospheric absorption bands and windows are marked, using today's usual nomenclatures. This spectrum demonstrates the necessity of integrations over λ for infra-red wavelength bands, as discussed in section 2.2. Only within actual window areas and for distances larger than some 100 m exponential approximations may be used, e.g. for the 8 to 13 μm band, mostly used with thermal imaging devices of the first generation.

Even if much relevant empirical and theoretical material is available, and already used for computer codes, like LOWTRAN (resolution $\Delta(1/\lambda) \geq 20 \text{ cm}^{-1}$) and HITRAN (line by line model) [11], see also section 2.5, also with respect to molecular absorption further research is still necessary. New high quality spectral transmission measurements and broad band transmission measurements (e.g., see project OPAQUE, section 4) under different meteorological conditions, and as a function of range, should allow to improve such models. But in contradiction to aerosol and hydrometeor effects, molecular absorption and scattering can be handled theoretically and by models with a quality, sufficient already for very much of today's system analysis problems, see Fig.3.

2.4.2 Aerosol Effects

The term aerosol is frequently used to describe suspended solid, liquid and mixed particles in the atmosphere, small enough not to fall rapidly under the force of gravity such as rain drops, and that are not produced in the context of thermodynamical processes, such as cloud and fog droplets, that are usually handled as hydrometeors (sometimes also as aerosols). The diameter range for aerosols is 10^{-3} to about $50 \mu\text{m}$, overlapping with that of cloud and fog droplets, as well as with that of fine drizzle droplets [7] with falling speeds between cm s^{-1} and m s^{-1} . Typical overall aerosol concentrations near ground are lying between 50 and 10^5 cm^{-3} . Visually aerosols are producing haze or dust, equivalent to decreasing transmission and contrast, i.e. visibility. The composition, optically described by m , see section 2.3 and Eq.(11), and the size distribution of actual aerosols are highly variable, related to meteorological and orographical conditions. Sea and land are producing aerosols of different type, that will be modified and mixed, up to their transportation, to relative humidity and their lifetime. Especially over seas and near to the sea surface (including sea spray) the aerosol is not known at all with an accuracy necessary for military system analysis, e.g. for sea scimmer analysis. But also at land and for aerospace, especially long range transmission in the stratosphere, much aerosol research is still necessary to derive in models and accurate in situ and remote sensing measurement methods. Particle size distributions can be measured in situ with modern optical means (e.g. Instruments of Royco and Particle Measuring Inc., USA), but there is still a lack of methods to measure the complex index of refraction m in situ, and certainly for reliable remote sensing methods.

In the wavelength range $0.3 \mu\text{m} < \lambda < 15 \mu\text{m}$ aerosol particles are acting as Mie scatterers up to $m(\lambda)$ and absorbers up to $x(\lambda)$, see Eq.(11). The absorption effect is small in the visible range, but has to be taken into account for infra-red wavelengths, where it is not known accurately up till now. To get a feeling for

the impact of aerosol size distributions on the wavelength dependency of the scattering coefficient β_A , it may be used the so-called Junge aerosol distribution:

$$\frac{dN}{d \log r} = c r^{-\nu}, \quad (17)$$

that is a good first order approximation for haze over land and diameters around visual wavelengths. N = aerosol concentration, r = aerosol radius $d/2$; c and ν are constants, describing aerosol concentration and distribution resp. ν usually is lying between 2.5 and 4; values between 3 and 3.5 may be used as an first order approximation for visual ranges larger than 1 km, and up to aerosol diameters of about some μm . Mie's theory allows to calculate the spectral scattering coefficient for this distribution:

$$\beta_{\lambda A} \sim \lambda^{-(\nu-2)} = \lambda^{-(1 \text{ till } 1.5)} \quad (18)$$

for $\nu = 3$ till 3.5. For visual ranges V_N between about 1 km and the Rayleigh range 337 km, β_A is lying therefore between about 4 km^{-1} and 10^{-2} km^{-1} , see Eq. (16). Visual ranges smaller than about 1 km are seldom; ranges of some 100 m and less, occurring more often, are caused by hydrometeors, like clouds, fog or precipitation.

Fig.4 allows to discuss the impact of different aerosol diameter ranges on the spectral scattering coefficient $\beta_{\lambda A}$, following F.Volz, e.g.[3]. Assuming a Junge distribution with $\nu = 3$ for $0.1 \mu\text{m} \leq d \leq 20 \mu\text{m}$ the spectral scattering coefficients for these diameters has to be added, weighted by that distribution. It follows, that for a certain wavelength λ particles around $d = \lambda$ are the most effective scatterers. For wavelengths $\lambda > d_{\text{max}}$ Rayleigh scattering ($\sim \lambda^{-4}$) results, for $d_{\text{min}} \leq \lambda \leq d_{\text{max}}$ with $\nu = 3$ a λ^{-1} -relation is present, and for $\lambda < d_{\text{min}}$ more or less wavelength independent, i.e. geometrical scattering is indicated. Deviations from a Junge distribution have a strong impact on the wavelength dependency around $d = \lambda$, as shown by an example in Fig.4.

This simple physical discussion shows clearly the impact of giant aerosol particles of some μm on infra-red transmission. There is no strong correlation between the concentration of them and that of aerosols with smaller diameters, because of different production and transportation mechanisms. Much research is necessary, based on aerosol size distribution measurements up to $50 \mu\text{m}$ and their correlation with transmission and scattering, as well as the meteorological and orographical conditions. Fig.5 presents an example of size distributions, quite similar up to some μm , but differing very much around $20 \mu\text{m}$, quite typical for overland, near ground situations. The visual range V_N not at all can be used to characterize such distributions as a whole. It was almost the same for both measurements, but infra-red transmission would have been quite different. No simple standard method exists up till now, comparable with the determination of visual range V_N , to derive in a figure, describing aerosol extinction in the middle and far infra-red area, aside from thermal or laser transmission measurements over some 100 m themselves, see section 4.

For particle diameters up to some μm there exist several well established models, e.g. [11,19], that may be used for system analysis. More models and especially models for larger particles are necessary, including studies of available and new approximation functions to describe them by a set of parameters instead of actually measured distributions.

2.4.3 Hydrometeor Effects

Hydrometeors are precipitation particles like rain, snow and hail, but also fog and cloud droplets (sometimes classified as aerosols); furthermore also dew as well as hoar- and whitefrost and frozen fog are hydrometeors, not relevant to atmospheric propagation, but to target/background radiation characteristics.

Fog and cloud droplets with diameters between 0.1 and 1 μm resp., and about 20 μm and more [19] in case of fog, may be handled similar to aerosols. In the visible range fog and clouds are "white" because of $\lambda < d_{\text{eff}}$, because the corresponding size distributions are peaking at some μm , aside from special "blue" fogs with very small fog droplets, peaking around 1 μm . Around 10 μm a "pseudo window" appears, found by measurements and Mie calculations [6], see Fig.6. Wavelength independent calculations, based on the visual range V_N in fog and clouds (some $m \leq V_N \leq$ some 100 m, e.g. $4 \cdot 10^3 \text{ km}^{-1} \leq \sigma \leq 7 \text{ km}^{-1}$), as incorporated in LOWTRAN 3 B as a zero order approximation, may be used up to wavelengths of 1 or some μm , but are only zero order approximations for the 8-13 μm thermal band, for what Mie calculations are necessary, because there $d \approx \lambda$ holds.

Precipitation offers droplets in case of rain between about 100 μm and 5 mm, where they are breaking up through hydrodynamic effects. Larger particles exist only as solid hydrometeors, like snow, graupel and hail, the latter may occur up to some cm diameter. For wavelengths up till 15 μm they all are producing geometrical scattering, so that the non spherical shapes do not cause much problems. For mm waves especially the effects of rain droplets has to be handled by Mie's theory, including the contribution of the non spherical droplet shape to depolarization effects. For visible and infra-red wavelengths the drop size distribution of rain can be described by the rain rate RR in mmh^{-1} , i.e. by the Marshall-Palmer distribution [13]:

$$N(d) = N_0 \exp - \Lambda d, \quad (19)$$

with the intercept parameter $N_0 \approx 8000 \text{ m}^{-3} \text{ mm}^{-1} \approx \text{const.}$ and the slope factor

$$\Lambda = 41 \text{ RR}^{-0.21}$$

in cm^{-1} for RR in mmh^{-1} . The wavelength independent transmission may be calculated by a geometrical model [20] taking into account this distribution and the fact, that the Mie extinction efficiency factor Q_{ext} is approaching 2 for large values of the Mie size parameter $d\pi/\lambda$, see left end of single size curves in Fig.4. In addition a constant terminal drop velocity $v(d) \approx 10 \cdot (1 - \exp - 5.5 d)$ in m s^{-1} has to be assumed. Fig.7 shows calculated transmission values for different ranges as a function of rain rate RR, that would have to be multiplied by the transmission of the rainless case, especially in the infra-red range with respect to molecular absorption. The aerosol concentration during rain is rather small, so that aerosol extinction may be neglected. Fig.8 shows an example [21] of simultaneous transmission measurements along a 160 m path, but folded, i.e. along a 320 m transmission range, at 0.63 μm (HeNe-laser) and at 10.6 μm (CO_2 -laser) together with visibility measurements using a backscatter device (Videograph, Impulsphysik Hamburg) and the determination of meteorological quantities, especially of rain rate. In Fig.8 the transmission at 0.63 μm , at 10.6 μm , in the visible band and that, calculated by this model, may be compared with the measured rain rates. The correlation coefficients between these functions all are about 0.8. Elaborated models of this type may be incorporated in future versions of LOWTRAN. But more measurements of rain drop size distribution and typical rain inhomogeneities are still necessary, especially with respect to sub-mm and mm wave transmission and scattering.

2.5 Transmission Computer Code LOWTRAN

The already mentioned transmission computer code LOWTRAN [11], as established by the AFGL of the USA is the best available tool to calculate horizontal and slant path transmission in the atmosphere with wavelength resolutions of $\Delta(1/\lambda) \geq 20 \text{ cm}^{-1}$ for $0.25 \mu\text{m} \leq \lambda \leq 28.5 \mu\text{m}$ (i.e. $0.5\% \leq \Delta\lambda/\lambda \leq 5\%$). The accuracy is some percent, decreasing to maybe 10% near the slopes of absorption bands, see Fig.3. The latest version (3B) includes several standard aerosol models. Reliable models for hydrometeor effects have to be added in the future. For details and distribution procedures of this computer code see [11]. Fig.3 presents an example.

3. ATMOSPHERIC VISION3.1 General Vision Formula and Perception Criteria

Aside from double ended optical/optronical systems, e.g. communication links, that can be described by atmospheric transmission including turbulence effects, see lecture 3, the propagation of optical signals suffers not only from atmospheric transmission, but also from atmospheric path radiance, aside from the influence of meteorological, i.e. atmospheric conditions on initial target and background radiances. These three general effects, transmission, path radiance and initial scene radiance are strongly related. Vision theories or models are describing system performance, including optical/optronical device characteristics and the perception capability of an observer, or an automatic perception system, with respect to a certain perception task. Zero - (detection) and one-dimensional (line scanner) systems may be included, as well as passive and active systems. Only applied in the context of such models atmospheric propagation quantities are applicable to system analysis and the forecasting of "optical weather", i.e. of application oriented figures.

As mentioned in lecture 1 and summarized in its Fig.2, the initial scene information is either produced by reflection ($\lambda < 3 \mu\text{m}$ and active) or emission ($\lambda > 3 \mu\text{m}$) in the scene. It has to be described by an initial radiance L_i^T for the scene elements i . The corresponding apparent radiance L_i at an observation site is given by

$$L_i = \tau L_i^T + L^A \leq L_i^T, \quad (20)$$

because the initial radiance is reduced by atmospheric transmission $\tau < 1$, and atmospheric path radiance L^A , not carrying image information, is added. The latter is produced by scattering of radiation from ambient natural or man made sources ($\lambda < 3 \mu\text{m}$), or the system source itself in the case of active systems, and therefore strongly related to the irradiance of the scene. For $\lambda > 3 \mu\text{m}$ atmospheric emission is adding path radiance. The general vision signal

$$\Delta L = \tau \Delta L^T < \Delta L^T \quad (21)$$

has to be perceived to discriminate between two different scene elements, necessary to perform a certain perception task. If this is possible, is up to the relevant signal-to-noise ratio:

$$\boxed{S/N = \frac{\Delta L}{\sigma_{\Delta}} \geq p \gg 1,} \quad (22)$$

σ_{Δ} = rms noise of ΔL , p = perception threshold, e.g. for an human observer about 2.5. Eq.(22) may be called general vision formula [15], because it allows the description of all vision processes, at least for the wavelength range $0.3 \mu\text{m} \leq \lambda \leq 15 \mu\text{m}$. It includes human vision, i.e. the well known theory based on contrast loss [14] by Koschmieder, as shown in [15], see also [1, paper 40]. It allows to calculate the maximum perception range as a function of scene characteristics, atmospheric conditions affecting scene and propagation medium, device characteristics and perception task:

$$R_{\text{max}} = R_{\text{max}}(\text{scene, atm., device, task}) . \quad (23)$$

Observation task, are usually described by the spatial resolution necessary to fulfil a certain task with respect to a certain target, e.g. 1 lp/target, 3.5 lp/target and 7 lp/target for detection, recognition and identification resp. This would define the scene element i in the above presented general formulae.

3.2 Atmospheric Path Radiance

Scene characteristics, i.e. reflection and emission as a function of geophysical conditions cannot be discussed within this context. It may be mentioned only, that thermal signatures and reflectivities at relevant laser wavelengths, e.g. at $1.06 \mu\text{m}$ and especially at $10.6 \mu\text{m}$ of different targets and backgrounds (incl. background clutter problems and camouflaging), and their dependency on meteorological conditions are not at all known to an extent, necessary for system analysis today. Therefore many extended current research programmes are devoted to these problem areas. For human vision and image intensifier passive vision the scene irradiation during day and night has to be known. Many research projects in the past were devoted to that, e.g. [9], and sufficient data seem to be available.

Atmospheric path radiance, produced by scattered ambient radiation is directly related to the irradiance of the scene under usual conditions. Following Koschmieder [14, 15] for passive systems ($\lambda \leq 3 \mu\text{m}$) it can be described by the horizon radiance L^H and the extinction coefficient σ :

$$L^A = L^H (1 - \exp - \sigma R) . \quad (24)$$

For inhomogeneous conditions Duntley introduced the atmospheric path function L'^A as path radiance per unit path length, sometimes called differential path radiance. For homogeneous conditions it holds the relation $L^H = L'^A \sigma$. Further theoretical work and measurements on L'^A are still the key to improved vision theories and models for $\lambda \leq 3 \mu\text{m}$ in the passive case, especially for slant path vision. For active systems see [1, paper 40] and [16], offering in its part II a perception model for gated viewing systems.

In the case of thermal path radiance it follows also Eq.(24), certainly using only $\tau(R)$, because no exponential transmission law is applicable in general, see section 2.2. Because $\tau \rightarrow 0$ for $R \rightarrow \infty$, i.e. the emissivity $\epsilon \rightarrow 1$ (Kirchhoff's law: $\epsilon = \alpha = 1 - \tau$ in the atmosphere) $L^H \rightarrow L_0$, where L_0 is the spectrally relevant blackbody radiation at ambient temperature T_0 . Thermal path radiance therefore is given by

$$L^A = L^H (1 - \tau(R)) = L_0 (1 - \tau(R)) . \quad (25)$$

So, aside from vision along inhomogeneous paths, where L'^A has to be studied and applied, the critical magnitude path radiance can be handled, if atmospheric transmission $\tau_{\lambda}(R)$ is known and horizon radiance. Problem areas with respect to $\tau_{\lambda}(R)$ were mentioned already earlier, but still measurements (see section 4) are necessary to prove also

these relations for path radiance under a large variety of real conditions, because many assumptions have to be made, to derive them, that could not be discussed here in detail.

3.3 Perception Range Modelling Concepts

The classical example of a perception range model is Koschmieder's theory of human vision, based on atmospheric contrast loss as produced by path radiance, and on a contrast threshold $K_{\min} = 0.02$ to characterize "device and perception task" for human vision. If the contrast, as usual in physiological optics is defined by $K = (L_1 - L_2) / L_2$, it follows from Eq. (20) and (24), that the apparent contrast at an observation site is given by

$$K = K_0 \frac{L_2^T}{L_2(R)} \exp - \sigma R \geq K_{\min} . \quad (26)$$

where $K_0 =$ initial contrast and $K_{\min} =$ contrast threshold ≈ 0.02 . Against the horizon Eq. (26) reduces to an exponential contrast loss law, because of $L^H = L_2^T = L_2(R)$. For the observation of a "black", i.e. non-radiating target for $\lambda < 3 \mu\text{m}$, $L_1^T = 0$ and therefore $K_0 = -1$, so that in this special case

$$K = -\exp - \sigma R \geq K_{\min} . \quad (27)$$

The maximum perception range in this case is called visual range V_N (Normsichtweite), that therefore is defined by

$$V_N = \frac{3.912}{\sigma} \triangleq \tau = 0.02 , \quad (28)$$

if $K_{\min} = 0.02$. V_N will be measured photopically or sometimes near $0.55 \mu\text{m}$, if not estimated by human observers as still usual in meteorology. V_N is the distance over what a black target against the horizon may be observed, i.e. detected, or based on this theory, along what the transmission in the visual band (photopic or around $0.55 \mu\text{m}$) is 0.02. Scattering methods can be used also for its determination, because extinction in the visible band is produced almost only by scattering, and path radiance is produced by scattering as mentioned. Sometimes the definition, presented as Eq. (28) is also applied to other wavelength bands, to define a characteristic atmospheric range $V_N(\lambda, \Delta\lambda)$. For the following it may be remembered, that V_N is in fact a maximum perception range R_{\max} with respect to a specified scene (visually "black" target against the horizon), a special device (human eye), and a well defined task (detection), as a function of atmospheric conditions. Only based on the assumptions involved in Koschmieder's theory, these conditions can be characterized by the extinction coefficient σ only. This human vision theory, based on contrast loss, may be derived from the general vision formula, Eq. (22), if the contrast is introduced and quantum-noise limited vision is assumed or a contrast limited device [15].

To derive in maximum propagation ranges R_{\max} the general vision formula Eq. (22) may be simply rewritten for the threshold case as following:

$$\begin{aligned} \tau(R_{\max}) \Delta L^T &= p \sigma \Delta , \\ \text{ASD} &= \text{MNSD} . \end{aligned} \quad \left. \vphantom{\begin{aligned} \tau(R_{\max}) \Delta L^T &= p \sigma \Delta , \\ \text{ASD} &= \text{MNSD} . \end{aligned}} \right\} (29)$$

ASD, the apparent signal difference, is a function of the scene conditions, the atmospheric conditions (and the task) at R_{\max} . MNSD, the minimum necessary signal difference, is a function of the device, the task (and the path radiance) at R_{\max} . For thermal vision, for example, ASD is an apparent temperature difference (ATD),

and MNSD a minimum necessary temperature difference (MNTD). The task enters the ASD by the definition of the relevant area of scene elements, e.g. the relevant initial temperature difference ΔT^T , that may be different for different perception tasks. With similar temperatures in the scene ($\Delta T \ll T_0$) the thermal path radiance does not explicitly enter the MNTD, because that is given for a certain ambient temperature T_0 . In the case of recognition, i.e. for 3.5 lp/target and a square target, i.e. the 4 bar pattern with aspect ratio 1:7, the MNTD is the well-known MRTD (minimum resolvable temperature difference), used to characterize thermal imaging systems. Fig.9 shows typical curves for the apparent signal difference ASD and the minimum necessary signal difference MNSD, let say in the above mentioned case the apparent temperature difference ATD, and for recognition, the MRTD. The intersection of both curves presents the maximum perception range R_{max} . This model allows to separate environmental aspects from device and perception features as much as possible. Different devices, would result in different MNSD-curves, a variety of environmental conditions would be equivalent to a set of ASD-curves with the same starting point at $R = 0$ or maybe also with different starting points, because of the interrelation between scene and propagation medium characteristics. For more details of thermal range models see [17], and [18] presenting especially this concept.

More generally it does not exist a maximum perception range R_{max} rather than a decreasing perception probability as a function of range, $P_p(R)$. Eq.(22) and (25) can be generalized, to cover this, by introducing a function p instead of a threshold figure. In Fig.9 it would have to be added a third dimension, i.e. the probability to fulfil a certain perception task. Instead of R_{max} , usually given for a 50% probability, it would follow $P_p(R)$.

Summarizing this section, it was shown that atmospheric propagation and meteorology are key areas to calculate the apparent signal difference at an observation site, being the input to each vision model. The same holds for the apparent contrast, if it is a relevant assessment figure, and for spatially dc-radiance levels, affecting quantum-noise limited systems.

4. MEASUREMENT PROJECT OPAQUE

Having mentioned throughout this lecture many measurements necessary to be performed in the future, it may be meaningful to draw the attention to an extended current measurement project, that will offer a large data basis for future atmospheric optical and system analysis purposes. It is the project OPAQUE (optical and infra-red atmospheric quantities in Europe), organized and performed by a NATO research study group (AC/243 (Panel IV/RSG.8)), where Canada, Denmark, F.R.Germany, France, Italy, The Netherlands, U.K. and the U.S.A. are cooperating [1, paper 14] and Reference [1] of lecture 1.

At 6 OPAQUE-stations in Western Europe, to what in the near future a 7th will be added, all relevant atmospheric optical and infra-red quantities are hourly measured over a period of at least 2 years, together with the usual meteorological figures. Fig.10 presents an example of such an OPAQUE - station.

For this routine measurement programme broad-band quantities in the visible (photopic) and thermal range were chosen, aside from additional laser transmission and scattering, as well as mm wave transmission projects at some stations. As shown earlier photopic magnitudes allow to determine radiation quantities relevant to image intensifier vision with an acceptable accuracy.

The basic data set, collected hourly at each station is defined by:

σ	= photopic extinction coefficient, i.e. visual range V_N ,
E_h	= " irradiance of a horizontal plane,
E_v	= " " of a vertical plane (N, E, S, W),
L_p	= " path radiance towards E, with $R = 100$ m,
F_p	= " differential path radiance (N, E, S, W),
E_{Si}	= " and spectral irradiance by the sun, at 8 channels,
T_i	= thermal transmission at 4 channels, with $R = 500$ m,
δT	= temperature fluctuations, i.e. microturbulence,
MET	= temperature, humidity, pressure, rain rate, wind speed and direction at 2 m and 10 m.

All measurements are performed at about 2 m height over ground, aside of the additional wind measurement at the usual meteorological height of 10 m. It is used, if applicable, a common time constant of about 10 s. Many additional measuring equipments are installed at the OPAQUE-stations, e.g. for the determination of

$n(r)$	= aerosol size distribution (almost at all stations),
$\tau_\lambda, \beta_\lambda$	= laser transmission and scattering,
E_{Sk}, E_{Gr}	= radiation flux from sky and ground,
δI	= turbulence induced laser beam and thermal beam fluctuations, i.e. microturbulence,
	- hemispherical/cloud pictures,
	- aerosol samples, e.g. index of refraction,
	(- visual weather observations),
	(- atmospheric optical quantities in aerospace, collected by two national (USA and F.R.G.) flight programmes).

The calibration of the measuring equipment was established by calibration roundtrips of mobile stations and intercomparison trials at certain sites. The intercomparative calibration of aerosol counters and thermal transmissometers were the first extensive trials of this type at all. Reports are available to the participating countries. Most of the stations are computer controlled, and are automatically operating since the beginning of 1977, aside from service and calibration activities, and aside of the 7th station, mentioned above. The data collected at these stations are digitally collected and offered in a common format to the OPAQUE data-bank at U.K., and will be available to all participating countries. They will form a unique data basis on atmospheric optical and infra-red quantities.

As mentioned earlier similar programmes, not necessarily performed at a routine basis, have to be performed in the future, especially at actual coastal areas, over seas and in aerospace. Long range transmission studies are necessary, as well as much detail work on aerosols and hydrometeors, to summarize only the most essential problem areas for research under natural conditions. Battle polluted environments up till now are only studied in a limited way, and are asking for many future research activities in atmospheric optics, e.g. [10].

5. CONCLUSIONS

It was tried within this lecture to cover the broad field of atmospheric propagation, including comments on atmospheric vision, for the wavelength range $0.3 \mu\text{m} \leq \lambda \leq 15 \mu\text{m}$, and perception range modelling concepts. Sub-mm and mm wave effects were mentioned also in some cases. Because most of the sections contain already final remarks on the state of the art and necessary future research, and because of the broad problem area touched, it does not seem to be meaningful to repeat these concluding statements here again.

It may finally be mentioned only, that today's available numerical computer techniques allow extensive quick numerical calculations. But especially this fact is often inducing such extended calculations before the atmospheric propagation problem, as affecting a certain optical/optronical system or a class of systems, has been analyzed completely, and all major effects and their interrelation, limiting the system, are identified and studied. If this lecture was only helpful to increase the general overview, absolutely necessary for such an analysis, it may have been already effective.

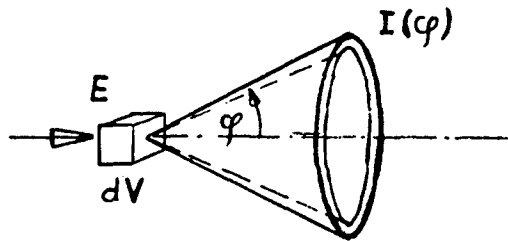
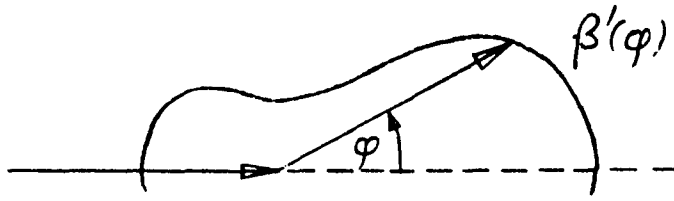
REFERENCES

- [1] Optical Propagation in the Atmosphere, 1976; NATO-AGARD Conference Proceedings No.183 (Symposium held in Lyngby, Denmark, Oct.1975; Session IV: Non-Linear Propagation)
- [2] High Power Laser Propagation, F.G.Gebhardt, 1976; Appl.Optics, Vol.15, p.1476
- [3] Geophysics II, 1957, Ed.S.Flügge/J.Barthels; Encyclopedia of Physics, Vol.XLVIII, Springer Verlag Berlin
- [4] Handbook of Geophysics (USAF), 1960; The Macmillan Company, New York
- [5] Physics of the Atmosphere, 1962, P.N.Tverskoi; Israel Program for Scientific Translations (from Russian) Ltd.
- [6] Optics of the Atmosphere-Scattering by Molecules and Particles, 1976, E.J.McCartney; J.Wiley & Sons, New York
- [7] Atmospheric Aerosols, 1977, S.Twomey; Elsevier Scientific Publishing Company, Amsterdam
- [8] Radiation in the Atmosphere (Structure and Radiation Properties of Aerosols and Clouds/Remote Sensing and Satellite Measurements), 1977, Ed.H.-J.Bolle; Science Press Princeton (Proc.of the Symposium on ..., Garmisch, F.R.Germany, Aug.1976)
- [9] Atmospheric Optical Environment, 1972, M.L.Vatsia;U.S.Army Electronics Command, Report No. ECOM-7023
- [10] A Review of Atmospheric Transmission Information in the Optical and Microwave Spectral Regions, 1976, A.R.Downs; U.S. Ballistic Research Laboratories, Report No.BRL-MR-2710
- [11] Atmospheric Transmission from 0.25 to 28.5 μm : Supplement LOWTRAN 3B(1976), 1976, J.E.A.Selby, E.P.Shettle, and R.A.McClatchey; U.S. Air Force Geophysics Laboratory, Report No.AFGL-TR-76-0258
- [12] e.g., Applied Optics, Atmospheric and Oceanic Physics, Atmospheric Environment, Contributions to Atmospheric Physics, Infrared Physics, Journal of Aerosol Science, Journal of the Atmospheric Sciences, Journal of the Optical Society of America, Optik; meteorological journals

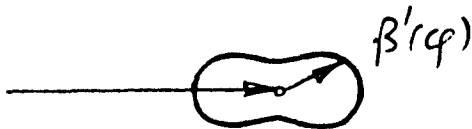
- [13] The Distribution of Rain Drops with Size, 1948, J.S.Marshall and W.M.K.Palmer; J.Met., Vol.5, p.165
- [14] Vision through the Atmosphere, 1952, W.E.K.Middleton; Univ.of Toronto Press
- [15] Atmospheric Vision $0.35 \mu\text{m} \leq \lambda \leq 14 \mu\text{m}$, 1975, D.H.Höhn; Appl.Optics, Vol.14, p.404
- [16] Gated Viewing, Part I, 1976, T.Bakker e.a.(Phys.Lab.TNO, The Netherlands), and Part II, 1976 (to be published 1978) D.H.Höhn e.a.(FFO, F.R.Germany); Report No.FFO 1976/1 and FFO 1976/2
- [17] Night Vision Laboratory Static Performance Model for Thermal Viewing Systems, 1975, J.A.Ratches e.a.; U.S. Army Electronics Command, Report No.ECOM-7043
- [18] FFO - Thermisches Reichweitenmodell 1 (FFO Thermal Range Model 1), 1977, W.Wittenstein, W.Büchtemann and D.H.Höhn; FFO, F.R.Germany, Report No.FFO 1977/23, to be published.
- [19] Size Distribution of Fog and Cloud Droplets and their Volume Extinction Coefficients at Visible and Infrared Wavelengths, 1976, F.Tampieri and C.Tomasi; Pageoph, Vol.114, p.571
- [20] Modelling of Atmospheric IR Extinction by Rain and Considerations on Natural Rain Drop Size Distributions, 1977, W.Jessen; FFO, F.R.Germany, Report No.FFO 1977/16 (OPAQUE R/GE 7703)
- [21] Operational Modelling of the Aerospace Propagation Environment, to be published; NATO-AGARD Conference Proceedings No...., (Symposium to be held in Ottawa, Canada, April 1978, paper on: The Influence of Meteorological Parameters on Atmospheric Transmission at $10.6 \mu\text{m}$ (CO_2 -Laser Radiation) and $0.63 \mu\text{m}$ (HeNe-Laser Radiation) from Measurements and Calculations, 1978, J.Abele, H.Raidt, W.Jessen and R.Kirschmer)

Acknowledgement:

I am grateful to my colleagues of the FFO, especially to the members of the Division on Atmospheric Optics and Meteorology, for many stimulating discussions.



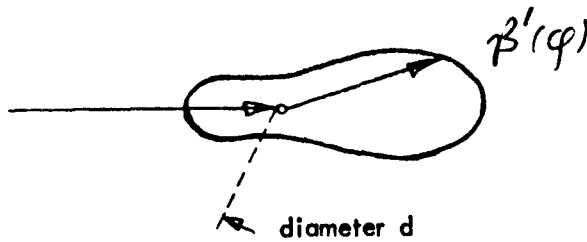
scattering:
 geometry,
 definitions



Rayleigh scattering

$d \ll 0.2 \lambda$

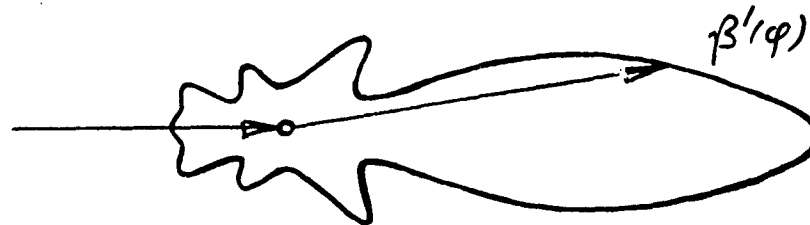
$\beta'(\phi) \sim (1 + \cos^2 \phi); \beta_\lambda \sim \lambda^{-4}$



Mie scattering

$0.2 \lambda \leq d \leq 5 \lambda$

forward sc.; $(\beta_\lambda \sim \lambda^{-1}?)$



geometrical scattering

$d \geq 5 \lambda$

mostly forw.sc.; β indep. of λ

Fig.1 : General types of atmospheric scattering; definition of symbols, schematical relative scattering functions $\beta'(\phi)$ for Rayleigh, Mie, and geometrical scattering together with the relevant wavelength λ /diameter d ranges; partly from [6].

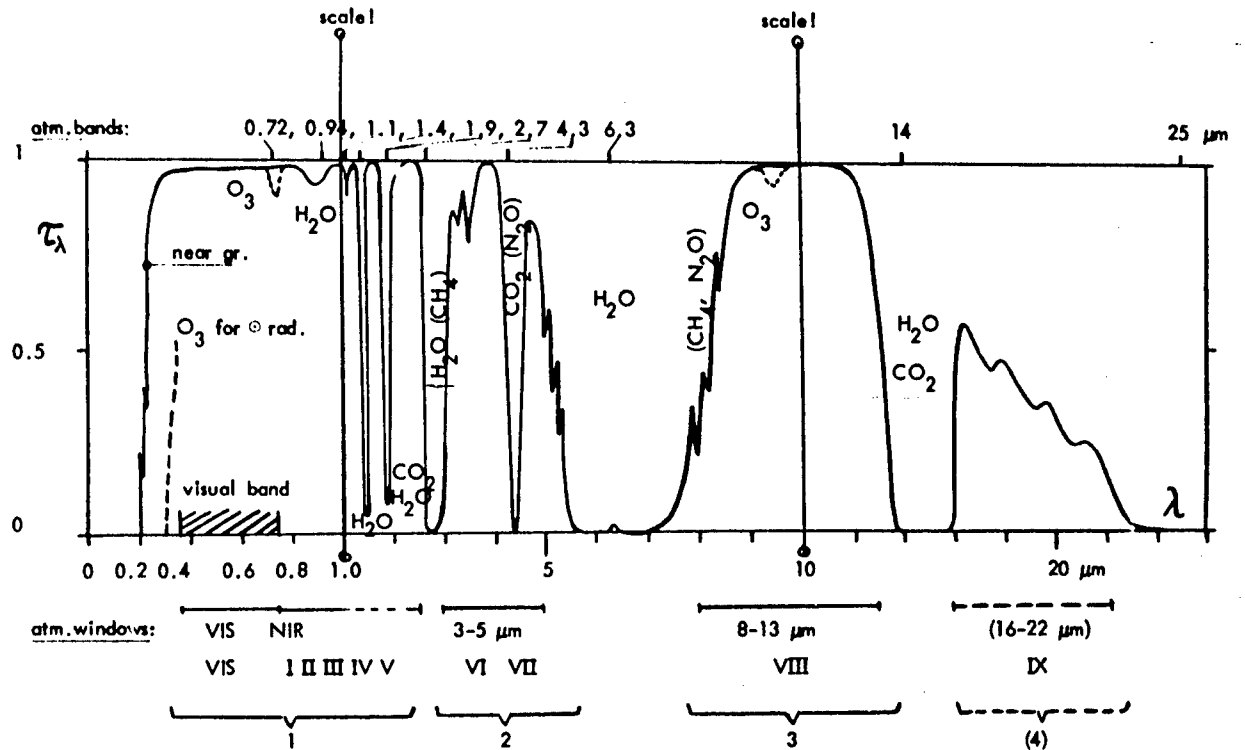


Fig.2 : Schematic low resolution atmospheric transmission spectrum with indications of the most relevant atmospheric absorbing molecules and the usual description of atmospheric bands and windows.

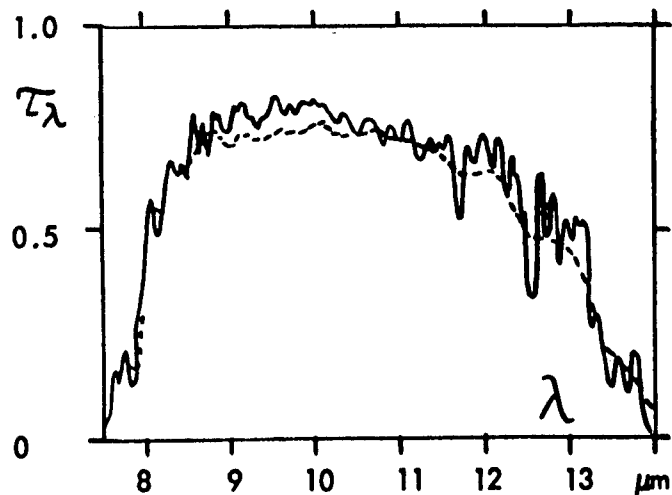


Fig.3 : Comparison between measured (Gebbie e.a.:-) and calculated (----) spectral transmission within the 8 to 13 μm band for a 1 nautical mile path (1.7 pr.cm H₂O), using LOWTRAN 3 B; from [11].

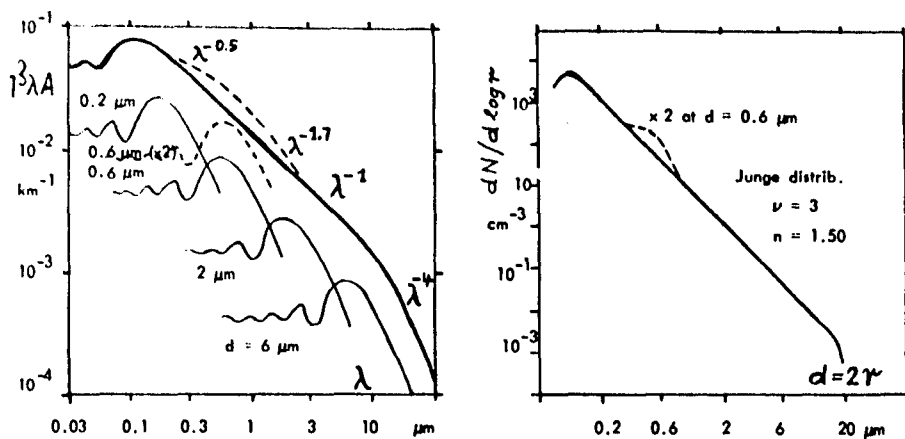


Fig.4 : Aerosol scattering coefficient $\beta_{\lambda A}$ as a function of wavelength λ , as realized by a Junge distribution of the aerosol ($\nu = 3$), and the impact of a deviation of such a distribution, schematical; following F.Volz [3, Section 2: Strahlung in der unteren Atmosphäre (radiation in the lower atmosphere)].

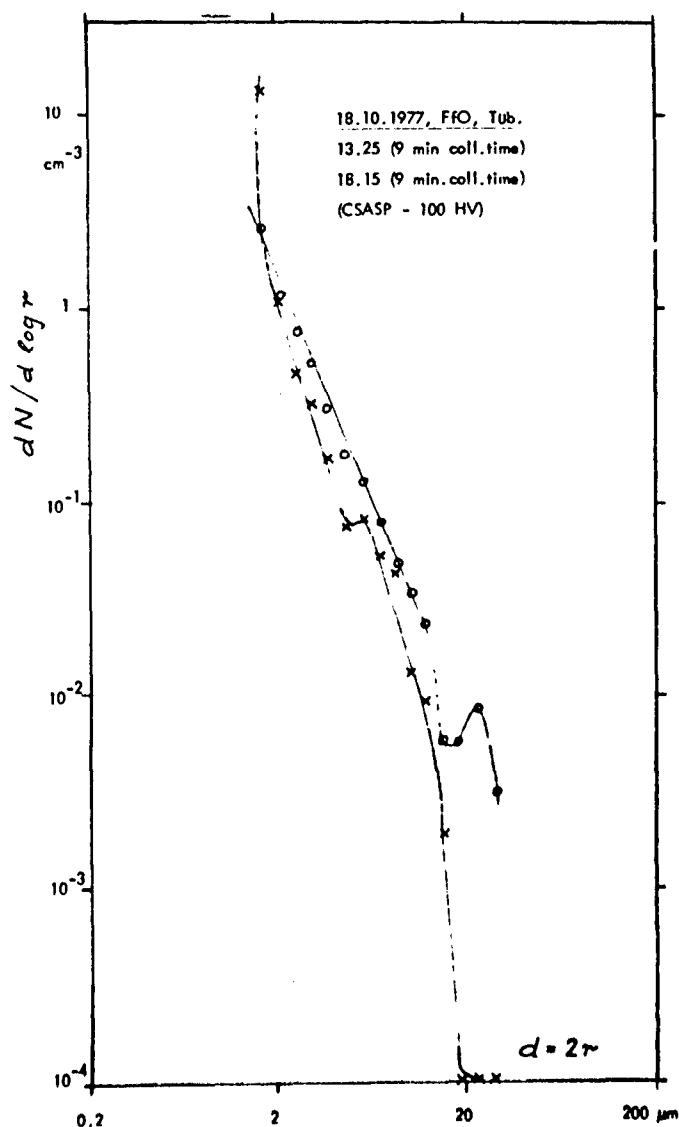


Fig.5 : Aerosol size distributions for almost the same visual range V_N with strongly different concentrations of giant aerosol particles around $20 \mu\text{m}$, affecting thermal transmission drastically; measured by J.Abele, 1977, FfO, Tübingen, to be published in [21].

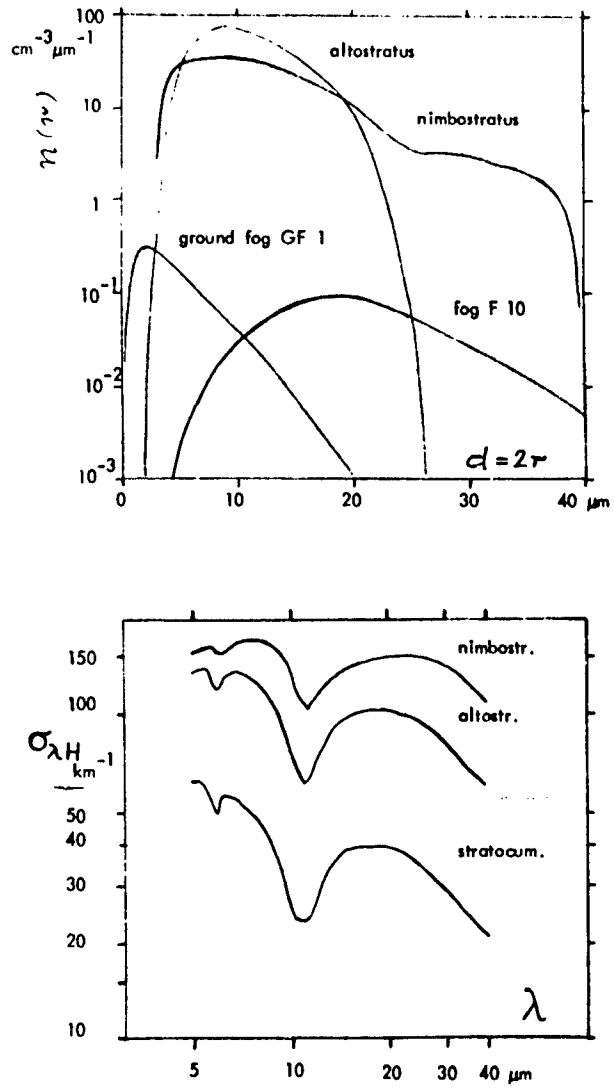


Fig. 6 : Typical fog and cloud droplet size distributions and spectral extinction coefficients for cloud distributions; from [6,19].

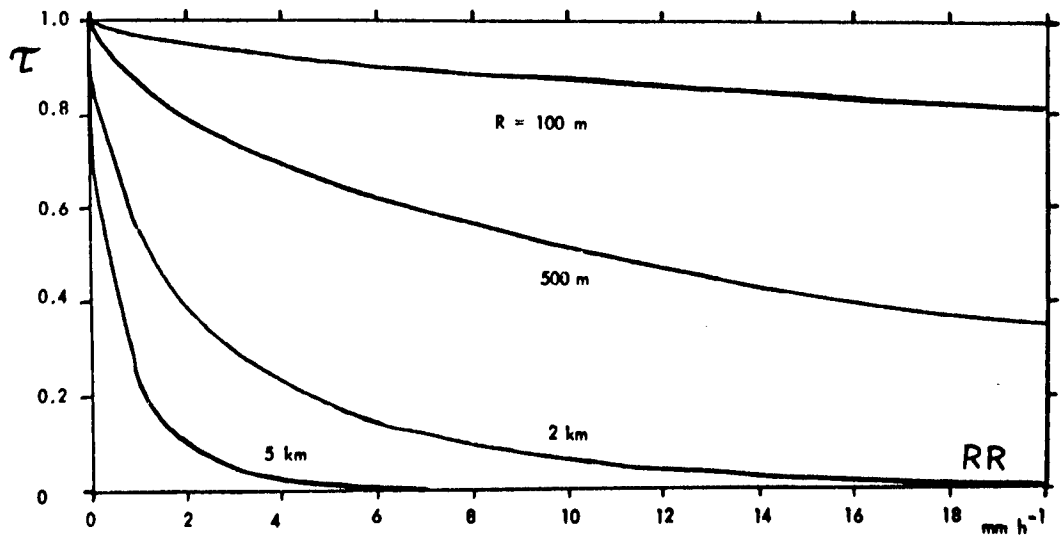


Fig. 7 : Transmission through rain as a function of rain rate RR for several ranges R as calculated by a model; from [20].

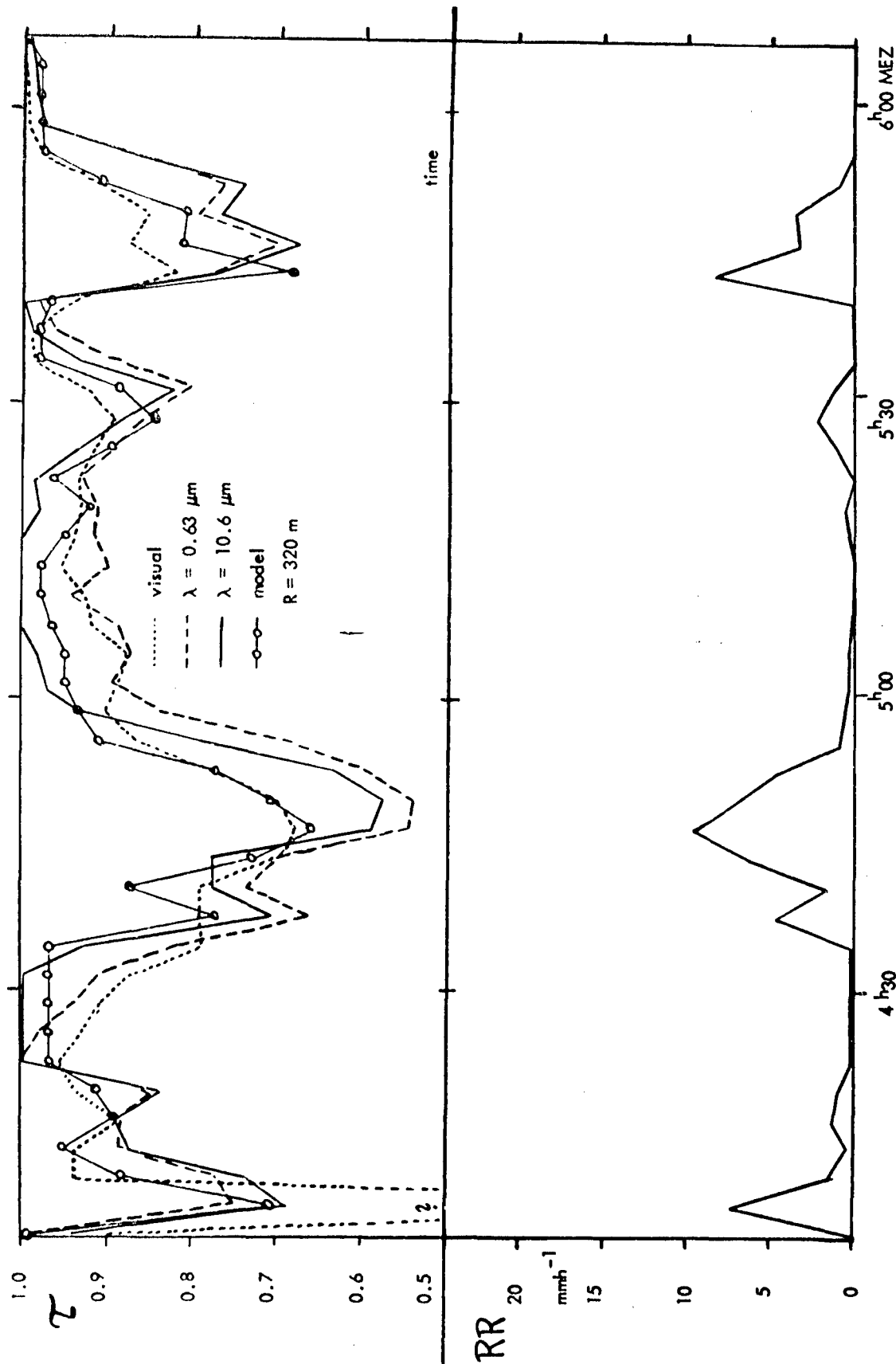


Fig.8 : Transmission through rain as measured in the visible band, and at $0.63 \mu\text{m}$ and $10.6 \mu\text{m}$, compared with that, predicted by a model [20]; to be published in [21].

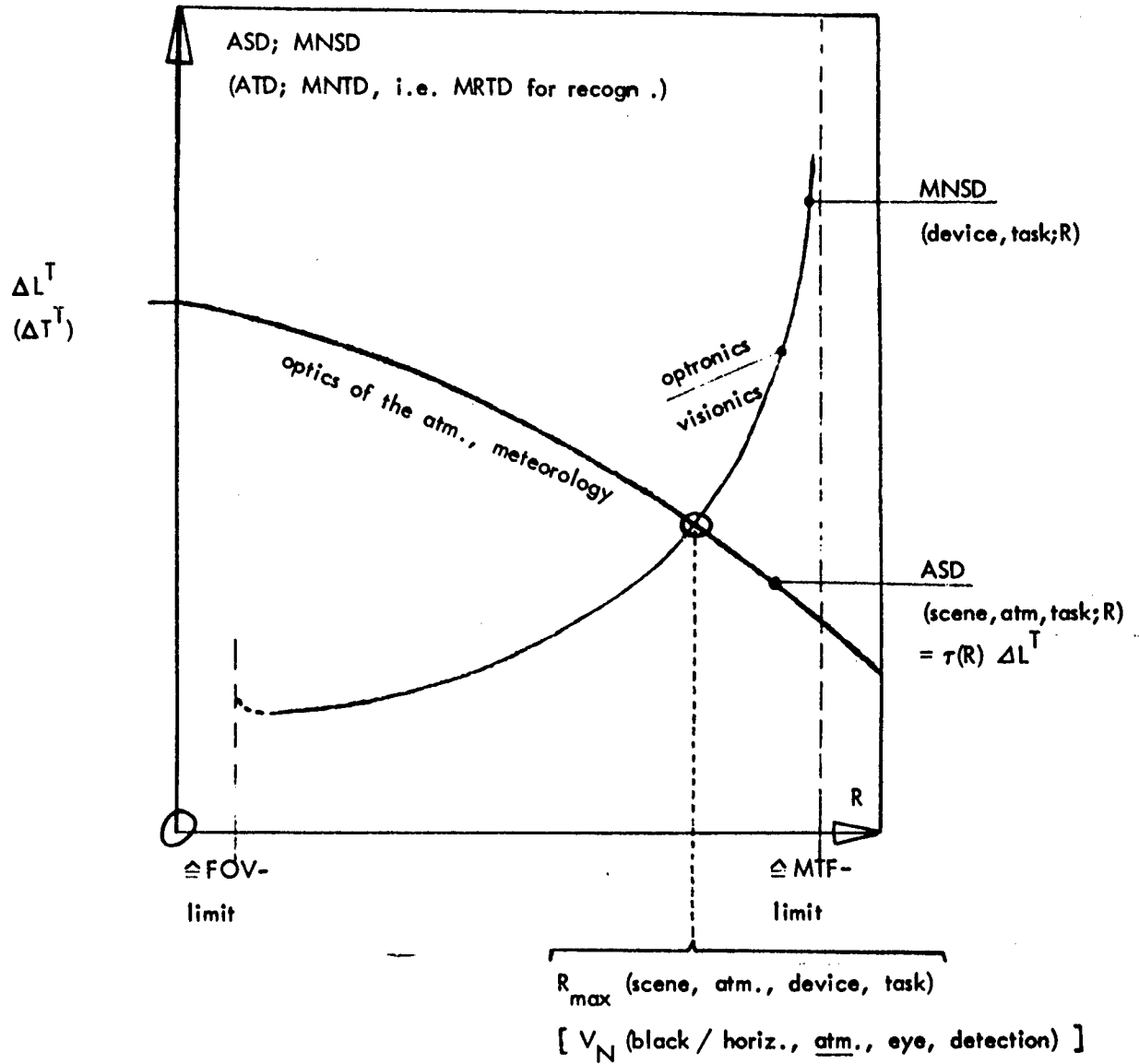


Fig.9 : Concept of perception range modelling. The intersection of the apparent signal difference ASD with the minimum necessary signal difference MNSD offers the maximum perception range R_{max} , if not the perception probability $P_p(R)$ is determined, equivalent to a third dimension in Fig.9. For thermal vision the relevant magnitudes are given in brackets.

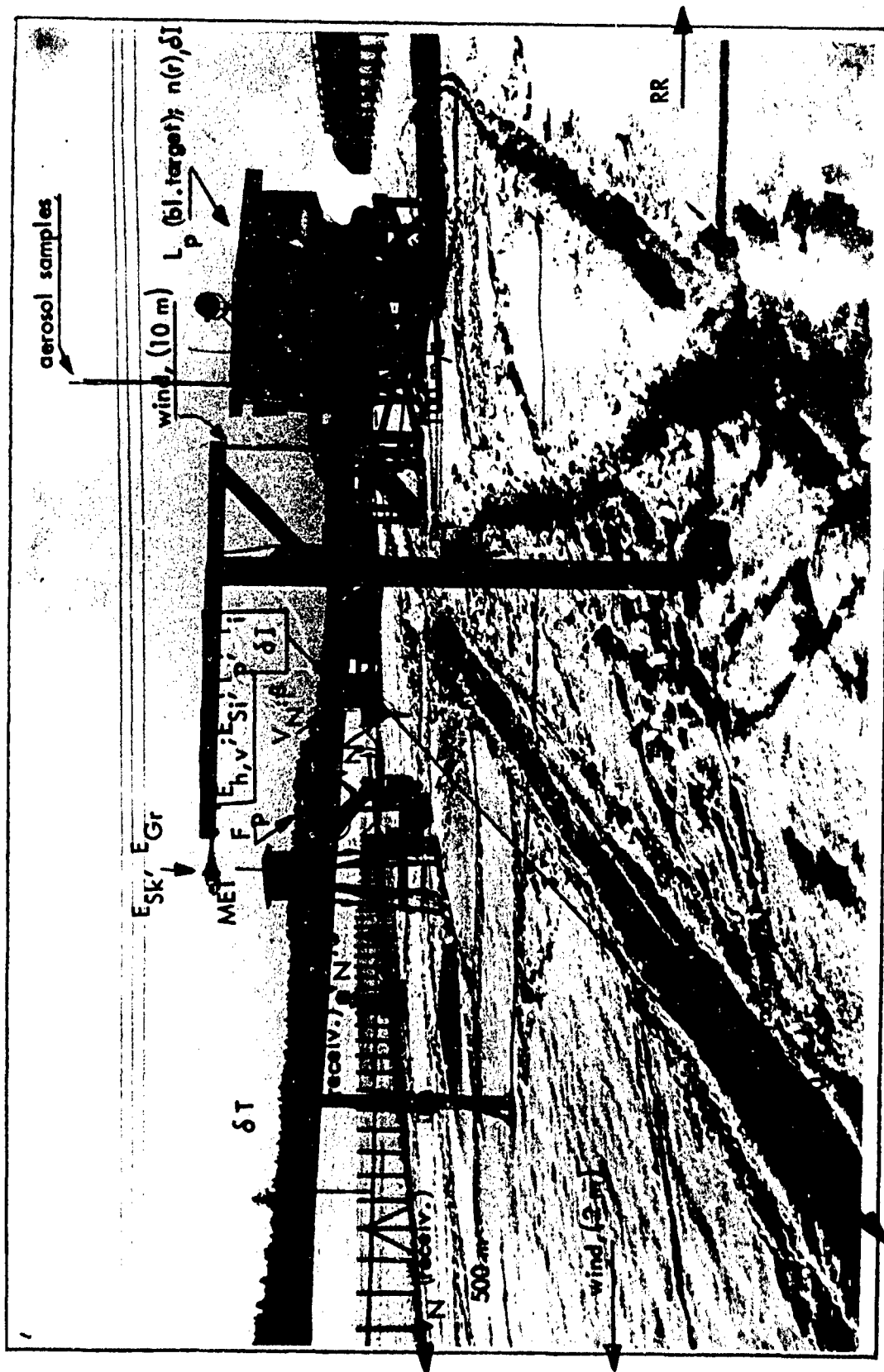


Fig.10 : German OPAQUE - station, situated in Southern Germany at the Schwäbische Alb, 750 m above NN, with indications of the parameters, measured there; see also tabulation in section 4.

PROPAGATION PROBLEMS RELATIVE TO LASER
TRANSMISSION

by

Mario Bertolotti

Istituto di Fisica-Facolta' di Ingegneria
Universita' di Roma, Roma, Italy

SUMMARY

Atmospheric transmission and scattering of monochromatic beams are considered. The effects of atmospheric turbulence are then described. After short theoretical introduction, the more important effects are described and discussed. Thermal blooming is finally discussed in both cases of cw and pulse operation.

CONTENT

1. ATMOSPHERIC ABSORPTION AND SCATTERING

- 1.1. Molecular extinction
- 1.2 Extinction due to aerosols
- 1.3 Fog and rain extinction

2. ATMOSPHERIC TURBULENCE

- 2.1 Introductory remarks and theoretical background
- 2.2 Effects of turbulence on laser beams
 - a) beam spread and average intensity
 - b) spatial coherence of the electric field
 - c) intensity fluctuations
 - d) phase fluctuations
 - e) angle of arrival fluctuations

3. BLOOMING

1. ATMOSPHERIC ABSORPTION AND SCATTERING

The light traveling through the atmosphere, suffers an attenuation which is due to the absorption from the various constituents that form the atmosphere and an attenuation due to scattering of radiation out of the incident beam direction from molecules or small particles-suspended in the atmosphere (dust, water droplets, etc.). This radiation is not absorbed but the effect of diffusion in directions different from the one of beam propagation results the same in an attenuation of the transmitted beam.

Sometimes it happens that this radiation is sent back in the beam direction because of multiple scattering (forward scattering).

To these effects other phenomena add due to casual fluctuations in the index of refraction of the atmosphere, due to turbulence. The intensity $I(x)$ of a laser beam propagating in an homogeneous atmosphere for a path length x can be written as (Bouguer law)

$$I(x) = I_0 e^{-\gamma x}, \quad (1)$$

where I_0 is the incident light intensity, and γ is the extinction coefficient. It is usually given in Km^{-1} and it takes into account all interactions which extract energy from the laser beam.

The coefficient γ can be considered the sum of various components

$$\gamma = \gamma_m + \gamma_a + \gamma_f + \gamma_p, \quad (2)$$

each one taking into account the effects due to molecules (γ_m), aerosol (γ_a), fog (γ_f) and precipitation (γ_p). We will consider these contributions separately.

1.1 Molecular extinction

The molecular extinction coefficient γ_m is the sum of the molecular absorption coefficient K_m and the molecular scattering coefficient σ_m , i.e.

$$\gamma_m = K_m + \sigma_m \quad (3)$$

The molecular scattering coefficient σ_m is essentially due to Rayleigh and Mie scattering. The absorption coefficient K_m is rather complex to be calculated.

The relative transmission of primary constituents of the atmosphere is shown in Fig. 1 as a function of wavelength (λ). There are visible regions of high transparency (windows) at wavelengths in the ranges from 1 to 2 μ , 3.5 to 5 μ , and 8 to 14 μ . The curves of Fig. 1 have a relatively poor spectral resolution. Practically the atmospheric absorption changes drastically as a function of wavelength.

Besides the absorption due to the fixed atmospheric constituents it is necessary to take into account also the absorption due to components which can be in variable concentrations. Water vapor and CO₂ are the more important.

The coefficients K_m (H₂O) have been measured by various authors (2)(3)(4)(5) for different laser wavelengths. As an example

$$K_m(\text{H}_2\text{O}) \approx 0.03 \text{ Km}^{-1} \text{ mm}^{-1} \text{ of precipitable water for He-Ne} \quad (4)$$

$$K_m(\text{H}_2\text{O}) = 7.0 \times 10^{-6} p_{\text{H}_2\text{O}} (P + 88 p_{\text{H}_2\text{O}}) (\text{Km}^{-1}) \text{ for CO}_2 \quad (5)$$

where $p_{\text{H}_2\text{O}}$ is the partial pressure of water vapor in Torr, and P is the total atmospheric pressure (in Torr).

For CO₂ beams also absorption by CO₂ is important (6)(7)(8). Stephenson and collab. (6) give

$$K_m(\text{CO}_2) = 0.436 c \left(\frac{295}{T}\right)^{3/2} e^{-2210/T} \quad (6)$$

where T is absolute temperature and c is CO₂ concentration in ppm (normal values of c range from 330 ppm in dry atmosphere up to 900 ppm during the night near vegetation). Other wavelengths have been considered by J.Y.Wang (9).

1.2 Extinction due to aerosols

The aerosol extinction coefficient γ_a is the most difficult to evaluate. Transmission of radiation through the atmosphere depends strongly from scattering and absorption of aerosols, which can consist of dust and combustion products, salt particles, industrial pollutants, living organisms and, the most important, water droplets.

Mie theory can be used to derive absorption and scattering coefficients K_a and σ_a for spherical particles if the complex refractive index and the number density and size distribution are known (10). Every irregularity in particle size gives however strong changes.

Atmospheric aerosol is present in every state of the atmosphere but with a highly variable concentration in time and in space. The size distribution ranges in a large interval of radii for natural particles between about 10⁻³ μm up to 10² μm and can have a considerable complexity.

Moreover many particles of natural aerosols, which are a mixture of water soluble and insoluble components, are subjected to strong changes in size when relative humidity changes.

Let us consider an atmosphere where the aerosol sizes in the unitary volume are characterized by a distribution function $f(r)$. Many distribution function have been considered.

The extinction coefficient can be written in general as

$$\gamma_a = \int_0^\infty f(r) c(r, \lambda) dr, \quad (7)$$

where $c(r, \lambda)$ is the extinction cross-section of a particle of radius r at wavelength λ . It is convenient to use an extinction efficiency factor

$$Q_{\text{ext}} = \frac{c(r, \lambda)}{\pi r^2} \quad (8)$$

Therefore

$$\gamma_a = \int_0^\infty f(r) Q_{\text{ext}}(r, \lambda) \pi r^2 dr. \quad (9)$$

The dependence of Q_{ext} from the particle radius is shown in Fig. 2 for spherical water droplets not absorbing (refractive index 1.33) by using the dimension parameter

$$\kappa = 2\pi r / \lambda \quad (10)$$

For wavelengths larger than $3\mu\text{m}$, absorption of liquid water must be considered. It is

$$Q_{\text{ext}} = Q_{\text{abs}} + Q_{\text{scat}} \quad (11)$$

The complete solution of the scattering problem may be found and results for Q are tabulated.

The natural scatterer size distribution can be approximated by many models and many calculations have been done on the resulting attenuation (11) to (17). Recently Shettle and Fenn (18) have given aerosol models for various altitudes. For altitudes near the ground the range of conditions is represented by three different aerosol models, rural, urban and maritime.

These models are assumed to be the sum of two log-normal distributions

$$\frac{dN(r)}{dr} = \sum_{i=1}^2 \frac{N_i}{\log_{10} r \cdot \sigma_i \sqrt{2\pi}} \exp \left\{ - \frac{(\log r - \log r_i)^2}{2\sigma_i^2} \right\}, \quad (12)$$

where $N(r)$ is the cumulative number density. The parameters defining the size distributions are given in Table I.

Table I
(Size distributions)

(normalized to 1 particle/cm³)

Type of aerosol	$N_1^{(*)}$	r_1	σ_1	$N_2^{(*)}$	r_2	σ_2
Rural	0.9999975	0.005 μ	0.475	$2.5 \cdot 10^{-6}$	0.5	0.475
Urban	0.9999975	0.005 μ	0.475	$2.5 \cdot 10^{-6}$	0.5	0.475
Maritime-continental origin	1	0.005 μ	0.475	-	-	-
Maritime-sea spray origin	1	0.3 μ	0.4	-	-	-

(*) $N_1 + N_2 = 1$

The maritime aerosol is composed by salt particles which are caused by the evaporation of seaspray droplets plus a continental component. The properties of the seaspray produced component, especially in the lower 100 m or so above the water, depend strongly on relative humidity and also windspeed.

The number of seaspray produced aerosols increase with windspeed, especially the larger particles. The size distribution also is a function of relative humidity since the hygroscopic particles begin to grow by absorption of water, if the relative humidity reaches values above 70%. The dependence of humidity and windspeed has not been incorporated in the model which corresponds to moderate windspeeds and a relative humidity of $\approx 80\%$.

The coefficients for extinction, absorption and scattering are shown in Figs. 3. Some examples of calculated atmospheric transmittances are shown in Table 2 which gives total atmospheric transmittances for a 1 Km horizontal path at ground level through atmosphere of different optical properties. The transmittances are derived from the coefficients for molecular absorption and scattering as well as aerosol absorption and scattering.

Table 2

Aerosol Model	Visibility	Transmittance		
		$\lambda = 0.55\mu\text{m}$	$\lambda = 1.06\mu\text{m}$	$\lambda = 10.591\mu\text{m}$
rural	50 Km	0.925	0.970	0.694
	10 Km	0.677	0.843	0.673
urban	10 Km	0.677	0.822	0.673
	2 Km	0.142	0.368	0.578
maritime	10 Km	0.677	0.691	0.657
	2 Km	0.142	0.181	0.509

The scattering coefficient σ_s can also be found by means of an empirical relation from the knowledge of the optical visibility V

$$\sigma_s = \frac{3.5}{V} \left(\frac{0.53}{\lambda} \right)^{0.62 V^{1/2}} \quad (13)$$

where V is in Km, λ in μm and σ_s in Km^{-1} (19). The transmittances at $0.55\mu\text{m}$ in table 2 are therefore, by definition, identical if the visibility is the same.

The growth factor F of aerosol radius as a function of relative humidity RH is shown in Fig.4 (20).

From it we may expect a strong increase in the extinction of hygroscopic aerosol particles with an increase of relative humidity RH [s. Fig.5 ref. (12)]; it is a consequence of the combined effect of change in amplitude of size distribution and change in refractive index (21).

One of the best calculation for σ_s has been made by Barnhardt and Straete (17) for the $10.6\mu\text{m}$ wavelength. They have calculated σ_s as a function of relative humidity for various aerosol kinds classified as a mixture of two fundamental types; continental and maritime.

Their results are shown in Fig.6.

1.3 Fog and rain extinction

An empirical relation between fog extinction coefficient at $10.6\mu\text{m}$ and at $0.53\mu\text{m}$ (22) is

$$\gamma_f(\lambda = 10.6) = 0.38 \gamma_f(\lambda = 0.53) \quad (14)$$

For rain, Sokolov (23) finds that γ_p is connected to precipitation velocity as shown in Table 3.

Table 3

precipitation velocity (mm/hour)	1	5	10	25	50	100
$\gamma_f(\lambda = 0.63\mu\text{m})$	0.25	0.69	1.04	1.80	2.88	4.19
$\gamma_p(\lambda = 10.6\mu\text{m})$	0.25	0.69	1.04	1.82	2.90	4.27

From Table 3 it is seen that there is no substantial difference in attenuation between these two wavelengths.

Scattering by rain is a multiple scattering phenomenon difficult to analyze quantitatively. A theoretical estimation in single scattering can be made by assuming that for λ between $0.4\mu\text{m}$ and $15\mu\text{m}$ rain droplets can be considered large with Q_{ext} practically equal to two.

Therefore

$$\gamma_p = 2N \int_{r_1}^{r_2} \pi r^2 f(r) dr = 2G, \quad (15)$$

where

$$G = N \int_{r_1}^{r_2} \pi r^2 f(r) dr, \quad (16)$$

is the geometrical cross-section of droplets per volume unity. Therefore we may expect that the extinction coefficient for rain is independent of λ between $0.4\mu\text{m}$ and $15\mu\text{m}$.

The empirical relation between γ_p and the precipitation velocity J (mm/hour)

$$\chi = 0.21 J^{0.74} \quad (\text{Km}^{-1}) \quad (17)$$

Additional data can be found in ref.(24).

2 - ATMOSPHERIC TURBULENCE

2.1 - Introductory remarks and theoretical background

When a laser beam propagates through the turbulent atmosphere it suffers a degradation due to the random changes of the refractive index.

The structure of turbulence is described by statistical fluctuations in air velocity. Two basic mechanisms are responsible for velocity turbulence: wind shear and convective heating from the ground.

As a result of these turbulences, eddy air currents are produced. For instance air blown over obstacles breaks up into eddies, the largest of which being determined by the size of the obstacle. Due to viscosity if the energy in the eddy exceeds a critical level determined by the Reynold's number, the velocity fluctuations within the eddy are no longer stable, and the eddy breaks up into smaller eddies. Further breakup occurs until the eddy is reduced to sufficiently small size where viscous effects become dominant thereby dissipating the available energy into heat.

When the process is selfsustaining each eddy of a given size transfer the same amount of energy to its immediately smaller neighbor. A range of size or scales of eddies is then found to exist, extending from an outer scale L_0 to an inner scale l_0 . Close to ground it is often assumed that the outer scale is of the order of the height above the ground and ranges typically between 1 to 100 m. The inner scale is of the order of 1 to 10 mm near the ground.

Each eddy can be thought of as a parcell of air, a turbulent blob with its own characteristics velocity, temperature, refractive index, etc.

The propagation of optical waves is influenced mainly by changes in the refractive index which depend directly of temperature fluctuations resulting from the turbulent mixing of air blobs induced by temperature gradients in the atmosphere. It can be shown (25) that in the atmosphere, when conditions for homogeneous turbulence exist, the power spectrum of velocity fluctuations is proportional to the power spectrum of the index of refraction fluctuations. The fluctuations in the index of refraction are functions of the position r and time t , so that the index of refraction n can be written as

$$n(r,t) = 1 + n_1(r,t) \quad (18)$$

where n_1 is the fluctuation in the index of refraction. For clear-air atmospheric turbulence it is generally reasonable to assume that n_1 is small and that its temporal dependence is mainly due to atmospheric winds, so that $n_1(r,t) \approx n_1[r - V(r)t]$ where $V(r)$ is the local wind velocity. This last assumption is known as "Taylor's frozen-flow hypothesis", and appears to hold in most practical situations.

Let us now ignore, for the moment, the effect of atmospheric winds and concentrate on the spatial variations of n_1 . Here we shall only need to calculate integrals of n_1 of the form $\int f(x)n_1(x)dx$, and these are generally Gaussian random variables. Therefore, we shall only be interested in the first two moments of n_1 . It is clear that the first moment $\langle n_1 \rangle = 0$ where $\langle \cdot \rangle$ denotes an ensemble average. We must now specify the covariance $\langle n_1(r)n_1(r') \rangle$.

We shall assume that the random medium is locally stationary; that is, if we define $R = (r+r')/2$ and $\rho = r-r'$ then the moment $\langle n_1(r)n_1(r') \rangle$ varies much more rapidly with ρ than it does with R . For this case the covariance of n_1 may be written as

$$\langle n_1(r)n_1(r') \rangle = \iiint d^3k \Phi_n(R,k) e^{i k \rho} \quad (19)$$

The function $\Phi_n(R,k)$ is known as the wavenumber spectrum of the index-of-refraction fluctuations, and for well-developed turbulence in the earth's atmosphere is given approximately by

$$\Phi_n(R,k) = \frac{0.033 C_n^2 \exp[-(\frac{kL_0}{2\pi})^2]}{[k^2 + L_0^{-2}]^{11/6}} \quad (20)$$

In Eq.(20), the quantity C_n^2 is known as the index-of-refraction structure constant, and is a measure of the magnitude of the fluctuations in the index of refraction. The values of C_n^2 can be taken as indicative of the turbulence strength. The following classification is sometimes used

weak turbulence	$C_n^2 = 64 \cdot 10^{-18} \text{ m}^{-2/3}$
intermediate turbulence	$C_n^2 = 16 \cdot 10^{-16} \text{ m}^{-2/3}$
strong	$C_n^2 = 25 \cdot 10^{-14} \text{ m}^{-2/3}$

In general C_n^2 will vary with altitude, and the values listed here are meant to characterize average day-time conditions a few meters above the earth's surface. The exact variations with altitude depends upon the local terrain.

The earliest attempts to study propagation in a random medium employed the geometric-optics approximation; however, this was shown to be of very limited utility since results obtained by geometric optics are valid only for propagation paths of order $\kappa \ell^2$, where κ is the signal wave-number. In the late 1950's Tatarski (25) developed a new technique, based on the Rytov approximation, which had a much greater range of validity than the geometric-optics method. In this method the electric field E of a narrow-band beam propagating in a random medium is written as

$$E = \exp(\psi) = \exp(\chi + iS), \quad (21)$$

and ψ is next written as

$$\psi = \psi_0 + \psi_1, \quad (22)$$

where ψ_0 satisfies the vacuum equation

$$-\nabla^2 \psi_0 + (\nabla \psi_0)^2 + \kappa^2 = 0, \quad (23)$$

and $\psi_1 = \chi_1 + iS_1$ has a solution given by

$$\psi_1(z) = \frac{\kappa^2}{2\pi E_0(z)} \iiint d^3z' n_1(z') E_0(z') \frac{e^{i\kappa|\vec{z}-\vec{z}'|}}{|\vec{z}-\vec{z}'|}, \quad (24)$$

where $E_0 = \exp \psi_0$. From Eq.(24) it is possible to calculate the moments of the log-amplitude χ_1 and the phase S_1 . It is quite clear from Eq.(24) that the moments of ψ_1 can be expressed in terms of the moments of the index of refraction fluctuation n_1 . Solution (24) is however obtained under the assumption that $|\nabla \psi_1| \ll |\nabla \psi_0|$ which leads to an important restriction on the range of validity of the Rytov method. When the Rytov method was first developed it appeared to give quite good agreement with all the available experimental data, which had been taken over propagation paths of less than 1 Km in the atmosphere. However, in the late 1960's when experiments were performed using horizontal propagation paths much greater than 1 Km, it was found that the experimental data deviated significantly from predictions made using the Rytov method. In particular, it was found that if the propagation path x is such that the parameter $\sigma_x^2 = 1.23 \kappa^{7/6} C_n^2 x^{11/6}$ is greater than 0.3, the Rytov approximation is invalid. It was soon recognized that, because the Rytov approximation is equivalent to the scatter of the incident wave by a series of random phase screens it did not adequately account for multiple scatter of the electromagnetic wave by the turbulent eddies. This pushed to develop new theories which properly include multiple scatter, and led to an exploration of several different techniques. However, the technique which to date appears to be most successful in overcoming the limitations of the Rytov method and is easiest to understand is the Markov approximation (25)(26)(27)(28). In this approximation a light beam is considered which is propagating along the x axis in a medium with random index of refraction fluctuations, and the electric field is written as

$$E = u(x, y, z) e^{i\kappa x} \quad (25)$$

To obtain solutions for the moments $\langle u(x, y) \rangle$, $\langle u(x, y) u^*(x, y) \rangle$, etc., where $\rho \equiv (y, z)$ it is first assumed that the index-of-refraction fluctuation n_1 is delta-function correlated in the direction of propagation, so that the turbulent eddies look like flat disks oriented normally to the propagation path. The moments of the field are then obtained by using the Novikov-Furutsu formula (29), which states that if n_1 is a Gaussian random variable and $\Phi[\Lambda]$ is an arbitrary functional of n_1 , then

$$\langle n_1(z) \Phi[\Lambda] \rangle = \iint_{-\infty}^{+\infty} d^3z' \langle n_1(z) n_1(z') \rangle \left\langle \frac{\delta \Phi[\Lambda]}{\delta n_1(z')} \right\rangle. \quad (26)$$

It can be demonstrated (25) that the conditions required for the validity of the approximations made in this method are that

$$\kappa l_0 \gg 1, \quad (27a)$$

and

$$\kappa C_n^2 L_0^{5/3} \ll 1. \quad (27b)$$

The condition in Eq.(27a) requires that the scattering pattern of even the smallest turbulent eddies must be primarily in the forward direction, while that requirement expressed by Eq.(27b) is that there be very little attenuation (due to scatter) of the signal over one wavelength.

If we substitute numbers typical of C_n^2 , L_0 and l_0 in the earth's atmosphere we find that the condition in Eq. (27b) is really not very restrictive, and that the Markov approximation is valid over horizontal propagation paths of many hundreds or thousands of kilometers in the Earth's atmosphere; this is quite an improvement over the Rytov approximation, which was valid only over distances less than about 1 Km.

It is so possible to derive the equations satisfied by the higher order moments of the field; the equation satisfied by second moment

$$\Gamma_2(x, \rho_1, \rho_2) = \langle u(x, \rho_1) u^*(x, \rho_2) \rangle, \quad (28)$$

can be obtained and its solution is

$$\Gamma_2(x, \rho_1, \rho_2) = \left(\frac{\kappa}{2\pi x} \right)^2 \iint_{-\infty}^{\infty} d^2 \rho'_1 \iint_{-\infty}^{\infty} d^2 \rho'_2 u_0(\rho'_1) u_0^*(\rho'_2) \cdot \exp \left\{ i \frac{\kappa}{2\pi} \left[(\rho'_1 - \rho_1)^2 - (\rho'_2 - \rho_2)^2 \right] - \frac{\pi \kappa^2}{4} \int_0^x d x' H \left[\kappa', \frac{x'}{z} (\rho_1 - \rho_2) + (\rho'_1 - \rho'_2) \left(1 - \frac{x'}{x} \right) \right] \right\}, \quad (29)$$

where for the spectrum Φ_n given in Eq.(22)

$$H(x, \xi) = 1.88 C_n^2(x) |\xi|^{5/3} \left[1 - 0.705 \left(\frac{|\xi|}{L_0} \right)^{1/3} \right], \quad (30)$$

provided $l_0 \ll |\xi| \ll L_0$. Equation (29) gives the general spatial coherence function of the beam; the intensity distribution $I(x, \rho) = \langle u(x, \rho) u^*(x, \rho) \rangle$ can be obtained from Eq.(29) simply by setting ρ_2 equal to ρ_1 .

It is also possible to derive the equation satisfied by the fourth moment of the field

$$\Gamma_4(x, \rho_1, \rho_2, \rho_3, \rho_4) = \langle u(x, \rho_1) u^*(x, \rho_2) u(x, \rho_3) u^*(x, \rho_4) \rangle.$$

However in this case a solution in closed form cannot be obtained.

This is unfortunate since a knowledge of Γ_4 is necessary in order to calculate intensity scintillations, beam wander, aperture averaging, and a number of other measurable effects. However, a number of approximate solutions, valid for different ranges of σ_r^2 have recently been developed and will be discussed in the following.

2.2. Effects of turbulence on laser beams

We will now consider the various effects of turbulence on the parameters of a laser beam. Let us consider a receiving equipment composed of a lens and a photomultiplier at its focus. The voltage across its output terminals constitutes the received signal. In the vacuum, or in an homogeneous atmosphere, the laser beam is directed along the optical axis, and the photomultiplier receives practically the full energy of the beam.

A turbulent atmosphere causes the beam parameters to fluctuate at random, and will distort the beam producing one or more of the following effects.

A) Beam spreading.

The unperturbed beam has its own spread due to diffraction. Turbulence causes further beam spread and the beam cross-section fluctuates in size (breathing).

B) spatial coherence

The spatial coherence of the beam is shown to decrease with its traveling in the turbulent atmosphere.

C) Intensity fluctuations.

Interference produces amplitude fluctuations on the receiving surface (scintillation). As a result we have fluctuations in the received power that, turbulence being equal, depend on the receiver aperture size and on the path length.

In telecommunications these fluctuations impose a lower limit to the depth of amplitude modulation, and finally inhibit its use for analogical modulation. The temporal changes of these fluctuations are also of interest for these systems.

D) phase fluctuations.

The phase along the arriving wavefront changes in a random way. Two points on the wave surface of the unperturbed wave, do not have, generally the same phase. Their phase difference changes at random (spatial phase fluctuations).

In telecommunication it is desirable to have coherence over the whole receiving surface; therefore this phenomenon poses an upper limit to the receiver dimensions.

Fluctuations in the transit time (due to fluctuations in the propagation velocity) cause random phase changes over a point of the receiver. These fluctuations produce a parasite modulation that perturbs the signal modulation.

F) angle of arrival fluctuations.

The angle formed by the normal to the wavefront and the propagation direction undergoes casual changes. If there is a lens, in the receiver, these fluctuations produce displacements of the image point of the beam on the focal plane (image-dancing or quivering). Therefore to receive the signal we must increase the aperture surface at the receiver.

When the path is long, the wavefront can be thought of as divided into coherence regions. Each coherence region presents its own incidence angle with causal changes (crumbling of the wavefront, boiling or image blurring).

Not all these phenomena are mutually independent. We will in the following describe them.

A) Beam spread and average intensity

In the absence of turbulence, a laser beam exiting from an aperture of diameter D would, in the far field, have an angular spread $\theta_0 \approx \lambda/D$, where λ is the signal wavelength. When turbulence is present the situation becomes much more complex because the beam is scattered by the moving turbulent eddies. This gives rise to an angular beam spread which may be much greater than θ_0 ; in addition other effects such as beam wander or even breakup of the beam into an ensemble of individual beams may occur.

When discussing the radius of a beam propagating in a turbulent medium it is necessary to distinguish between its short- and long-term spread. In general, when a laser beam interacts with the turbulent eddies it is found that those eddies which are large compared with the diameter of the beam tend to deflect the beam, whereas those eddies which are small compared with the beam diameter tend to broaden the beam, but do not deflect it significantly. Consequently, if we had a photographic plate at a distance x into the random medium and took a very short exposure picture we would observe a broadened laser spot (due to the small eddies) of radius ρ_s which is deflected (due to the large eddies) by a distance ρ_c , as indicated pictorially in Fig.7. Now, because the turbulent eddies are flowing across the beam, the beam will be continually deflected in different directions in time intervals of order $\Delta t = D/|V|$, where V is the transverse flow velocity of the turbulent eddies. The time history of the beam wander is shown in Fig.8. Because the spot dances from position to position in times of order Δt , it is clear from Fig.8 that if we took a picture, with an exposure time much longer than Δt , of the received spot we would see a broadened spot with a meansquare radius $\langle \rho_L^2 \rangle$ given by

$$\langle \rho_L^2 \rangle = \langle \rho_s^2 \rangle + \langle \rho_c^2 \rangle, \quad (31)$$

ρ_s is the short-term beam spread and ρ_c is the long-term beam spread.

Unfortunately, the model given above does not give the whole story, and only holds in the limit when the turbulence is relatively weak. When the turbulence is strong the beam no longer wanders significantly, but rather breaks up into multiple beams. In this case a short exposure picture of the received spot would consist not of a single spot, but of a multiplicity of spots at random locations on the receiving aperture. The long-exposure picture, however, would be a blurred version of the short exposure, but with approximately the same total diameter.

If the initial field distribution in the beam has the Gaussian form

$$u_0(s) = \exp \left\{ -\frac{2s^2}{D^2} - \frac{ik^2 s^2}{2F} \right\}, \quad (32)$$

i.e. a beam with an initial diameter D and a radius of curvature F one finds

$$\langle s_L^2 \rangle \approx \frac{4x^2}{\kappa^2 D^2} + \frac{D^2}{4} \left(1 - \frac{x}{F}\right)^2 + \frac{4x^2}{\kappa^2 \rho_0^2} \quad \text{for } x \ll (\kappa^2 C_n^2 l_0^{5/3})^{-1} \quad (33a)$$

$$\langle s_L^2 \rangle \approx \frac{4x^2}{\kappa^2 D^2} + \frac{D^2}{4} \left(1 - \frac{x}{F}\right)^2 + 4.4 x^2 C_n^2 l_0^{-5/3} \quad \text{for } x \gg (\kappa^2 C_n^2 l_0^{5/3})^{-1} \quad (33b)$$

where, for homogeneous turbulence (i.e. C_n^2 not depending on distance)

$$\rho_0 = 1.06 \kappa^{-6/5} C_n^{-6/5} x^{-1/5}.$$

The first two terms in Eq.(33a) and Eq.(33b) represent the beam spreading in vacuum; the last term represents the additional spread due to the scattering of the beam by the turbulent eddies.

The validity of Eq.(33a) has been studied somehow and seems to be confirmed (30).

In atmospheric turbulence $(\kappa^2 C_n^2 l_0^{5/3})^{-1}$ is of order of 100 Km.

Average Intensity

The formal expression for the long term averaged beam intensity is given by Eq.(29) with $\rho_1 = \rho_2 = \rho$. In particular, for a Gaussian initial field distribution $u_0(\rho)$, the long-term averaged intensity can be found by using the results of Eq.(33a) and Eq.(33b), along with energy conservation. That is, since the turbulent eddies are much larger than the signal wavelength, nearly all of the energy is scattered in the forward direction. Consequently $\langle I(x,0) \rangle \langle s^2(x) \rangle$ is approximately a constant. If we denote the intensity at $x = 0$ by I_0 , we then have for the axial intensity (31)

$$I_0 \frac{D^2}{4} \approx \langle I(x,0) \rangle \langle s^2(x) \rangle. \quad (34)$$

We next substitute Eq.(33a) into Eq.(34) to obtain, for $x \ll (\kappa^2 C_n^2 l_0^{5/3})^{-1}$,

$$\langle I(x,0) \rangle \approx \frac{\left(\frac{D^2}{4}\right) I_0}{\frac{4x^2}{\kappa^2 D^2} + \frac{D^2}{4} \left(1 - \frac{x}{F}\right)^2 + \frac{4x^2}{\kappa^2 \rho_0^2}}. \quad (35)$$

For $x \gg (\kappa^2 C_n^2 l_0^{5/3})^{-1}$ we have to use instead Eq. (33b). The approximate result in Eq. (35) agrees quite well with more rigorous theoretical results (25), (32) and also with experimental data (33).

If the Flux $P_0 = \pi D^2 I_0 / 4$ through the transmitting aperture is held fixed, Eq.(35) predicts that, in turbulence, there is a limiting value of the intensity at the focus ($x = F$) of the beam, no matter how large the initial diameter D of the beam is made. This maximum intensity is

$$\langle I_{\max} \rangle = \frac{0.165 P_0}{C_n^{14/5} F^{14/5} \kappa^{2/5}}. \quad (36)$$

Kallistрова and Kon (34) have made detailed measurements of the focused beam intensity in turbulence; they have found that there is a limit to the intensity of a focused beam, and that Eq. (36) is a good approximation to that limit. The short term averaged intensity is considered by (34a).

B. Spatial coherence.

The function $\overline{T}_2(x, \rho_1, \rho_2) = \langle u(x, \rho_1) u^*(x, \rho_2) \rangle$ is a measure of the long-term spatial coherence of the electric field, in a plane transverse to the direction of propagation of the beam. This function is important for interferometry experiments in radio astronomy, and because it determines the signal-to-noise ratio in an optical

heterodyne receiver (35). Exact expressions for T_1 in the limiting cases of plane and spherical waves have been available for some time; however, the general solution for T_1 for a finite beam has only more recently been derived (25)(32)(36) and numerically evaluated (31). In particular, the general solution for the coherence relative to the average center of the beam is given by Eq. (29), with ρ_1 set equal to zero. We will not present the general solution for T_1 here, but will rather present an approximate evaluation of Eq. (29) for the case when the initial electric field of the beam is given by Eq. (32). We then find that the long-term coherence function $M(x, \rho)$, which measures coherence relative to the undisplaced center of the beam, is (36)

$$M(x, \rho) = \frac{T_1(x, 0, \rho)}{T_1(x, 0, 0)} = \exp \left\{ - \left(\frac{\rho}{\rho_b} \right)^{5/3} \right\}, \quad (37)$$

where

$$\rho_b = \rho_p \left[\frac{(1 - \frac{\kappa}{F})^2 + \frac{4\kappa^2}{\kappa^2 D^2} \left\{ 1 + \frac{1}{3} \left(\frac{D}{\rho_p} \right)^2 \right\}}{1 - \frac{13}{3} \left(\frac{\kappa}{F} \right) + \frac{11}{3} \left(\frac{\kappa}{F} \right)^2 + \frac{4\kappa^2}{3\kappa^2 D^2} \left\{ 1 + \frac{1}{4} \left(\frac{D}{\rho_p} \right)^2 \right\}} \right]^{1/2}, \quad (38)$$

ρ_p is the plane-wave coherence length given by

$$\rho_p = \kappa^{-6/5} x^{-1/5} C_n^{-6/5}, \quad (39)$$

and it is assumed that $l_0 \ll \rho_p \ll L_0$. The simplified expression in Eq. (37) can be shown (31) to be a good approximation to the exact results obtained from Eq. (29). It can also be demonstrated that the same trends, as predicted by Eq. (37), are observed experimentally. For example, consider the plane-wave limit in which

$$M(x, \rho) = \exp \left\{ - \left(\frac{\rho}{\rho_p} \right)^{5/3} \right\}. \quad (40)$$

Gilmartin and Holtz (37) have found experimentally that ρ_p varies as $k^{-6/5}$, as predicted by Eq. (39). Further verification is found in recent Soviet experiments (38) which indicate that ρ_p varies as $k^{-6/5} x^{-3/5} C_n^{-6/5}$, in complete agreement with Eqs. (39) and (40).

It is important to emphasize that ρ_b is the long-term averaged (over times much larger than $\Delta t = D/V$) coherence length of the beam. If measurements relative to the instantaneous center of the wandering beam are made over times much shorter than Δt some short-term length ρ_b' which is greater than ρ_b . The short term coherence length has not been studied in any rigorous fashion; however, a rough approximation (39) is readily obtained, and it is found that the short-term beam coherence length ρ_b' is also given by Eq. (38), except with ρ_p replaced by ρ_{ps} which for $\rho_p/D < 1$ is given by

$$\rho_{ps} = \rho_p \left[1 + 0.37 \left(\rho_p / D \right)^{1/3} \right]. \quad (41)$$

C. Intensity fluctuations

If we measure the intensity of a laser beam across its traveling direction in a turbulent medium, we would find that the measured value of I would fluctuate with time about its average value $\langle I \rangle$. As an example Fig. 9 shows power fluctuations measured with an aperture of 7 cm over a path 145 Km long (40). It is desirable to be able to predict the magnitude of the intensity scintillations, since this is an important consideration in the design of any receiver system. At present, extensive experimental data on the intensity scintillation are available, but the theory is complete only for the limiting case of weak turbulence. For the case of weak turbulence it is conventional to calculate the variance and covariance of the logarithm of the amplitude fluctuations rather than of the intensity fluctuations. This presents no great difficulty because if the log-amplitude χ , is normally distributed, it can be shown that

$$\beta_\chi(x, \rho_1, \rho_2) = \langle \chi_1(x, \rho_1) \chi_2(x, \rho_2) \rangle, \quad (42)$$

is related to

$$b_I(x, \rho_1, \rho_2) = \frac{\langle I(x, \rho_1) I(x, \rho_2) \rangle - \langle I(x, \rho_1) \rangle \langle I(x, \rho_2) \rangle}{\langle I(x, \rho_1) \rangle \langle I(x, \rho_2) \rangle}, \quad (43)$$

via

$$B_x(x, \rho_1, \rho_2) = \frac{1}{4} \ln [1 + b_I(x, \rho_1, \rho_2)] \quad (44)$$

We shall, therefore, present the theoretical results for B_x ; the results for b_I follow from Eq. (44).

The ensemble average in Eq.(42) can be readily evaluated by using the Rytov method; the quantity $\chi_1(x, \rho_1)$ can be calculated by taking the real part of Eq.(25). This result is then multiplied by $\chi_1(x, \rho_2)$ and ensemble averaged, with Eq.(21) used to evaluate $\langle n_1(x, \rho_1) n_1(x, \rho_2) \rangle$. A good approximation for B_x in the case of a plane wave can be obtained for the case when the turbulence is homogeneous (i.e., C_n^2 independent of x). In that case, (41)

$$B_x(x, \hat{\rho}) = \frac{1}{4} b_I(x, \hat{\rho}) = \frac{1.23 \kappa^{7/6} C_n^2 x^{11/6}}{4} \left[1 - 10.9 \left(\frac{\hat{\rho}^2}{\lambda x} \right)^{3/6} + 10.7 \left(\frac{\hat{\rho}^2}{\lambda x} \right) \right], \quad (45)$$

provided $\ell_0 \ll \hat{\rho} \ll (\lambda x)^{1/2}$. This expression is valid only for $\sigma_I^2 = 1.23 \kappa^{7/6} C_n^2 x^{11/6} \leq 0.3$. It has been compared in detail with experimental data and the agreement is quite favorable (42), provided $\sigma_I^2 < 0.3$. This point is quite evident from Fig.10; there calculations of

$$\sigma_I^2 = \frac{\langle I^2 \rangle - \langle I \rangle^2}{\langle I \rangle^2} = \exp \left\{ 4 B_x(x, 0, 0) \right\} - 1,$$

for a unit-amplitude plane wave are compared with experimental data. Finally we note from Eq.(45) that in weak turbulence the characteristic transverse length for correlation of the intensity fluctuations is $(\lambda x)^{1/2}$; we shall see later that in strong turbulence there is an entirely different characteristic correlation length for the intensity fluctuations.

Scintillations in strong turbulence

A great deal of effort has been devoted to attempting to explain the reasons for the failure of the Rytov method when the turbulence is strong and to develop new theories which are adequate when $\sigma_I^2 > 1$. Most of this effort has been an attempt to obtain solutions of the equation giving T_4 since the intensity fluctuations are directly related to T_4 through

$$\langle I(x, \rho_1) I(x, \rho_2) \rangle - \langle I(x, \rho_1) \rangle \langle I(x, \rho_2) \rangle = T_4^I(x, \rho_1, \rho_2, \rho_1, \rho_2) - T_2^I(x, \rho_1, \rho_2) T_2^I(x, \rho_2, \rho_1)$$

In the plane wave limit it has been shown by several different techniques that for $\sigma_I^2 \gg 1$ an approximate solution for the normalized intensity scintillation $b_I(x, \rho)$ in homogeneous turbulence is (43)

$$b_I(x, \hat{\rho}) = \exp \left\{ -2 \left(\frac{\hat{\rho}}{\rho_p} \right)^{3/2} \right\} + \frac{1}{(\sigma_I^2)^{1/4}} \left\{ f \left[\frac{\hat{\rho}}{(\lambda x)^{1/2} \sigma_I^{6/11}} \right] + g \left[\frac{\hat{\rho} \sigma_I^{6/11}}{(\lambda x)^{1/2}} \right] \right\}, \quad (46)$$

where b_I is defined in Eq.(43), $\hat{\rho} = |\rho_1 - \rho_2|$, ρ_p is the plane wave coherence length, defined in Eq.(39) and the functions $f(s)$ and $g(s)$ are shown in Fig.11. We can obtain the variance of the intensity fluctuations by setting $\rho = 0$ in Eq.(46); the result is

$$\sigma_I^2 = \frac{\langle I^2 \rangle - \langle I \rangle^2}{\langle I \rangle^2} = 1 + \frac{0.99}{(\sigma_I^2)^{2/5}} \quad (47)$$

This expression is in good agreement (42) with measurement; the decay of σ_I^2 to unity as $(\sigma_I^2)^{-4/5}$ has been predicted by a number of authors. In Fig.12 we present a comparison of the analytical predictions, made using Eq.(46), and recent Soviet measured data (43) for the covariance of the intensity fluctuations. The agreement is quite good. In Fig.12 the abscissa R is defined as $R = \hat{\rho} / (\lambda x)^{1/2}$. The sharp decay in $b_I(R)$ near $R = 0$ is governed by the first term in Eq. (46), whereas the long tail is governed by the second term; the last term is important in the transition region between the first two terms.

It is important to note that the nature of the intensity covariance function b_I is quite different in strong turbulence than in weak turbulence; this is evident from Fig.13. We observe that in weak turbulence the intensity fluctuations are correlated over transverse distance ρ of order $(\lambda x)^{1/2}$. However, in strong turbulence we see from Eq.(46) and Fig.13 that the correlation is over transverse separations

$$\hat{\xi} \sim \xi_p = \frac{0.36 (\lambda x)^{1/2}}{(\sigma_1^2)^{3/5}} \quad (48)$$

Since $\sigma_1^2 \gg 1$ in strong turbulence it is clear from Eq.(48) that the correlation distance is much shorter in strong turbulence than in weak turbulence. Although Eqs.(46) and (47) are strictly valid only for plane waves it is expected that they will also yield a fair approximation for finite beams, except possibly in the focal plane. In fact it has been shown (44) that for $\sigma_1^2 \gg 1$ and

$$\sigma_1^2 \gg 0.5 \left[\frac{4x}{\kappa D^2} + \left(\frac{\mu D^2}{4x} \right) \left(1 - \frac{\mu}{F} \right)^2 \right]^{5/6} \quad (49)$$

the properties of the intensity scintillations of the beam are independent of its initial structure. Therefore for sufficiently strong turbulence the normalized scintillations of a plane wave are the same as those of a finite beam; this effect has also been observed experimentally (45)(42).

Aperture averaging

The intensity fluctuations σ_I^2 shown in Fig.10 and discussed previously are really those which would be measured by a receiving aperture with an infinitesimally small diameter. In practice the receiving aperture has a finite diameter and the intensity fluctuations measured will not be σ_I^2 but rather an average of the fluctuations over the whole aperture. Let us consider the fluctuations δP_R in the power received by a circular aperture of diameter D' when a signal of intensity I is incident on it,

$$\delta P_R = P_R - \langle P_R \rangle = \iint_{D'} d^2 \rho_1 [I - \langle I \rangle] .$$

The mean-square fluctuation in the received power is

$$\begin{aligned} \langle \delta P_R^2 \rangle &= \iint_{D'} d^2 \rho_1 \iint_{D'} d^2 \rho_2 [\langle I(\rho_1) I(\rho_2) \rangle - \langle I(\rho_1) \rangle \langle I(\rho_2) \rangle] \\ &= \iint_{D'} d^2 \rho_1 \iint_{D'} d^2 \rho_2 B_I(x, \rho_1, \rho_2), \end{aligned} \quad (50)$$

where

$$B_I(x, \rho_1, \rho_2) = \langle I(\rho_1) \rangle \langle I(\rho_2) \rangle b_I(x, \rho_1, \rho_2),$$

and b_I is defined in Eq.(43). Let us now define $G(D')$ as the ratio of the received power fluctuations in an aperture of diameter D' to those measured by a point aperture. By using Eq.(50), it is straightforward to show (25) that for a plane wave

$$G(D') = \frac{1}{\pi(D')^2} \int_0^{D'} \frac{b_I(x, \hat{\rho})}{b_I(x, 0)} \left\{ \cos^{-1} \left(\frac{\hat{\rho}}{D'} \right) - \frac{\hat{\rho}}{D'} \left[1 - \left(\frac{\hat{\rho}}{D'} \right)^2 \right]^{1/2} \right\} \hat{\rho} d\hat{\rho} \quad (51)$$

$G(D')$ can be readily calculated for both strong and weak turbulence; and the result is shown in Fig.14. We observe that as the diameter of the receiving aperture is increased the magnitude of the fluctuations in the received power decreases; this effect is known as aperture averaging, and has been observed experimentally (45)(46). From Fig.14 we can note that in weak turbulence ($\sigma_1^2 \ll 1$) the fluctuations in the received power are significantly reduced whenever the aperture diameter D' exceeds $(\lambda x)^{1/2}$. However, in strong turbulence ($\sigma_1^2 \gg 1$) there is a significant reduction in the fluctuations whenever the receiving aperture diameter exceeds $\xi_p = 0.36 (\lambda x)^{1/2} (\sigma_1^2)^{-3/5}$ which is much smaller than $(\lambda x)^{1/2}$ because $\sigma_1^2 \gg 1$.

Frequency spectrum of the intensity scintillations

In some applications it is desirable to know the frequency spectrum of the intensity fluctuations of a light beam which would be measured by a receiver in a turbulent medium. This spectrum $W_I(\omega)$ is given by

$$W_I(\omega) = \int_0^\infty d\tau \cos \omega \tau [\langle I(x, \rho_1, t) I(x, \rho_2, t+\tau) \rangle - \langle I(x, \rho_1, t) \rangle \langle I(x, \rho_2, t+\tau) \rangle] , \quad (52)$$

where ω is the frequency and $I(x, \rho, t)$ is the instantaneous intensity at the position (x, ρ, t) at the time t . In writing Eq.(52), it has been implicitly assumed that the turbulence is a (temporally) stationary random process; for frozen flow this is a good assumption. For strong turbulence the expression in Eq.(52) has been evaluated in some cases (47). For weak turbulence, it is customary to study the frequency spectrum $W_x(\omega)$ of the log-amplitude fluctuations. This is related to the results obtained previously via

$$W_x(x, \rho, \omega) = \int_0^{\infty} d\tau \cos \omega \tau B_x(x, \rho, \rho, \tau).$$

Approximate analytical expressions for $W_x(\omega)$ have been obtained in a number of limiting cases, (25)(48)(49)(50). Experimental measurements of W_x and W_I have been made for both weak and strong turbulence (51)(52)(53). For the case of propagation in the clear atmosphere it is found that; for propagation paths such that the turbulence parameter $\sigma_I^2 \ll 1$, the width of the frequency spectrum $W_x(\omega)$ is of the order $V/(\lambda x)^{1/2}$, which is typically about 10 to 100 Hz. For paths such that $\sigma_I^2 \gg 1$, the width of the frequency spectrum is of order V/ρ , which is typically about 100 to 1000 Hz.

Probability distribution of the intensity

In some applications, such as the calculation of the probability of error in a communications link, it is desirable to know the probability distribution satisfied by the received intensity. For the case when $\sigma_I^2 \ll 1$, it has been found, that the probability distribution of the intensity is very nearly log-normal. That, is for a unit amplitude plane wave, the probability density $p(I)$ satisfies

$$p(I) = \frac{1}{(2\pi)^{1/2} \sigma_I I} \exp \left\{ - \left(\ln I + \frac{\sigma_I^2}{2} \right)^2 (2\sigma_I^2)^{-1} \right\}, \quad (53)$$

where $\sigma_I^2 = 4 B_x(x, 0) = \ln(1 + \sigma_I^2)$. The above result is physically reasonable since it implies that $\chi = (1/2) \ln(I)$ is normally distributed. By returning to Eq.(25), we see that $\chi = \text{Re}(\Psi_1)$ is essentially the sum of a large number of independent forward scatterings; therefore, by virtue of the central limit theorem χ is a normally distributed random variable.

Experimental measurements have been made (43)(54); for $25 < \sigma_I^2 < 100$, and for $0 < \sigma_I^2 < 0.3$ the distribution in Eq.(53) is reasonably accurate. However, for $1 < \sigma_I^2 < 25$, the measured probability distribution appears to deviate significantly from the result in Eq.(53). This is especially true for $1 < \sigma_I^2 < 4$.

D - Phase fluctuations

The phase fluctuations can be calculated in the weak turbulence case by taking the imaginary part of Eq.(25) to obtain the phase $S_1(x, \rho)$ and then obtaining

$$B_s(x, \rho, \rho) = \langle S_1(x, \rho) S_1(x, \rho) \rangle.$$

More often it is interesting to calculate the phase structure function defined as

$$d_s(x, \rho, \rho) = \langle [S_1(x, \rho) - S_1(x, \rho)]^2 \rangle. \quad (54)$$

For the case when $\sigma_I^2 < 0.3$ by employing the Rytov method, for a plane wave we have

$$d_s(x, \hat{r}) = \begin{cases} \frac{1}{2} d_1(\hat{r}) & \ell_0 \ll \hat{r} \ll (\lambda x)^{1/2} \\ d_1(\hat{r}) & \hat{r} \gg (\lambda x)^{1/2} \end{cases} \quad (55)$$

where $d_1(\hat{r})$ for $\ell_0 \ll \hat{r} \ll L_0$ is given by

$$d_1(\hat{r}) = 2.92 |\hat{r}|^{1/3} \kappa^2 x C_n^2. \quad (56)$$

Eqs.(55) and (56) are found to be valid also in strong turbulence, as proved also by Ishimaru (56a).

For large values of \hat{r} Tatarski (57) finds

$$B_s(x, \rho, \rho) = 0.73 C_n^2 \kappa^2 x |\hat{r}|^{-1/3} k(181/\ell), \quad (57)$$

where $f(|\hat{\rho}|/l)$ is an adimensional function whose behavior is shown in Fig.15, and the scale l is defined through

$$0.41 C_n^2 \kappa^{7/6} l^{11/6} = 1.$$

The phase structure function's dependence on the 5/3 power of the separation distance $\hat{\rho}$ between points, for small $\hat{\rho}$ values, has been experimentally verified by many authors.

For large values of $\hat{\rho}$ the phase structure function shows saturation properties. Bertolotti et al. (58)(59) have made measurements of the phase structure function on paths of 0.5 Km and 3.5 Km by using a particular kind of interferometer that allows simultaneous measurements for ray couples of different separation.

Fig.16 shows some curves of the phase structure function obtained in different conditions. The dotted line is the 5/3 power law that best fits the initial part of the curve, from which the C_n^2 value can be deduced.

A saturation for $\hat{\rho}$ values of the order of 10 cm is clearly seen.

Similar results have also been obtained by Burlamacchi et al.(60). Other authors in different ambiental conditions, have found agreement with the 5/3 power law up to much larger values of $\hat{\rho}$ (61)(62).

Fig.17 shows on probability paper the statistical distribution of phase differences for two distances between the beams. The experimental points are consistent with a normal distribution.

The spectrum $W_s(\omega)$ of the phase fluctuations can be obtained by evaluating

$$W_s(\omega) = \int_0^{\infty} d\tau \cos \omega \tau \langle \Delta S(t) \Delta S(t+\tau) \rangle, \quad (58)$$

where $\Delta S(t) = S(x,0,t) - S(x,\rho,t)$, and t is the time variable. If we assume that the turbulent flow is frozen, than the product $\langle \Delta S(t) \Delta S(t+\tau) \rangle$ can be rewritten as

$$\langle [S_s(x,0,t) - S_s(x,\rho,t)] [S_s(x,-v\tau,t) - S_s(x,\rho-v\tau,t)] \rangle, \quad (59)$$

where v is the flow velocity of the turbulence in the direction transverse to the direction of propagation. If Eq.(59) is used in Eq.(58) we find for a plane wave that

$$W_s(\omega) = \begin{cases} 0.0326 \\ 0.0652 \end{cases} \left\{ v^{5/3} C_n^2 \kappa^2 \left[1 - \cos\left(\frac{\omega \rho}{v}\right) \right] \frac{\left(\frac{2\pi}{\omega}\right)^{5/3}}{\left[1 + \left(\frac{1.07v}{\omega L_0}\right)^2 \right]^{4/3}} \right. \quad \begin{matrix} l_0 \ll \rho \ll (\lambda \kappa)^{1/2} \\ \rho \gg (\lambda \kappa)^{1/2} \end{matrix} \quad (60)$$

where the expression (55) is used for the phase structure function. For a spherical wave the expression is the same with the substitution $[1 - \cos(\omega \rho / v)]$ with $[1 - \cos(\omega \rho N) / \omega \rho / v]$. This expression has been experimentally verified (61)(63)(64)(65). Fig.18 (61) shows experimental points obtained for different ρ values.

E - Angle of arrival fluctuations

A wave propagating in vacuum has a uniform wavefront; however, because different portions of the wavefront experience different phase shifts, a signal propagating in a random medium has random surfaces of constant phase, such as shown in Fig.19. This phase distortion leads to fluctuations in the angle of arrival α of the wavefront; these are the cause of image jitter in a telescope, an effect which is well known to astronomers.

Means-Square Angle of Arrival

Consider a receiving aperture of diameter D' . The phase difference ΔS across this aperture can be approximated by

$$\Delta S \approx \kappa D' \sin \alpha \approx \kappa D' \alpha.$$

Therefore, the mean-square angle-of-arrival fluctuations can be written as (s. Fig. 19)

$$\langle \alpha^2 \rangle \approx \frac{\langle \Delta S^2 \rangle}{\kappa^2 D'^2} = \frac{d_s(x, 0, D')}{\kappa^2 D'^2} \quad (61)$$

If we use Eq. (56) in Eq. (61) we have the result, for a plane wave in nearly homogeneous turbulence,

$$\langle \alpha^2 \rangle = \begin{cases} 1.46 \\ 2.92 \end{cases} C_n^2 \times (D')^{-1/3} \quad \begin{matrix} L_0 \ll D' \ll (\lambda x)^{1/2} \\ L_0 > D' \gg (\lambda x)^{1/2} \end{matrix} \quad (62)$$

In strong turbulence the following expression is sometimes used

$$\langle \alpha^2 \rangle = \begin{cases} 2.192 \\ 2.92 \end{cases} \times C_n^2 (D')^{-1/3} \quad \begin{matrix} L_0 \ll D' \ll \rho_p \\ L_0 \gg D' \gg \rho_p \end{matrix} \quad (63)$$

If we compare Eqs. (62) and (63) we see that, except for a slight difference in the value of the numerical coefficient, the results are identical. This same conclusion can be shown to hold for a spherical wave, and we can infer that it also holds for an arbitrary beam, except possibly in the focal plane. This conclusion explains why predictions made using the weak turbulence theory were able to give good agreement with experimental results taken for $\sigma_1^2 \gg 1$.

Angle of Arrival Spectrum

The spectrum $W_\alpha(\omega)$ of the fluctuations in the angle of arrival can be obtained through the relation

$$W_\alpha(\omega) = \frac{W_s(\omega)}{\kappa^2 D'^2} \quad (64)$$

A plot of the normalized angle-of-arrival spectrum is shown in Fig. 20. Note that the spectrum decays sharply (as $\omega^{-8/3}$) when $(\omega D'/V) \gg 1$.

From Fig. 20 we also observe that if $D' \ll L_0$ nearly all of the angle of arrival fluctuations will have frequencies $f = \omega/2\pi$ in the interval

$$\frac{0.01V}{2\pi D'} \leq f \leq \frac{10V}{2\pi D'} \quad (65)$$

3. BLOOMING

High power laser beams propagating through the earth's atmosphere are subjected to all the previously studied turbulence effects, and at the same time, creates a new effect; the so called thermal blooming phenomenon. Blooming is produced by the absorption of laser radiation by the atmosphere which alters the temperature of the ambient air and, in turn, its refractive index. The altered index changes the characteristics of the propagation of the laser beam. Generally, the temperature change is positive, causing the air to act like a thick, weak diverging lens and thereby enlarging the beam size in the focal plane.

Thermal blooming is a non-linear phenomenon. According to the kind of laser beam under consideration different effects are obtained (66).

a - cw thermal blooming

If a cw laser beam, focussed at range f , is turned on at a specified time, the beam begins the blooming first and most rapidly in the focal volume. The beam spreading travels backward towards the laser source (transient cw thermal blooming). If a steady transverse wind is present, however, the heated air is swept out of the beam and a steady state evolves. Beam slewing leads also to a steady state for similar reason. The steady state is first reached for the beam in the vicinity of the aperture; with the passage of time the beam reaches the steady condition at longer and longer ranges, until the entire region between aperture and focal plane becomes time independent. This will not occur however, if wind and slewing combine algebraically to be zero somewhere along the beam; then the beam will be steady for all ranges short of the zero wind point, the so-called stagnation point, and time-dependent at longer ranges.

This kind of thermal blooming is called stagnation zone blooming.

The time for the onset of the steady state is of the order of the wind transit time d/V at the aperture (d = aperture diameter of the beam, V = transverse component of wind). Fig.21 shows a photograph of a cross-section of a steady state cw bloomed (66).

CW stagnation zone blooming is as frequent a phenomenon as the cw steady state case, but is considerably more complicated.

b - pulse blooming

Short, high power, high energy, single pulse beams also suffer a variety of thermal bloomings different from the CW steady state kind.

When a single laser pulse of length τ_p is transmitted in the atmosphere, the laser heating of the air within the beam will generate a transverse density gradient which will be time varying. The characteristic time of this phenomenon is the hydrodynamic time $\tau_H = d/2 V_s$ (V_s = sound speed) which is the time required for a sound wave to cross the beam. When $\tau_p/\tau_H \ll 1$ the air density changes do not have time to develop completely and thermal blooming will be small. On the other hand τ_p cannot be made too small while maintaining a large pulse energy because the power density will then increase and the atmospheric breakdown limit may be exceeded.

The hydrodynamic time is proportional to the beam radius, thus thermal blooming is much greater near the focus than near the laser transmitting aperture. Also the changes in the index of refraction are larger in the focus. Qualitatively, thermal blooming causes an expansion of the beam relative to its initial size and hence a lowering of the beam intensity in the region of the beam axis. The ratio of the on-axis intensity of the distorted beam to the on-axis intensity of the undistorted beam in the focal plane in the short-time regime can be put in the form (67)

$$I/I_0 = 1 - \delta_0 E t^3 / E_f \tau_p \tau_H,$$

where δ_0 is a numerical parameter of the order of 0.4, E is the total pulse energy, E_f contains the hydrodynamic parameters. The beam behavior off-axis as a function of time is illustrated in Fig.22, where the normalized intensity, at any range z and time t is plotted against a normalized radial coordinate $r/a\sqrt{d(z)}$ being a the gaussian beam spot and $d(z)$ the beam size at distance z . The curves give the irradiance profiles at any range and time for which $\delta_0 E t^3 / E_f \tau_p \tau_H$ is 0 (upper curve), 0.1, 0.2, 0.3, 0.4, 0.5 (lower curve).

More detailed informations on the various kind of blooming are in refs.(68).

BIBLIOGRAPHY

- 1) H.L.Hackfort : Infrared Radiation - McGraw Hill Book Co.New York 1960
- 2) J.H.McCoy,D.B.Rensch,R.K.Long : Appl.Opt.8, 1471 (1969)
- 3) D.E.Burch AMS, Boston 1972
- 4) P.J.Wyatt,V.R.Stull,G.N.Plass.Appl.Opt. 3, (1964) 229 e 243
- 5) M.S.Shumate, R.T.Meuzies, J.S.Margolis, e L.C.Rosengren - Appl.Opt. 15, 2480 (1976)
- 6) J.C.Stephenson,W.A.Heseltine e C.B.Moore e 399 (1967) Appl.Phys. Letters 11, 164
- 7) P.K.L.Yin e R.K.Long : Appl.Opt.7, 1551 (1968)
J.H.McCoy e R.K.Long : Appl.Opt.8, 111 (1969)
- 8) V.A.Borisov : Optical Technology 37, 426 (1970)
- 9) J.Y.Wang - Appl.Opt. 13, 56 (1974)
- 10) H.C.van de Hulst - Light Scattering by Small Particles - John Wiley Sons, Inc. New York, 1957
- 11) D.B.Rensch e R.K.Long - Appl.Opt. 9, 1563 (1970)
- 12) J.A.Hodges - Appl.Opt.11, 2304 (1972)
- 13) W.C.Wells, G.Gal,M.W.Munn - Appl.Opt.16, 654 (1977)
- 14) J.Heintzenberg e M.Baker - Appl.Opt. 15, 1178 (1976)
- 15) H.R.Carlson,M.E.Milham,R.H.Frickel - Appl.Opt. 15, 2454 (1976)
- 16) W.Gruner,D.H.Hohn,H.Raidt. Atmospherische Transmission Report Ffo 1974/33
- 17) E.A.Barnhardt and J.L.Streete , Appl.Opt.9, 1337 (1970)
- 18) E.P.Shettle and R.W.Fenn - AGARD Conf.Proceedings No.183 on Optical Propagation in the Atmosphere - AGARD 1976 paper 2.
- 19) H.S.Stewart and R.F.Hopfield - Appl.Optics and Optical Engineering Kingslake ed.vol.1 Academic Press 1965 pagg.127-152
- 20) K.Fisher - Blitr.zur Phys.der Atm. 43, 244 (1970)
- 21) V.N.Aref'ev and V.I.Dianov-Klokov - Sov.J.Quant.Electron. 6, 499 (1976)
- 22) V.P.Bisyarina, I.P.Bisyarina e A.V.Sokolov - Radio Engineering and Electronic Physics 16, 1589 (1971)
- 23) A.V.Sokolov - Radio Engineering and Electronic Phys. 15 , 2175 (1970)
- 24) V.E.Zuev - in Laser Monitoring of the Atmosphere - ed.E.A. Hinkley - Springer Verlag, New York 1976 p.29
- 25) V.I.Tatarski : Wave Propagation in a Turbulent Medium McGraw-Hill Book Co.Inc. New York 1961
- 26) V.I.Tatarski : JETP 29, 1133 (1969)
- 27) W.Klyatskin : JETP 30, 520 (1970)
- 28) V.Klyatskin and V.Tatarski - JETP 31, 335 (1970)
- 29) E.Novikov , JETP 20, 1290 (1965) - K.Furutsu J.Res.Nat.Bur.Stand. 67D, 303 (1963)
- 30) M.Kallistrova and V.Pokasov - Radiophys.Quantum Electron.14, 940 (1971)
H.Raidt - AGARD Conf.Proceedings No.183 on Optical Propagation in the Atmosphere AGARD 1976 paper 21.
- 31) R.L.Fante : PIEEE 63, 1669 (1975)
- 32) R. Fante : J.Opt.Soc.Amer. 64, 592 (1974)
- 33) I.Starobinets - Radiophys.Quantum Electron. 15, 738 (1972)
V.Mironov,S.Khmelevstov - Radiophys.Quantum Electron. 15, 567 (1972)
- 34) M.Kallistrova and A.Kon - Radiophys.Quantum Electr.15, 545 (1972)
- 34a) J.R.Dunphy and J.R.Kerr - Appl.Opt.16, 1345 (1977)
- 35) D.Fried - PIEEE 55, 57 (1967)
- 36) H.Yura - Appl.Opt.11, 1399 (1972)
H.Yura - AGARD Conf.Proceedings No.183 on Optical Propagation in the Atmosphere AGARD 1976 paper 18.
- 37) T.Gilmartin and J.Holtz - Appl.Opt. 13, 1906 (1974)
- 38) A.Gurvich,N.Time,L.Turevtseva, V.Turchin - Izv.Akad.Sci.USSR Fiz.Atmos.Okeana 10, 484 (1974) (in russian)
- 39) H.Yura - J.Opt.Soc.Amer. 63, 567 (1973)
- 40) A.L.Buck - Appl.Opt.6, 703 (1967)
- 41) A.Ishimaru - Radio Sci. 4, 295 (1969)
- 42) R.Fante - J.Opt.Soc.Amer.62, 548 (1975)
- 43) M.Gracheva,A.Gurvich,S.Kashkarov,V.Pokasov - Aerospace Corp.Library Services, Translation LRO-73-T-28
- 44) R.Fante - J.Opt.Soc.Amer. 62, 608 (1975)
- 45) G.Homstad,J.Strohbehn,R.Berger,J.Heneghan - J.Opt.Soc.Amer.64, 162 (1977)
- 46) J.Kerr,J.Dunphy - J.Opt.Soc.Amer. 63, 1 (1973)

- 47) G.W.Reinhardt and S.A.Collins jr. - J.Opt.Soc.America 62, 1526 (1972)
H.Yura - J.Opt.Soc.Amer. 64, 357 (1974)
V.A.Banakh and V.L.Mironov - Sov.J.Quant.Electron. . 5, 1178 (1976)
- 48) S.Clifford - J.Opt.Soc.Amer. 61, 1285 (1971)
- 49) G.Reinhardt and S.Collins - J.Opt.Soc.Amer. 62, 1526 (1972)
- 50) N.Time - Radiophys.Quantum Electr. 14, 936 (1971)
- 51) J.Dunphy and J.Kerr - J.Opt.Soc.Amer. 63, 981 (1973)
- 52) A.Gurvich and V.Tatarski - Radio Sci. 10, 3 (1975)
- 53) P.Madics, R.Lee, A.Waterman - Radio Sci. 8, 185 (1973)
- 54) A.Gurvich, M.Kallistrova and N.Time - Radiophys.Quantum Electron. 11, 771 (1968)
J.W.Strohbehn, T.I.Wang, J.P.Speck - Radio Sci. 10, 59 (1975)
- 55) D.De Wolf - PIEEE 62, 1523 (1974)
- 56) K.Gochelashvii and V.Shishov - Opt.Acta 18, 313 (1971)
- 56a) A.Ishimaru - Appl.Opt. 16, 3190 (1977)
- 57) V.I.Tatarski - Propagation of waves in Turbulent Atmosphere (in russian) Moscow Nauka 1967
- 58) M.Bertolotti, M.Carnevale, L.Muzii and D.Sette - Appl.Opt. 7, 2246 (1968)
- 59) M.Bertolotti, M.Carnevale, L.Muzii and D.Sette - Appl.Opt. 9, 510 (1970)
- 60) P.Burlamacchi, A.Consortini, L.Ronchi - Alta Frequenza 38 - Special Issue on URSI Symposium on Electrom.Waves, Stresa Italy June 24-29, 1968 pag.149.
- 61) S.F.Clifford, G.M.B.Bouricius, C.R.Ochs, M.H.Ackley - J.Opt.Soc.Amer. 69, 1279 (1971)
- 62) G.M.B.Bouricius, S.F.Clifford - J.Opt.Soc.America 60, 1484 (1970)
- 63) P.Madics, R.Lee, A.Weterman - Radio Sci. 8, 185 (1973)
- 64) A.Gurvich, M.Kallistrova, N.Time - Radiophys.Quantum Electron. 11, 771 (1968)
- 65) T.Arsen'yan et al. - Radiophys.Quantum Electron. 15, 937 (1972)
- 66) J.N.Hayes - AGARD Conf.Proceedings n.183 on Optical Propagation in the Atmosphere paper n.29.
- 67) A.H.Aitken, J.N.Hayes, P.B.Ulrich - Appl.Opt. 12, 193 (1973)
- 68) AGARD Conference Proc.n.183 on Optical Propagation in the Atmosphere- AGARD 1976 Session IV.

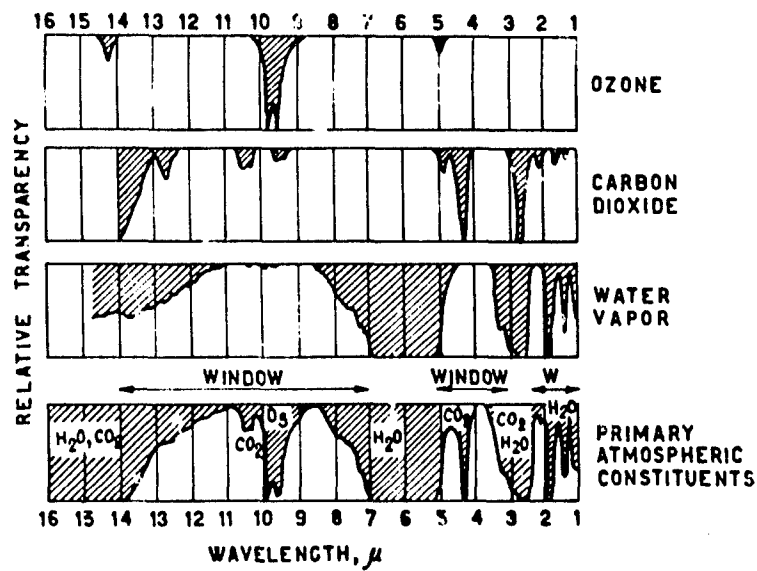


Figure 1

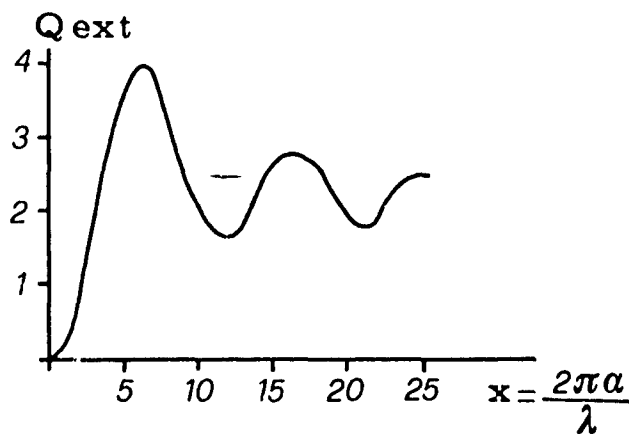
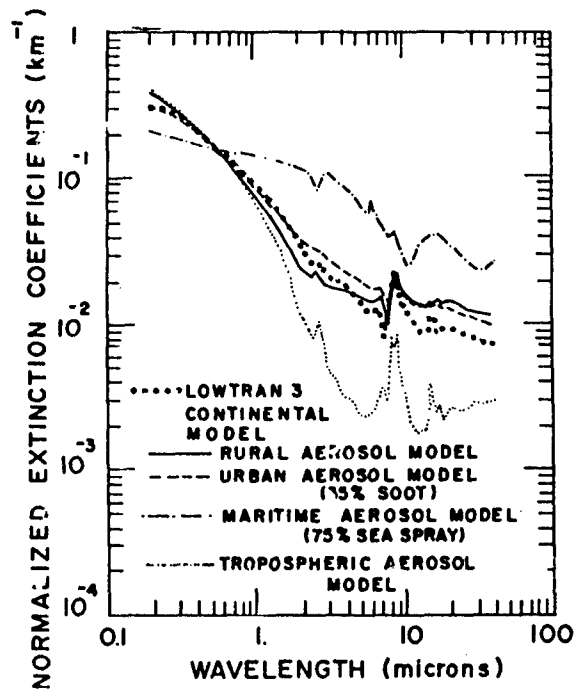
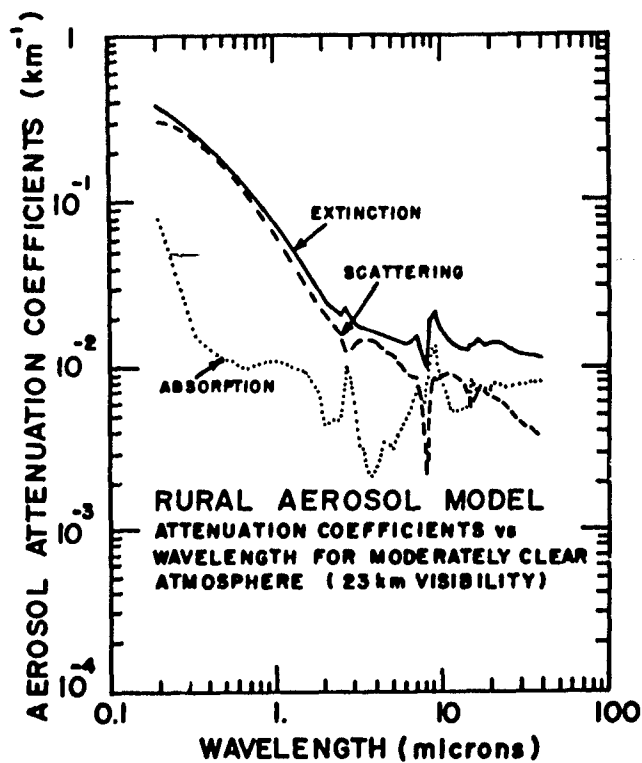


Figure 2



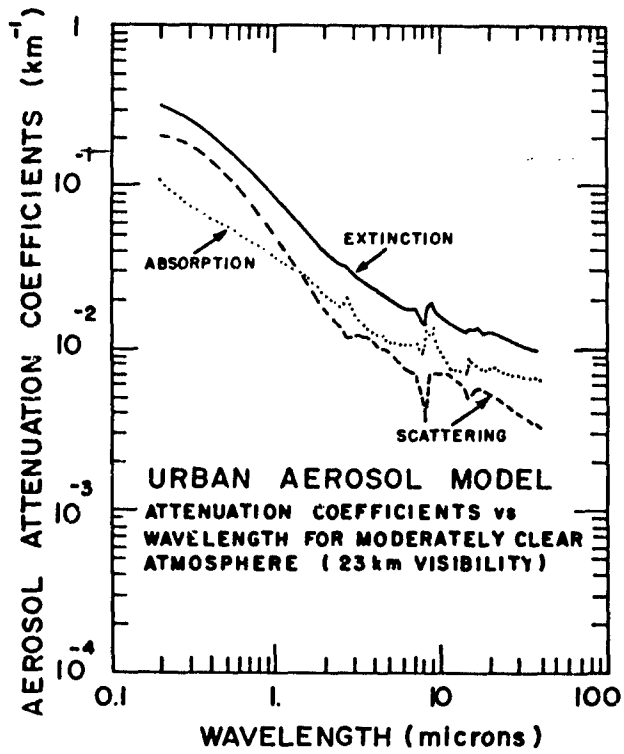
Extinction coefficients for the lower atmospheric aerosol models as a function of wavelength. The particle concentrations have been normalized so the extinction at 0.55 microns corresponds to a 23 km meteorological range, to facilitate a comparison of the wavelength dependence of the extinction for the different models.

Figure 3a



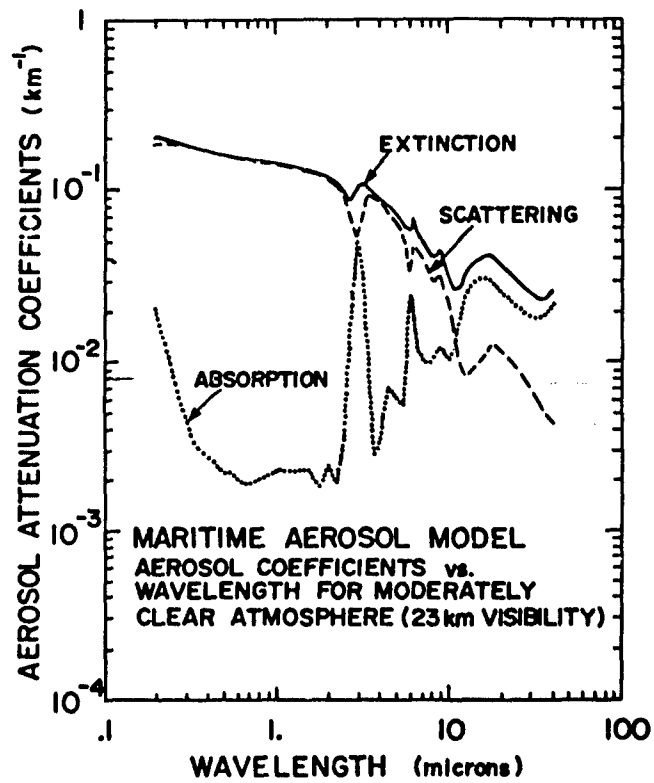
Scattering (dashed line), Absorption (dotted line) and Extinction (solid line) coefficients for the Rural Aerosol Model. As in Figure 3a the extinction coefficient is normalized to give a meteorological range of 23 km at 0.55 microns.

Figure 3b



Same as Fig.3b for the Urban Aerosol Model.

Figure 3c



Same as Fig.3b for the Maritime Aerosol Model.

Figure 3d

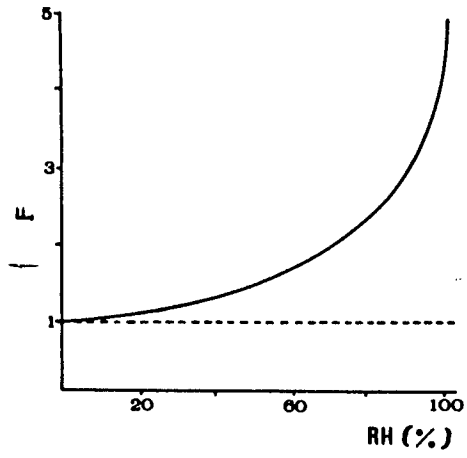


Figure 4

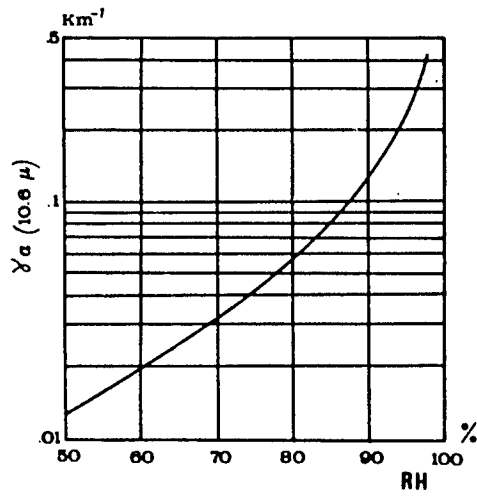


Figure 5

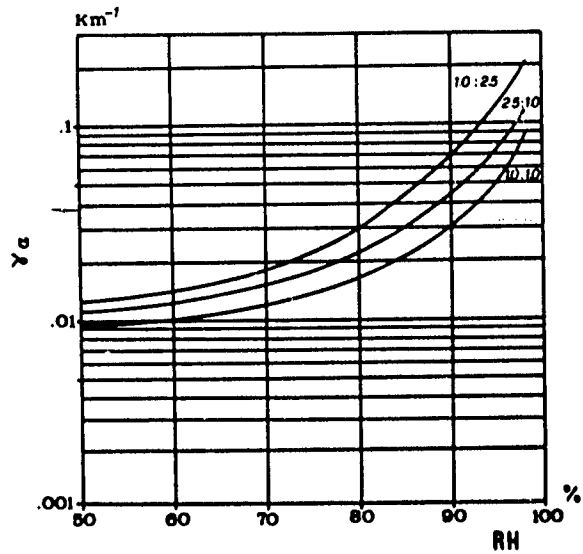


Figure 6

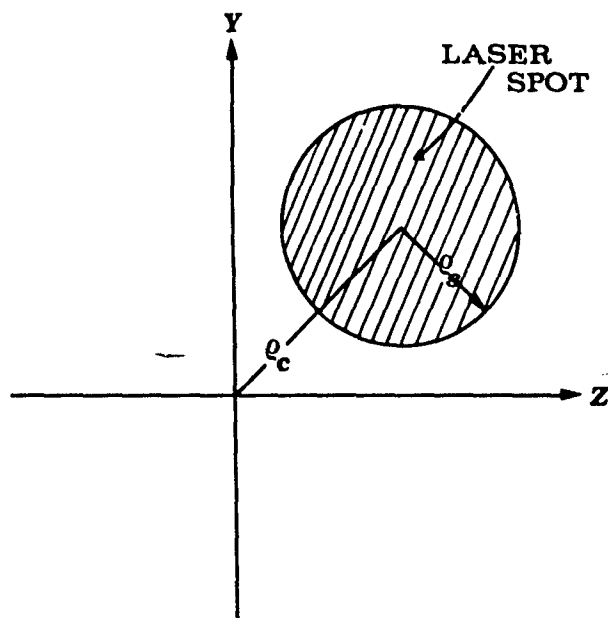


Figure 7

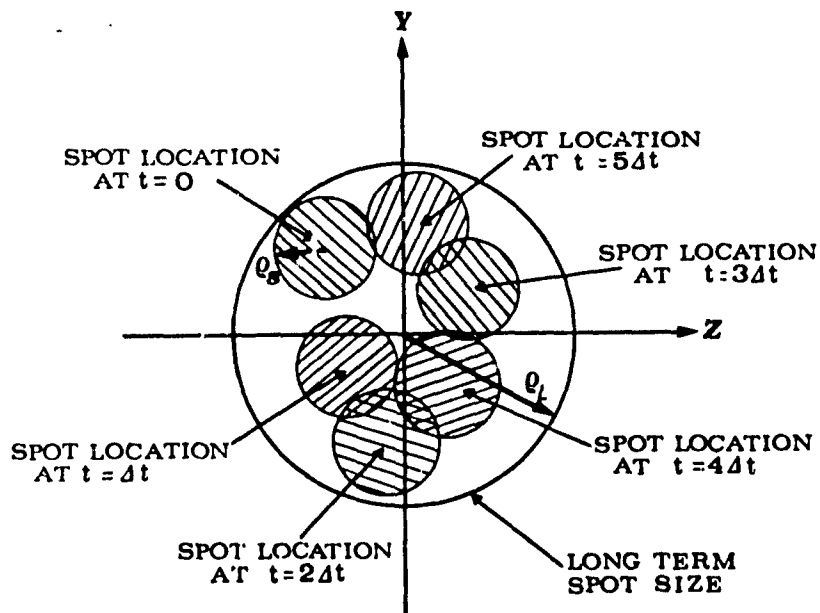


Figure 8

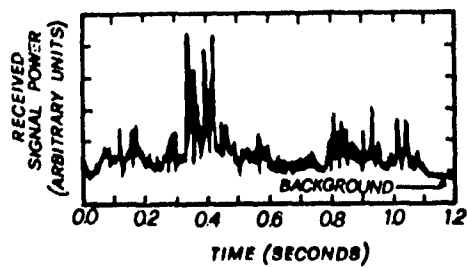


Figure 9

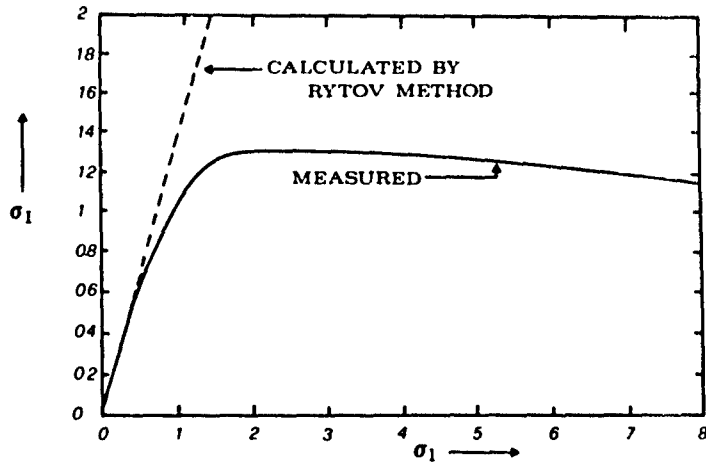


Figure 10

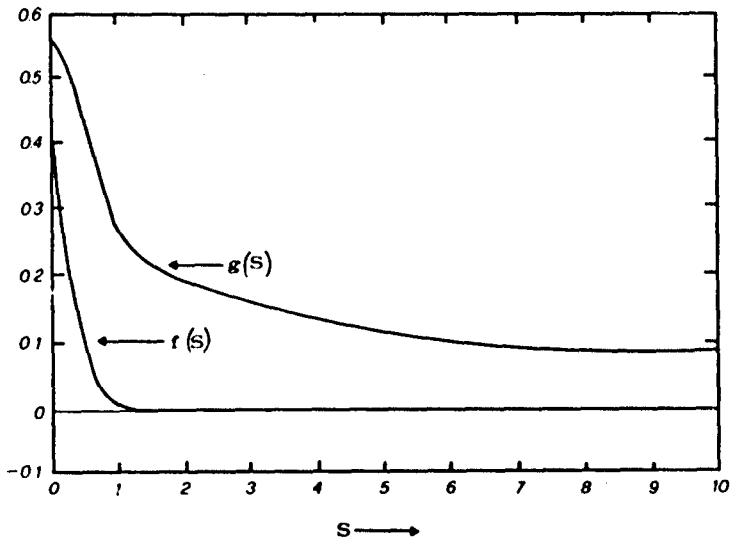


Figure 11

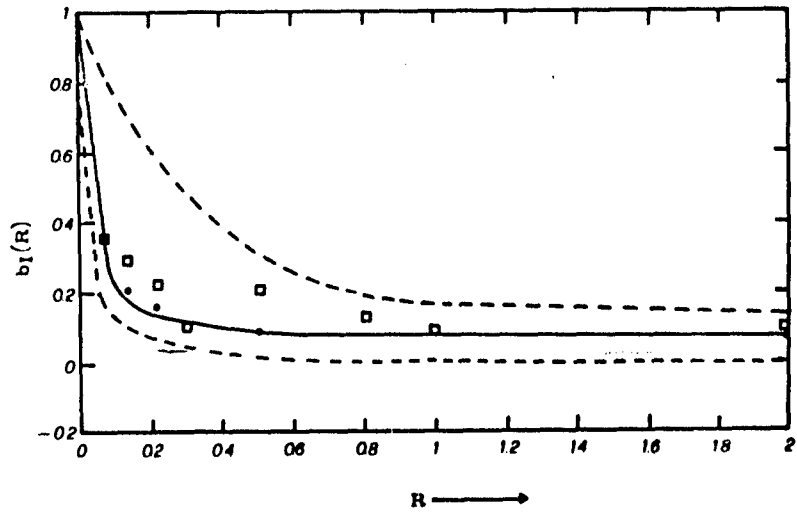


Figure 12

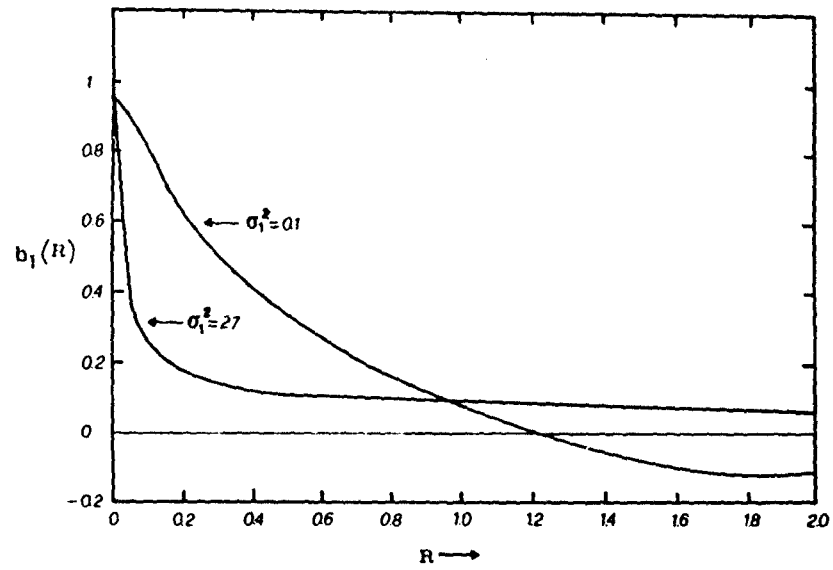


Figure 13

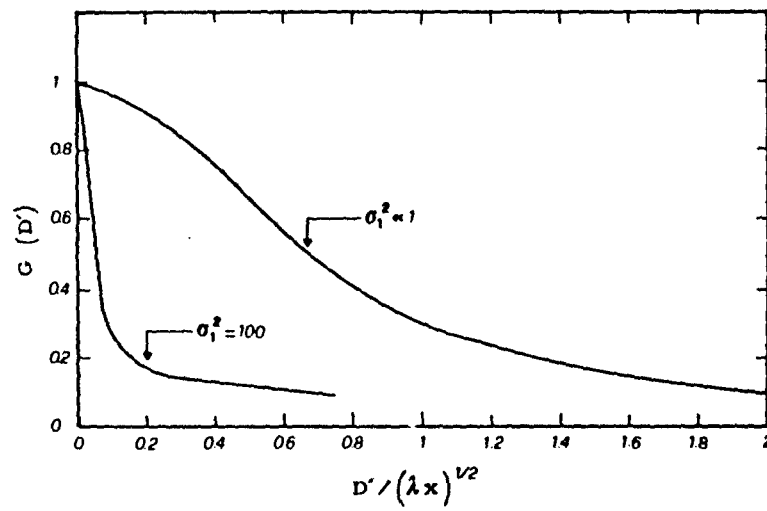


Figure 14

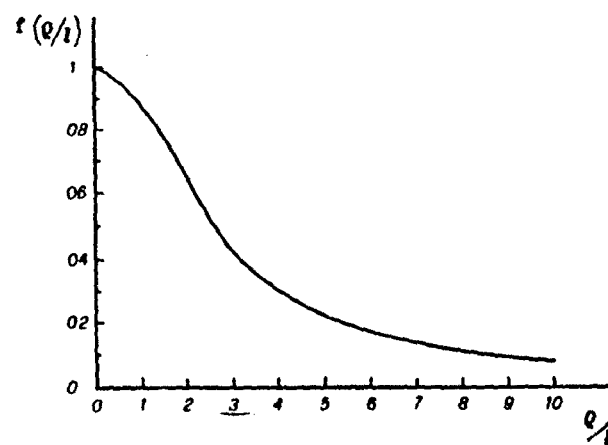


Figure 15

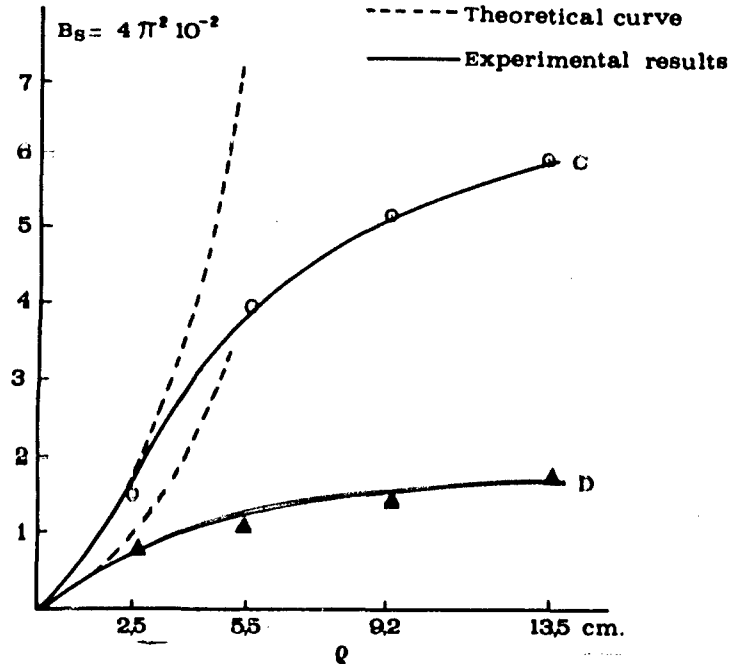


Figure 16

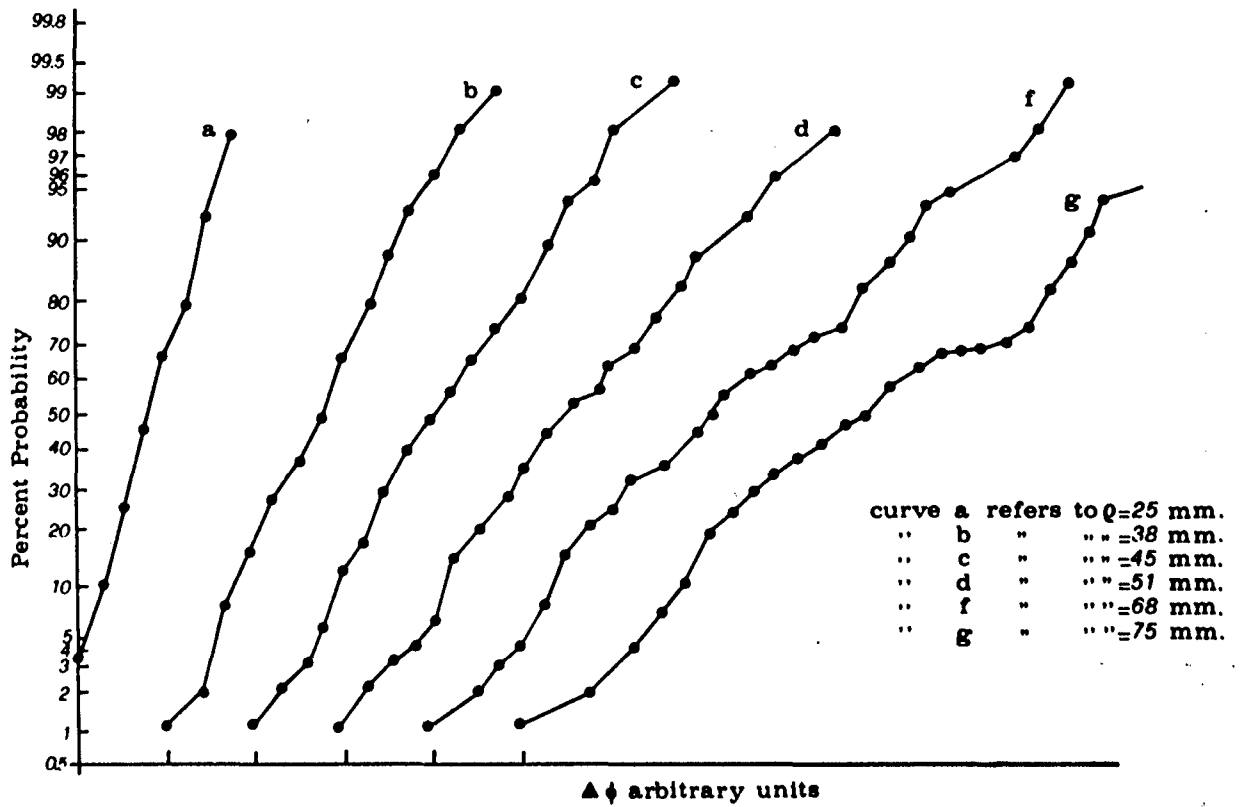


Figure 17

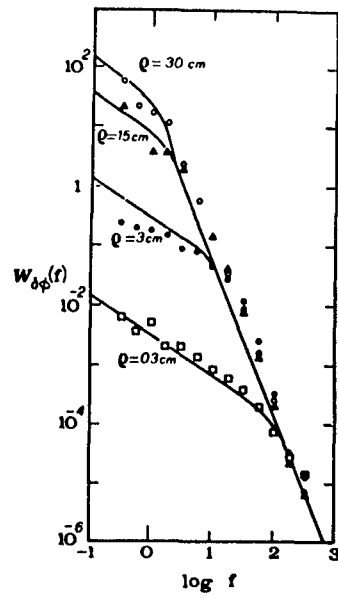


Figure 18

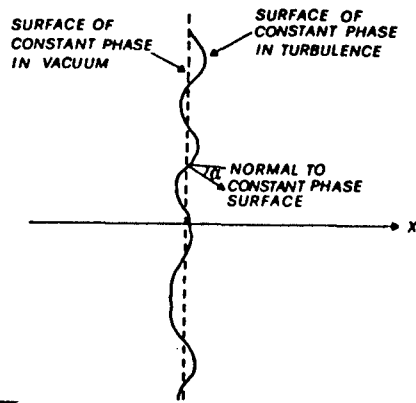


Figure 19

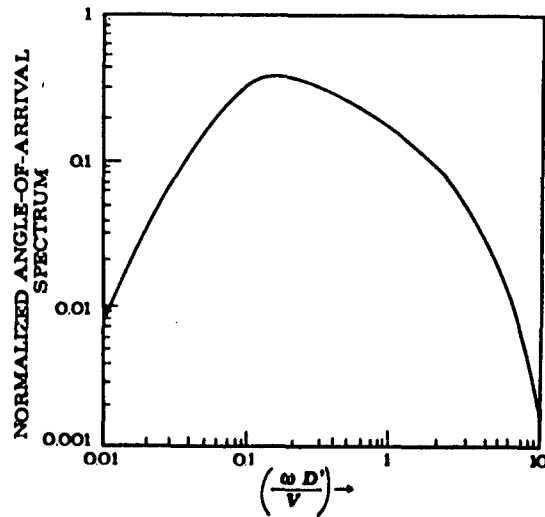
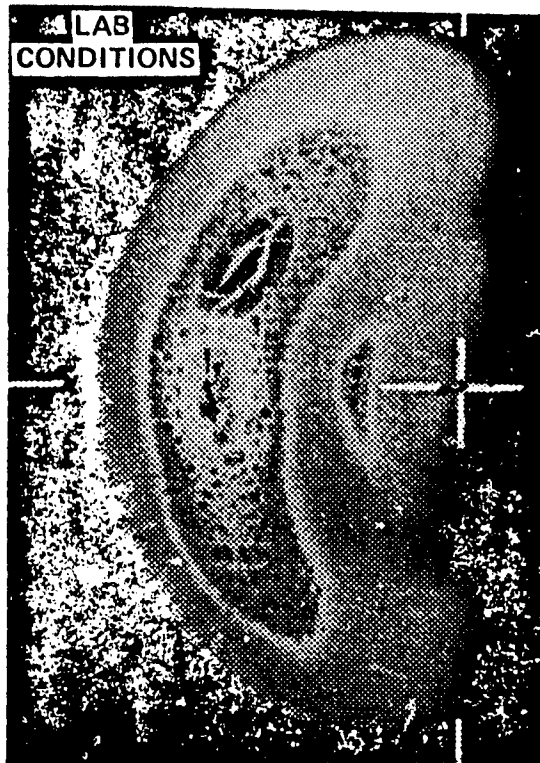


Figure 20

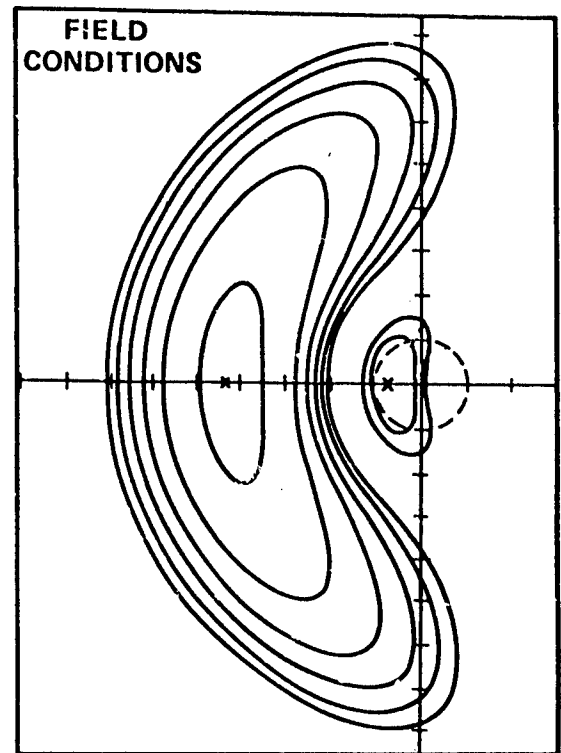
EXPERIMENT



1.2 mm

$N = 13$
 $F = 2.6$
 $N_a = 0.41$

THEORY



3.6 cm/div

$N = 16$
 $F = 2.8$
 $N_a = 0.134$

CW Steady State Thermal Blooming, one point comparison between experiment and theory. The left hand portion of the figure is a photograph showing the structure of a bloomed beam under the laboratory conditions indicated on the figure, while the right hand figure is an isoirradiance contour plot derived from theory. The comparison is not precise as can be seen by the difference in the corresponding dimensionless parameters, but close enough to show that quantitative prediction of CW steady state thermal blooming is reliable. (This figure is by courtesy of Dr. Fred Gebhardt, United Technology Research Laboratory and Dr. L.C. Bradley and Dr. J. Herrmann of Lincoln Laboratory.)

Figure 21

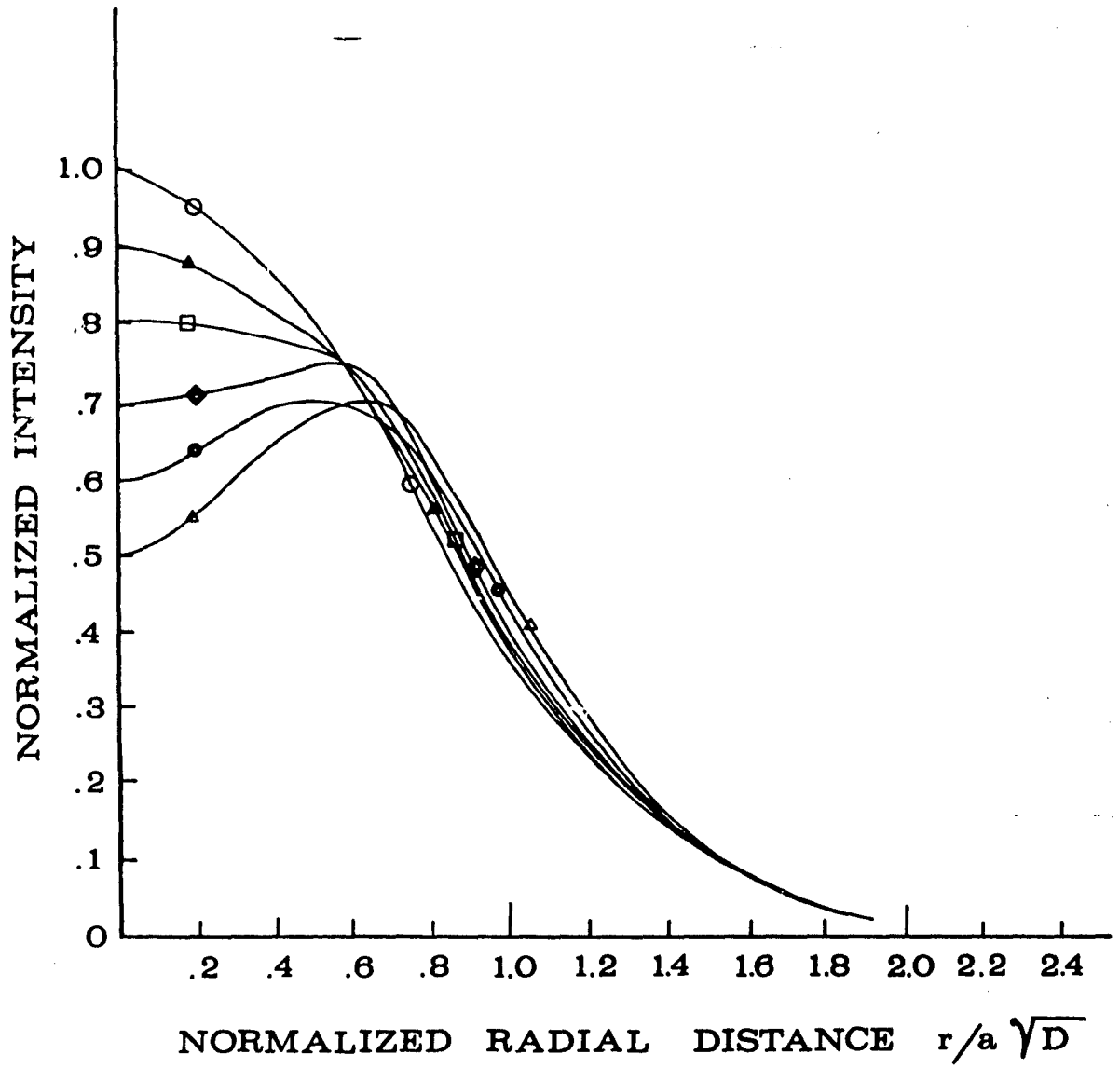


Figure 22

INTRODUCTION TO RADIO WAVE PROPAGATION EFFECTS ON SYSTEMS

Jules Aarons
 Space Physics Division
 Air Force Geophysics Laboratory
 Hanscom AFB, MA 01731

1. INTRODUCTION

The optimum path of electromagnetic waves is through a vacuum. Since Nature abhors a vacuum she introduced the earth's atmosphere - at least that is the way it must seem to engineers vexed with propagation problems. The atmosphere mainly hinders propagation - only in a few systems does it provide means for guiding the energy.

The two regions of interest to this study are the lower atmosphere, the meteorological region, and the ionized upper atmosphere, the latter ranging from 60 km to several thousand kilometers from the earth's surface.

The lower atmosphere is of importance in refraction and absorption processes at wavelengths below 3 cm at all angles of elevation. It is also of importance at all wavelengths at angles of elevation below 5°.

The ionosphere is used as a component of various systems from 10 KHz to 30 MHz; it has effects on radio wave propagation of major or minor significance at frequencies to 6 GHz.

2. THE IONOSPHERE AS A SYSTEM COMPONENT

2.1 ELF, VLF, LF.

The ionosphere is used as a tool for communications and navigation - as a system component. The electron layers at 60 km, the D layer, at 100 km, the E layer, and the highest layer, the F layer, form at various frequencies the components of a system.

Low frequency and very low frequency waves move from antenna to antenna along a guided path i.e., a waveguide mode with the upper wall the D layer, the bottom wall the earth's surface, and with gradients of electron density along the waveguide walls.

Applications of VLF signals are based on either the high potential of their phase stability (e.g., in radio navigation, in the distribution of standard frequency and time) or on their characteristic phase and amplitude behavior under the influence of disturbed boundary conditions in the earth-ionosphere waveguide (e.g., in monitoring solar particle and X-ray effects in the lower ionosphere and in locating underground discontinuities of electrical parameters such as ore deposits).

In systems where accurate position determination is important as in various LORAN C applications for accurate navigation, propagation over ground surfaces sets the system limitations. In addition there is a lack of knowledge of the morphology of the D region ion density and composition.

Normal high frequency communications in the range from 5 to 20 MHz utilize the F layer electron density, the portion of the ionosphere with maximum electron density. Signals are refracted at heights ranging from 100 km to 400 km depending on latitude, time of day, solar flux and other parameters.

Radio communications systems using the ionosphere in this manner depend on morphological models to forecast frequency channels. A model developed by the Institute of Telecommunication Sciences (Boulder, Colorado) from networks of ionosondes is the forecast tool of most groups with each user refining the model. The requirement is that the particular area is to be illuminated with radio energy. However the constraints of frequency utilization, of RF interference from other transmissions and of noise, man made and natural, may further limit the choice of frequency.

In systems where accurate position determination is important e.g., HF Direction Finding and HF Over the Horizon Radar the concept of the ionosphere as a horizontal stratified curved reflector comes into question as winds, waves, turbulence, instabilities and external electric fields can all deform the ionosphere to some extent and predictive models of these short lived phenomena are not available. However in this area various real time predictive methods are being used.

3. THE IONOSPHERE AS A NUISANCE

In the 1960's many new systems considered the ionosphere merely as an annoying degrading component not to be taken seriously. Radars were moved to the range above 400 MHz, where possible, to avoid ionospheric problems. Satellite communications services were placed in the 4 and 6 GHz region in part to avoid ionospheric problems and in part to avoid problems with the lower atmosphere. However, the advent of new radar systems requiring higher precision and more accurate target identification forced the reevaluation of the ionospheric time delay. The use of high data rates in satellite communication caused designers to deal with the loss of data bits by fading processes produced by ionospheric irregularities.

Satellite beacon transmissions from 20 MHz to 6 GHz have shown fading effects when signals traverse ionospheric irregularities with scales of 1 km or less. The regions of importance for this effect are the auroral region with some effects at polar and at

sub-auroral latitudes and the geomagnetic equatorial region ($\pm 20^\circ$).

The irregularities in the ionosphere effectively scatter, focus, and defocus the radio wave energy from satellites or reflected from targets beyond the ionosphere, increasing and decreasing signal level. The equatorial region produces the most intense effects with 3-4 dB peak to peak fades at 4 GHz noted. The high latitude region is most strongly affected during magnetic storms.

The fading produced by the intense small ionospheric irregularities must be a system design consideration in the frequency range 100-1600 MHz. At the higher frequencies an adequate signal margin will cause the system to ride out the fades. At frequencies from 100-600 MHz other methods are needed to mitigate the scintillation effects and to provide error-free operations.

Radio waves propagated through the earth's ionosphere suffer a time delay proportional to the number of free electrons in the medium through which the wave passes. A radar pulse for very accurate ranging must be corrected for the total electron content in its path. Thus the diurnal, latitudinal, and geomagnetic patterns must be studied and put into the form of models. In addition, new navigation systems such as the NAV/STAR Global Positioning System needs a correction model when only a single frequency receiver is used; with a simple model 50% of the error can be eliminated.

4. SOLAR EVENTS AND THEIR EFFECTS

Impulsive emissions of electromagnetic and particulate radiation by the sun cause direct and indirect effects on electromagnetic systems which operate in or through the near-earth space environment.

The frequency of occurrence of impulsive solar events and the intensity of these events is correlated, to some extent, with the 11-year cycle of solar activity. While the general modulation of the frequency of impulsive events can be approximately predicted, detailed forecasting depends on the capability to judge whether a particular region of solar activity will become the site of a solar flare that will emit a burst of X-rays, radio waves or energetic particles, and when the flare is most likely to occur. This judgement can be made only approximately. In 1977 the level of solar activity was increasing, and is expected to reach maximum levels in 1979-1980.

Four important phenomena generally result from any particular impulsive solar event: a burst of X-rays and EUV (extreme ultraviolet) radiation, a burst of radio noise, emission of energetic particles, and emission of a plasma blast wave. The effects of each of these are described below.

X-ray and radio bursts are the very first signatures of a solar event and serve as useful indicators for forecasters. The radio noise burst may directly affect radar and communications systems; thus, operators of these systems need to know whether an increase in noise is associated with a solar event in progress, a system malfunction or jamming by unfriendly forces. X-ray and EUV bursts of solar origin will, in general, change the properties of the ionosphere and may cause phenomena such as fadeouts on HF communications links. The rise time of these bursts is on the order of minutes; the typical duration may be of the order of an hour. Forecasting before the imminent occurrence of X-ray or radio bursts depends on relatively subjective interpretation by experienced observers of the configuration of solar magnetic fields in solar active regions and a knowledge of the past behavior of a particular region. Warning of the effects after an event has started has recently become a forecasting accomplishment primarily through recognizing solar radio burst characteristics.

Solar particle events are impulsive emissions of energetic protons (and heavier particles) and electrons from the sun, occurring in association with solar flares. These energetic particles propagate through interplanetary space at very high speed; the most energetic reach the earth in times as short as 20-30 minutes after their generation. An energetic solar particle event, as observed at the earth, may last for many hours or several days.

Solar particles are sufficiently energetic to penetrate to the D-layer of the polar ionosphere and cause additional ionization there. This phenomenon is called Polar Cap Absorption (PCA). Thus, in addition to direct effects on space systems, solar particle events also affect the propagation of electromagnetic waves through the polar ionosphere.

The typical large solar event which generates X-rays, radio noise and energetic particles also sends out a blast of solar plasma into the interplanetary medium. A shock wave associated with this cloud reaches the earth's orbit in three or four days and results in a geomagnetic storm and disturbances in the polar ionosphere, aurorae, and heating of the neutral atmosphere. Ionospheric disturbances may affect the propagation of HF in polar regions and cause increases in scintillations; changes in the properties of the aurorae may give rise to enhanced optical background.

5. TROPOSPHERIC EFFECTS ON MICROWAVE SYSTEMS

Tropospheric propagation variability affects the performance of microwave radar and communications systems. Forecasting can warn of unusual propagation and ameliorating actions can be taken; for the system user the knowledge of deficiencies in propagation during certain periods, the existence of holes in coverage or of false targets is of importance.

5.1 Effects on Systems.

The lower atmosphere does refract radio waves. When the path length is long i.e.,

at low angle of elevation, the refractive structure can bend or delay radio waves. If the refractive index decreased with altitude smoothly, exponentially or linearly, and if the atmosphere were horizontally homogeneous, refraction effects could be calculated and taken into account by the system. The real atmosphere contains both vertical and horizontal gradients which produce serious problems.

The two phenomena of importance are large vertical gradients near the earth's surface (surface ducts) and similar large gradients over small height intervals at altitudes to 15,000 feet, the elevated layers. The most serious effects are in situations where the transmission paths are nearly horizontal or where the path terminals or the radar and its target are at the altitude of the layer.

5.2 Effects on Radars.

With radars looking out over the sea at low elevation angles, effects appear in the following ways: echoes appear where they should not and targets that should have been observed fail to appear. With enough knowledge of the refractive structure (refractometers in aircraft for example) performance could have been explained. Tests have shown that radiosonde measurements overhead of the radar can be used but the horizontal variability of meteorological conditions makes this method of limited utility.

Serious degrading can be produced by unusual gradients or ducting. Within a given surveillance volume of a radar, performance can be seriously degraded with little or no warning to the operator. These radar "holes" are regions where performance is below normal due to defocusing.

Although the accuracy of meteorological forecasts has been considerably improved in recent years by computer technology, spaceborne measurements etc., the resulting warnings of nonstandard propagation are still disappointingly crude. The intensity of the departure from normal conditions, the time duration, and the precise spatial distribution of the affected regions is not at present accurately predictable.

Due to the computer processing of radar echoes the use of other methods of correcting for tropospheric effects has been decreased. It is possible for example to use radar meteorological information for correction of angular errors by the programming of the processing of radar tracks is just starting to be able to handle such information.

5.3 Troposcatter Communications.

The increasing use of satellite communications will lessen the importance of troposcatter systems. However, in a military climate a diversity of communications channels is needed.

Unusual atmospheric profiles can degrade troposcatter communications to an extent which depends on the path length and the vagaries of the geographical conditions of the path. The loss in performance is almost never complete and the duration of poor performance rarely exceeds a few hours. However it is helpful for the tropocircuit operators to know when degradation is to be expected so that operating bandwidth can be reduced. Satellite cloud photography may very well provide the basis of a future system to warn operators of degrading meteorological conditions.

5.4 Precision Tracking of Targets.

Tracking errors multiply very rapidly as the line of sight to the target approaches the horizon. The development of laser tracking technology has reduced the importance of its radar counterpart in situations where all-weather operation is not a requirement.

6.0 IN SITU TECHNIQUES

Table I lists for convenient reference the in situ methods used for measuring atmospheric refraction. There are many variations to each instrumentation method. The following describes the basic features, advantages, and limitations of these measurement means.

TABLE I
IN SITU MEASUREMENTS

Technique	Parameter(s) Measured	Remarks
Radiosonde	Temperature Pressure Humidity	Each parameter measured separately. Radio refractivity must be calculated.
Refractometer	Refractivity	Measures refractivity directly.
Humidiometer	Water Vapor Density	Temperature and pressure must be measured independently. Refractivity must be calculated but humidity is its most important constituent.

Radiosondes are the most widely used instruments for obtaining information on the atmosphere as a function of height. Weather stations throughout the world launch radiosondes daily (usually at 0000 and 1200 UT). These data have been valuable for describing the average properties of atmospheric refraction on a global scale. Table II lists techniques of measuring tropospheric parameters from ground or airborne platforms; Table III from satellites.

7.0 SUMMARY

I have tried to provide a background for current interest in radio wave propagation. More demands are placed on communication systems for reliability and for message expansion. Greater accuracy is demanded from navigation and detection systems. These newer needs have caused propagation specialists to intensify studies in the areas indicated.

8.0 ACKNOWLEDGEMENT

The author acknowledges the extensive use of introductory and explanatory material from reports of the USAF Scientific Advisory Board.

TABLE II
REMOTE PROBING - GROUND-BASED OR AIRBORNE MEASUREMENTS

Technique	Parameters Affecting Measurement	Remarks
Acoustic Sounding	Temperature and wind inhomogeneities.	Vertical backscatter sounders measure regions of temperature inhomogeneities associated with stratification and convective processes. Forward or bistatic sounders can be used to measure wind. Acoustic sounders are useful for profiles within first km of the atmosphere.
Radio Acoustic	Temperature profiles.	Accurately measures temperature profile. Potential application to measuring winds, useful for profiles within first few km.
FM-CM Radar	Refractive inhomogeneities associated with stratification and convective processes. Rain	Does not measure the atmospheric refractivity. Useful within the first km of the atmosphere for studies of in-cloud distribution of rain. High range resolution (~1 m).
Radar (high power)	Refractive inhomogeneities associated with stratification and convective processes. Rain.	Does not measure refractivity. Useful for probing the atmosphere at extended ranges of several tens of kilometers.
Radiometer	Temperature Profiles. Atmospheric refraction.	Temperature profiles have limited spatial resolution. Provides a measure of the integrated refractivity. Multi-wavelength optical radiometers provide a coarse measure of the water vapor content.
Lidar	Particulate concentration. Temperature.	Conventional Rayleigh backscatter is used to measure particulate concentration - well developed. Some relation between particulate concentration and refractivity. Raman scattering can be used to measure temperature and humidity profiles. Differential absorption techniques can potentially measure water vapor content.
Transmission Probing	Atmospheric refraction. Winds.	Effective for probing large regions. Can be used by airborne or ground systems. Transmitters can be sources of opportunity or specially configured for particular applications. Beyond-the-horizon transmission techniques are particularly effective in defining regions of atmospheric stratification.

TABLE III
REMOTE PROBING - SATELLITE METHODS

Technique	Measurement	Remarks
Cloud Cover	Optical and IR. Photography to delineate cloud patterns and heights	High spatial resolution over large portions of the earth. Define basic air mass and cloud pattern distributions over large portions of the earth.
Radiometer	Integrated water content. Winds over oceans. Regions of precipitation. Surface temperature.	Present radiometer methods have a coarse height resolution and limited use in the measurement of atmospheric refractivity near the earth's surface.
Transmission (RF)	Total refraction. Multifading from atmospheric layers.	Beacons could be used to provide information on atmospheric refraction and ducting environment. Occultation measurements could be developed.
Satellite of Opportunity	Measure atmospheric refraction from ground-based radar.	With known satellite ephemeris data, radars can track satellites for diagnostic tests on the radar and provide a measure of atmospheric refraction.

HIGH FREQUENCY RADIOWAVE PROPAGATION IN THE IONOSPHERE

by

T.B. Jones
 Physics Department
 University of Leicester
 Leicester, U.K.

1. Basic Concepts1.1 The Ionosphere

Above about 60 km, layers of free electrons form in the upper atmosphere due to the ionizing action of incoming solar radiations and particles. These ionized layers can reflect HF radiowaves and their physical characteristics will greatly influence the propagation parameters for any HF circuit^{1,2}.

The distribution of electron density with height in the ionosphere varies with time of day, season and geographical location. However three basic regions can be identified as indicated in Figure 1. In the lowest layer (D-region) the electron density is insufficient to reflect HF waves and they penetrate the region to be reflected at higher levels. Considerable attenuation of the waves takes place in the D-region as a result of the high values of electron collision frequency at these low heights. Both E- and F-layers reflect HF waves and play an important role in the propagation of these waves to great distances. It should be noted that in summer the F-region subdivides into F₁ and F₂ layers.

The features of the ionospheric layers can be determined by a radar technique¹ in which the time of flight (t) of a radio pulse reflected in the ionosphere is measured. For ionosphere studies, the pulses are transmitted vertically into the ionosphere and the transmitter and receiver are co-located. If the pulse is assumed to travel with the free space velocity (c) the equivalent path P' can be written

$$P' = 2h' = ct \quad \dots (1)$$

where h' is the equivalent height of reflection assumed to be equal to P'/2 at vertical incidence.

In practice the frequency of the sounding wave is varied and the resulting changes of h' with frequency are displayed in the form of an ionogram. An example of a mid-latitude vertical incidence ionogram showing E- and F-layer reflections is reproduced in Figure 2. Due to the influence of the earth's magnetic field the ionosphere is birefracting and two echo returns are obtained for a given frequency, corresponding to the ordinary (O) and extraordinary (X) modes of propagation. Both O and X components are visible in Figure 2. The frequency at which the sounding wave penetrates the layer is called the critical frequency. Thus we have two critical frequencies for each layer (e.g. f_{0E}, f_{XE} and f_{0F} and f_{XF}) corresponding to the two magneto-ionic modes of propagation.

For practical purposes we must turn our attention to propagation at oblique incidence, bearing in mind the basic concepts of reflecting layers introduced above.

1.2 Reflection at Oblique Incidence

Suppose for simplicity that the ground and the ionosphere are plane and parallel. Furthermore, consider the ionosphere to consist of a number of slabs of constant electron density, the density increasing from slab to slab with increasing height (Figure 3). Snell's Law can be applied at the boundary between each slab. Thus

$$\mu_0 \sin \phi_0 = \mu_1 \sin \phi_1 = \dots = \mu_n \sin \phi_n \quad \dots (2)$$

If the refractive index μ_n becomes sufficiently small, ϕ_n will approach 90° and total reflection will occur at the point of grazing incidence.

The refractive index outside the ionosphere μ_0 is unity and ϕ_0 is the initial angle of incidence. Hence

$$\begin{aligned} 1 \cdot \sin \phi_0 &= \mu_n \sin 90 \\ \sin \phi_0 &= \mu_n \end{aligned} \quad \dots (3)$$

The refractive index of the ordinary wave component is given by

$$\mu^2 = 1 - \left[\frac{f_N}{f} \right]^2 \quad \dots (4)$$

where f is the wave frequency and f_N the plasma frequency. At vertical incidence the reflection condition becomes f = f_N and we will write f = f_v to represent the vertically incident frequency reflected at the level where the plasma frequency = f_N.

For the oblique case we have, by substitution into equation (3),

$$\begin{aligned} \sin^2 \phi_0 &= 1 - \left[\frac{f_N}{f} \right]^2 = 1 - \left[\frac{f_v}{f} \right]^2 \\ f &= f_v \sec \phi_0 \end{aligned} \quad \dots (5)$$

Thus a frequency f incident at an angle ϕ_0 will be reflected from the same electron density (true height) as the equivalent vertical incidence frequency $f_v = f \cos \phi_0$; hence a given ionospheric layer will always reflect higher frequencies at oblique incidence than at vertical incidence.

Two other important relationships should be noted in connection with oblique propagation. Breit and Tuve's theorem³ states that the group (or equivalent) path P' between a transmitter T and receiver R is given by the length of the equivalent triangle TAR (see Fig. 4). The second theorem due to Martyn⁴ states that the virtual height of reflection of an obliquely incident wave is the same as that of an equivalent vertical wave, i.e.

$$P'(f) = 2h'(f_v \sec \phi_0) \quad \dots (6)$$

No formal proof of these relationships is given here as they may readily be found in the literature (e.g. Davies²).

1.3 Calculation of Maximum Frequencies

The theorems of Breit and Tuve and of Martyn indicate that for a plane ionosphere the reflection process can be represented by a mirror-like reflection at a height equal to the virtual height h' of reflection of the equivalent vertical frequency.

The variation of h' with frequency is obtained from a conventional vertical-incidence ionogram. The relationship between oblique and equivalent vertical frequencies for a plane reflector (see Fig. 4) at height h' is given by

$$f_{\text{oblique}} = f_v \sec \phi_0 = f_v \sqrt{1 + \left[\frac{D}{2h'} \right]^2} \quad \dots (7)$$

To determine f_{oblique} for a given f_v , we require h' as a function of frequency from an ionogram and the relationship between $\sec \phi_0$ and h' and D. This information can be presented graphically in the form of a transmission curve⁵ (shown in Fig. 5) which represents a graphical solution for the two conditions above. The intersection of the transmission curve with the ionogram gives the equivalent reflection heights for that frequency over the oblique path of length D. Thus the oblique ionogram can be built up as indicated in Figure 5. It should be noted that higher frequencies can be propagated at oblique incidence and that the highest frequency possible does not correspond to the layer-critical frequency. The oblique ionogram has two branches which move together joining at the highest frequency which can be reflected obliquely. Frequencies below this "junction frequency" can be propagated via two paths and are termed the high- and low-angle ray, respectively.

The junction frequency is the highest frequency which is propagated by specular reflection over the distance D. For shorter distances it will penetrate the layer, hence D is known as "skip distance" which is the shortest range at which reception of this frequency is possible. The skip distance will increase with increasing frequency.

For a fixed frequency the paths of rays leaving the transmitter are shown in Figure 6. For low angles of propagation, path (1) is long and the range is large. As elevation angle increases, range decreases (2) until the skip distance is reached (3). For still higher angles of elevation the range increases rapidly (4 and 5) and eventually penetration occurs (6). The small bundle of rays between the skip ray and the penetrating ray is dispersed over a great range. Although the signal strengths are very low, workable signals can be received over high angle paths.

For a curved earth and curved ionosphere the equivalence theorems are no longer valid. $\sec \phi_0$ depends not only on h' and D but also on the electron density distribution and will therefore differ as the ionosphere changes (e.g. with time of day). The expressions to determine $\sec \phi_0$ become complicated and for most purposes it is sufficiently accurate to introduce a correction factor k so that the secant law becomes⁶

$$f_{\text{oblique}} = k f_v \sec \phi_0.$$

1.4 Multi-Path Propagation

So far we have considered a single-hop reflection from one reflecting layer. In general, reflections can occur from both E- and F-layers and signals are often propagated via multiple hops. Hence the propagation path may involve

- a) Multiple-hop propagation
- b) Multiple-layer propagation
- c) Low- and high-angle rays
- d) Both ordinary and extraordinary magneto-ionic components.

The possibility of multiple-path propagation greatly influences the quality of HF reception. Since each mode is received over a different path, mutual interference will take place. Moreover the fading rate, absorption loss and group delays will be different for the various paths which combine at the receiver to form the total signal. Thus considerable distortion of the transmitted information is likely under multi-path conditions.

The active modes of propagation for a given circuit can be determined experimentally when oblique sounding facilities are available over the path; alternatively the modes can be determined using transmission curves in conjunction with a vertical-incidence ionogram. In addition, there are prediction methods involving ionospheric models and these techniques are discussed in another lecture of this series.

1.5 MUF and LUF

For a given separation between transmitter and receiver and a particular ionospheric electron density profile, only waves within a certain range of frequency will reach the receiver. The high-frequency limit is apparently determined by penetration of the waves through the ionosphere whereas the low-frequency limit is determined by the increase in absorption as the transmitted frequency decreases. These limits are referred to as the Maximum Usable Frequency (MUF) and Lowest Usable Frequency (LUF), respectively^{2,6}.

Inspection of Figure 5 suggests that the junction frequency corresponds to the path MUF for a single-hop path. There are occasions, however, notably in summer, when the F-region divides into two separate layers (F₁ and F₂), when the MUF corresponds to the junction frequency of the lower layer (smaller critical frequency) rather than to that of the layer with the highest critical frequency. This situation is illustrated in Figure 7. A similar situation can arise during the presence of enhancements in the E-layer, known as sporadic-E conditions.

In practice the MUF is not a sharp limit and propagation is often possible on frequencies greater than the classical MUF. The Maximum Operational Frequency (MOF) may be appreciably higher than the MUF. This extension arises since neither the ground nor the ionosphere are smooth reflectors, as assumed in the simplified theory. Scattering from irregularities will therefore allow signals to propagate to distances beyond the limit of the refracted wave. Ionospheric tilts can also play an important role in extending the operational frequency above the MUF.

The absorption (L) of a radiowave in the ionosphere increases as the wave frequency decreases since

$$L \propto \frac{1}{f^2} \quad \dots (7)$$

when the wave frequency f exceeds the electron gyrofrequency. The sensitivity of a receiver is usually limited by external noise which increases as the frequency is reduced. Thus there is a frequency limit below which the signal-to-noise ratio exceeds the acceptable value for the service required. The Lowest Usable Frequency is termed the LUF and is to some extent dependent on the engineering characteristics of the system (e.g. transmitter power).

The optimum working frequency, or the Frequency for Optimum Transmission (FOT), is usually found to be close to the MUF and is empirically fixed at 0.85 of the monthly median value of the MUF. Other factors, such as the sensitivity of the circuit to multi-path interference, will also govern the choice of the FOT.

It should be noted that in addition to absorption limitations the signal can lose energy after it has been transmitted by several other mechanisms such as those listed below:

- a) Spatial spreading of the energy
- b) Polarization changes due to the magneto-ionic nature of the propagation medium
- c) Curvature of the ionosphere leading to focussing and defocussing
- d) Scatter processes.

These processes complicate the evaluation of the expected performance of an HF circuit.

2. Scatter Propagation

2.1 Ground Scatter

Both the ground and the ionosphere are not smooth reflectors since they contain irregularities of many kinds. According to Rayleigh's criterion a surface cannot be regarded as smooth if it has irregularities which are greater than $1/25$ of a wavelength. In addition to the specularly reflected wave, which decreases in energy with increasing roughness, some of the incident energy is scattered in all directions.

A ground scatter situation is illustrated in Figure 8. After reflection in the ionosphere at B, the wave is incident on the ground at R, where it is specularly reflected and continues to propagate to greater distances. A small fraction of the wave energy at R (about 1% for average ground conditions) is scattered into a solid angle of 2π . A small fraction of this signal will travel back along the original propagation path to the transmitter site^{8,9}. A receiver co-located with the transmitter can then detect this energy which has a travel time of twice the group path TAR. The scatter with the minimum time delay will come from the near edge of the skip distance. If the transmitted frequency is increased, the skip distance increases and consequently the time delay of the backscatter increases. For frequencies close to the layer-critical frequency (zero skip distance) the backscatter returns merge into the two-hop vertical-incidence trace on an ionogram-type display (see Fig. 9). This figure shows that the returned energy is concentrated into a rather limited path range and returns from all distances greater than the skip are not observed. This feature is due to the focussing effect which occurs at the skip distance, returns from greater ranges being too weak to register on the display¹⁰. The backscatter is characterised by rather rapid fading due to the interaction of many waves returned from various parts of the ground along slightly different paths. Changes in the ionosphere produce different phase variations in these paths which result in mutual interference at the receiver and so reduce the "quality" of the signal.

Reception within the skip distance can occur via backscatter modes. If the distance between the transmitter and receiver (T and R in Fig. 10) is less than the skip distance, no reception via a specular path is possible. Signals can be received at R, however, which are scattered outside the skip around the transmitter which also lies outside the receiver skip area (shaded area in Fig. 10)⁶.

The backscatter process enables signals to be received from the ground over the curvature of the earth's surface. It is thus possible to illuminate an area for radar purposes well beyond the limit of conventional line-of-site radars. Information can be obtained regarding the terrain and other reflecting objects. When the Doppler frequency of the returned signals is processed some information regarding target movement can be obtained.

Backscatter sounding can be used to determine the characteristics of the ionosphere at points remote from the transmitter and receiver. This is important when ionospheric characteristics are to be measured at locations inaccessible to vertical-incidence sounders (e.g. mid ocean). From this information the MUF and FOT can be determined for point-to-point transmissions which are reflected in the remote region of the ionosphere.

An interesting application of backscatter radar is found in sea surface studies¹¹. The long ocean swells produce a diffraction grating effect which gives rise to Bragg reflection of the incident wave. By measuring the time delay and Doppler shifts of the scattered signals, detailed information regarding the sea state and the magnitude, speed and direction of the dominant waves can be obtained.

2.2 Ionospheric Scatter

The ionosphere has so far been considered to be a perfectly smooth reflector. This is not the case in practice since many types of disturbance can occur which distort the iso-ionic contours. Thus true specular reflection seldom occurs and some scattering of the incident wave energy takes place. Frequently the F-layer ionization becomes very disturbed and many field-aligned irregularities are produced in the electron density. During these conditions, known as spread F, strong scattering of the signal can occur. This produces rapid fading due to the mutual interference of waves propagating over the various scattered paths. These effects are particularly marked at equatorial latitudes where Spread-F conditions frequently occur. Very high fading rates, known as "flutter fading" are produced by low-latitude Spread F¹².

HF waves can also be scattered from the lower ionosphere when meteor showers are present. The meteors produce long trails of overdense ionization in the height range 80 - 100 km. These are strong scatterers of radio waves and operational communication systems have been developed using meteor forward scatter¹³.

3. Ray Tracing

3.1 Basic Concepts

In sections 1 and 2 the propagation characteristics of the wave between transmitter and receiver have been dealt with from an experimental standpoint. Frequently expensive sounding techniques are not available and some method of calculating the propagation parameters is required. If a model of the electron density height distribution is known, or can be derived say from vertical-incidence ionograms, then the trajectory of the ray through the ionosphere can be determined. This procedure is known as ray tracing¹⁴. The simplest form of ray tracing has already been referred to in section 1 where the ionosphere was represented by a series of horizontal slabs of ionization and Snell's Law was applied to determine the ray path, as illustrated in Figure 3. This approach is clearly oversimplified since no account is taken of factors such as the curvature of the earth and the ionosphere, the influence of the earth's magnetic field and the effect of electron collisions. In modern ray-tracing analysis all these factors are included and the appropriate equations are solved numerically in a high-speed computer to yield the ray trajectory given the launch angle in azimuth and elevation. Calculation of the parameters such as attenuation, polarization, relative phase and time of flight are generally included in these analyses. It is often difficult to find rays which connect specific transmitter and receiver locations and frequently rays are determined for a range of launch angles until one is found that produces the required range and direction.

3.2 Ray-Tracing Techniques

3.2.1 No magnetic field

If the influence of the earth's magnetic field is neglected the ray path can be determined from the principles of geometrical optics. For the ray geometry shown in Figure 11 the following relationship can be applied:

$$\text{Group Path } P' = ct = \int_S \mu' ds$$

$$\text{Phase Path } P = \frac{c}{\omega} \int_S \underline{k} \cdot d\underline{s} = \int_S \mu ds \qquad \text{Absorption } L = \int_S K ds$$

where \underline{k} is the wave propagation vector, ω the angular wave frequency, c the free space velocity, and K the absorption coefficient. The angle subtended at the centre of the earth θ can be expressed as:

$$\theta = \int \frac{a \cos \Delta dh}{(a+h)^2 \sqrt{\mu^2 - [a/(a+h)]^2 \cos^2 \Delta}}$$

where the symbols are defined in Fig. 11.

$$P' = \int \frac{dh}{\sqrt{\mu^2 - [a/(a+h)]^2 \cos^2 \Delta}}$$

$$P = \int \frac{\mu^2 dh}{\sqrt{\mu^2 - [a/(a+h)]^2 \cos^2 \Delta}}$$

$$S = \int \frac{\mu dh}{\sqrt{\mu^2 - [a/(a+h)]^2 \cos^2 \Delta}}$$

These ray equations can be integrated numerically for any distribution of electron density. This approach has been adopted by Croft¹⁵. Alternatively, some model of the ionospheric electron density height profile can be adopted which allows the equations to be integrated analytically; this approach clearly limits the type of ionospheric profile but does provide useful results in a limited number of cases¹⁶.

3.2.2 Magnetic field included

The ionosphere becomes an anisotropic medium when the influence of the earth's magnetic field is taken into consideration. Thus the direction of energy flow no longer coincides with the direction of the propagation vector k . Snell's Law applies to the k direction but not to the ray direction¹⁷. A number of ray-tracing techniques have been developed which include the magnetic field effects, such as those of Bremner¹⁸, Booker¹⁹ and Hazelgrove²⁰. A detailed discussion of these techniques lies outside the scope of this lecture but some comments are included concerning the ray-tracing programme developed by Jones²¹ since this is widely available (ITS Report OT 75-76). The ITS programme is based on the Hazelgrove equations and can be applied to a wide variety of ionospheric models. For example, either tabulated or analytical electron density (or collision frequency) profiles can be used. Moreover the effects of tilts and waves can be included as perturbations in the $N(h)$ distribution. The coordinates of the transmitter can be specified in three dimensions (latitude, longitude and height above the earth's surface) and the receiver can be at any height. The earth's magnetic field can be represented in a number of ways, for example by an earth-centred dipole.

When the transmitter location, frequency, the launch elevation and azimuth angles and the ionosphere model are specified, the programme computes the parameters shown in Table 1. The programme enables the propagation parameters along any ray path to be determined. Moreover, when many ray paths are traced features such as focussing and defocussing zones, skip distances, great circle deviations etc. become apparent¹⁴. An example of focussing effects is reproduced in Figure 12. It must be emphasised that the usefulness of any ray-tracing calculation will depend on how well the ionospheric model adopted represents the real situation. The technique is very powerful for the initial planning and evaluation of any HF circuit.

4. Channel Evaluation and Selection

The optimum frequency for any given HF circuit will depend on several factors. As we have seen the ionosphere plays an important role in determining the MUF and LUF but other influences, such as interference, fading and the signal information rates, are important considerations in selecting the "best" frequency. If all the parameters influencing the system can be monitored, then it should be possible to determine experimentally the optimum frequency for a particular type of transmission. Unfortunately, it is not always possible to monitor every conceivable parameter; however considerable improvements can be achieved when only a limited amount of information concerning the propagation channel is available for evaluating its performance (channel evaluation). Three major types of channel estimation and evaluation systems have been developed for transmission from a remote or mobile user to a base station and these will now be discussed briefly²².

4.1 Oblique Sounding Systems

In this system the transmitter of an oblique ionosonde is operated at the base station and the signals are received at the remote site. These signals are evaluated at the remote site and a frequency near the MUF, free of interference, is selected for communicating with the base station. The pulse transmissions from the base station can be coded to contain information regarding the local interference levels and preferred frequencies, etc. A network of fixed pulse sounders has been developed for channel estimation in the U.S. known as the "Common User Radio Transmission System (CURTS)"²³, which can provide channel estimation facilities over a wide range of latitude and longitude.

A somewhat similar system for ground-to-air use, known as "Channel Evaluation and Calling (CHEC)", has been developed in Canada²⁴. In this system transmissions are made from the base station on each of the frequencies assigned to the user, as opposed to the continuous sweep of an oblique sounder. The base transmitter emits a signal for several seconds on each assigned channel which contains a calling code, data on the base station interference levels and a C.W. section. At the remote station, specified by the calling code, the base interference levels are decoded and the signal strengths in each of the

channels are measured. A special-purpose processor then computes the optimum channel for transmission to base using the signal-to-noise information, measured signal levels and the assumption that reciprocity along the path holds. Considerable improvement in performance has been obtained using the CHEC system.

4.2 Backscatter Systems

In this type of channel estimation a backscatter sounder (transmitter and receiver co-located) is operated at the base station and the propagation conditions are determined from the backscatter ionograms²⁵. No processing is undertaken at the remote location and the channel selection is carried out entirely at the base station. Interference levels and the ionospheric propagation conditions are contained in the backscatter ionogram; however these are difficult to interpret, particularly when many modes of propagation are active. This procedure is especially useful when it is desired to illuminate a specific region from the base station rather than obtain optimum performance for a point-to-point link.

Improvements can be made to the backscatter technique by coding the transmitted pulse and/or by activating transponders placed at known ranges from the base station.

4.3 Pilot-Tone Systems

A somewhat different approach to channel selection can be achieved by inserting C.W. tones into the data spectrum of the transmitted signal and the tones are also radiated on the other channels available^{26,27}. At the receiver the phase of the pilot tone is measured and this enables the relative state of the channel to be specified in terms of predicted error rates. This type of system can be developed so that a receiver modem (equalizer) can be adjusted in real time to track the effect of multi-path propagation and so remove most of the errors produced by these effects. These systems require the insertion of the pilot tone at the transmitter and rather specialized decoding and tracking at the receiver if their full capabilities are to be realized.

The adoption of any form of channel estimation technique will generally lead to improved system performance. These systems are, however, not widely used since they involve additional expense in hardware and in most cases require specialized knowledge to interpret the data in terms of the optimum working frequency.

5. Summary

The performance of an HF radio circuit is controlled to a large extent by the ionosphere. The path parameters, such as the MUF and LUF, can be determined by direct experiment or, alternatively, they can be calculated from ionospheric models by prediction and ray-tracing methods. In assessing the most suitable frequency for a given link, factors other than propagation conditions must be considered, e.g. noise and transmitter power. A number of techniques for evaluating the complete channel response have been developed and when these are employed a considerable improvement in system performance can be obtained.

References

1. Ratcliffe, J.A., Sun, Earth and Radio, World Univ. Lib. (1970).
2. Davies, K., Ionospheric radio propagation, U.S. Dept Commerce NBS, Monograph 80 (1965).
3. Breit, G. and Tuve, M.A., A test for the existence of the conducting layer, Phys. Rev. **28** (1926) 554.
4. Martyn, D.F., The propagation of medium waves in the ionosphere, Proc. Phys. Soc. **47** (1935) 323.
5. Smith, N., The relation of radio sky wave transmission to ionosphere measurements, Proc. IRE **27** (1939) 332.
6. Dieminger, W., Ionospheric propagation of HF radiowaves, AGARD Lect. Ser. 29 (1968).
7. Appleton, E.V. and Piggott, W.R., Ionospheric absorption measurements during a sun spot cycle, J. atmosph. terr. Phys. **5** (1954) 141.
8. Abel, W.G. and Edwards, L.C., The source of long distance backscatter, Proc. IRE **39** (1951) 1538.
9. Møller, H.G., Further results of sweep frequency oblique incidence measurements, J. atmosph. terr. Phys. **12** (1958) 173.
10. Shearman, E.D.R., The technique of ionospheric investigation using ground scatter, Proc. IEEE **103**, Pt B (1956) 121.
11. "Radio Oceanography", Special Issue of Trans. IEEE Antennas and Propagation, **AP25**, January (1977).
12. Davies, K and Barghausen, A.F., The effect of spread F on the propagation of radiowaves near the equator, In: Spread F and its Effects on Radio Propagation and Communications, AGARDOGRAPH No. 95 (1966).

13. Sugar, G.R., Radio propagation by reflection from meteor trails, Proc. IEEE 52 (1964) 116.
14. Jones, T.B. (Ed.), Oblique Ionospheric Radiowave Propagation, AGARD Conf. Proc. No. 13 (1969).
15. Croft, T.A. and Hoogasian, H., Exact ray-tracing calculations in a quasi-parabolic ionosphere with no magnetic field, Radio Science 3 (1968) 69.
16. Appleton, E.V. and Beynon, W.J.G., The application of ionospheric data to radio communications problems. Pt II. Proc. Phys. Soc. 59 (1947) 58.
17. Budden, K.G., Radiowaves in the Ionosphere, Cambridge Univ. Press (1961).
18. Bremmer, H., Terrestrial Radio Waves, Elsevier Publ. Co., Amsterdam (1949).
19. Booker, H.G., The application of the magneto-ionic theory to radio waves incident obliquely upon a horizontally stratified medium, J. geophys. Res. 54 (1949) 243.
20. Hazelgrove, J., Ray theory and a new method for ray tracing, In: Physics of the Ionosphere, Phys. Soc. Lond. (1954).
21. Jones, R.M. and Stephenson, J.J., A versatile three-dimensional ray tracing computer program for radiowaves in the ionosphere, O.T. Rep. 75-76, U.S. Dept. Commerce.
22. Darnell, M., Channel estimation techniques for HF communications, AGARD Conf. Proc. CP-173, Ch. 16 (1975).
23. Probst, S.E., The CURTS concept and current status of development, In: Ionospheric Radio Communications, Plenum Press (1968) 370.
24. Stevens, E.E., The CHEC sounding system, In: Ionospheric Radio Communications, Plenum Press (1968) 359.
25. Burdick, B.J., Chisholm, J.H. and Nichols, B.E., Polar ionosphere modelling based on HF backscatter beacon and airborne ionosonde measurements, AGARD Conf. Proc. CP-173, Ch. 30 (1975).
26. Betts, J.A. and Darnell, M., Real time HF channel estimation by phase measurements on low level pilot tones, AGARD Conf. Proc. CP-173, Ch. 18 (1975).

Acknowledgement

The diagrams used in the lecture are based on the published work of the following authors:

Figure 2 J.A. Ratcliffe [1]

Figures 3-10 W. Dieminger [6]

Figures 11-12 K. Davies [2] and AGARD Lecture Series 29 (1968).

TABLE 1: Typical Output Parameters of Jones 3D Ray-Tracing Program

Height of ray point above ground
Range of ray point projected on the earth's surface
Azimuth deviation at ray point
Elevation angles at ray point
Wave polarization
Group path
Phase path
Absorption
Doppler frequency shift

The program also indicates the position at which reflection occurs and the location at which the ray reaches the ground after reflection (for further details see OT Report 75-76).

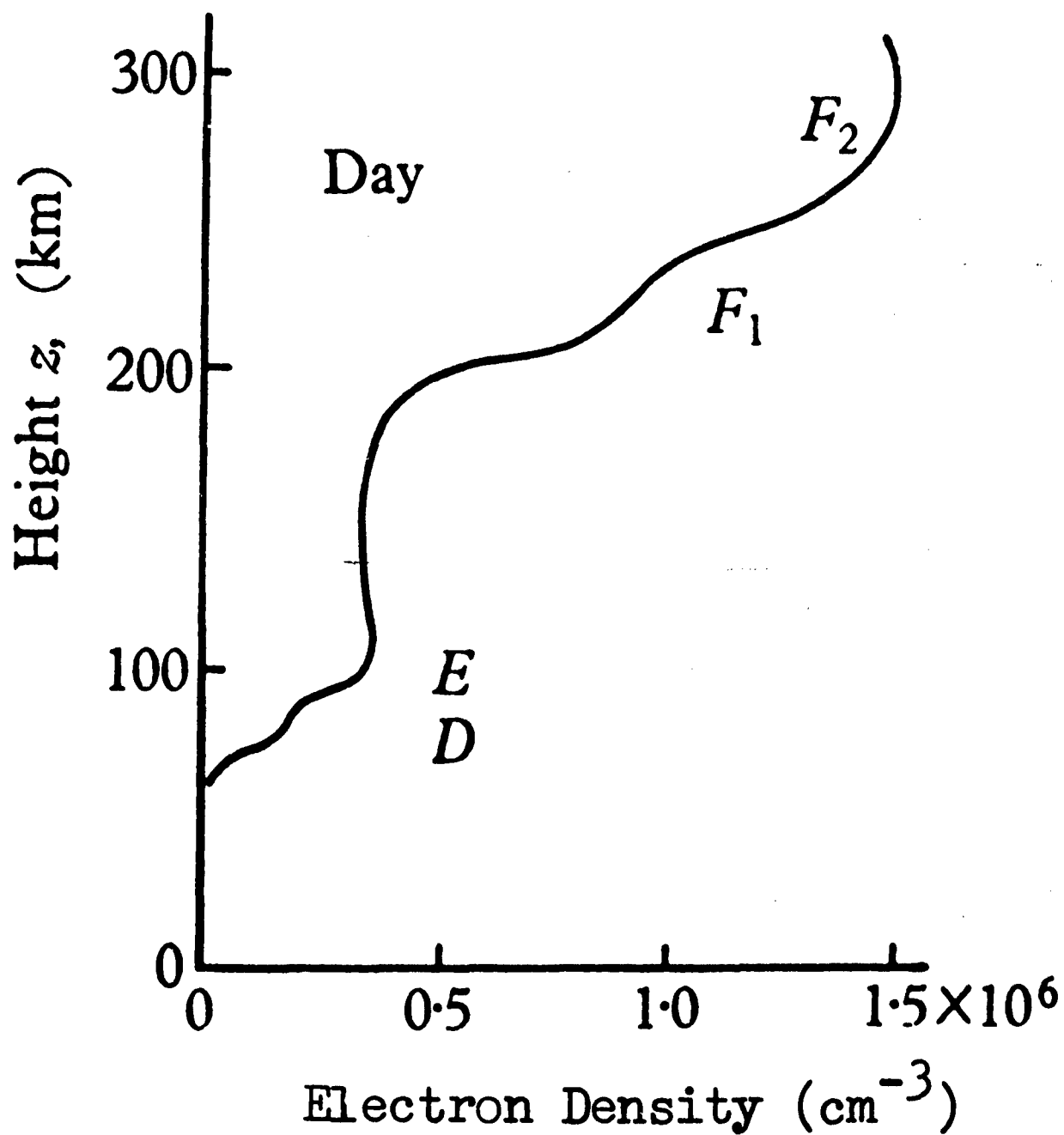


Fig. 1. Typical electron density height distribution in the mid-latitude ionosphere during summer.

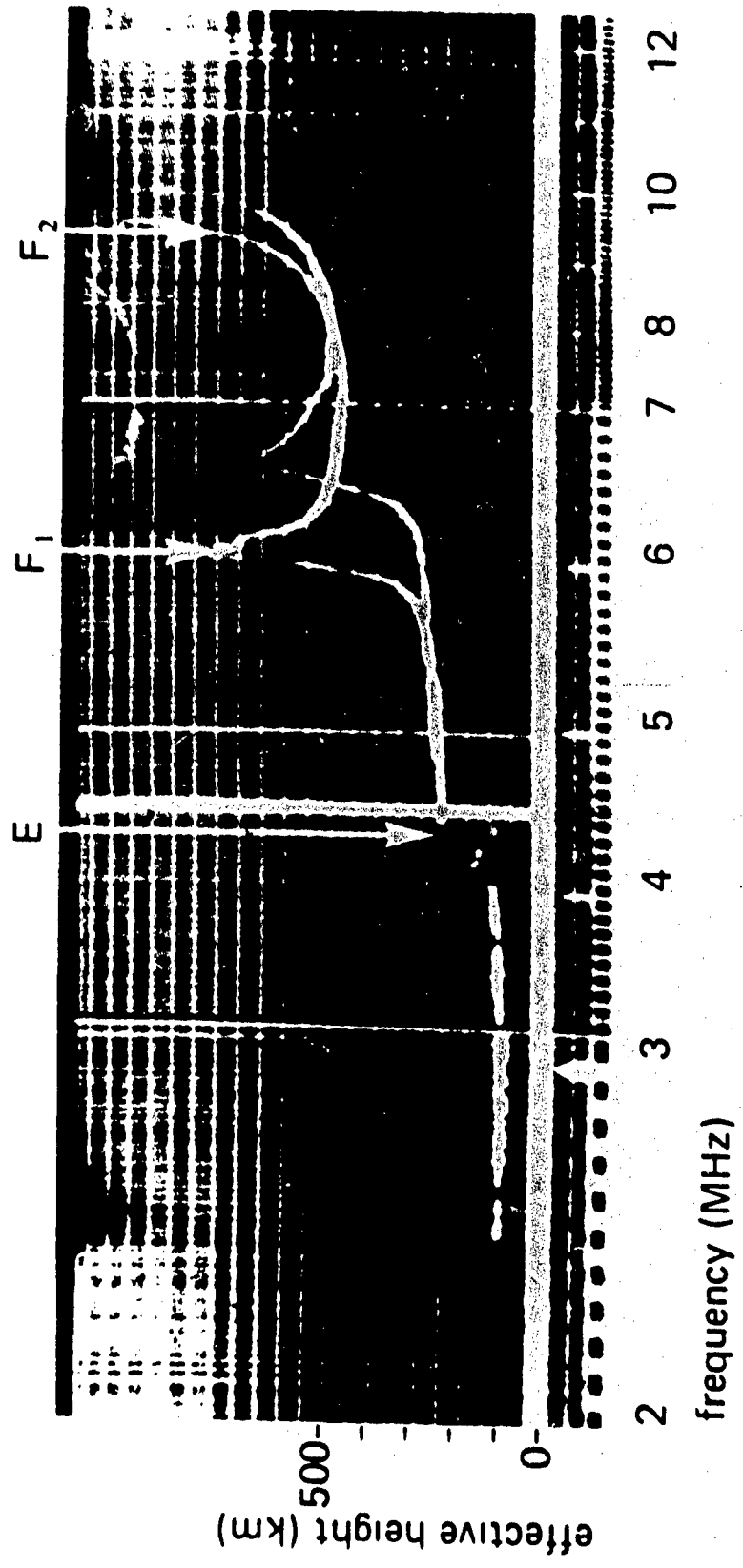


Fig. 2. Mid-latitude ionogram indicating variation of equivalent height with frequency. Ordinary mode critical frequencies of E, F₁ and F₂ layers are indicated. Note magneto-ionic splitting (after Ratcliffe, 1970).

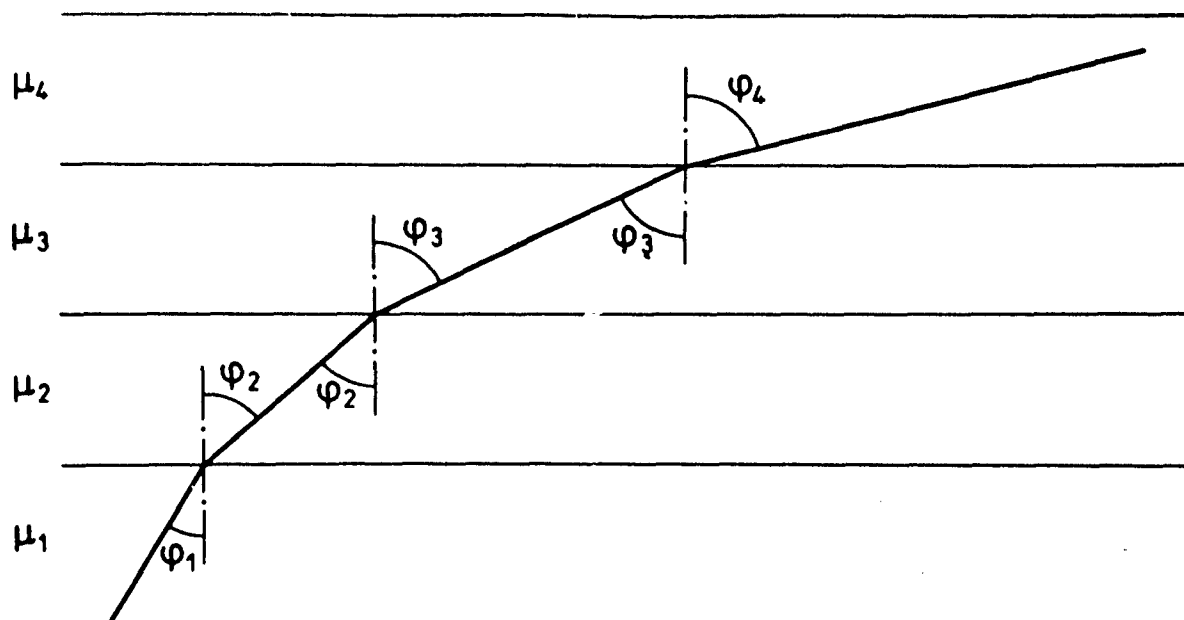


Fig. 3. Refraction in a layered medium (after Dieminger, 1968).

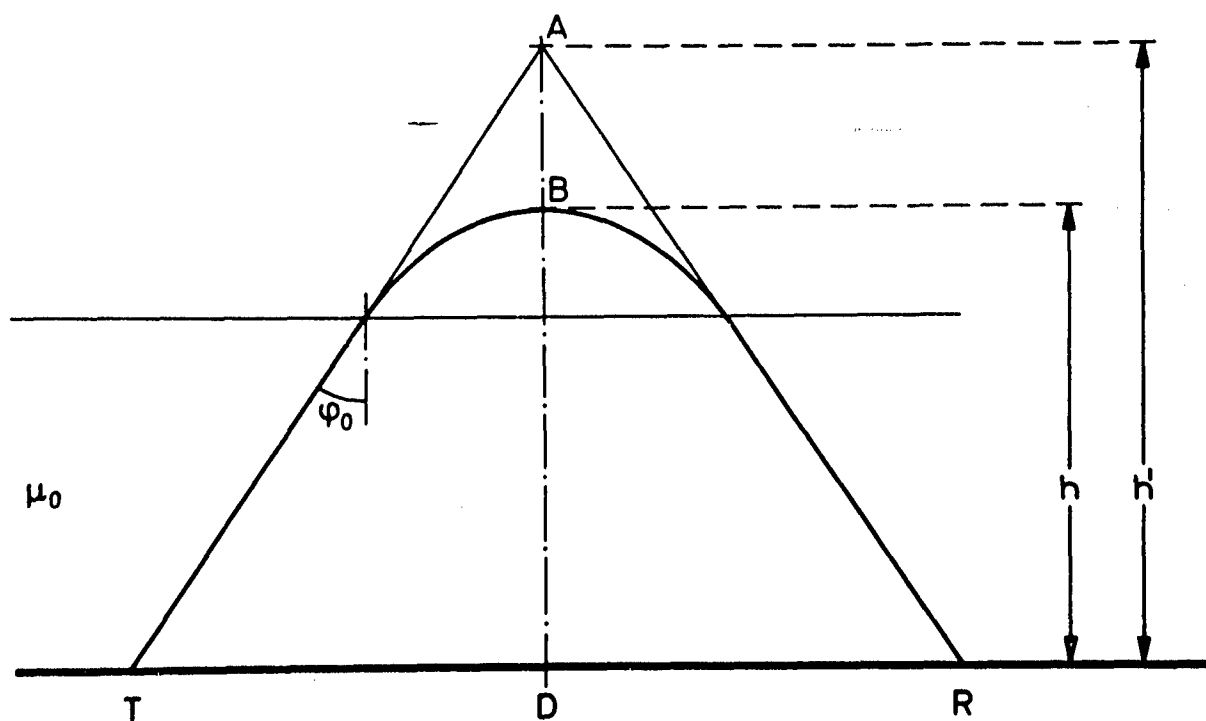


Fig. 4. True path and virtual path (after Dieminger, 1968).

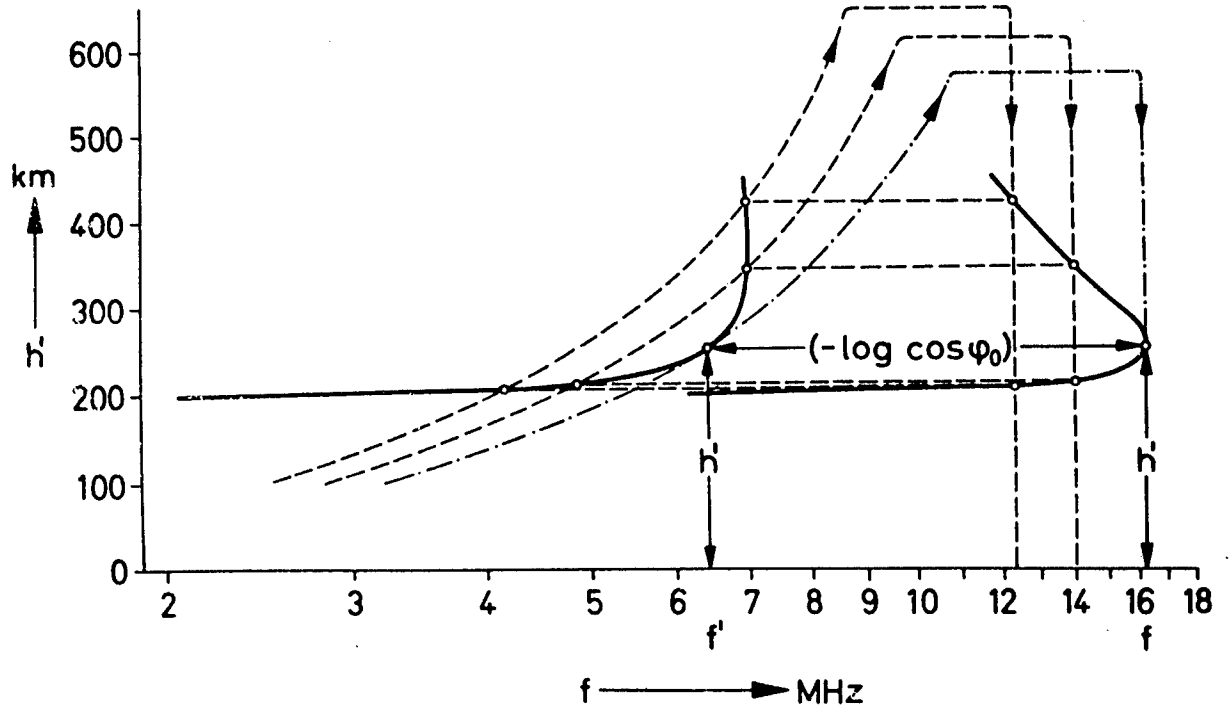


Fig. 5. Use of transmission curves (after Dieminger, 1968).

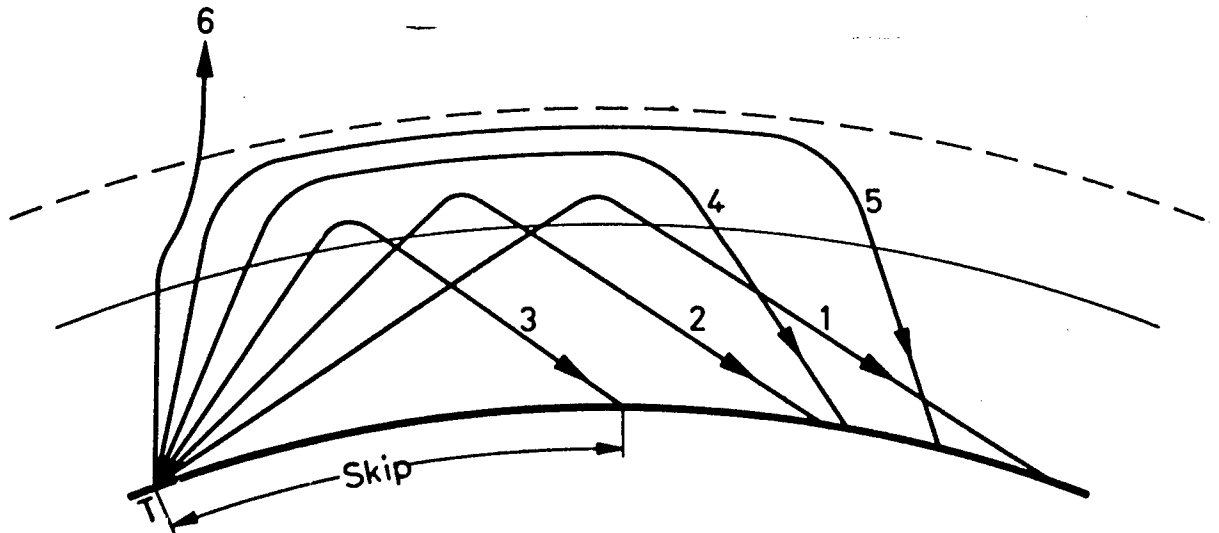


Fig. 6. Ray paths for fixed frequency and variable angle of elevation (after Dieminger, 1968).

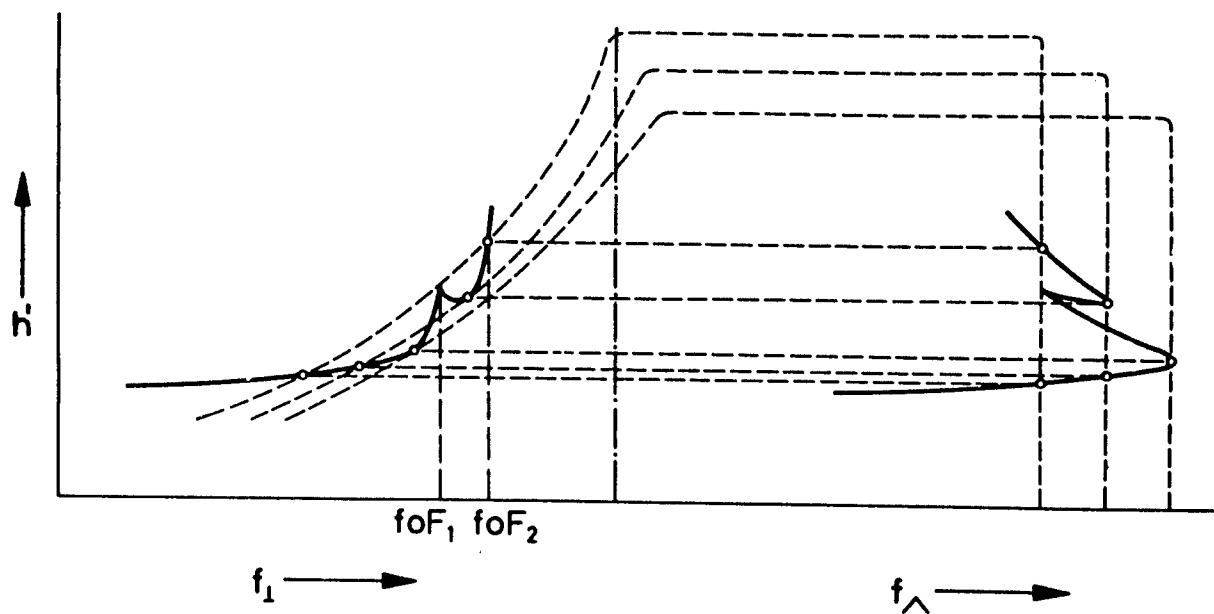


Fig. 7. MUF determined by the F_1 -layer (after Dieminger, 1968).

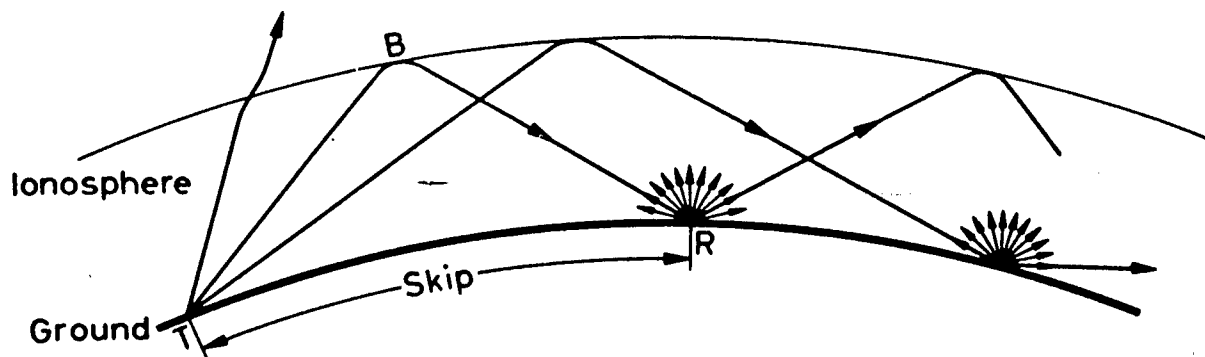


Fig. 8. Geometry of ground backscatter (after Dieminger, 1968).

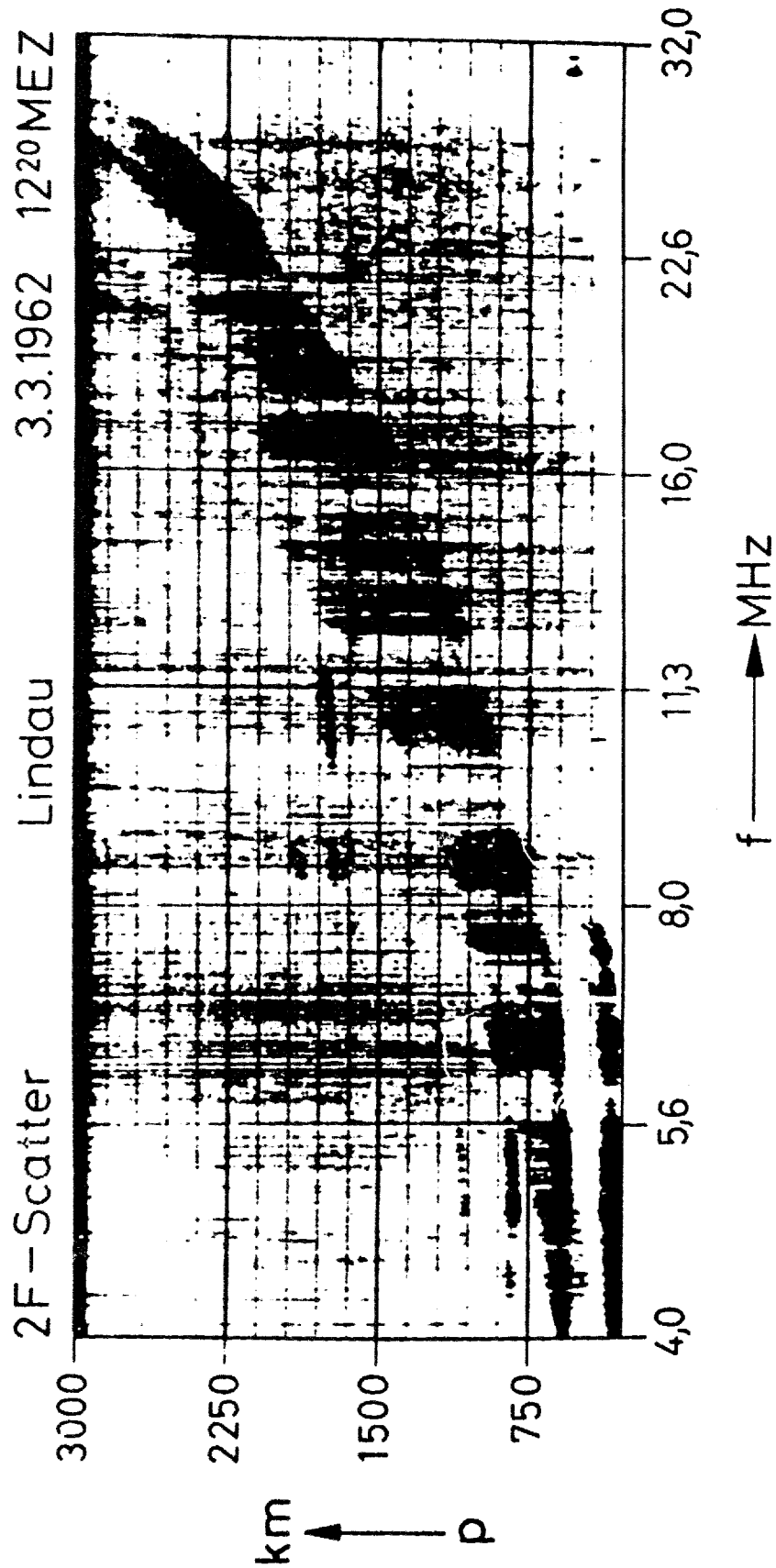


Fig. 9. Backscatter record as obtained at Lindau (peak power 250 kW, antenna gain 10 dB) (after Dieminger, 1968).

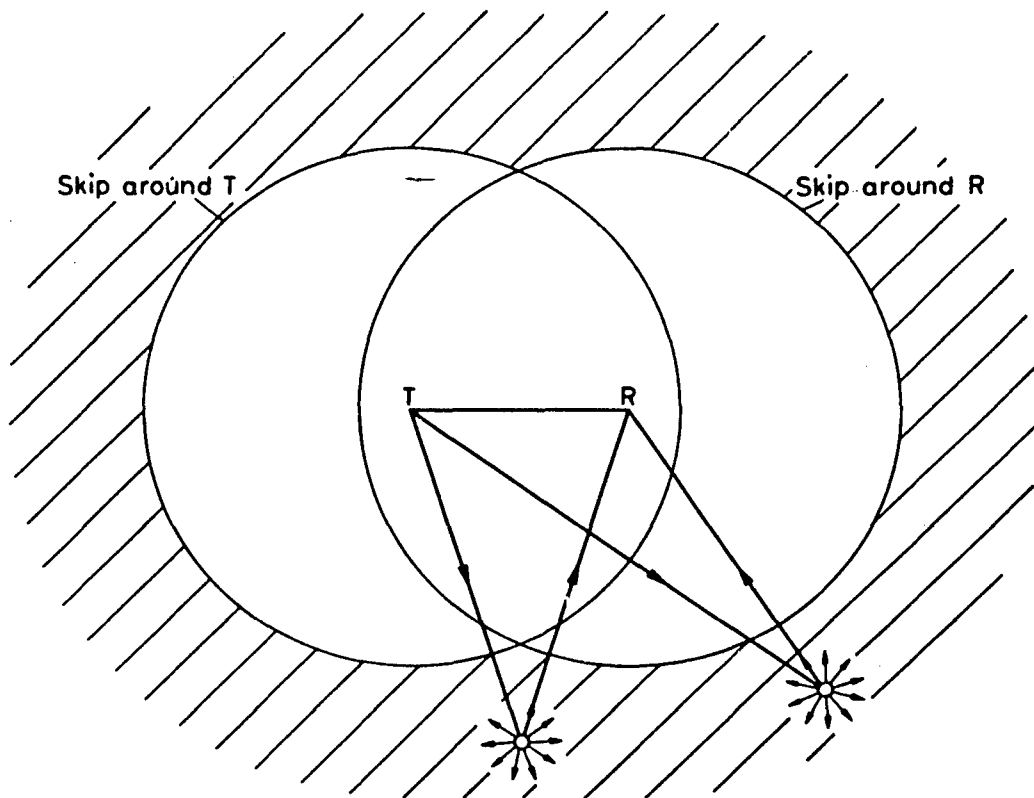


Fig. 10. Reception inside the skip distance (after Dieminger, 1968).

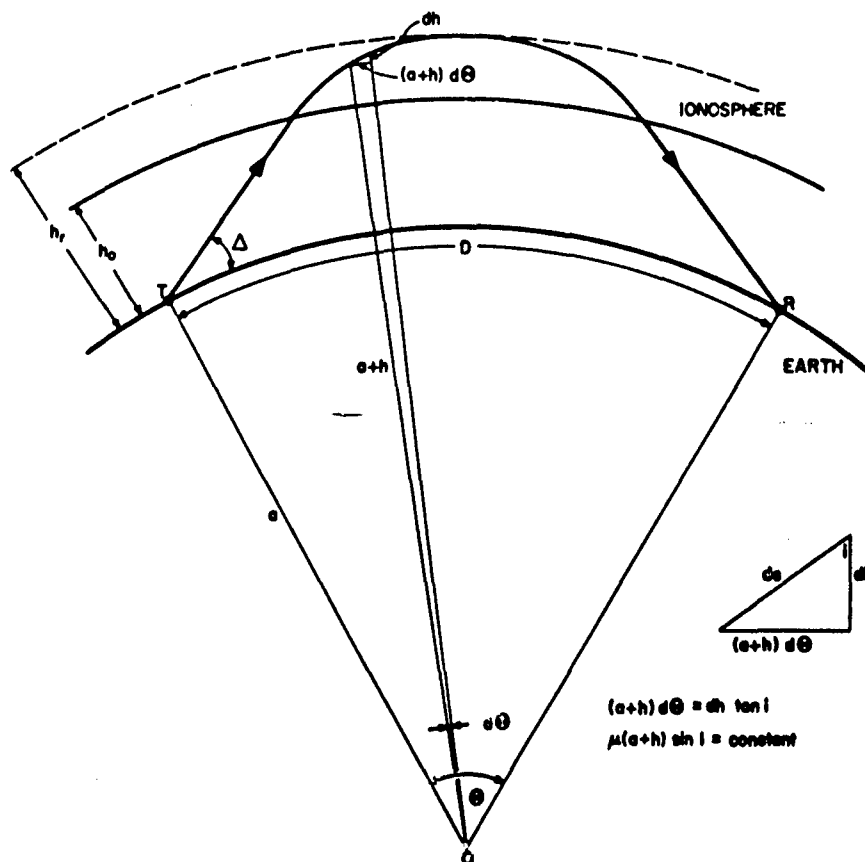


Fig. 11. Ray path geometry for a spherically stratified ionosphere (after AGARD lecture series 29, 1968).

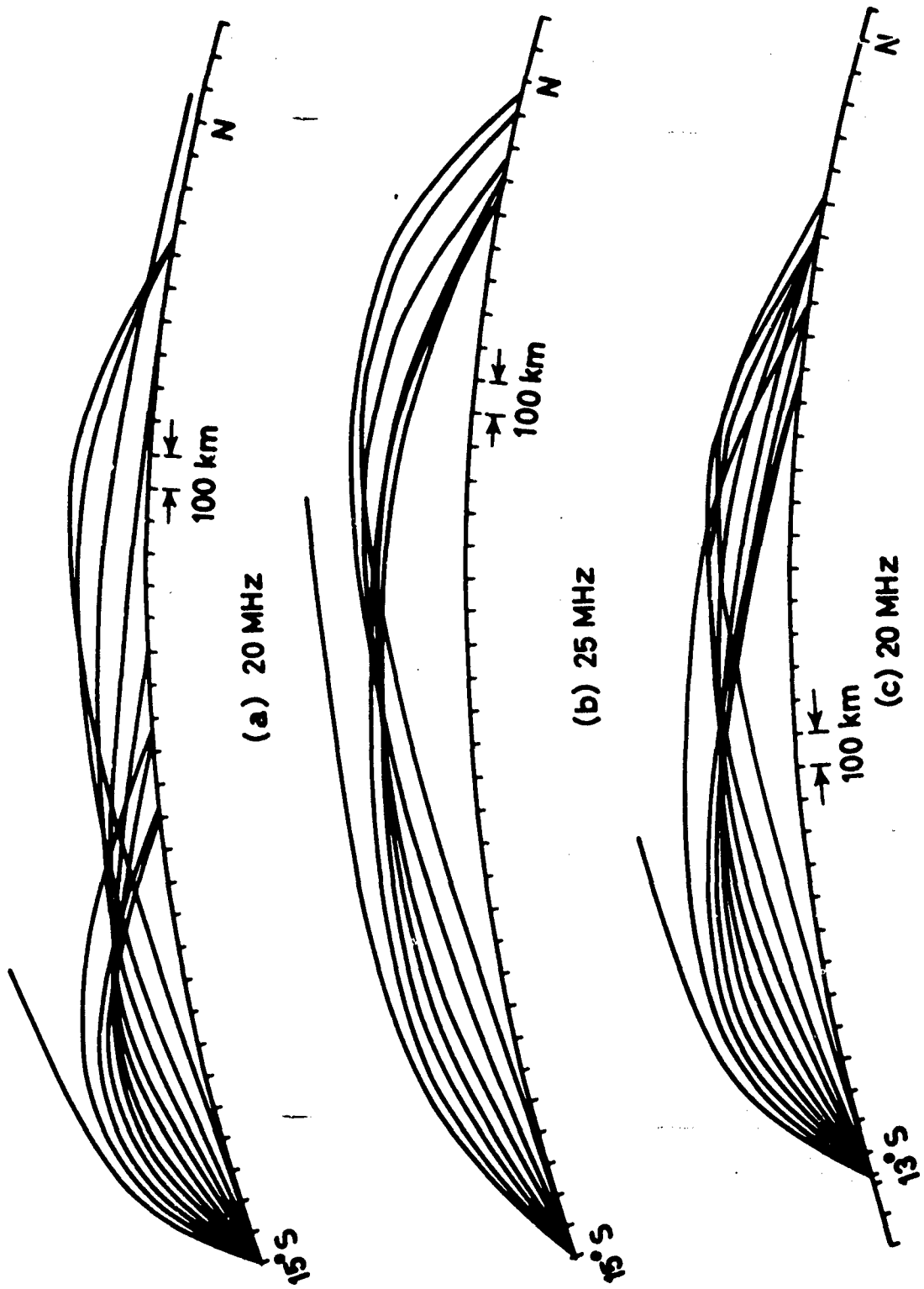


Fig. 12. North-south ray paths across the magnetic equator (notice the concentration of the power in a small area on the ground) (after Davies, 1965).

FORECASTING AND PREDICTION OF IONOSPHERIC PARAMETERS

Kenneth Davies
 Space Environment Laboratory
 NOAA Environmental Research Laboratories
 Boulder, Colorado 80302, U.S.A.

1. INTRODUCTION

1.1 Societal Concerns

The ionosphere is usually defined as that part of the atmosphere (above about 50 km) that contains sufficient ionization to affect the propagation of radio waves. The importance of the ionosphere to society follows directly from this definition because radio is a primary means of telecommunications especially when one or both of the terminals is mobile (e.g., airplane, ship, automobile). The ionosphere affects radio waves in two ways: (a) advantageously by reflection and thus enabling communications such as on high frequencies and (b) adversely by scattering, absorbing and producing undesirable effects such as fading and interference between transmitters on the same carrier frequency. These effects on the radio frequency spectrum are summarized in Table 1.

Besides its relevance to radio communications there are other important aspects of the ionosphere as for example: (a) its role in disturbing the Earth's magnetic field, (b) production of aurora, scientific exploration, etc. A list of some typical users, civilian and military, is given in Table 2. Geomagnetic disturbances produce considerable voltages in large conductors such as: electrical power systems (see Slothower and Albertson, 1967; Albertson and Van Baelen, 1969), the 1,100 km Alaska Pipeline (EOS, Sept. 1977), etc. Geomagnetic disturbances can also affect the prediction of volcanic activity based on magnetic fluctuations (see Decker, 1978) and also mineral exploration. From a scientific point of view the ionosphere is of interest as an enormous plasma laboratory which is not confined by the walls of the ionization chamber. It is in the ionosphere that most of the solar extreme ultraviolet (EUV) and X radiation is absorbed. A large variety of plasma instabilities and physical processes have been discovered in the ionosphere, thus providing an interaction between aeronomy, ionospheric and magnetospheric physics and plasma physics. An understanding of these plasma phenomena is essential in the prediction of many ionospheric effects which are of importance to society. The societal implications of weather and climate changes makes it vital to study the physical processes in the upper atmosphere and the magnetosphere with a view to finding the coupling mechanisms between solar activity, interplanetary magnetic variations and weather.

Ionospheric predictions are of course only one in a host of geophysical predictions that are of direct concern to society. These fields include for example: earthquakes, volcanoes, landslides, hurricanes, tornadoes, floods, tsunamis. Since national resources are limited the amount of effort that should be expended on the preparation and improvement of ionospheric predictions must be balanced against the demands of other disciplines. For example, an ionospheric storm does not threaten human lives directly whereas the July 28, 1976 earthquake took some 600,000 lives in Tangshan, the May 8, 1902 eruption of Mont Pelé, Martinique, killed around 30,000 and some 200,000 persons were drowned in Bengal floods (see Landsberg, 1978). Thus it is wise to keep a perspective when allocating resources to the various fields. This brings up also a question of how precise a prediction can and should be. In particular there is no point in refining a prediction system beyond the stage at which a user can take advantage of it.

In this lecture we shall consider the needs for long-term (years) predictions and short-term (minutes to days) forecasts of ionospheric conditions and the various techniques used in preparing predictions and forecasts. The propagation of radio waves will be discussed briefly in Section 2 and predictions in the spatial, temporal and frequency domains will be covered in Section 3 together with the question of the accuracies of the predictions. Short-term phenomena, which tend to be correlated with solar disturbances, are treated in Section 4.

1.2 Need for Ionospheric Predictions

By far the major concern with the ionosphere is its influence on the effective management and efficient utilization of the radio frequency spectrum for communications, navigation, and surveillance. Radio is particularly important for: (1) mobile communications using high frequency reflections, (2) communications in sparsely populated areas where alternative systems are either non-existent or uneconomical, (3) communications in high latitudes where the ionosphere is frequently disturbed and may include (1) and (2). Ionospheric communications are of particular relevance to NATO in northern Europe, the North Atlantic and over the North Polar Cap, and, hence, ionospheric conditions are of considerable importance.

The following three aspects of radio communication are of importance: (1) safety, (2) commercial and (3) personal. In the case of safety a good forecast can be of value in saving lives, e.g. launching rescue missions. On the other hand, commercial usage is basically a matter of economics and, in general, personal communications are matters of convenience. Thus forecasts and predictions have various values depending on the usage. In the effective utilization of the radio frequency spectrum we are concerned

with the following properties: (1) The frequency spectrum is used--not consumed; it is wasted when not in use. (2) It has the dimensions of space, time and frequency than can be shared provided that effective predictions are available. (3) The spectrum is an international resource--available to all. (4) The spectrum is wasted when assigned to tasks that can be done better in other ways. (5) The spectrum is wasted when its characteristics are not correctly applied. (6) It is subject to pollution and, therefore, needs policing.

One of the greatest pressures on the overcrowded radio spectrum is that resulting from the increasing mobility of the world's population and, especially, military personnel. There are more people on the move at higher speeds and radio is about the only means of communication. Communications insures more efficient business, public and private safety and national security. Thus any medium, such as the ionosphere, that affects radio waves, both advantageously and/or adversely, is of vital concern to society.

One of the most important applications of long term ionospheric predictions is in the management of the radio spectrum; i.e., to circuit planners and operators and to national and international regulatory agencies both civilian and military. This includes: the allocation of frequencies, required transmitter powers, antenna configurations, scheduling, etc. Operators are primarily concerned with frequency predictions as an indicator of when to change operating frequency. Predictions are of use in determining the degree of mutual interference between radio transmissions and with interference between radio transmissions and other spectrum users such as the radio astronomers. Ionospheric predictions are important in military communications both to insure adequate liaison and to minimize false alarms to surveillance systems.

1.3 Need for Ionospheric Forecasts

The term forecast is used to denote a relatively short-term, for example less than the 27 day solar rotation period, prognosis of ionospheric conditions. Here again radio users are probably the main beneficiaries. Forecasts generally are concerned with aspects of ionospheric disturbances frequently associated with solar flares. These disturbances include for example: sudden ionospheric disturbances--see Table 3, polar cap absorptions and ionospheric storms. These disturbances cause serious disruption of radio traffic, and other uses of the ionosphere, and consequently the forecasts tend to concentrate on qualitative aspects such as indicating that a storm is likely within the next two to three days. In addition to these forecasts there is a "warning" service based on real-time data which informs a user that a disturbance is already in progress. Forecasts and warnings are of considerable value to station operators, both civilian and military, because they enable the operators to: (a) provide for alternative means of communication, (b) pass priority material before the radio circuit closes, (c) initiate or delay rescue operations, and (d) determine that the cause is natural rather than equipmental and thus avoid the unnecessary expense of calling a service man. Short term forecasts are particularly valuable to operators in high latitudes in which ionospheric communications are the only contacts with the outside world. For effective utilization of ionospheric forecasts educated operators are essential.

In addition to the communications-related roles, forecasts have other uses as for example: (1) alert geophysical prospectors that magnetic measurements are suspect, (2) alert scientists that the time is opportune to launch, or delay launch, of certain rocket experiments, (3) warn electric power companies of the possibility of distribution outages.

2. THE IONOSPHERE AND RADIO WAVES

2.1 Refraction and Reflection

Some of the important ionospheric radio effects are illustrated in Figure 1 which refers to the high frequency spectrum but is not confined thereto. Because of the presence of free ions, particularly electrons, the refractive index of the ionosphere is often less than unity so that radio waves are refracted away from the vertical. If the refractive index becomes sufficiently low the angle of refraction reaches 90° and reflection occurs. The processes of refraction, reflection, absorption, wave polarization, etc., are dealt with in considerable detail by Ratcliffe (1959), Budden (1961), Kelso (1964) and Davies (1969) with more elementary discussions by Ratcliffe (1970), Davies (1965) and Lied (1967) which are well worth reading.

In the absence of electron collisions and of an external magnetic field, or on sufficiently high radio frequencies, the real refractive index μ is given by:

$$\mu^2 = 1 - 80.61 \frac{N}{f^2} \quad (1)$$

where N is the electron number density in m^{-3} and f is the radio frequency in Hertz. From equation (1) we see that refraction increases with increase of electron density and decreases with increase of wave frequency. The maximum, or critical, frequency f_c reflected from an ionospheric layer with vertical propagation is given by

$$f_c^2 = 80.61 N_{max} \quad (2)$$

The maximum frequency f_{\max} reflected with oblique propagation over a distance d is related to f_c thus

$$f_{\max} = M(d) f_c \quad (3)$$

where $M(d)$ is the maximum useable frequency, or MUF, factor which depends on distance, d , and on the height and shape of the ionospheric layer profile. Various methods have been devised to determine MUF factors such as the parabolic layer method (Appleton and Beynon, 1940, 1947) and the graphical method of Smith (1939).

Electrons have several effects on radio rays other than refraction as for example: defocussing, group retardation, phase path, which in turn modify the amplitude, time of arrival, angle of elevation, etc. Even in the cases of VHF satellite-to-ground transmissions, where the refraction is insufficient to appreciably modify the physical ray path, the effects on time of flight, carrier phase and wave polarization are appreciable. The excess time delay t_g introduced by the electrons is

$$t_g = 0.135 N_T / f^2 \quad \mu \text{ sec} \quad (4)$$

where N_T is the total columnar electron content per square meter along the ray path.

The presence of the geomagnetic field renders the ionosphere birefringent to radio waves. On entry into the ionosphere a radio wave is, in general, split into an ordinary wave and an extraordinary wave which, to a large extent, propagate independently. With reference to the geomagnetic field B_0 the sense of rotation, or polarization, of the ordinary wave is left-handed whereas the extraordinary wave is right-handed, i.e. the rotation of the H, E vectors and the motions of the electrons. An important frequency for the propagation of radio waves is the electron gyro- or cyclotron frequency f_H given by

$$f_H = \frac{1}{2\pi} \frac{e}{m} B_0 = 2.80 \times 10^{10} B_0 \quad \text{Hz} \quad (5)$$

where e/m is the electron charge/mass ratio. In the ionosphere $f_H \approx 1.5$ MHz, i.e. in the middle of the medium frequency band. At this frequency the electrons driven by the extraordinary wave tend to resonate and absorb power from the radio wave. The refractive indices of radio waves in the ionosphere is given by the Appleton equation the properties of which have been discussed extensively elsewhere (e.g., Budden, 1961; Davies, 1969; Ratcliffe, 1959). On frequencies well above the cyclotron frequency and well above the plasma frequency $f_N = \sqrt{80.61N}$, the waves often propagate as if traveling nearly parallel to the geomagnetic field and the refractive indices are given approximately by

$$\mu^2 = 1 - \frac{80.61N}{f(f \pm f_H \cos \theta)} \quad (6)$$

where θ is the angle between the direction of propagation and the magnetic field, the + and - signs denote the ordinary and extraordinary waves respectively. From (6) we see that the magnetic field affects the extraordinary wave more than the ordinary wave. With transverse propagation the refractive index of the ordinary wave is the same as the no-field case, i.e. equation (1). Furthermore, with vertical (normal) propagation the ordinary wave is reflected from the same true height as would be the case in the absence of a magnetic field.

Because the refractive index is frequency dependent the medium is dispersive and a wave packet (modulated signal) will move with the group velocity v_g which, in general, differs from the phase velocity v_p of the individual wave crests. On high frequencies $v_p > c > v_g$ so that individual crests appear at the back of a packet, or pulse, move through the packet and disappear at the front. The energy travels with the group velocity. Because the refractive index depends on direction, the medium is anisotropic and so the direction of energy flow differs from the direction of phase propagation--see Davies (1969, Chapter 7).

2.2 Absorption

When a radio wave traverses an ionized plasma the electric field of the wave sets the electrons in motion. The oscillating electrons radiate and the net effect is to change the phase of the advancing wave. When sufficient molecules are present the moving electrons collide and the direction of electron motion is changed so that the reradiated energy is not coherent with the advancing wave and the wave is attenuated. The energy lost in collisions degenerates into thermal motion and thermal radio noise. The microscopic processes involved in absorption are discussed by Ratcliffe (1959) which is well worth reading.

Absorption is of great practical importance in telecommunications, especially in the medium-frequency and high-frequency bands (≈ 0.3 to 30 MHz). In an absorbing medium the wave amplitude decreases exponentially with distance d , i.e.

$$A \propto 10^{-(\kappa d/20)} \quad (7)$$

where κ is the absorption per unit distance in decibels, which is given by

$$\kappa = 4.6 \times 10^{-2} \frac{N\nu}{(\omega \pm \omega_H)^2 + \nu^2} \frac{1}{\mu} \text{ dB/km} \quad (8)$$

In (8) ν is the electron collision frequency, $\omega = 2\pi f$ and $\omega_H = 2\pi f_H$. Equation (8) enables us to identify two types of absorption: (1) deviative absorption ($\mu \neq 0$) which occurs near the top of the ray path or where marked wave retardation occurs and (2) non-deviative absorption, which occurs in regions where $\mu = 1$ but $N\nu$ is large, i.e. 70 to 90 km. With medium- and high-frequency waves the nondeviative absorption index reduces to

$$\kappa = 4.6 \times 10^{-2} N\nu / (\omega \pm \omega_H)^2 \quad (9)$$

so that absorption decreases with increase of frequency, furthermore the absorption of the extraordinary wave is greater than that of the ordinary wave especially on medium waves ($\omega \sim \omega_H$).

2.3 Scattering

The theory of radio ray propagation in the ionosphere is based on the idea of an infinite uniform medium. When the medium changes slowly the theory holds for most practical cases as is borne out by radio soundings of the ionosphere--i.e., sharp traces on ionograms. When the ionosphere contains irregularities, e.g. clouds of electrons, partial reflections, coupling between ordinary and extraordinary waves, diffraction, fading, etc., occurs.

Partial reflections occur when there is a sudden change $\Delta\mu$ of refractive index μ (e.g. see Born and Wolf, 1959, section 1.5.2) such as exist in the D region and sporadic E. With vertical propagation the partial reflection coefficient is given approximately by

$$\rho = \frac{\Delta\mu}{2\mu} \quad (10)$$

Observations of partial reflections have been used by Belrose (1970) to determine electron density profiles in the D region.

Sporadic E, at heights between about 100 and 120 km, often occurs in the form of patches of small flat "pancakes". Partial reflection occurs because, although the "pancakes" are totally reflecting (overdense), radio waves penetrate between the clouds.

Scattering of radio energy takes place from ionized meteor trails (see Davies, 1965, chapter 8) and from turbulence in the D region. The F region is characterized by strong irregularities in the form of cylinders aligned along the geomagnetic field. These cause the phenomenon of spread F on ionograms--Figure 2--which is particularly severe near the geomagnetic equator (on equinox evenings) and near the auroral zones. The superposition of scattered wavelets leads to very rapid "flutter" fading which can seriously distort radio signals. Another form of scatter involving normal ionospheric reflection is backscatter, or sidescatter, from irregular structures on the Earth's surface (e.g., mountains, sea surface). Scattering from individual electrons is called incoherent scatter or Thomson scatter (see Farley, 1970). It is a most useful technique for studying the electron distributions, temperatures and motions in the ionosphere.

An extensive discussion of the effects of ionospheric scattering on very-long-distance radio communications is given by Whale (1969).

3. PREDICTIONS

3.1 Predictions in the Time Domain

Essentially this is the answer to the question "How can we predict the state of the ionosphere at some future time based on past observations?". Since about 1933 systematic radio soundings of the ionosphere have been made at a steadily growing number of geographical locations. Since 1962 these have been supplemented by satellite-borne sounders (e.g., see Proc. IEEE, 1969). The incoherent, or Thomson, scatter technique has been used at a very few locations. Ionograms give the time of arrival as a function of frequency over the approximate frequency range 1.6 MHz to 25 MHz. These photographic (or digital) records give information on the layers of the ionosphere (see Table 4) such as the critical frequencies, shape and height, minimum frequency (a measure of absorption), off-vertical echoes, etc. From these data it has been possible, for given locations, to establish the dependence of various parameters on Zurich sunspot number R and solar zenith angle χ .

From the point of view of radio communications the most important parameter of an ionospheric layer is its critical or penetration frequency (ordinary wave). Some important features are: (a) The seasonal variation of foE and foF1 are in phase with the solar zenith angle whereas foF2 tends to be in antiphase (winter anomaly), at least in

middle latitudes--see Figure 3. (b) The F1 layer disappears in some winters and at night. (c) There is a marked increase in the critical frequencies in sympathy with the sunspot cycle--Figure 4.

The E and F1 layers.

To a first approximation

$$foE = 0.9\{(180 + 1.44R) \cos \chi\}^n \text{ MHz} \quad (11)$$

where n varies between 0.1 in high latitudes to about 0.4 near the equator with an overall average of 0.25 giving foE within about 0.2 MHz.

The F1 layer critical frequency is given by:

$$foF1 = (4.3 + 0.1R) \cos^{0.2} \chi \quad (12)$$

The F1 layer is present only during the day, it is more evident in summer than in winter, at high sunspot numbers and during ionospheric storms (when foF2 is depressed).

The D layer

Turning to the D region, the most important radio aspect is absorption which depends on the path integral of the product Nv. The diurnal variation of D region absorption L is given by

$$L = 430(1 + 0.0035R) \cos^n \chi / (f \pm f_H)^2 \text{ dB} \quad (13)$$

In middle and low latitudes the exponent n is in the range 0.7 to 1.0 with an average near 0.75. In high magnetic latitudes the value of n is much smaller (= 0.1) and the absorption is generally higher than in middle latitudes. Equation (13) does not allow for the "winter anomaly" in which the absorption, on a given radio frequency and angle χ , is higher in winter than in summer. The anomalous absorption occurs on groups of days; days of high absorption in one sector, e.g. North America may be days of low absorption in another sector, e.g. Europe. The winter anomaly is not present in high latitudes during the long winter night. Neither does (13) account for enhanced absorption following flares, ionospheric storms, etc.

The F2 layer

By far the most important layer from the radio viewpoint is the F2 layer. The long term variation of foF2 is related to the sunspot number for $R < 110$ as shown in Figure 4. For values of R above about 110 the foF2 plateaus; at least this is what has happened during the past 3 or 4 cycles. There is, of course, no guarantee that all cycles behave similarly.

The diurnal and seasonal variations of foF2 are very complicated and do not follow any simple dependence on χ . As seen in Figure 3 the critical frequencies are higher in winter than in summer for middle latitudes. This winter anomaly is believed to result from chemical changes in the neutral atmosphere that increase the electron loss processes during the summer. Standard methods of time series analysis can be applied to existing data, e.g. Fourier series and Fourier integrals and used for prediction. Another method has been developed by Paul (1972) called anharmonic frequency analysis. This method is applicable when the time series contains a relatively small number of discrete frequencies. Frequencies and amplitudes of the various components are evaluated whereas in Fourier series amplitudes are evaluated for prescribed frequencies. Analyses of this type can be applied to data for a large number of stations and used to predict global distributions of foF2. Similar treatments can be applied to other irregular parameters such as sporadic E, spread F, radio noise, etc.

In the preparation of long term predictions no attempt is made to estimate the day-to-day variations in critical frequency since these are rather localized in both space and time. The first step is to establish the dependence of foF2 and M(3000)F2 on sunspot number using 12-month running means for each hour.

3.2 Prediction in the Space Domain

The spatial or geographical structure of the ionosphere has been deduced from long time series of data obtained from the world-wide sounding network of ionosondes. The number of stations contributing to this network has grown from a few in the early 1930's to around 150 during the International Geophysical Year (1957-58) and has been roughly constant thereafter, i.e. closures have been compensated by new installations.

The most widely used predictions are those developed in the Department of Commerce, Boulder, Colorado using a numerical mapping system developed by Jones and Gallet (1962). The term numerical map is used to denote a function Γ of latitude, longitude and time and is obtained by fitting certain (Fourier) polynomial series to the ionospheric data. The Fourier coefficients vary with geographic coordinates. The numerical map is particularly useful when incorporating additional data and also when large numbers of propagation paths are involved.

The graphical forms of numerical maps are illustrated in Figures 5 and 6 which show zero distance maximum usable frequency or penetration frequency of the extraordinary wave $f_x F_2 = f_o F_2 + \frac{1}{2} f_c$, with vertical sounding. These maps show that the maximum of $f_x F_2$ lies not at the subsolar point but in two zones one north of the other south of the magnetic dip equator.

Using this method the Consultative Committee on International Radio (CCIR) of the International Telecommunications Union (ITU) has published an Atlas of Ionospheric Characteristics (CCIR Report 340, 1966). The Atlas is in two forms: (1) on punched cards for computer usage, and (2) in the form of charts, for two levels of solar activity 0 and 100. For values of $R > 150$, R is set equal to 150, linear interpolation and extrapolation is used for $0 < R < 150$.

Numerical maps have been constructed for other ionospheric parameters: for $f_o E_s$ (Leftin, Ostrow and Preston, 1968), for the sporadic-E blanketing frequency $f_b E_s$ (Leftin and Ostrow, 1969), $f_o E$ (Leftin, 1976) and occurrence of spread F (Davis, 1972). The technique has been applied also to the representation of the daily departures of the $f_o F_2$ from the monthly median (Jones, Gallet, Leftin and Stewart, 1973).

Vertical to Oblique Conversion

Given the ionospheric parameters at a given geographical point it is necessary to predict the propagation conditions using that point (e.g., as the midpoint of a propagation path). This is usually done, assuming that the ionosphere is concentric, by the use of nomograms (or equivalent numerical techniques) given for example by Davies (1965, Chapter 7) and the CCIR Report 340. Of course, in practice the ionosphere is not concentric and errors in predicting propagation paths can arise. In this case recourse to ray tracing techniques is necessary to determine the ray path between given transmitter and receiver. An example of a double-bounce ray path across the equatorial bulge, shown in Figure 7, could not be predicted from concentric geometry. For ray tracing it is necessary to predict the ionospheric densities as a function of height. Such predictions are available using numerical models (see Jones and Stewart, 1970) as shown in Figure 8 or parabolic models (see Barghausen et al., 1969).

Ionospheric Scintillations

Some of the undesirable aspects of the ionosphere are its adverse effects, e.g. the amplitude and phase fluctuations, on radio signals from satellites to Earth. A global model of scintillations has been developed by Fremouw and Rino (1973). This model takes into consideration sunspot number, season, local time, frequency, and geographical locations. An output of such a model, given in Figure 9, shows that scintillation is important in the equatorial zone and, to a lesser extent, in the auroral zone.

Radio Noise

Signal-to-noise ratio is a primary concern of radio operators and planners so that global maps of radio noise levels are an essential part of the trade. World distribution and characteristics of atmospheric radio noise have been published by CCIR (Report 322, 1963). There are several types of noise, e.g. noise internal to the receiver and external noise which in turn can be subdivided into several types such as atmospheric, galactic and man-made. Atmospheric noise dominates on frequencies below about 30 MHz and the CCIR report presents world maps of mean noise power on an effective frequency of 1 MHz for four seasons: winter, spring, summer and autumn, for 4-hour periods in local time as illustrated in Figure 10. Graphs are also provided for extrapolating to radio frequencies other than 1 MHz, together with the standard deviations of the data. The noise levels are for a bandwidth of 1 kHz and must be corrected for the appropriate operational bandwidth. One of the main shortcomings with these noise maps is the lack of directional information. The atmospheric noise sources (e.g., thunderstorms) are usually located in specific areas, thus the directivity of a receiving antenna may differentiate in favor of or against the noise level.

Total Electron Content

For a number of (radio) purposes, the total content integrated along a path through the ionosphere is required. Some examples of the use of total electron content (TEC) include: (1) excess time delay of a radio signal over that in free space, (2) change in phase path, (3) angle of refraction of a satellite-to-ground raypath, and (4) angle of rotation of the electric field of a radio wave.

The excess time delay is given by equation (4) while the change in phase path (see Lawrence, Little and Chivers, 1964)

$$P = \frac{40.53}{f^2} N_T \quad \text{meters} \quad (14)$$

where N_T is the integrated electron content in a column of 1 m^2 along the raypath. The refraction angle τ caused by an horizontal gradient of total content is

$$\tau = \frac{2332}{f^2} \frac{dN_T}{dx} \quad \text{degrees} \quad (15)$$

and the doppler shift Δf resulting from a time rate of change in N_T

$$\Delta f = - \frac{1.352 \times 10^{-7}}{F} \frac{dN_T}{dt} \quad (16)$$

The Faraday rotation of the electric field is

$$\begin{aligned} \Omega &= 4.840 \times 10^{-5} \int f_L N ds \quad \text{degrees.} \\ &= 4.840 \times 10^{-5} F N_F \end{aligned} \quad (17)$$

where f_L is the electron gyrofrequency corresponding to the component of the geomagnetic field (B_z) along the raypath, F is a weighted mean of f_L and N_F is the Faraday electron content up to a height of about 2000 km (see Davies, Fritz and Gray, 1976). Davies, Fritz and Gray (1976) give a method for the prediction of total electron content N_T from Faraday content (the latter being easier to measure) viz

$$N_T = N_F(LT) + 0.1N_F(12) \quad (18)$$

where $LT \equiv$ local mean time and $N_F(12)$ is the noon value.

Models for the prediction of vertical electron content for systems engineers and planners have been constructed by Klobuchar and Aarons (1973). For many purposes monthly median maps are required whereas for some purposes, especially those for which horizontal gradients are important, require a "snapshot" of the ionosphere. By combination of geostationary and orbiting satellite data Davies, Hartmann and Leitinger (1977) have constructed "real time" contour maps of total electron content such as that shown in Figure 11.

3.3 Prediction in the Frequency Domain

High Frequencies

We start our discussion of ionospheric prediction in the frequency domain with the high frequency band (approximately 2 to 30 MHz) because its usage is almost entirely dependent on the ionosphere. The ground range is restricted essentially to line-of-sight and within this range communication is far better carried on higher frequencies where the bandwidth is more adequate.

There are numerous systems available for calculating the required radio parameters necessary for a specified circuit performance. Some countries have developed their own systems to take account of the special ionospheric conditions prevailing there. Others rely on one of the world-wide systems such as that developed at the Institute of Telecommunications Science in the U.S.A. (see for example Roberts and Rosich, 1971; Barghausen, Finney, Proctor and Schultz, 1969; Haydon, Leftin and Rosich, 1976). There are certain basic monthly median ingredients which all systems must contain, these include: the zero-distance MUF, information on the height of the ionosphere to enable the determination of the $M(d)$ factor and the angles of elevation, a measure of the ionospheric absorption to determine signals strength (lowest usable frequency), and radio noise levels.

The first quantity that must be determined is the usable bandwidth, i.e. the maximum and lowest usable frequencies. To obtain the optimum working frequency (FOT -- French initials) an allowance of 15% is made for the fluctuations about the monthly medians. Thus:

$$FOT = 0.85 \times (\text{median MUF}) \quad (19)$$

The idea is that the FOT should be as high as possible to minimize ionospheric absorption (see Equation (2.2)) but sufficiently below the median MUF to allow reflection 90% of the time. Having selected an optimum frequency it is necessary to establish that it is not cut off by an underlying layer and that it lies above the LUF set by absorption, noise, antenna, etc. Having established that the frequency is usable it is necessary to determine the transmitter power required for a specified grade of service.

An additional constraint on frequency selection is imposed by electromagnetic compatibility, namely the need to avoid interference. Frequencies are assigned on a priority basis by national administrations. The radio frequency allocation system tends to be inflexible and, once an operator has been allocated a specific frequency, the extent to which he (she) can utilize propagation predictions is severely circumscribed. The overuse of equation (19) to determine the FOT has proven counterproductive. Since the world's population is concentrated in a relatively few geographical areas, most radio circuits will tend to have approximately the same FOT. The resulting spectrum congestion makes such frequencies far from optimum and radio operators often find that frequencies near the LUF give better performance for the weaker signal is more than compensated by the lower interference.

Medium Frequencies

The MF band (approximately 300-2000 kHz) is one of the most intensively exploited parts of the radio spectrum because of the presence of the AM broadcast band (\approx 500-1600 kHz). The operation of the broadcast band depends mainly on a dominant ground wave so that the sky wave is usually undesirable as it leads to fading and interference. During the day the sky wave is absorbed and the AM band operates satisfactorily. At night, when D region absorption practically disappears, the sky wave is enhanced and the result is interference between stations using the same channel. This is an example of a poor allocation of the frequency spectrum to do a job that would be better done at much higher frequencies (e.g., VHF), however, the enormous financial investment in equipment prevents correction of the mistake.

Broadcast stations are divided into (a) clear, (b) regional, and (c) local channels. A clear channel is essentially assigned solely to one station and is allowed 50 kW power (in the U.S.A.). Regional and local channels are shared and limited to low powers. Local stations are sometimes restricted to daylight operation.

Methods for calculating signal strengths on medium frequencies which encompasses the AM broadcast band are given by CCIR (Report SG-6, 1976). The field strengths depend on local time, sunspot number, magnetic latitude, path length, transmitter power, frequency, etc. Because of the congestion in this part of the spectrum, experimentation is severely limited and so our knowledge of ionospheric radio is least on frequencies we use most. Much of the data for MF predictions have been gathered in Europe (see Ebert, 1962) and in the U.S.A. (see Norton, 1959). There is considerable uncertainty in the measurements: for example, it is unclear whether the signal strength increases or decreases with carrier frequency. There appears to be little seasonal variation in signal strength.

When these prediction systems were applied to the magnetic equatorial zone they were found to be inadequate, the observed field strength was found to be less than the predicted value. The main reason for this is that vertical antennas used in AM broadcasting excite mostly the ordinary wave in Europe and the U.S.A. because the magnetic field is nearly vertical whereas at the magnetic equator the magnetic field is horizontal and the extraordinary wave is excited. We see from equation (9) that on MF ($\omega = \omega_H$) the extraordinary wave is heavily absorbed and the echo is weak.

Wave polarization is important on medium frequencies ($f < f_H$) because mismatch can occur between an ionospheric echo (mostly ordinary) and a receiving antenna. The echo will be largely oriented parallel to the magnetic field so that an antenna perpendicular to this direction (horizontal) will pick up a relatively small fraction of the echo (see Davies, 1969, Chapter 13).

Other Frequencies

Predictions of signal strengths on very-low and low-frequencies are made from CCIR Reports (SG-6, 1976, p. 125) and (SG-6, 1975). These frequencies are important in navigation, e.g. OMEGA. Again the signal strengths depend on local time, geomagnetic location, etc.

Above the high frequency band lies the very high frequency (VHF) band over which the ground wave dominates and any sky wave is a nuisance. Not infrequently intense sporadic E results in long distance propagation of VHF signals that produce unwanted co-channel interference. A prediction model for estimating VHF field strengths in middle latitudes is given in the Annex to CCIR (1976). Frequencies above about 100 MHz are rarely reflected from the ionosphere but ionospheric irregularities do produce undesirable scintillation on satellite communications up to frequencies of 6 GHz.

Extrapolation in the Frequency Domain

One important aspect of prediction is the extrapolation of known conditions in one part of the frequency spectrum to another. Predictions of this nature have not been uniformly successful in the past. The discovery of the ionosphere itself was the result of a wrong prediction. In 1901 Marconi successfully established radio communication across the Atlantic in the face of theoretical predictions that radio waves could not possibly bend around the Earth. About World War I the prevailing prediction, based on the Austin-Cohen formula, was that, for long distance transmission, long waves were superior to short waves. This prediction was upset around 1923 when the American Radio Relay League (amateurs) showed that high frequencies would propagate over large distances with relatively little attenuation (see Davies, 1969, Chapter 1).

In the 1950's it was predicted that HF communication would be replaced by higher frequencies which were reliable especially in high geomagnetic latitudes, for example meteor scatter and D region forward scatter. It is interesting to note that the Canadian meteor scatter (JANET) system was blacked out in its first week of trials by a polar cap absorption (see Folkestad, 1968, page 440).

With the advent of satellite communications the prediction (based on equation (1)) was that signals on VHF and SHF would be free of undesirable scintillations because of the inverse square dependence. The occurrence of scintillations on frequencies up to the GHz range came as a shock. It now appears that the depth of amplitude scintillations falls off more like the inverse frequency rather than its square. This type of

prediction is very important because historically most of our knowledge about the ionosphere have been collected at lower frequencies and extrapolated to higher frequencies. Of course it must be realized that, in general, ionosphere effects do diminish with increase of radio frequency.

While on this topic it is important to consider predictions of what will happen to the ionosphere because of the advertent and inadvertent modification by man. Examples abound such as increasing transmitter power in order to overcome high interference levels. Not only does this compound the congestion aspects but, to some extent, is self defeating because high power radio signals enhance the absorption in the D region (e.g., the Luxemburg effect)--see for example Megill (1965), Davies (1969)--and create irregularities and absorption in the F region--see Utlaut (1975). Before the Platteville heating experiments (Utlaut, 1975) it was predicted that F region absorption would decrease with heating because the electron-ion collision frequency decreased with increase of electron temperature. Observations showed that "broadband" attenuation of the ordinary wave results from heating. The production of spread F was essentially not predicted yet it is the dominant consequence of F region heating--see Davies (1978).

Another example of the need for ionospheric prediction arises from the proposal to establish, in geostationary orbit, a satellite power station (see Glaser, 1977; Brown, 1973). The following questions arise in this connection: (1) What will happen as the result of heating the D and lower E regions where the electron loss rate decreases with increase of electron temperature? (2) Will there be appreciable scattering of microwave energy (≈ 2.5 GHz) out of the beam? (3) Will the beam itself create irregularities? (4) Will the chemical pollution of the neutral F region deplete the electron concentration there? The latter effect could have a profound effect as shown by Mendillo et al. (1975) in the case of the launch of Skylab. Other questions regarding chemical modification are: Will chemical modification create dynamical (Rayleigh-Taylor) instabilities that can simulate the natural spread F?, and "Will the ionospheric modification produce a "duct" in the plasmasphere enabling radio signals to propagate to the magnetic conjugate area?.

3.4 Accuracy of Predictions

The questions often arise "How accurate are these predictions?" and "Do we need greater accuracy?". There are no simple answers to these questions because we need to define what we mean by accuracy and what benefits accrue from a more precise prediction of a given ionospheric parameter. The answers depend also on the particular parameter, for example foF2. The predicted foF2 depends, among other things, on the accuracy of the predicted sunspot number or other index which may not be an ionospheric parameter, on geophysical location, season, etc. The critical frequencies of the E and F1 layers are relatively well behaved and, for an accurate sunspot number, the predicted monthly median values are within about 5% of those observed. The monthly median foF2, one of the more variable ionospheric characteristics, can be predicted with an accuracy of within 10 per cent even at Churchill, Canada in the highly variable auroral zone (see Folkestad, 1968, page 257).

It must be remembered that the accuracy of a monthly median is not necessarily the relevant quantity. The standard deviation of foF2 in middle latitudes is of the order of 20% of the monthly median. Thus an accurate median is of little value for day-to-day operations and such predictions should be viewed more as a useful guide to intelligent planners and operators rather than as a precise evaluation of ionospheric conditions. This is borne out by predictions of critical frequencies of sporadic E. Although predicted monthly median fEs may be within 0.7 MHz of the observations, there are times when it is completely absent, i.e. indistinguishable from the regular E. Barghausen et al. (1969) have compared predicted and observed signal strengths over selected paths. For one 1200 km path they find that at night the agreement is within ± 2 dB and at noon within about 6 dB. For a second 2600 km path the two sets of data agree within about 7 dB.

As mentioned above these numbers concerning accuracy can have little meaning except to a particular user. For long-term (solar cycle) planning the present ITS predictions are often sufficient to enable the circuit designers to request a range of frequencies and to select antenna systems and transmitters with the appropriate characteristics. Day to day operations are quite a different matter as will be discussed below.

4. FORECASTING

4.1 Forecasting Solar Flares

Predictions of ionospheric conditions for times less than the 27-day solar rotation period are herein called forecasts. Rather than the numerical specification of a parameter (e.g., foF2) forecasts generally are concerned with more qualitative aspects such as the probable occurrence of an X-ray flare and, hence, of a polar cap absorption (PCA) and an ionospheric storm. The effects of these disturbances, particularly PCAs and storms is so catastrophic that it is much more important to know that one is likely than to worry about the fine details. An important service, allied to forecasting, is that of disturbance warning which is a notification that an event is in progress. Forecasting and warning essentially require the same solar observations, the main difference being in the customer requirements and the rapid communications facilities needed for notification.

There are two preliminary data gathering stages in the preparation of these forecasts, viz: solar and geophysical. The solar data include optical (e.g., H α) observations of the structures, locations and evolutions of active regions (e.g., plages, filaments, etc.), radio bursts and, from satellites, X-rays, extreme ultraviolet and particle fluxes in space. Essentially all solar X-ray flares large enough to affect radio waves are detected by satellites near the Earth. Because of the high time resolution (≈ 3 sec) and intensity resolution the early rise in emission can be detected minutes before the flare intensity is high enough to produce significant ionospheric effects. The geophysical data include: the geomagnetic field, ionospheric radio soundings, cosmic radio noise and monitoring of radio circuits from VLF through HF.

Solar flares are large explosions observed in red H α (6563 A), X-ray, EUV, radio emissions, etc. The area and intensity of a flare increase rapidly to a peak in a few minutes and decay relatively slowly, the larger the peak optical intensity the longer the duration which may last from 3 or 4 min to 2 or 3 hr; the average lifetime is about 30 min. Solar flares are assigned an "importance" based on area (0 to 4) and brightness (faint F, normal N, bright B) which replaces an older range between 0 and 3+ (see Solar-Geophysical Data, 1977).

For the forecasting of sudden ionospheric disturbances the X-ray ($\frac{1}{2}$ A to 8 A) flare is important. These X-ray flares are rated C, M and X according to their fluxes (E) in the 1-8 A range as measured by satellites, i.e. C: $10^{-3} < E < 10^{-2}$; M: $10^{-2} < E < 10^{-1}$; X: $10^{-1} < E \text{ erg cm}^{-2} \text{ sec}^{-1}$. Class X flares produce SIDs that affect radio communications, so it is important to estimate their probability of occurrence. Radio noise bursts are categorized as follows:

- Type 1 or noise storms are characterized by a background continuum with superimposed bursts. This type can persist for hours or days. They usually follow a flare and are associated with strong magnetic fields.
- Type 2 or slow drift bursts in which the radio frequency falls (from say 100 MHz to 10 MHz) during their 10 to 20 min lifetime. They tend to be associated with large flares and indicate that material is being ejected from the Sun and a shock wave is propagating towards the Earth.
- Type 3 or fast drift bursts in which the radio frequency falls (from say 500 MHz to 10 MHz) in a few seconds. Type 3 bursts are thought to be associated with streams of relativistic electrons.
- Type 4 and 5 bursts are broadband continuum radiations. Type 4 lasts from 10 min to several hours whereas Type 5 lasts for about 1 min. Synchrotron radiation from relativistic electrons spiraling in coronal magnetic fields are thought to cause Type 4 bursts which correlate with Forbush decreases in cosmic noise and with geomagnetic storms. Identification of radio noise bursts is, therefore, a valuable tool in the forecasting of the terrestrial effects of solar flares. It must be realized that solar activity interpretation and, hence, forecasting is largely an art developed by experienced observers. Few, if any, flares have identical characteristics and some large optical flares produce small terrestrial effects whereas a medium size optical flare may well result in a large terrestrial effect.

Turning to forecasting procedures; as of 1971 there were about 14 centers issuing short-term forecasts of solar activity and/or ionospheric parameters. Generally, the solar forecasts consist of collecting optical observations, e.g. locations and sizes of active regions, filaments, fibrils, plages, etc., solar magnetic field, solar radio noise amplitude over a wide frequency range, solar X-rays, satellite particle measurements, and ground-based ionospheric measurements. The development of active areas in particular is used by experienced observers to infer the occurrence of a flare within the following few (1 to 3) days. From comparison of prevailing conditions on the Sun with previous patterns, experienced observers can estimate the possibility that if a flare occurs it will be accompanied by X-rays, high energy protons, etc. Combining these data with radio noise observations and other information gives added weight to the forecast.

4.2 Terrestrial Effects of Solar Flares

A group of phenomena classified as sudden ionospheric disturbances, listed in Table 3, are caused by solar electromagnetic radiation that arrive on Earth at about the same time as the visible light. The effects are mostly caused by ionization enhancements in the D region which affect the reflection of VLF and LF and enhance the absorption of HF and VHF. Enhanced ionization in the E and lower F regions produce sudden frequency deviations which are closely related to enhancements of solar EUV and hard X-rays. Sudden ionospheric disturbances are daylight hemisphere phenomena that produce HF radio blackout (several minutes) but a few last up to one hour. In 1937 a year of high sunspot numbers 33 SWFs lasting more than 1 hr were observed at Washington, D.C. whereas in 1944, at sunspot minimum, only 2 were observed lasting for 1 hr. During intense SIDs the absorption in the D region can increase by a factor of 10 (see Davies, 1965, Chapter 6). Some flare effects are gradual, rather than sudden, and vary as $\cos^{\theta} \chi$ so that the magnitude is largest near the subsolar point and small in polar regions and near the sunrise and sunset lines.

The sequence of events following a large flare is illustrated in Figure 12. High energy (1 to 20 MeV) solar protons arrive at the Earth from 15 min to several hours after the flare occurrence and these are deflected by the geomagnetic field to the polar caps where they produce intense ionization in the D region resulting in polar cap absorption. Polar cap absorption produces serious disruption of radio traffic over the polar caps from VLF through VHF. Fortunately, however, the effects are largest during

daylight, although the enhanced absorption reappears for from 1 to 10 days. The daytime absorption is about four times that at night. PCAs are not normally accompanied by either geomagnetic or auroral disturbance, except in the later stages when a storm sets in.

By far the most important of the short time disturbances is the ionospheric storm which tends to originate near the auroral zone and extend to middle and low latitudes where it causes disruption of radio traffic. Storms are produced by charged particles, mostly electrons with energies of the order of 1-10 kev. Ionospheric storms are related to geomagnetic storms which may last from a few hours to several days. D-region enhancements are often called auroral absorptions because they are most intense near the auroral zone. In middle latitudes the most serious feature of a storm is the depression of the critical frequencies of the F2 layer (see Figure 13).

4.3 Sudden Ionospheric Disturbances

The forecasting of sudden ionospheric disturbances amounts essentially to the forecasting of X-ray flares. The magnitude of an SID depends upon the magnitude of the flare X radiation, on the solar zenith angle and, to some extent, on prevailing ionospheric conditions. Essentially all solar X-ray flares that can be observed from the Earth (i.e., on the front of the Sun) are being detected by satellite instruments on such satellites as Solrad Hi, GOES, SMS-1. Because of the high time resolution (≈ 3 sec) and sensitivity the early rise in emission can usually be detected minutes before the X-ray intensity is high enough to produce significant ionospheric effects (X flare).

In the present state of the art it appears that while forecasters can predict that a flare will occur in the next several days they cannot accurately predict when the flare will erupt, its size nor its duration. It should be remembered, however, that forecasts of no-flare occurrence can be of considerable value.

The forecasting of ionospheric effects above the D region (e.g., SFDs) depends on forecasting an EUV flare (Donnelly, 1976). Ionospheric effects of this nature do not disrupt radio communications and therefore are of little practical importance.

There is no simple method for predicting the magnitude of an ionospheric effect of a flare. One approach is to estimate the enhancement in solar radiation and, hence, make model calculations of the changes in the electron density profile of the D layer. From this it is possible to calculate, using propagation theory, the effects on VLF phase (see Morfitt, 1971) and the enhanced absorption of HF waves (see Bleiweiss, 1972). For most operational purposes, a knowledge that an SID is imminent is all that an operator needs in order to take corrective action. Fortunately, SIDs are sufficiently short-lived that a radio communicator can "sit it out" provided he is aware of the cause.

4.4 Polar Cap Events

Polar cap events are large increases in D-region ionization that occur more-or-less uniformly over the cap (Lied, 1967, page 94). Although they are usually termed polar cap absorptions (PCAs) they also affect VLF, LF, etc., waves propagating over the polar caps. The prediction of PCAs has been discussed by Cook and McCue (1975). Proton flares may be accompanied by an SID, ground-level cosmic ray increase, type 4 radio bursts, etc. Proton flares appear to occur in regions of high magnetic field gradient and are accompanied also by high radio fluxes on metric and centimetric wavelengths (Castelli et al., 1967) with a minimum on decimetric wavelengths giving a U-shaped spectrum. Croom (1970) has proposed a criterion that on 19 GHz a peak noise flux increase of more than 50% and an overall flux increase of 10% for longer than 5 min indicates a proton flare. These types of criteria are used by forecasters to predict the occurrence of polar cap events.

Once a PCA has been forecast its development can be predicted from climatological considerations based on previous patterns. For example, a typical sequence of events in a PCA has on August 16-18, 1958 been described by Lied (1967, page 63). A flare (importance 3+) occurred at 0433 UT, followed by an SCNA which lasted for about 10 min with peak absorption of about 2 dB on 27.6 MHz. The PCA started in northern Norway, about 2 hours later the maximum absorption was about 13 dB, followed by a minimum around midnight and increasing again to around 16 dB next day. A magnetic sudden commencement and storm occurred that day with absorption peaking around 10 dB. The difference in the magnitude of the day and night absorption results from the nighttime attachment of free electrons, in the D region, to neutrals to form stable negative ions. During the day the electrons are detached by solar radiation.

The occurrence of PCAs follows the sunspot cycle as shown in Figure 14. There is no evidence of a seasonal variation in occurrence. During 1957-58 one day out of 8 had PCA. The most likely duration of events is about 2 days but can last up to 6 or 7 days (Warwick and Haurwitz, 1962).

4.5 Ionospheric and Geomagnetic Storms

From the point of view of radio communications ionospheric and geomagnetic storms are by far the most important of the terrestrial consequences of solar disturbances. Flares are thought to produce shock waves in the interplanetary medium that strike the

Earth's magnetosphere producing changes in the geomagnetic field and causing the precipitation into the ionosphere of energetic stably-trapped particles. While some of these magnetospheric energetic particles may originally come from the Sun some are thought to come from the ionosphere. The arrival of the shock wave compresses the magnetosphere and produces a magnetic sudden commencement (SC) as shown in Figure 15. After the SC there is an increase in the horizontal component (the initial phase), followed by a decrease below normal (main phase) and a recovery phase. The intensity of a magnetic disturbance is measured by the logarithmic K and linear A indices (see Rostoker, 1972).

The effect of a storm on the ionosphere is illustrated in Figure 16 for the variation of total electron content (it applies also to N_{F2}) over North America. Mendillo (1973) has shown that provided the sudden commencement occurs sufficiently early in the day an enhancement of TEC (positive phase) occurs near 1800 local time on that day (storm day 1) with a sharp decrease followed by below normal values on succeeding days (negative phase). The negative storm is particularly important because the usable HF radio spectrum is compressed by the decrease in MUF (especially when there is enhancement of D region absorption and, hence, of the LUF).

Ionospheric storms are more frequent at high sunspot numbers and negative effects tend to occur in summer and positive effects in winter. Negative storms are mostly confined to middle latitudes with equatorial negative storms occurring only during the most intense disturbances. Having formed, an area of depressed foF2 will tend to move around the Earth with the Sun starting in the morning sector and ending in the afternoon sector.

In addition to flare associated magnetic storms, there are recurrent storms caused by sectors in the solar wind sweeping past the Earth. Since these sectors rotate with the Sun, these storms tend to recur every synodic solar rotation of approximately 27 days. The recurrent storms are most evident in years of low sunspot number when the background magnetic activity is low. At these times a storm may recur two or three times. The recurrent storms are associated with particular regions on the Sun such as coronal holes (see Bohlin, 1976).

Forecasts of solar-terrestrial conditions are made by a number of organizations, one of which is the Space Environment Services Center (SESC) of the National Oceanic and Atmospheric Administration (NOAA) in Boulder, Colorado. SESC is a national and international focal point for real-time solar and geophysical data. It maintains a continuous watch on the Sun by satellites, by optical and radio telescopes located around the world. An elaborate communications system links SESC with the observatories so that it is immediately aware of solar activity. The communications links are vital to the dissemination of forecasts which includes event notification. Forecasting itself goes on continuously and three forecasts are issued daily. Event notification involves the alerting of individuals and organizations of the occurrence of prevailing conditions. A sample forecast is shown in Figure 17. The solar-geomagnetic data are converted by the Global Weather Central of the USAF into a plain language HF radio propagation report, an example of which is shown in Figure 18.

4.6 Short-Term Prediction of F2 Parameters

The forecasts discussed in section 4.5 provide information on the general state of the ionosphere, information is sometimes required to improve frequency usage, i.e. MUF. The ITS system (Barghausen, 1969, section 8.4) includes the capability of short-term F2 MUF predictions based on the local magnetic K index. The ratio $P = (\text{daily MUF})/(\text{monthly median MUF})$ is determined as a function of K for each hour, i.e.:

$$P = P_0 + bK \quad (20)$$

where P and b are constant for given location and hour. These coefficients are determined for several geomagnetic latitude zones, several levels of sunspot numbers and eight local time intervals (00-03, etc.). The average of four previous K values is used in the prediction. With this technique Barghausen et al. (1969) report that error reductions of MUF as large as 23% are possible in the auroral zone and 15% in middle latitude. It may be borne in mind that while the foF2 may be depressed during magnetic activity, sporadic E (fEs) may be enhanced and the net effect could be an increase in MUF especially near the auroral zone.

Most short-term predictions, like the ITS system, are based on modifying the monthly median curve. The main difficulty with this approach is that any individual daily curve shows little similarity to the median curve. Indeed predicting the shape of the diurnal variation of say foF2 has proven to be difficult and statistics show that it is no easier to predict 6 hours in advance than 6 months in advance.

4.7 Accuracy of Forecasts

As in the case of long-term predictions the question of accuracy of forecasts cannot be answered simply. Various statistical studies have been made (e.g., Agy, 1970, Chapter 5) which show that forecasts of solar activity can be made with high accuracy (80% to 90%) and that some 50% to 70% of the more outstanding events have been announced in advance. Also while statistical improvements in foF2, etc., can be achieved by short-term modifications, this may be of little benefit to the operator unless he has

rapid access to the information and the ability to use the information, e.g. change transmitter frequency. Further although the climatological (average) picture of ionospheric storms has been established with reasonable confidence it may be of little value in forecasting the detailed history of an individual storm. It is now clear that at a given geographical location no two storms are exactly alike and a given storm, at different locations, rarely produces identical ionospheric responses.

The value of a forecast is, therefore, much more important than accuracy in a purely numerical sense. Most users are more concerned with catastrophic events than in minor disturbances so that statistics may be misleading. Thus a particular forecaster may err in forecasting 98 small events but, if he correctly forecasts the two major storms, his statistics may be poor but his reputation good. The latter argument has been cited to support unconventional methods such as that based on planetary conjunctions (Nelson, 1963; Blizzard, 1970).

Short-term forecasts are of considerable value to certain users especially those in isolated high-latitude locations where ionospheric radio is the sole link with the outside world. Some ways in which forecasts have been, and are, of value include: (a) priority material can be passed before the radio channel closes, (b) the operator can switch to an alternative link such as cable, satellite, low-latitude relay, if any of these (more expensive) links are available, (c) the operator is warned that his equipment is not necessarily malfunctioning and does not require servicing, an expensive operation at an isolated location.

In using the ionosphere, predictions and forecasts should be used mainly as a guide in determining a course of remedial actions. Educated operators are essential for effective utilization of radio circuits and a small investment in training may be a far better investment than in expensive equipment. It should also be emphasized that the value of a forecast depends largely on how quickly the information can be communicated to the user. This has improved greatly in recent years with the use of computers and satellite communications circuits.

5. CONCLUDING REMARKS

In this lecture an attempt has been made to give a broad picture of the needs for which such predictions are prepared. Broadly speaking the present ionospheric prediction systems are adequate for the long-term planning of frequency allocations on an international basis and for the design of many long-distance HF communications circuits.

On the other hand, short-term forecasts are, generally, inadequate to insure that the necessary corrective action be undertaken. At the present time, prospects for improvement are moderate to poor. Indeed financial cutbacks have resulted in a deterioration in forecasting services in the past few years. The biggest improvements in recent years, in both long-term and short-term predictions have largely resulted from technological advances in data acquisition, processing and distribution.

REFERENCES

- Albertson, V. D. and J. A. Van Baelon (1969), Electric and Magnetic fields at the earth's surface due to auroral currents, *IEEE Trans.*, PAS-89, 578-584.
- Appleton, E. V. and W. J. G. Beynon (1940), The application of ionospheric data to radio communications problems, Pt. I, *Proc. Phys. Soc.*, 52, 518.
- Appleton, E. V. and W. J. G. Beynon (1947), The application of ionospheric data to radio communications problems, Pt. II, *Proc. Phys. Soc.*, 59, 58.
- Barghausen, A. F., J. W. Finney, L. Lee Proctor and L. D. Schultz (1960), Predicting long term operational parameters of high-frequency sky-wave telecommunications systems, ESSA Tech. Rept. ERL 110-ITS 78, U.S. Dept. of Commerce, Boulder, CO 80302.
- Belrose, J. S. (1970), Radio wave probing of the ionosphere by the partial reflection of radio waves, *J. Atmos. Terr. Phys.*, 32(4), 567-596.
- Bleiweiss, M. P. (1972), Solar X-ray spectrum definition and the prediction of ionospheric radio wave propagation, Technical Report No. NELC/TR 1840, Naval Electronics Laboratory Center, San Diego, California.
- Blizzard, J. B. (1970), Long range solar flare prediction, in Ionospheric Forecasting, ed. V. Agy, AGARD Conf. Proc. No. 49, London, Tech. Edit. and Reprod.
- Bohlin, J. D. (1976), The physical properties of coronal holes, Physics of Planetary Environments, I, ed. D. J. Williams, Am. Geophys. Union, pp. 114-128.
- Born, M. and E. Wolf (1959), Principles of Optics, London, Pergamon Press.
- Budden, K. G. (1961), Radio Waves in the Ionosphere, Cambridge, The University Press.
- Castelli, J. P., J. Aarons and G. A. Michael (1967), Flux density measurements of radio bursts of proton-producing flares and non-proton flares, *J. Geophys. Res.*, 72, 5491-98.
- CCIR (1964), World Distributions and Characteristics of Atmospheric Noise, Report 322, International Telecommunication Union, Geneva.
- CCIR (1966), CCIR Atlas of Ionospheric Characteristics, Report 340, Geneva, International Telecommunication Union.
- CCIR SG-6 (1975), Ionospheric Propagation (SG-6), CCIR XIIIth Plenary Assembly; Geneva; Volume VI, Geneva, International Telecommunication Union.
- CCIR SG-6 (1976), Conclusions of the Interim Meeting of Study Group 6 (Ionospheric Propagation), Geneva, 16 Feb. - 3 March 1976, DOC 6/177-E, Geneva, International Telecommunication Union.

- Cook, F. E. and C. G. McCue (1975), Solar-terrestrial relations and short-term ionospheric forecasting, Radio Elec. Engr., 45(112), 11-30.
- Croom, D. L. (1970), 19-gigahertz (1.58 centimeter) solar radio bursts as indicators of proton events, J. Geophys. Res., 75, 6940-49.
- Davies, K. (1965), Ionospheric Radio Propagation, NBS Monograph 80, U.S. Govt. Printing Office, Washington, DC 20402; also Dover Publications Inc., New York (1966); also (In Japanese) Corona Press Ltd., Tokyo (1966).
- Davies, K. (1969), Ionospheric Radio Waves, Ginn-Blaisdell, Waltham, Mass.
- Davies, K. (1978), Artificial modification of the ionosphere, AGARD Lecture Series 93.
- Davies, K., R. B. Fritz, and T. B. Gray (1976), Measurements of the columnar electron contents of the ionosphere and plasmasphere, J. Geophys. Res., 81, 2825-2833.
- Davies, K., G. K. Hartmann and R. Leitinger (1977), A comparison of several methods of estimating the columnar electron content of the plasmasphere, J. Atmos. Terr. Res., 39, 571-580.
- Decker, R. W. (1978), State-of-the-art in volcano forecasting, in Geophysical Predictions, ed. H. Landsberg, National Research Council, Washington, DC 20814.
- Donnelly, R. F. (1976), Empirical models of solar flare X-ray and EUV emission for use in studying their E and F region effects, J. Geophys. Res., 81, (25), 4745-4753.
- Ebert, W. (1962), Ionospheric Propagation on Long and Medium Waves, Tech. Doc. 3081-E, Brussels, The European Broadcasting Union.
- EOS (1977), Trans. Am. Geophys. Union, 58(9), 846.
- Farley, D. T. (1970), Incoherent scattering at radio frequencies, J. Atmos. Terr. Phys., 32(4), 693-704.
- Folkestad, K., ed. (1968), Ionospheric Radio Communications, Plenum Press, New York.
- Fremouw, E. J. and C. L. Rino (1973), An empirical model for average F-layer scintillation at VHF/UHF, Radio Sci., 8, 213-222.
- Glaser, P. E. (1977), Solar power from satellites, Phys. Today, 30, 30-38.
- Haydon, G. W., M. Leftin and R. Rosich (1976), Predicting the performance of high frequency sky wave telecommunications systems, OT Report 76-102, U.S. Dept. of Commerce, Boulder, CO 80302.
- Jones, W. B. and F. G. Stewart (1970), A numerical method for global mapping of plasma frequency, Radio Sci., 5, 773-784.
- Jones, W. B. and R. M. Gallet (1962), Representation of diurnal and geographic variations of ionospheric data by numerical methods, Radio Sci., 66D(4), 419-438.
- Jones, W. B., R. M. Gallet, M. Leftin and F. G. Stewart (1973), Analysis and representation of the daily departures of the foF2 from the monthly median, OT Report 73-12, U.S. Dept. of Commerce, Boulder, CO 80302.
- Kelso, J. M. (1964), Radio Ray Propagation in the Ionosphere, New York, McGraw Hill Co.
- Klobuchar, J. A. and J. Aarons (1973), Numerical Models of Total Electron Content Over Europe and the Mediterranean and Multi-station Scintillation Comparisons, AGARDograph No. AG-166A, London, Tech. Edit. and Reprod. Ltd.
- Landsberg, H. E. (1978), Geophysical predictions overview, in Geophysical Predictions, National Research Council, Washington, DC 20814.
- Lawrence, R. S., C. G. Little and H. J. A. Chivers (1964), A survey of ionospheric effects upon earth-space radio propagation, Proc. IEEE, 52(1), 4-27.
- Leftin, Margo (1976), Numerical representation of monthly median critical frequencies of the regular E region (foE), OT Report 76-88, U.S. Dept. of Commerce, Boulder, CO 80302.
- Leftin, M. and S. M. Ostrow (1969), Numerical maps of foEs for solar cycle minimum, ESSA Tech. Rept. ERL 124-ITS 87, U.S. Dept. of Commerce, Boulder, CO 80302.
- Leftin, M., S. M. Ostrow and C. Preston (1968), Numerical maps of foEs for solar cycle minimum and maximum, ESSA Tech. Rept. ERL 73-ITS 63, U.S. Dept. of Commerce, Boulder, CO 80302.
- Lied, F. (1967), High Frequency Radio Communications, AGARDograph 104, Maidenhead, England, Technivision.
- McIntosh, P. S. and M. Dryer, eds. (1972), Solar Activity and Predictions, Progress in Astronautics and Aeronautics, Volume 30, MIT Press, Cambridge, Mass.
- Megill, L. R. (1965), Self distortion of radio signals in the D region, Radio Sci., 69D, 367.
- Mendillo, M. (1973), A study of the relationship between geomagnetic storms and ionospheric disturbances at mid-latitudes, Planet. Space Sci., 21, 349-358.
- Mendillo, M., G. S. Hawkins and J. A. Klobuchar (1975), A sudden vanishing of the ionospheric F region due to the launch of Skylab, J. Geophys. Res., 80, 2217-2228.
- Morfitt, D. G. (1971), Analysis of a Multimode Propagation Concept for Predicting VLF Signal Strengths at Night, Technical Report No. NELC/TR 1798, Naval Electronics Laboratory Center, San Diego, California.
- Nelson, J. H. (1963), Circuit reliability, frequency utilization, and forecasting in the high frequency communication band, in The Effect of Disturbances of Solar Origin on Communications, AGARDograph 59, Oxford, Pergamon Press.
- Norton, K. A. (1959), Transmission loss in radio propagation II, NBS Tech. Note 12, U.S. Dept. of Commerce, Boulder, CO 80302.
- Paul, A. K. (1972), Anharmonic frequency analysis, Math. Comp., 26(118), 437-447.
- Proc. IEEE (1969), Special issue on Topside Sounding and the Ionosphere, 57(6), 859-1170.
- Ratcliffe, J. A. (1959), The Magneto-Ionic Theory, Cambridge, The University Press.
- Ratcliffe, J. A. (1970), Sun, Earth and Radio, London, Weidenfeld and Nicolson.
- Roberts, W. M. and R. K. Rosich (1971), Ionospheric Predictions, OT Report 13, U.S. Dept. of Commerce, Boulder, CO 80302.
- Rostoker, G. (1972), Geomagnetic indices, Rev. Geophys. Space Phys., 10, 933-950.
- Slothower, J. C. and V. D. Albertson (1967), The effects of solar magnetic activity on electric power systems, J. Minn. Acad. Sci., 34, 94-100.

- Smith, N. (1939), The relation of radio sky wave transmission to ionosphere measurements, Proc. IRE, 27, 332.
- Solar-Geophysical Data, (1977), NOAA-EDS, U.S. Dept. of Commerce, Boulder, CO 80302.
- Utlaut, W. F. (1975), Ionospheric modification induced by high-power HF transmitters--a potential for extended range VHF-UHF communications and plasma physics research, Proc. IEEE, 63, 1022-1043.
- Warwick, C. S. and M. Haurwitz (1962), A study of solar activity associated with polar-cap absorption, J. Geophys. Res., 67, 1317-32.
- Whale, H. A. (1969), Effects of Ionospheric Scattering on Very Long Distance Radio Communication, New York, Plenum Press.

Table 1. THE RADIO SPECTRUM

Name	Frequency Range	Primary Propagation Modes	Primary Uses
Very Low Frequency (VLF)	3 - 30 kHz	Waveguide (between Ground and Lower Ionosphere) and Ground Wave	Navigation, Communications Standard Frequency and Time
Low Frequency (LF)	30 - 300 kHz	Waveguide and Ground Wave	Maritime, Loran C, Broadcasting
Medium Frequency (MF)	300 - 3000 kHz	E Region Reflection (Night) and Ground Wave	Maritime, Aeronautical, International Distress AM Broadcasting, Maritime and Land Mobile
High Frequency (HF)	3 - 30 MHz	Reflection from E and F Regions	Maritime and Aeronautical Fixed Services, Broadcasting, Amateurs, Citizens
Very High Frequency (VHF)	30 - 300 MHz	Line of Sight, Scatter from ionospheric Irregularities, E _s	Television, FM Broadcasting Public Safety, Mobile, Aeronautical
Ultra High Frequency (UHF)	300 - 3000 MHz	Line of Sight, Affected by ionospheric Irregularities	Space Communications, Television, Radar, Broadcasting, Navigation Fixed, Mobile
Super High Frequency (SHF)	3000 - 30,000 MHz	Line of Sight, Tropospheric, Affected by Ionospheric Irregularities	Space Communications, Television, Radar, Broadcasting, Navigation Fixed, Mobile

Table 2. Typical Users of the Ionosphere

1. Military
 - 1.1 Communications, point to point
 - 1.2 Navigation
 - 1.3 Surveillance, e.g. over the horizon radar
2. Civilian
 - 2.1 International broadcasters
 - 2.2 Commercial communicators
 - 2.3 Industrial companies (communications)
 - 2.4 Industrial companies (prospecting)
 - 2.5 Power companies
 - 2.6 Amateur radio operators
 - 2.7 Scientists
 - 2.8 Government communications.

TABLE 3.

SUDDEN IONOSPHERIC DISTURBANCES

PHENOMENON	FREQUENCY BANDS INVOLVED
Sudden Frequency Deviation (SFD)	HF
Short-Wave Fadeout (SWF)	HF and Lower VHF
Sudden Phase Anomaly (SPA)	VLF
Sudden Enhancement of Atmospherics (SEA)	LF
Sudden Enhancement of Signal (SES)	VLF
Sudden Cosmic Noise Absorption (SCNA)	HF and Lower VHF

Table 4. Ionospheric layers

Name	Height Range km	Approximate Peak Densities m^{-3}
C	50 - 60	10^8
D	60 - 90	10^9
E	90 - 140	10^{11}
F1	140 - 200	2×10^{11}
F2	> 200	10^{12}
Plasmasphere	≈ 1000	10^{10}

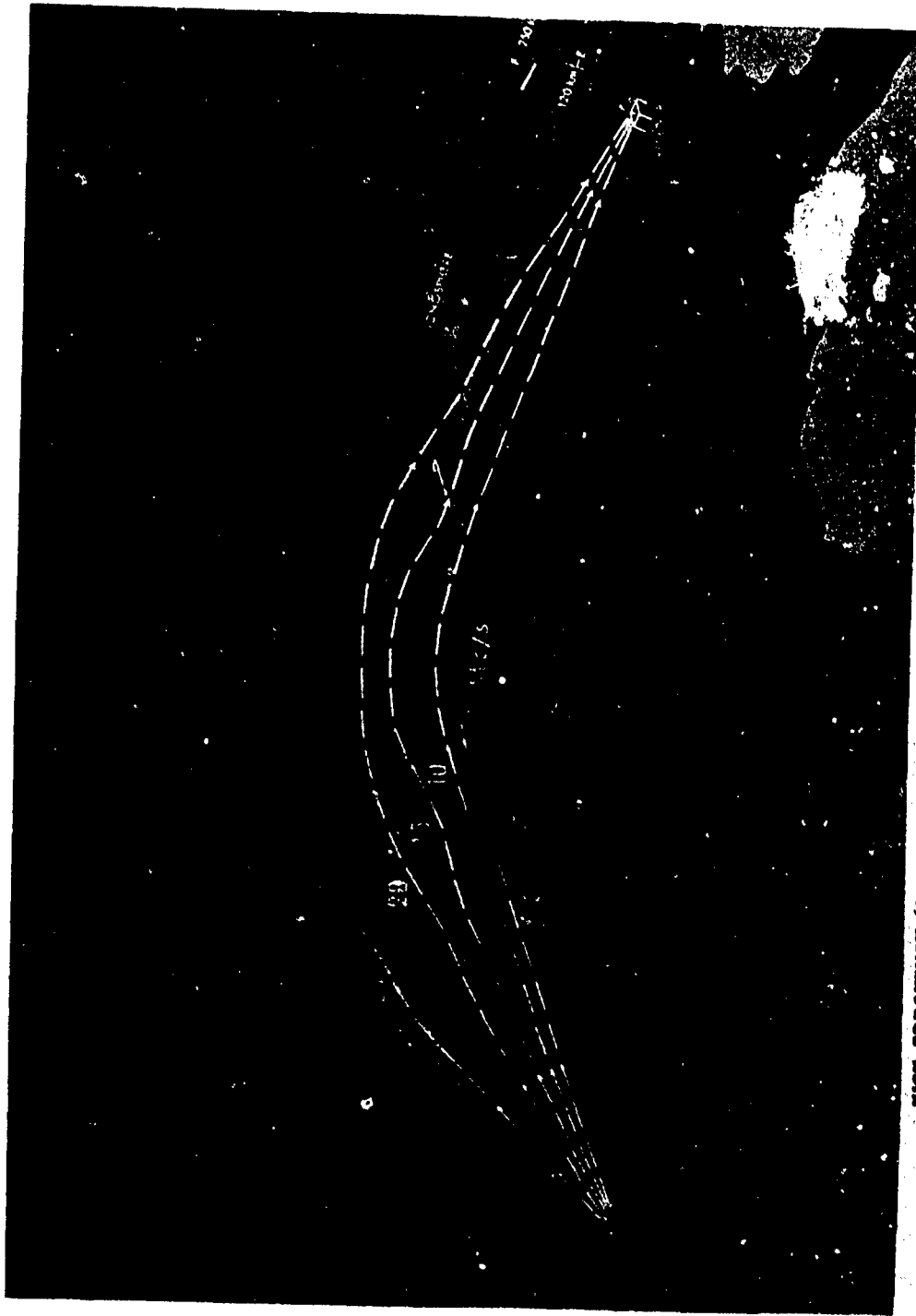


Fig.1 Illustrating refraction, reflection, penetration and absorption of radio signals in the ionosphere

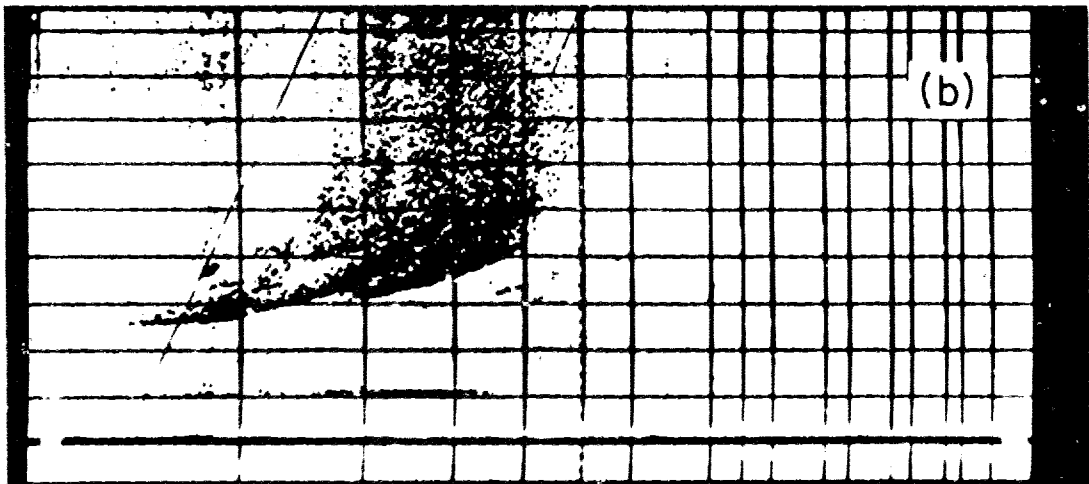
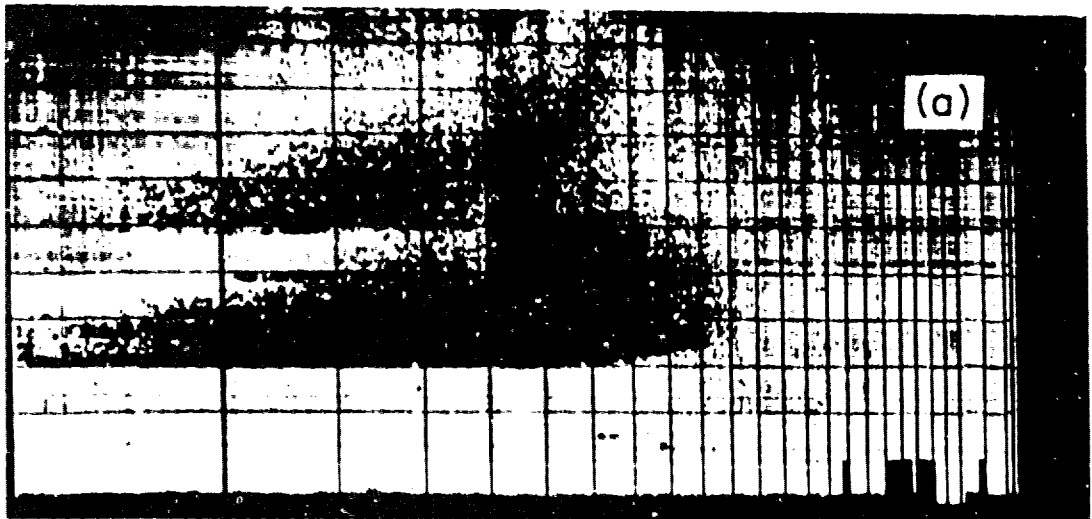


Fig.2 Ionogram showing spread F

Best Available Copy

JANVIER - JANUARY - ENERO; 00h; $R_{\text{ion}} = 0$; EJF (ZERO) F2 (MHz)

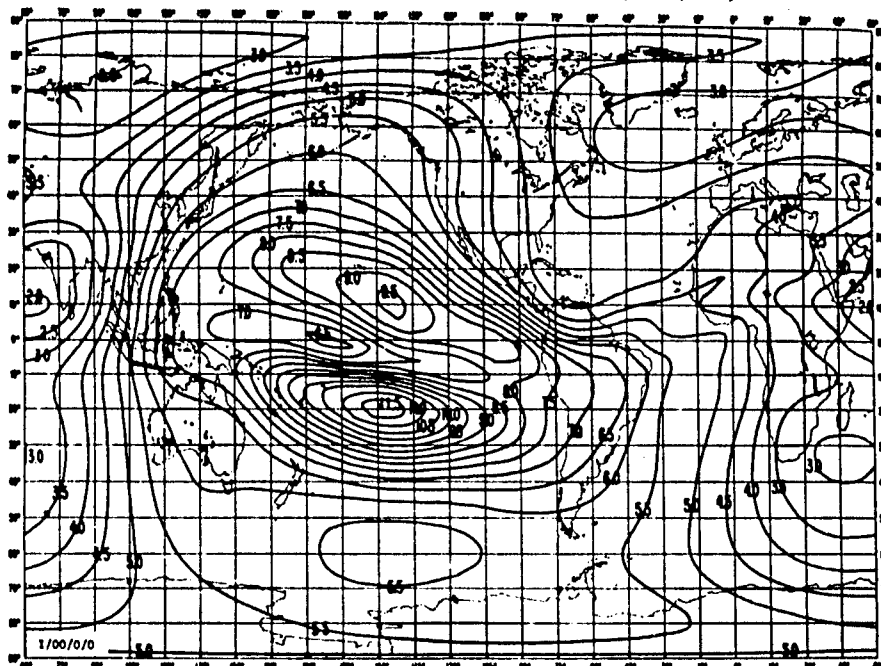


Fig.5 Global map of F2 MUF(o) R = 0

JANVIER - JANUARY - ENERO; 00h; $R_{\text{ion}} = 100$; EJF (ZERO) F2 (MHz)

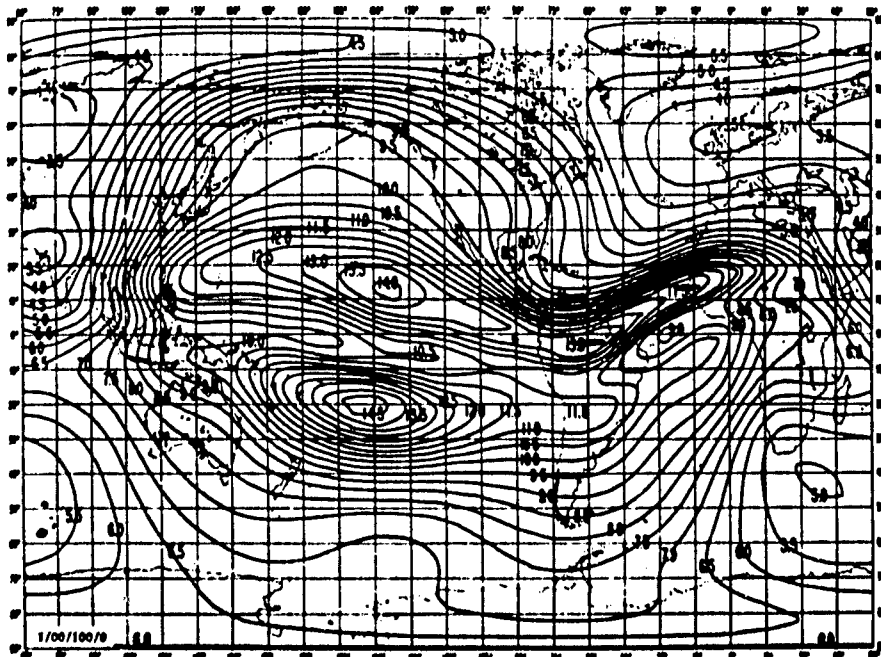


Fig.6 Global map of F2 MUF(o) R = 100

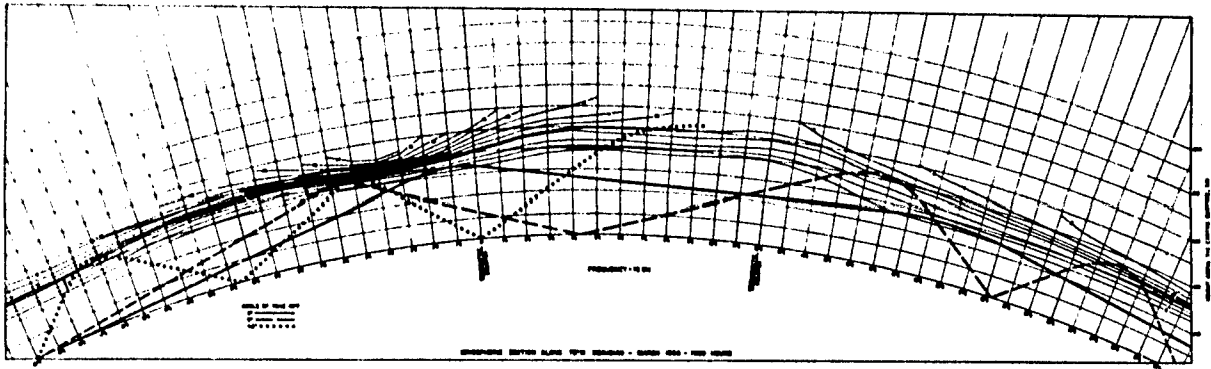


Fig.7 Transequatorial ray path

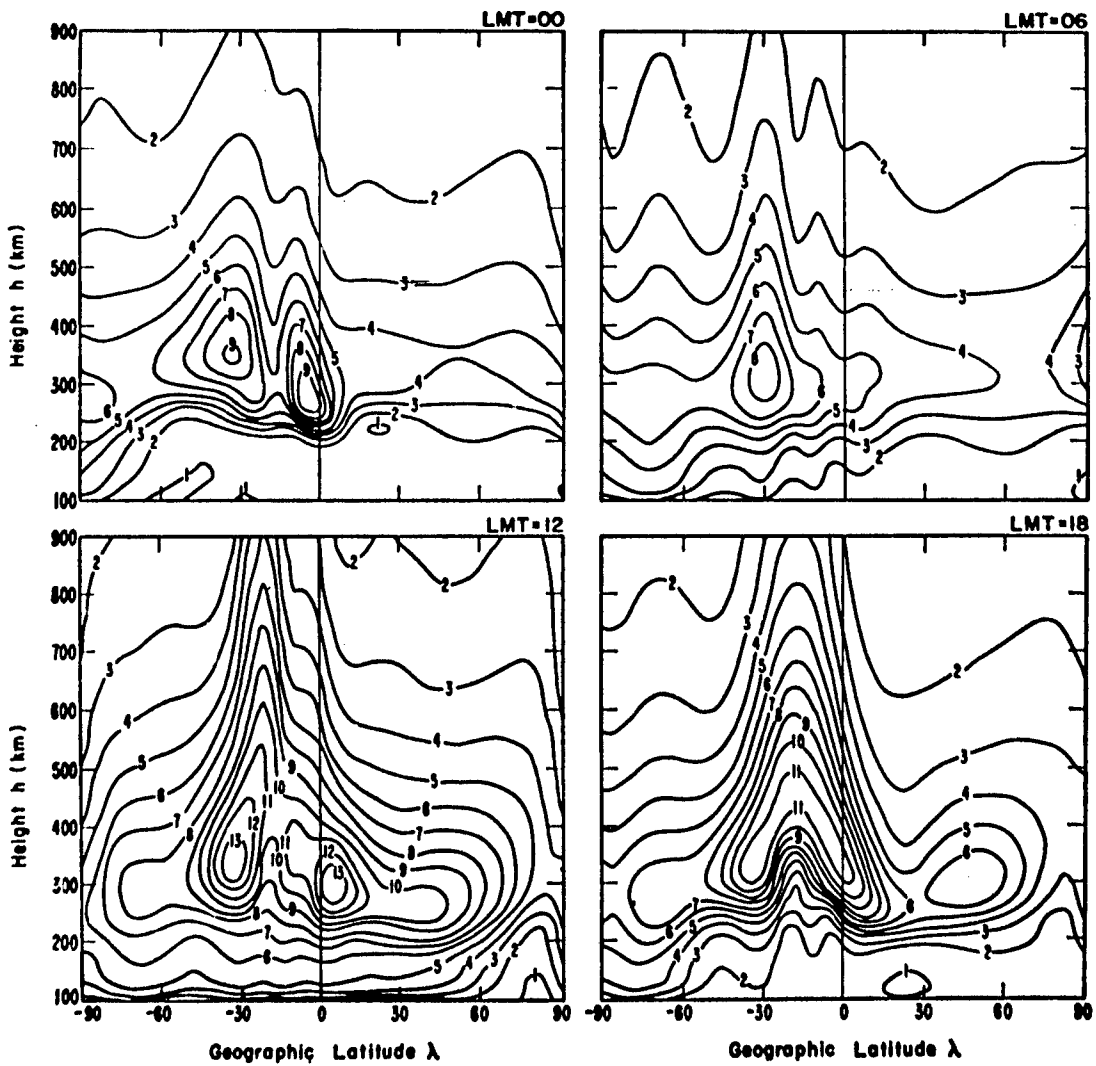


Fig.8 Cross section of plasma frequency f_N from numerical map for November 1966 (from Jones and Stewart, 1970, Fig.4)

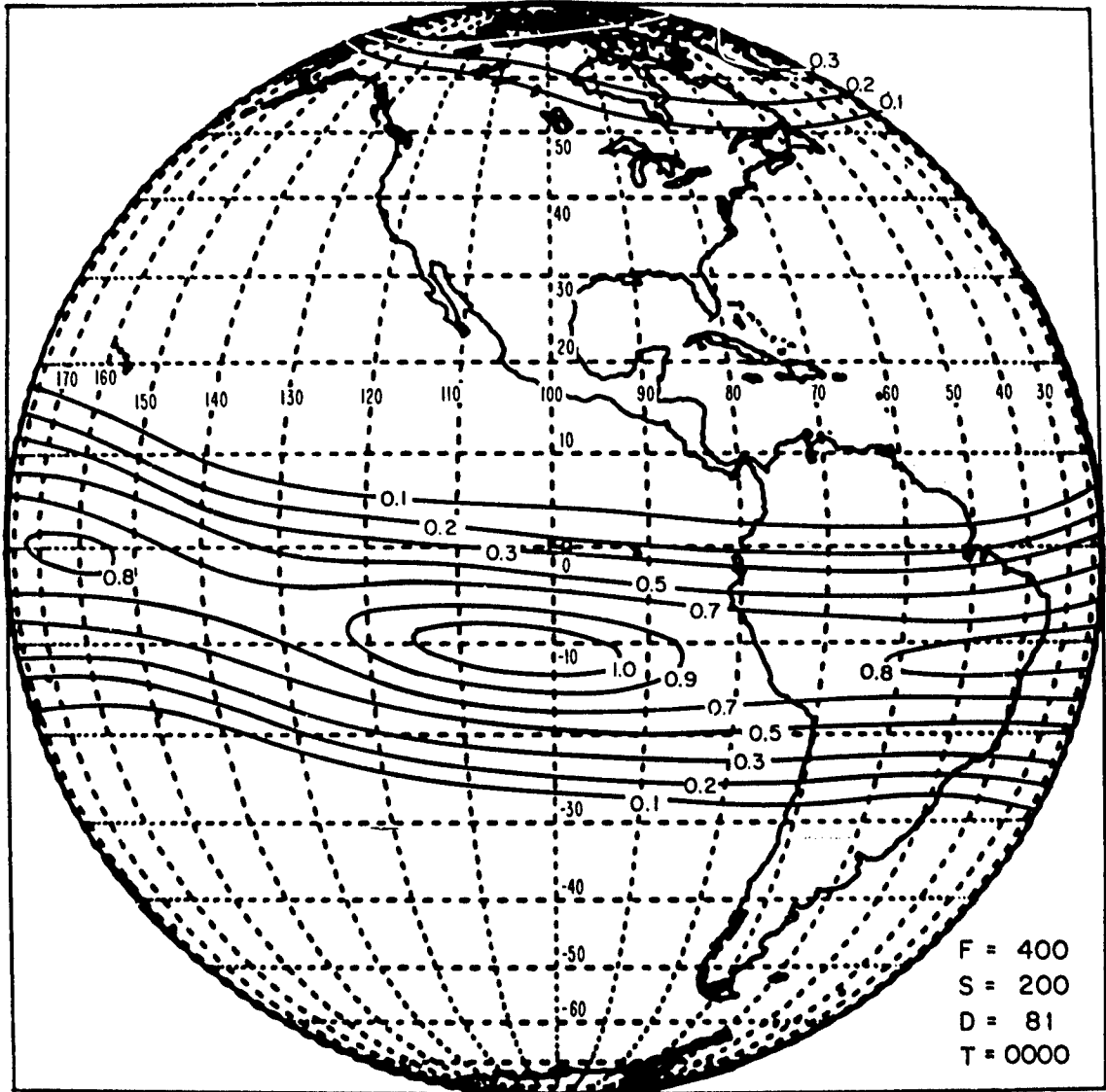


Fig.9 Map of contours of satellite radio scintillations based on the Fremouw and Rino model



Fig.10 World map of atmospheric radio noise

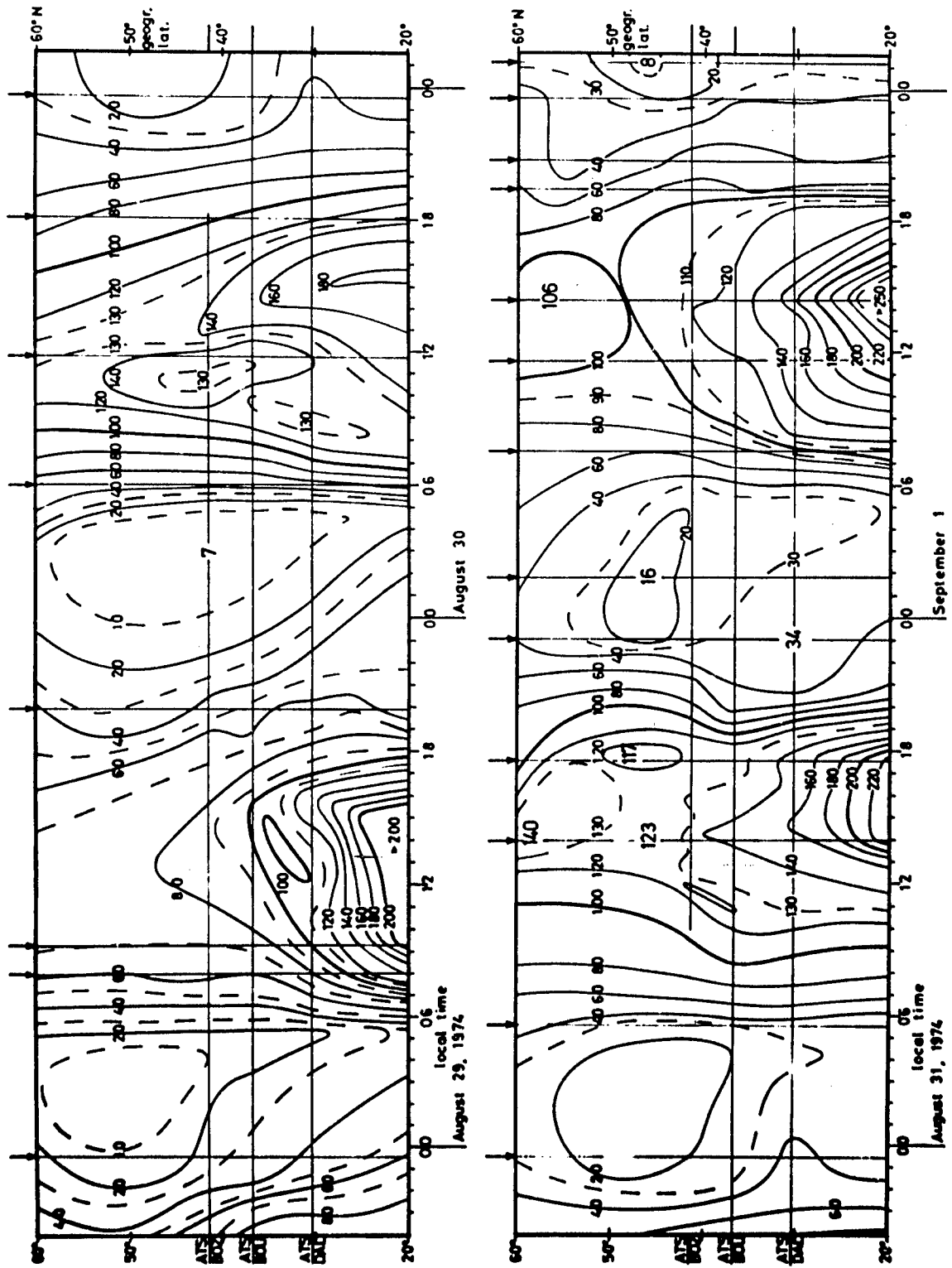


Fig.11 Contour map of total electron content

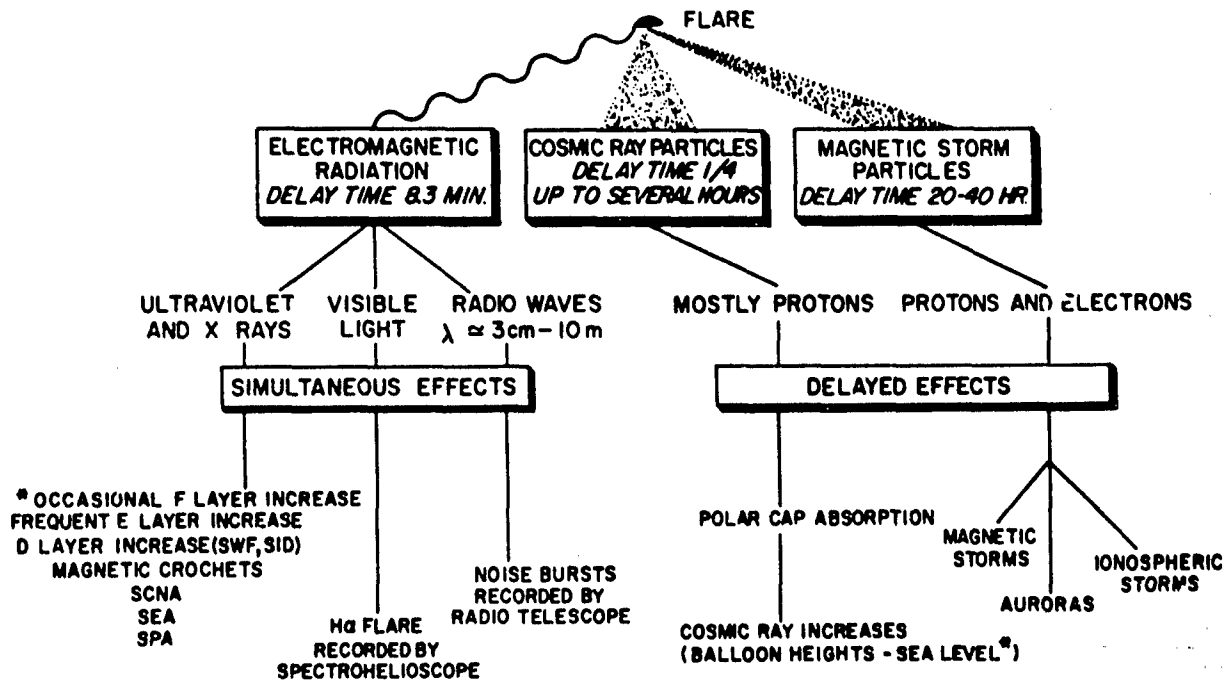


Fig.12 Terrestrial effects of a solar flare

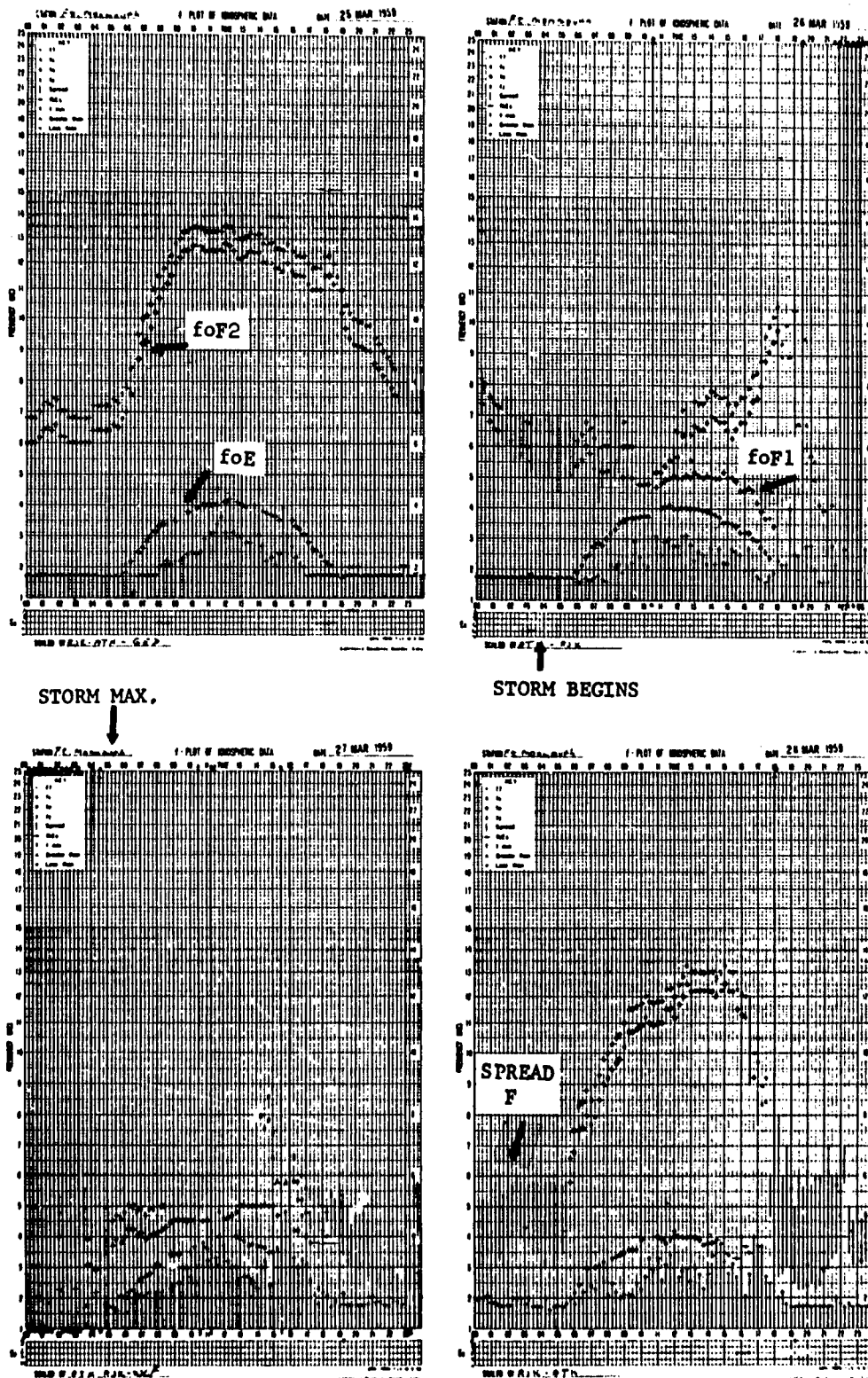


Fig. 13 f-plot showing depression of foF2 during storm

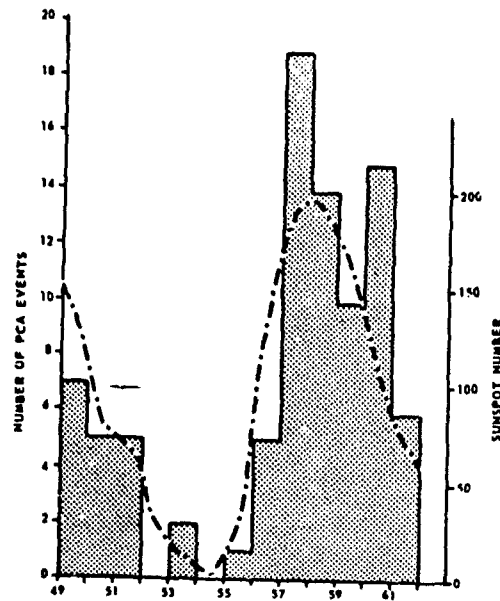


Fig. 14 Solar cycle occurrence of PCAs

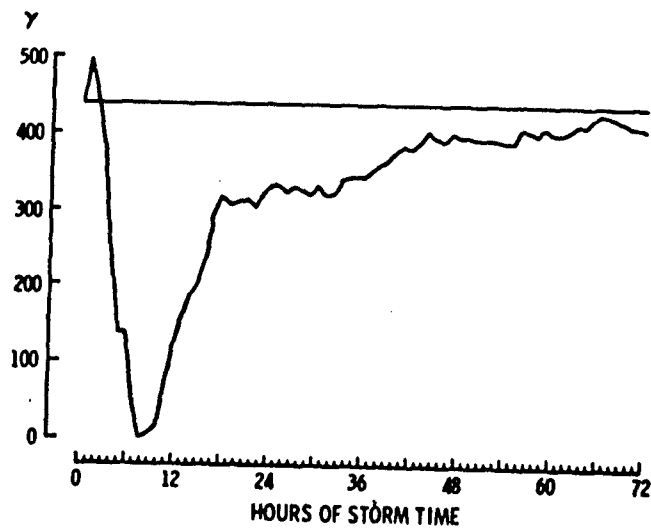


Fig. 15 Magnetic storm sequence

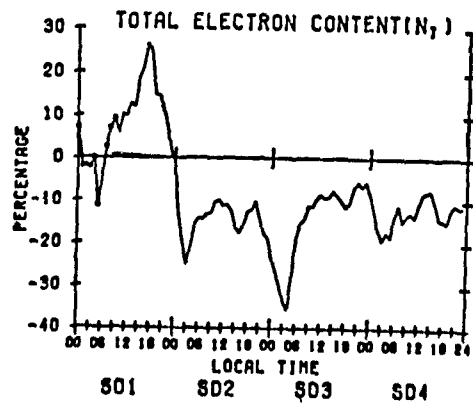


Fig. 16 Storm variation of Faraday content (Mendillo)

NNNN
 KBOU
 HFUS BOU 192200
 FROM SPACE ENVIRONMENT SERVICES CENTER BOULDER COLO
 SDF NUMBER 200
 JOINT AFGWC/SESC PRIMARY REPORT OF SOLAR AND GEOPHYSICAL ACTIVITY ISSUED
 2200Z 19 JULY 1974
 IA. SOLAR ACTIVITY HAS BEEN VERY LOW WITH THREE NON-ENERGETIC SUBFLARES
 REPORTED DURING THE PAST 24 HOURS. REGIONS 438 (S08W72) AND 443 (SL2E06)
 HAVE BEEN STABLE. MINOR INTENSITY FLUCTUATIONS HAVE OCCURRED IN REGIONS
 442 (SLOW34) AND 445 (S04W37). AN ACTIVE PROMINENCE (SL3E90) PARTIALLY
 ERUPTED, AND THEN TOTALLY DISSIPATED, BETWEEN 0715-0840Z. NO OTHER ACTI-
 VITY HAS BEEN REPORTED TO SUBSTANTIATE AN ACTIVE RETURN OF OLD REGION 435.
 IB. SOLAR ACTIVITY IS EXPECTED TO REMAIN LOW.
 II. THE GEOMAGNETIC FIELD HAS BEEN QUIET. IT IS EXPECTED TO BE QUIET TO
 UNSETTLED.
 III. EVENT PROBABILITIES 20 - 22 JULY
 CLASS M 03/03/03
 CLASS X 01/01/01
 PROTON 01/01/01
 PCAF GREEN
 IV. OTTAWA 10.7 CM FLUX
 OBSERVED 19 JULY 84
 PREDICTED 20 - 22 JULY 83/85/85
 90-DAY MEAN 19 JULY 90
 V. GEOMAGNETIC A INDICES
 OBSERVED FREDERICKSBURG 18 JULY 06
 ESTIMATED AFR/AP 19 JULY 04/06
 PREDICTED AFR/AP 20 - 22 JULY 07/08 - 09/10 - 11/12
 SOLTERWARN
 SPAN
 BT

Fig.17 Sample solar/geophysical forecast

AIR FORCE GLOBAL WEATHER CENTRAL
 DAILY PRIMARY HF RADIO PROPAGATION REPORT
 PART I. DESCRIPTION OF GENERAL HF RADIO PROPAGATION CONDITIONS
 FOR THE 24 HOUR PERIOD ENDING 12240Z JAN 77.
 HF PROPAGATION CONDITIONS WERE GENERALLY FAIR TO GOOD IN MOST
 AREAS EARLY IN THE RADIO DAY, BECOMING GENERALLY GOOD DURING
 THE LATTER HALF. MUFs ON LOW LATITUDE CIRCUITS CONTINUED TO
 BE SOMEWHAT LOWER THAN SEASONAL NORMALS, GENERALLY NEAR 20 TO
 30 PERCENT. THE PREDAWN DIP IN MUFs WAS LESS PRONOUNCED
 HOWEVER, SOME AREAS WERE STILL ENCOUNTERING DIFFICULTIES
 IN LOCATING SUITABLE WORKING FREQUENCIES DURING THE TRANSITION
 PERIOD. MUFs TENDED TO REMAIN SLIGHTLY ABOVE NORMAL AFTER
 LOCAL SUNSET ON MID LATITUDE PATHS, RESULTING IN
 THE DAYTIME FREQUENCIES OPERATING LATER THAN HAS BEEN THE CASE
 DURING THE PAST FEW DAYS. CONDITIONS OVER THE HIGH LATITUDES
 WERE GENERALLY GOOD, ALTHOUGH SHORT PERIODS OF INTENSE
 ABSORPTION, AND CONSEQUENTLY REDUCED SIGNAL STRENGTHS AND
 ELEVATED NOISE LEVELS OCCURRED BETWEEN LOCAL MIDNIGHT AND
 DAWN. THE GEOMAGNETIC FIELD WAS UNSETTLED TO ACTIVE UNTIL
 1500Z, BECOMING QUIET FOR THE REST OF THE DAY.
 PART II. SUMMARY OF POSSIBLE HF RADIO PROPAGATION DISTURBANCES
 ON SUNLIT PATHS FOR THE 24 HOUR PERIOD ENDING 122400Z JAN 77.

BEGIN	END	CONFIRMED	FREQUENCIES AFFECTED
1315Z	1341Z		
1746Z	1825Z		
1924Z	1944Z		
2144Z	2220Z	YES	UP TO 11 MHz

PART III. OUTLOOK FOR GENERAL HF RADIO PROPAGATION CONDITIONS
 FOR THE 24 HOUR PERIOD BEGINNING 130400Z JAN 77.
 HF PROPAGATION CONDITIONS WILL CONTINUE TO SHOW IMPROVEMENT
 OVER MOST AREAS. MUFs WILL REMAIN GENERALLY BELOW SEASONAL
 NORMALS OVER THE LOWER LATITUDES, BUT WILL BE NEAR NORMALS
 ELSEWHERE. THE GEOMAGNETIC FIELD SHOULD BE GENERALLY
 QUIET, ALTHOUGH SOME SLIGHTLY UNSETTLED PERIODS ARE LIKELY
 FOR BRIEF PERIODS DURING THE NIGHTTIME HOURS. THE CHANCE OF
 A SOLAR FLARE INDUCED SHORT WAVE IS MODERATE.

Fig.18 Sample HF radio propagation forecast

IONOSPHERIC EFFECTS ON SATELLITE NAVIGATION AND
AIR TRAFFIC CONTROL SYSTEMS

J.A. Klobuchar
Air Force Geophysics Laboratory
Hanscom AFB, Bedford, MA 01731

SUMMARY

The electrons in the earth's ionosphere can produce severe limitations on the performance of modern satellite navigation systems. In this paper those characteristics of the ionosphere which are of potential concern to advanced navigation systems will be described and various techniques for correcting for some of these effects will be outlined. The most important limitation to an advanced navigation system is the range error introduced by the group path delay effect of the ionosphere. Fortunately, the ionosphere is a dispersive medium and the use of a two-frequency measurement of the actual group delay can result in almost complete correction for this time delay error at the cost of the use of a second frequency with sufficient spacing from the normal system operating frequency. Lacking a second operational system frequency various model representations of ionospheric time delay are available. The advantages and limitations of various types of models are also discussed.

1. INTRODUCTION

The electrons in the earth's ionosphere can be a major limiting factor in the range accuracy of modern satellite navigation systems. In this paper those characteristics which are of potential concern to advanced satellite navigation and air traffic control systems will be described and various methods of correcting for these effects will be outlined.

At frequencies of approximately 100 MHz and higher the major effects which the ionosphere has upon radio waves passing through it are: 1) time delays greater than the free space wave velocity; 2) polarization rotation of linearly polarized waves; 3) angular refraction or bending of the ray path from a geometric straight line; 4) phase advance of the carrier phase with respect to the free space phase scintillation. Absorption of radio waves above 100 MHz is generally negligible. Fortunately, the ionosphere is a dispersive medium; that is, these effects are all a function of frequency, and this fact can be utilized to advantage to mitigate many potential ionospheric problems to satellite navigation systems. Each of these effects on transionospherically propagated radio waves will be described.

2. IONOSPHERIC TIME DELAY

2.1. The First Order Effect

The additional time delay over the free space transit time between a signal transmitted from above the ionosphere and a user on or near the earth's surface is given by $\Delta T = 40.3 / cf^2$ TEC (seconds) where TEC is the total number of electrons, called Total Electron Content, along the path from the transmitter to the receiver; c is the velocity of light in meters/second, and f is the system operating frequency in Hertz. The TEC is generally expressed as the number of electrons in a unit cross section column of one square meter area along this path. Extreme values of this TEC parameter vary from 10^{16} el/m² to 10^{19} el/m². A plot of time delay versus system operating frequency for TEC covering these extreme values is shown in figure 1. Note that, at a system operating frequency of 1 GHz, for example, a TEC of 10^{18} el/m², a value frequently exceeded in low and mid-latitude parts of the world, a time delay of 134 nanoseconds or 132 feet (40.2 meters) of range error will be encountered by the radio wave. At 100 MHz this same TEC value would produce a range error of over 13,000 feet or 4 kilometers! Obviously, the TEC parameter is of potentially great importance to precision satellite navigation systems.

2.2. Examples of Typical TEC Values

Fortunately, sufficient ionospheric TEC data is now available from various locations throughout the world to be able to describe the diurnal, seasonal, geographic, solar cycle and magnetic activity dependence of this parameter so that systems design engineers are able to determine the potential effects on any new satellite navigation system. In fact, analytic models of the TEC parameter exist which could be used to estimate the time delay due to the ionosphere. The accuracy and limitations of the typical types of models will be described in a later section of this report, but they are useful now in giving an overall, world-wide view of ionospheric time delay. Figure 2 shows the result of the Bent¹ model when calculated on a global basis for March 1968, a solar maximum year of an average solar cycle. This figure

illustrates the world-wide time delay for a system operating frequency of 1.6 GHz at a universal time of 00 hours. Note from the figure that the regions of maximum time delay occur near the equator at plus and minus 15 to 20 degrees of latitude. These TEC contours move along approximate lines of constant magnetic latitude from east to west as the earth rotates.

2.3. Variability of Ionospheric Time Delay

While a model can give a representation of approximate world-wide TEC behavior, actual continuous TEC data recorded at various stations has been recorded to give monthly average and statistical values. An example of a year's TEC data taken at Hamilton, Massachusetts, with the daily values for each month overplotted, is given in figure 3. Note the large day-to-day variability within each month and the seasonal changes, with the lowest TEC values occurring during the summer months and the largest values during the equinoxes. Some, but by no means all, of the daily variability of TEC about the monthly mean curve is due to magnetic storms which have been extensively studied for the behavior of the TEC parameter². Other departures from monthly median behavior occur with no clear reason, such as a magnetic disturbance or enhanced solar activity.

The distribution of the differences of TEC from monthly mean values is approximately normal or Gaussian. The standard deviation of daily TEC values from the average behavior for Hamilton, Mass. for 1969 is given in figure 4 separately for the winter, summer and equinox seasons as a function of local time of the day. The percentage standard deviation is perhaps most important during the mid-day period when the absolute values of TEC are highest. During this mid-day period the standard deviation is approximately 20 percent. Figure 5 shows similar data for the solar minimum period of 1974-75 when the mid-day standard deviation of TEC at Hamilton is between 20 and 25 percent. The nighttime values of standard deviation are considerably higher, but the absolute TEC values are much lower at night during solar minimum conditions than at other times. Figures 6, 7, and 8 illustrate the diurnal and seasonal variation of the standard deviation of the TEC parameter at several stations during the solar maximum year of 1969 for the summer, winter and equinox seasons respectively. Again during the mid-day period the standard deviation is generally less than 25 percent, though at night, especially for the Honolulu station during equinox, the percentage standard deviations are considerably higher. Figure 9 shows the seasonal dependence of the standard deviation for the same stations for the important mid-day period, for each month of 1969. Data for Hong Kong are for 1968. A good working number for systems engineers to use for design purposes for the standard deviation of ionospheric time delay, based upon much available data, is 25 percent.

2.4. Worst Case TEC Statistics

While the standard deviation does give a good estimate of the variability of ionospheric time delay, there are rare times when the distribution of TEC values departs greatly from a normal curve. Such an instance was measured in December 1971 at Hamilton, Mass. and is illustrated in figure 10 which shows monthly TEC overplots. The extremely large TEC value seen in the December overplots occurred on 17 December 1971 during a large magnetic storm. While the storm had been in progress for several hours, no indication of this extremely large TEC value was discernable ahead of its occurrence. Thus, this example of extreme statistics was unpredictable, and probably represents a true worst case departure from monthly average conditions. Any system design engineer must be careful to consider worst case TEC values, even though they occur infrequently. An example of worst case navigation system design for TEC geographic variability was given by Elrod⁵ in which a proposed real time correction system was based upon an observed worst case gradient in TEC among several monitoring stations within the continental United States (CONUS). Elrod concluded that over one hundred TEC monitoring paths would be required in the CONUS to satisfactorily measure the worst case TEC gradient. For rms conditions, however, considerably fewer stations are required.

2.5. Two-Frequency Ionospheric Time Delay Corrections

If the navigation system bandwidth is large enough so that two, fairly widely spaced bands can be used for ranging, the ionospheric time delay error can be reduced to an acceptable level automatically, and can be made transparent to the system user. Because the ionospheric time delay is a function of frequency we can write:

$$\delta T_1 = \frac{K}{cf_1^2} \text{TEC}, \quad \delta T_2 = \frac{K}{cf_2^2} \text{TEC}$$

where δT_1 is the value needed to correct for the ionospheric error on the frequency f_1 , and δT_2 is the ionospheric error encountered on the frequency f_2 . If the normal system operational frequency is f_1 and we choose f_2 at a lower frequency for ionospheric correction purposes, we obtain

$$\Delta(\delta T) = \frac{K \cdot \text{TEC}}{c} \left(\frac{1}{f_2^2} - \frac{1}{f_1^2} \right) = \delta T_1 \left(\frac{f_1^2}{f_2^2} - 1 \right)$$

or

$$\delta T_1 = \frac{f_2^2}{(f_1^2 - f_2^2)} \Delta(\delta T)$$

The value $\Delta(\delta T)$ is obtained from the difference of the simultaneous measurements of the total range, including ionospheric time delay, at the two frequencies f_1 and f_2 , since the geometric distance is, of course, the same at all frequencies. The quantity $f_2^2 / f_1^2 - f_2^2$ is called the ionospheric scaling factor. For small ratios of f_1/f_2 this factor is much larger than unity and the required precision of the differential measurement may be unreasonably large. A plot of this quantity, normalized by f_1 , is given in figure 11.

In this derivation we have not considered the contribution of receiver noise to the differential measurement accuracy. This contribution has been considered by Cretcher⁴ for the NAVSTAR-GPS advanced satellite navigation system.

2.6. Examples of Two-Frequency Ionospheric Time Delay Systems

The United States Department of Defense is currently developing, under tri-service sponsorship, an advanced satellite navigation system called NAVSTAR-Global Positioning System (GPS). The GPS is now in the initial stages of its validation phase with systems tests currently underway to prove the concept and accuracy requirements.⁵ The GPS will basically consist of three constellations of 8 satellites each, in 12 hour synchronous orbits, at 63 degrees inclination. The system is user passive. The transmissions from each satellite give the satellite ephemeris, clock error and capability of determining the ionospheric time delay correction along the direction to the satellite. The latter capability is achieved by the use of two carrier frequencies spaced sufficiently far apart to enable a direct measurement of the ionospheric time delay to be made. The ephemeris and satellite clock frequency standard error are sent at low data rates on carriers that are modulated with pseudo-random noise codes. Each user must have knowledge of the unique PRN codes which will enable him to synchronize his receiver to each of the satellites. He does this by locally generating the PRN code for each satellite and shifting his locally generated code in time until he obtains correlation with the transmitted code. The codes are designed for low correlation at all phases except the correct shift. The pseudorange must be determined in this manner from four satellites, rather than three, to correct for the user's own possible clock errors. The satellite orbits are chosen such that for all time at least four satellites are in view of any point on the earth. Satellites at optimum viewing angles are chosen to obtain the maximum geometric precision in the measurements. Elevation angles from 5 degrees to the zenith are used. Due to tropospheric time delay errors elevation angles lower than 5 degrees are avoided.

The operational frequency of this system is 1.6 GHz. To allow users with high accuracy position requirements to automatically correct for the ionospheric time delay, a second frequency at 1.2 GHz is available. The actual ionospheric time delay is obtained by measuring the difference in arrival time of 10 MHz modulation envelopes on both the carriers. This is an actual measurement of the modulation or group delay. The dependence of the ionospheric scaling factor with choice of the secondary frequency f_2 , is shown in figure 11. For the GPS pair of frequencies, if a correction accuracy of 3 meters, corresponding to a 10 nanosecond ionospheric time delay at f_1 , is required for the first order ionospheric term, then a differential measurement accuracy of 3.9 nanoseconds will be required. The assumption is made here that the modulation on both carriers is actually transmitted with a known phase difference from the satellite, including possible antenna differential phase shift at the two carrier frequencies with respect to their modulation frequencies. Also, the effects of receiver noise are neglected.

Another example of two-frequency ionospheric time delay corrections will be taken for the 225-400 MHz frequency band. Suppose a satellite ranging system at, say 400 MHz, is contemplated. Assume that a correction for an electron content of 10^{18} el/m² is required. At 400 MHz this value of TEC corresponds to an ionospheric time delay of 840 nanoseconds, or 250 meters of range error. To determine the 840 nanosecond delay at 400 MHz, further suppose that a second system frequency at 350 MHz is utilized. The differential delay will then be 4.27 times smaller, or 197 nanoseconds. To measure this differential time delay to a one percent precision requires a 2 nanosecond accuracy.

2.7. Higher Order Correction Terms

The differential time delay example for an assumed 400 MHz frequency system illustrates another point; namely that, at the approximate 99 percent correction level, higher order effects may be appreciable, and the simple first-order $1/f^2$ relationship may not remain valid. This has been considered by daRosa⁶ and also by Yeh⁷ for the case of mean pulse arrival times. Suffice it to say here that systems designers should not attempt to utilize the simple $1/f^2$ relationship without considering higher order ionospheric effects when their required ionospheric correction becomes greater than approximately 98 percent of the total ionospheric time delay.

3. FARADAY POLARIZATION ROTATION

3.1. Frequency Dependence

When a linearly polarized radio wave traverses the ionosphere the wave undergoes rotation of the plane of polarization. At 100 MHz and higher frequencies the amount of this polarization rotation can be described by

$$\Omega = \frac{2.36 \times 10^{-5}}{f^2} \int B \cos \theta N dl \text{ (radians)}$$

where the quantity inside the integral is the product of electron density times the longitudinal component of the earth's magnetic field integrated along the radio wave path. Many ionospheric workers have used this effect, named for Michael Faraday who first observed polarization changes in an optical experiment, to make measurements of the TEC of the ionosphere. Since the longitudinal magnetic field intensity changes much slower with height than the electron density of the ionosphere, the equation can be rewritten as

$$\Omega = \frac{K}{f^2} B_L * TEC$$

where $B_L = B \cos \theta$ taken at a mean ionospheric height, usually near 400 kilometers, $K = 2.36 \times 10^{-5}$ and TEC is $\int N dl$. Typical values of polarization rotation for northern mid-latitude stations viewing a geostationary satellite near their station meridian are given in figure 12 as a function of system frequency and total electron content. In fact, the largest portion of TEC data available today from stations throughout the world have come from Faraday rotation measurements.

For satellite navigation and communication designers, however, the Faraday polarization rotation effect is a nuisance. If a linearly polarized wave is transmitted from a satellite to an observer on or near the earth's surface the amount of polarization rotation may be nearly an odd integral multiple of 90 degrees, thereby giving no signal on the receiver's linearly polarized antenna, unless the user is careful to re-align his antenna polarization for maximum received signal.

3.2. Circular Polarization

This problem is overcome by the use of circular polarization of the correct sense at both the satellite and at the user's receiver. Generally, the mobile user finds it difficult to utilize circular polarization due to the continual vehicle directional changes; thus he settles for a received linear polarization. The 3 dB loss between transmitted circular polarization and received linear polarization is a necessary price to pay for user antenna maneuverability and simplicity.

4. ANGULAR REFRACTION

The refractive index of the earth's ionosphere is responsible for bending of radio waves from a straight line geometric path between satellite and ground. This angular refraction or bending produces an apparent higher elevation angle than the geometric elevation. Millman et al., has derived several expressions relating the refraction to the resultant angular bending. Perhaps the easiest expressions to use, as given by Millman, relate the ionospheric range error to angular refraction:

$$\Delta E = \frac{(R + r_0 \sin E_0) (r_0 \cos E_0)}{h_1 (2r_0 + h_1) + r_0^2 \sin^2 E_0} \frac{\Delta R}{R}$$

where E_0 is the apparent elevation angle, R is the apparent range, ΔR is computed from $\Delta R = (48.3/f^2) * TEC$, r_0 is the earth's radius and h_1 is the height of the centroid of the TEC distribution, generally between 300 and 450 km.

For high elevation angles and satellites well above most of the ionization, the angular refraction can be expressed as:

$$\Delta E = \frac{\cos E_0}{2h_1} \Delta R$$

For low elevation angles: $\Delta E = \cot E_0 \frac{\Delta R}{R}$

Typical values of elevation refraction error at 1.6 GHz for an assumed worst case elevation angle of 5 degrees and a 10^{19} el/m² ionosphere will be 0.3 milliradians. For the same viewing angle and TEC and an operation frequency of 400 MHz the angular refraction error will be approximately 4 milliradians. Generally the range error itself is the main ionospheric problem for advanced navigation systems, and elevation angle errors are insignificant. Satellite detection radar systems, on the other hand, do have the requirement to know accurate pointing elevation angles for their large aperture arrays, though generally the accurate tracking is done by using range rate information, and elevation angle is of secondary importance as long as the radar can see the target.

5. IONOSPHERIC PHASE PATH LENGTH EFFECTS

5.1. Phase Path Changes

In addition to group path length increases, the Faraday polarization rotation effect, and the angular refraction of radio waves, the phase of the carrier of radio frequency transmissions is changed by the ionosphere. Actually, the RF phase is advanced with respect to its phase in the absence of an ionosphere. The amount of this phase path decrease can be expressed as:

$$\phi = \frac{1.34 \times 10^{-7}}{f} \text{ TEC (cycles)}$$

where f is the system operating frequency in Hertz, and TEC is in el/m^2 column. In practice, the amount of this phase advance cannot readily be measured on a single frequency and two, coherently derived frequencies are used for this measurement. For the pair of frequencies to be used by NAVSTAR/GPS the differential phase shift between 1.2 GHz and 1.6 GHz referenced to the latter frequency is:

$$\Delta\phi = \frac{1.34 \times 10^{-7}}{1.6 \times 10^9} * \left[\frac{m^2 - 1}{m^2} \right] * \text{TEC (cycles)}$$

where $m = f_1/f_2 = 1.28$, $\Delta\phi = 3.34 \times 10^{-17} * \text{TEC}$ or $2.99 \times 10^{16} \text{ el}/\text{m}^2$ per complete 2π cycle of differential carrier phase between 1.2 and 1.6 GHz, measured at 1.6 GHz. With a reasonable carrier signal to noise ratio, this differential carrier phase can be measured to within, say ten degrees, or less than $6.1 \times 10^{16} \text{ el}/\text{m}^2$. Since the TEC is generally much greater than 3×10^{16} , there is a $2N\pi$ ambiguity in the differential phase measurement.

As an ionospheric monitoring tool the combination of differential carrier phase and differential modulation phase provides an excellent means of determining ionospheric electron content along the ray path to the satellite as the differential modulation phase has an almost negligible chance of having an ambiguity. It, of course, provides corrections to the radial distance between the satellite and user for the apparent path shortening due to ionospheric phase path effects. The amount of this phase path change during the course of a period before dawn to mid-day, corresponding to a TEC change from perhaps 10^{16} to $10^{18} \text{ el}/\text{m}^2$, would be 33 cycles at 1.6 GHz. Since cycle length at this frequency is 19 centimeters, the two frequency correction in this example is correcting for a phase change of 6.3 meters during this time period. Remember that the satellite is farther away by 6.3 meters than the carrier phase measurements would indicate. Corrections for the ionospheric phase advance are particularly necessary for precise time transfer via satellite.⁹ Attempts have been made by Schwab and Prozeller¹⁰ to utilize single-frequency measurements of combined phase and group path delays to correct for first order ionospheric effects on the low-orbit Transit navigation satellites.

5.2. Doppler Shift

Since frequency is simply the derivative of phase, an additional Doppler shift results due to changing TEC. This additional frequency shift is generally small compared to the normal geometric Doppler shift, but can be computed by:

$$\Delta f = \frac{d\phi}{dt} = \frac{1.34 \times 10^{-7}}{f} \frac{d(\text{TEC})}{dt} \quad (\text{Hertz})$$

For high orbit satellites where the diurnal changes in TEC are greater than geometric ones an upper limit to the rate of change of TEC is approximately $0.1 \times 10^{16} \text{ el}/\text{m}^2$ per second. This value yields an additional frequency shift of less than one tenth of a Hertz at 1.6 GHz which would not be significant compared with a typical required receiver loop bandwidth of at least a few Hertz. At 400 MHz a similar rate of change of TEC would produce a frequency shift of approximately 0.3 Hertz, probably still not significant. During times of severe phase scintillation, which can occur even at GigaHertz frequencies, the TEC likely does not change in a rapid manner to yield greater ionospheric Doppler shifts, but the phase of the incoming RF signal can have a large random fluctuation superimposed upon the changes associated with the normal rate of change in TEC. This large, random component may actually spread out the spectrum of the received signal sufficiently to cause the receiver to lose phase lock as the received signal phase may have little energy left in the stable carrier, and instead may be spread over several Hertz, with little recognizable carrier remaining.

5.3. Phase-Coherent Integration

When radio signals of nearly-precisely-known received frequency are below the receiver noise level it may be possible to significantly enhance the signal-to-noise ratio and hence, to detect the signal, if phase-coherent signal integration can be done. Since the received signal frequency is not precisely known, due, if nothing else, to unknown geometric Doppler shift, a search for the signal phase or, rather, signal rate of change of phase with respect to a receiver standard phase is performed, usually in a digital manner. A constant ionospheric TEC will have no effect upon this process. A linearly changing TEC will simply change the received signal frequency slightly; while a non-linear TEC change will result in non-linear received signal phase changes, that is, changes in received signal frequency with time, and hence lack of continued coherency of the received signal phase, unless second order phase changes are searched for in the detection processing. While it is not anticipated that modern satellite navigation and communication systems will have to resort to phase coherent integration

it is a potentially serious problem for weak signal detection via transionospheric propagation, especially for modern satellite detection radar systems.

The times and geographic regions where strong phase scintillation at UHF and higher frequencies is likely to occur can be determined by referring to the available morphology of amplitude scintillation. Though it is possible to have strong phase scintillation without severe amplitude scintillation the morphology should be approximately the same. Aarons et al¹¹ has reviewed the global morphology of ionospheric amplitude scintillations and also scintillations in the equatorial region¹² which can produce severe effects for navigation and communications systems operating at UHF and L band. The effects of the irregularities which produce both amplitude and phase scintillations on these potential systems is outside the scope of this paper.

6. Model Algorithms of Ionospheric Time Delay

Instead of making direct measurements of ionospheric time delay by using the two-frequency method outlined above, the systems design engineer may choose to make use of a model representation of TEC to correct for ionospheric time delay. Since models generally are made to represent average conditions; updated values of some of the model parameters may be required to provide increased accuracy. First, the current state of the art models will be discussed; then a simple, first order model, deliberately designed to correct for approximately 50% of the rms time delay, will be described. Finally, some comments will be made on real time model updating and the correlation distance of TEC data.

6.1. State of the Art Models-Physical Models

A physical model is one in which attempts are made to mathematically describe the physical processes which result in the free electrons in the earth's ionosphere. Given all the initial conditions of the earth's atmosphere, the solar ionizing radiation which impinges upon it, and a knowledge of the many reaction rates involved, electron density profiles as a function of geographic position and height can be calculated. Such electron density values can then easily be integrated along any radio wave path used to compute ionospheric time delay at a system operating frequency. The Penn State Model^{13,14} is perhaps the most well known physical model.

While physical models certainly have the greatest long term potential of solving and describing the world-wide time delay, at present their use and accuracy is severely limited by a knowledge of the input conditions. Also, considerable computer resources are required to run such models. Their use by system design engineers for other than initial, order of magnitude, time delay results for planning purposes is not recommended at this time.

6.2. State of the Art Models-Empirical Models.

Empirical models are simply mathematical descriptions of available experimental data. Perhaps the most complete empirical model of the ionosphere which exists is the ITS-78 model¹⁵ of foF2, proportional to the density of the peak of the F2 region of the ionosphere. This model representation incorporates the experimental results from over 150 ionospheric sounders located throughout the world. These results are modelled in a diurnal form by Fourier temporal coefficients and in geographic form by Legendre orthogonal polynomials. Empirical models have been constructed by Chiu¹⁶, Flattery et al.¹⁷ and of electron density height profiles by Yip et al¹⁸ using ITS-78 as a basis for N_{max} .

While it is generally agreed that the ITS-78 analytic representation is the best world-wide empirical model available to describe the behavior of the peak of the ionospheric F2 region, foF2, which is directly proportional to the density at the peak of the F2 region, called N_{max} , the relationship between N_{max} and TEC, the parameter required for ionospheric time delay, is not well known. The major diurnal and seasonal changes in the ratio of TEC/ N_{max} are known for mid-latitude stations, but the day-to-day variability and the geographic dependence of this ratio are largely unknown. Also, there are insufficient data available from which extensive studies of this ratio can be made. Even though there are perhaps as many as thirty stations from which direct TEC data has been taken in the past, there are probably no more than 12 locations from which enough TEC data is available to represent the seasonal and solar cycle behavior. Thus, there is insufficient TEC data to make a world-wide model directly from this parameter. The lack of data in the near-equatorial region is particularly limiting to any potential direct TEC model.

An ionospheric profile model from which TEC can be easily obtained has been developed by Bent¹ in which he used the analytic representation of ITS-78 as a base and developed topside ionospheric thickness parameter values from the Alouette satellite topside sounder. His model, while world-wide in application contains topside information mainly from the 70 W longitude meridian region, and is expected to work best in that region. The Bent model is perhaps the best presently available state of the art empirical TEC model.

6.3. A Simple First Order Model

Klobuchar¹⁹ constructed an algorithm of ionospheric time delay for users who could not carry large computer resources with them on their operational system. It was designed to obtain an approximate 50% correction for ionospheric time delay including day-to-day variability. His model representation attempts to fit the monthly average TEC at those time of the day when time delay values are greatest. He makes no attempt to update for day-to-day variability, though the model representation can easily be adapted for this purpose. Only eight coefficients are used to represent the world-wide behavior of ionospheric time delay. In one proposed operational use these eight coeffi-

icients would be transmitted from the navigation satellite to user link. The coefficients could be changed on a daily basis, if necessary, although sufficient operational ionospheric monitoring stations must be implemented to generate the coefficients for this algorithm. Additional features of this operational algorithm include numerous approximations to the geometrical calculations required for off-zenith viewing of the satellite, and for conversion from geodetic to the geomagnetic coordinates used in ordering the ionospheric correction coefficients.

6.4. Model Updating with Near-Real-Time Data

The existing models of TEC fairly well represent the monthly average values at many locations; certainly over the CONUS region average models have a remaining bias which is small compared to the day-to-day variability. In the near-equatorial regions, except for a few locations where much actual TEC data is available, such as at Hawaii and at Hong Kong, there is little available data against which the models may be tested. The near-equatorial regions are very important for world-wide navigation systems which require TEC corrections because the highest TEC values are found in this part of the world.

To make any significant improvement upon the monthly average climatology of TEC near-real-time measurements must be made. DuLong²⁰ has shown that, for data taken from the same location in the same direction, useful improvements to climatology can be made with data up to three hours old. Table I, derived from DuLong shows the percent TEC remaining after correction for near-real-time TEC data. The improvement over monthly climatology's refreshingly high during solar maximum daytime periods when the absolute values of TEC are highest, which is when a good correction is most required. During solar minimum periods a three hour forward prediction based upon actual measurements, in the same direction as the one for which an updated TEC value is required, is not any better than the use of a monthly or seven day running value. The three hour useful time interval for near-real-time measurements should be treated as a maximum value, however. During the sunrise and sunset periods the useful time interval over which a measurement can improve upon climatology is shorter, due to the large geographic gradients which exist during those periods.

The NAVSTAR-GPS will be a significant new source of potential TEC data for near-real-time model updating as well as for scientific use. The use of the two frequencies on board the GPS will provide TEC to an accuracy better than 10^{16} el/m², which is approximately the smallest TEC value observed, and represents approximately one percent of the total mid-day TEC during solar maximum conditions at a near-equatorial anomaly location.

6.5. Geographic Correlation Distance of Time Delay

Even if a near-real-time measurement can be used almost simultaneously to correct for a system located some distance from the measurement location the system designer must decide if an rms type of improvement is adequate or if he must design an ionospheric correction method to work under absolute worst case condition. The Elrod³ study concluded that worst case conditions would require approximately 120 real time ionospheric monitoring stations located throughout the CONUS region alone. This number of ionospheric monitoring stations, if implemented, would not only adequately serve as ionospheric correction for the proposed ASTRO-NAV navigation system, but would be a significant new source of ionospheric data available to the ionospheric scientific community, twenty times the number of stations presently monitoring TEC from within or near the CONUS. If only rms corrections are required, the station spacing can be much greater. Klobuchar and Johanson²¹ have shown that, for the CONUS region, for a 50% improvement in TEC prediction over the monthly median value, TEC monitoring stations must be spaced approximately 2400 kilometers apart in longitude and 1600 kilometers in latitude. Note, however, that a 50% improvement over the monthly median values, only decreases the rms error from approximately 20% of the monthly median to 10%. These results assume that the observations can be implemented into an operational system within a few minutes of time.

7. CONCLUSIONS

All the ionospheric effects considered in this paper are inversely proportional to some power of the system operating frequency. Therefore, as the frequency is raised the ionospheric effects become smaller. In some cases it may be possible to utilize an operational frequency high enough that ionospheric errors are small, or similar in magnitude, to other system errors. In the case where ionospheric time delay is a problem, the best solution from the ionospheric point of view is to use two, relatively widely spaced frequencies to actually measure the ionospheric time delay and to automatically correct for this effect along the actual system radio wave paths. If a two-frequency method is considered for use, the two frequencies should be coherent enough so that differential phase delay as well as differential group path delay can both be measured. Thus, a coarse and a fine measurement of ionospheric time delay and its temporal variations can be obtained.

If a two frequency system is impractical there are several models of ionospheric time delay from which to choose. Also, the choice of whether, how often, and at how many locations to update the models must be considered. Finally, the choice of model complexity versus expected model improvement must be considered; perhaps for some users a 50% rms correction for ionospheric time delay errors is sufficient. For the CONUS

region models are good representations of the actual monthly average conditions. For any world-wide system models are of poorer quality, especially in the equatorial region where they may be most required.

8. ACKNOWLEDGEMENTS

In presenting the statistics of data used in this study several different experimenters have been responsible for data collection from various stations. The use of data from the following is gratefully acknowledged: TEC data from Stanford and Edmonton, provided by A.V. daRosa; from Aberystwyth by L. Kersley; from Hong Kong by G.O. Walker; and from Hawaii by H.T. Roelofs.

9. REFERENCES

1. Bent, R.B., S.K. Llewellyn, G. Nesterczuk, and P.E. Schmid, "The Development of a Highly-Successful Worldwide Empirical Ionospheric Model and Its Use in Certain Aspects of Space Communications and Worldwide Total Electron Content Investigations", in Effects of the Ionosphere on Space Systems and Communications, J.M. Goodman, Ed, Naval Research Laboratory, Washington, D.C. 20375, 1975. US Government Printing Office stock No. 008-051-00064-0.
2. Mendillo, M. and J.A. Klobuchar, "An Atlas of the Midlatitude F-Region Response to Geomagnetic Storms", AFCRL-TR-74-0065, February 1974.
3. Elrod, B.D., "Correction for Ionospheric Propagation Delay in ASTRO-DABS - The Dual Frequency Calibration (DFC) Method", Mitre Technical Report MTR-6896, April 1975.
4. Cretcher, C.K., "Ionospheric Effects in NAVSTAR-GPS", in Effects of the Ionosphere on Space Systems and Communications, J.M. Goodman, Editor, Naval Research Laboratory, Washington, D.C. 20375, 1975. US Government Printing office stock No. 008-051-00064-0.
5. Lassiter, E.M., and B. Parkinson, "The Status of the Development of the NAVSTAR-Global Positioning System", Navigation, Volume XXV, Nr. 97, pp 13-26, January 1977.
6. da Rosa, A.V., "Propagation Errors in VHF Satellite-to-Aircraft Ranging", IEEE, Transaction on Antennas and Propagation, Vol AP-17, pp 628-633, September 1969.
7. Yeh, K.C., "Mean Arrival Time and Mean Pulsewidth of Signals Propagating Through a Dispersive and Random Medium", IEEE Transactions on Antennas and Propagation, Vol AP-25, No. 5, pp 710-713, September 1977.
8. Millman, G.H., and G.M. Reinsmith, "An Analysis of the Incoherent Scatter-Paraday Rotation Technique for Ionospheric Propagation Error Correction", General Electric Technical Information Series, R74EMH2, February 1974. Available from HMES Technical Publications, Box 1122 (CSP4-24), Syracuse, New York 13201.
9. Hanson, D.W., and W.F. Hamilton, "Satellite Broadcasting of WWV Signals", IEEE Transactions on Aerospace and Electronic Systems, Vol AES-10, No. 5, pp 562-573, September 1974.
10. Schwab, V. and E.F. Prozeller, "Single-Frequency Refraction-Free Satellite Navigation", Johns Hopkins University-Applied Physics Laboratory Technical Memorandum, TG-1221, January 1974.
11. Aarons, J., H.E. Whitney, and R.S. Allen, "Global Morphology of Ionospheric Scintillation", Proceedings of the IEEE, Vol 59, pp 159-172, January 1971.
12. Aarons, J., "Equatorial Scintillations: A Review", AFGL-TR-76-0078, April 1976.
13. Nisbet, J.S., "On the Construction and Use of a Simple Ionospheric Model", Radio Science, Vol 6, No. 4, pp 437-464, April 1971.
14. Nisbet, J.S., "Models of the Ionosphere", in Atmospheres of Earth and the Planets, pp 245-258, D. Reidel Publishing Co., Dordrecht-Holland, 1975.
15. Jones, W.B. and P.G. Stewart, "A Numerical Method for Global Mapping of Plasma Frequency", Radio Science, Vol 5, No. 5, pp 773-784, May 1970.
16. Chiu, Y.T., "An Improved Phenomenological Model of Ionospheric Density", Journ. of Atm. and Terrestr. Phys., Vol 37, pp 1563-1570, 1975.

17. Flattery, T.W., and A.C. Ramsay, "Derivation of Total Electron Content for Real Time Global Applications", in Effects of the Ionosphere on Space Systems and Communications, J.M. Goodman, Ed, Naval Research Laboratory, Washington, D.C. 20375, 1975, US Government Printing Office Stock No. 008-051-00064-0.
18. Yip, K.W., and O.H. von Roos, "A New Global Ionospheric Model", Jet Propulsion Laboratory Deep Space Network Progress Report 42-30, September and October 1975, California Institute of Technology, Pasadena, California, December 15, 1975.
19. Klobuchar, J.A. "A First-Order, Worldwide, Ionospheric Time-Delay Algorithm", AFCRL-TR-75-0502, 25 September 1975.
20. DuLong, D.D., "Reduction of the Uncertainty of Radar Range Correction", AFGL-TR-77-0125, June 1977.
21. Klobuchar, J.A., and J.M. Johanson, "Correlation Distance of Mean Daytime Electron Content", AFGL-TR-77-0185, 22 August 1977.

	<u>SEASON</u>			
	WINTER	VERNAL EQUINOX	SUMMER	AUTUMNAL EQUINOX
	<u>SOLAR MAXIMUM (Rz=110)</u>			
TOTAL R (MR. AT 400 MHz.)	258	327	189	310
% REMAINING AFTER MONTHLY MEAN CORR.	18	17	16	18
% REMAINING AFTER 3 HOUR OLD MEAS.	12	11	11	10
% REMAINING AFTER 1 HOUR OLD MEAS.	7	6	7	4
% REMAINING AFTER 30 min. OLD MEAS.	5	4	5	3
	<u>SOLAR MINIMUM (Rz=10)</u>			
TOTAL R (MR. AT 400 MHz)	77	77	69	86
% REMAINING AFTER MONTHLY MEAN CORR.	18	24	17	14
% REMAINING AFTER 3 HOUR OLD MEAS.	18	20	17	18
% REMAINING AFTER 1 HOUR OLD MEAS.	11	11	8	10
% REMAINING AFTER 30 min. OLD MEAS.	9	7	5	6

TABLE 1.

Total range error and percent error remaining after correction for monthly mean value, and after correction including actual data, along same direction, taken at different times before required value. All data are for the daily maximum TEC value. (Derived from DuLong²⁰).

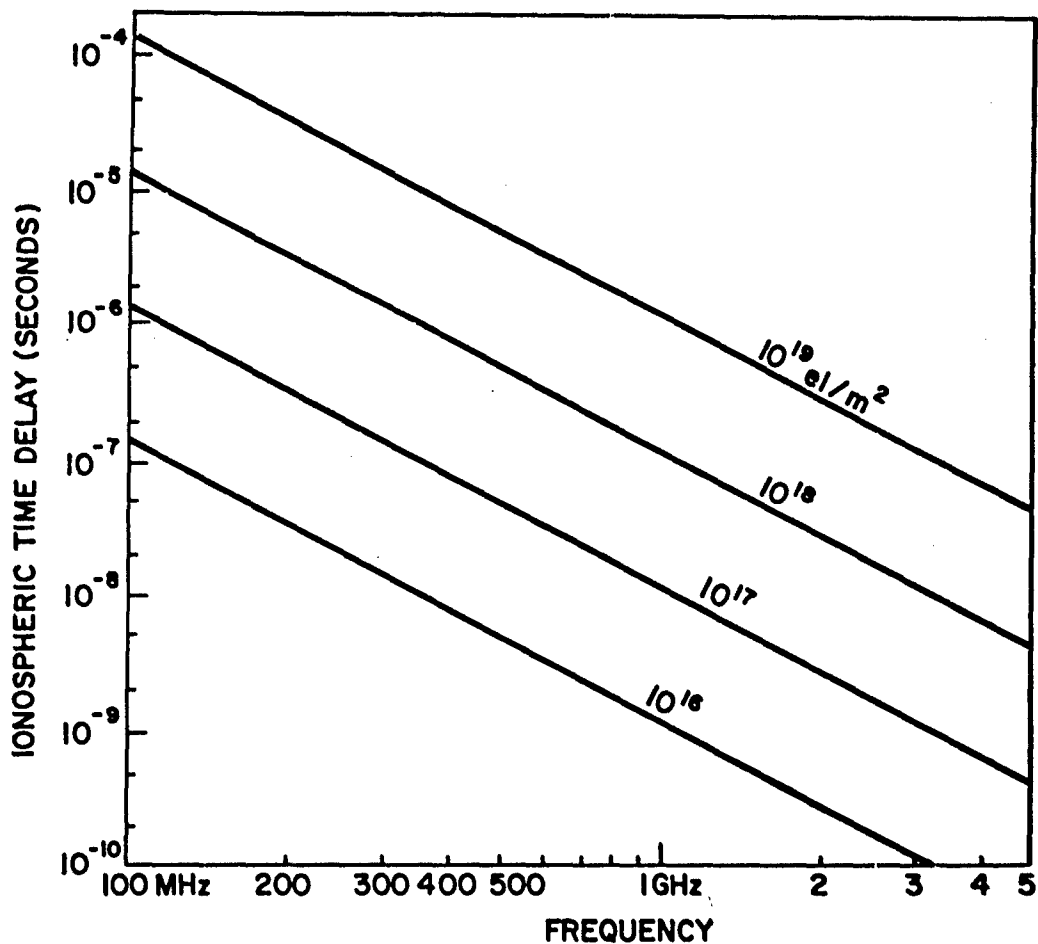


Fig. 1. Ionospheric time delay versus frequency for several values of TEC.

IONOSPHERIC TIME DELAY (BENT MODEL)
(NANOSECONDS AT 1.6 GHz)

00 h UT, MARCH 1968

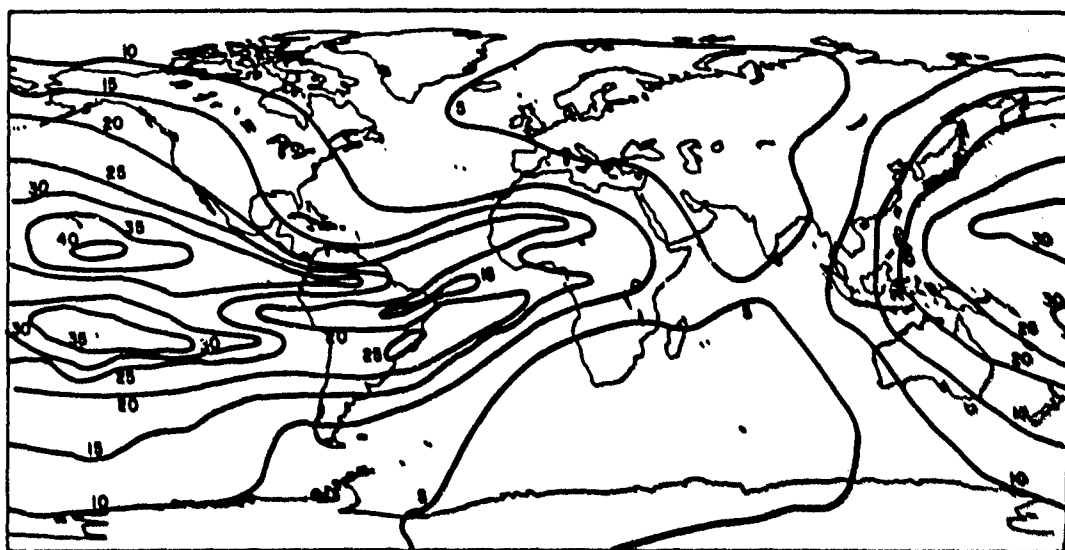
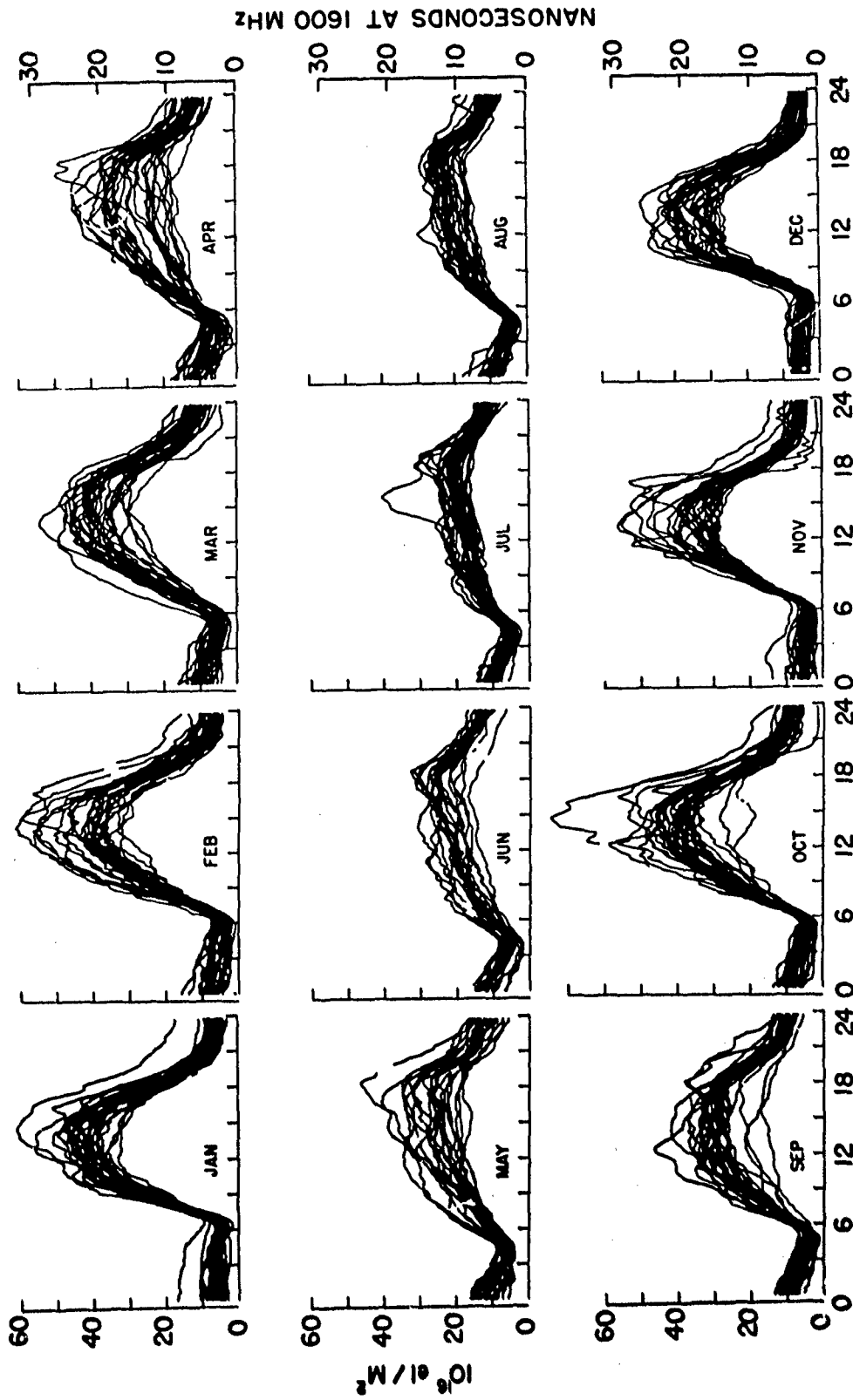


Fig. 2. Worldwide average vertical ionospheric time delay at 1.6 GHz for 00 hours universal time March, 1968, an average solar maximum year.



LOCAL MEAN TIME

**TOTAL EQUIVALENT VERTICAL ELECTRON CONTENT FROM HAMILTON, MASS. (looking towards
ATS-3), 1968**

Fig. 3. Monthly overplots of equivalent vertical TEC from Hamilton, Massachusetts for the year 1968, a solar maximum year.

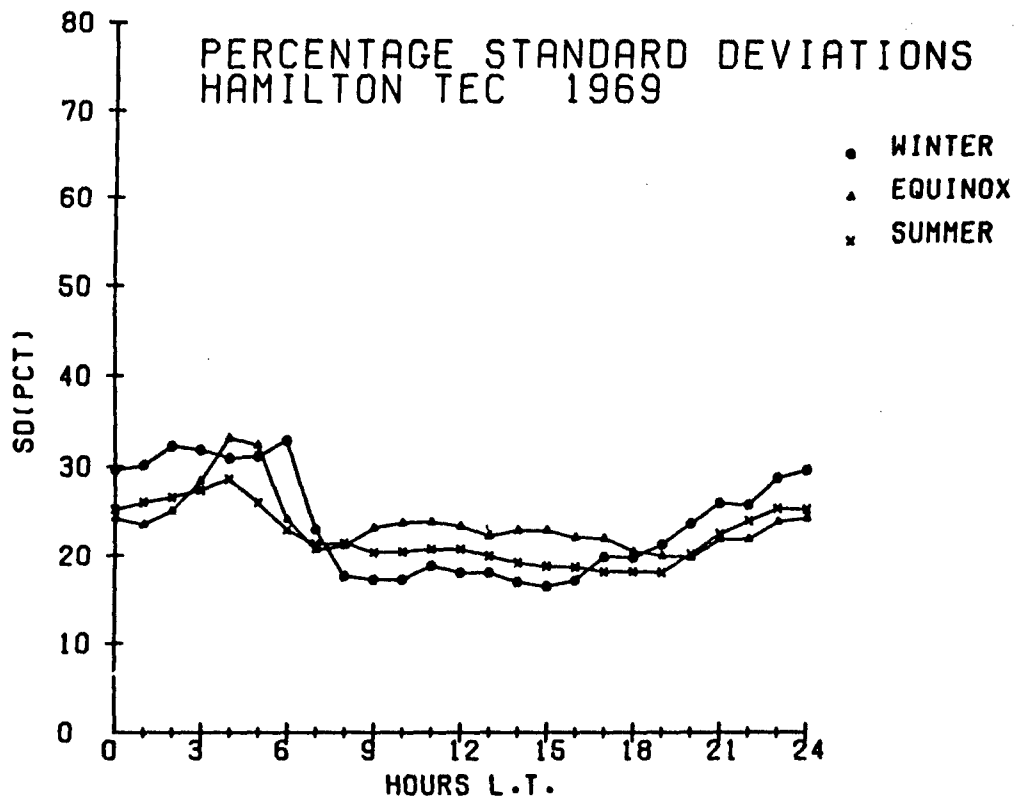


Fig. 4. Percentage standard deviation of TEC versus local time for Hamilton, Massachusetts for the seasons of the year 1969, a solar maximum year.

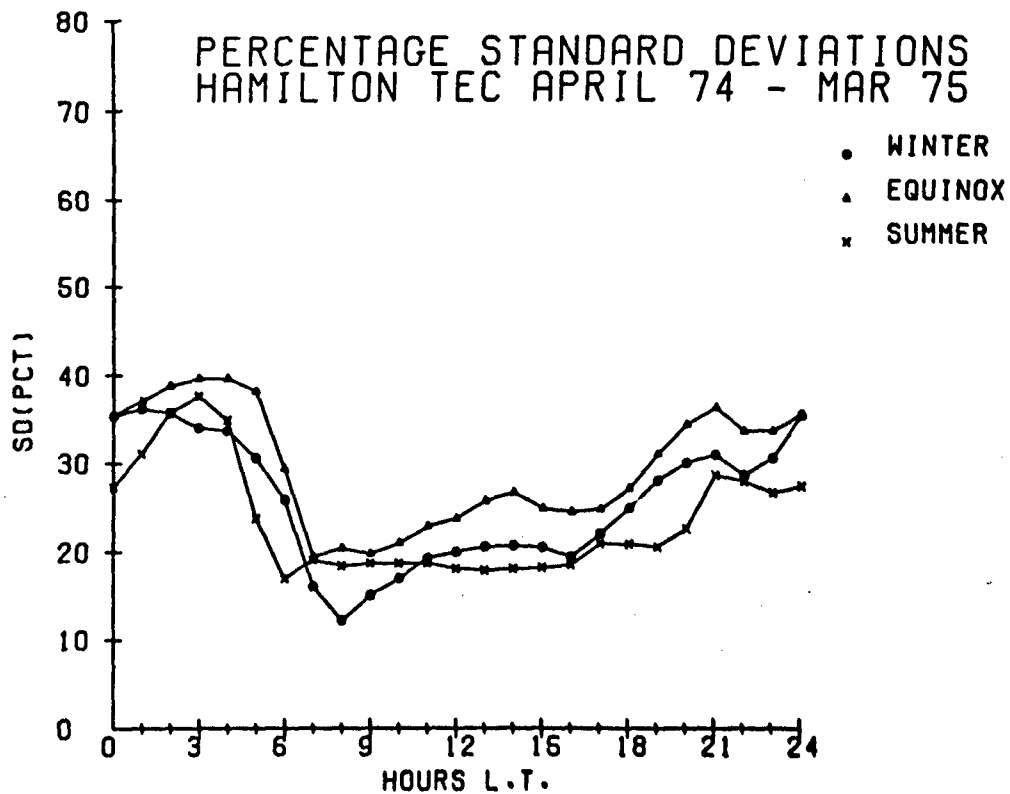


Fig. 5. Percentage standard deviation of TEC versus local time for Hamilton, Massachusetts for the seasons of the period April 1974 through March 1975, a near solar minimum period.

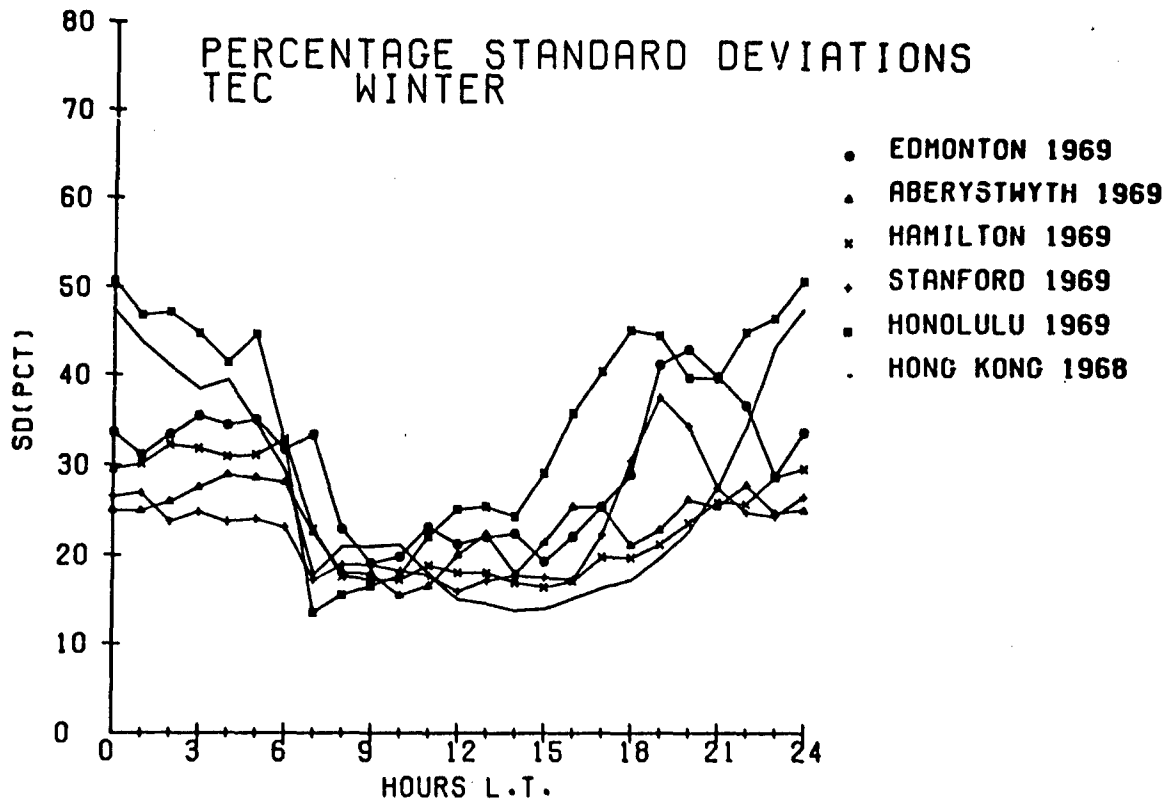


Fig. 6. Percentage standard deviation of TEC versus local time for the summer season for several stations for the solar maximum year 1969. The data from Hong Kong is for 1968.

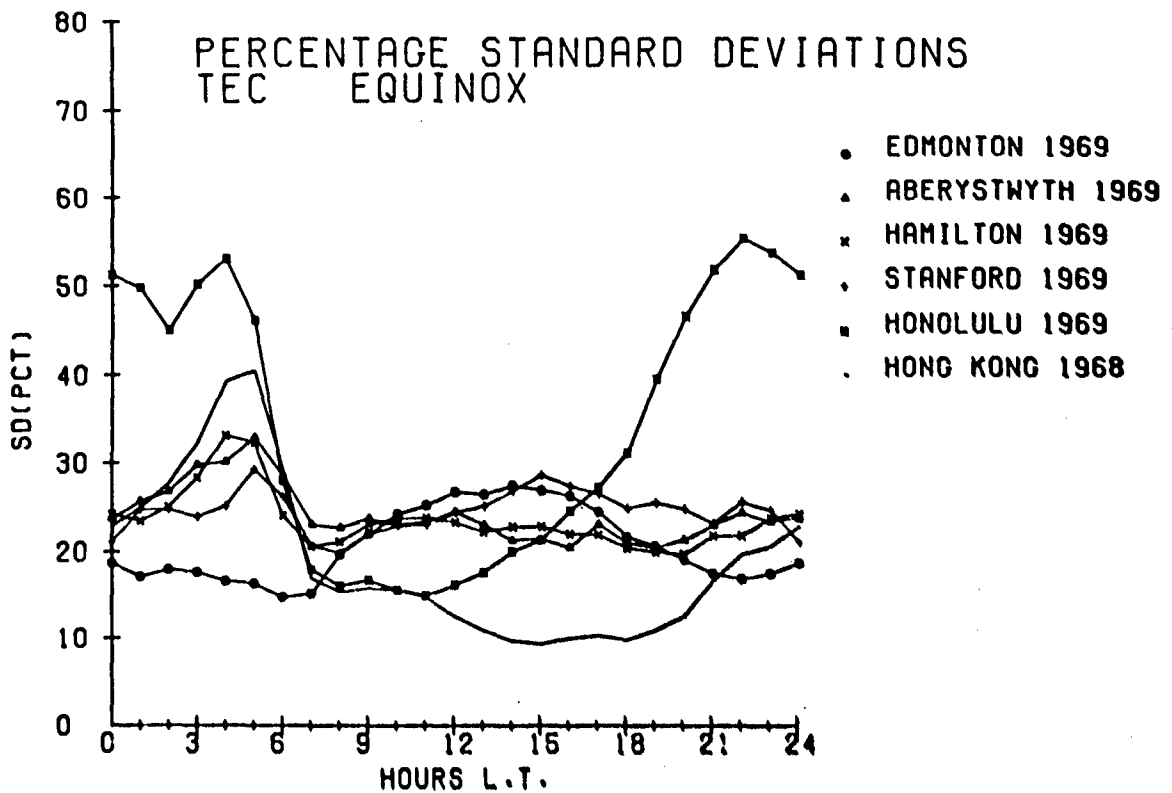


Fig. 7. Percentage standard deviation of TEC versus local time for the winter season for several stations for the solar maximum year of 1969. The data from Hong Kong is for 1968.

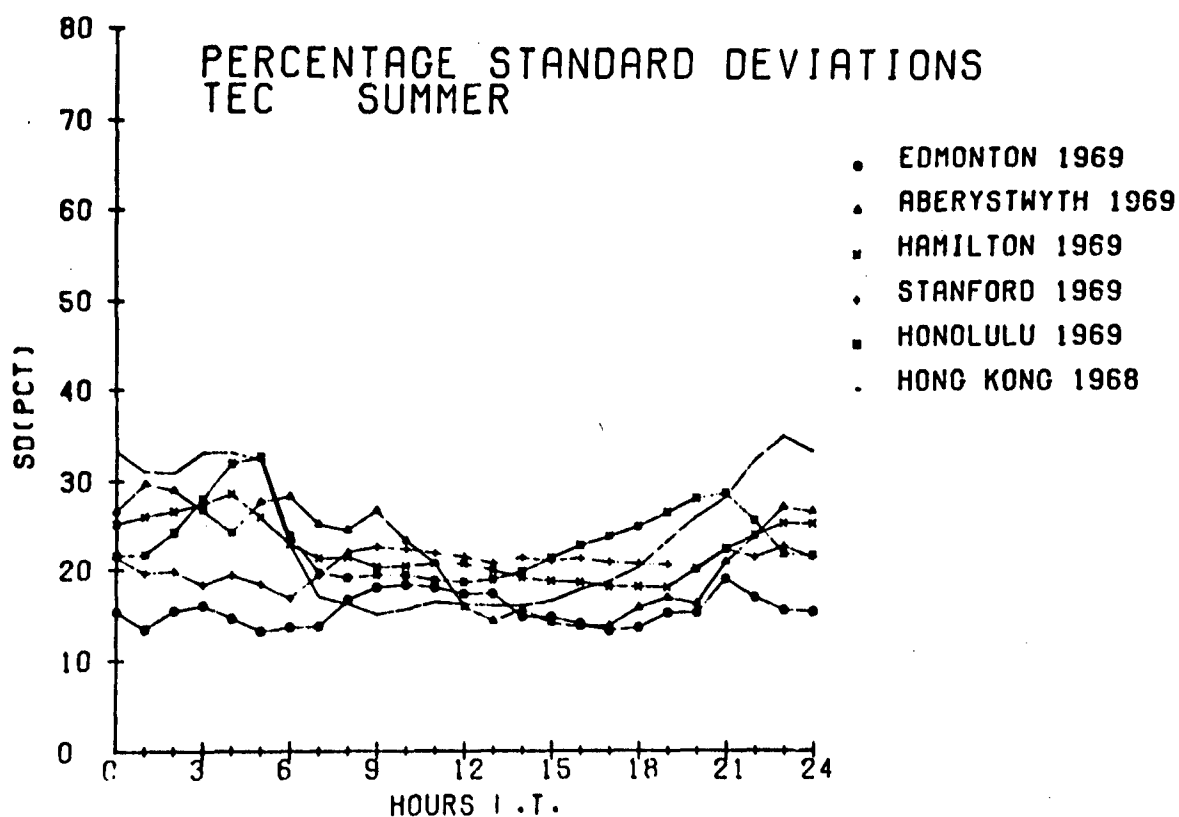


Fig. 8. Percentage standard deviation of TEC versus local time for the equinox seasons for several stations for the solar maximum year of 1969. The data from Hong Kong is for 1968.

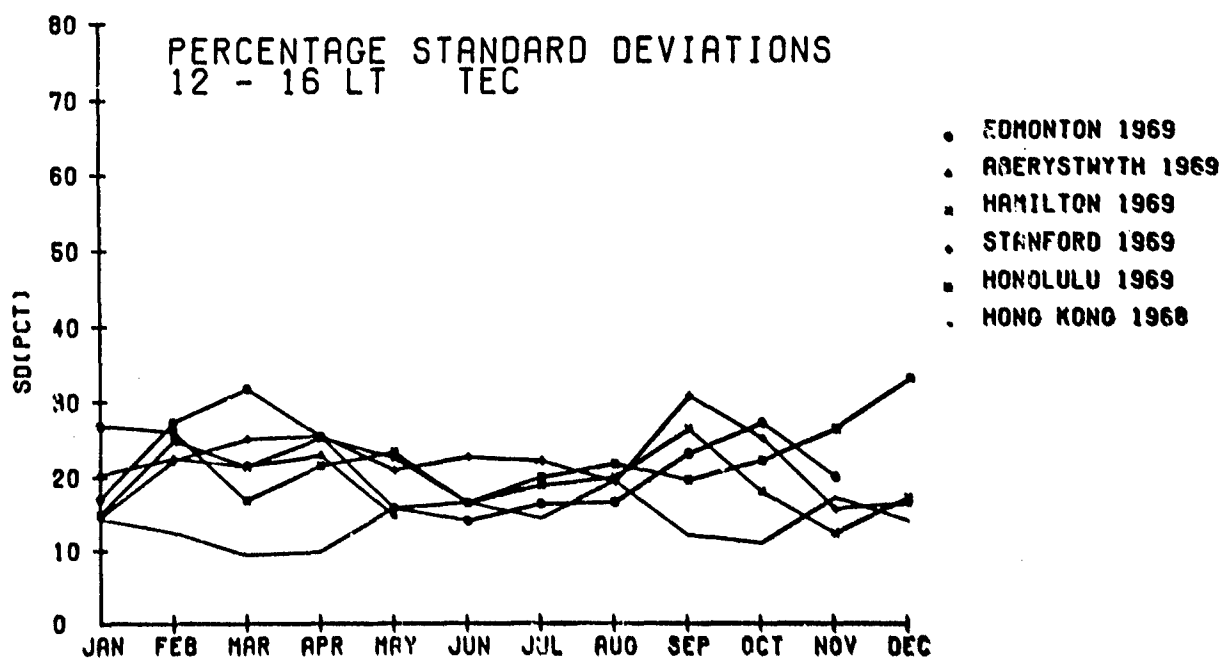


Fig. 9. Percentage standard deviation of TEC for the 12-16 hour local time period versus month of the year 1969 for several stations. Data from Hong Kong is for 1968.

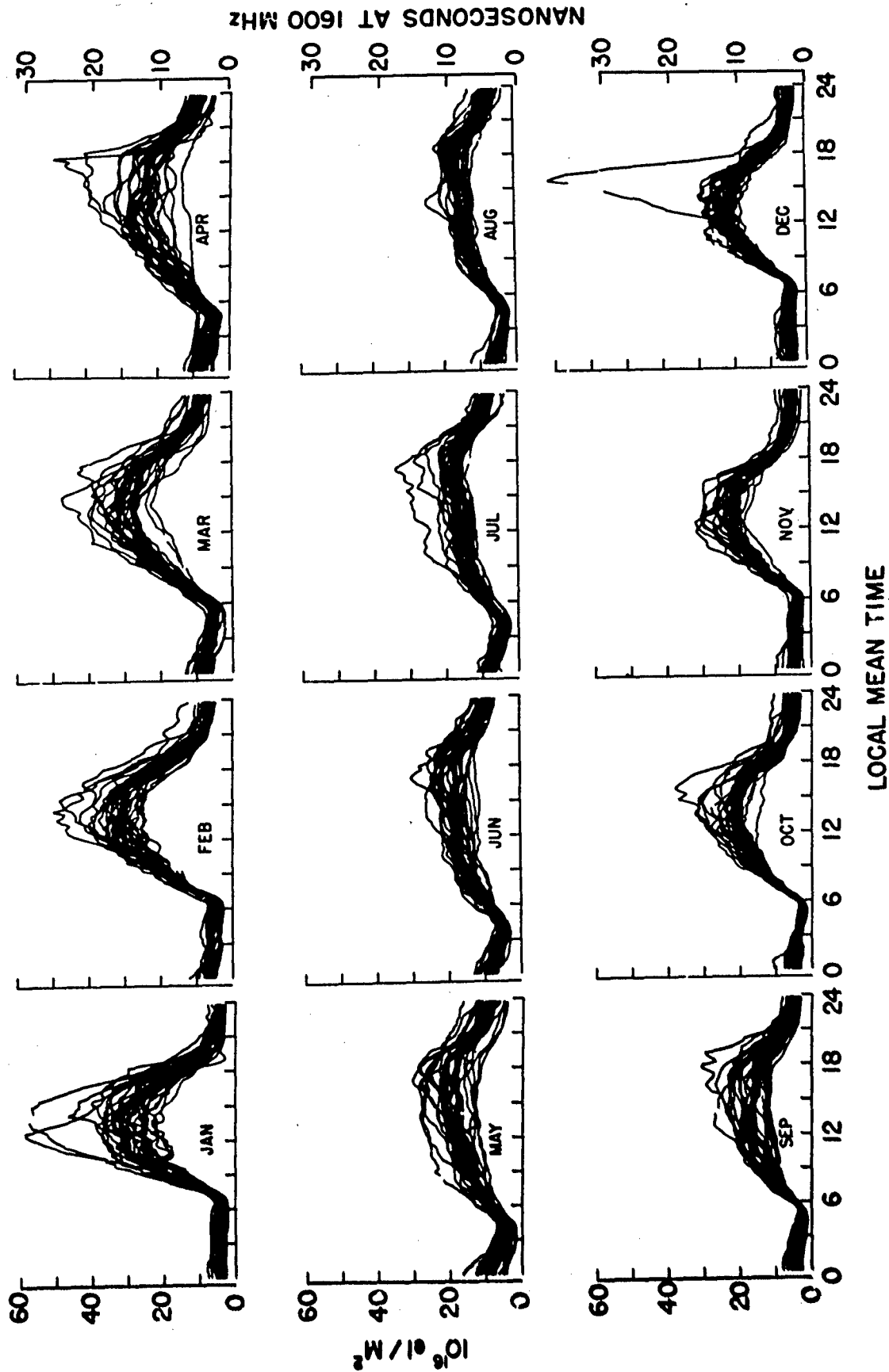


Fig. 10. Monthly overplots of equivalent vertical TEC from Hamilton, Massachusetts for the year 1971.

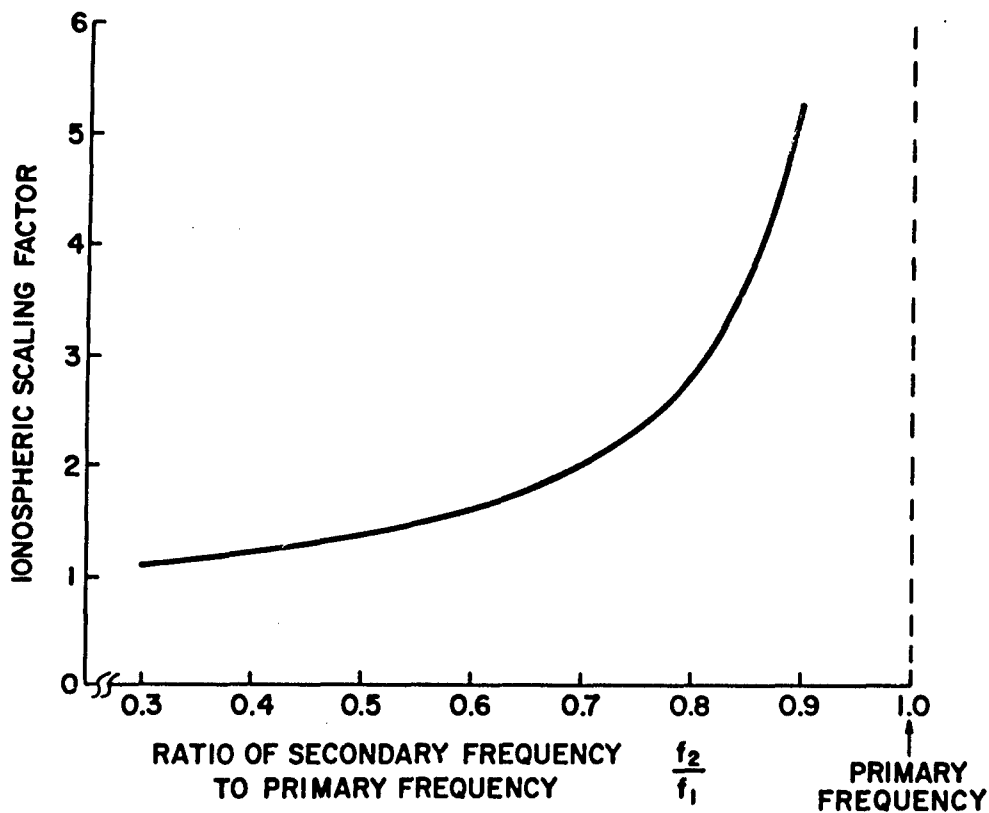


Fig. 11. Ionospheric scaling factor for two frequency differential time delay measurements versus the ratio of the secondary to the primary frequency.

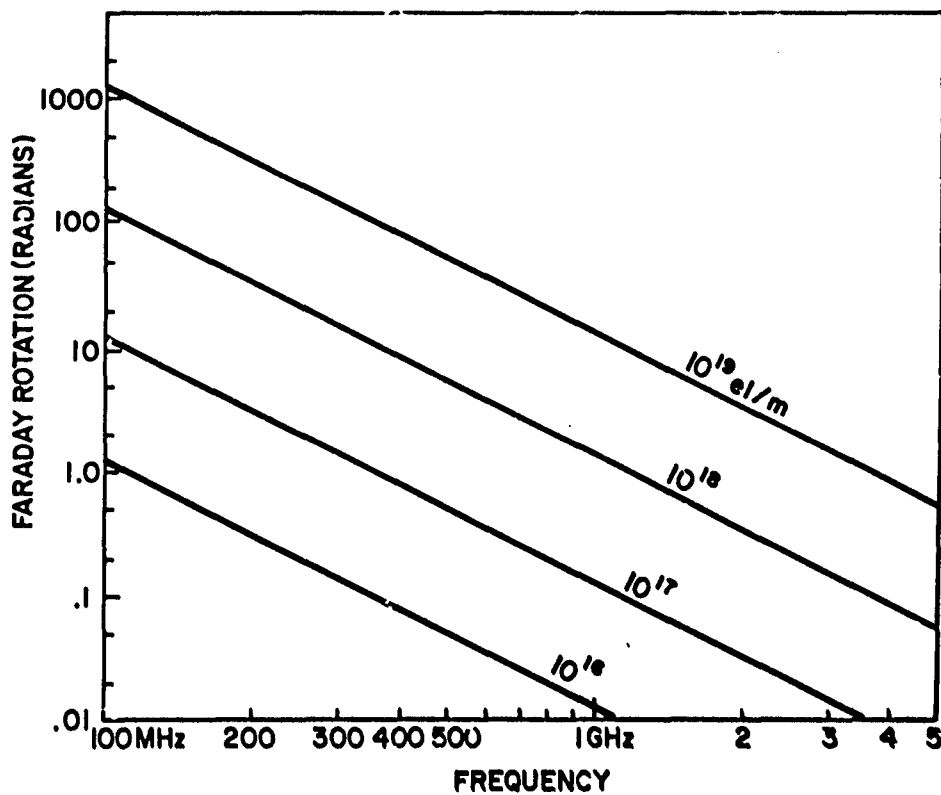


Fig. 12. Approximate Faraday rotation as a function of frequency for a northern mid-latitude station viewing a geostationary satellite along the station meridian.

IONOSPHERIC SCINTILLATIONS: AN INTRODUCTION

Jules Aarons
Air Force Geophysics Laboratory
Hanscom AFB, MA 01731

1. INTRODUCTION

A radio signal traversing the ionosphere will be modified by the medium due to the presence of irregularities with wavelengths from a few meters to a few kilometers. Scintillations or fluctuations in received signal level are variations of amplitude, phase, polarization, and angle of arrival produced when the waves pass through electron density irregularities. The scintillations can become severe and present problems for communications, navigation and detection systems. Transmissions from or to satellites have been affected from 20 MHz thru 6 GHz. In system operations, attention must be paid to this phenomenon at equatorial latitudes by MARISAT and AEROSAT (the L Band Maritime and Aeronautical Satellite Systems) and by NAVSTAR-GPS (the L Band Global Positioning System). At both equatorial and high latitudes scintillation effects will be seen on UHF communications systems (100 - 600 MHz).

2. AMPLITUDE SCINTILLATIONS

Scintillations in amplitude can be characterized by a depth of fading index and a fading period. A useful index to compare scintillation data is the scintillation index, S_4 , which is defined as the square root of the variance of received power divided by the mean values of the received power (Briggs and Parkin, 1963). An alternative, less rigorous quantitative measure of scintillation index has been adopted by the Joint Satellite Studies Group (JSSG) to ensure a standard method of data scaling in long-term statistical analysis.

The definition is: $SI_{JSSG} = P_{max} - P_{min} / P_{max} + P_{min}$ where P_{max} is the power amplitude of the 3rd peak down from the maximum excursion of the scintillations and P_{min} is the power amplitude of the 3rd peak up from the minimum excursion, measured in dB (Whitney et al., 1969).

The equivalence of selected values of these indices is indicated below.

S_4	dB _{JSSG}	SI_{JSSG}
.075	1	11
.17	3	32
.3	6	59
.45	10	81

The nature of amplitude fluctuations will be shown in a composite figure 1. Figure 1 is a tracing of observations made of equatorial scintillations at Huancayo, Peru while observing the synchronous satellite, LES-6. It can be noted that the median signal is increased during periods of scintillation activity as well as decreased in level. The probability of time the signal is below specified, graphed signal levels is shown for this 15 minute sample as well as statistics on fade duration.

2.1 Latitudinal Variation of Scintillation Activity.

The global picture of scintillations is complex but from the systems point of view the virulent areas are centered about the auroral oval and the equatorial region. The irregularity structure during magnetically quiet nights is pictured in Figure 2. Since the density of hatching is an attempt to describe the depth of fading, it should be noted that equatorial scintillations are of greater intensity than high latitude effects. At high latitudes, present data indicate that the maximum intensity of scintillation occurs in the auroral oval, although irregularity intensity is high over the polar latitudes. The data base for polar scintillation statistics is sparse. Middle latitude scintillation is observed, but it is generally of lesser intensity than high or equatorial latitude fading.

2.2 High Latitude Scintillations.

Optical aurora, the visual displays predominantly in the green line, 5577 Å, are familiar phenomena. Recently the aurora has been dramatically illustrated by the Defense Meteorological Satellites with an illustration shown in Figure 3. The most intense scintillations are in the high latitude region observed above discrete and diffuse aurora. Scintillations are predominantly an F layer phenomenon with activity ranging from 200 km to 800 km at high latitudes while the aurora as shown in the DMSP photographs is dominated by activity at 100 km.

Compared to mid-latitude levels, scintillation of radio signals increases considerably when the ray path traverses the high latitude region. The increase starts with the boundary of low level irregularities located at night in the same region as the ionospheric trough. Scintillations maximize above the aurora (Martin and Aarons, 1977). At polar latitudes scintillation level is high but somewhat

lower than at auroral latitudes.

During magnetic storms, scintillation levels increase dramatically with local excursions of the magnetic field. Statistically scintillation levels increase with K_p and with AE index (Basu, 1975).

Recent analysis (Aarons et al., 1976) of data of several high latitude stations show a general trend of an increase of scintillation excursions with both increasing solar flux and increasing K_p . This trend is affected by the seasonal character of the scintillation excursions. These are shown in Figures 4a and 4b for a station at $\sim 63^\circ A$ under both quiet and disturbed magnetic conditions.

2.3 Radar Observations.

Using 400 MHz radar signals obtained from skin tracking of satellites, Evans (1973) made a series of measurements at Millstone Hill, Massachusetts. He identified a scintillation boundary, using the S_4 value of 0.04 as the criterion as to whether the entry into the high latitude irregularity region had been reached. His results were similar to those of Aarons and Allen (1971) in that the lowest latitude of 57° was reached before midnight for this region (Fig. 5).

He found that the probability of observing large scintillations increased during magnetically disturbed periods. The highest scintillation indices ($S_4 + 1.0$ and transverse angle scintillations $\sigma_{TR} > 20$ m leg) were largely confined to periods when magnetic storms were in progress, including some in the daytime.

Evans found the amplitude during scintillation most closely followed a Nakagami m distribution with a Rayleigh distribution obtained for $m = 1$.

The mean scintillation index as a function of invariant latitude varied with magnetic activity. At latitudes above 53° , a higher K_p was associated with increased scintillation, while below 53° there was a small decrease in scintillation with increasing K_p .

2.4 In Situ Measurements.

Perhaps the largest contribution to new measurements of global morphology of irregularities in the period between 1970 and the present comes from the in situ measurements of various ionospheric parameters. These include electric fields, thermal electrons, suprathermal electrons, and ion density measurements.

Correlating in situ measurements with scintillations can only be done with several caveats. In situ measurements give no indication of thickness, an effect of importance on scintillation excursions (Singleton, 1974). In situ measurements are frequently higher in altitude than the 350 km level found to be the predominant height of the (often) thin layer irregularities. In situ measurements unless configured carefully do not show the effects of irregularity elongation, field alignment or zenith angle. More basically, however, in situ measurements may measure the causal element for the production of the irregularities (suprathermal electrons), for example; therefore the ambient atmosphere must be taken into consideration.

One series of significant measurements was obtained with an electrostatic probe on ISIS-1; thermal positive ion observations were made (Sagalyn et al., 1974). A spatial resolution of 150 meters was possible. The equatorial boundary of the irregularity region was defined as the latitude of onset of persistent small scale ionization irregularities extending over at least a few degrees in latitude with amplitudes amounting to 20 percent or more of the mean background levels.

The boundary of the irregularity zone was found to be 3° to 9° closer to the pole in the southern hemisphere than in the northern hemisphere. The seasonal variation of the mean location was small. The boundary is closest to the pole in June and farthest in December. No poleward boundaries for the irregularity zone were found; the inhomogeneities extend across the pole. Comparison of the irregularity boundary of this technique and that of the scintillation boundary were excellent at night and between 21 and 06 local time but differed at 1700 LT (Figure 6).

The severe topside irregularity zone was observed using the ionosounder on ISIS-2 (Dyson and Winningham, 1973). On the dayside of the earth the equatorward boundaries of this zone and of the < 300 eV electron precipitation coincide. However, the boundary does not coincide with electron precipitation above 300 eV. The zone extends beyond the poleward boundary of the particle precipitation, probably due to magnetospheric convection transporting irregularities poleward of the region of production.

2.5 Equatorial Scintillations.

In the equatorial region, the typical development of scintillation from an ionosphere devoid of intense irregularities to that where deep fading is observed is often abrupt and dramatic as shown in three photographed sections of paper tape recordings made in Natal, Brazil (Fig. 7). The start of scintillations can often be noted to take place within a few seconds, a single fade. An example of the fast onset, the deep rapid continuous fluctuation and finally the slowing and more sporadic fading is shown in the top panel of the figure. The observations illustrated are of the 254 MHz transmissions of LES-6. The use of a large antenna (in this case, 28 ft in diameter) has allowed deep fading to be observed, frequently of the order of 20 dB below mean level. Rapid deep fading characterizes the beginning of the scintillation activity as shown in Figure 7a. As the night progresses, the scintillation frequently becomes more sporadic with interludes of low level fading (Fig. 7b). The small scale irregularities are contained in the large scale patches that move across the path. Finally, at the end of the scintillation activity, the scintillations change character, and one notes long fades that may remain below fade margins of 6 dB for 3 to 37

seconds (Fig. 7c).

The patterns of scintillation activity show great variety. One pattern that has been observed frequently is of a patchy nature. Scintillations on one satellite path start and stop during the night several times, with the patch moving through the propagation path in times of the order of 20 minutes to several hours. A compressed time scale was used in Figure 8a (Natal, Brazil) compared to the data in Figure 7. Similar lifetimes of the patches of irregularities, as well as their velocities, have been reported in transequatorial studies of irregularities by HF transmissions (Crochet, 1972). Figure 8b shows lifetimes of the patches using this technique (Rottger, 1973).

In the equatorial region, experiments were performed to study the development and maintenance of the large scale irregularity patches (several hundred kilometers EW and many times that NS) which often contain the small scale irregularities of approximately 3 m to 1 km which produce VHF to microwave scintillation.

The top panel of Figure 9 shows an upwelling into the middle and upper F layer of a localized depletion of electron density formed in the lower F region. This "plume" forms at 1945 LT from a thin layer of bottomside irregularities, followed at 2045 LT by a second plume, emerging from a much wider and more disturbed layer of irregularities. The two lower panels show scintillations observed on LES-9 signals at Ancon and Huancayo. The propagation path from Ancon to LES-9 traverses the disturbed ionosphere 300 km east of Jicamarca and that from Huancayo to LES-9 475 km east of Jicamarca. The time history of the formation of the plume over Jicamarca and the onset times of scintillations at Ancon and Huancayo show a clear eastward drift of an irregularity region of well defined extent. The two plumes seen in the backscatter record result in one extended scintillation event, suggesting a rather large extent in height of irregularities responsible for the scintillations.

Figure 10 shows typical patch 3-dimensional structure at local times depending on the stage of formation or dissolution. With the formation of a thin layer of irregularities (\sim 1930 local time) UHF scintillations start with 5 dB peak to peak values typical. Fading rates (on the ground) are typically 10/min. During the formation of the plume scintillations show greater depth (\sim 20 dB peak to peak); irregularity thickness increases as well as strength of returns; rates exceed 10/min. It is during this time that microwave scintillations are probably observed.

After formation an irregularity structure moves east at speeds between 50 and 150 m sec⁻¹. Scintillations observed during this phase are still high. At a later stage irregularities within a specific patch begin to decrease in intensity, resulting in lower scintillation levels. Limited observations suggest that the eastward motion of these patches slows down in the later stage, around midnight.

2.6 Seasonal and Solar Cycle Dependence.

There are clearly seasonal maxima of the occurrence of equatorial scintillations. The precise pattern varies as a function of longitude and solar flux. The seasonal pattern and the solar cycle dependence can best be illustrated with the aid of Figures 11a and 11b, utilizing observations at Huancayo, Peru of ATS-3 transmitting at 137 MHz.

Figure 11a utilizes data taken at the peak of the present solar cycle (August 1969 to July 1970) with another period (Figure 11b) centered around a minimum in the solar cycle (August 1973 to July 1974). There is a higher occurrence of deep scintillations (a scintillation index (SI) greater than 60 (6 dB peak to peak)) with an S_4 of 0.3 during a year of high solar flux (August 1969 to July 1970) than during a year with low solar flux (August 1973 to July 1974). The magnetic index K_p range is in both cases from 0-3 to avoid possible confusion with magnetic storm effects. Similar solar cycle dependence has been reported at Accra (Koster, 1972).

As for seasonal pattern, Mullen and Hawkins (1975) found that the peak of the equinoctial activity took place in November and March at Accra, Ghana, whereas Huancayo data show a diffuse maximum from October through March, with only a slight decrease in scintillation activity in December.

For African longitudes, observing from Ghana, Koster (1972) found equinoctial maxima with clear minima near the solstices.

The seasonal pattern for the eastern region of Asia is not clearly ascertained. Nichols (1974) found the seasonal pattern and distribution of 250 MHz fades shown in Figure 12 for his Kwajalein Islands observations. Some data from the high latitude edge of this longitudinal region (Calcutta) indicates that a maximum of occurrence takes place in the June to July period.

Taur (1973) using 4 and 6 GHz data found maximum occurrence in February to April and September to November. He worked with global statistics. Basu et al., (1976) presented the estimated worldwide equatorial morphology of percentage scintillation greater than or equal to 4.5 dB at 140 MHz for Nov-Dec 1969 and 1970 during 1900-2300 LT on magnetically quiet days based on 250 Ogo-6 orbits (Fig. 13). A great variability in occurrence as a function of longitude is seen.

As for magnetic dependence, data from Huancayo, Peru indicates a complex dependence varying with month and time of day. Koster (1972) showed that scintillation is frequently inhibited during large magnetic disturbances at Accra, Ghana. A table summarizing much of scintillation morphology is shown in Table 1 (G. Millman, 1977, private communication).

2.7 Geometrical Considerations.

The intensity at which scintillations are observed depends upon the position of the observer relative to the irregularities in the ionosphere that cause the scintillation. Keeping both the thickness of the irregularity region and ΔN , the electron density deviation of the irregularity, constant, geometrical factors have to be considered to evaluate data and to predict scintillation effects at a particular location. Among

these are:

(a) Zenith distance of the irregularity at the ionospheric layer. One study (Wand and Evans, 1975) found the intensity of scintillation may be related approximately to the zenith path values by the secant of the zenith distances to 70° ; below that an elevation angle dependence ranging between $1/2$ and the first power of the zenith angles should be used.

(b) Propagation angle relative to the earth's magnetic field. Performing this calculation demands the use of an irregularity configuration and the consideration of Gaussian or a power law model for the irregularities. At high latitudes irregularities in one study were elongated along the earth's magnetic field with a cylindrical form of axial ratio of 5 along the lines of force. Sheet-like irregularities with forms of 10:10:1 have also been found in recent auroral studies (Rino, private communication). For equatorial latitudes, this elongation along the lines of force may be of the order of 50 to 100 (Koster, 1963).

(c) The distance from the irregularity region to the source and to the observer (near the irregularities, only phase fluctuations are developed). As noted in Mikkelsen et al., (1977) and Crane (1977), the theoretical scintillation index can be expressed in terms of the above factors when dealing with ionospheric irregularities represented by a Gaussian power spectrum.

Scintillation levels relative to zenith values for an assumed irregularity correction of 5:2:1 (sheet-like irregularities) are shown in Figure 14 for a sub-auroral station at 54° invariant latitude. Looking "up" the lines of force produces an increasing index by a factor of 3.5 (at the field point). Looking perpendicular to the lines of force reduces the scintillation relative to its zenith value of 1. Low angles of elevation produce high multiplying factors.

2.8 Frequency Dependence.

Observations (Fremouw et al., 1978) employing ten frequencies between 138 MHz and 2.9 GHz transmitted from the same satellite, show a consistent $\lambda^{1.5}$ behavior of S_4 for S_4 less than about 0.6. The frequency dependence is less steep for stronger scintillation, with S_4 attaining a maximum value near unity with a few rare exceptions. The same observations show that the phase scintillation index, σ_ϕ (defined as the standard deviation of phase in the fluctuation-spectral range containing intensity scintillations), varies as λ under most conditions, a result also obtained by Crane (1976). Figure 15 expresses these results in scatter diagram form for intensity and phase scintillation. Under extremely disturbed conditions, it appears that the frequency dependence of σ_ϕ is less steep for values greater than a few radians. In general, however, definitive measurements of phase scintillations have only begun.

2.9 Fading Period.

The fading period of scintillation varies over quite a large range and can be as long as several minutes at equatorial latitudes (Koster, 1966). The fading period depends both upon the apparent motion of the irregularities relative to the ray path and in the case of strong scintillation on its severity. For strong scintillation with $S_4 > 0.4$ or where peak to peak fading is greater than 8 dB, the fading period is shorter than for weak scintillation with the same relative velocity. The fading period of gigahertz scintillation at the equator ranges from 2-15 seconds. The gigahertz measurements were in the weak scintillation limit and were made when both the transmitter and receiver were stationary; therefore the observed fading periods reflect the motion of the ionospheric irregularities.

From the point of view of having order of magnitude ideas of the fading period, the concept of the Fresnel zone can be used to explain the weak scintillation observations in scale size and fading period. The scale size r_0 is $r_0 = \sqrt{\lambda z_1(z_2 - z_1)}/z_2$ where z_2 is the length of the path from the satellite to the ground and z_1 is the distance to the irregularities; the fading period would be r_0/v . The above expression for r_0 implies that both scale size and fading period are proportional to $\sqrt{\lambda}$.

The fading rate is a function of ground pattern size and motion of the ionospheric winds, the observer and the source. Essentially at all latitudes the ground pattern size is frozen when observing low altitude satellite signals. When observing synchronous satellites from ground stations the wind pattern determines the fading rate.

3. SIGNAL CHARACTERISTICS

3.1 Signal Statistics.

The amplitude, phase, and angle-of-arrival of a signal will fluctuate during periods of scintillation. The intensity of the scintillation may be characterized by the variance in received power or by the variance in the logarithm of received power. The measure S_4 is defined as the square root of the variance of received power divided by the mean value of the received power (Briggs and Parkin, 1963). The measure σ_ϕ is the square root of the variance of the logarithm of the received power (Tatarski, 1967). For periods of scintillation having a constant value of either one of these measures, the signal level fluctuations may be described by an empirical probability density function (pdf). Sample empirical pdfs are given in Fig. 16 for several S_4 values.

The phase of the received signal also may vary. Phase scintillation is defined as those phase variations that are as fast or faster than the slowest intensity scintillations. The strength of phase scintillation may be characterized by the standard deviation of phase, σ_ϕ . Empirical pdfs for phase fluctuations are given in Fig. 17 for the same cases shown in Fig. 16. The data depicted in Fig. 16 and 17 were obtained at a

midlatitude station at 150 and 400 MHz (Crane, 1977).

Attempts have been made to model the observed amplitude pdf. Whitney et al. (1972) and Crane (1977) have constructed model distribution functions based upon the use of the Nakagami-m distribution ($m = (S_4)^{-2}$) and have shown that the models provide a reasonable approximation to their observed empirical distribution functions. In addition, the Rayleigh pdf provided a good fit to the data under conditions of very strong scintillation ($S_4 \gg 0.9$). The Nakagami-m distribution is a Rayleigh distribution for $m = 1$ (strong scintillation), and is a log-normal distribution for $m > 1$ (weak scintillation).

The log-normal and Nakagami-m distributions are both characterized by a single parameter which can be related to either S_4 or σ_χ . More complex models exist with more parameters that can be adjusted to fit the data. A leading candidate from models in this class is the two-component Gaussian statistics model (Fremouw et al., 1978). The received complex electric field can be modelled as the product of the focus and the scatter components, which are statistically independent. The empirical pdfs can be fitted by using the six parameters that describe the statistical characteristics of the two components.

3.2 Spectrum of Amplitude and Phase Fluctuations.

The signal fluctuations may also be described by spatial or temporal power spectra (Rufenach, 1972). Temporal power spectral density estimates for scintillation observed at 150 and 400 MHz using a low orbiting satellite are depicted in Fig. 18 (Crane, 1976). The power spectral density values were normalized to have the same values at frequencies near 5 Hz. The observations were also compared with a theoretical model based upon an irregularity power-law spectrum giving weak scintillation. The data and theoretical model show that the spectra for log-amplitude fluctuations peak at a frequency near $f = 0.4 v/r_0$ where v is the relative velocity of the irregularities normal to the line-of-sight (drift velocity) at the location of maximum fluctuations in the electron density, and r_0 is the size of the first Fresnel zone at the same point. The power spectrum for log-amplitude fluctuations decreases with increasing frequency as f^{-3} (the high-frequency asymptote). The data have this form until masked by modulation noise. A power spectrum obtained for equatorial scintillation of 4 GHz signals for the geostationary Intelsat IV satellite is depicted in Fig. 19 (Tsur, 1976). The power spectrum of intensity fluctuations for strong scattering in the equatorial region has been measured using 136 and 360 MHz transmissions from ATS-6 (Whitney and Basu, 1977). In the case of strong scattering the transition frequency, demarcating the low frequency and high frequency slopes, increases and the high frequency slope may also increase to as much as f^{-6} .

The power spectrum for phase fluctuations shown in Fig. 18 continues to increase with decreasing frequency, showing the domination of phase fluctuations by the large-scale refractive-index changes as predicted by geometrical optics. These data show that for a sufficiently long observing time the variance of log-amplitude (proportional to σ_χ^2) reaches a fixed level, but the variance of signal phase continues to increase with increasing observing time. Since the power spectrum for phase fluctuations behaves approximately as f^{-3} , and doppler or angle-of-arrival fluctuations may be related to the temporal or spatial derivative of the phase fluctuations, the power spectra for doppler fluctuations will vary as f^{-2} . The angle-of-arrival or doppler variances will also continue to increase with increasing observing time.

The data depicted in Fig. 18 were obtained using a rapidly moving line-of-sight to a low orbiting satellite. During the portion of the satellite pass used to generate the spectra, the ionosphere could be considered frozen. The temporal fluctuations, therefore, may be interpreted as spatial fluctuations. The scale sizes at a height of 300 km are indicated on the second scale. For a geostationary satellite, the spatial fluctuations will not change, but the temporal fluctuations will. The spatial fluctuations may be expressed either as fluctuations at a point in the ionosphere or fluctuations on the ground (and normal to the line-of-sight). At the ground, the peak of the log-amplitude power spectrum occurs at scale sizes near $\lambda = 2.5 r_0 z_2 / (z_2 - z_1)$. The data shown in Fig. 18 are for motion of the satellite nearly perpendicular to the magnetic field. The resultant scale sizes, therefore, are for a direction perpendicular to the field. For a direction along the field, the scale size increases by the axial ratio of the irregularities.

3.3 Diversity Schemes.

Diversity schemes attempt to reduce the effects of fading during a scintillation event by combining two signals that are fading independently. For a Rayleigh process, signal fades are greater than 18.4 dB for one percent of the time. For two independent Rayleigh processes, the larger of the two signals at any sample point fades to 9.5 dB for one percent of the time yielding a gain in protection against fading of 9 dB. In general the diversity gain depends upon the correlation between the two samples of the fading process. If the correlation coefficient is less than 0.6, the diversity gain is 8 dB or better. A correlation coefficient of 0.6 may be used as a threshold for diversity action for a fading process although it strictly applies only to a Rayleigh fading (strong scintillation). In the limit of weak scintillation, a correlation coefficient less than 0.6 occurs between observations at two frequencies for signals propagating along the same path only if the carrier frequencies are separated by more than a factor of three, suggesting that frequency diversity is not generally effective in combating scintillation (Crane, 1977). Simultaneous fluctuations on orthogonal-polarized channels are also highly correlated for frequencies above 100 MHz (Koster, 1966; Whitney and Ring, 1971; Crane, 1977).

Two diversity schemes are viable for both weak and strong scintillation conditions.

time and space. Time diversity requires that the same message be sent at two different times separated far enough for the correlation coefficient to be less than 0.6. Space diversity requires that the same message be detected at two receiving points separated far enough for the coefficient to be less than 0.6. One experimental set up and illustrative material are shown in Figure 20 (Whitney, personal communication). The correlation function may be calculated from the power spectrum for the received signal fluctuations. The time separation corresponding to a correlation coefficient of 0.6 as computed for the spectra described in Section 2.3.2 is given by $\tau = 0.3 r_0/v$. For space diversity, the distance for a correlation coefficient of 0.6 is $l = 0.3 r_0 z_2 / (z_2 - z_1)$ for a direction normal to the line-of-sight and normal to the field, and $l = 0.3 r_0 z_2 \alpha / (z_2 - z_1)$ for a direction normal to the line-of-sight in the direction of the field, where α = axial ratio of the irregularities. For oblique incidence, the projection of these distances onto the ground is required for the estimation of diversity distance.

Diversity schemes are normally only required to overcome the effects of intense scintillations; weak scintillations are offset by a reasonable fade margin. Measurements of the spatial cross-correlation function for strong scattering conditions have given typical values for the correlation coefficient of 0.6 for 300 m. antenna separation and 0.3 for 1000 m. separation (NELC measurements at Guam, September 1976, reported at Interagency Coordination Committee and Group-Ionospheric Scintillation, 26 January 1977). The corresponding drift velocity of the irregularities was approximately 50 m. per second. It was measured with E-W antenna baselines which would be parallel to the expected drift velocity vector. Other antenna orientations would require greater baselines to achieve the necessary decorrelation. Therefore space diversity seems only practical for ground stations.

Another means for characterizing signals is shown in Figure 21. Here a 15 minute data sample is analyzed to determine the percentage of zero error messages which may be put thru the system with given system margins. One can note that if the link margin for the receiving system is reduced (in this example) by -4 dB then only 13% of the messages will be received error free. In this case the data, taken on magnetic tape, has been processed so that 4 second messages are put thru the system. Only those 4 second messages with cross hatching are received perfectly. When one analyzes the statistics of signal fading the resulting curve on the left hand side is noted. The periods of scintillations above and below the link margins are shown on the lower right. Thus the designer of equipment can with statistics of this sort determine the trade-off for mitigating scintillations or can give to the user the hard facts of living with the percentage of time when scintillation activity produces an unacceptable error rate.

4. CONCLUSION

The systems engineer utilizes irregularity data to develop means to mitigate the effects of this fading or provides enough signal margin to regard the phenomenon as a non-problem. The systems operator must be given a realistic appraisal of the probability of occurrence of errors in his messages or identification of targets.

Much has to be done to understand the phenomena of irregularity formation, development and dissipation. More data is needed to evaluate the phase fluctuation parameters to be encountered on different paths.

There is a great deal of activity in this field of radio wave propagation due to its possible impact on systems. The work outlined will introduce many aspects of the present state of knowledge in the field.

5. ACKNOWLEDGEMENTS

A portion of the material in this paper is from CCIR documents to which the author has contributed.

6. REFERENCES

- Aarons, J. and Allen, R.S. (1971) Scintillation boundaries during quiet and disturbed magnetic conditions, J. Geophys. Res., 76, 170-177.
- Aarons, J., Mullen, J., Whitney, H., Martin, E., Bhavnani, K. and Whelan, L. A high-latitude empirical model of scintillation excursions: Phase 1, AFGL-TR-76-0210, 17 Sept. 1976.
- Basu, Sunanda (1975) Universal time seasonal variations of auroral zone magnetic activity and VHF scintillations, J. Geophys. Res., 80, 4725-4728.
- Basu, Sunanda, Masu, S., and Khan, B.K. (1976) Model of equatorial scintillations from in-situ measurements, Radio Sci., 11, 821-832.
- Briggs, B.H. and Parkin, I.A. (1963) On the variation of radio star and satellite scintillation with zenith angle, J. Atmos. Terr. Phys., 23, 339.
- Crane, R.K. (1976) Spectra of ionospheric scintillations, J. Geophys. Res., 81, 2041.
- Crane, R.K. (1977) Ionospheric scintillation, Proc. IEEE, 65, 180-199.

- Crochet, M. (1972) Propagation transequatoriale en dehors d'un grand cercle en ondes decametriques, Partie I: Mise en evidence et morphologie, Ann. Geophys., 28, 27-35.
- Dyson, P.L., and Winningham, J.D. (1973) Topside Ionospheric Spread F and Particle Precipitation in the Dayside Magnetospheric Clefts, AFCRL F19628-72-C-0230.
- Evans, J.V., ed. (1973) The Millstone Hill Radar Propagation Study: Scientific Results, Lincoln Lab., Technical Report.
- Fremouw, E.J., Livingston, R.C., Rino, C.L., Cousins, M., Fair, B.C., and Leadbrand, R.L. (1978) Complex-signal scintillation - Early results from the DNA-002 coherent beacon, Radio Sci., 13 (1).
- Koster, J.R. (1963) Some measurements of the irregularities giving rise to radio star scintillations at the equator, J. Geophys. Res., 68, 2579.
- Koster, J.R. (1966) Ionospheric studies using the tracking beacon of the Early Bird synchronous satellite, Ann. de. Geophys., 22, 435-439.
- Koster, J.R. (1972) Equatorial scintillations, Planet. Space Sci., 20, 1999-2014.
- Martin, E. and Aarons, J. (1977) F-layer scintillations and the aurora, J. Geophys. Res., 82, 2717-2722.
- Mikkelsen, I.S., Aarons, J., and Martin, E. (1977) Geometrical considerations of 136 MHz amplitude scintillation in the auroral oval, Accepted for publication in J. Atmos. Terr. Phys.
- Mullen, J. and Hawkins, G. (1975) Equatorial scintillation at 136 MHz observed over half a sunspot cycle, Effect of the Ionosphere on Space Systems and Communications, John Goodman, ed., NTIS CSCL 04/1 N75-30714#, Naval Research Lab, Washington, D.C.
- Nichols, B.E. (1974) UHF Fading from a Synchronous Satellite Observed at Kwajalein, October 1968 through June 1970, Tech. Note, Lincoln Laboratory, 1974-19, Air Force Contract F19628-73-C-0002.
- Rottger, J. (1973) Wave-like structures of large scale equatorial spread-F irregularities, J. Atmos. Terr. Phys., 35, 1195-1206.
- Rufenach, C.L. (1972) Power law wave number spectrum deduced from ionospheric scintillation observations, J. Atmos. Terr. Phys., 77, 4761.
- Sagalyn, R.C., Smiddy, M., and Ahmed, M. (1974) High latitude irregularities in the top side ionosphere based on ISIS-I thermal ion probe data, J. Geophys. Res., 79, 4252.
- Singleton, D.C. (1974) The dependence of high-latitude ionospheric scintillation on zenith angle and azimuth, J. Atmos. Terr. Phys., 36, 113.
- Tatarski, V.I. (1967) Radio Propagation in a Turbulent Medium, English-translation by P. Silverman, McGraw-Hill, New York.
- Taur, R.R. (1973a) Ionospheric scintillations at 4 and 6 GHz, COMSAT Technical Review, 3.
- Taur, R.R. (1976) Simultaneous 1.5 and 4 GHz ionospheric scintillation measurements, Radio Sci., 11, 1029.
- Wand, R.H. and Evans, J.V. (1975) Morphology of ionospheric scintillation in the auroral zone, Proceedings of the IES Symposium, Naval Research Laboratory, Arlington, VA.
- Whitney, H.E., Malik, C., and Aarons, J. (1969) A proposed index for measuring ionospheric scintillations, Planet. Space Science, 17, 1069-1073.
- Whitney, H.E. and Ring, W.F. (1971) Dependency of scintillation fading of oppositely polarized VHF signals, IEEE Trans. Ant. Prop., AP-19.
- Whitney, H.E., Aarons, J., Allen, R.S., and Seeman, D.R. (1972) Estimation of the cumulative amplitude probability distribution function of ionospheric scintillations, Radio Sci., 7, 1095.
- Whitney, H.E. and Basu, S. (1977) The effect of ionospheric scintillation on VHF/UHF satellite communication, Radio Sci., 12, 123-133.

SOLAR-GEOPHYSICAL AND TEMPORAL DEPENDENCE OF IONOSPHERIC SCINTILLATION

PARAMETER	LATITUDE REGION		
	EQUATORIAL	MID-LATITUDE	HIGH-LATITUDE
Activity Level	Exhibits Greatest Extremes	Generally Very Quiet to Moderately Active	Generally Moderately Active to Very Active
Diurnal	Maximum-Nighttime Minimum-Daytime	Maximum-Nighttime Sporadic-Daytime	Maximum-Nighttime Minimum-Daytime
Seasonal	Longitudinal Dependent Accra, Ghana Maximum-November and March Minimum-Solstices Huancayo, Peru Maximum-October through March Minimum- May through July Kwajalein Islands Maximum-May Minimum-November and December	Maximum-Spring Minimum-Winter	Maximum-Summer Minimum-Winter
Solar Cycle	Occurrence Increases with SSN	Insufficient Data	Occurrence Increases with SSN
Magnetic Activity	Longitudinal Dependent Accra, Ghana Occurrence decreases with K_p Huancayo, Peru March Equinox- Occurrence decreases with K_p June Solstice Occurrence increases with K_p September Equinox 0000-0400 Hrs. LT, Occurrence increases with K_p	Independent of K_p	Occurrence Increases with K_p

TABLE 1.

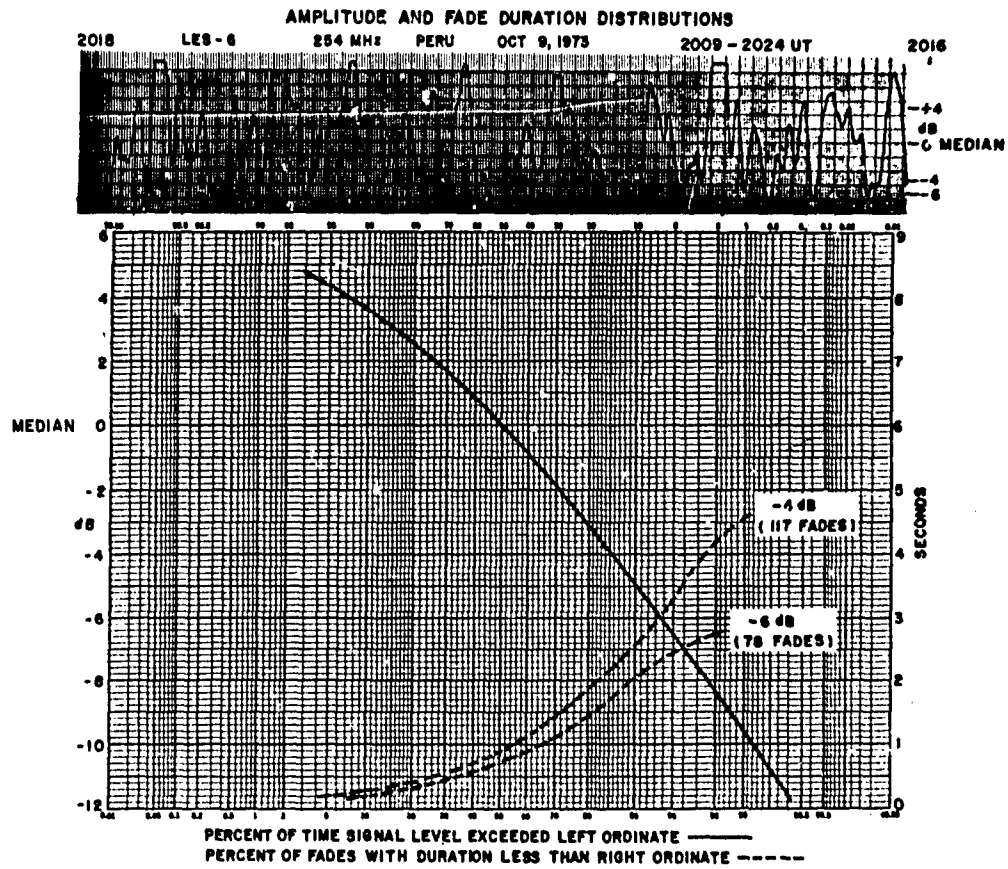


FIG. 1 Retracing of Huancayo, Peru LES-6 observations with statistics on fade duration and probability of time signal is below certain levels.

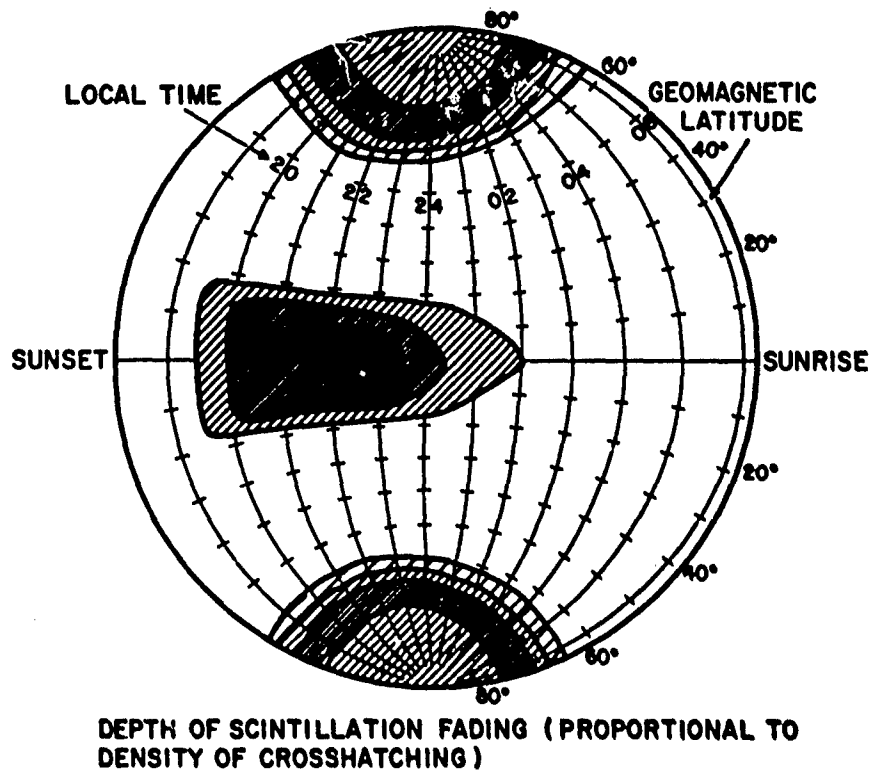


FIG. 2 Irregularity structure during magnetically quiet nights.

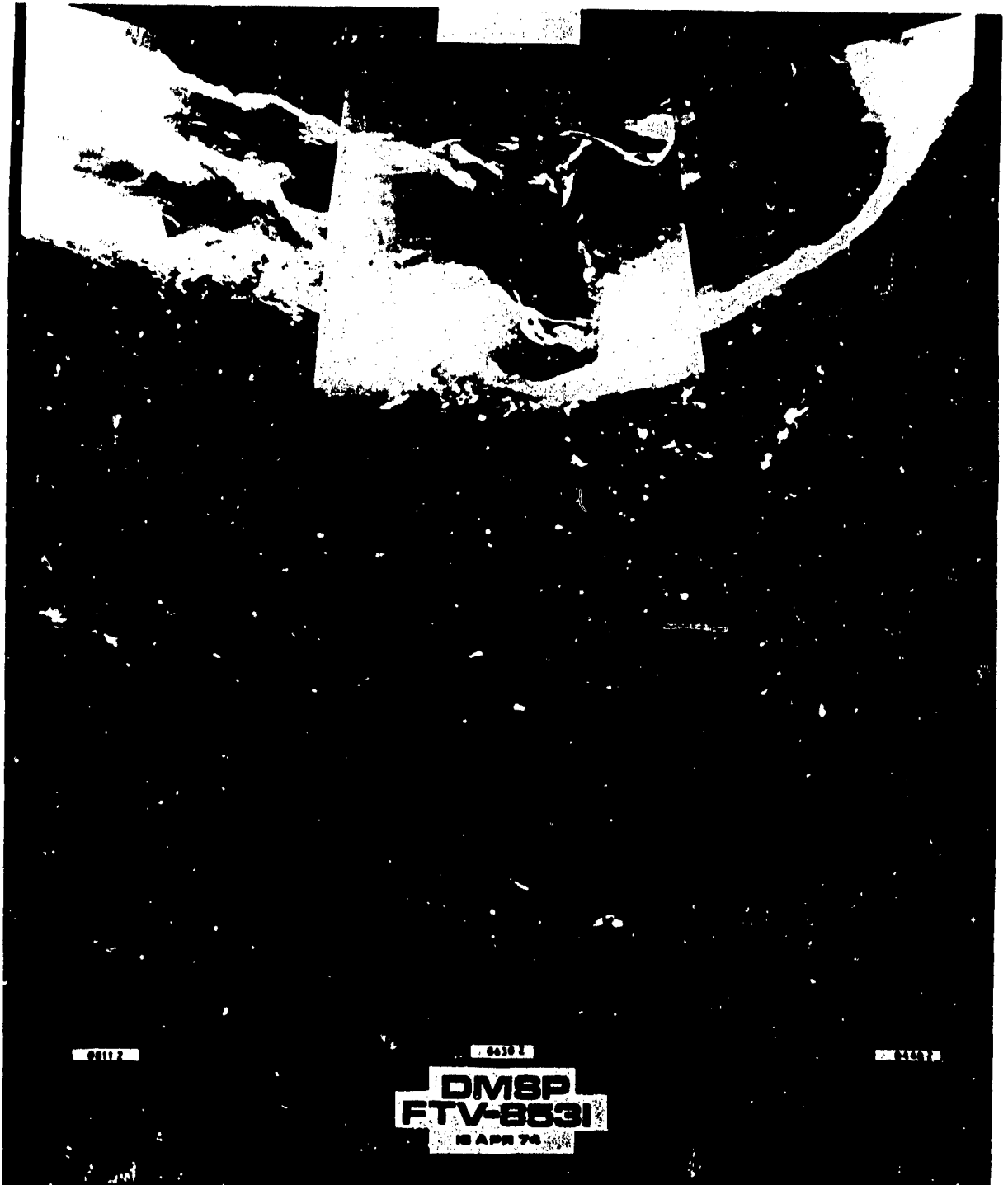


FIG. 3

Defense Meteorological Satellite Photograph at 3 times combined to illustrate aurora above North America on 18 April 1974.

MEAN SCINTILLATION INDEX ATS-3 137MHz NARSSARSSUAQ
1968-1974 Kp = 0-3

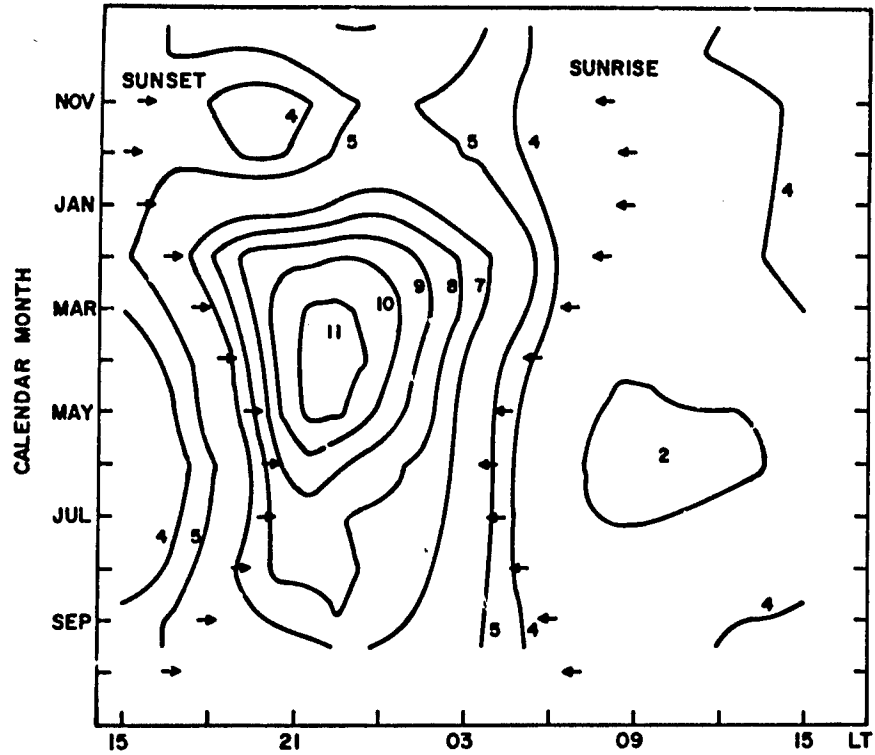


FIG. 4A

Seasonal character of scintillation excursions (dB) of Narssarssuaq, Greenland observations (63°A) under quiet magnetic conditions.

MEAN SCINTILLATION INDEX ATS-3 137MHz NARSSARSSUAQ
1968-1974 Kp = 4-9

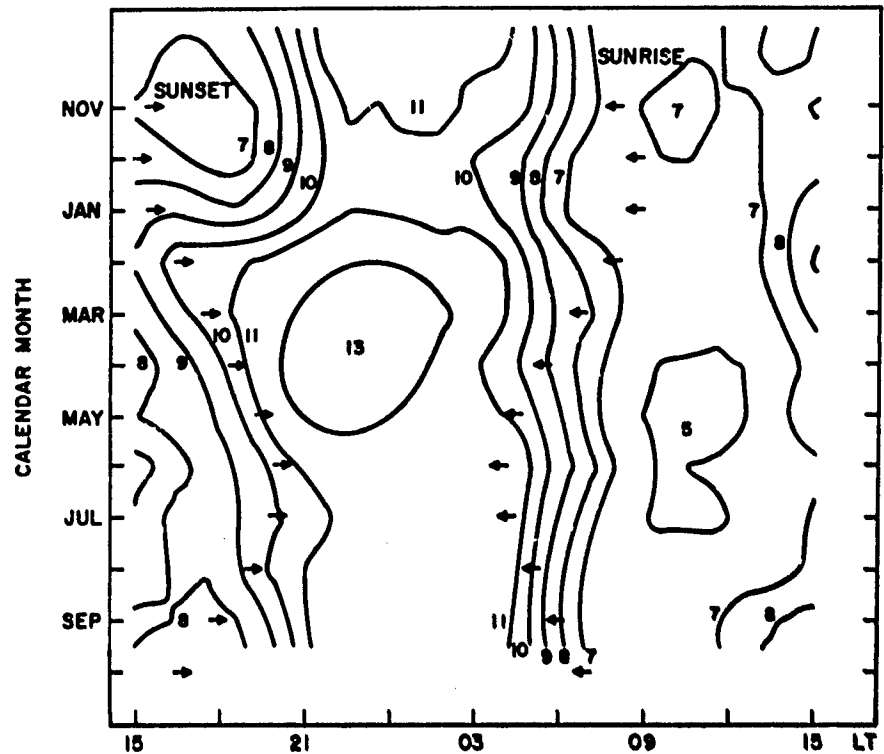
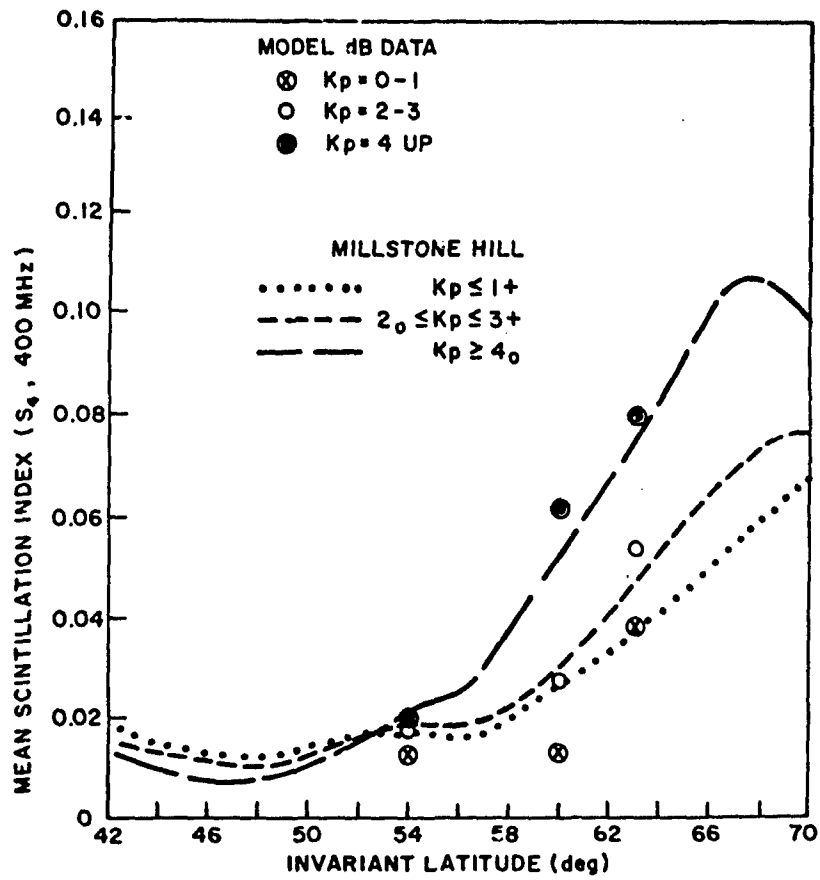


FIG. 4B

Seasonal character of scintillation excursions (dB) of Narssarssuaq, Greenland observations (63°A) under disturbed magnetic conditions.



MEAN SCINTILLATION INDEX FOR DIFFERENT LEVELS OF MAGNETIC ACTIVITY (FROM EVANS' MILLSTONE HILL OBSERVATIONS)

FIG. 5 Mean scintillation level over a range of invariant latitudes for different levels of magnetic activity. (From Evan's Millstone Hill observations)

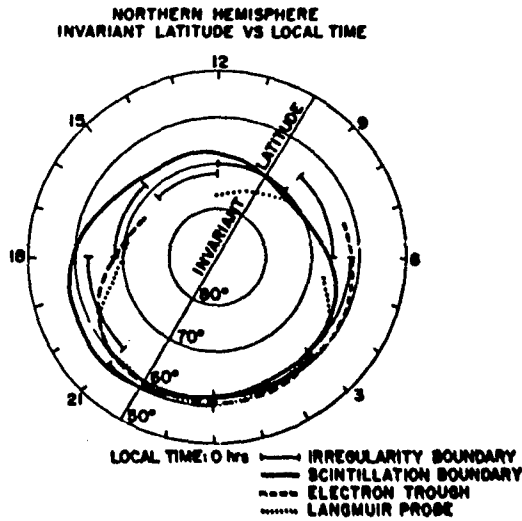


FIG. 6 Comparison of equatorward boundary from ISIS-1 data with other boundaries: Scintillation boundary - Aarons, Kp=1; Electron trough - Muldrew, Kp=2; Langmuir Probe - Dyson, Kp ≤ 3+.

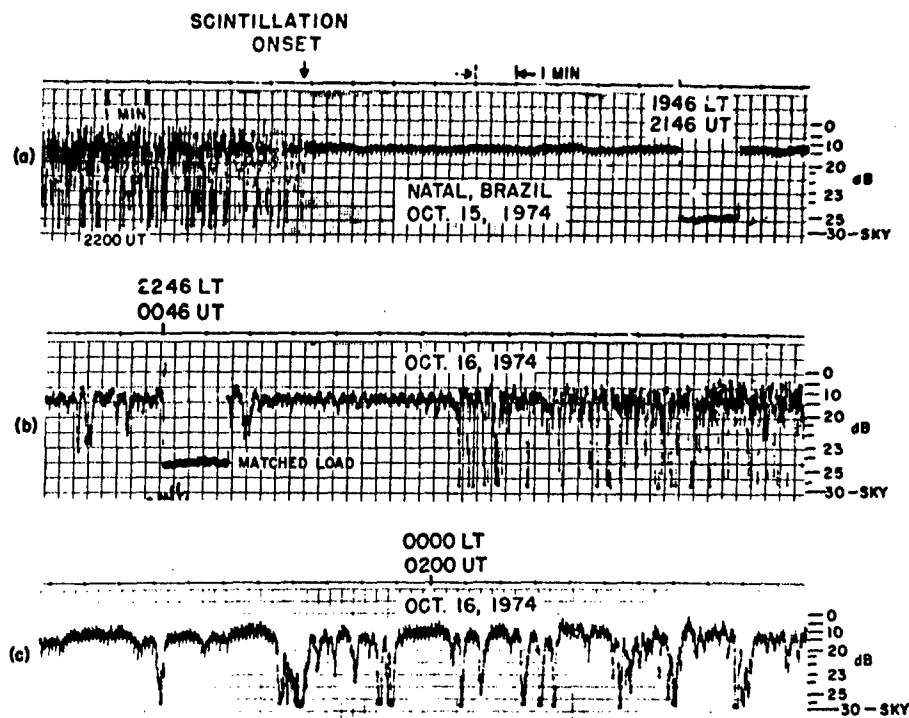
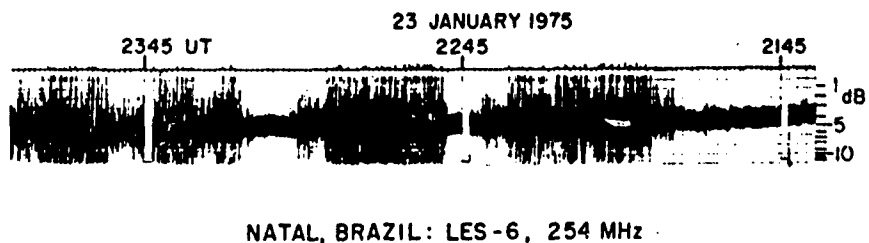


FIG. 7(a,b,c) LES-6 observations recorded at Natal, Brazil on Oct. 15-16, 1974, showing scintillation onset and cessation.



NATAL, BRAZIL: LES-6, 254 MHz

FIG. 8A Observations of LES-6 recorded at Natal, Brazil on Jan. 23, 1975, showing scintillation starting and stopping several times as the irregularity patch moves through the propagation path.

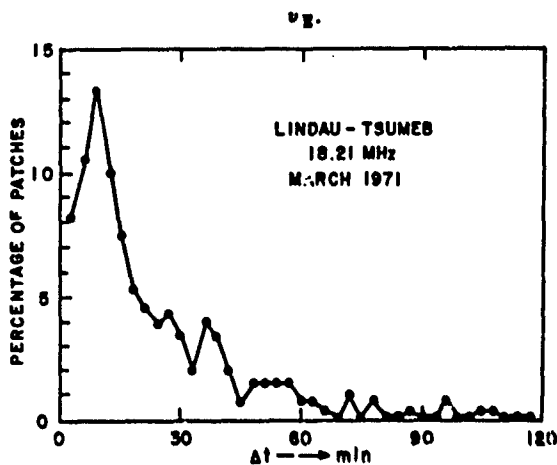


FIG. 8B Lifetimes of irregularity patches measured in transequatorial studies using HF transmissions (Rottger, 1973).

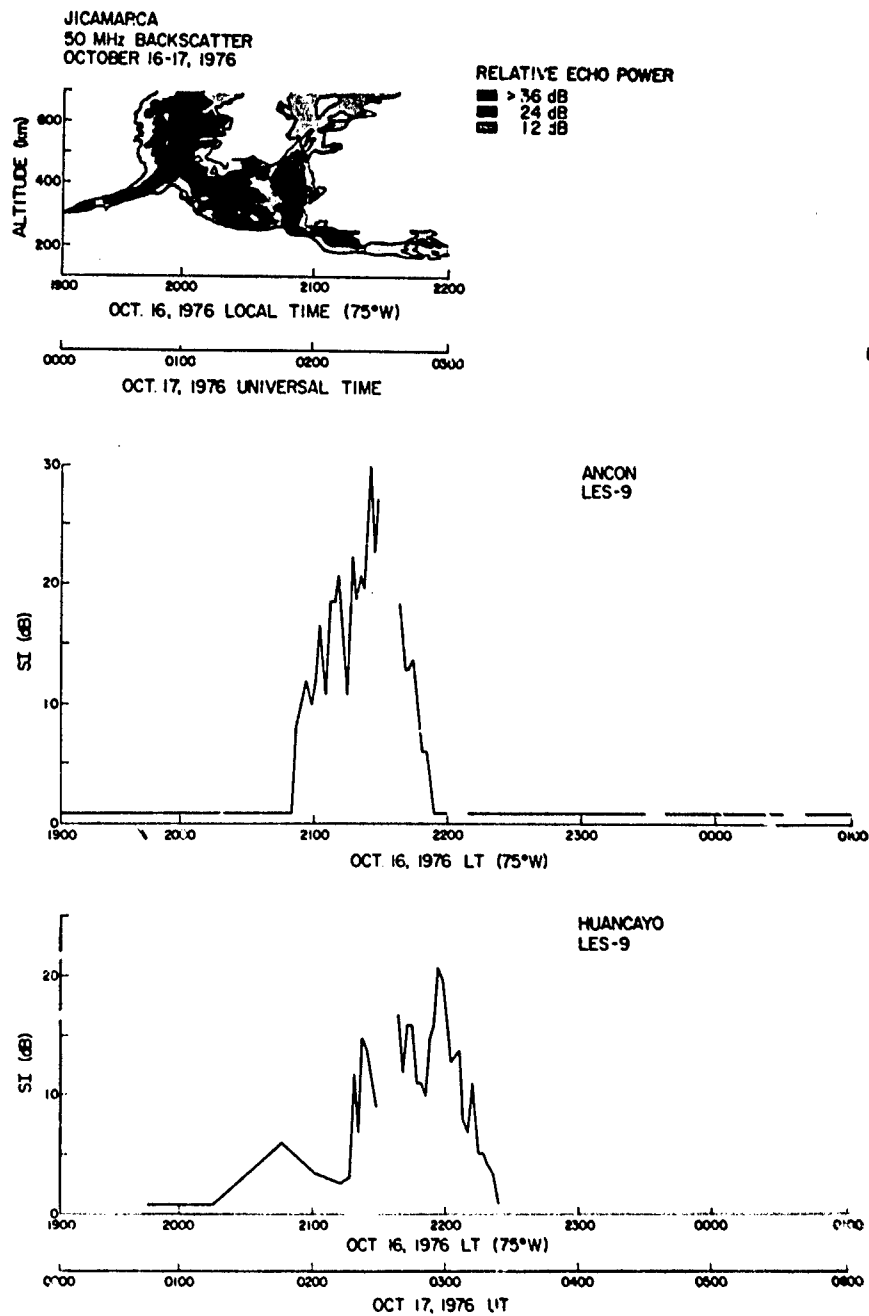


FIG. 9

Backscatter and scintillation data showing the relation of a "plume" to abrupt scintillation onset at 2 observatories, Ancon and Huancayo, Peru.

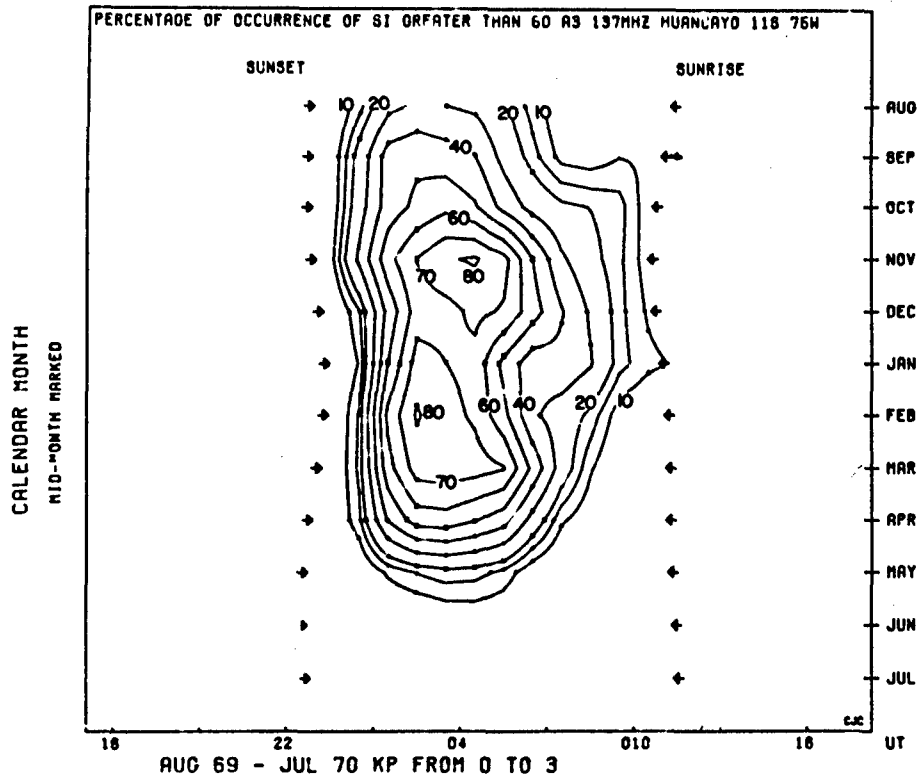


FIG. 11A

Seasonal character of scintillation observations from Huancayo, Peru during solar maximum period.

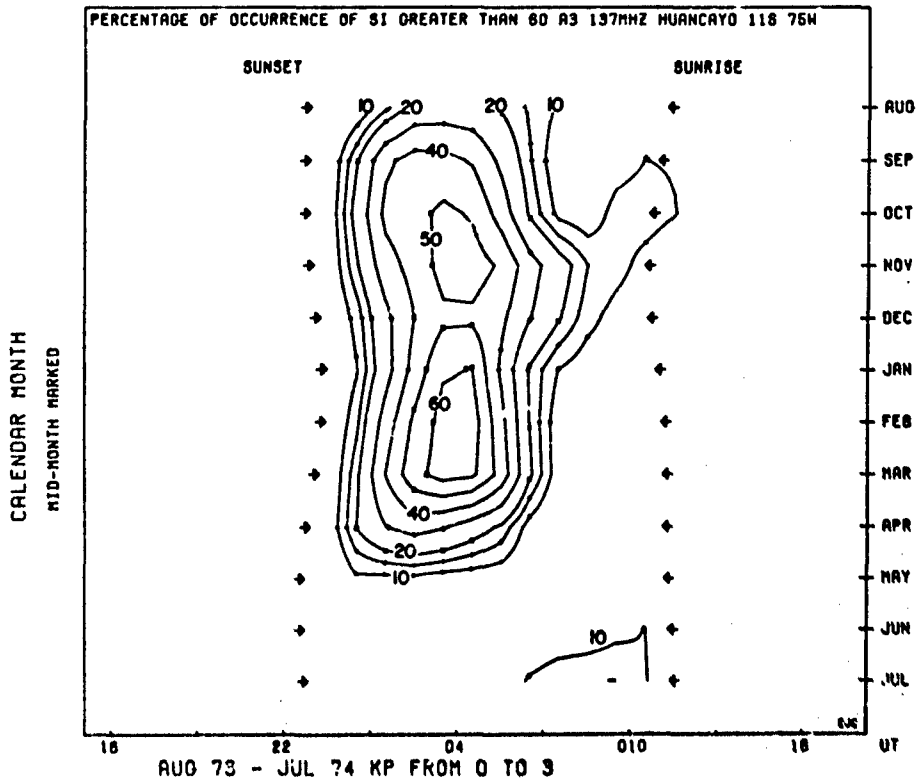


FIG. 11B

Seasonal character of scintillation observations from Huancayo, Peru during solar minimum period.

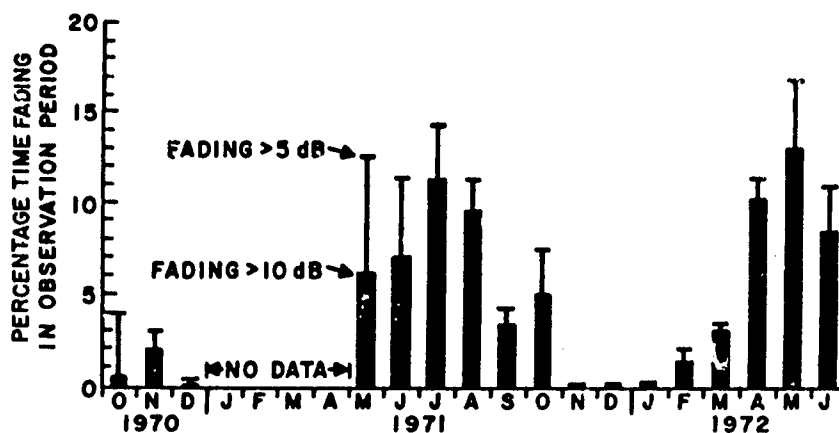


FIG. 12 Fading on 254 MHz as observed at Kwajalein. Maximum scintillation occurs from April to October.

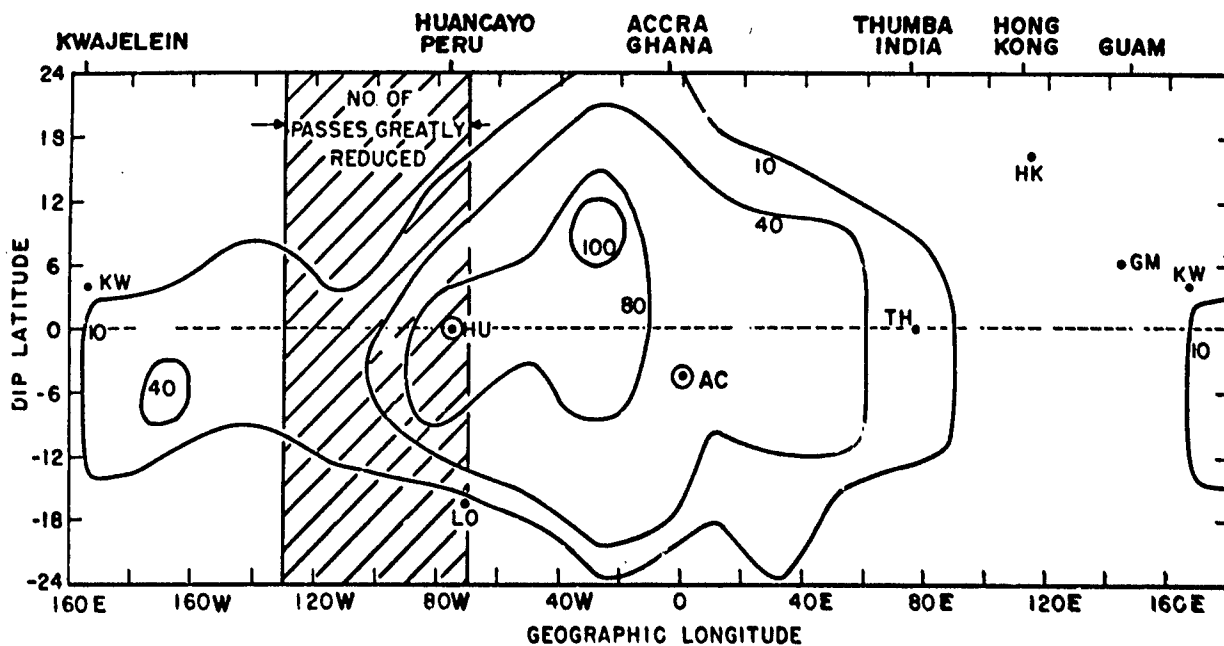


FIG. 13 Percentage occurrence of scintillations ≥ 4.5 dB at 140 MHz (1900-2300 LMT, Nov.-Dec., 1969, 1970) $A_p \leq 12$ over a wide longitudinal swath using scintillation data and Ogo-6 observations.

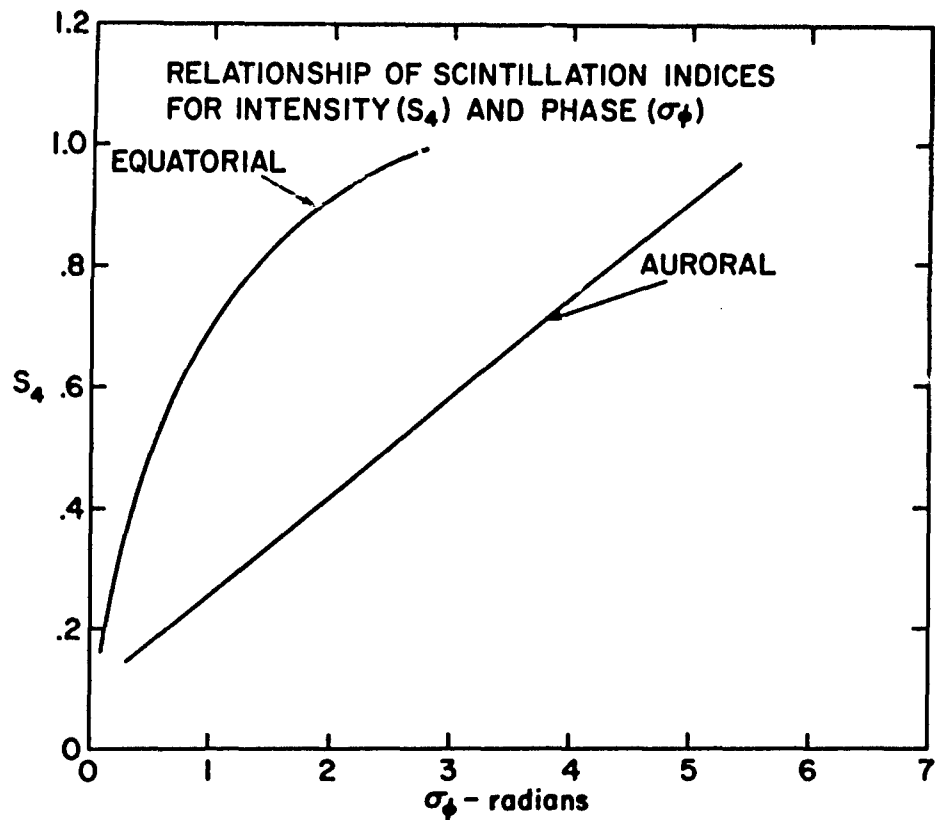


FIG. 14

Graph of correction factors for Sagamore Hill under assumption of elliptical column irregularity model.

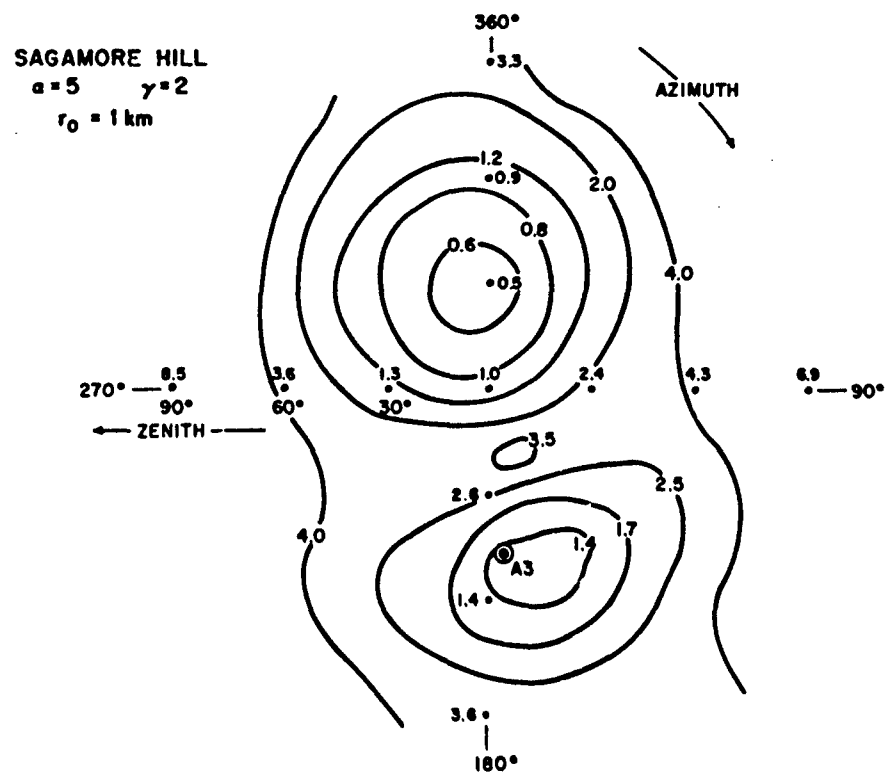


FIG. 15

Scatter diagram of scintillation indices for intensity (S_4) and phase (σ_ϕ) for 43 doubly detrended VHF data segments ranging in length from 20 to 80 sec. Equatorial data from Ancon and Kwajalein and high latitude data from Poker Flat and SRI.

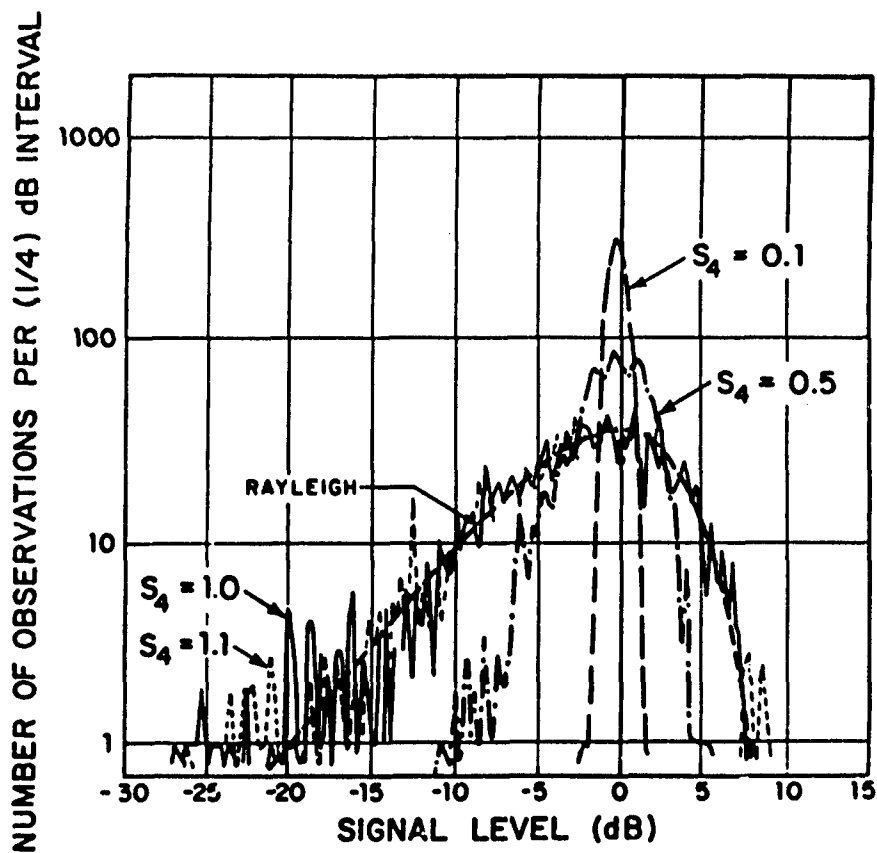


FIG. 16

Empirical amplitude probability density functions. Data obtained from Millstone Hill Radar Facility (Crane, 1974).

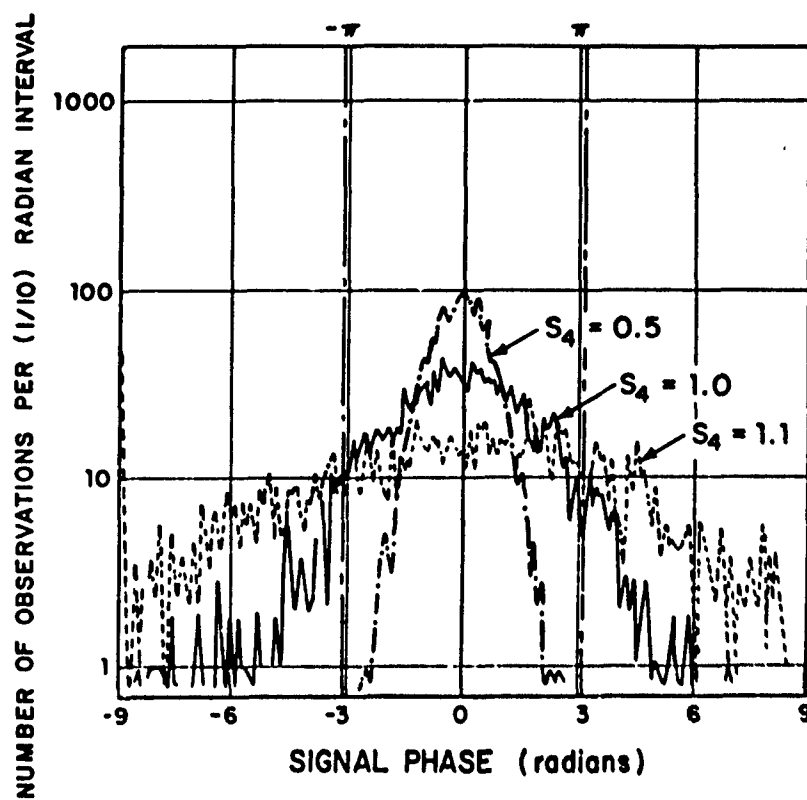


FIG. 17

Empirical phase probability density functions. Data obtained from Millstone Hill Radar Facility (Crane, 1974).

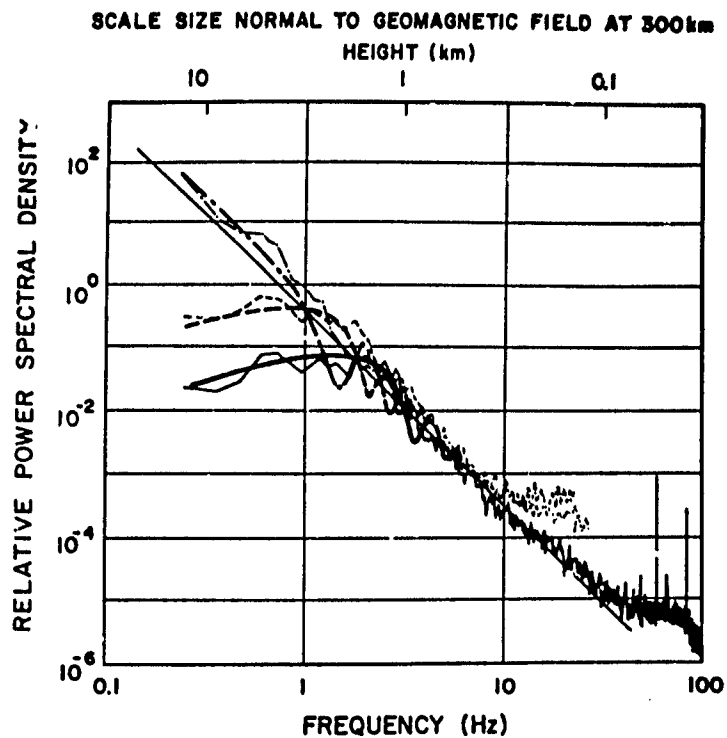


FIG. 18

Power spectral density estimates for low orbiting satellite at 150 and 400 MHz: — 400 MHz log amplitude, --- 150 MHz log amplitude, -.- 150-400 MHz differential phase. Light lines for experimental data, heavy lines for theoretical estimates. Millstone Hill Radar Facility, 29 June 1971, 0151 UT, Object 2965.

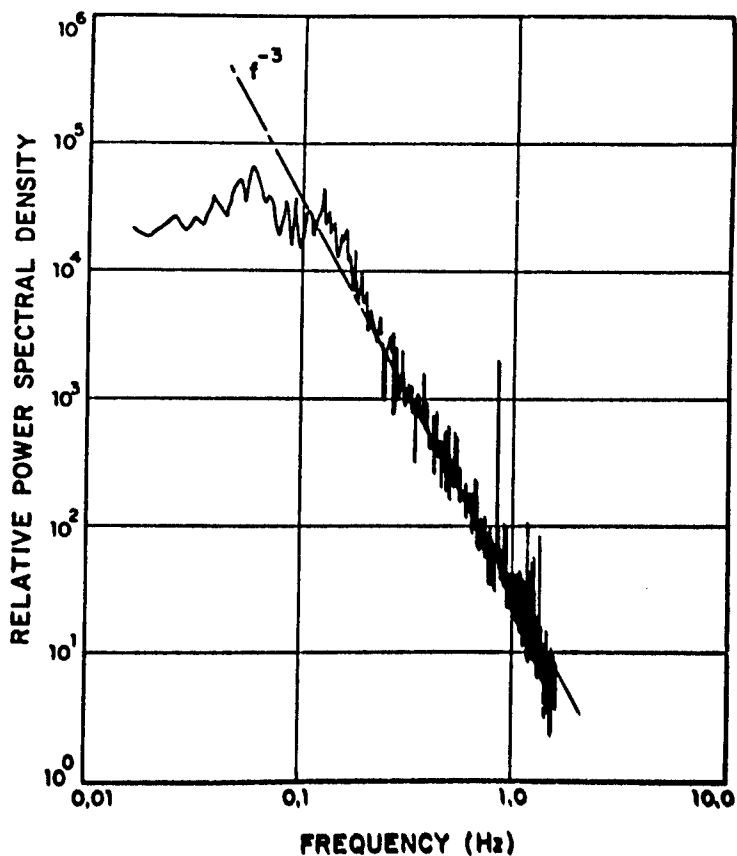


FIG. 19

Power spectral density estimates for a geostationary satellite at 3.95 GHz. Hong Kong Earth Station, 3 October 1972, 2100 LT, Intelsat IV.

SPACED RECEIVER STUDIES ANCON, PERU

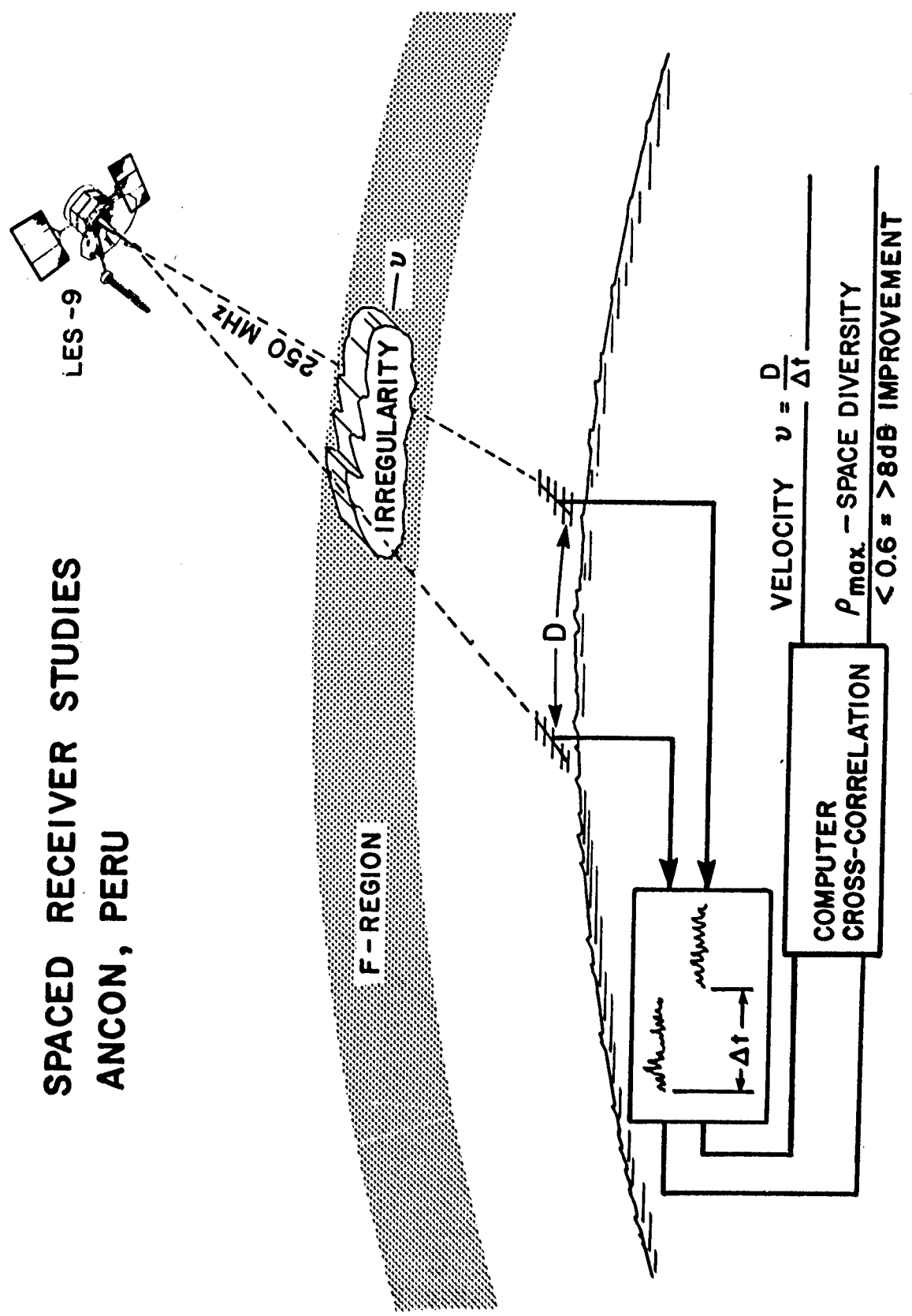


FIG. 20 Experimental set-up and illustrative material for measuring space diversity.

SCINTILLATION AND FADE DURATION ANALYSIS

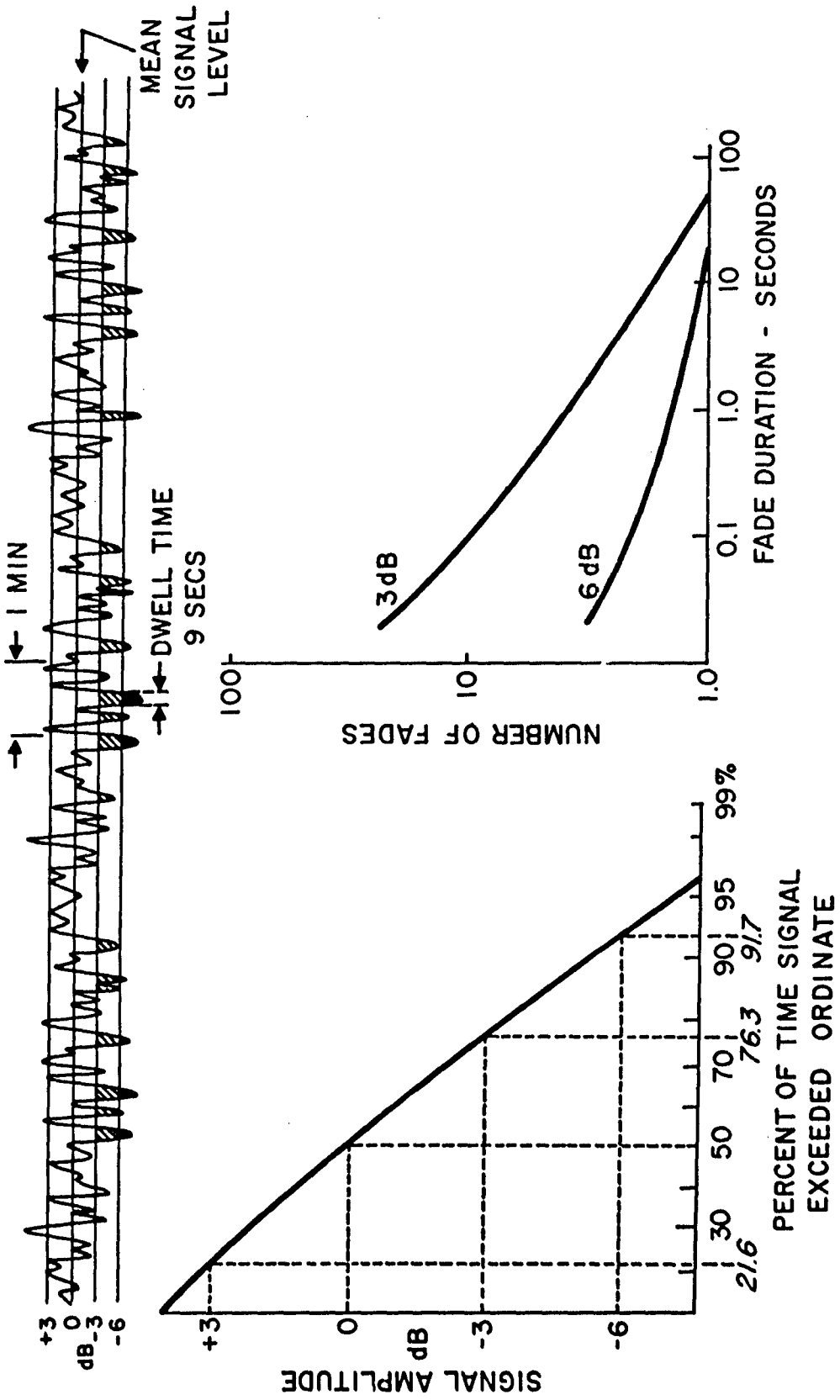


FIG. 21 Tracing of 15 min. data sample with analysis of percent of time signal is below certain levels and fade duration.

ARTIFICIAL MODIFICATION OF THE IONOSPHERE

Kenneth Davies
 Space Environment Laboratory
 NOAA Environmental Research Laboratories
 Boulder, Colorado 80302, U.S.A.

1. RADIO HEATING OF THE IONOSPHERE

1.1 The Luxemburg effect

The earliest indication that man could change the ionosphere occurred in 1933 when Tellegen (1973) reported that the signals received in Holland from the Swiss radio station at Beromuster (650 kHz) appeared to be modulated with signals from the powerful station at Luxemburg (252 kHz, 200 kW). The large frequency difference between the two carriers ruled out any possibility that the interaction was equipmental. It was found that this phenomenon, called cross-modulation, was quite common when the unwanted, or disturbing, station was located near the transmission path of the wanted station to the receiver.

The cause of cross-modulation, given by Bailey and Martyn (1934), is as follows: the electric field of the disturbing wave imparts energy to the D region electrons. This energy is converted into heat by electron-neutral collisions thus raising the electron temperature and, hence, the electron collision frequency ν . When the angular frequency of the wanted wave is much greater than the collision frequency the absorption of the wanted wave is proportional to ν and, hence, it varies with the electron temperature which, in turn, varies with the modulation of the disturbing signal. At the peaks of the disturbing wave the absorption of the unwanted signal is maximum and vice versa. The theory of the Luxemburg effect has been considered by Bailey and Martyn (1934), Ratcliffe (1959, Chapter 4; 1970, Chapter 8), Ratcliffe and Shaw (1948) and by Kelso (1964, section 5.10). The Luxemburg effect results in a form of interference between two stations.

1.2 Electron heating and cooling

Let us consider briefly the simple theory of electron heating. On the average, an electron is gaining energy u from the disturbing wave and losing some energy via electron-neutral collisions. The net rate of gain of electron energy

$$\frac{du}{dt} = \nu(u) (\epsilon(u) - g(u)(u - u_g)) \quad (1)$$

where $\epsilon(u)$ is the average energy gained between successive collisions and $g(u)$ is the fraction of excess electron energy lost per collision. The loss term in equation (1) is based on laboratory experiments which show that, for electrons in nitrogen and for small excess energies, the mean loss of energy per collision is proportional to the excess of electron energy over the thermal gas value u_g . As indicated in equation (1) the proportionality factor is itself a function of electron energy. The laboratory measurements together with theoretical calculations (see Thrane, 1966) indicate that g has a value around 4×10^{-3} which is much greater than the value of 7.8×10^{-5} for elastic collisions in nitrogen. This difference is due to the fact that electron cooling proceeds via rotational excitation of N_2 molecules for which

$$g = 20 T_g^{-3/2} \quad (2)$$

In the D region $T_g = 200^\circ\text{K}$.

To determine the rate of energy gain we determine the power absorbed by a cylinder of unit cross section and height dh from a wave of power flux P (see Davies, 1969). The power absorption coefficient is twice that of the amplitude absorption coefficient κ (since $P \propto A^2$). Therefore, the power absorbed is $2\kappa Pdh$ which equals the power gained by Ndh electrons so that

$$\epsilon(u) = \frac{2\kappa(u)P}{\nu(u)N} \quad (3)$$

where N is the electron density and $\kappa(u)$ depends on u via $\nu(u)$. For small constant heating powers ϵ is almost independent of u , i.e. $\kappa = \kappa(u_0)$, $\nu = \nu(u_0)$, and the increase in electron energy is given by:

$$u(t) = \frac{\epsilon(u_0)}{g(u_0)} (1 - \exp(-g(u_0)\nu(u_0)t)) \quad (4)$$

The variation of $u(t)$ is shown in Figure 1. If the disturbing wave is shut off (square wave) the electron energy decays exponentially with a relaxation time $\tau(u_0)$ where

$$u - u_0 = (u' - u_0) \exp\left[-\frac{t - t'}{\tau(u_0)}\right] \quad (5)$$

where u' is the value of u at the instant (t') the power is cut off and

$$\tau(u_0) = \frac{1}{g(u_0)v(u_0)} \quad (6)$$

Since τ is proportional to $1/v$ it is small in the lower parts of the D region, where v is large, and increases with height. Thus the response of the ionosphere, at different heights, to a pulse of disturbing wave is somewhat like that sketched in Figure 2.

The exact dependence of $g(u)$ and $v(u)$ on electron energy u has not been established. For small excess energies the following formulas are thought to hold:

$$v(u) \propto u \quad (7)$$

$$g(u) = 3 \times 10^{-3} \frac{300}{T_e} \quad (8)$$

Let us consider briefly the meaning of collision frequency which plays such an important part in the absorption of radio signals. In the theory of absorption (e.g., Ratcliffe, 1959, Chapter 5) it is assumed that any elastic collision between an electron and a molecule completely destroys the ordered momentum of the electron. In the D region the electron to neutral number density is less than 10^{-7} so that electron-neutral collisions only need be considered. On the basis of simple ballistic theory the mean collision frequency ν should be proportional to the square root of the electron energy u , i.e. $\nu = \sigma V n = \sigma \sqrt{u} n$ where n is the neutral number density, V is the mean speed and σ the electron cross section. Encounters between charged and neutral particles involve coulomb (electrical) interactions (see Davies, 1969, Chapter 11) so that the effective cross section is a function of electron energy. In nitrogen, near thermal energies, the collision cross section is found to be proportional to electron velocity so that $\nu \propto nu$. Phelps and Pack (1961) give

$$\nu = 1.12 \times 10^{-13} u n(N_2). \quad (9)$$

where u is in electron volts. In air, Phelps and Pack (1966) give

$$\nu = (1.12 \times 10^{-13} n(N_2) + 7 \times 10^{-14} n(O_2)) u \text{ sec}^{-1} \quad (10)$$

For air this reduces to

$$\nu_M = 6.34 \times 10^5 p \text{ sec}^{-1} \quad (11)$$

where p is the atmospheric pressure in Newtons m^{-2} and ν_M is the collision frequency of an electron gas all with energy kT_e , with k = Boltzmann Constant.

In the usual radio propagation theory, e.g. the Appleton equation, the mean collision frequency ν_A is related to ν_M for the cases of $\nu \ll \omega$, and $\nu \gg \omega$ by the following:

$$\begin{aligned} \nu \ll \omega, & \quad \nu_A = 2.5\nu_M & (a) \\ \nu \gg \omega, & \quad \nu_A = 1.5\nu_M & (b) \end{aligned} \quad (12)$$

Some experimental data on the height variation of ν_M are given in Figure 3 (Thrane, 1966). When the propagation is quasi-longitudinal the absorption coefficient κ (with $\nu = \omega$) is given by

$$\kappa = 1.327 \times 10^{-5} \frac{N}{\nu_M} \zeta_{5/2} \left(2\pi \frac{f \pm f_L}{\nu_M} \right) \quad (13)$$

where the + and - signs refer to the ordinary and extraordinary waves respectively. $\zeta_{5/2}$ is a semi-conductor integral (see Sen and Wyller, 1960; Davies, 1969) and f_L is the gyrofrequency for the longitudinal component of the geomagnetic field.

1.3 Cross Modulation

Cross-modulation (Luxemburg Effect) has been used to study the electron density distribution in the D region by measuring the interaction of two pulsed radio signals. The method was first used by Fejer (1970; 1971) and it has been employed by others to determine both the electron density and collision frequency profiles. Because the collision frequency affects both the real (phase μ) and imaginary (amplitude κ) parts of the refractive index, heating the D region electrons will produce both phase and amplitude modulation. The phase advance $\Delta\phi$ is related to the change $\Delta\mu$ in real part of the refractive index by

$$\Delta\phi = \frac{\omega}{c} \int \Delta\mu \, ds = \frac{\omega}{c} \int \left(\frac{\partial\mu}{\partial\nu} \right)_N \Delta\nu \, ds \quad (14)$$

and the corresponding change ΔL in absorption

$$\Delta L = \int \Delta\kappa \, ds = \int \left(\frac{\partial\kappa}{\partial\nu} \right)_N \Delta\nu \, ds \quad (15)$$

where ds is an element of the ray path and $(\partial\mu/\partial\nu)$ and $(\partial\kappa/\partial\nu)$ can be calculated from theory. In this treatment it is assumed that the electron density is not affected by the heating. Typically, observations show $\Delta L = 0.4$ dB and the phase interaction $\Delta\phi = 10^{-2}$ radian. The phase interaction technique was pioneered by Weisbrod, Lee and Ferraro (1964).

An experimental arrangement is shown in Figure 4. A "wanted" transmitter T_1 emits a pulsed high frequency radio wave on a frequency f_1 and pulse repetition frequency p_1 . This wave is reflected vertically, from E- or F-layers; a "disturbing" wave with frequency f_2 and repetition rate p_2 ($= p_1/2$) is emitted from T_2 . The transmitters are timed so that every second wanted pulse meets a disturbing pulse at a height h_0 in the D region. Thus, alternate wanted pulses travel down through a layer whose properties have just been changed by the disturbing pulse. The pulse repetition frequency p_1 is sufficiently low that the D-region electrons have time to cool between pulses ($\approx 10^{-3}$ sec). The phase and amplitude of the received pulses are modulated with the frequency p_2 . The detailed theory of wave interaction is given by Thrane (1966), Weisbrod et al. (1964), Smith et al. (1965) together with the means of deducing electron density and collision frequency profiles. Some sample profiles obtained by this technique are shown in Figures 5 and 6.

1.4 Gyrointeraction

To obtain maximum wave interaction one requirement is that there be maximum absorption of the disturbing wave. One way of accomplishing this is to polarize the disturbing wave so that, on entry into the ionosphere, all the incident power goes into the extraordinary wave whose absorption coefficient is given by

$$\kappa = 4.6 \times 10^{-2} \frac{N\nu(u)}{(\omega - \omega_H)^2 + \nu^2(u)} \text{ dB/km} \quad (16)$$

This expression shows that the absorption of the disturbing wave is large when the wave frequency ω approaches the gyrofrequency ω_H ($= 2\pi f_H$). The interaction process is called gyrointeraction.

The variation with frequency of absorption coefficient κ_D of the disturbing wave for given values of N , ν and f_H (≈ 1.5 MHz) is shown in Figure 7. It would be expected that the total absorption would be greatest when $f_D = f_H$. In practice, this may not necessarily occur because near the gyrofrequency the power in the disturbing wave is absorbed low in the ionosphere where

$$\kappa_D \sim \frac{N}{\nu} \quad (17)$$

so that an increase of collision frequency may lead to a decrease in the absorption. Furthermore, if the collision frequency is greater than $2\pi(f_w - f_u)$, where f_w is the frequency of the wanted wave, the absorption coefficient of the wanted wave κ_w will also vary as $1/\nu$ and the absorption of the wanted wave in the presence of the disturbing wave may be less than it is in the absence of the disturbing wave. The full theory of gyrointeraction is complicated and will not be considered here (see Smith et al., 1965). It predicts that the absorption of the wanted wave will change with frequency of the disturbing wave with a double hump centered on the gyrofrequency, as sketched in Figure 7. Further discussion on gyrointeraction using high power waves is given by Smith and Loch (1974), by Kissick and Ferraro (1974) and Jones (1974).

1.5 Self-distortion

Self-distortion refers to the effect on a radio signal of its own heating of the ionosphere. The theory of self-distortion (sometimes called self-demodulation) is similar to that of wave interaction. The best treatment is a numerical (computer) solution in which the energy absorbed from the wave is calculated and used to determine the increase in electron energy and, hence, a modified electron collision frequency which is used to recalculate the absorption.

Numerical methods for calculating self-distortion, based on the above principle, have been given by Megill (1965) for the case of a nondeviating ionosphere in which the effects of the geomagnetic field are neglected. In Megill's method, it is assumed that the power P in the incident wave is modulated according to:

$$P(t) = P_0(1 - a \cos 2\pi f_m t)^2 \quad (18)$$

in which f_m is the modulation frequency. The amplitude modulation depth, M is given by

$$M = \frac{A_{\max} - A_{\min}}{A_{\max}} \quad (19)$$

In the absence of absorption

$$M = \frac{2a}{1+a} \quad (20)$$

Taking into account the energy dependences of the collision frequency ν and of g , together with the distribution of energy (e.g., Maxwellian), Megill has calculated: (1) the change in M due to nonlinear absorption, (2) the phase shift in the fundamental component of the modulation envelope (frequency = f_c) and (3) the second harmonic generated by the nonlinearity. When absorption occurs in a region in which the collision frequency is larger than the angular-wave frequency, the demodulation will be negative, i.e. the modulation will be enhanced. The percent demodulation is defined as $100(M_{in} - M_{out})/M_{in}$, where M_{in} and M_{out} represent the depths of modulation before and after absorption. The demodulation can be positive or negative depending on the assumed profiles of electron density and collision frequency and on the wave and modulation frequencies. Megill's (1965) opinion is that --"it is nearly impossible to make general statements concerning this effect, except to point out that the range can run as much as 16% demodulation, i.e. the emerging wave may be about 67% modulated, as compared with an ingoing 80%, to a negative demodulation of about 8%. Again it may be said that these effects are more extreme in a constant electron-density model than in the real atmosphere because there are competing effects entering at different altitudes."

An example (after Megill, 1965) of the effect of demodulation on amplitude and phase is given in Figure 8. The amplitude change is of the order of 5% (0.4 dB) and the phase advance is approximately 20° ($360^\circ \equiv$ full modulation cycle). Megill finds that, depending on the D-region electron-density model, the wave and modulation frequencies, the percent demodulation can vary between about -9 and 17, while the phase shift can amount to around 27° .

One consequence of self-demodulation is the adverse effect of increasing the effective power of radio transmitters. The higher the power, the greater is the ionospheric absorption and so the net effect is self-defeating. For example, Megill (1965) has shown that with a carrier frequency of 1 MHz and 80% modulation with frequency 1000 Hz, the propagation loss caused by self-demodulation is of the order of 10 dB (i.e., a factor of about 3).

1.6 F-region heating

1.6.1 The Platteville Experiment

In the electron heating experiments discussed above electromagnetic energy is converted into heat via electron-neutral collisions; this is sometimes called resistive heating. In these experiments, with the exception of gyrointeraction, the radio frequencies are removed from any resonant frequencies of the ionospheric plasma. In the high-power F-region heating experiments carried out in Platteville, Colorado (see Utlaut and Cohen, 1971; Utlaut, 1974, 1977) and in Arecibo, Puerto Rico (Gordon and Carlson, 1977) frequencies near foF2 have been used to excite plasma resonance oscillations and, hence, irregularities in the ionospheric plasma.

Let us first consider the experimental facility at Platteville, Colorado operated by the Institute for Telecommunications at Boulder, Colorado. The variable frequency (5 to 25 MHz) transmitter is capable of delivering about 2.0 megawatts to a large ring-array antenna (Figure 9), which provides a power-aperture product of about 10^6 megawatt-square meters. The antenna is designed to operate between frequency limits of 5 to 10 MHz approximately the diurnal range of the foF2. The width of the antenna beam is about 16° (between half-power points) at the middle of the frequency band. This antenna, which consists of crossed dipoles, can be excited to radiate right-handed or left-handed (with respect to the geomagnetic field) waves that generate extraordinary and ordinary waves respectively in the ionosphere. These waves have different propagation velocities and ray paths in the ionosphere; e.g., for waves incident normally on a flat ionosphere, the extraordinary ray is deflected toward the equator whereas the ordinary ray is deflected towards the nearer pole--see Figure 10. On a given frequency the ordinary wave is reflected at a higher height than is the extraordinary wave (see Davies, 1969, Chapter 7; Cohen and Whitehead, 1970). The consequence of this magnetoionic deviation (not simple refraction) is that the heated volume should be centered magnetically north (ordinary) or south (extraordinary) of the zenith. The geometry of the Platteville experiment is shown in Figure 11. The diagnostic ionosonde is located at Erie.

1.6.2 The Arecibo facility

The Arecibo facility (Gordon, Carlson and Showen, 1971) was originally constructed for radar-astronomy and radio astronomy by Cornell University. Its salient feature is a 305 m spherical antenna built over a limestone sink hole. For ionospheric modification studies, an appropriate high frequency log periodic feed was installed at the focal point of the spherical dish. This antenna (5 to 12 MHz range) is about 10° in angular halfwidth. The RF transmitter is identical to one of those used at Platteville and, together with the high gain of the antenna, produced an effective power output within

about 3 dB of that at Platteville (Utlaut, 1975). An important diagnostic tool at Arecibo is the incoherent scatter radar which detects radio energy scattered by many individual electrons (see Farley, 1970).

1.6.3 Deviative absorption

Let us consider briefly some differences between the nondeviative absorption of the radio signals in the D region discussed in the case of wave interaction and the deviative absorption in the case of F-region heating. The absorption per unit distance (κ) is given by

$$\kappa = 4.6 \times 10^{-2} \frac{1}{\mu} \frac{N\nu}{(\omega \pm \omega_H)^2 + \nu^2} \text{ dB/km} \quad (21)$$

where the symbolism is given in a companion lecture (Davies, 1978). Nondeviative absorption occurs when the refractive index $\mu = 1$ and $N\nu$ is large. On the other hand deviative absorption occurs when $\mu \rightarrow 0$, i.e. near reflection with vertical propagation. In the D region, the electron collisions are mostly with neutral molecules (ν_{en}) whereas in the F region, where the neutral number density is much smaller, the dominant collisions are with positive ions (ν_{ei}). The electron-ion collision dependence on electron temperature (T_e) (e.g., see Whitehead, 1970) is

$$\nu_{ei} = T_e^{-3/2} \quad (22)$$

so that an increase of electron temperature by radio heating should result in a decrease of absorption rather than an increase.

The heating and hydrodynamic expansion of the F layer caused by radio absorption occurs in several stages (see Meltz and LeLevier, 1970). During the first minute, thermal energy is imparted to the electron gas and the electron temperature is raised, field-aligned pressure gradients are established, and the plasma begins to expand along the geomagnetic field--see Figure 12. Plasma density changes are less than 1% during this initial phase and the incident wave field is essentially unperturbed. During the next several minutes, the plasma expands and the F region electron density decreases slowly ($\approx 14\%$ at Arecibo (Gordon and Carlson, 1974) and 7% at Platteville (Utlaut and Violette, 1972)) while the electron and ion temperatures approach a steady state. The next stage, which occurs from about 3 to about 5 min after onset of heating, is very complicated and is characterized by self-focusing and, possibly, defocusing of the incident radio signals caused by changes in refractive index.

Radio wave heating near the reflection level (with vertical propagation) is enhanced by the fact that as the refractive index goes to zero so does the magnetic field of the wave. Thus, at the (vertical) reflection height, the radio wave is an electrostatic wave rather than an electromagnetic wave. Furthermore, the ordinary-wave electric field is linear and parallel to the geomagnetic field. On the other hand the electric field of the extraordinary wave at reflection is circularly polarized and is perpendicular to the geomagnetic field. The local electric field must be obtained from the wave equations either by exact "full-wave" solution or, approximately, from the WKB method. The latter is poor near reflection, but may be sufficiently accurate on frequencies slightly above the penetration frequency.

1.6.4 Electron temperature

Electron cooling is thought to be via three main processes: (1) elastic collisions with ions, (2) fine-structure transitions in the $O(^1P)$ ground state of atomic oxygen, and (3) the rotational excitation of molecular nitrogen. Near and above the F peak the dominant loss is by elastic collisions with ions but below 280 km the major collision loss is through fine-structure transitions. Typical cooling times are about 10 to 30 sec. Thomson (1970) has calculated that the maximum temperature change, near the center of the Platteville beam, is about 470°K by day and 550°K at night.

1.6.5 Wide band attenuation (WBA)

Many unanticipated phenomena have been observed with the Platteville heater and new understandings have been gained in the field of plasma physics, because of the ability to carry out experiments on the ionosphere. One phenomenon, which occurs during times other than ± 4 h from local noon, is called wide band attenuation and it is illustrated in the ionograms of Figure 13. It is observed when ordinary-wave heating is used. The WBA results in the disappearance of the diagnostic o-wave at all frequencies above, and perhaps a few tens of kilohertz below, the heater frequency. When WBA occurs, its onset is within a few seconds of heater turnon and it disappears within seconds of turnoff. The cause of the attenuation, which exceeds 10 dB, is not clear (see Utlaut, 1975).

Experiments, in which the heater polarization was switched rapidly between ordinary and extraordinary (Utlaut, 1974), showed that WBA appeared and disappeared quickly as the heating wave was changed to and from the ordinary polarization. This indicates that the responsible mechanism must have a fast response time (≈ 1 min), i.e. it cannot be simply heating and cooling. Utlaut (1974) points out that parametric instabilities (Perkins and Kaw, 1971; DuBois and Goldman, 1965; Weinstock, 1974) develop and quench

rapidly, probably within a few milliseconds, and suggests that they are a more likely cause of WBA than is diffraction or scattering of the o-wave diagnostic wave by ionospheric irregularities.

1.6.6 Airglow

Airglow, from excited oxygen atoms, at 6300 Å has been observed particularly when the ordinary wave is used for heating. An example is shown in Figure 14 in which the heater frequency is kept fixed at 5.3 MHz and the foF2 (> 5.3 MHz) is undergoing its diurnal decay. The intensity modulation is induced by cycling the ordinary heating-wave on and off at 6-min intervals, e.g. see Utlaut and Cohen (1971). This enhancement of the normal airglow indicates the existence of collisional excitation of atomic oxygen by electrons. This process requires significant numbers of electrons with energies greater than 2 eV. For a Maxwellian distribution of energies this requires electron temperatures of around 2000°K. The more likely explanation involves a nonthermal energy distribution having high-velocity electrons produced by excitation of a plasma instability.

At Arecibo red-line enhancement and suppression have been observed. Suppression of roughly 1% is observed with x-wave heating, implying a temperature-dependent reduction in the recombination rate. O-wave heating results in enhancement--see Gordon and Carlson (1974).

1.6.7 High-power heating of the D region

Measurements of the cross-modulation imposed on signals with frequencies as low as 20 kHz, that traverse the heated D region over Platteville, have been made by Jones et al. (1972) and Jones (1974). The magnitude of the cross-modulation, observed on WWVB (60 kHz), was much greater (= 30%) with extraordinary wave heating than with the ordinary wave (= 10%). This is consistent with modern nonlinear heating theory (Utlaut, 1974a).

1.7 Field aligned irregularities

1.7.1 Spread F

The ionosonde used to diagnose the Platteville modifications was located at Erie--see Figure 11--about 26 km west of Platteville but well under the heated region. The first and most consistent phenomenon observed after the Platteville transmitter was turned on was the production of spread F. Spread F describes the appearance of diffuse traces on ionograms as seen in Figure 13. Spread F occurs frequently in certain geographical locations but rarely over Colorado by day. Artificial spread F, however, is produced at any time of day, with heater frequencies ranging from at least 0.5 to 1.05 of the critical frequency and with either ordinary or extraordinary heating waves. The diffuse echoes begin on ionograms within seconds of heater turnon and they persist for varying durations, after turnoff, depending on time of day. In the daytime, it may persist for 5 to 10 min in the upper (F2) region, but for about one minute in the F1 region. After sunset, it may persist for 10 to 20 min and when generated after midnight it has been seen for several hours until sunrise.

A second phenomenon observed, when the heater is on for 10 min or more, is a satellite trace paralleling the predisturbed echo trace on the ionogram--see Figure 13c. The trace tends to move, with time, away from the original trace as the heating continues and, after the heating ceases, to move back and eventually merge with the original trace. This sequence of events is evidence of the creation of a major bulge in the isoionic electron density contours as heated electrons are redistributed along the geomagnetic field (Utlaut et al., 1970; Utlaut, 1974).

The Boulder and Arecibo ionograms, during heating, exhibit the same general characteristics, although details vary possibly because of differences in field-line geometry and incident powers (see Gordon and Carlson, 1974).

1.7.2 Sky maps

A large circular phased array for a high-frequency radar was located about 11 km east of Platteville and it has been used by Allen, Thome and Rao (1974) to observe the angular spectrum of spread-F echoes from a modified ionosphere. The angular spectrum has a systematic dependence on sounding frequency, range, Doppler shift and heater power. The results of ray tracing simulation support the view that the spread-F is caused by magnetic field-aligned ducts within the heated volume. A sequence of Doppler spectrum and sky map, shown in Figure 15, illustrate the dynamic behavior. The first map was obtained prior to heating and shows a single echo a few degrees from the zenith; this shows the ionosphere to be smooth and slightly tilted. After 16 sec of heating, several echoes appear along with a broadening spectrum. This continues to develop with prolonged heating until a stable situation is attained after 3 min. The movement of the center of the echo pattern (towards the south and west) is caused by a traveling ionospheric disturbance.

1.7.3 Field aligned scatter

Artificial spread-F (ASF) is believed to be caused by field-aligned scatter (FAS) from irregularities embedded in the heated volume. A model of these Platteville heater-induced irregularities is shown in Figure 16. These irregularities scatter radio waves on frequencies as high as 50 MHz (Thome and Blood, 1974; Fialer, 1974). In the case of

FAS the dominant returns are located where the radar beam is orthogonal to the earth's magnetic field. The presence of FAS has been confirmed by Thome and Blood (1974), Fialer (1974), Minkoff et al. (1974), Minkoff and Weissman (1977) with a radar located at the White Sands Missile Range and by Carpenter (1974) using a VHF (157 MHz) and UHF (435 MHz) system between Stanford, California and White Sands.

1.7.4 Plasma line scatter

In FAS the frequency of the received echo is essentially the same as that transmitted. Another weaker type of scatter has been observed which results in received echoes with two frequencies one of which is shifted up and the other down from the emitted frequency by an amount nearly equal to the frequency used for heating the ionosphere. This type of scatter is called plasma line scatter (PLS). This observation led plasma theorists to the discovery of a new mode of plasma reaction in which beating between two high-frequency waves, the heating wave and an electrostatic plasma wave, generates a low frequency plasma wave which propagates transverse to the magnetic field and produces small scale (≈ 3 meter) field-aligned density structures (Utlaut and Violette, 1974; Perkins, 1974). The differences between FAS and PLS are discussed by Utlaut (1974) who points out that with FAS the strongest returns occur in the perpendicular configuration whereas with PLS the maximum backscattered signal comes from the region of maximum heating at which the ionospheric plasma frequency equals the heater frequency.

1.7.5 Ion-acoustic scatter

A third type of scatter is thought to result from Bragg-type scattering from ion-acoustic waves which propagate nearly along the geomagnetic field--called ion-acoustic scattering (IAS). The received signal differs only by a few kilohertz (i.e., ion-acoustic frequencies) from the transmitter frequency--see Utlaut (1975).

1.7.6 E region scatter

So far we have discussed F region effects close to the heated region. Effects in the E region (100-120 km) have been reported both from Platteville and Arecibo. Utlaut and Violette (1972) report short-lived E echoes on ionograms on frequencies above foF2. The echoes appear to be from partially reflecting sporadic E. Similar sporadic E echoes have been observed at Arecibo (Gordon and Carlson, 1974). Wright (1975) has attributed Es echoes to stimulated particle precipitation.

1.8 The Satellite Power Station

A suggestion under consideration by NASA is to place in synchronous orbit a large ($\approx 70 \text{ km}^2$) solar-power collector and to transmit the power to earth by microwaves ($f \approx 2.5 \text{ GHz}$). Microwave power transmission is a three-step process consisting of: (1) generation of microwave power from DC, (2) the formation of a highly collimated beam of microwaves for transmitting the power, and (3) the capture and rectification of power on the earth (Brown, 1977; Glaser, 1977). The technology exists for an efficient, reliable and safe system with power handling capability of 5 to 10 gigawatts.

The immediate concern regards the effects on the ionosphere of the very high power fluxes of about 100 Wm^{-2} which are very much greater than the Platteville flux of a few tens of microwatts per square meter although less than the total insolation of $1,388 \text{ Wm}^{-2}$. Although the power flux of the solar-satellite beam is very much greater than that of the Platteville heater the power absorbed in the ionosphere is not nearly as much because of the inverse frequency law of radio absorption. Nevertheless, a great deal of power is available for heating the lower ionosphere where most of the resistive heating takes place.

This subject has been considered recently by Perkins and Roble (1978) who calculate the effect of resistive heating by radio waves on ionospheric temperatures, electron densities and airglow emissions. They study two cases: (1) a 3 GHz, 10 GW microwave beam from the proposed power satellite and (2) 15 MHz beams with powers of 1 MW and 3 MW launched by the Arecibo antenna. These two cases have similar intensities and geometries of resistive heating. The most dramatic effects are predicted for the E-region, where a thermal runaway will take place because the electron cooling by O_2 and N_2 rotational bands decreases with increase of electron temperature (equation (8)). The E region temperature will increase roughly from 200°K to about 1000°K , see Figure 17, at which level it is stabilized by electron cooling via vibrational excitation of O_2 and N_2 , the vibrational energy eventually being radiated in the infrared. In the lower ionosphere the electron density in the radiowave beam is enhanced primarily because of the decrease in recombination rate with increase of electron temperature. In the lower E region the electron density may increase by a factor of about three.

In the F region, where thermal conductivity plays an important role, temperature increases of 200° to 500°K will occur along the geomagnetic field lines passing through the radio beam. The electron density profiles calculated for the undisturbed ionosphere and for the maximum heating case are shown in Figure 18.

The consequences of this modification of the ionosphere on radio communications can be estimated. Assuming that the electron temperature increases by a factor of 3 and that the D region electron density increases by a factor of 2 then the product $N\nu$ and, hence, the nondeviative absorption of a radio signal will increase by a factor of about

10 (20 dB). While this is a large increase its extent is limited and its location is well defined so that radio circuits through the modified region can be avoided. Of course, a large number of such power links could affect the power requirements of some HF communications circuits.

An increase in the peak electron density of the E layer by a factor of 2 to 3 will increase the foE by around 50%. This will have some adverse effect on radio propagation: for example, an increase in the lower cut-off frequency for propagation via the F2 layer.

2. CHEMICAL MODIFICATION OF THE IONOSPHERE

2.1 Reasons for some modifications

The introduction of various impurities into the ionosphere serves several purposes, e.g.:

- (A) Deliberate modification
- (1) To act as tracers for the study of ionospheric parameters, e.g. barium releases.
 - (2) To induce instabilities into plasma to create plasma irregularities and thus simulate natural disturbances.
 - (3) Inject plasma beams along geomagnetic field lines to study the magnetosphere.
 - (4) Create "holes" in the ionosphere leading to "field-aligned" ducts for possible radio communications.
- (B) Inadvertent modification
- (1) Exhaust gases from rockets.
 - (2) Possible diffusion of chemicals (e.g., freon) from the ground.

Thus chemical seeding of the upper atmosphere can have beneficial and potentially hazardous consequences for the ionosphere. We shall consider some of these chemical modifications and their consequences.

2.2 The effect of chemical impurities on the electron losses

Ionospheric electrons and ions are produced mostly by photoionization of atoms and molecules by solar extreme ultraviolet (100 Å to 1200 Å) and X radiation (1 Å to 100 Å). For example, in the F2 layer where atomic oxygen dominates



In principle the electrons could disappear by the reverse process but the direct electron-atomic ion recombination rate is so low that the F2 layer, once ionized, would take years to disappear. In practice, rapid recombination requires the presence of molecular ions so that excess energy and momentum can be absorbed. In the F region the neutral molecules are mostly O₂ and N₂ and these react with O⁺ to produce the diatomic ions O₂⁺ and NO⁺:



(24)

The O₂⁺ and N₂⁺ can react quickly with electrons



(25)

where the asterisks denote excited states.

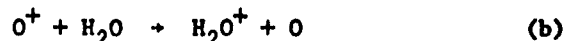
We can see that chemical modification can be used to modify the above processes in two ways:

- (1) The introduction of a chemical with a low ionization potential will increase the production rate, for a given insolation, and thus, the local electron density.
- (2) The introduction of a molecular gas with a high affinity for electrons or a high charge exchange coefficient will increase the loss rate and, hence, produce a hole in the plasma.

2.3 Inadvertent modification

To illustrate an effect of the inadvertent pollution of the ionosphere we consider the discovery by Medillo et al. (1975) that the exhaust plume of the Saturn V rocket, which launched NASA's Skylab, caused a sudden and large-scale depletion of the electron content of the F region. The observed effect consisted of a large (~ 50%) bite out in the Faraday electron content between ATS3 satellite and ground that occurred near 1240, 75° WMT, on May 14, 1973, which lasted for several hours (see Figure 19). The Skylab depression of TEC is much larger than the storm depletion. Observations from several sites revealed that a "hole" in the F region was created with a radius of approximately 1000 km. The onset of the depletion occurred within 10 min of the launch of Skylab. The specific mechanism that created the hole was the rapid ion-atom interchange reactions

between the natural O^+ and the hydrogen and water vapor molecules in the plume, from the second-stage engines, followed by dissociative recombination (equations (24) and (25)), i.e.



and



It should be noted that the dissociative recombinations (equations (25) and (27)) proceed at a relatively fast rate so that the electron loss rates are determined by the slower atom-ion reactions.

In the F region the continuity equation takes the form

$$\frac{dN_F}{dt} = q - \beta N_F \quad (28)$$

where, in the present case, N_F is the columnar electron content measured by the Faraday technique (see Titheridge, 1972), q is the total production rate and β is an effective linear loss coefficient. Under normal conditions β is of the order of $2 \times 10^{-5} \text{ sec}^{-1}$ whereas from Figure 19 $\beta \sim 280 \times 10^{-5} \text{ sec}^{-1}$, i.e. over 100 times the normal value. Mendillo et al. (1975) show that the insertion of H_2 and H_2O , from the known characteristics of the jet engines, leads to an effective loss coefficient similar to that observed. These authors comment: The exhaust was composed of 70% water vapor and 30% unused hydrogen. When converted to particle flow per second, each engine ejects 7.8×10^{27} water molecules and 3.3×10^{27} hydrogen molecules at a speed of 4.5 km s^{-1} . Such flow rates represent extraordinary additions to the ambient atmosphere of species never found in quantity in the F region. With the cluster of 5 engines releasing over 1 ton s^{-1} of such gases one might expect to find a variety of dynamical and chemical processes with direct ionospheric consequences.

Although the above chemical modification represents an extreme example, smaller, but deliberate, seeding of the F2 region with H_2O and H_2 can produce required modifications (e.g., see Mendillo and Forbes, 1977; Bernhardt, da Rosa and Park, 1977). Side effects of chemically induced depletion of the ionosphere include: (a) increase of electron temperature, (b) decrease of ion temperature, (c) enhancement of airglow, (d) formation of depleted ducts extending into the magnetosphere that can guide radio waves, and (e) production of a focusing lens affecting radio waves traversing the ionosphere.

2.4 Deliberate modification

2.4.1 Metallic ions

Many experiments have been carried out to test the effect of chemicals on the ionosphere (see Haerendel, 1977). The most commonly used modification is the release of gases in the upper atmosphere. The cheapest way is by chemical reactions such as the barium-copper oxide reaction, which yields a neutral metal vapor. The ionization, provided by EUV illumination, is greater than the ambient because of the lower ionization potential of metallic ions. Metal ions above the turbopause ($\approx 120 \text{ km}$) have a much longer life-time than the times for transport, in contrast to the life-times of the dominant ions NO^+ and O_2^+ . As the metallic cloud is only partially ionized we have a diffusing neutral gas, that gives information on the properties of the neutral atmosphere, whereas the behavior of the ionized cloud depends also on the interaction with the ambient ionosphere and on the local magnetic and electric fields. To determine these physical properties, e.g. diffusion, E fields, it is necessary to measure the motions of the neutral and ion clouds.

Experiments with barium have been reported by Föppl et al. (1967). The Ba^+ cloud, with a width of a few km transverse to the geomagnetic field, is generated within about 5 sec of release and expands mainly along the magnetic field lines. The clouds were observed photographically from two ground stations for triangulation. After the initial cloud expansion, caused by excess pressure during release, the neutral cloud expands by diffusion. The neutral cloud tends to drift with the ambient neutral wind whereas the motion of the ionized cloud is affected also by $E \times B$ drift so that the two clouds diverge with time as seen in Figure 20. For photographic contrast these seeding experiments must be conducted near sunrise and sunset only. Observations by Föppl et al. (1967) at Sardinia yield neutral horizontal speeds between 60 and 150 m s^{-1} . Ion motions parallel and perpendicular to the magnetic field are approximately 60 m s^{-1} and 40 m s^{-1} .

Barium ion releases at F-region heights (see Stoffregen, 1970) produce disturbances in the E region. Such effects could be caused by ion-cloud triggering of particle precipitation (Stoffregen, 1970) or by currents flowing along magnetic field lines to short circuit the polarization field in the cloud via the E layer where the electrical conductivity is high (Haerendel et al., 1967). This model is illustrated in Figure 23. The reason for the current flow is that the electrons and ions in the cloud, under the action of the ambient electric field, move with slightly different speeds producing a polarization field-charge separation. At F-region heights the electrons cannot move easily in the direction of the electric field. In the E region the ion conductivity is large so that the electrical circuit can be more easily completed via the E region than via the F region. At the foot of the magnetic field lines in the E region there will be regions of enhanced and depleted plasma densities.

2.4.2 Electron attachment

Some chemicals have a high affinity for electrons so that their injection into the ionosphere has relatively little effect except to remove electrons and replace them with heavy negative ions. Such a chemical is sulfur hexafluoride which was used in Project Firefly (see Paul et al., 1968) to create an electron hole near the daytime F2-layer peak. The electron removal is



The inertia of a heavy negative ion is so great that it does not affect the propagation of HF radio signals so, that as far as radio waves are concerned, there is a "hole" in the F2 region. An ionogram taken following the release is shown in Figure 21 and illustrates the complicated nature of the echoes. The lower panel shows a synthetic ionogram obtained by ray tracing (Paul et al., 1968) while Figure 22 gives an example of the radio raypath through the hole.

A sequence of ionograms obtained during this experiment confirmed the theoretical calculations of the descent of heavy molecules in the atmosphere. A total of 22.7 kg (10^{26} molecules) of SF_6 was released at 222 km, a little below the F2 peak, and produced a spherical cloud with a radius of about 3 km. As the cloud descends under gravity it eventually assumes a "pancake" shape. The shape of the electron hole is somewhat different because the initial spherical hole is modified by inward diffusion of ambient electrons along the geomagnetic field so that the hole will become elongated along the field at a rate such that it doubles its vertical extent in a time of the order of 2 min.

2.4.3 Shaped charges

Shaped or hollow charges have been effective tools for the injection of ion beams along magnetic lines of force up to high altitudes, i.e. into the magnetosphere (Wescott et al., 1974). Forward speeds between 8 and 15 km s⁻¹ are characteristic of the fast part of the velocity distribution.

The injection of plasma into the ionosphere and/or magnetosphere can set up Alfvén waves which propagate nearly along the geomagnetic field thus modification of one region can be communicated to other regions (see Scholer, 1970).

2.5 Effect of hydrogen on the equatorial ionosphere

The equator is a particularly interesting place to study seeding of the ionosphere because the magnetic field B_0 is horizontal and perpendicular to the gravity vector g . Under these conditions a plasma drifts with velocity

$$\underline{u} = \frac{g \times B_0}{\omega_H B_0} \quad (30)$$

where ω_H is the gyrofrequency. Although this drift is small (~ 1 cm s⁻¹) the ion current establishes an electric polarization field at an inhomogeneity. This field is normally short circuited by currents that flow via the lower F and E regions where the transverse (Pedersen) conductivity is high during the day (Haerendel, 1977). At sunset this conductivity is reduced and a situation develops where a heavy fluid rests on a lighter one at the steep ledge of the F2 layer which is inherently unstable (the Rayleigh-Taylor instability). It is now believed, by some, that equatorial spread F is initiated by this process.

A feature of this instability is that the irregularity creates elongated bubbles which rise to several hundred km, even above the F2 peak (see Woodman and La Hoz, 1976). Inside these "holes" short-wave irregularities from that are responsible for radio scattering. Figure 24 is an example of rising patches of 3 m irregularities as measured by the Jicamarca radar (Woodman and La Hoz, 1976). One surprise, reported by Haerendel (1977), is that when barium was placed in a (theoretically) unstable F-layer during spread-F no visible fine structure was observed. This is one of the few examples of barium clouds without striations and the anomaly is still not explained.

The serious effects of equatorial irregularities on communications makes further understanding of this instability of practical importance. The required (unstable) conditions might be produced by seeding the equatorial ionosphere with H_2 gas inducing the ion-atom interchange of equation (26). The electron "hole" will expand along the geomagnetic field line. Theoretical modeling by Anderson and Bernhardt (1978) shows that: (1) H_2 gas is more effective than H_2O since it diffuses faster, thus depleting the electron density further along the field. (2) The optimum altitude is approximately 300 km because at higher altitudes the H_2 gas diffuses away too rapidly.

2.6 Communications aspects of ionospheric modification

2.6.1 Radio modification

Some consequences of radio heating of the ionosphere have already been mentioned.

- (1) Interference between broadcasting stations caused by wave interaction.
- (2) Self-demodulation in the D region, when high powers are employed, partially offsetting the increase in power.
- (3) Production of F-region irregularities that enable field-aligned scatter. This scatter can be used for a direct link between transmitter or receiver or it might be used to modify the angle of incidence in the F2 layer and enable the launch of the signal into a propagation mode (e.g., whispering gallery, field-aligned duct) and thus propagate to long distances. Since irregularities can be generated at all local times FAS can provide 24-hour operations by choosing the appropriate frequency for ionospheric modification.

Inadvertent ionospheric modification by high-power (e.g., 10MW) HF transmitters that already exist could result in undesirable communications effects. While these transmitters are designed primarily for oblique circuits there may be sufficient side-lobe emission to produce F-region effects and, thus, degrade communications circuits (see Albrecht, 1977, pages RTD 11-5, 6).

2.6.2 Chemical modification

Chemical modification might be used in several ways to facilitate or hamper ionospheric radio communications:

- (1) Plasma seeding at high altitudes may be used to create an artificial duct in the magnetosphere and thus enable propagation of radio waves from VLF through VHF.
- (2) Overdense seeding (e.g., barium clouds) can be used to scatter waves which might be used directly or used to modify the angle of incidence of radio signals on the reflecting layer.
- (3) Underdense seeding (e.g., H_2 , H_2O , etc.), near the magnetic equator, creates irregularities in the form of holes that can be used to simulate natural equatorial spread-F. Normally this phenomenon has adverse effects on radio communications (e.g., flutter fading, scintillation)--see Aarons (1978).

3. NUCLEAR EXPLOSIONS

One of the most devastating means of ionospheric modification is by nuclear explosions. These often produce violent chemical and dynamic effects throughout the upper atmosphere some of which last for several days. Low altitude explosions produce large acoustic-gravity waves that travel large distances (e.g., Kanellakos, 1970; Row, 1970; Baker and Davies, 1968; Georges, 1968). High altitude explosions produce X-rays that ionize the D region and result in high absorption of radio signals. They also modify the energetic charged-particle populations in the radiation belts surrounding the earth. Particle precipitation from these modified belts ionize the D region and affect the phase of long distance VLF propagation for many days. The D-region effects are noticed first at two places one near the explosion and the other at the far end of the geomagnetic field line. With time the trapped electrons drift in an easterly direction and after about one hour they envelope the whole earth.

4. CONCLUDING REMARKS

We have seen that the ionosphere can be altered by radio and by chemical means and that such alterations may be advantageous or adverse from the point of view of the radio communicator. From the viewpoint of military communications F-region modification provides a relatively secure means of communications because of the highly aspect sensitive characteristics of field-aligned scatter.

There are several means of modification that have not been discussed here but nevertheless are of considerable importance. One example is the modification of the magnetosphere by the injection of very-low-frequency waves that leads to stimulation of VLF radio emissions (Helliwell et al., 1977). A number of other aspects of modification are presented in the AGARD Conference Proceedings on Non-Linear Effects in Electromagnetic Wave Propagation (Fejer, 1974).

REFERENCES

- Aarons, J. (1978), Ionospheric scintillation, Lecture E, AGARD Lecture Series 93. This volume.
- Albrecht, H. (ed.) (1977), Artificial Modification of Propagation Media, AGARD Conf. Proc. 192, Tech. Edit. and Reprod. Ltd., London.

- Allen, E. M., G. D. Thome and P. B. Rao (1974), HF phased array observations of heater-induced spread-F, *Radio Sci.* 9, (11), 905-916.
- Anderson, D. N. and P. A. Bernhardt (1978), Modeling the effects of an H₂ gas release on the equatorial ionosphere, *J. Geophys. Res.*, 83, in press.
- Bailey, V. A. and D. F. Martyn (1934), The influence of electric waves on the ionosphere, *Phil. Mag.*, 18, 369.
- Baker, D. M. and K. Davies (1968), Waves in the ionosphere produced by nuclear explosions, *J. Geophys. Res.*, 73, (1), 448-451.
- Bernhardt, P., A. V. da Rosa and C. G. Park (1977), Chemical depletion of the ionosphere, AGARD Conf. Proc. No. 192, editor H. J. Albrecht, Tech. Edit. and Reprod., London.
- Brown, W. C. (1977), Transmission of power from space to earth, AIAA-EEI-IEEE Conf. on New Options in Energy Technology, San Francisco.
- Carpenter, G. B. (1974), VHF and UHF bistatic observations of a region of the ionosphere modified by a high power radio transmitter, *Radio Sci.* 9, (11), 965-969.
- Cohen, R. and J. D. Whitehead (1970), Radio-reflectivity detection of artificial modification of the ionospheric F layer, *J. Geophys. Res.*, 75, (31), 6439-6445.
- Davies, K. (1969), *Ionospheric Radio Waves*, Ginn-Blaisdell, Waltham, Mass.
- Davies, K. (1978), Forecasting and prediction of ionospheric parameters, AGARD Lecture Series No. 93. This volume.
- DuBois, D. F. and M. V. Goldman (1965), Radiation induced instability of electron plasma oscillations, *Phys. Rev. Letters*, 14, 544-546.
- Farley, D. T. (1970), Incoherent scattering at radio frequencies, *J. Atmos. Terr. Phys.*, 32, 693-704.
- Fejer, J. A. (1961), The absorption of short radio waves in the ionospheric D and E regions, *J. Atmos. Terr. Phys.*, 23, 260.
- Fejer, J. A. (1970), Radio wave probing of the lower ionosphere by cross-modulation techniques, *J. Atmos. Terr. Phys.*, 32, 597-607.
- Fejer, J. A., editor (1974), *Non-Linear Effects in Electromagnetic Wave Propagation*, AGARD Conf. Proc. 138, AD-781510, National Tech. Information Service, Springfield, Virginia.
- Fialer, P. A. (1974), Field-aligned scattering from a heated region of the ionosphere--Observations at HF and VHF, *Radio Sci.*, 9, (11), 923-940.
- Föppl, H., G. Haerendel, L. Haser, J. Loidl, P. Lütjens, R. Lüst, F. Melzner, B. Meyer, H. Neuss and E. Rieger (1967), Artificial strontium and barium clouds in the upper atmosphere, *Planet. Space Sci.*, 15, (2), 357-372.
- Georges, T. M., editor (1968), *Acoustic-gravity waves in the atmosphere*, U.S. Government Printing Office, Washington, D. C.
- Glaser, P. E. (1977), Solar power from satellites, *Phys. Today*, 30, 30-38.
- Gordon, W. E. and H. C. Carlson (1974), Arecibo heating experiments, *Radio Sci.*, 9, (11), 1041-1047.
- Gordon, W. E. and H. C. Carlson (1974), Parametric instabilities in the ionosphere excited by powerful radio waves over Arecibo, AGARD Conf. Proc. No. 138, Tech. Edit. and Reprod. Ltd., London.
- Gordon, W. E. and H. C. Carlson (1977), The heating experiment at Arecibo, AGARD Conf. Proc. No. 192, editor H. J. Albrecht, Tech. Edit. and Reprod., Ltd., London.
- Gordon, W. E., H. C. Carlson and R. L. Showen (1971), Ionospheric heating at Arecibo: First tests, *J. Geophys. Res.*, 76, 7808-7813.
- Haerendel, G. (1977), Modification of ionized media by chemical substances--a review of physical processes, AGARD Conf. Proc. No. 192, editor H. J. Albrecht, Tech. Edit. and Reprod., Ltd., London.
- Haerendel, G., R. Lüst and E. Rieger (1967), Motion of artificial ion clouds in the upper atmosphere, *Planet. Space Sci.*, 15, (1), 1-18.
- Helliwell, R. A., J. P. Katsufakis and P. A. Bernhardt (1977), Modification of the propagation characteristics of the ionosphere (and magnetosphere) by injection into the magnetosphere of whistler-mode waves, AGARD Conf. Proc. No. 192, editor H. J. Albrecht, Tech. Edit. and Reprod. Ltd., London.

- Jones, T. B. (1974), Modification effects in the ionospheric D region, AGARD Conf. Proc. No. 138, Tech. Edit. and Reprod. Ltd., London.
- Jones, T. B., K. Davies and B. Weider (1972), Observations of D region modifications at low and very low frequencies, *Nature*, 238, 33-34.
- Kanellakos, D. P. (1970), Spatial and temporal models of the TID from a low-altitude nuclear explosion, from Phase and Frequency Instabilities in Electromagnetic Wave Propagation, editor K. Davies, AGARD Conf. Proc. No. 33, Technivision, Slough, England.
- Kelso, J. M. (1964), Radio Ray Propagation in the Ionosphere, McGraw-Hill.
- Kissick, W. A. and A. J. Ferraro (1974), Wave interaction using a partially reflected probing wave, AGARD Conf. Proc. No. 138, Tech. Edit. and Reprod. Ltd., London.
- Lee, H. S. and A. J. Ferraro (1969), Winter D-region electron concentration and collision frequency features obtained with high power interaction measurements, *J. Geophys. Res.*, 74, 1184-1194.
- Megill, L. R. (1965), Self distortion of radio signals in the D region, *Radio Sci.*, 69D, 367.
- Meltz, G. and R. E. LeLevier (1970), Heating the F region by deviative absorption of radio waves, *J. Geophys. Res.*, 75, (31), 6406-6416.
- Mendillo, M. and J. Forbes (1977), Spatial-temporal development of molecular release capable of creating large-scale F-region holes, AGARD Conf. Proc. 192, editor H. J. Albrecht, Tech. Edit. and Reprod. Ltd., London.
- Mendillo, M., G. S. Hawkins and J. A. Klobuchar (1975), A sudden vanishing of the ionospheric F region due to the launch of Skylab, *J. Geophys. Res.*, 80, 2217-2228.
- Minkoff, J. (1974), Radio frequency scattering from a heated ionospheric volume. 3. Cross section calculations, *Radio Sci.*, 9, (11), 997-1004.
- Minkoff, J. and I. Weissman (1977), A review of VHF/UHF scattering from a heated ionospheric volume, AGARD Conf. Proc. 192, editor H. J. Albrecht, Tech. Edit. and Reprod. Ltd., London.
- Paul, A. K., G. H. Smith and J. W. Wright (1968), Ray-tracing synthesis of ionogram observations of a large local disturbance in the ionosphere, *Radio Sci.*, 3, (1), 15-26.
- Perkins, F. W. (1974), A theoretical model for short-scale field-aligned plasma density striations, *Radio Sci.*, 9, (11), 1065-1070.
- Perkins, F. W. and P. K. Kaw (1971), On the role of plasma instabilities in ionospheric heating by radio waves, *J. Geophys. Res.*, 76, 282-284.
- Perkins, F. W. and R. G. Roble (1978), Ionospheric heating by radio waves: Predictions for Arecibo and the satellite power station, *J. Geophys. Res.*, 83, in press.
- Phelps, A. V. and J. L. Pack (1961), Drift velocities of slow electrons in helium, neon, argon, hydrogen and nitrogen, *Phys. Rev.*, 121, (3), 798-806.
- Ratcliffe, J. A. (1959), The Magneto-Ionic Theory, Cambridge, The University Press.
- Ratcliffe, J. A. and I. J. Shaw (1948), A study of the interaction of radio waves, *Proc. Roy. Soc. A* 193, 311.
- Row, R. V. (1970), Localized low-altitude sources and acoustic gravity wave perturbations of the ionosphere, from Phase and Frequency Instabilities in Electromagnetic Wave Propagation, editor K. Davies, AGARD Conf. Proc. No. 33, Technivision, Slough, England.
- Scholer, M. (1970), On the motion of artificial ion clouds in the magnetosphere, *Planet. Space Sci.*, 18, (7), 977-1004.
- Sen, H. K. and A. A. Wyller (1960), On the generalization of the Appleton-Hartree magnetoionic formula, *J. Geophys. Res.*, 65, 3931.
- Smith, R. A. and R. G. Loch (1974), Electron heating of the ionosphere by powerful gyrowaves, AGARD Conf. Proc. No. 138, Tech. Edit. and Reprod. Ltd., London.
- Smith, R. A., I. A. Bourne, R. G. Loch, C. S. G. K. Setty, T. N. R. Coyne, P. H. Barratt and B. S. N. Prasad (1965), Radio Wave Interaction using Gyro-Waves, Report AFCRL-65-460, Bedford, Mass.
- Stoffregen, W. (1970), Electron density variations observed in the E-layer below an artificial barium cloud, *J. Atmos. Terr. Phys.*, 32, 171.

- Tellegen, B. D. H. (1933), Interaction between radio waves, *Nature*, 131, 840.
- Thome, G. D. and D. W. Blood (1974), First observations of RF backscatter from field-aligned irregularities produced by ionospheric heating, *Radio Sci.*, 9, (11), 917-921.
- Thomson, J. A. (1970), Energy deposition in artificial ionospheric heating experiments, *J. Geophys. Res.*, 75, (31), 6446-6452.
- Thrane, E. V. (1966), Experimental Studies of the Structure of the Ionospheric D-Region, NDRE Report No. 54, Norwegian Defence Research Establishment, Kjeller, Norway.
- Thrane, E. V. and W. R. Piggott (1966), The collision frequency in the E- and D-regions of the ionosphere, *J. Atmos. Terr. Phys.*, 28, (8), 721-737.
- Utlaut, W. F. (1974), A survey of ionospheric modification effects produced by high-power HF radio waves, AGARD Conf. Proc. No. 138, Tech. Edit. and Reprod. Ltd., London.
- Utlaut, W. F. (1975), Ionospheric modification induced by high-power HF transmitters--a potential for extended range VHF-UHF communications and plasma physics research, *Proc. IEEE*, 63, 1022-1043.
- Utlaut, W. F. (1977), Ionospheric modification induced by high-power HF transmitters--potential for communication and plasma physics research, AGARD Conf. Proc. No. 192, editor H. J. Albrecht, Tech. Edit. and Reprod. Ltd., London.
- Utlaut, W. F. and R. Cohen (1971), Modifying the ionosphere with intense radio waves, *Science*, 174, 245-254.
- Utlaut, W. F. and E. J. Violette (1972), Further ionosonde observations of ionospheric modification by an high-powered HF transmitter, *J. Geophys. Res.*, 77, 6804-6818.
- Utlaut, W. F. and E. J. Violette (1974), A summary of vertical incidence radio observations of ionospheric modification, *Radio Sci.*, 9, (11), 895-903.
- Utlaut, W. F., E. J. Violette and A. K. Paul (1970), Some ionosonde observations of ionospheric modification by very high power, high frequency ground-based transmissions, *J. Geophys. Res.*, 75, (31), 6429-6435.
- Weisbrod, S., H. S. Lee and A. J. Ferraro (1964), Investigation of phase interaction as a means for the study of the lower ionosphere, *J. Geophys. Res.*, 69, 2337.
- Weinstock, J. (1974), Enhanced airglow, electron acceleration, and parametric instabilities, *Radio Sci.*, 9, (11), 1085-1087.
- Wescott, E. M., E. P. Rieger, H. C. Stenbaek-Nielsen, T. N. Davis, H. M. Peak and P. J. Bottoms (1974), L = 1.24 conjugate magnetic field line tracing experiments with barium shaped charges, *J. Geophys. Res.*, 79, (1), 159-168.
- Whitehead, J. D. (1970), Some F-region parameters measurable in the Boulder heating experiment, *J. Geophys. Res.*, 75, (31), 6417-6418.
- Woodman, R. F. and C. La Hoz (1976), Radar observations of F-region equatorial irregularities, *J. Geophys. Res.*, 81, (31), 5447-5466.
- Wright, J. W. (1975), Evidence for precipitation of energetic particles by ionospheric heating transmissions, *J. Geophys. Res.*, 80, 4383-4386.

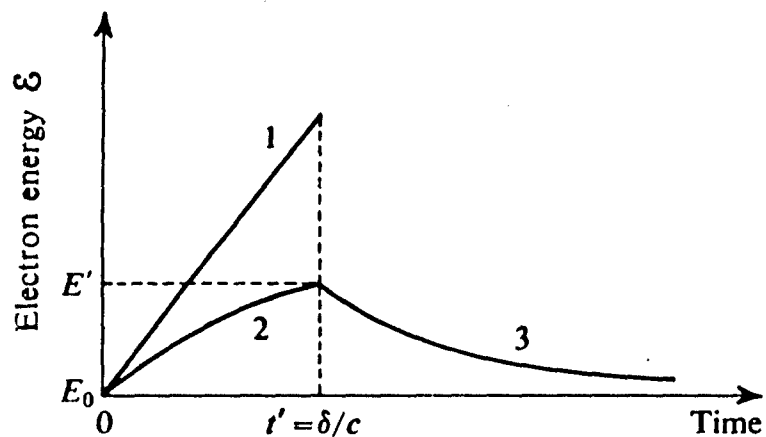


Fig.1 Time variations of electron energy resulting from square-wave heating

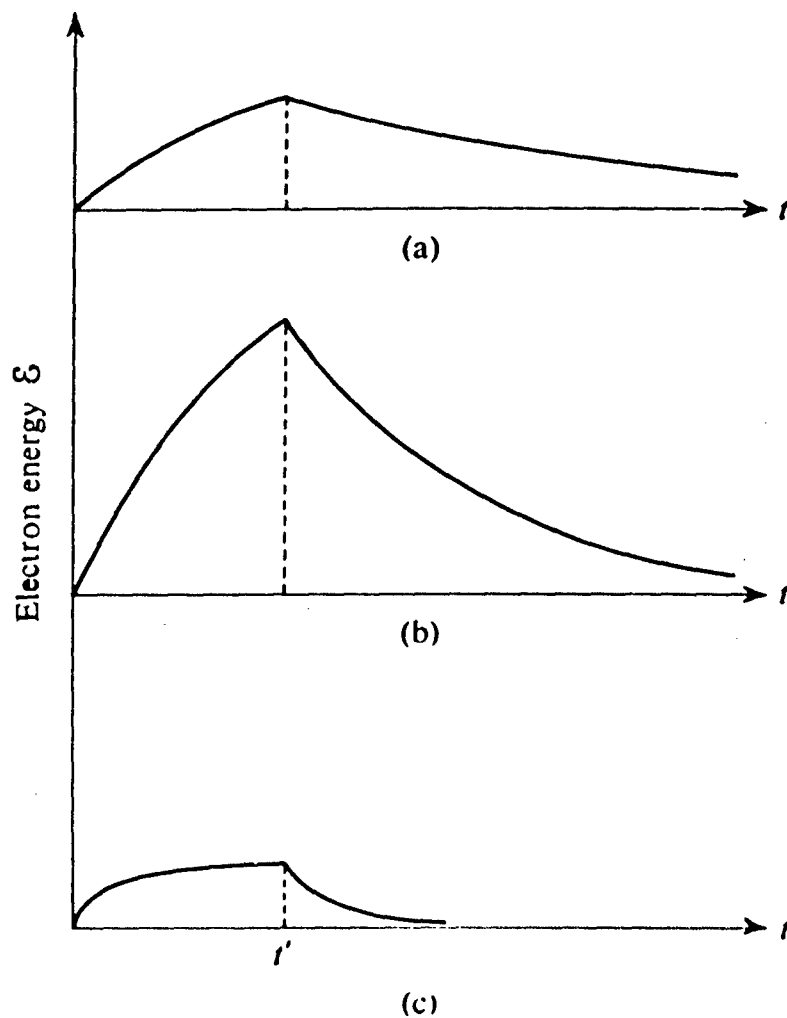
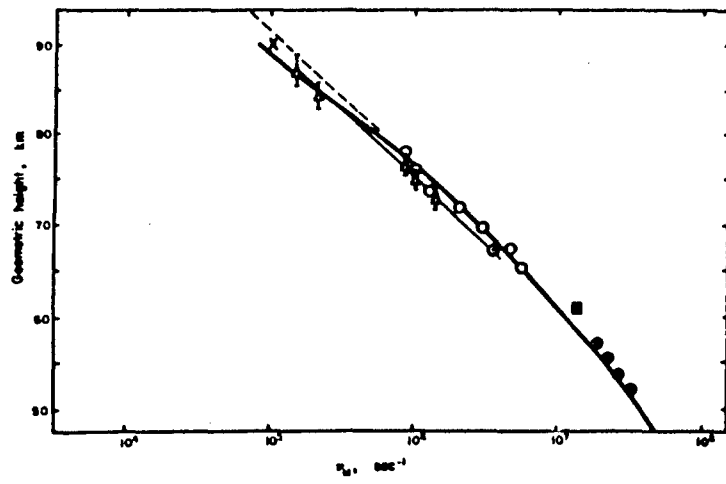
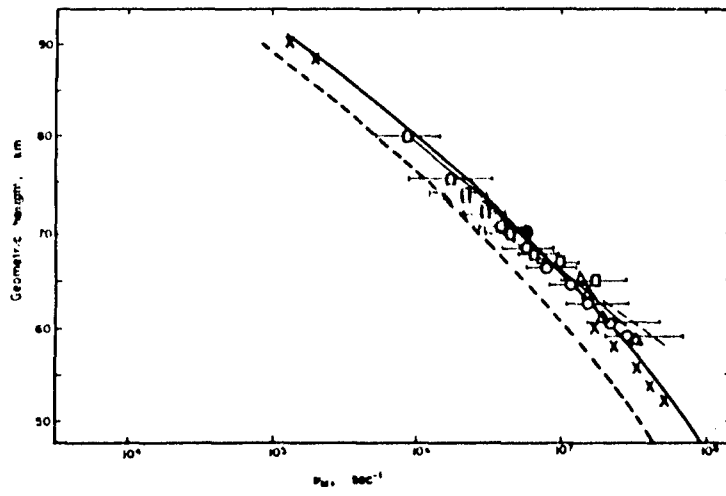


Fig.2 Response of the ionosphere, at different heights, to a heating pulse
(a) near 100 km; (b) near 75 km; (c) near 500 km



(a)



(b)

Fig.3 Height variations of ν_M (after Thrane and Piggott, 1966)
 (a) winter and spring; (b) summer and autumn

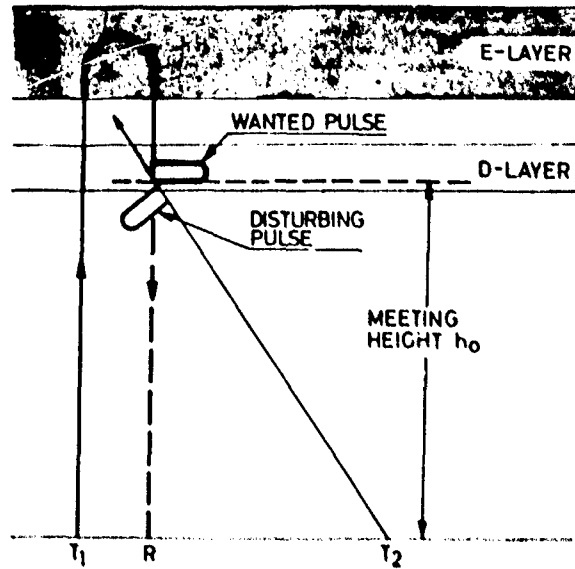


Fig.4 Experimental arrangement for Fejer-type cross-modulation

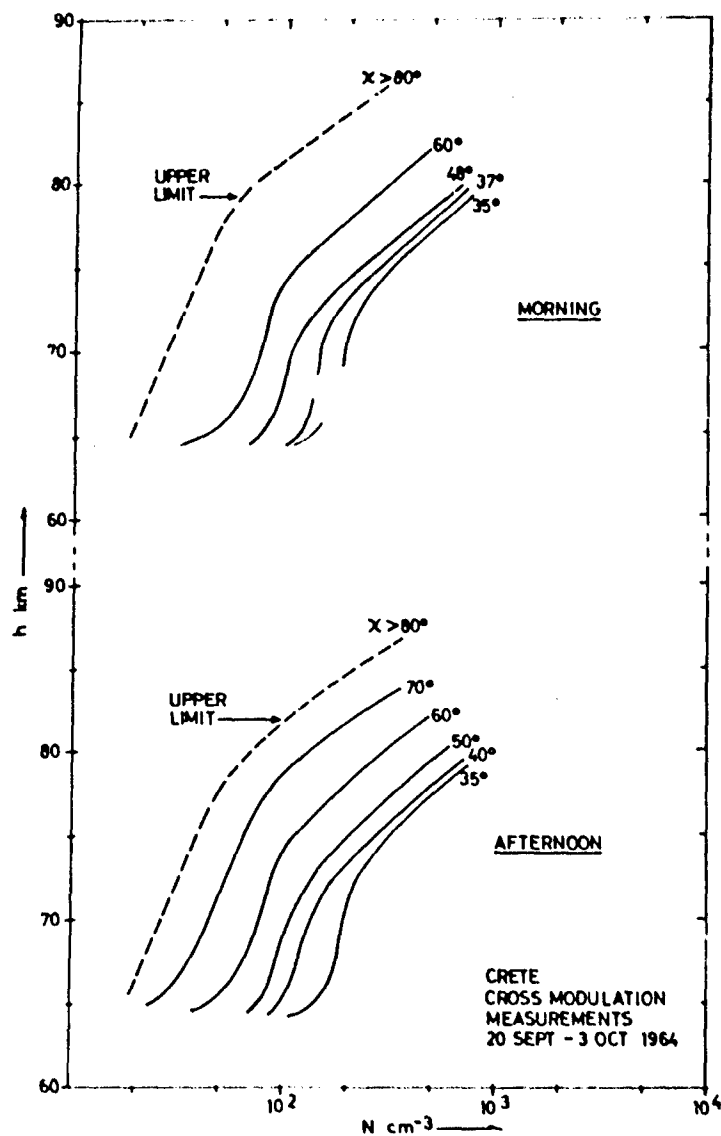


Fig.5 Electron-density profiles obtained from cross modulation (after Thrane, 1966)

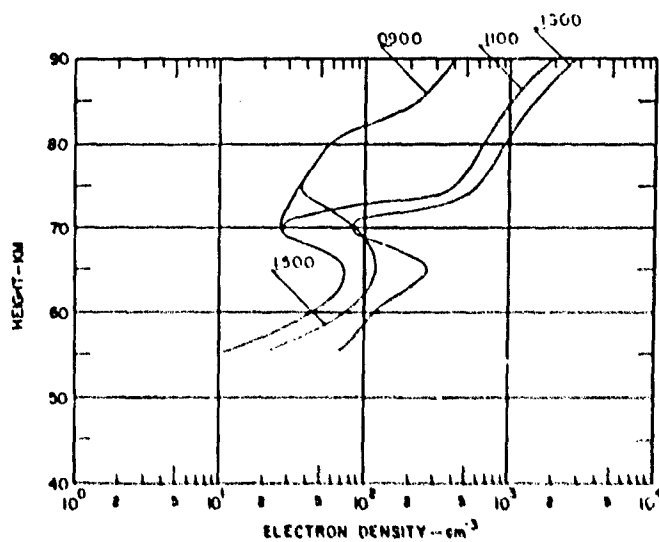


Fig.6 Sample electron-density profiles (after Lee and Ferraro, 1969)

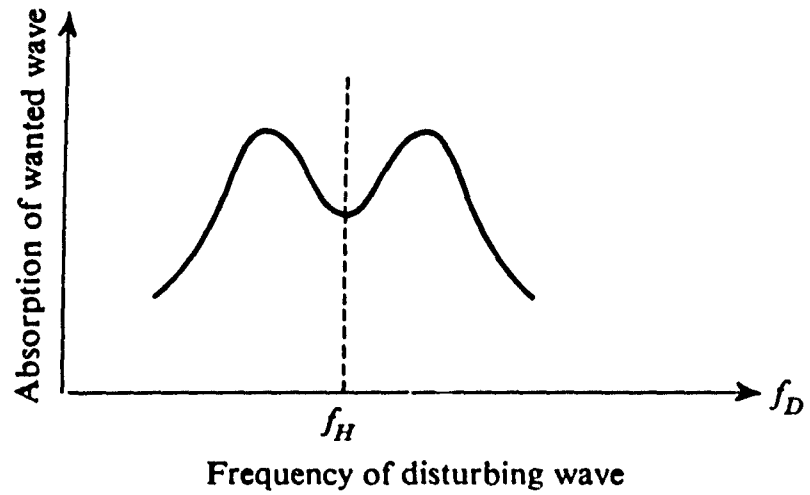


Fig.7 Sketch of the expected variation of the absorption of the wanted wave as the disturbing-wave frequency f_D varies through the gyrofrequency f_H

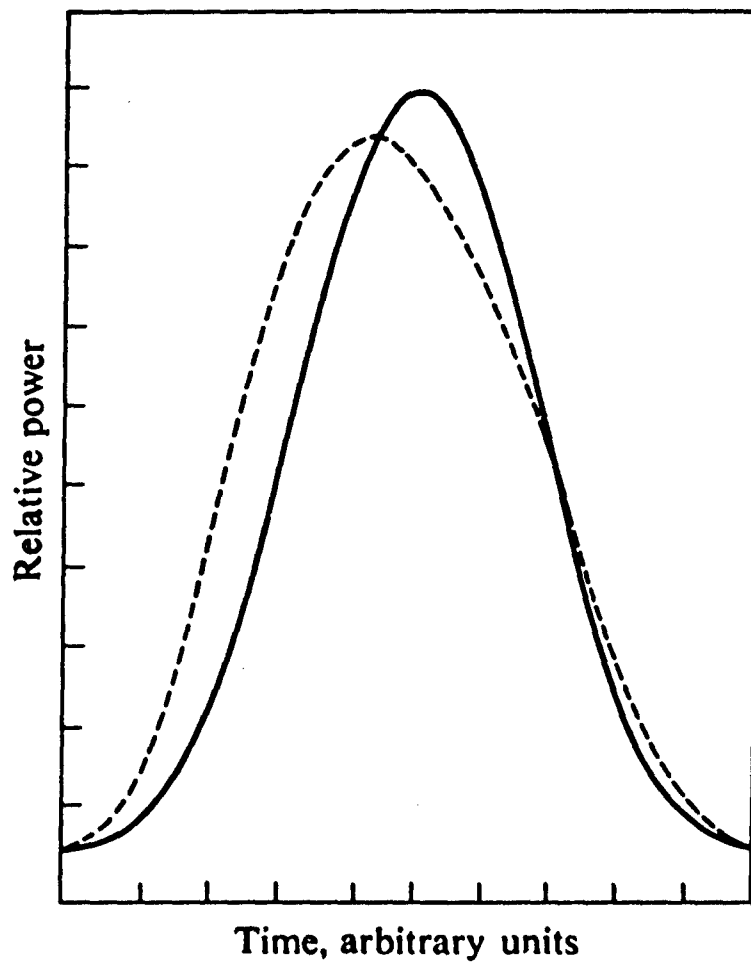


Fig.8 Modulated wave form before and after self-distortion. The solid line is the incident wave and the dashed line the emerging wave (after McGill, 1965)

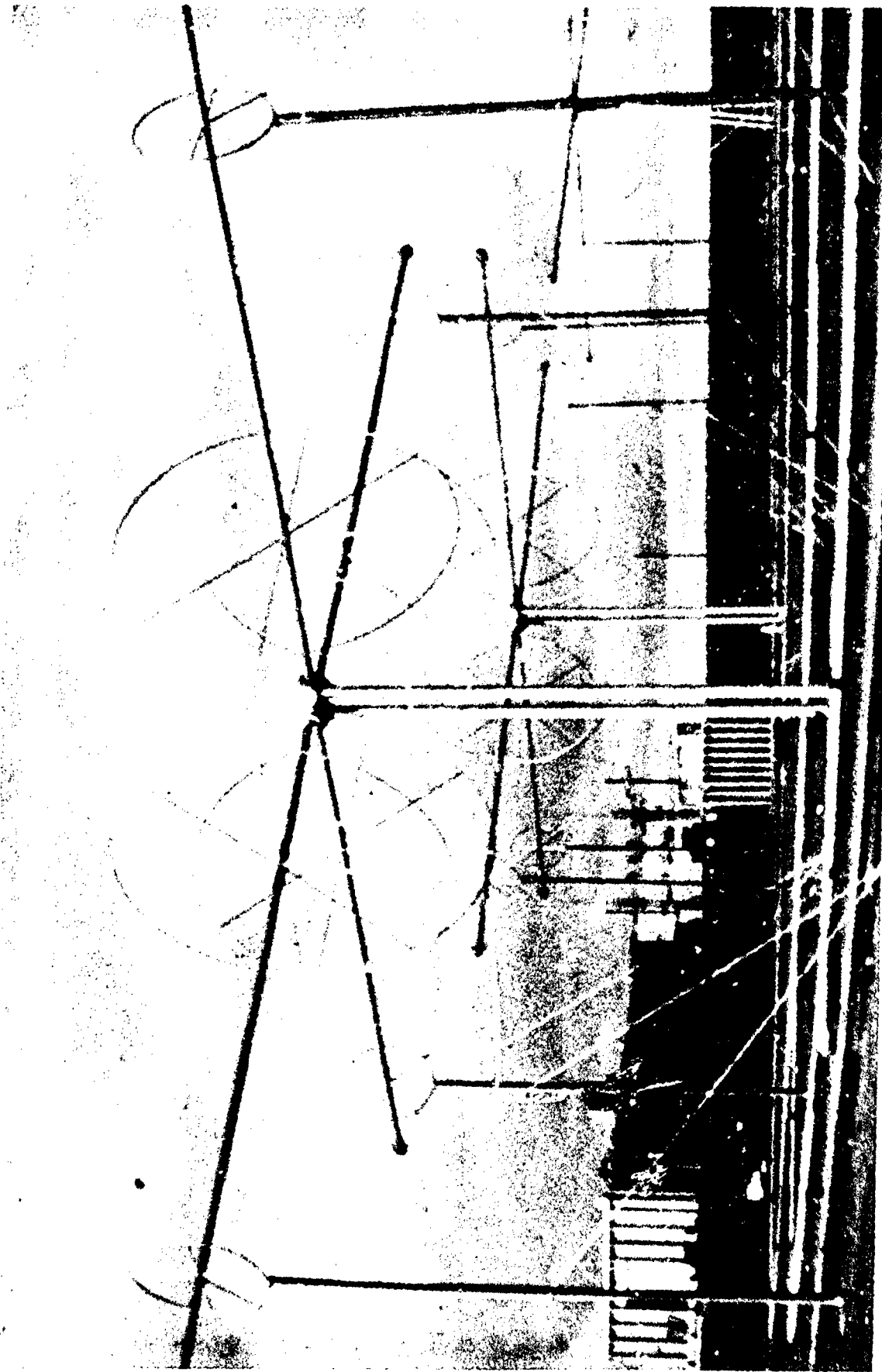


Fig.9(a) The Platteville antenna

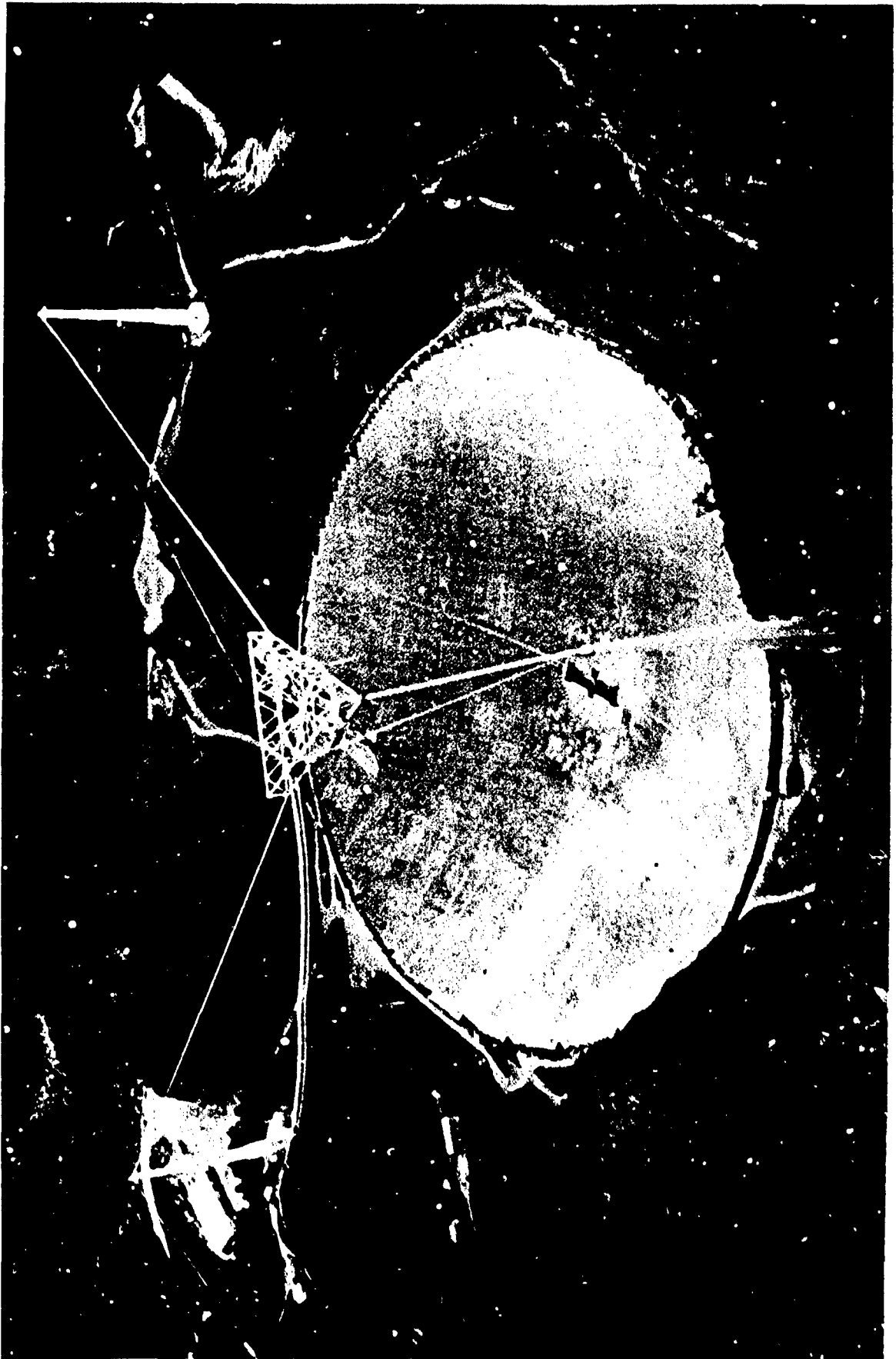


Fig.9(b) The Arecibo antenna

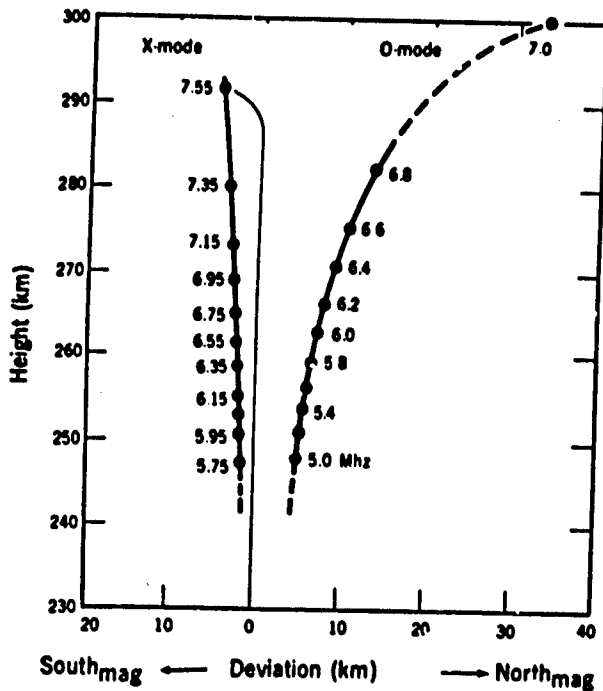


Fig.10 Ordinary and extraordinary ray paths over Platteville (after Utlaut and Cohen, 1971)

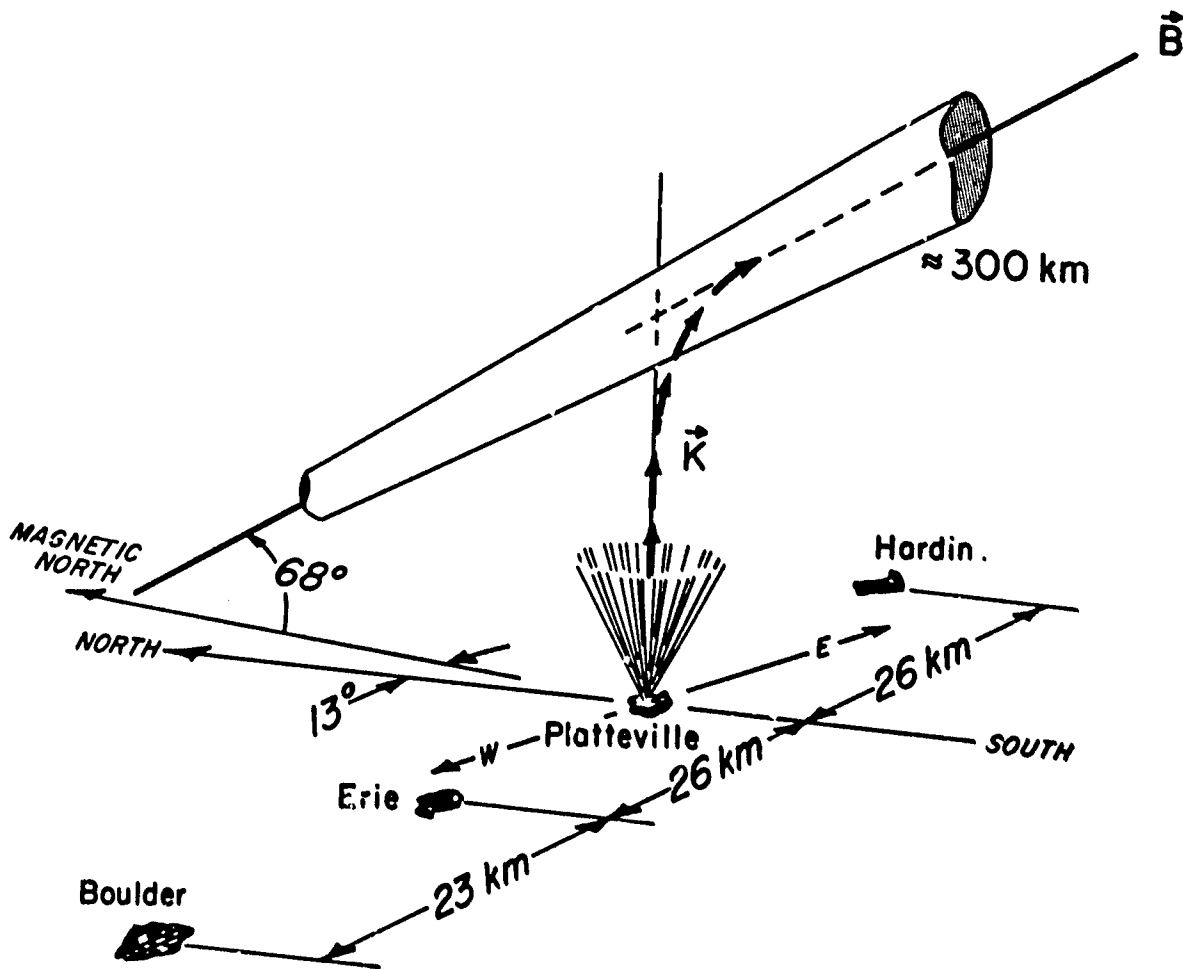


Fig.11 Schematic view of the Platteville transmitter facility (after Utlaut, 1970)

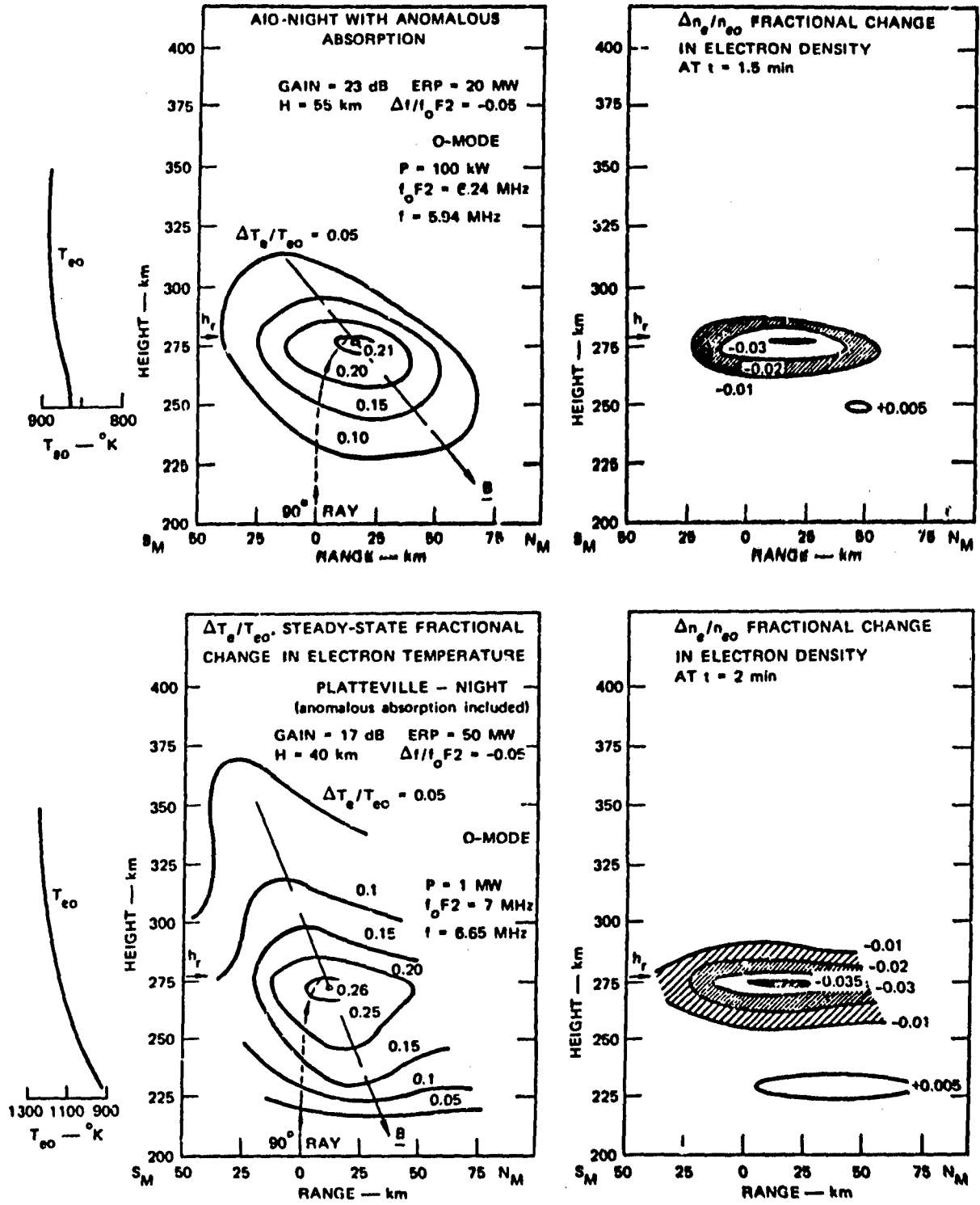


Fig. 12 Contours of calculated fractional change in electron temperature and density expected above Arecibo (upper) and Platteville (lower) (after Meltz)

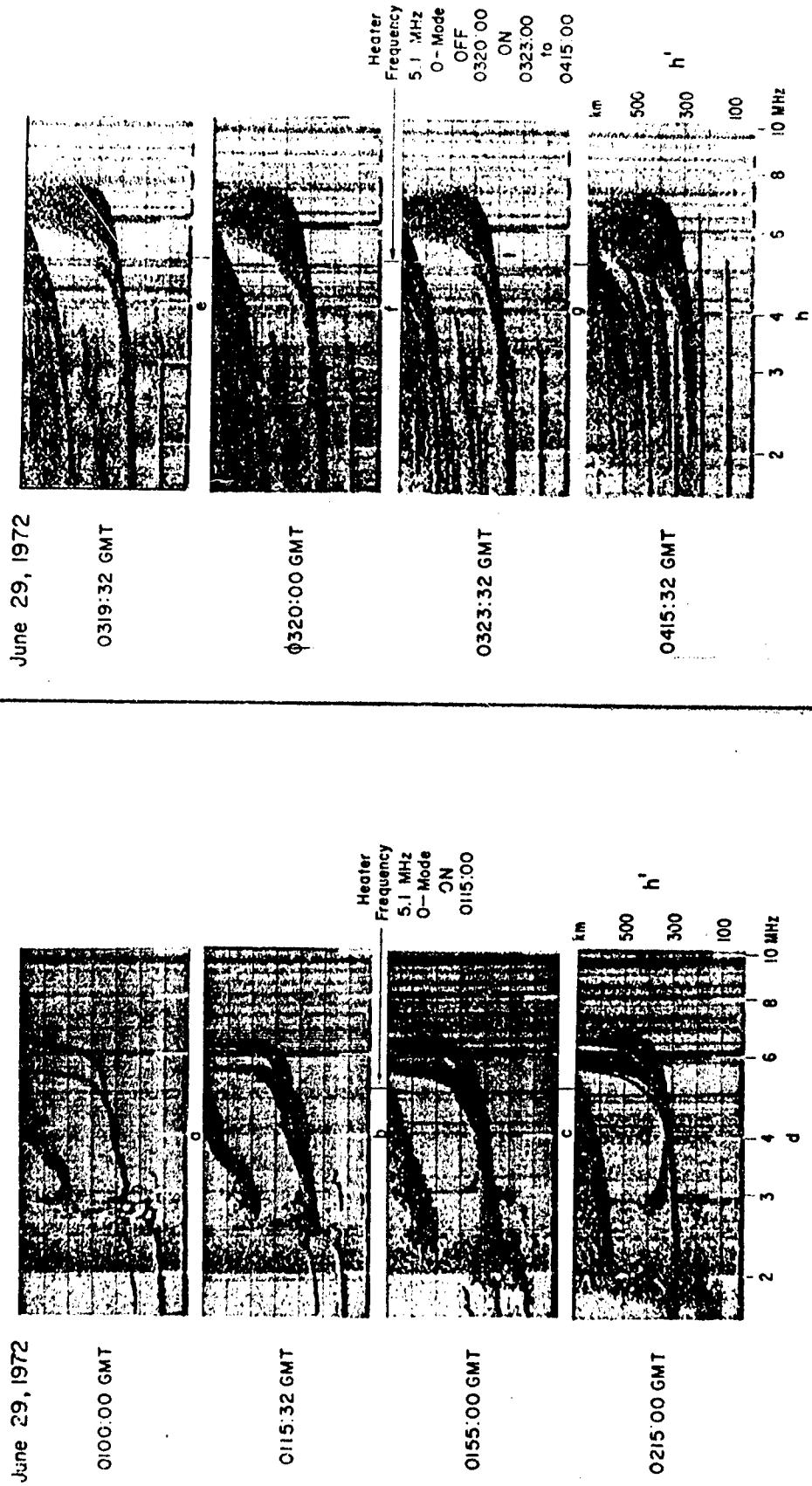


Fig. 13 Ionograms taken at Erie illustrating artificial spread F, IF2 satellite trace and wide-band attenuation resulting from the Platteville heater (after Utlaut, 1975)

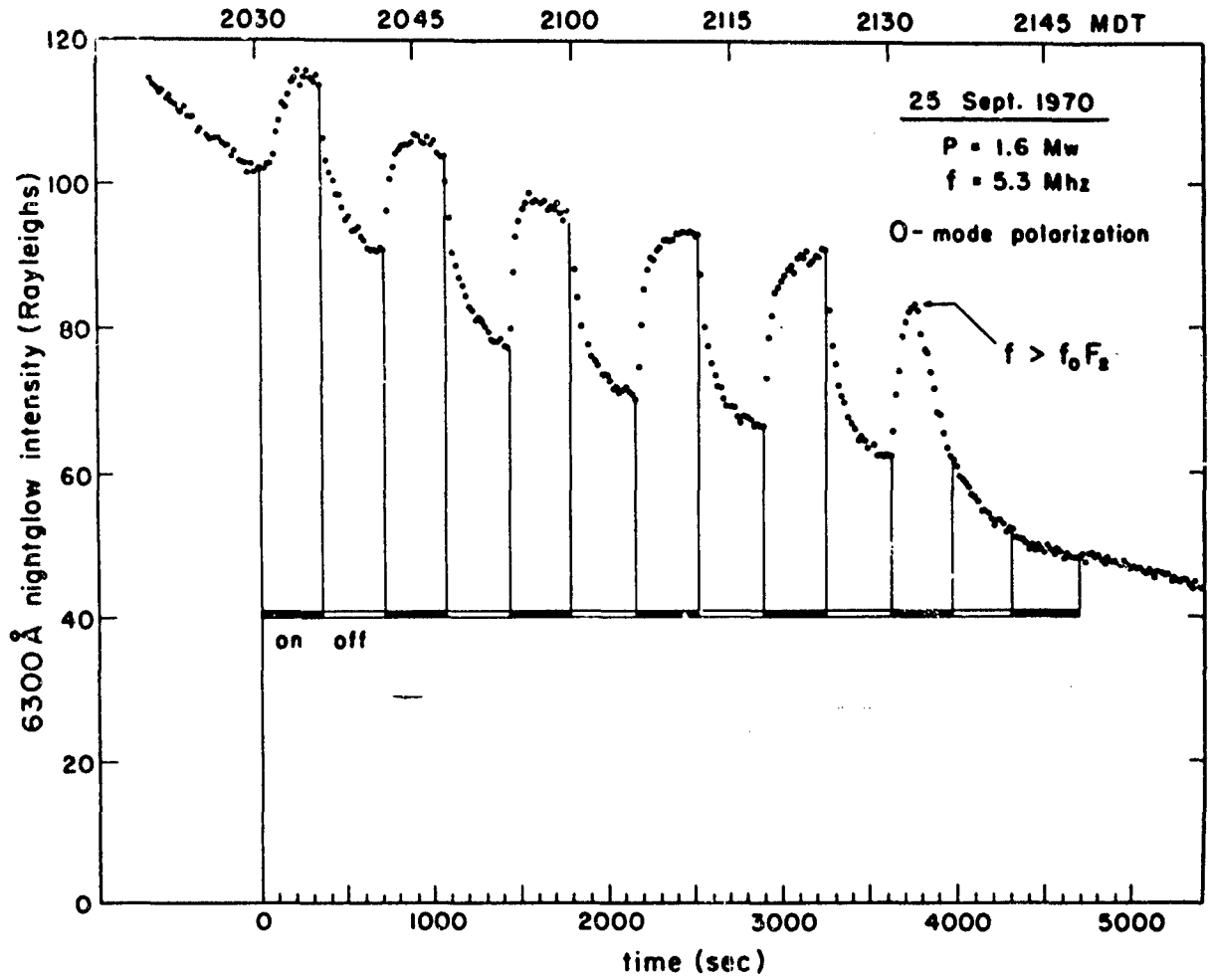


Fig.14 Intensity modulation at 6300 Å by cycling the o-wave heater on and off at 6-minute intervals

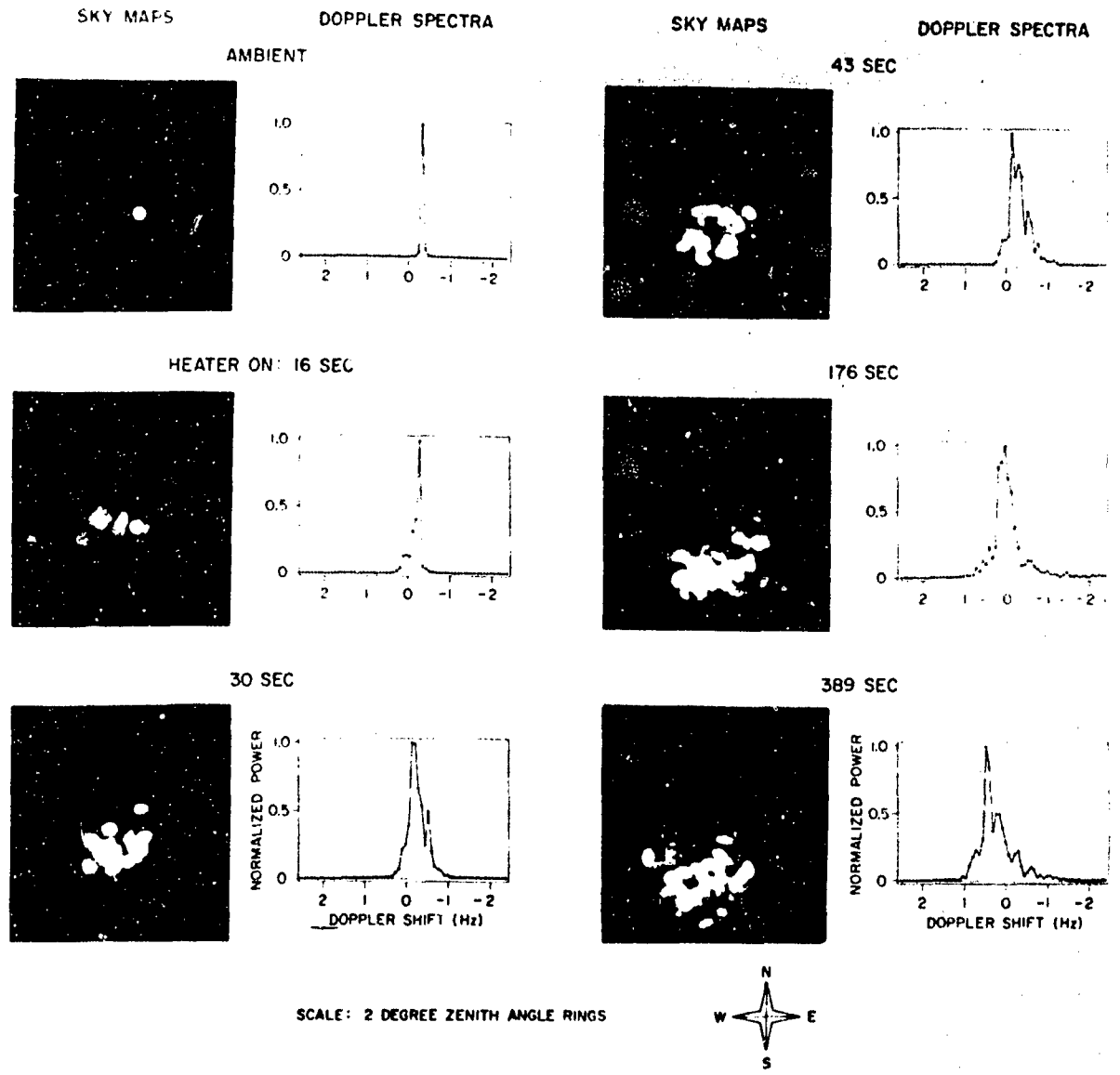


Fig.15 Time sequence of Doppler spectrum and sky map pairs taken during a heater turn-off (after Allen, Thome and Rao, 1974)

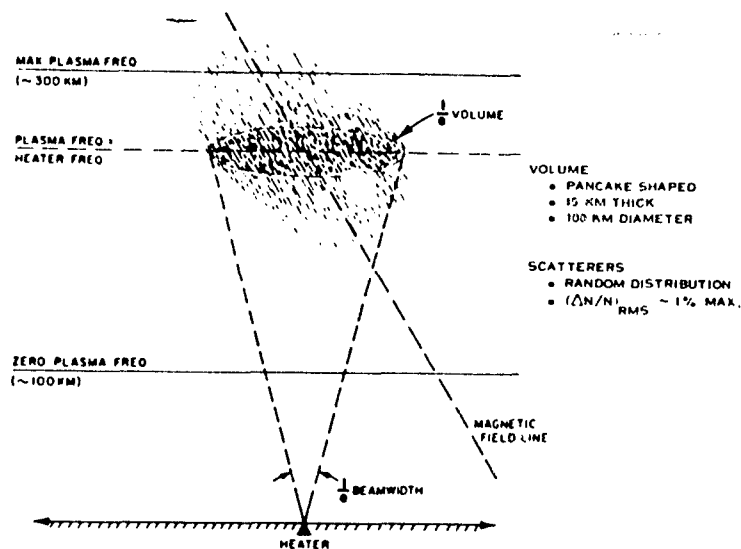


Fig.16 Physical model of Platteville heater-induced electron density irregularities for FAS (after Rao and Thome, 1974)

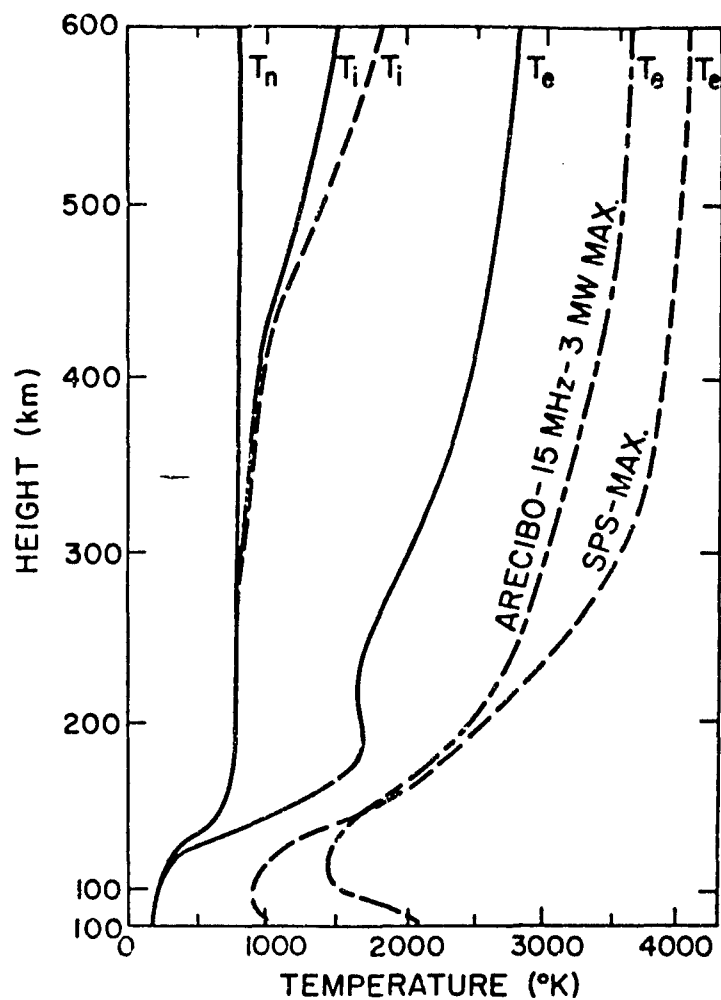


Fig.17 Vertical profiles of electron temperature. The dashed curve is for heating by the satellite power station and long-and-short dashed curve is for heating by a 15 MHz, 3 MW Arcibo heater. T_n , T_i are the neutral gas and ion temperatures for both SPS and Arcibo (After Perkins and Robie, 1978)

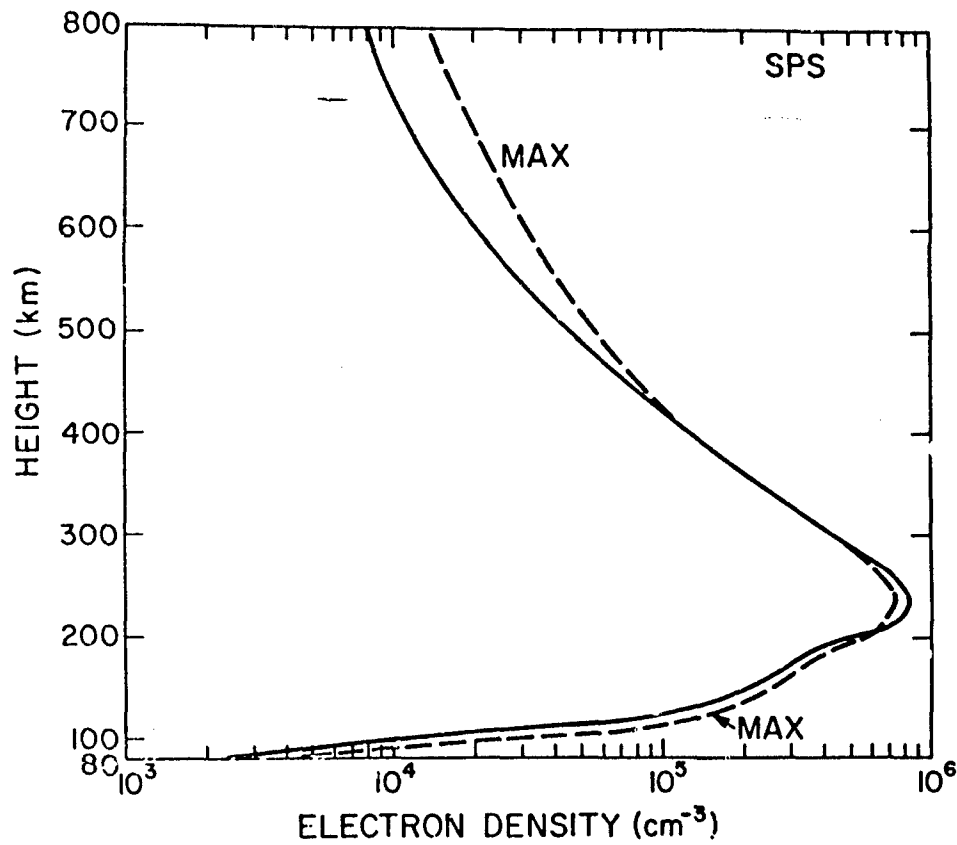


Fig.18 Calculated vertical profiles of electron density (cm^{-3}). The solid curve is the undisturbed day profile and dashed curve is that three hours after heating by SPS (after Perkins and Roble, 1978)

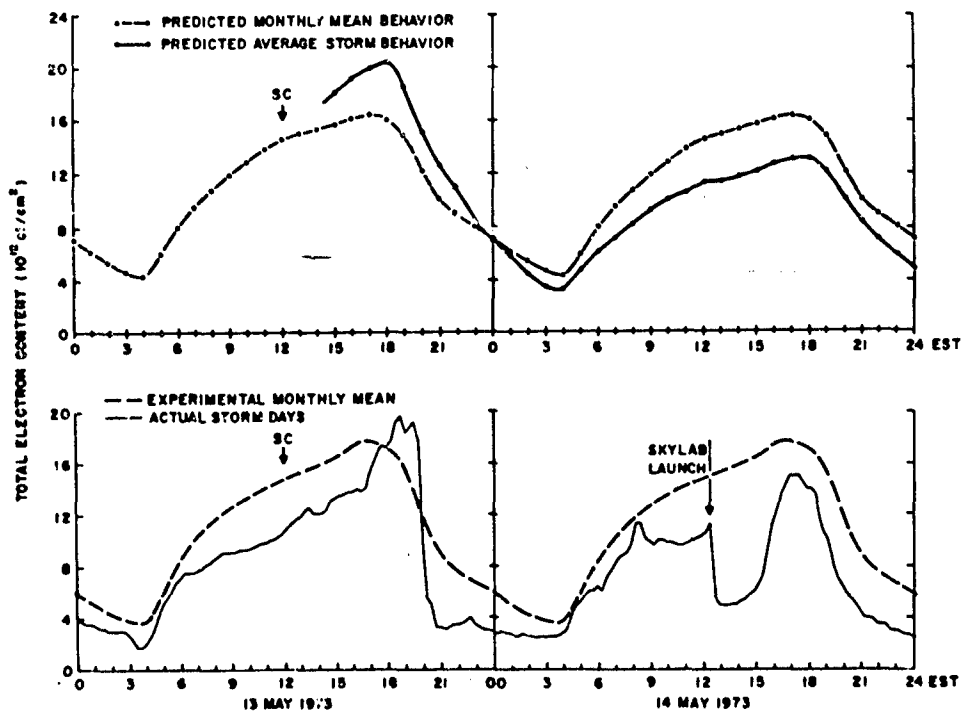


Fig.19 A comparison of the Sagamore Hill predicted monthly mean total electron content and its average storm-time correction for May 1973 with the observed monthly mean and the behavior during the geomagnetic storm period May 13-14. The Skylab depression is considerably larger than the natural depletion

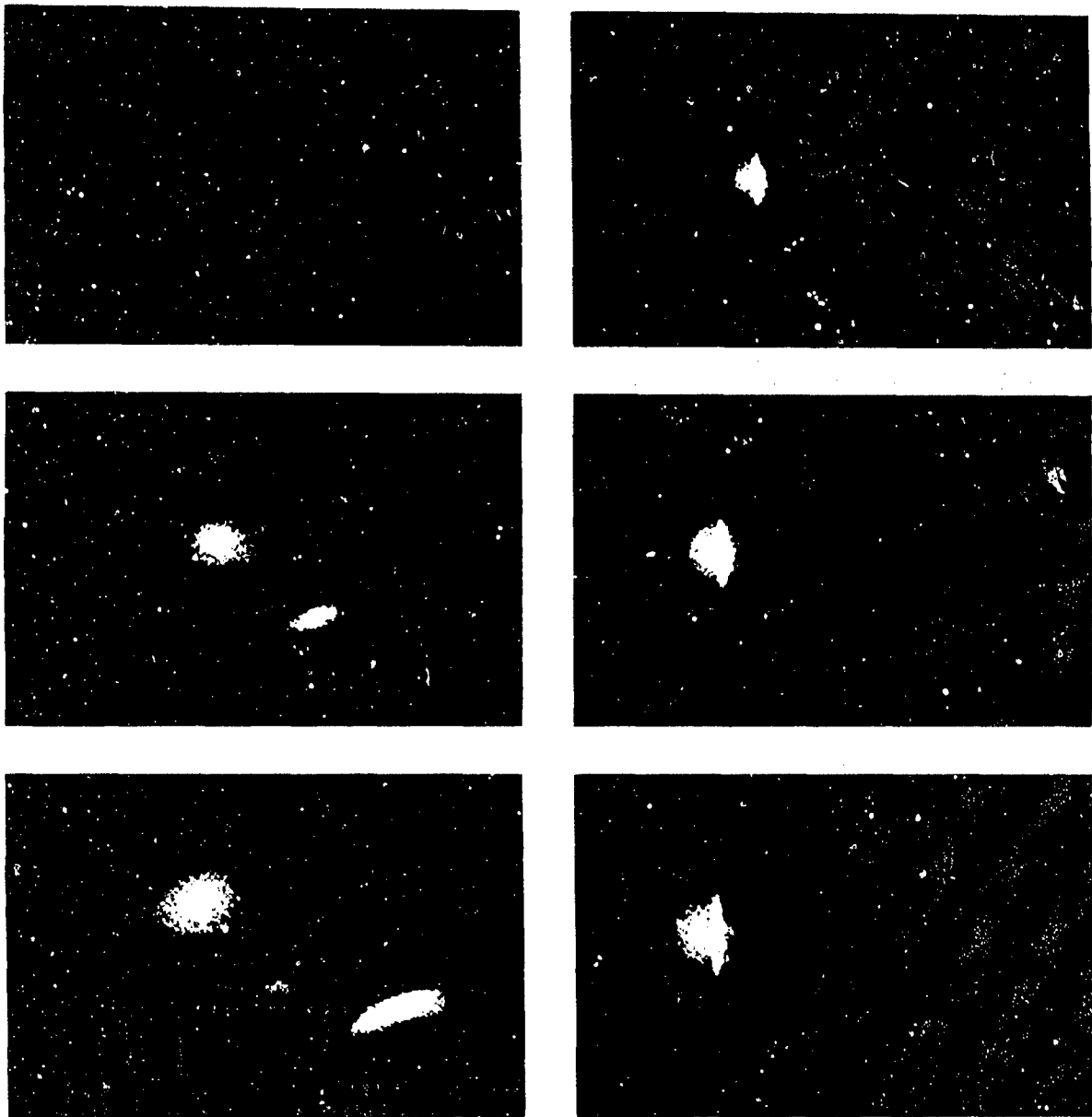


Fig.20 Photographs of barium ion (elongated shapes) and neutral strontium (spherical shapes) at three subsequent times (after Haerendel, Lüst and Rieger, 1967)

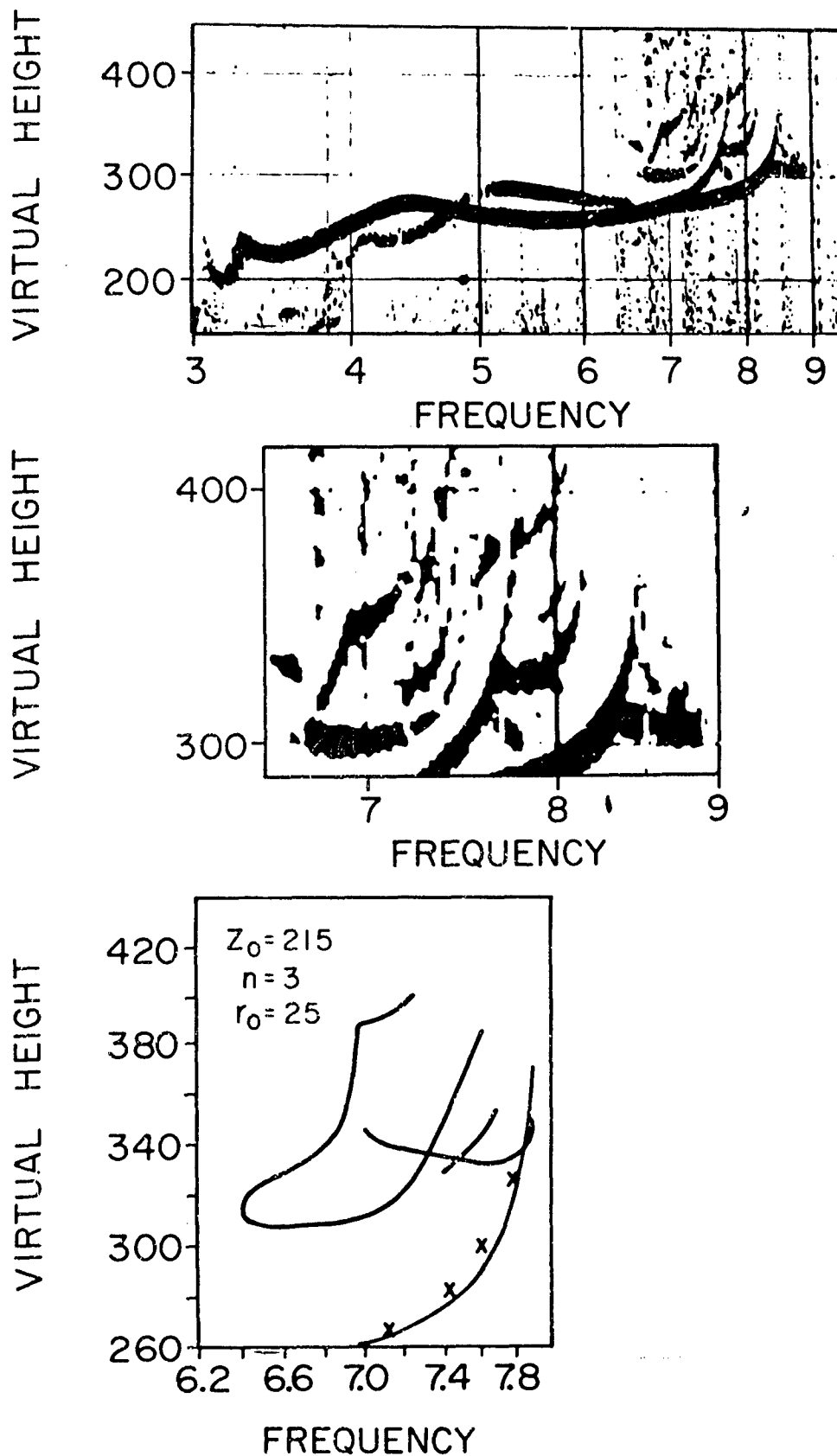


Fig.21 Ionogram taken during Firefly MARTHR

- (a) Portion between 3 and 10 MHz
- (b) Enlargement of section between 6.2 and 7 MHz showing oblique echoes from a "hole" in the ionosphere.
- (c) Synthetic ionogram obtained by ray tracing. The lowest curve is that for vertical incidence; the x's are corresponding observed points.

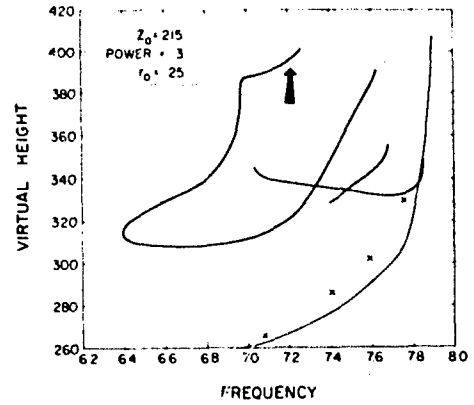
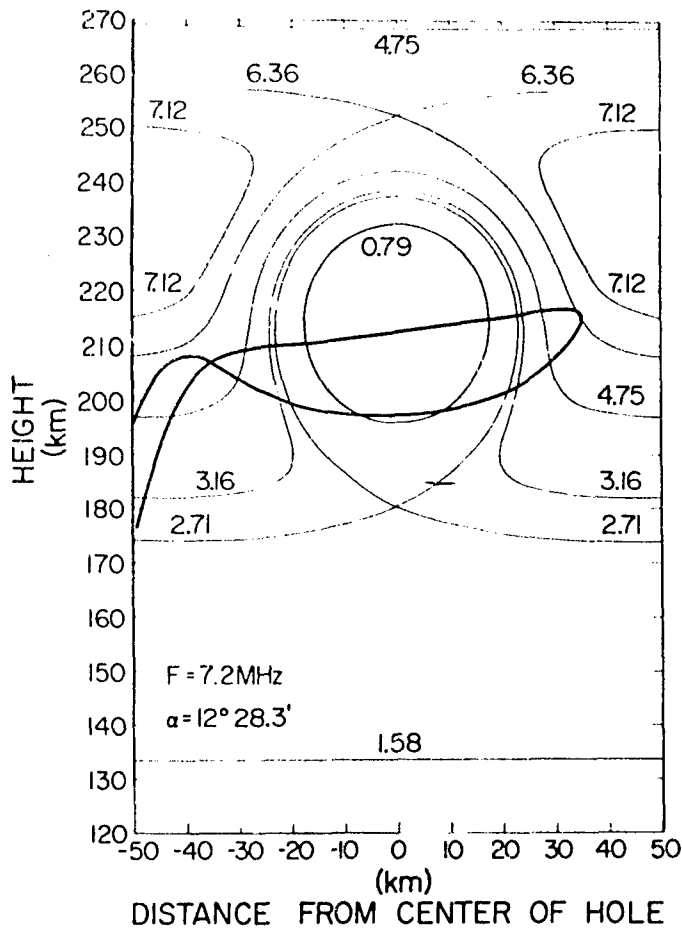


Fig.22 Path of 7.2 MHz ray entering ionosphere at angle of $12^\circ 28.3'$ from the vertical

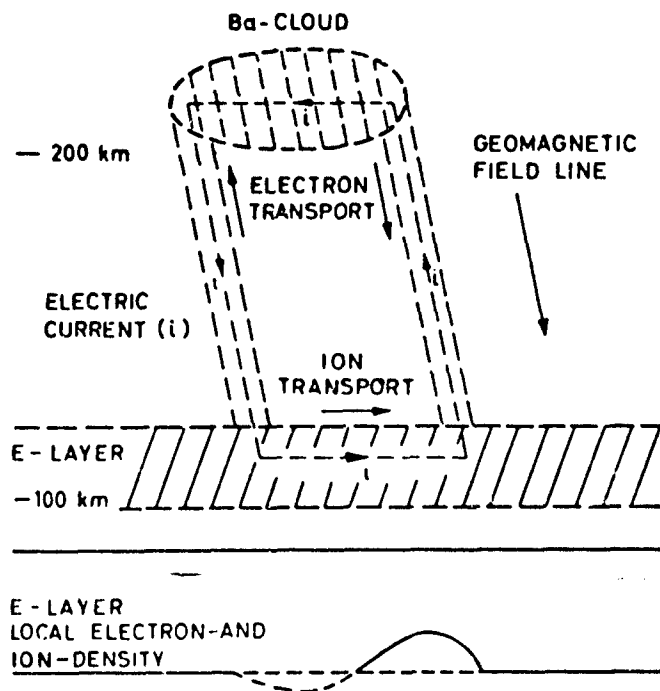


Fig.23 Possible current flow between F-region cloud and its image in the E region (after Stoffregen, 1970)

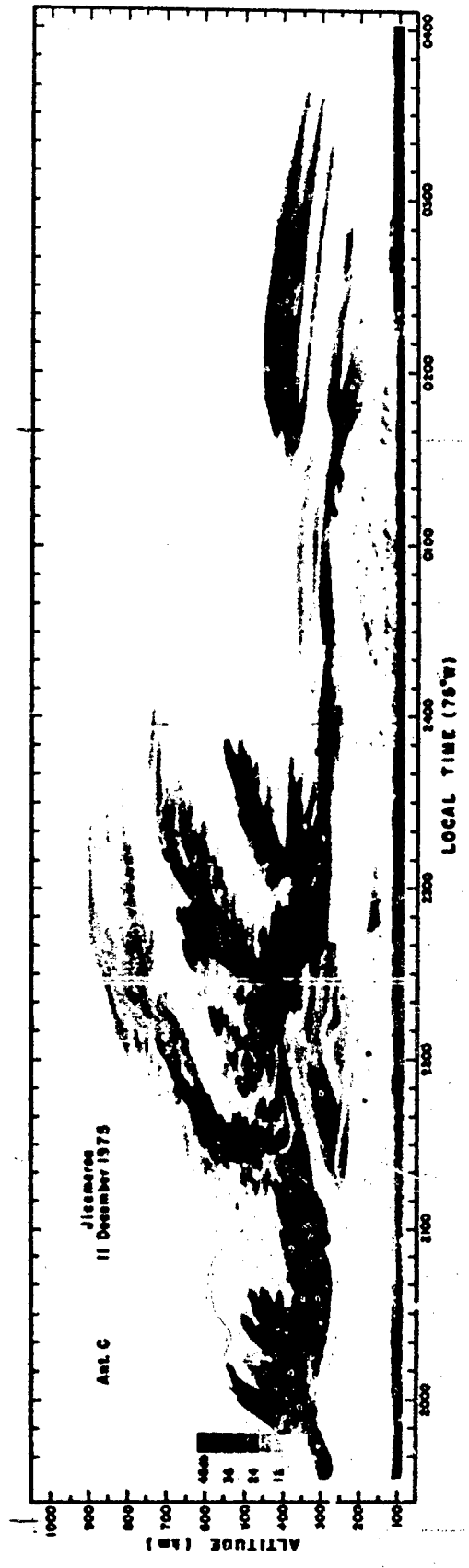


Fig. 24 Radar echoes from equatorial spread-F at Jicamarca showing plumes of rising irregularities (Woodman and La Hoz, 1976)

THE PROPAGATION OF LOW AND VERY LOW FREQUENCY RADIOWAVES

by

T.B. Jones

Physics Department, University of Leicester, UK

1.1 Basic Concepts

The propagation of low (30 to 300 kHz) and very low (10 to 30 kHz) radiowaves has been of considerable importance since the earliest days of radio. Radiowaves in these frequency bands are reflected from the lowest region of the ionosphere (D-region) which is normally penetrated by HF transmissions. Little attenuation of VLF and LF signals occurs on reflection in the ionosphere and consequently they propagate to considerable distances (as demonstrated by Marconi in 1901).

The great disadvantage of VLF/LF systems is the very limited bandwidth available and the high cost and low efficiency of the transmitting installations. Because of the inherent stability of this type of propagation it is used for worldwide navigation, timing and frequency comparison systems. VLF waves have relatively large penetration depths into both land and sea and they can therefore be used for subsurface communications.

1.2 The Breakdown of Ray Optics

In order to evaluate the performance of any radio system it is necessary to calculate the propagation characteristics of the signal. At VLF and LF the medium through which the waves propagate (i.e. the ionosphere) can vary appreciably within the space of one wavelength (one wavelength at 10 kHz is equivalent to 30 km). Conventional ray optics breaks down in these circumstances and "full-wave" solutions become necessary in which the wave fields are calculated at many points in the course of the wavelength.

When propagation takes place to great distances further complications occur in that a large number of ray paths can be established between the transmitter and receiver. This can conveniently be represented in terms of waveguide mode propagation, where the earth and the ionosphere form the walls of a spherical waveguide. A combination of full-wave and waveguide mode analyses enables the phase, amplitude and polarization of VLF and LF waves propagated to great distances to be determined for any type of ionospheric model and propagation path.

1.2.1 Full-Wave Methods

The differential wave equations governing the propagation of radiowaves in the ionosphere are linear and homogeneous, thus the sum of any solution is itself a solution. In the usual methods of calculation [1] the differential equations satisfying some field component of the wave are first formulated. Solutions are then obtained at great heights, well above the reflection levels, and these correspond to purely upgoing waves. Connection formulae are applied to obtain solutions down through the ionosphere. Below the ionosphere these are separated out into upgoing and downgoing waves. From these the reflection coefficients are calculated, which will depend on the polarization of the incident wave. In general, the incident and reflected waves do not have the same polarization and the reflection properties must be completely specified by the four parameters R_1, R_2, R_3, R_4 .

Numerical methods for full-wave solution of the wave equations have been extensively discussed in the literature [2,3]. These methods differ in detail but to illustrate the procedure the Pitteway solution is outlined since this has been widely employed by many groups of workers.

The equation of motion of a single electron in the wave field may be written [4] as

$$P = \epsilon_0 M E \quad \dots (1)$$

where the susceptibility tensor M is given by

$$M = -X \begin{vmatrix} U & jY_z & -jY_y \\ -jY_z & U & jY_x \\ jY_y & -jY_x & U \end{vmatrix}^{-1} \quad \dots (2)$$

The conventional notation of the magneto-ionic theory [1] is used throughout.

Following Pitteway, the coordinate axes are defined by the earth's field and are chosen so that Y_x vanishes. Y is assumed constant at all heights.

The four wave field equations can be written in matrix form

$$e' = -jkTe \quad \dots (3)$$

where e is the column vector

$$e = \begin{vmatrix} E_x \\ -E_y \\ H_x \\ H_y \end{vmatrix}$$

and \mathbb{I} is a 4×4 matrix.

$$\mathbb{I} = \begin{pmatrix} -j\ell B_1 & \ell B_2 & \ell m B_3 & 1 - \ell^2 B_3 \\ j m B_1 & -m B_2 & 1 - m^2 B_3 & \ell m B_3 \\ -\ell m + j B_4 & 1 - \ell^2 - B_5 + \frac{X Y_y^2}{\alpha} & -m B_2 & \ell B_2 \\ 1 - m^2 - B_5 & -\ell m - j B_4 & -j m B_1 & j \ell B_1 \end{pmatrix}$$

where

$$\begin{aligned} B_1 &= X Y_y / \alpha \\ B_2 &= X Y_y Y_z / \alpha \\ B_3 &= U(U^2 - Y^2) / \alpha = 1 + X(U^2 - Y_z^2) / \alpha \\ B_4 &= X Y_z (U - X) / \alpha \\ B_5 &= X U (U - X) / \alpha \\ \alpha &= U(U^2 - Y^2) - X(U^2 - Y_z^2) \end{aligned}$$

The incident wave normal has direction cosines ℓ , m , n and the functional dependence comes through the variation of X and U with height.

The four linear differential equations (3) are integrated numerically. The computer forms derivatives of (3) at the starting values (at great heights) and uses these to calculate the wave fields at a slightly lower height. Fourth-degree polynomials are used to fit the solutions of the differential equations by calculating four separate sets of derivatives at each height. The process is then repeated towards the bottom of the ionosphere until free space is reached. Here the solution is separated into upgoing and downgoing components and the reflection and conversion coefficients determined.

Care must be taken during the numerical integration to ensure that the two solutions remain independent. Suitable constraints are applied to the solutions at each integration step so that the second solution is not swamped by the dominant solution. Full details of these techniques are given by Pitteway [3].

Various other types of numerical full-wave analysis have been developed (e.g. [5]). They all enable the complex reflection and conversion coefficients to be determined for any given height distribution of electron density and collision frequency. Parameters such as the wave frequency, path azimuth, angle of incidence, and geomagnetic field intensity are easily varied. Thus the reflection parameters of VLF and LF waves can be calculated for conditions representative of any time of day, season and geographical location. Clearly this technique provides a powerful aid in the design and operation of any VLF/LF radiowave system.

1.2.2 Waveguide Mode Propagation

The theory of VLF radiowave propagation in the terrestrial waveguide has been extensively developed by Budden [6], Wait [7] and others.

At these frequencies for long-range propagation the earth behaves like a good electrical conductor with a reflection coefficient approaching +1 while the ionosphere has a reflection coefficient approaching -1. It is convenient thus to treat the earth and the ionosphere as the two boundaries of a spherical waveguide and to consider propagation to great distances in terms of waveguide modes.

A vertical electric antenna situated on the surface of the earth will excite transverse magnetic waveguide modes (TM modes). For each mode there are three parameters which govern the characteristics of the mode, i.e. the attenuation rate in dB/m; the phase velocity of the mode, usually quoted relative to the velocity of light, v/c ; and the excitation factor Λ , which is approximately the ratio of the power launched into the earth ionosphere waveguide to that launched into a flat waveguide with perfectly conducting boundaries. To indicate how these parameters vary with frequency, Figs. 1, 2 and 3 show theoretically derived values by Wait and Spies [8] of v/c , attenuation and Λ for modes 1 and 2, for a representative model of the ionosphere boundary for both daytime and night-time with the lower boundary of the waveguide being sea water (effectively a perfect electrical conductor of conductivity, $\sigma_g = \infty$). In these curves the ionospheric boundary is represented by a conductivity parameter σ_r which varies in an exponential manner with height:

$$\sigma_r = (\sigma_r)_0 \exp \beta (Z - Z_0)$$

Z is a measure of distance above a reference level Z_0 where the conductivity parameter has a value $(\sigma_r)_0$ and β is a constant. The values of β suggested by Wait and Spies [8] to represent the day and night profiles of the conductivity of the lower ionosphere are 0.3/km and 0.5/km respectively.

From these curves a number of general features are immediately discernible which experimental results can test. Mode 2 suffers a larger attenuation than mode 1 and this difference is more marked for the lower frequencies. Also, the difference in the phase velocity between night and day conditions of mode 1 is larger at the lower than at the higher frequencies. This indicates that at large distances from a transmitter where mode 1 would be the dominant mode both by day and night, the diurnal phase delay

pattern should (a) increase in magnitude linearly with distance, and (b) have a larger magnitude the lower the frequency. Both these indications are borne out by the experimental results. For distances closer to a transmitter the effects of the second mode should become more marked. This is especially so at the higher frequencies since at these frequencies, as may be seen from Fig. 3, the second mode is more easily excited in the waveguide; at 20 kHz, for example, the excitation factor for mode 2 is some 10-15 dB greater than for mode 1 under night conditions while at 10 kHz they are more or less equally excited. Fig. 4 shows a theoretical estimate of the diurnal phase delay variation at 16 kHz based on the waveguide model stated above, where the reference heights for day and night are 75 and 88 km respectively. This theoretical curve shows the effect of the second mode in the departure of the curve from a linear form. Of special interest is the manner in which the theoretical curve fits the experimental data for distances in the 1000-3000 km range. A corresponding curve for 10 kHz is also shown, from which it is evident that the effect of the second mode is much smaller, due to (a) its larger attenuation rate under day conditions, and (b) the larger excitation factor of mode 1 at this frequency compared to 16 kHz.

The general characteristics of VLF propagation as outlined above have been derived from the theoretical approach pioneered by Wait [7] and Budden [6] and verified by experimental measurements. The theory was limited to the simple model of the ionospheric boundary. Experimental measurements, undertaken in connection with navigational aid development, indicated areas where theory could not account for measured data. Theoretical advances by Galejs [9] and Pappert [10] enabled an arbitrary ionospheric profile, together with an arbitrary terrestrial magnetic field, to be incorporated in the waveguide model. These, together with an appropriate choice of a lower ionosphere model, have allowed much better correlation between theory and experiment.

1.2.3 LF Propagation

The waveguide mode theory of propagation is useful when one is restricted to considering not more than, say, a few modes. This holds for frequencies less than about 30 kHz. At high frequencies it is more appropriate to view propagation in terms of wave-hops [11], though Johler [12] has developed a theory covering the frequency range from VLF to MF which considers propagation in terms of spherical wave functions.

In the wave-hop theory, the full-wave solution for propagation between a spherical earth and a concentric ionosphere can be expanded into a series of complex integrals. If these integrals are replaced by their saddle-point approximations the series can be identified as the ray-hop series of geometric optics, and thus these integrals are called wave-hops. The saddle-point approximation is inadequate near and beyond the caustic and in this area the wave-hops can be evaluated by numerical integration or by summing a residue series. Berry and Chrisman [11] represent the series in the form

$$E_{\text{--}} = E_0 + \sum_{j=1} R_j I_j$$

where E_0 is the groundwave and R_j is the ionospheric reflection coefficient as discussed earlier in this paper. The path integral I_j takes into account ground conductivity, path length, reflection height and earth curvature.

2 Propagation Characteristics of VLF/LF Radiowaves

Attention is now given to the experimental investigation of the propagation of VLF and LF waves via the ionosphere. Following Marconi's successful transatlantic transmissions in 1901, rapid progress was made in developing the LF band for communication purposes. The early experiments soon showed that the signal strength varied with time of day, and marked differences were noted in the signal strength received during day time and at night. However, it was not until the work of Appleton and Barnett in the mid-1920's that these changes were conclusively associated with changes in the reflecting layer. Much larger signals were received at night at all frequencies although deep fading did occur. Daytime conditions were found to be more stable, however, and choice of frequency was important as there was evidence suggesting that the signal strength increased with decreasing frequency. The transition from day to night and vice versa was not a smooth one and the signal strength passed through more than one maximum and minimum value.

In the presence of a reflecting layer, interference might be expected between the direct groundwave and the reflected signal. Hollingsworth [13], using a frequency of 21.4 kHz, demonstrated the interference as a series of well-defined maxima and minima of signal strength with increasing distance from the transmitter. From these observations he deduced an equivalent height of 75 km for the reflecting layer for summer midday conditions. Propagation anomalies associated with solar and magnetic disturbances were also noted. The influence of the earth's magnetic field was appreciated even at this early stage and Round et al. [14] noted that propagation from east to west was more difficult than from north to south.

In the 1930's the use of VLF/LF radiowaves for communication purposes declined although there was great interest in developing low frequency techniques for studying the lower ionosphere. The development of atomic frequency standards in the 1960's allowed the phase stability of VLF propagation to be fully exploited and led to a renewed interest in the VLF band.

2.1 Undisturbed Conditions

Comparison of the phase of the downcoming skywave with that of the direct groundwave provides an interferometer technique which allows accurate measurements of the changes in the apparent height of the reflecting layer [15]; a typical example of these results is reproduced in Fig. 5, and shows changes of phase with time of day of the 16 kHz skywave received at a distance of 90 km from the transmitter. The phase changes behave in a very regular manner and if there is no phase change on reflection, then the

phase variations correspond to the variations of the reflection height of the lower ionosphere. During the day this behaviour is very regular and shows a weak solar zenith angle dependence which can be represented as

$$h = h_0 + A(t) \log_e (\sec \chi)$$

h and h_0 are the apparent heights of reflection when the sun's zenith angle is χ and zero degrees respectively. $A(t)$ is a constant for any given day.

The change in apparent height from day to night at 16 kHz was found to be 17 and 13 km for summer and winter conditions respectively. On frequencies near 100 kHz the change during the day-night transition in winter is about 7 km, while in summer the absorption of the signals is so large that no measurements could be made.

In addition to these steep incidence observations, measurements were made to distances of up to 1000 km. Up to 500 km the 16 kHz observations were very similar to the steep incidence results; however beyond this range the phase of the signal starts to advance about 1 hour before sunrise and remains fairly constant during the day, showing very little zenith angle dependence. These results have been interpreted in terms of two reflecting layers in the D-region where the lower layer reflects the waves at distances of 500 km or more. The behaviour of the two layers is different and thus suggests that they are formed by different mechanisms. Similar results were obtained using higher frequencies.

Detailed investigations of the propagation of LF waves to distances of up to 1000 km indicate that the behaviour of radiowaves in the 100-700 kHz band can be quite different to that at lower frequencies. Marked fading effects were observed at night and these frequencies were also sensitive to transient disturbances in the D-region. The variation of signal strength as a function of distance from the transmitter shows many maxima and minima as a consequence of interference between ground- and skywaves; this is illustrated in Fig. 6 for 85 kHz transmissions in the UK [16].

Studies of VLF/LF wave propagation at high latitudes have been made by Belrose and co-workers and very large disturbances are noted during geomagnetic storms [17]. At very high latitudes the diurnal phase and amplitude variations are considerably modified since some part of the propagation path remains entirely sunlit or in darkness for long periods. Many of these unusual features have been commented on by Belrose [17].

In all these experiments the absorption of the LF waves was found to be considerably greater than for the VLF waves. Bracewell et al. [16] studied the frequency dependence of the reflection coefficients. Below 20 kHz the variation from night to day is from a coefficient of 0.50 to about 0.10 in summer, whereas at 100 kHz, for the same conditions, it varies from 0.20 to a value less than 0.0001. During winter day-time the medium is a much better reflector, giving reflection coefficients of 0.35 (< 20 kHz) and 0.03 (~ 100 kHz). As the path becomes more oblique the reflection coefficient increases to a maximum at grazing incidence.

The phase and amplitude variations of VLF waves propagated to great distances have been studied extensively [18]. The very marked changes which occur in the diurnal pattern of phase variation has been summarized by Belrose [17] and is reproduced in Fig. 7. It is evident from the figure that the greatest phase changes occur at sunrise and sunset and these phase transitions have been extensively studied [19]. In general, the sunrise/sunset behaviour has been explained in terms of waveguide modes converted by the sunrise/sunset discontinuity in the ionospheric boundary of the earth-ionosphere waveguide interfering with those which propagate through the discontinuity unmodified. The propagation of VLF waves over high latitude paths exhibits some novel features since the diurnal changes are produced when only part of the path is illuminated. Some interesting mode structures can occur in these cases.

2.2 Disturbed Conditions

The lower ionosphere is sensitive to a number of geophysical disturbances such as those resulting from solar flare and magnetic storm activity. During flare conditions, the solar X-ray flux is enhanced and additional ionization is produced in the D-region. The effective reflection height is decreased and a phase advance is noted on short propagation paths. On certain long propagation paths a phase retardation is noted during flare activity and can be explained by waveguide mode interference [20]. In addition to the phase anomalies, the amplitude of the signal is also affected. The exact form of the amplitude change can be quite complex and depends on both the path and the frequency.

In contrast to the short period-disturbances induced by the flare enhancement of solar X-rays a number of long duration disturbances are also observed.

On high latitude paths (> 60°) phase and amplitude anomalies are observed during solar cosmic ray events. The cause of these events, which last for several days, is enhanced ionization of the D-region by solar protons in the energy range 80-100 MeV which are emitted during solar flares. In general this produces a lowering of the reflection heights of the VLF and LF waves and a corresponding change in the received phase. The night-time phase is depressed and the diurnal phase variation can disappear entirely. The night-time amplitude is less than normal but during the day the signal level is normal or even increased. These effects are dependent on the latitude of the propagation path.

Perhaps the best known disturbance effects on VLF/LF propagation are those associated with geomagnetic storms. During magnetic storms, anomalies are produced in both the phase and amplitude of VLF and LF waves propagated over both short and long paths. These events are of long duration, lasting for up to ten days or more. The main features associated with the storm activities at LF have been summarized by Lauter and Sprunger [21] who note that the sudden commencement of the geomagnetic storm does not affect the received signal strength. The main phase of the storm produces deep fading at night and this is known as the primary storm effect. No daytime anomalies are noted during the main phase of the storm. For

large storms high absorption sets in 3 or 4 days after storm commencement and continues for several days; this is the so-called storm after-effect. Similar behaviour has been noted on VLF signals propagated at steep incidence. The phase of the VLF signals is sensitive to storm effects and phase advances are noted, particularly at night, as shown in Fig. 8. For long-path VLF propagation both the night- and daytime phase is advanced and the regular day/night transition is displaced. Further, anomalies in the phase and amplitude of VLF and LF propagation have been reported which are related to changes in the temperature at stratospheric heights (i.e. 1 mb pressure level). The phase of both LF and VLF signals are found to be advanced during some periods in winter when anomalies in the D-region electron density exist. These winter anomalies, first noted as increases in the absorption of high-frequency radiowaves, are related to stratospheric warmings, and deviations from the normal VLF and LF diurnal patterns have been noted during these events.

Propagation anomalies are also produced by meteor showers, nuclear detonations and during solar eclipse. These are transient disturbances and their magnitudes are normally much less than the normal diurnal changes. For this reason they are not considered to be major disruptive factors in practical VLF/LF propagation systems.

2.3 Applications of VLF/LF Propagation

When dealing with communication or navigational radio systems in the VLF to LF bands, which operate over distance of 1000 km or more, the influence of the ionosphere on the propagation of the radiowaves, which carry the information necessary for communication or navigation, becomes very marked. While it is true that this type of long-range circuit can operate only because the ionosphere exists, the variability of the ionosphere is the major cause of the unreliability of such systems.

In the case of long-range radio navigational aids, it is usually the relative phase of transmitted signals that is of prime importance and it is the prevailing ionospheric conditions, which govern the variability of the phase delay of the transmitted signals, that ultimately define the accuracy and reliability of such systems. Radio aids to navigation such as Decca (70-130 kHz) and Loran C (100 kHz) give remarkable accuracy while the received signals are within groundwave propagation range. When ionospheric propagation starts to make a contribution to the received signal the accuracy of the system deteriorates markedly.

As examples of this type of application one VLF (Omega) and one LF (Loran C) navigation system will now be described in some detail and the propagation limitations discussed.

3 The Omega Navigation System

3.1 Basic Concepts

Omega is a world-wide navigational aid [22] using frequencies in the 10-14 kHz band, at present being operated by the US Navy. A pair of transmitting stations provides the navigator with a family of hyperbolic lines-of-position (l.o.p.), and eight transmitting stations with 5000-6000 km baselines will give global coverage. The eight transmitters, named A, B, C ... H, will radiate the frequency format shown in Fig. 9. All transmitters are phase-synchronized and repeat their individual radiated format every 10 secs, the 10 second period beginning at 00.00 hrs and synchronized to UT2.

The 10.2, 11 $\frac{1}{2}$ and 13.6 kHz transmissions are the basic navigation frequencies; other radiated frequencies, unique to each transmitter, may be used for navigation by distance measurement based on a cycle-counting technique.

The Omega frequency of 10.2 kHz is accepted as the basic frequency for navigation and charts depicting Omega l.o.p.'s for a frequency of 10.2 kHz are presently available for most areas of the world. These 10.2 kHz l.o.p.'s have ambiguities spaced by 15 km on the baseline joining two transmitters and for marine use, where the vessel is slow moving, the resolution of these 15 km ambiguities can be achieved by dead reckoning means. However, if necessary, the 13.6 kHz transmissions could be utilized in conjunction with the 10.2 kHz transmissions to give ambiguous l.o.p.'s separated by some 45 km on the baseline.

The exact positions of these l.o.p.'s on a chart, relative to known geographic coordinates, are governed by the value of the propagation velocity, v , that is used for the appropriate frequency. For 10.2 kHz the standard value used is given by $c/v = 0.9974$ where c is the velocity of propagation in free space (299 792.5 km/s).

Since the velocity of propagation is a function of many geophysical parameters such as ground conductivity, direction of propagation, effective height of ionospheric reflection, the l.o.p.'s will vary about the charted values, both temporally and spatially. How can these variations be corrected and what is the final accuracy of the system are important questions for the ionospheric physicist.

3.2 Propagation Aspects in Omega

For frequencies appropriate to Omega the broad features of the propagation characteristics may be explicitly stated. Only two modes, namely modes 1 and 2, are of importance in the context of Omega, and over the frequency band covered, 10-14 kHz, mode 2 is excited more than mode 1 by some 1-4 dB. Further, mode 2 is propagated with a higher phase velocity than mode 1 and hence, as the modes travel away from a transmitter, they will move in and out of phase with one another, causing an interference effect which will be apparent in the magnitude of the resultant field strength. Fig. 10 depicts such an interference effect, measured on board a high speed aircraft, appropriate to the 10.2 kHz transmission from Omega

Trinidad under night conditions.

From the experimental and theoretical considerations of VLF propagation discussed earlier, the lower frequency band of 10-14 kHz has definite advantages over the higher frequencies for navigational purposes. The main advantage is that, due to the frequency dependence of the attenuation and excitation factors of the modes, the second mode perturbing effects are much smaller in this lower frequency band. At frequencies below 10 kHz the attenuation rates increase rapidly to high values. This, coupled with the economics of designing efficient ground transmitting aerials at this end of the band, effectively puts a lower limit of about 8 kHz to the optimum band for navigation use. These considerations have led to the Omega World-Wide Navigational System choosing its main frequency of transmission as 10.2 kHz.

Of particular importance to navigational purposes is the overall stability of propagation. This is best demonstrated by considering the long-term monitoring of a l.o.p. at fixed sites. Fig. 11 illustrates the monthly mean value and its variability (standard deviation) for the two l.o.p.'s (B-A) and (D-B) derived from the 10.2 kHz transmissions from Omega Trinidad (B), Omega Norway (A) and Omega New York (D). It is evident (a) the standard deviation of l.o.p.'s is small, being of the order 5 cels (1 cel is 1/100th of a lanewidth), and (b) there is a very marked dependence of the l.o.p. reading on time of day [23]. It is this characteristic of Omega to show small variability in its l.o.p.'s on a world-wide basis that gives rise to its widespread use as a navigation aid.

An important aspect of the Omega system is the ability to predict and correct for the 'stable' propagation effects. Swanson [24] has reviewed the techniques used to do this and only some aspects of this large problem are touched on here.

The modes excited by a VLF transmitter propagate with different phase velocities and consequently give rise to a series of maxima and minima in the field strength of the received signal as one moves away from the transmitter. As one travels through a minimum in the field strength pattern the phase of the received signal changes; the deeper the minimum the more rapid and greater is the phase change.

Under day conditions, at 10.2 kHz, one may experience up to $\pm 25 \mu\text{s}$ change in the time delay of the received signal as one passes through the deepest minimum in field strength. This would be equivalent to an error of 14 km in an l.o.p. over a range of some 200-500 km from the transmitter.

At night this modal interference can be more severe and it is possible at 10.2 kHz, for propagation towards magnetic east, for the second mode to dominate over the first mode beyond the position of the first minimum in field strength. Consequently, at a greater range, when the first mode is dominant, the phase error is at least one cycle (or an l.o.p. is in error by one position line, 15 km) when reference is made to single-mode propagation. This magnitude of errors occurs over a distance of some 400-700 km from the transmitter, smaller errors occurring at ranges out to some 2000 km from a transmitter.

Fig. 12 illustrates this effect for daytime conditions where the relative phase delay of the 10.2 kHz and 13.6 kHz transmissions from Omega Trinidad are plotted. This also shows the marked non-reciprocal propagation characteristics of VLF propagation where propagation towards the magnetic west is attenuated more severely than towards the magnetic east, the difference under day conditions at 10.2 kHz being some 4 dB/Mm (6 dB/Mm, west; 2 dB/Mm, east). This fact, together with the lower attenuation by night than by day, results in a 10.2 kHz signal propagating to the magnetic west being attenuated to a level comparable to the signal propagating to the magnetic east at some 10 Mm to the west of the transmitter. Thus as well as an area at the antipodes, there will exist an area, for transmitters situated in low latitudes, some 10 Mm to the magnetic west of the transmitter where the phase of the received signal may be unstable - due to the interference between signals arriving by more than one propagation path.

Disturbances in phase and amplitude occur during geophysical disturbances and these can be classed in two main groups. First there are sudden phase anomalies associated with solar flares. During 1968 some 350 SPA's were observed at Farnborough (UK) on the 10.2 kHz transmission from Omega Trinidad. The average maximum phase delay was 10 μs which corresponds to a change in l.o.p. at Farnborough of 1.5 km if the second path involved suffered no effect. If both paths are affected, the change in l.o.p. is less. It should also be noted that these large deviations occur only for a limited period (3-4 mins) near the maximum of the solar flare event.

The second class of disturbances is more infrequent than SPA's and refers to disturbances produced in the lower ionosphere over polar regions by high energy solar particles, in certain extreme cases extending down to latitudes lower than the auroral zone by some 5-10 degrees. While these disturbances are relatively infrequent, their effect on VLF propagation can last for several days. In 1968 ten such solar proton events, resulting in large disturbances to VLF propagation over polar regions, were observed in the U.K., occurring on a total of 43 days of the year. Similar to solar flare effects, no loss of signal is observed at 10.2 kHz during such disturbances and the phase delay decreases. The magnitude of this decrease during daylight conditions over the propagation path is a maximum on the first day of the event and slowly recovers to quiet conditions during the succeeding days. Maximum phase delays from 10-60 μs have been observed and, in a similar manner to solar flare effects, can be interpreted in terms of l.o.p. variations.

3.3 Lane Resolution

For sufficiently slow moving vehicles the ability to resolve the 15 km position line ambiguities of the 10.2 kHz transmissions is not paramount and reception of only one frequency may be sufficient for most purposes. With appropriate corrections for diurnal variations in the phase delay an accuracy approaching 1-2 km may be achieved. However, for quickly moving vehicles, use of three or more frequencies of transmission will probably be necessary in order to resolve completely all the ambiguous position lines. The three Omega transmission frequencies of 10.200, 11.333 and 13.600 kHz allow the 1133 and 1400 Hz resolving frequencies to be used for position line resolution, with corresponding position line spacings

of 135 and 45 km. The important question then arises of whether the phase variability of the resolving frequencies is sufficiently small to allow the appropriate position line in the next finer mesh of position lines to be unambiguously determined [25].

One of the main sources of phase variability in VLF propagation is that of interference between the two propagating waveguide modes. Because of the lower attenuation rates of the waveguide modes at night this interference effect will be strongest under these conditions. It is extremely difficult to measure the phase-delay variation with distance of a single carrier frequency, but the difference in phase delay between two close transmission frequencies as a function of distance is amenable to measurement and is, in fact, the required parameter to evaluate the variability of the resolving frequencies.

Some experimental results [25] indicate that the amount of second mode present at night at considerable distances from the transmitter (up to 7000 km) is very much greater than theory originally predicted (Fig. 13). In fact the magnitude of the phase-delay variations of these resolving frequencies under night conditions are such that the position lines laid down by the 1133 Hz frequency may not be resolved using the lower frequency. Under day conditions the corresponding phase-delay variability is smaller by nearly an order of magnitude and position line resolution is then entirely feasible.

3.4 Effects of the Earth's Surface

The major portion of the earth's surface is covered by water and, as far as VLF propagation is concerned, behaves as a perfect conductor. When propagation occurs over the land surfaces of the earth the waves propagate with higher attenuation rates but it is only in areas of extremely low conductivity, such as the ice-cap regions of the world, where the attenuation rates become excessive (of the order 20-40 dB/Mm) [26]. Loss of signal is then likely for paths traversing the Greenland ice-cap or Antarctica, and hence puts a limitation on the number of position lines available in areas close to such ice-caps.

The phase velocity of the propagating signal can also be affected when the waves cross a conductivity discontinuity on the earth's surface, such as a coast line. Indications are that in the context of the accuracy of Omega quoted in preceding sections this effect is not important, but may become so if use is made of Omega in its differential mode of operation. Fig. 14 illustrates the effects of the Greenland ice-cap on the phase and amplitude of signals transmitted from Omega Norway.

In propagating over large extents of land the phase velocity is decreased on its sea path value by some 0.05 - 0.10% where the conductivity lies between 10^{-2} and 3×10^{-3} S/m which is typical of the major portion of continents. Over a land path of some 5000 km this would result in an error of some 5 km. This type of error is probably amenable to being calibrated out of the system.

4 The Loran C Navigation System

4.1 Basic Concepts

Loran C is a very accurate navigation system which utilizes a frequency in the LF band (100 kHz). The system depends on reception of the groundwave signal and considerable reduction in position accuracy can occur if skywaves are received at the instant when the groundwave phase is measured. The general propagation characteristics of LF skywaves have already been discussed (section 2). It must be remembered that neither their phase nor their amplitude is as stable as for VLF waves and consequently LF skywave propagation cannot be used as successfully for navigation purposes as the VLF signals of the Omega system. To achieve the full accuracy of the Loran C system measurements are therefore confined to groundwave signals only.

The LF transmitting stations are grouped together in a 'chain', usually consisting of a 'master' and two or more 'slaves', and cover a geographical region of approximately 2000 km radius. The locations of the stations comprising the North Atlantic chain are indicated on the map in Fig. 15 as a typical example of a Loran 'chain'. The pulses transmitted from each of the transmitters are accurately synchronized and the position of the receiver is determined by measuring the time delay between the signals received from the different stations in the chain. Position fixing to within 150 m at ranges of 1800 km is typical for the system [27]. Each station transmits a unique coded pattern of pulses to ensure correct identification and to reduce mutual interference.

At the receiver the signal will consist of a pulse that has travelled along the earth's surface and a skywave component which will have been reflected one or more times in the ionosphere. This situation is reproduced in Fig. 16.

The transmitted pulse width is 250 μ sec and it has a steep leading edge rising to its full amplitude after 70 μ sec. In the receiver the time of arrival of the pulse is measured at the zero crossing of the third cycle of the 100 kHz carrier, i.e. 30 μ sec after the start of the pulse. This time can be measured with an accuracy of 0.1 μ sec. Thus interference between ground- and skywaves can only occur if the time delay between the two propagation paths is less than 30 μ sec. The propagation characteristics of the ground- and skywave signals are now described.

4.2 Groundwave Propagation

Away from the induction field of the transmitter the groundwave will be a surface wave whose amplitude and phase velocity will depend primarily on the conductivity of the earth's surface [28]. For propagation over sea water, with a conductivity $\sigma = 4$ mhos m^{-1} , to a range of 1000 km the phase velocity $v = 0.9995c$, where c is the free space velocity. At this range the attenuation is 10 dB in addition to

the spatial attenuation. For poorly conducting soil the corresponding values are $v = 0.9977c$ and $A = 26$ dB. For rough terrain even greater losses might be expected due to the changes in conductivity and mutual interference effects arising from the tilted surfaces. Detailed discussion of ground effects have been presented in the literature [29,30].

4.3 Skywave Propagation

LF radiowaves are reflected from the lowest region of the ionosphere (D-region) and their basic propagation characteristics have been described in section 2. It should be noted that the phase and amplitude of the reflected signals depend on the D-region electron density and collision frequency height profiles. Normal seasonal and diurnal changes will therefore be evident in these characteristics of the received signal. Since marked changes in the D-region electron density distribution occur during geomagnetic disturbances, the parameters of the received signal will also exhibit anomalies during these periods.

As indicated in section 1, simple ray theory cannot be used to calculate the propagation characteristics since the ionosphere can vary appreciably in the space of one wavelength ($\lambda = 3$ km). Mathematical techniques for dealing with these long wavelengths have been described in section 1.

4.4 Interference between Ground- and Skywaves

The relative time delay between reception of the ground- and skywaves at various ranges from the transmitter can be determined given a suitable model of the ionosphere. For propagation over sea water the time delay will never be less than $30 \mu\text{sec}$ for effective heights greater than 55 km. For propagation over land ($\sigma = 10^{-3}$ mhos m^{-1}) the corresponding height is 65 km. It should be noted that a small change in ionospheric reflection height may cause a large change in the distance at which interference can occur; however, for undisturbed night-time conditions interference should never occur.

The differences in propagation time have been calculated as a function of distance from the transmitter for both land and sea paths by Thrane and Larsen [31] and these results are reproduced in Figs. 17 and 18. Fig. 18 suggests that interference effects could seriously degrade system performance for land paths greater than about 1000 km.

At mid-latitudes phase stabilities of $\pm 1 \mu\text{sec}$ during daytime and from ± 4 to $\pm 8 \mu\text{sec}$ during night-time have been reported [32,33]. There is little information regarding performance at high latitudes but considerably poorer performance can be expected due to the influence of polar cap disturbances and the relatively low reflection heights of the 100 kHz signals in the polar ionosphere. In the case of a large polar cap disturbance changes in reflection height of as much as 30 km could occur, which would yield uncertainties in position fixing of approximately 10 km [31].

Loran C provides a highly accurate position system for ranges of up to about 1500 km; for greater ranges position accuracy can decrease because of the possibility of receiving skywave signals when the third zero crossing of the groundwave signal is measured.

5 Low Frequency Communications

The use of the low and very low frequency bands for communication purposes is restricted by the small bandwidth available and the slow data rates which this implies. A further restriction is the low radiation efficiency of the transmitters and the need for large, and therefore costly, antenna systems. However, the skywaves at these frequencies are much less affected by ionospheric disturbances than the high frequencies normally used for communications. The great stability, both in phase and amplitude, and the low attenuation rates involved combine to provide a very reliable though low data rate communications channel [34]. A further advantage at VLF is the rather deep penetration of these waves below the surface of the earth. Thus it is possible to receive VLF transmissions without being above the earth's surface, which is a major advantage in some applications.

The use of low frequency systems is particularly appropriate at high latitudes when frequent disturbances in the E- and F-regions of the ionosphere render HF communications notoriously unreliable, particularly during times of high sunspot activity. The low frequency systems are relatively unaffected by these disturbances.

At very low frequencies world-wide coverage can be obtained from a single transmitter and field strength can be calculated as indicated in section 1. This type of system can support only very low data rates but has the great advantage of very high reliability. In the LF band the service area is somewhat less, though the low attenuation rates (particularly at night) provide workable signals over many thousands of kilometres. One feature of LF propagation at night is the strong interference effects between sky- and groundwaves, particularly at ranges of up to about 1000 km. This situation is illustrated in Fig. 19. Difficulties can therefore arise if the receiver is located at a range from the transmitter corresponding to one of these minima. The use of more than one frequency channel can, however, usually resolve these difficulties since the two interference patterns will be mutually displaced.

The observations made concerning the VLF and LF navigation systems apply equally to communications on these frequency bands. They are invaluable for coverage of large areas with high reliability provided low data rates can be tolerated.

Summary

The distinctive features of VLF and LF propagation have been discussed and the specialized mathematical techniques necessary to calculate the propagation parameters described. Examples of VLF and LF systems, the Omega and Loran C navigators respectively, have been considered in detail in order to highlight the unique features of these long-wave systems. Some of the advantages and disadvantages of communications systems using these frequencies have also been noted.

7 References

1. Budden, K.G., Radiowaves in the Ionosphere, Cambridge Univ. Press (1961).
2. Barron, D.W. and Budden, K.G., The numerical solution of the differential equations governing the reflection of long radiowaves in the ionosphere, Pt III, Proc. Roy. Soc. A249, 387 (1959).
3. Pitteway, M.L.V., The numerical calculation of wave fields, reflection coefficients and polarizations of long radiowaves in the lower ionosphere, Pt I, Phil. Trans. Roy. Soc. A275, 219 (1965).
4. Banerjee, B.K., On the propagation of electromagnetic waves through the atmosphere, Proc. Roy. Soc. A190, 67 (1947).
5. Altman, C. and Cory, H., Application of thin-film optics to VLF radio propagation in the ionosphere, IEE Conf. Proc. No. 36, 98 (1967).
6. Budden, K.G., The Waveguide Mode Theory of Wave Propagation, Logos Press, London (1961).
7. Wait, J.R., Electromagnetic Waves in Stratified Media, Macmillan, New York (1962).
8. Wait, J.R. and Spies, K., Characteristics of the earth-ionosphere waveguide for VLF radio waves, N.B.S. Technical Note 300 (1964).
9. Galejs, J., Terrestrial Propagation of Long-Electromagnetic Waves, Pergamon Press, Oxford (1972).
10. Pappert, R.A., A numerical study of VLF mode structure and polarization below an anisotropic ionosphere, Radio Sci. 3, 219 (1968).
11. Berry, L.A. and Chrisman, M.E., The path integrals of LF and VLF wave hop theory, Radio Sci. 69D, 1469 (1965).
12. Jöhler, J.R., Spherical wave theory for MF, LF and VLF propagation, Radio Sci. 5, 1429 (1970).
13. Hollingsworth, J., The propagation of radio waves, J. Inst. elect. Engrs. 54, 579 (1926).
14. Round, H.J. et al., Report on measurements made on signal strength at great distances during 1922 and 1923 by an expedition sent to Australia, J. Inst. elect. Engrs. 63, 933 (1925).
15. Best, J.E., Ratcliffe, J.R. and Wilkes, M.V., Experimental investigation of very long waves reflected from the ionosphere, Proc. Roy. Soc. A156, 614 (1936).
16. Bracewell, R.N., Budden, K.G., Radcliffe, J.A., Straker, T.W. and Weeks, K., The ionospheric propagation of low and very low frequency radiowaves over distances less than 1000 km, Proc. Inst. elect. Engrs. 98, 221 (1951).
17. Belrose, J.S., Low and very low frequency radio wave propagation, AGARD Lect. Ser. No. 29, Ch. 4 (1968).
18. Burgess, B., The propagation of VLF waves over distances between 1000 and 3000 km, Radio Sci. 68D, 15 (1964).
19. Ries, G., Results concerning the sunrise effects of VLF signals propagated over long paths, Radio Sci. 2, 531 (1967).
20. Burgess, E. and Jones, T.B., Solar flare effects and VLF radiowave observations of the lower ionosphere, Radio Sci. 2, 619 (1967).
21. Lauter, E.A. and Knuth, R., Precipitation of high energy particles into the upper atmosphere at medium latitudes after magnetic storms, J. atmosph. terr. Phys. 29, 411 (1967).
22. Watt, D., VLF Radio Engineering, Pergamon Press (1967).
23. Swanson, E.R. and Tibbals, M.L., The Omega navigation system, J. Inst. Navigation 12, 1 (1965).
24. Swanson, E.R., Propagation effects in Omega, AGARD Conf. Proc. CP209, Ch. 15 (1976).
25. Burgess, B., Propagation effects and lane ambiguity resolution in Omega, Proc. Inst. elect. Engrs. 116, 1297 (1969).

26. Gary, J.H. and Crombie, D.D., Antarctic ice-cap attenuation rates of VLF signals determined from short and long great circle paths, *Radio Sci.* 7, 233 (1972).
27. Potts, C.E., Precise time and frequency dissemination via the Loran C system, *Proc. IEEE* 60, 530 (1972).
28. Watt, A.D., VLF Radio Engineering, Pergamon Press (1967).
29. Jöhler, J.R., Prediction of groundwave propagation time anomalies in the Loran C signal transmissions over land, AGARD Conf. Proc. CP 209, Ch. 12 (1976).
30. Horowitz, S. and Jöhler, J.R., Loran C/D coordinate prediction dependence on ground electrical properties, AGARD Conf. Proc. CP 209, Ch. 13 (1976).
31. Larsen, T.R. and Thrane, E.V., Ionospheric effects on Loran C in polar regions, AGARD Conf. Proc. CP 209, Ch. 14 (1976).
32. Doherty, R.H., Experimental observations and theoretical calculations leading to a model of the lower ionosphere, In: The Physics of the Ionosphere, Phys. Soc. Lond., p.428 (1963).
33. Shapiro, L.D., Loran C skywave delay measurements, *IEEE Trans. Instr. Meas.* IM-17, 366 (1968).
34. Williams, H.P. and Ince, A.N., Range of LF transmissions using digital modulation, *Proc. Inst. elect. Engrs.* 114, 1391 (1967).
35. Burgess, B. and Jones, T.B., The propagation of LF and VLF radiowaves with reference to some systems applications, *Radio elect. Engrn.* 45, 47 (1975).

Acknowledgements

The diagrams used in this lecture are based on the published work of the following authors:

Figs. 1-3	Wait, J.R. and Spies, K. [8]
Figs. 4,9-14,19	Burgess, B. and Jones, T.B. [35]
Figs. 5,6	Bracewell, R.N. et al. [16]
Figs. 7,8	Belrose, J.S. [17]
Figs. 15-18	Larsen, T.R. and Thrane, E.V. [31]

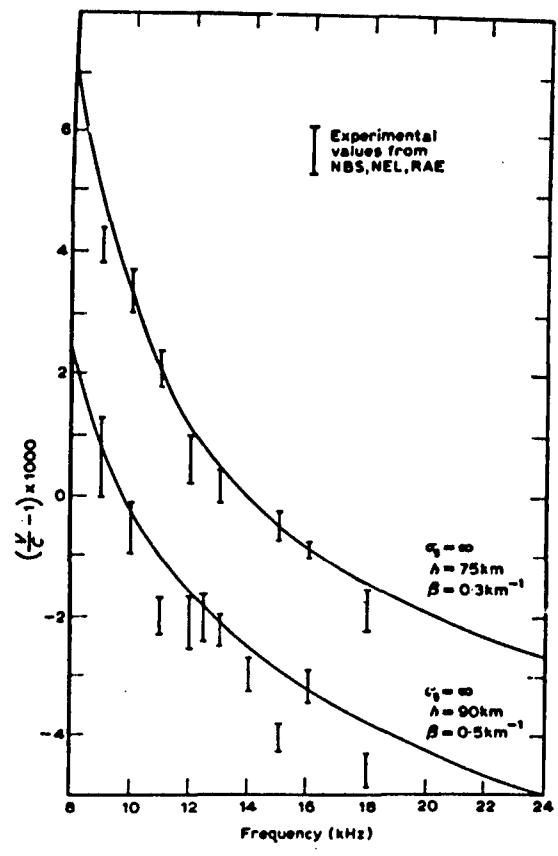


Fig. 1. Comparison of calculated and measured values of the phase velocity parameter (after Wait and Spies, 1964).

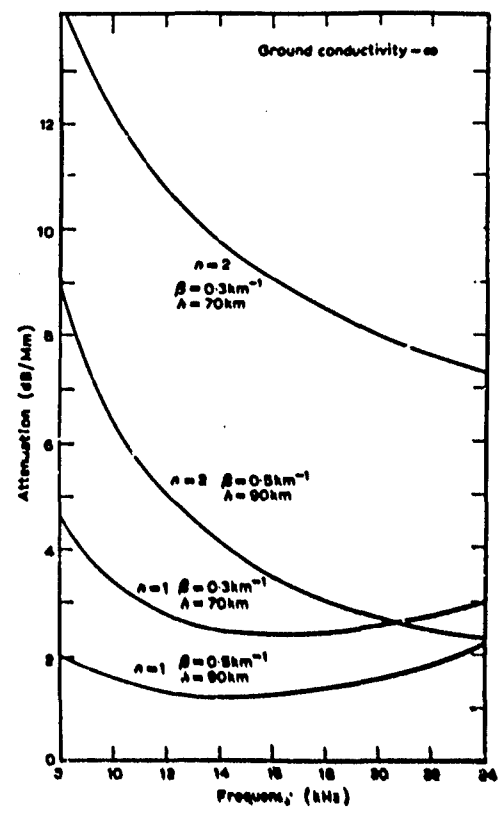


Fig. 2. Calculated attenuation rates for the first and second TN modes as a function of frequency (after Wait and Spies, 1964).

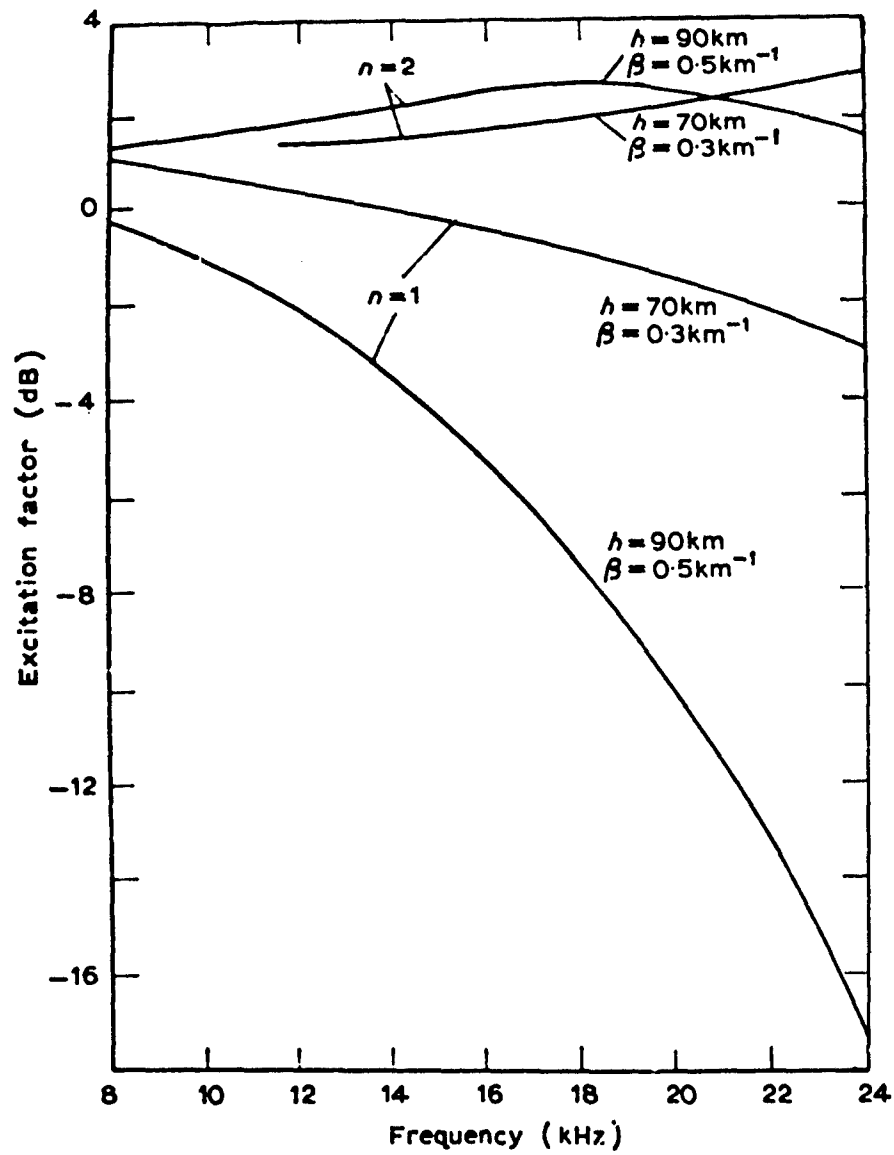


Fig. 3. Calculated excitation factors for day and night conditions (after Wait and Spies, 1964).

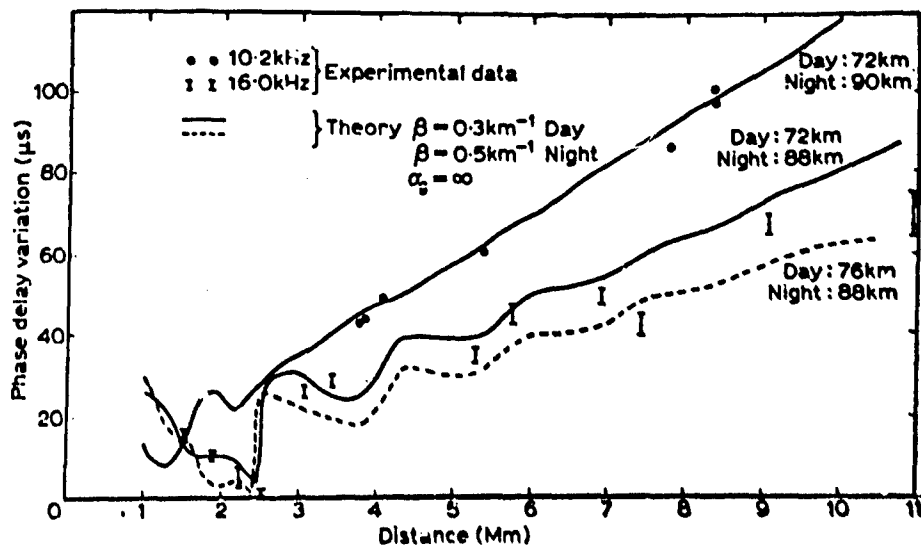


Fig. 4. Magnitude of diurnal phase delay variation versus distance for 10.2 kHz and 16 kHz (after Burgess and Jones, 1975).

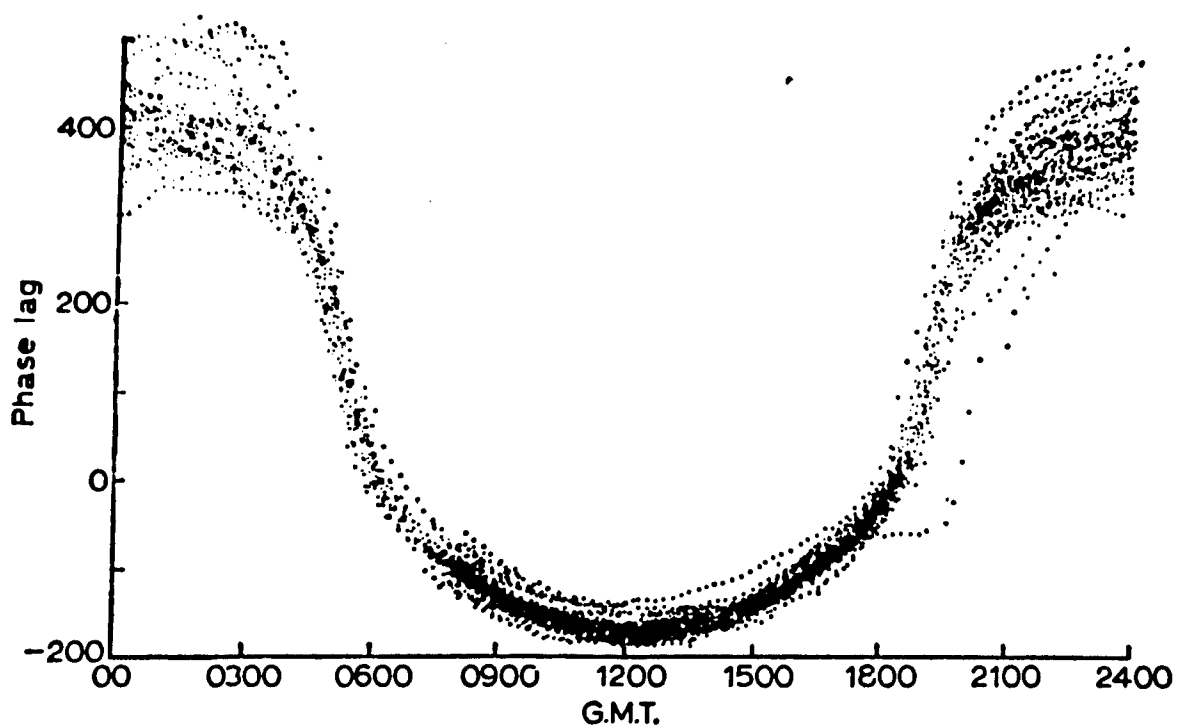


Fig. 5. Change of phase of skywave (16 kHz) with time of day (after Bracewell et al., 1951).

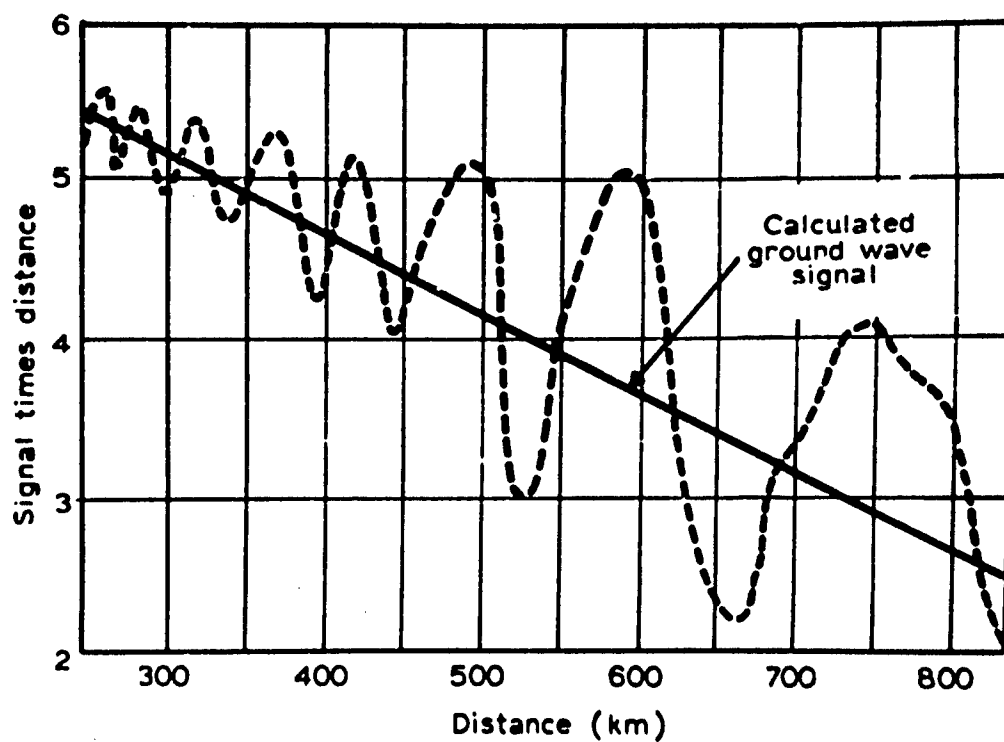


Fig. 6. Variation of signal strength as a function of distance from an 85 kHz transmitter (after Bracewell et al., 1951).

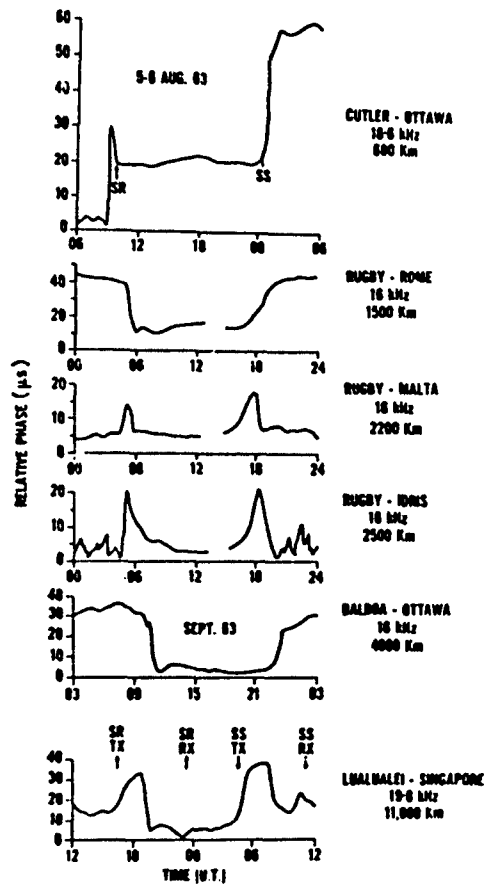


Fig. 7. Diurnal phase changes measured at various ranges from a VLF transmitter (after Belrose, 1968).

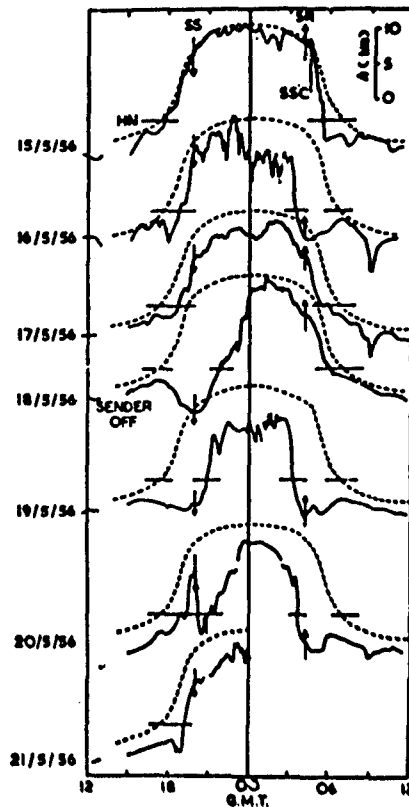


Fig. 8. Diurnal phase changes during and after a geomagnetic storm (after Belrose, 1968).

Station

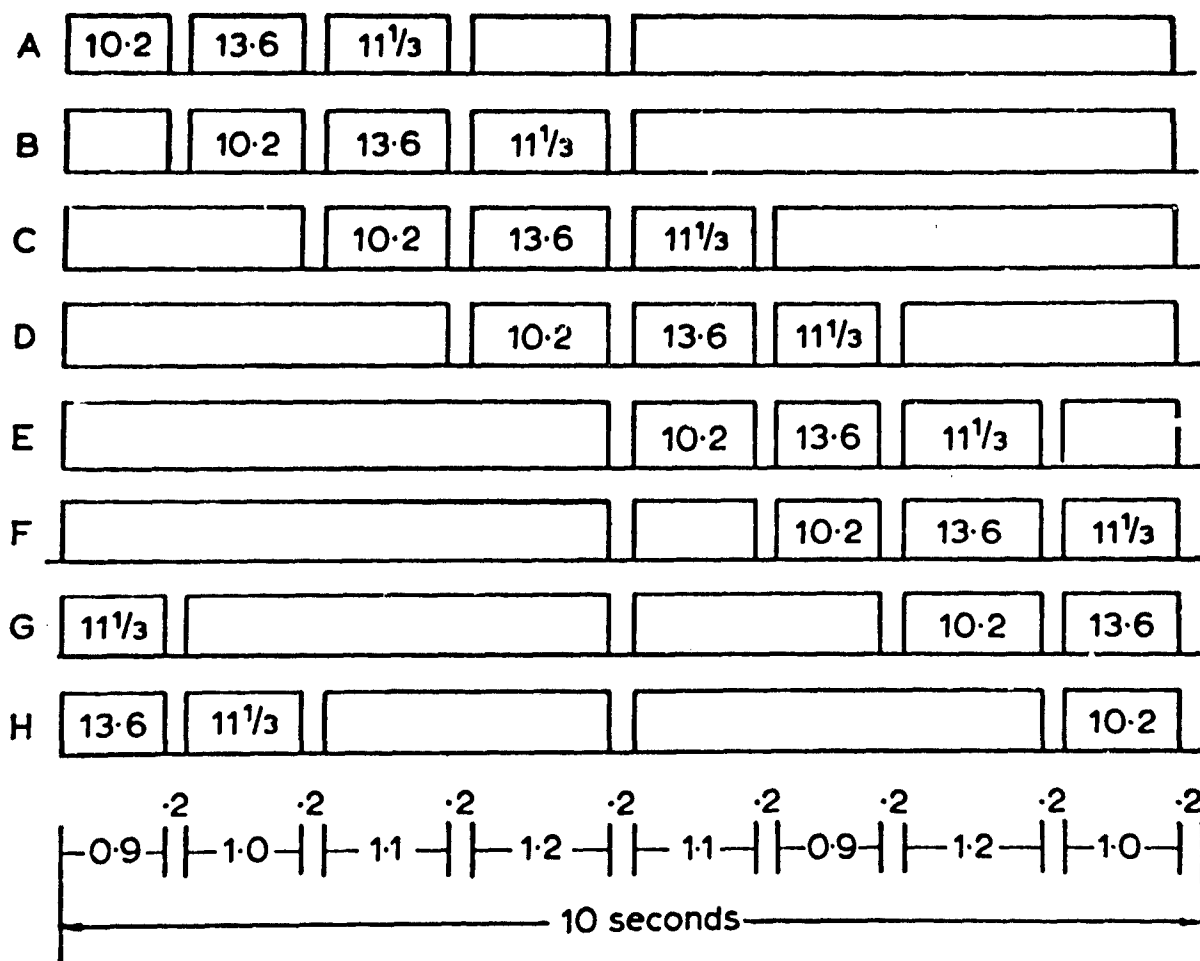


Fig. 9. Omega transmission format (after Burgess and Jones, 1975).

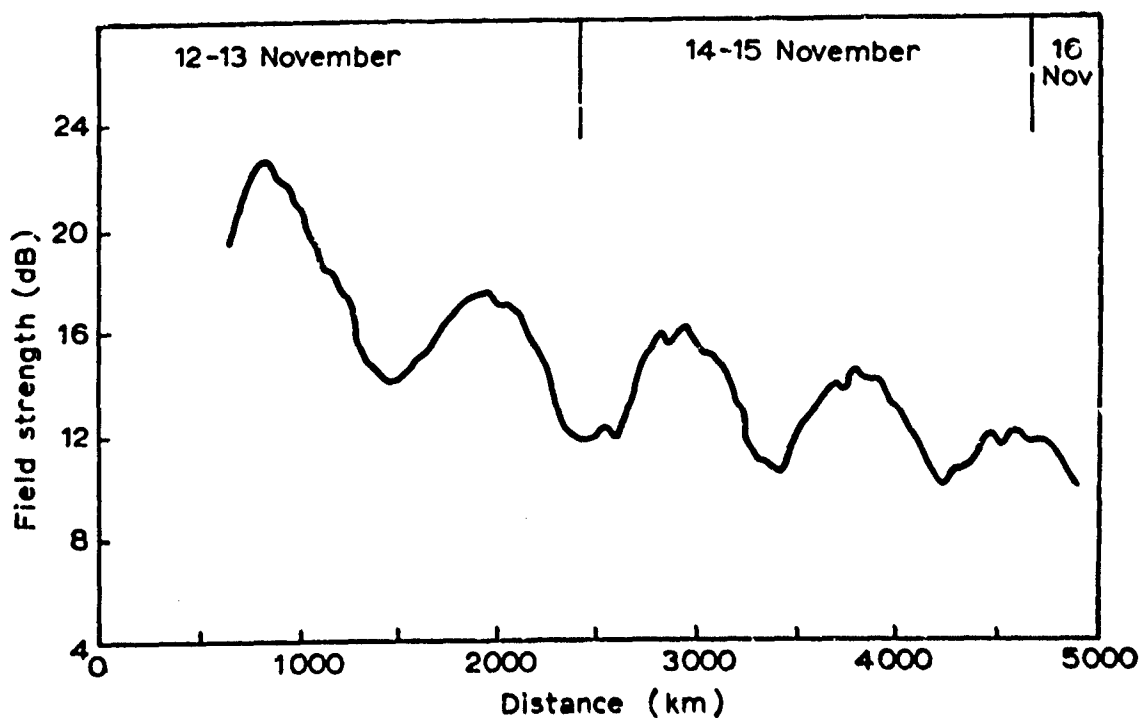


Fig. 10. Variation of 10.2 kHz field strength as a function of distance from the Omega Trinidad transmitter (after Burgess and Jones, 1975).

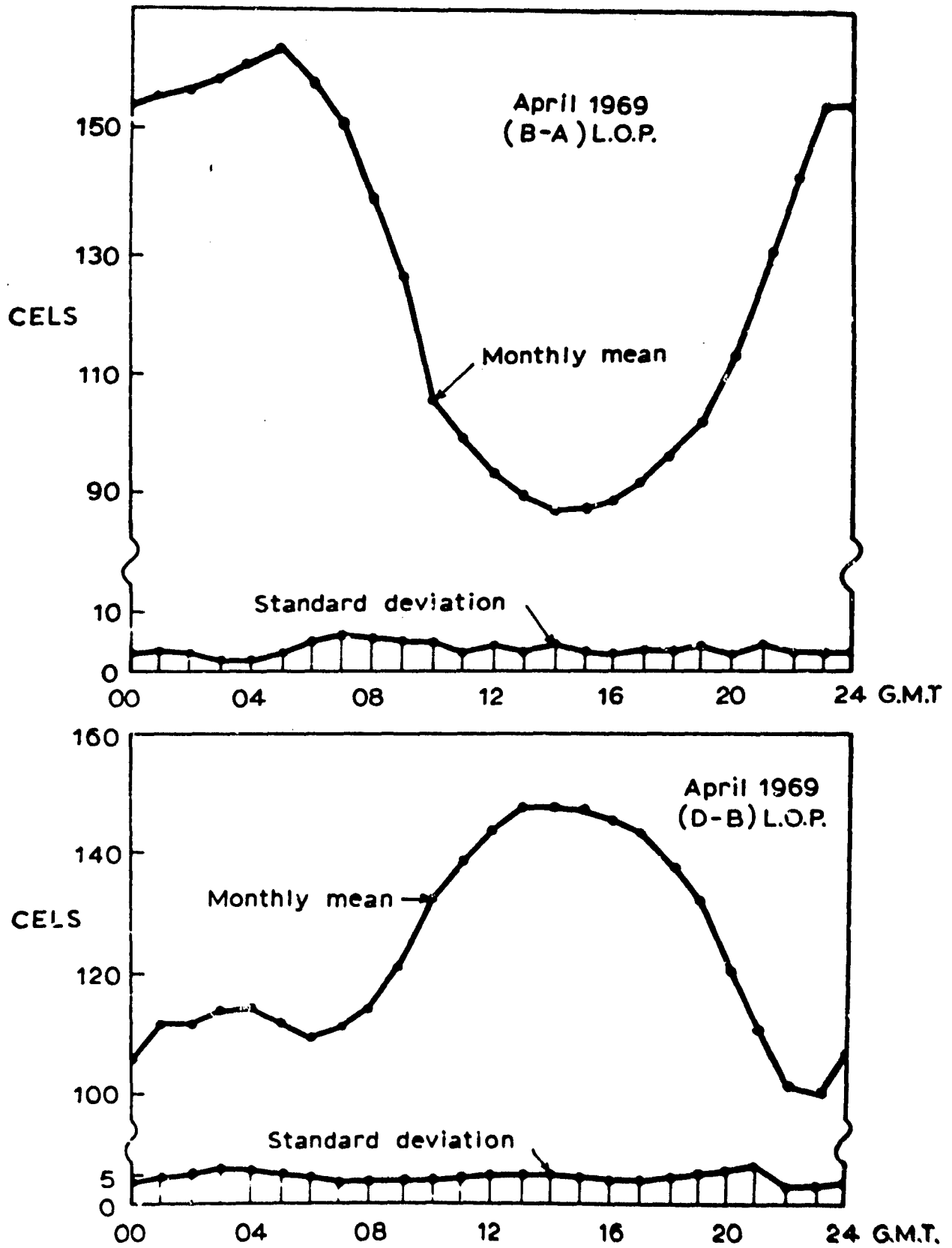
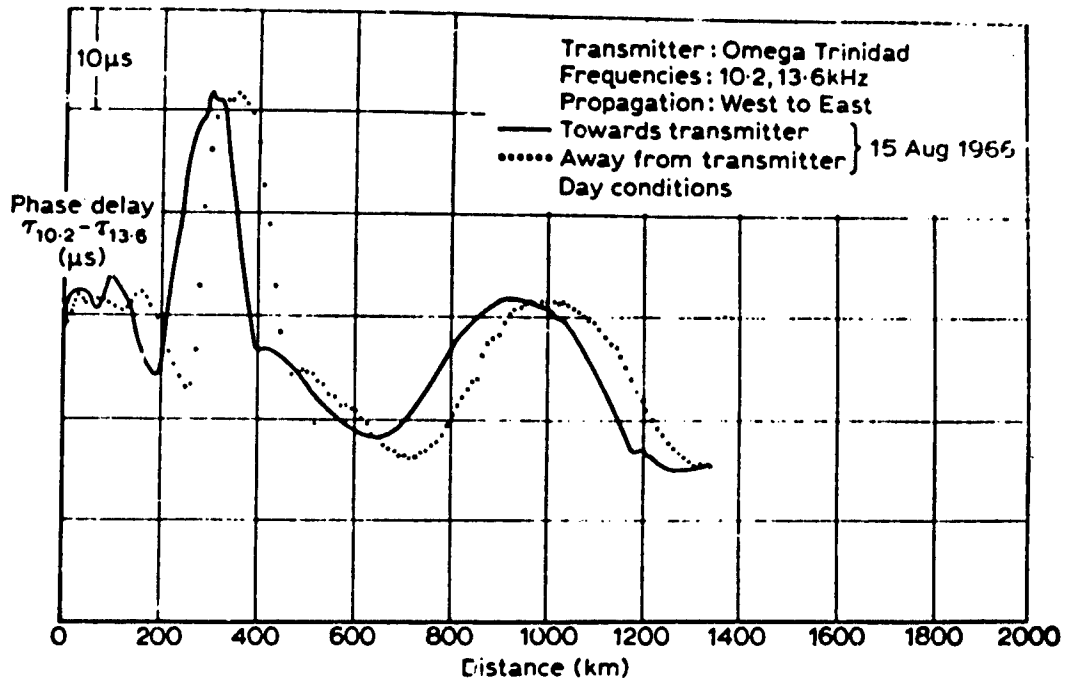
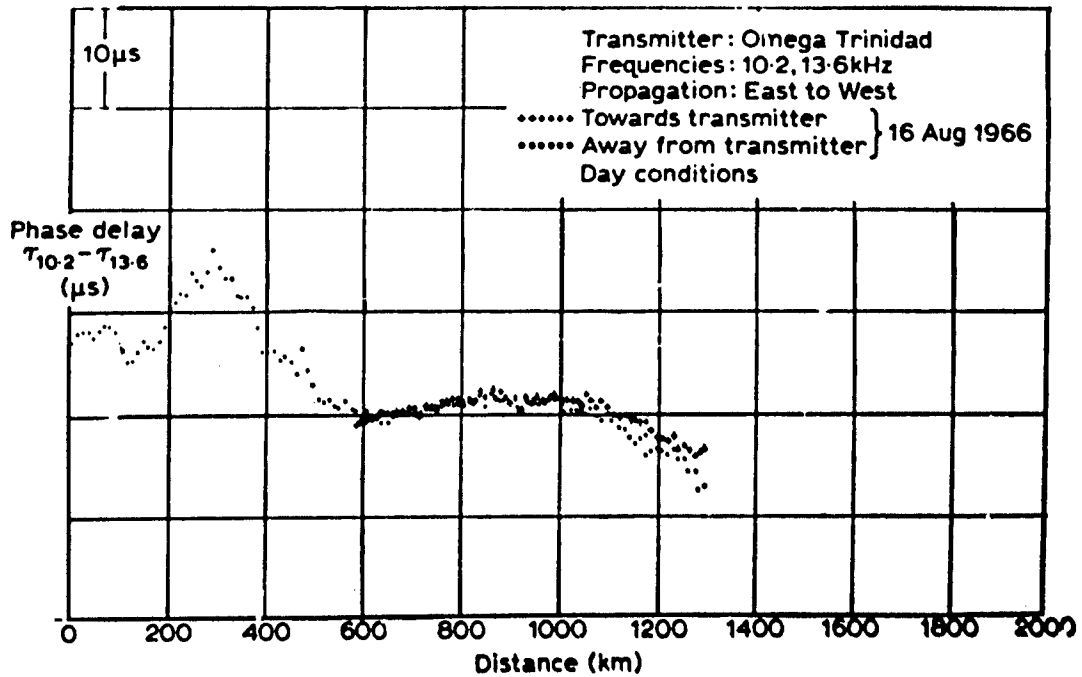


Fig. 11. Monthly mean value and standard deviation for the (B-A) and (D-B) Omega l.o.p.'s measured at Farnborough, U.K. (after Burgess and Jones, 1975).



(a)



(b)

12. a) Relative phase delay of 10.2 and 13.6 kHz signals as a function of distance from the Omega Trinidad transmitter. Daytime conditions, west to east propagation.
 b) relative phase delay of 10.2 and 13.6 kHz signals as a function of distance from the Omega Trinidad transmitter. Daytime conditions, east to west propagation.
 (after Burgess and Jones, 1975)

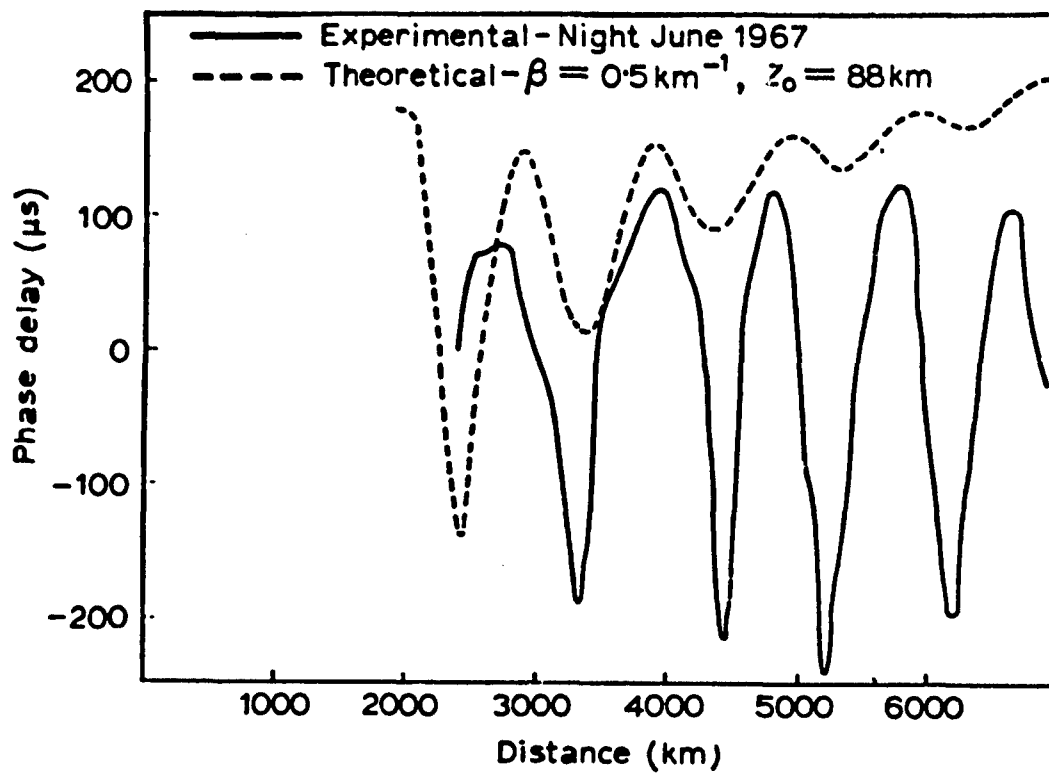
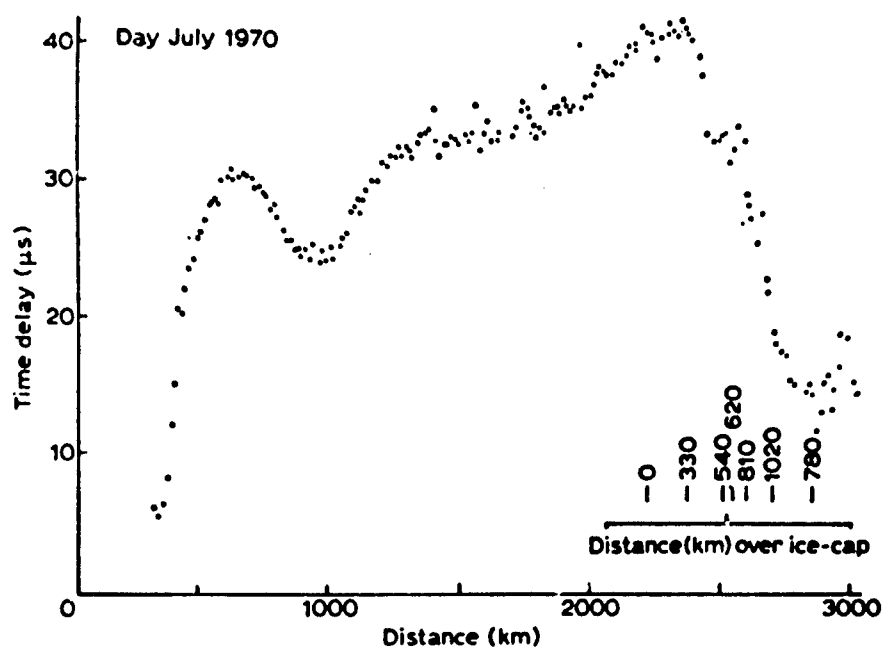
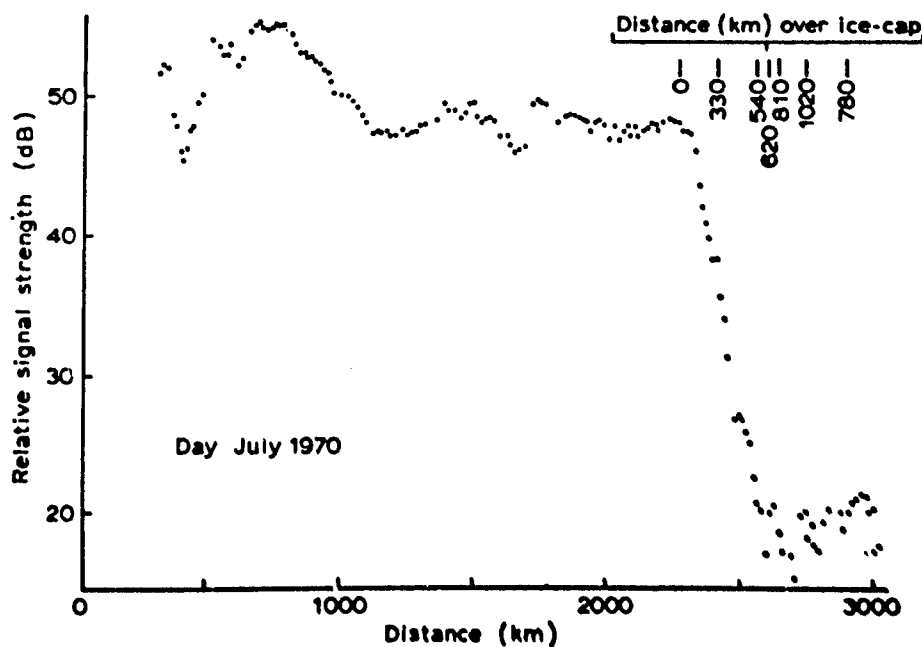


Fig. 13. Phase delay variability of the 262 Hz difference frequency referred to a 10.2 kHz carrier as a function of distance from the transmitter (Omega Trinidad). Night conditions (after Burgess and Jones, 1975).



(a)



(b)

Fig. 14. a) Time delay of 13.6 kHz relative to 10.2 kHz as a function of distance from the Omega Norway transmitter showing effect of Greenland Ice-cap.
 b) Signal strength at 13.6 kHz as a function of distance from the Omega Norway transmitter. Effect of Greenland Ice-cap is shown.
 (after Burgess and Jones, 1975)

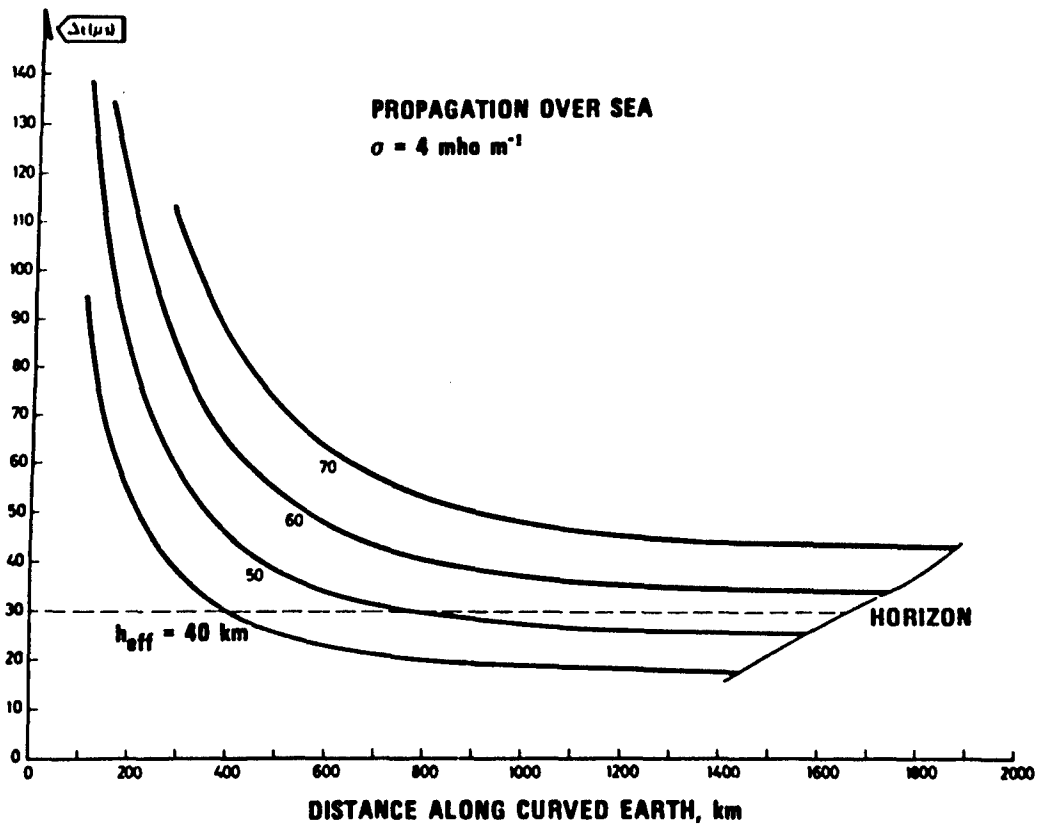


Fig. 17. Difference in propagation time (in μs) between groundwave and skywave vs propagated distance along the earth for various values of the effective reflection height. Propagation above sea (after Larsen and Thrane, 1976).

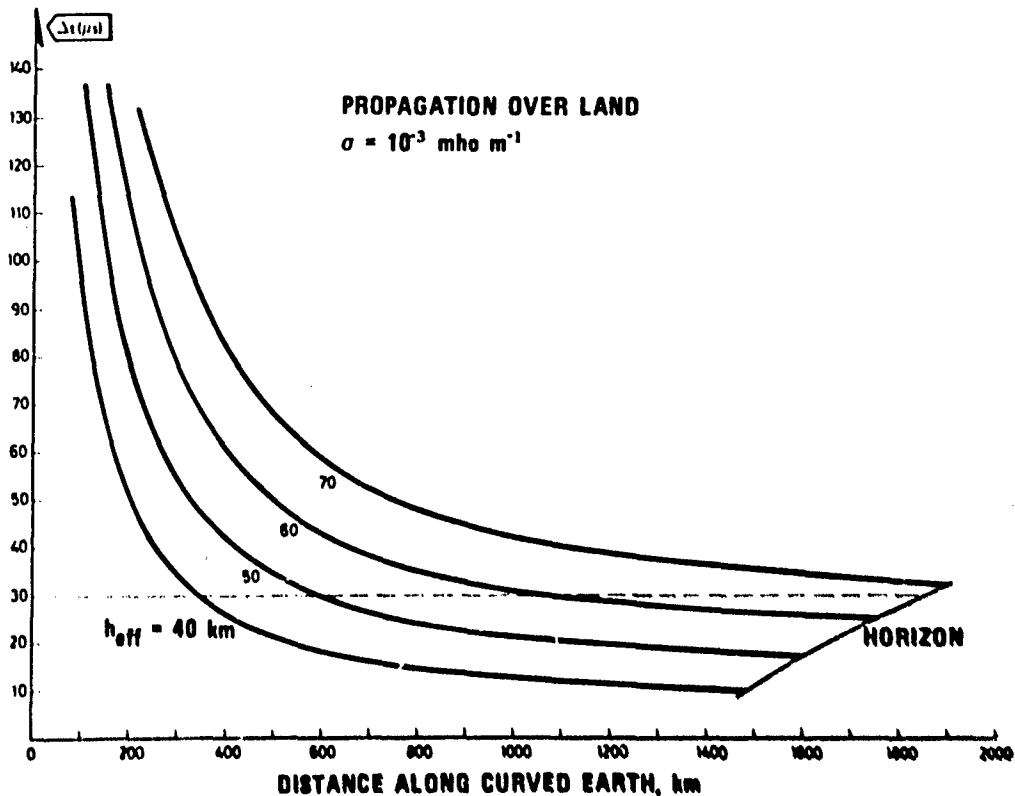
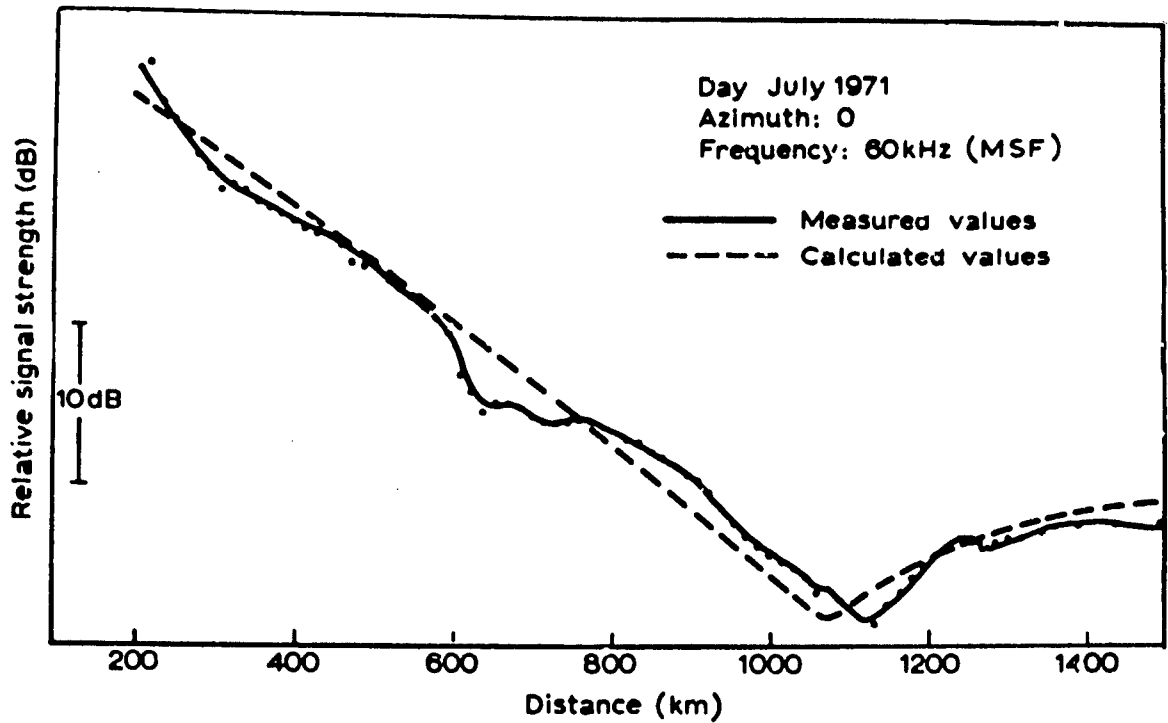
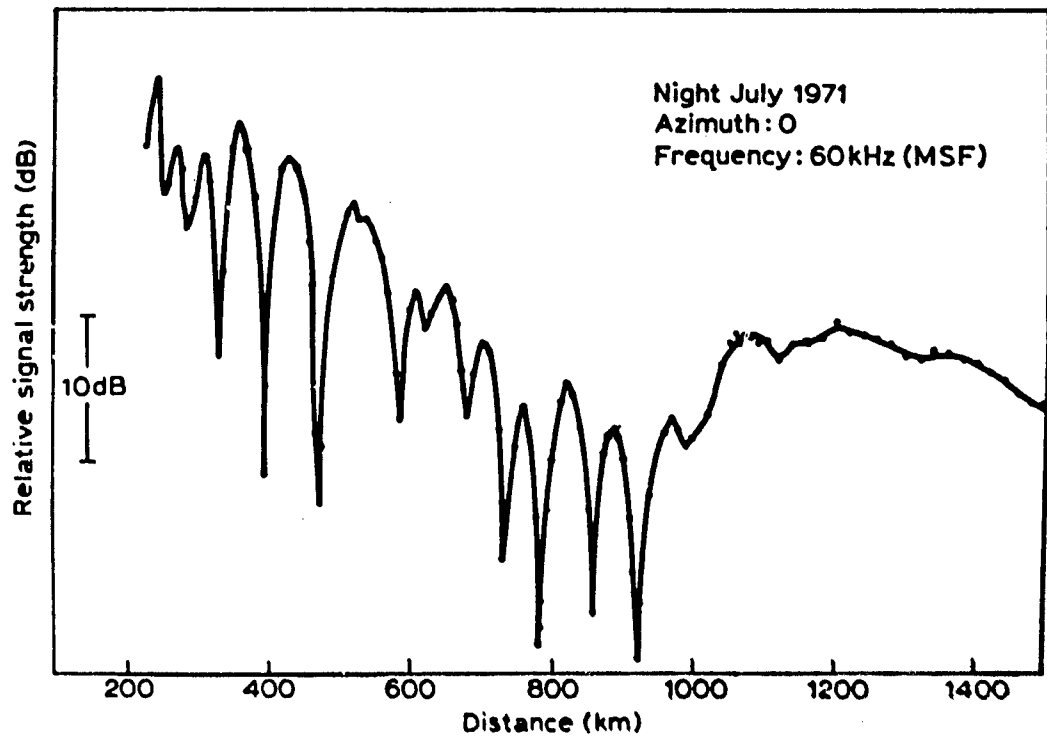


Fig. 18. Difference in propagation time (in μs) between groundwave and skywave vs propagated distance along the earth for various values of the effective reflection height. Propagation above poorly conducting land (after Larsen and Thrane, 1976).



(a)



(b)

Fig. 19. a) Signal strength variation with distance from a 60 kHz transmitter (MSF). Daytime conditions.
b) Signal strength variation with distance from a 60 kHz transmitter (MSF). Night-time conditions (after Burgess and Jones, 1975).

Remote Sensing

G.E. Peckham,
Heriot-Watt University,
Edinburgh EH14 4AS.

Abstract

The way in which emitted or reflected electromagnetic radiation may be used to obtain information about the atmosphere, land and sea is briefly described. The use of infrared scanners and radiometers on satellites to examine the land surface and properties of the atmosphere including temperature and composition, is described in more detail.

1.1 Introduction

Any method whereby we receive information about our environment without the use of instruments placed in situ comes under the heading "Remote Sensing". We may make use of radiation naturally present, either emitted by the target itself or reflected from some other source such as the sun. Examples of these techniques are photography and thermal mapping by infrared imagery. As an alternative to these passive systems, an active system may be used in which the target is illuminated by some artificial means. Examples are lidar and radar. Of course, it is not necessary to restrict the subject to the study of electromagnetic radiation. Acoustic sounding for example is used to study the atmosphere and the earth's interior. However, I shall be emphasising satellite sensors which can make use of only electromagnetic radiation.

Instruments may be mounted on a variety of platforms; ground base, ship, aircraft, balloon rocket or spacecraft. Some possible combinations of platforms, instruments and targets are shown in Figure 1. It is obvious that "Remote Sensing" is a very large field of study indeed and I cannot hope to cover the whole field. Accordingly I shall restrict my talk to only a few of these possibilities.

1.2 Properties of the atmosphere

A fundamental factor in the use of electromagnetic radiation for remote sensing is the transmission spectrum of the atmosphere. If the object is to view the earth's surface it will be necessary to use wavelengths where the atmosphere is transparent (the atmospheric windows). Measurements at wavelengths where the atmosphere absorbs can be used to obtain information about the atmosphere itself (composition and temperature). Absorption bands occur throughout the spectrum from ultraviolet to long radio waves with only a few windows where the atmosphere is more or less transparent, (see Figure 1). Ultraviolet radiation has sufficient quantum energy to cause electronic transitions in atoms. As wavelengths increase, the quantum energy gets less and by the time the visible part of the spectrum is reached, electronic transitions can no longer be excited so that the atmosphere becomes transparent except for the effects of suspended matter (aerosols) and clouds. The frequency of vibration of most molecules corresponds to the frequency of light in the infrared part of the spectrum and when a resonance occurs, strong absorption is found. In order to interact with electromagnetic radiation it is necessary for the vibrating molecule to have a dipole moment. The simple diatomic molecules of the major constituents (O_2 and N_2) have no dipole moment because of their high symmetry and so absorb only through weaker effects. Absorption in this part of the spectrum is mainly due to minor constituents, the three most prominent being carbon dioxide, water vapour and ozone. Frequencies in the far infrared to millimeter waves correspond to frequencies of molecular rotation and again many absorption bands due to minor constituents and water vapour are found. A strong absorption due to oxygen occurs at 5 mm wavelength which involves a magnetic dipole interaction.

1.3 Sensing the earth's surface

The reflection spectrum of the earth's surface is characteristic of the nature of that surface. By making measurements at a number of wavelengths, it is possible to distinguish between crop types, healthy and diseased plants, exposed minerals of different types, etc. In order to avoid interference from the atmosphere (in particular from water vapour and carbon dioxide), it is necessary to work in one of the atmospheric windows. The main regions of interest are:-

- (a) visible to near infrared used for photography, infrared mapping, lidar;
- (b) the thermal infrared window at $11 \mu m$ used for thermal mapping as this wavelength is close to the maximum in the thermal emission spectrum for normal temperatures;
- (c) wavelengths greater than 1 cm or so used for radar, and passive microwave radiometry.

The atmosphere is not entirely transparent even in these windows and allowance often has to be made for a few percent residual absorption, particularly if quantitative temperature measurements are to be made. Water vapour in particular has a complex spectrum which is far from completely understood. I shall concentrate on the use of the visible to near infrared window in this application.

1.4 Sensing atmospheric temperature and composition

The strengths of the atmospheric absorptions give information about the concentrations of minor constituents. This information is quite specific as each molecule has a distinctive absorption spectrum and it is frequently possible to find a wavelength at which only the particular molecule of interest absorbs. Techniques may be active using a laser backscattered from a reflector, natural terrain or aerosols, or passive using the sun as source. Problems arise in matching laser frequencies to the molecular absorptions as powerful tunable lasers are not available through much of the spectrum.

As an alternative to measuring the transmission directly it is possible to obtain much the same information by measuring the thermal emission. Kirchoff's law states that if an object absorbs a fraction β of the radiation incident upon it, then it emits that same fraction β of the blackbody radiation intensity at the appropriate temperature. If the temperature of the absorber can be estimated then its absorptance β , and hence the molecular concentration, can be obtained. The main problem is that everything else including the background against which the absorber is seen is also emitting radiation and the absorptance can only be estimated if there is a well defined temperature contrast to the background. The most straightforward way is to view the absorber against space using the limb sounding technique from spacecraft, aircraft or balloon. This technique has been used to study the concentrations of many molecules in the stratosphere from satellites such as Nimbus 6. The normal temperature distribution in the atmosphere does provide a temperature contrast to the earth's surface so that nadir looking instruments are also possible. This technique has been used for many years on meteorological satellites to map clouds and water vapour.

So far I have described how an estimate of atmospheric temperature can be used to deduce the amount of a minor constituent from a measurement of the emitted radiation in a suitable absorption band. It is possible to reverse this argument and to deduce the temperature from the observed emission if the amount of absorber is known. This is the principle behind a whole family of atmospheric temperature sounding instruments which have been flown on meteorological satellites. Usually the instruments have been infrared radiometers sensitive to the spectral region 14 to 15 μm , where there is strong atmospheric absorption due to CO_2 . Other instruments have used the 4.2 μm CO_2 band and the 5 μm O_2 absorption band. The purpose has been to obtain measurements of the vertical temperature profile of the atmosphere on a global scale.

2.1 Sensing the earth's surface

A whole series of satellites has been developed by NASA specifically to obtain information about the earth's surface. The first was ERTS1 (Earth Resources Technology Satellite), launched in 1972. The series has been renamed Landsat, and Landsat 2 and 3 are now in orbit. In parallel to this program, NASA developed an orbital Research Laboratory (Skylab) and this program also included many instruments designed to look at the earth's surface. A list of instruments carried by Landsat 1 and 2, and by Skylab is shown in Table 1.

Table 1. Landsat 1/2 and Skylab sensors and their spectral characteristics.

Spacecraft designation	Type of sensor	Spectral sensitivity range	Comments
Landsat 1/2	Return beam vidicon		
	TV camera		
	no. 1	475 - 575 nm	
	no. 2	580 - 680 nm	
MSS	Multispectral point scanner	no. 3	690 - 830 nm
		channel 1	500 - 600 nm
		channel 2	600 - 700 nm
		channel 3	700 - 800 nm
		channel 4	800 - 1100 nm
Skylab S-190	Multispectral camera cluster	no. 1	500 - 600 nm
		no. 2	600 - 700 nm
		no. 3	700 - 800 nm
		no. 4	800 - 900 nm
		no. 5	500 - 880 nm
		no. 6	400 - 700 nm
			Type of film: B&W:Panatomic-X B&W:Panatomic-X B&W:IR Aerographic B&W:IR Aerographic Colour:IR Aerochrome Colour:SO-242*
S-191	Infrared spectrometer	0.4 - 2.4 μm and 6 - 16 μm	Spectral resolution $2 \times 10^{-2} \mu\text{m}$ to $2.5 \times 10^{-1} \mu\text{m}$ (lower at longer wavelength)
S-192	Multispectral scanner	channel 1	410 - 460 nm
		channel 2	460 - 510 nm
		channel 3	520 - 556 nm
		channel 4	565 - 609 nm
		channel 5	620 - 670 nm
		channel 6	680 - 762 nm
		channel 7	783 - 860 nm
		channel 8	980 - 1080 nm
		channel 9	1.09 - 1.19 μm
		channel 10	1.20 - 1.30 μm
		channel 11	1.55 - 1.75 μm
		channel 12	2.10 - 2.35 μm
		channel 13	10.2 - 12.5 μm
S-193	Microwave system (passive + active) radiometer, scatterometer, altimeter	13.8 - 14.0 GHz	
S-194	L-band microwave radiometer	1.4 - 1.427 GHz	Centre frequency of 1.4135 GHz; bandwidth 27 MHz

* New film developed by Kodak, with high resolution at low contrast.

Landsat carries two instruments sensitive to visible and near infrared reflected sunlight. The vidicon camera system scans the image by electronic means whereas the multispectral scanner uses an elemental detector with a rotating mirror to scan across the satellite track and relies on the satellite motion to scan in the other dimension. A schematic diagram of these instruments is shown in Figure 3. The development of an improved near infrared multispectral scanner is under way. The new instrument includes channels sensitive to thermally emitted infrared radiation in addition to short wave channels.

Since Skylab was a manned spacecraft, cameras were used to record visible images on film which could in this case be recovered. In addition a 13 channel multispectral scanner was included together with a visible and infrared spectrometer. Both active and passive microwave systems were also carried. Skylab was an experimental mission unlike the Landsat series which are intended to provide a continuous service to users.

Landsat imagery has applications in many fields, including:
 Forestry; identification of tree types, extent of deforestation, disease, gale damage.
 Agriculture; crop types and yields, forecasts, disease, soil types and water content.
 Geology; lithologic mapping, identification of mineral ores, location of faults.
 Cartography; mapping remote areas, updating land use.

Many of these applications rely on the recognition of the spectral signature of a particular type of surface. Typical reflectivities for spectral bands, corresponding to those of the multispectral scanner, are shown in Figure 4. Obviously a direct display of the images in each of the four channels will be difficult to interpret and some method is needed to enhance the relatively small differences characteristic of particular surfaces. Such enhancement can be carried out optically or digitally. Image enhancement techniques can be divided into two types;

(a) Filtering and enhancement processes

Spatial filtering, e.g. a high pass filter enhances lines and edges, a notch filter can suppress particular frequencies, e.g. scan lines.

Directional filtering may be used to enhance edges aligned in a particular direction.

Matched filtering allows the filtering of particular two dimensional structures, e.g. spiral characteristic of tornadoes.

In density slicing, the brightness is quantised into 2 or more levels. Specific hues may be identified by density slicing a multispectral image.

Weighted averages over a number of multispectral channels may be used to form a compound image. In particular three such averages (differently weighted) may form a false colour display. The ratio of these weighted averages may be used to reduce dependence on the variable illumination of the scene. The brightnesses in the N spectral ranges will normally be highly correlated. It is often useful to choose N weighted averages so that these averages are uncorrelated. In a 3 channel system for instance, this allows most effective use of the 3 colours available in a false colour display. This may be looked on as an axis rotation in spectral space.

A powerful enhancement technique is that of histogram equalisation. Density slicing is carried out at brightness levels so spaced that an equal number of pixels fall into each category. This may with advantage follow an axis rotation in spectral space.

(b) Classification

Four different effects may be used for feature recognition. These are spatial, spectral, polarisation and temporal effects. Most important are spectral and spatial effects and spectral effects lend themselves most readily to automatic classification. The purpose of classification is to assign each element of the picture or pixel to a particular category, e.g. a particular land use. For this purpose each measurement may be visualised as a point in N dimensional space, where each axis represents the brightness recorded in one spectral channel. The N dimensional space is divided into regions (one for each category) by decision criteria. Various statistical rules are used to define the decision criteria to minimise error.

Decision criteria may be derived a priori by a supervised technique in which accurate ground truth is obtained for particular training areas and this is used to develop the decision criteria. An alternative unsupervised technique divides the remotely sensed data into classes depending on the clustering which occurs naturally in the N dimensional space. The category to which each class should be assigned is then found by obtaining ground truth for examples of each class.

An example of the use of such a classification scheme was a search for sulphide bearing ores in Pakistan reported by Schmit et al. (1975). The categories and classification limits are given in Table 2, and the resulting classification map is compared with ground truth in Figure 5.

Table 2. Digital classification table used in 1974 mineral evaluation in the Chagai District, Pakistan.

Class number	Rock type	Symbol	Multispectral scanner bands			
			4	5	6	7
1	Quartz High reliability diorite Low reliability Mineralised rock Pyritic High reliability rock Low reliability	-	46 to 50	52 to 60	50 to 60	18 to 22
2			44 to 45	52 to 60	45 to 49	18 to 19
3			41 to 45	47 to 54	39 to 44	16 to 17
4			41 to 45	47 to 54	39 to 44	16 to 19
5	Dry-wash alluvium	-	39 to 46	39 to 46	35 to 44	14 to 17
6			41 to 45	46 to 51	42 to 49	18 to 19
7	Boulder fan	+	33 to 40	39 to 46	30 to 35	9 to 16
8	Eolian sand	,	38 to 44	46 to 54	42 to 51	18 to 22
9			45	46 to 127	42 to 127	18 to 63
10	Various dark surfaces including hornfelsic rock outcrops, desert- varnished lag gravels, and detrital black sand	,	33 to 36	28 to 38	29 to 35	11 to 15
11			24 to 35	19 to 27	20 to 32	8 to 12
12			29 to 36	28 to 38	20 to 28	9 to 14

Part II

3 Atmospheric temperature sounding

Since 1960 a large number of satellites has been launched whose prime function has been the measurement of meteorological quantities. These satellites include the American Tiros and Nimbus series, several of the Russian Cosmos series, and the Russian Meteor operational weather satellites. Meteorological experiments have also formed part of the payload of many other satellites, for example the geostationary American ATS. An international plan for a series of geostationary satellites spaced around the equator to keep constant watch on the world's weather is now well under way with two American satellites, the European Meteosat and a Japanese satellite already in orbit.

Why has so much effort been devoted to satellite techniques when for many years apparently satisfactory measurements have been made by more conventional means? There are two main reasons. The first is that some measurements can be made satisfactorily only from satellites, for example, measurements of the radiation budget and large scale cloud features. The second is that satellite observations can cover the whole globe whereas the international network of radiosonde stations is concentrated on the continents of the northern hemisphere while the density of observations is inadequate in the arctic, the tropics, over oceans and in most of the southern hemisphere. This shortcoming is becoming steadily more apparent as attempts are made to increase the period of forecasts, to introduce numerical methods and to include the effects of sea surface temperature.

The most obvious features in a view of the earth from space are clouds and, since 1960, cloud photographs from the Tiros and Nimbus satellites have been used extensively in forecasting. In addition to the cloud cameras, the Tiros satellites carried instruments to measure the radiation emitted by the earth in the infrared region of the spectrum. Observations in a spectral window (e.g. 8 - 12 μm) where the atmosphere is transparent show low radiation from the cold clouds in contrast with higher radiation levels from the earth's surface. Observations of emitted radiation have the advantage that clouds may be seen during both day and night and also that an estimate of the height of the cloud top may be made from the known temperature structure of the atmosphere.

The distribution of water vapour may be measured in a similar way from observations in a region of the spectrum where water vapour absorbs. Meteosat includes a channel at 5.9 to 6.7 μm for this purpose.

In the case of water vapour and cloud, a knowledge of the vertical temperature structure of the atmosphere is used to deduce the distribution of the absorber. Conversely, if the distribution of the absorber is known, information about the temperature structure of the atmosphere can be obtained. CO_2 is known to be fairly evenly mixed and Tiros VII measured radiation in the 14 to 16 μm band, corresponding to the bending mode absorption of the CO_2 molecule. From these measurements, maps of stratospheric temperatures were produced. The Nimbus satellites have carried a series of more sophisticated temperature sounding instruments, the purpose of which has been to determine the entire vertical temperature structure of the atmosphere by making measurements at several wavelengths in the 15 μm CO_2 absorption band (or in some cases the 5 mm oxygen band).

The potential of satellite infrared radiometry is demonstrated by the emission spectrum (figure 6) recorded by the Fourier transform spectrometer (Iris) on Nimbus 4. The spectrum shows low emission from CO_2 at low temperatures, near the tropopause, but higher emission occurs where the atmosphere is more opaque at the band centre. This originates from CO_2 at higher temperatures in the stratosphere.

Satellite instruments have been used to measure cloud, water vapour and ozone distributions. Of the basic field quantities necessary to describe the dynamic state of the atmosphere (pressure, temperature, wind) only temperature has been measured so far although winds may be deduced indirectly by noting cloud movements. The measurement of the pressure field would be of great meteorological importance.

In the rest of this lecture, simple models of an atmospheric absorption band are used to describe the problems which are encountered in trying to deduce a vertical temperature profile from satellite radiation measurements.

3.1 Temperature sounding

Consider a slab of atmosphere containing a quantity of absorber du at a temperature T . At a frequency ν at which the absorption coefficient is k_ν , the emitted intensity in a vertical direction will be $k_\nu du B_\nu(T)$ where $B_\nu(T)$ is the Planck function at frequency ν and temperature T . Of this radiation a proportion $\tau_\nu = \exp(-\int_0^\infty k_\nu du')$ will reach the top of the atmosphere. The intensity at the top of the atmosphere is

$$I_\nu = \int_0^\infty B_\nu(T) k_\nu du' \tau_\nu = \int_0^1 B_\nu(T) d\tau_\nu \\ = \int_0^\infty B_\nu(T) \frac{d\tau_\nu}{dy} dy$$

in terms of an altitude variable $y = -\ln p$ where p is the pressure. The intensity I_ν is the weighted average of black body emission from the atmosphere, the weighting function describing the height from which radiation is emitted being $K(y) = (d\tau_\nu/dy)$. $K(y)$ must be known accurately to interpret the observed radiances in terms of a vertical temperature profile. This function may be found by numerical integration from tabulated line positions and strengths combined with laboratory measurements of the transmission of carbon dioxide.

However, the form $K(y)$ can be illustrated using simple models for the CO_2 absorption spectrum.

(1) *Monochromatic case* For a single collision broadened spectral line of strength S centred at frequency ν_0 the weighting function is

$$K(y) = 2 \frac{p_0^2}{p} \exp - \frac{p}{p_0}^2$$

where $p_0^2 = 2\pi(\nu - \nu_0)^2 (S \gamma_0 a)^{-1}$, γ_0 being the line halfwidth at 1 atm pressure and a the amount of absorber in a vertical column of atmosphere. This function has a peak at atmospheric pressure p_0 depending on the particular value of the absorption coefficient. The larger the absorption coefficient, the higher the peak. Its width at half height, however, is a constant 1.22 in the height variable y . This is equivalent to a width of 8.3 km assuming a scale height of 6.8 km.

(2) *Wide band case* To accept sufficient radiation to make the measurement in the presence of detector noise, it is necessary in practice to include a spectral interval of 3 to 10 cm^{-1} . This interval will include a number of absorption lines. The Elsasser model in which lines are assumed equally spaced may be

used to approximate the CO₂ absorption spectrum in this case. In the strong line limit this model gives for the weighting function

$$K(y) = (2/\pi)^{1/2} (p/p_0) \exp - p^2/(2p_0^2)$$

where $p_0^2 = \delta^2/\pi S a y_0$, δ being the line spacing. The function peaks at $p = p_0$, but now the half width is 1.80 in y (12.2 km).

This increase in width over the monochromatic case is understood easily as spectral regions near line centres will have high absorption coefficients and hence weighting functions peaking high in the atmosphere whereas in the wings of the lines the weighting functions will be lower. Averaging over a frequency band then produces a broad function.

(3) *Selective chopping* The highest 'wide band' weighting function that can be realised in the 15 μm CO₂ absorption band peaks at an atmospheric pressure of about 60 mbar (20 km). To achieve weighting functions higher than this, it is necessary to select radiation in the line centres and to reject that in the line wings. For appropriate pressures and path lengths, the line widths are of order 0.01 to 0.02 cm^{-1} , so that it is necessary to accept radiation from many lines to make a measurement in reasonable time in the presence of detector noise. It would be very difficult indeed to achieve this spectral selection by techniques such as interferometry. The solution to this problem was suggested by Smith and Pidgeon (1964). A cell containing an appropriately chosen pressure of CO₂ will absorb strongly only in the neighbourhood of the line centres. If such a cell is used to modulate the radiation in place of the usual opaque chopper, the radiometer becomes sensitive only to radiation in the line centres, and the weighting function peaks high in the atmosphere.

3.2 Retrieval of temperature profiles

Given an atmospheric temperature profile and the distribution and absorption properties of a particular constituent, it is not difficult to calculate the radiation emitted. The inverse problem where the radiances emitted in various spectral intervals are specified and the temperature profile must be deduced is less well defined. A number of spectral intervals are chosen within the CO₂ absorption band so that the weighting functions are scattered as widely as possible throughout the depth of the atmosphere. However, we have seen that the half width of a weighting function is about 10 km. Since this is similar to the depth of the troposphere, the weighting functions will show considerable overlap. This means that little extra information can be obtained by including more than six or so separate spectral intervals but this depends on the instrument noise characteristics. However, in order to specify a detailed temperature profile, it is necessary to give the temperature at many more than six heights.

One approach to this problem is to choose the most probable profile consistent with the observed radiances. Many sample profiles from radiosonde ascents are available and from these one can construct a covariance matrix, C , for the components of a vector B which describe the vertical radiance profile of the atmosphere. Assuming a gaussian distribution the probability of finding a particular profile B is proportional to $\exp(-\frac{1}{2}B^TC^{-1}B)$; we choose B to maximise this probability subject to the constraint that $KB = I$ where K is the matrix of weighting functions and I the vector of observed intensities. Using Lagrange multipliers we then find

$$B = C K^T (K C K^T)^{-1} I$$

This is a convenient form in that the vector of observations is simply multiplied by a matrix which may be pre-computed. In principle this linearity is not entirely accurate as the weighting functions themselves depend on the temperature profile. However it is usually sufficient to calculate the weighting functions for a standard atmosphere. Greater accuracy can be obtained by using different covariances for different geographical locations and seasons. The instrument noise characteristics may be included in the expression for B with little extra complication.

The most severe problem in carrying out the inversion is probably the presence of cloud. If cloud is thick, the instrument provides no information on temperatures below cloud top. In the case of broken cloud, its properties need to be known. The most accurate method is to obtain cloud information from another source, e.g. a radiometer operating in an atmospheric window, but cloud cover may be obtained by an extension of the inversion technique outlined above.

Another approach to the cloud problem has been to move away from the 15 μm region altogether and work in the 5 mm oxygen band. The drop in black body emission at the long wavelengths is compensated by the excellence of techniques for the detection of microwaves compared with infrared. Clouds are much more transparent at these longer wavelengths. Similar weighting functions may be achieved and microwave radiometers to some extent may replace infrared instruments for temperature sounding.

3.3. The instruments

The characteristics of some successful temperature sounding instruments are listed in Table 3. The instruments differ from each other mainly in the techniques used to select appropriate spectral intervals. All incorporate means for in-flight calibration. This is achieved by directing radiation from a black body emitting a known intensity into the instrument. Space is used as a zero reference.

Absolute calibration must be better than 1°K imposing severe conditions on stray radiation and reference blackbody design. The random noise level is a function of entrance aperture, field of view, spectral bandwidth, detector performance and signal integration times.

A single sounding from the Selective Chopper Radiometer on Nimbus 4 is shown in figure 7 compared with a radiosonde ascent. The weighting functions for this instrument, the top two of which were achieved by selective chopping, are also shown. Such profiles are obtained every 16 s. Recorded on magnetic tape, the satellite derived temperature patterns form a more complete data base for global scale atmospheric studies than has ever been available before. This is particularly so for the high stratosphere and the southern hemisphere where few radiosonde data are available.

As an example, a Fourier analysis of a sequence of stratospheric temperatures for latitude 60°S observed from the Nimbus 4 SCR clearly showed the presence of planetary scale waves in the temperature field. As the earth rotates under the satellite a static atmospheric temperature pattern would show components at 0, 1, 2 etc. cycles per day. However a peak occurred displaced to higher frequencies from the exact 2 cycles per day (see figure 8). This showed that the wavenumber 2 component of the temperature pattern is propagating to the east with a velocity of about 14° of longitude per day.

Table 3. Characteristics of some successful temperature sounding instruments

Experiment	Spectral selection	Number of channels	Spectral resolution	Field of view
IR interferometer spectrometer	Michelson interferometer †	Continuous, 5 - 25 μm ‡	5 cm^{-1}	8°
		Continuous, 6.25 - 50 μm §	3 cm^{-1}	5°
Satellite IR spectrometer	Grating spectrometer with array of detectors	7 in CO_2 band, † 1 in 11 μm window	5 cm^{-1}	12°
		14 including CO_2 § and water vapour	5 cm^{-1}	12° (scanned)
Selective chopper radiometer	Selective chopping with interference filters	6 in CO_2 band, § 1 in 11 μm window	0.01 - 10 cm^{-1}	10°
		16 including water vapour and window channels	0.01 - 10 cm^{-1}	1.5°
Vertical temperature profile radiometer	Interference filters	6 in CO_2 band 2 window 1 water vapour	3.5 - 10 cm^{-1}	2.2° (scanned)
IR temperature profile radiometer	Interference filters	4 in CO_2 band 2 window 1 water vapour		1.5° (scanned)
Nimbus microwave spectrometer	Microwave techniques	3 in 5 mm O_2 band 2 at 1 cm (water and liquid water)	220 MHz	10°
Pressure Modulation radiometer	Selective chopping by pressure modulation X	2	.001	20° x 4° (Doppler scanning)

†Interferogram is Fourier transformed to give spectrum

‡Nimbus 3, §Nimbus 4, ||Nimbus 5, Tiros, XNimbus 6

4 Remote sounding of stratospheric composition

In this section I want to describe a technique for the remote sensing of the composition of the stratosphere. This technique forms the basis for a proposal from a group under Professor J.T. Houghton at the University of Oxford for an experiment to be flown on Nimbus 6. The purpose of this experiment is to obtain information about photochemical processes in the stratosphere both in order to understand the normal behaviour of the stratosphere and to assess the effects of various pollutants that may be introduced into the stratosphere by man's activities. The concentrations of some of the more important constituents are shown in figure 9 as a function of height.

4.1 Limb sounding

The technique is based on limb sounding (see figure 10) in which the height from which radiation originates is defined by the direction of view rather than by the spectroscopic properties of the atmosphere, as in vertical temperature sounding. This technique can be used for temperature sounding, but it is particularly advantageous for composition measurement because (a) a much longer atmospheric path at a given level is available so that weak emission is enhanced, and (b) a zero radiation background is provided by space. Although the instrument can in principle see radiation originating from all heights above a minimum determined by the direction of view, it should be noted that because of the exponential decrease of pressure with height, for an evenly distributed absorber, most of the emission originates near this minimum height. Two thirds of the absorber along the path is present in a 5 km thick layer above the minimum height.

4.2 Pressure modulation

This is a technique for selecting and measuring the radiation emitted by a particular molecular species. A cell of gas in question is included in the optical path of the radiometer and its pressure varied cyclically (figure 11). The transmission of the cell, and hence the radiation falling on the detector, is modulated only at frequencies which lie within the absorption lines of the gas. The component of the output of the detector in phase with the modulation is then recovered by electronic processing in the usual way. Additional filtering requirements are not severe, as all that is required is to isolate the particular absorption band. Pressure modulation is a development from the technique of selective chopping, employed by the selective chopper radiometers on Nimbus 4 and Nimbus 5, and was used in a temperature sounding radiometer on Nimbus 6 (Houghton and Smith, 1970); because it employs only a single cell of gas the problems of balance inherent with a double beam system are eliminated. Emission from any gas can be detected provided that;

- a sufficiently strong emission band occurs in the infrared, at wavelengths where there is adequate thermal emission
- the gas is sufficiently stable and can be contained by the materials (optical and mechanical) which make up the modulator cell
- the absorption lines of the desired species do not overlap completely those of an unwanted species also present in the atmosphere.

4.3 Temperature measurement

The emission signals from the atmosphere in any spectral region depend on the atmosphere's transmission and on the mean temperatures along the path. In order to deduce emissivity and thence the concentrations of different constituents, it is necessary to know the atmosphere's temperature structure. Temperature can be measured by observing emission from CO_2 in its ν_2 band at 15 μm ; it being assumed that CO_2 dis-

tribution is uniform up to altitudes of 100 km or so. The derivation of temperature profiles from limb radiance observations has been considered in detail in recent papers (Gille (1971), Gille and House (1972)), and such measurements are made from the LRIR on Nimbus 6.

The addition of a PMR observing at the same time provides more information and enables altitudes to be probed than would otherwise be possible.

Because of the curvature of the atmosphere and because of the finite field of view of the radiometer, the radiation I reaching the instrument originates at various levels of the atmosphere, and can be written in the form,

$$I = \int_0^{\infty} B(T) \frac{dt}{dz} dz$$

dt/dz is usually known as the weighting function. Figure 12 shows values of the product of weighting function and blackbody function for a standard atmosphere, i.e. $B dt/dz$ for different directions of view and for a wide spectral interval. Integration over the field of view has also been carried out.

When a PMR is introduced into the system only the centres of the emission lines are chopped so that the effective spectral resolution of the PMR is of the same order as the width of the emission lines themselves (say $\sim 0.001 \text{ cm}^{-1}$). The effective emissivity in any particular case can, therefore, be much greater by several orders of magnitude and measurements may be made to much higher latitudes than is otherwise possible. The ultimate sensitivity of the instrument is limited by stray radiation, emitted from the scanning mirror and other parts of the instrument.

A useful bonus from the CO_2 band measurements is an accurate determination of the direction of view. Both the wide band radiation (I_{WB}) and the radiation measured by a PMR (I_{PMR}) are measured. It can be shown that at a suitable altitude ($\sim 50 \text{ km}$) in the atmosphere, ratio $I_{\text{WB}}/I_{\text{PMR}}$ is largely independent of temperature and depends only on atmospheric pressure (assuming a constant CO_2 mixing ratio). The pressure determined from this ratio determines the direction of view more accurately than the normal satellite altitude sensors.

5 Conclusions

In this talk I have been able to cover only a small part of the subject of remote sensing. The Landsat series has aroused world wide interest and many countries now use the images to investigate such factors as land use, location of mineral ores, crop yield forecasts, etc. The feasibility of determining the vertical temperature structure of the atmosphere from a satellite by measuring the emitted infrared or microwave radiation is now well established and instruments are now being incorporated in the TIROS series of operational weather satellites. Clouds remain a severe problem in retrieving accurate temperature profiles from these radiation measurements. The composition of the stratosphere and the nature of the photochemical reactions which take place there have been subject to intensive study in recent years. Because of the possibility that man made pollutants could cause unwelcome changes such as a reduction in ozone concentration and hence a higher ultraviolet intensity at the earth's surface. I have described an experiment to be flown on Nimbus 6 satellite which will allow the concentration of the minor constituents in the stratosphere to be monitored.

References

- Abel, P.G., Ellis, P.J., Houghton, J.T., Peckham, G.E., Rodgers, C.D., Smith, S.D. and Williamson, E.J., 1970: Remote sounding of atmospheric temperature from satellites: II The selective chopper radiometer, Proc. Roy. Soc. Lond., A320, 35-55.
- Carrett, E.C. and Curtis, L.F., 1976: Introduction to environmental remote sensing, Chapman and Hall, London.
- Ellis, P.J. et al., 1973: Remote sensing of atmospheric temperature from satellites: IV. The selective chopper radiometer for Nimbus 5, Proc. Roy. Soc. Lond., A334, 149-70.
- ESRO, 1973: The implications for European space programmes of the possibilities of manned missions, IV Earth resources, European Space Research Organisation Summer School.
- Gille, J.C. and House, F.B., 1971: On the inversion of limb radiance measurements, I Temperature and thickness, J. Atm. Sci., 28, 1427-1442.
- Gille, J.C., 1972: Limb scanning as a method for measuring the temperature structure of a planetary atmosphere. Temperature, its measurement and control in Science and Industry, Vol. 4.
- Houghton, J.T. and Smith, S.D., 1970: Remote sounding of atmospheric temperature from satellites: I Introduction, Proc. Roy. Soc. Lond., A320, 23-33.
- Houghton, J.T. and Taylor, F.W., 1973: Remote sounding from artificial satellites and space probes of the atmospheres of the earth and the planets, Rep. Prog. Phys., 36, 827-919. (Lists many further references).
- Kaplan, L.D., 1959: Inference of atmospheric structure from remote radiation measurements, J. Opt. Soc. Am., 49, 1004-7.
- Rodgers, C.D., 1971: Some theoretical aspects of remote sounding in the Earth's atmosphere, J. Quant. Spectrosc. Radiat. Transfer, 11, 767-777.
- Schmidt, R.G., Clark, B.B., Bernstein, R., 1975: A search for sulphide bearing areas using Landsat 1 data and digital image processing techniques, Proc. of the NASA Earth Resources Survey Symposium, Houston, Texas.
- Smith, S.D. and Pidgeon, C.R., 1964: Application of multiple beam interferometric methods to the study of CO_2 emission at $15 \mu\text{m}$, Mem. Soc. R. Sci. Liege, 9, 336-49.
- Staelin, D.H., 1969: Passive remote sensing at microwave wavelengths, Proc. IEEE, 57, 427-39.
- Thompson, W.I., 1971: Atmospheric transmission handbook, USA, Department of Transportation.

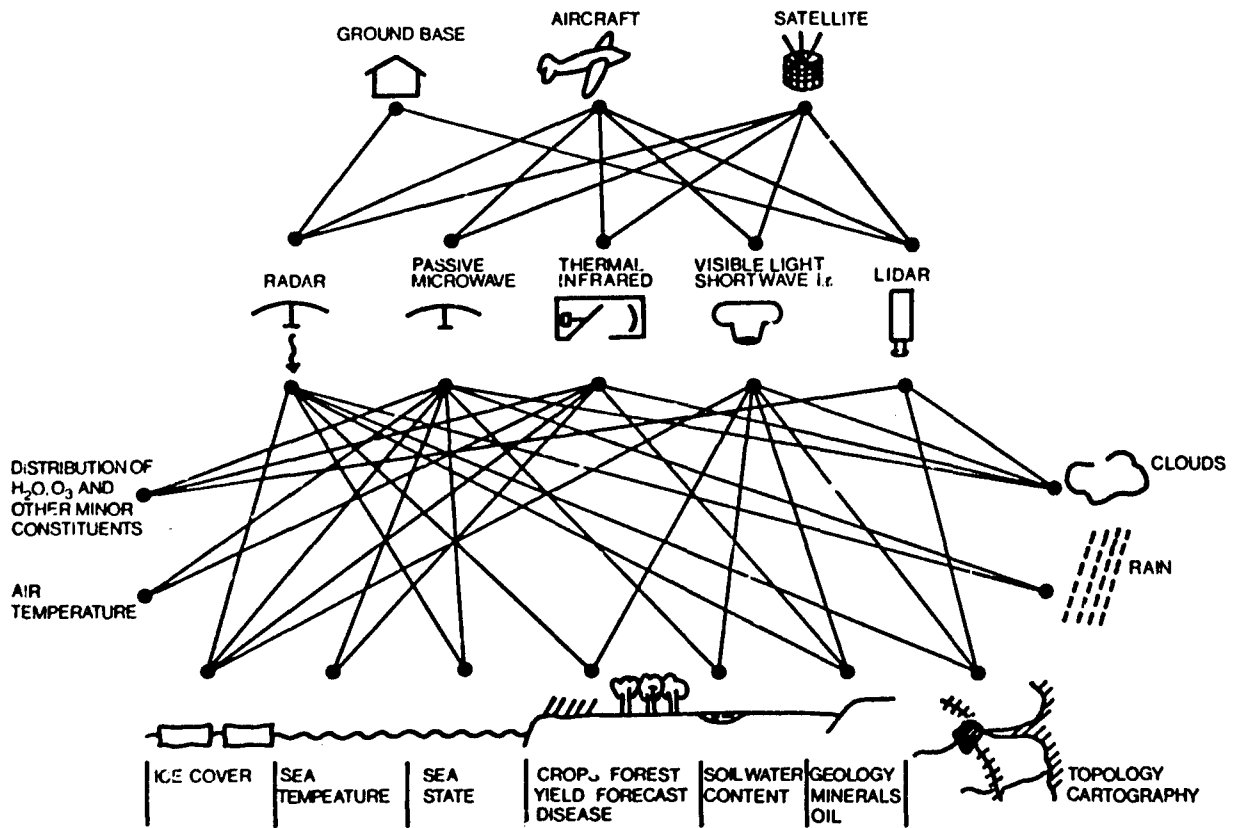


Figure 1. Remote sensing through the electro-magnetic spectrum.

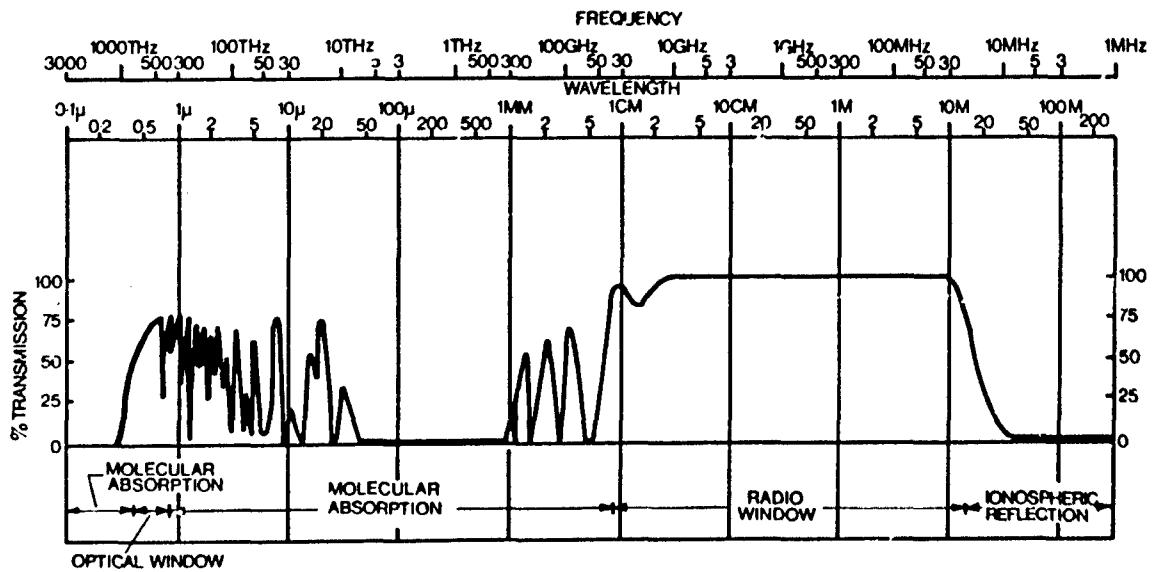


Figure 2. Electro-magnetic spectrum showing relative transparency of the Earth's atmosphere and ionosphere (Thompson, 1971).

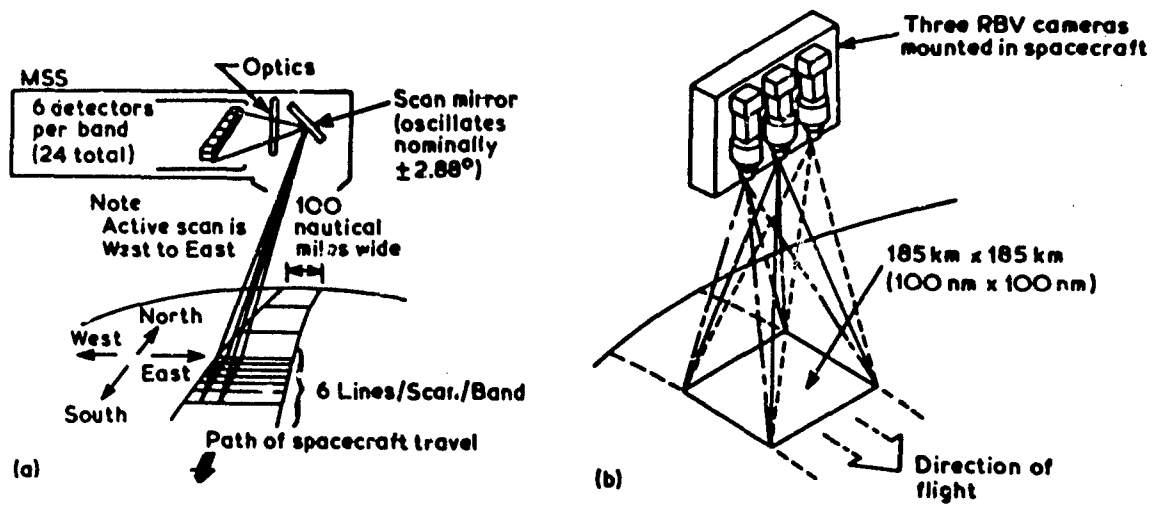


Figure 3. (a) Landsat 1 multispectral scanning system - scan pattern; (b) Landsat 1 return beam vidicon scanning pattern (source NASA).

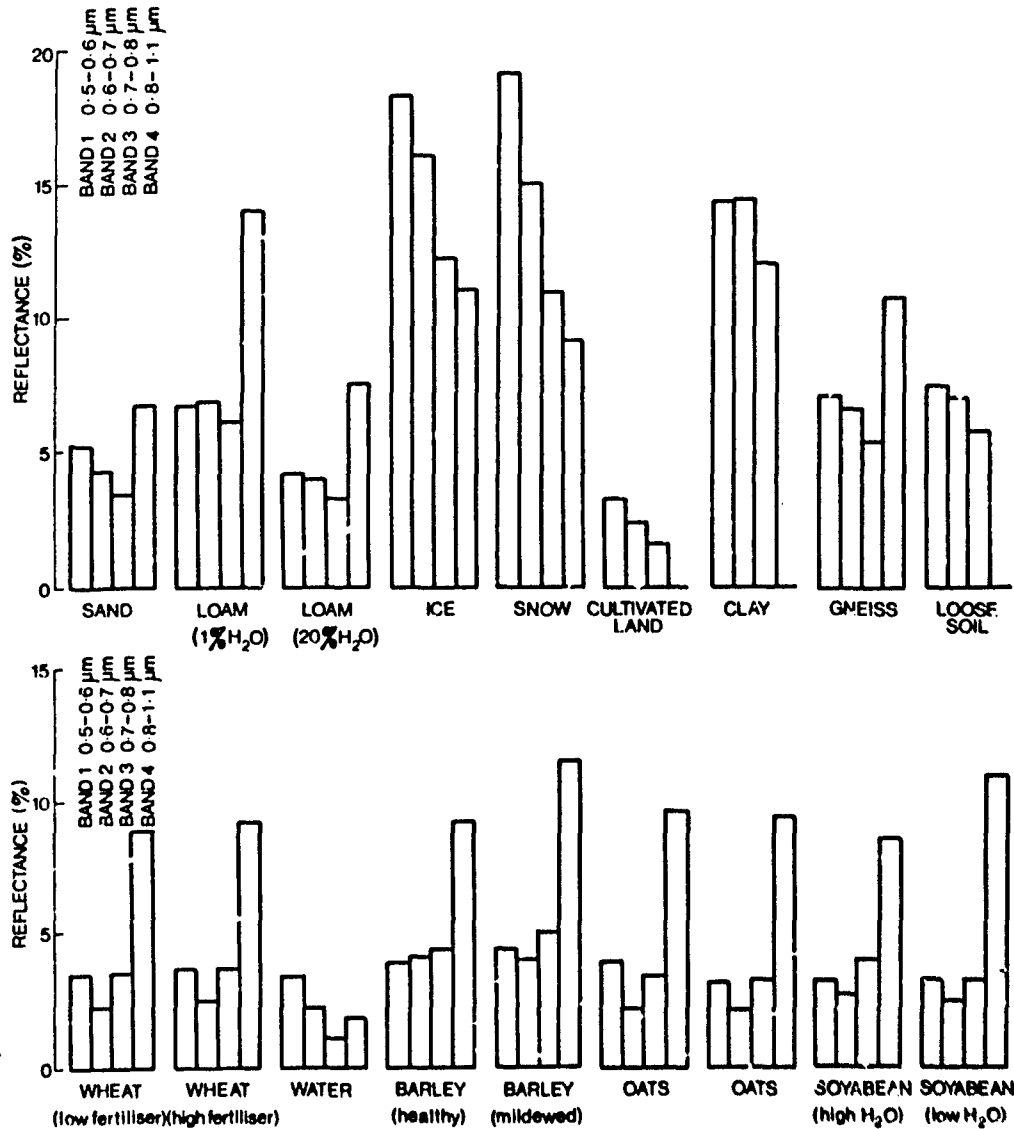


Figure 4. Reflectivity of various soils and crops in the four spectral bands covered by the multispectral scanner (MSS) on Landsat 1. (Data from aircraft and laboratory studies).

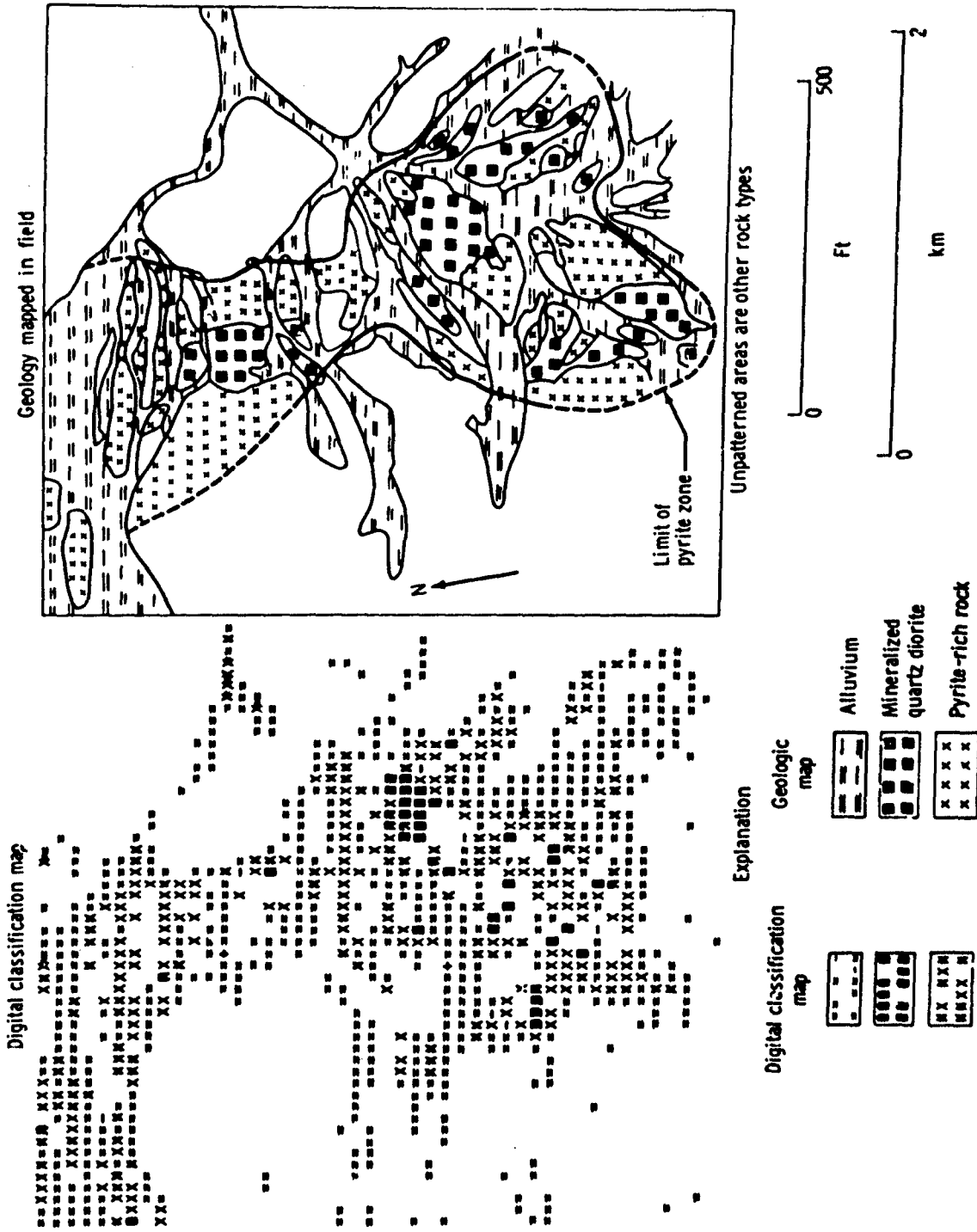


Figure 5. Comparison of digital-classification map made by using Table 1 and geology mapped in field studies (Saindak porphyry copper deposit, Pakistan).

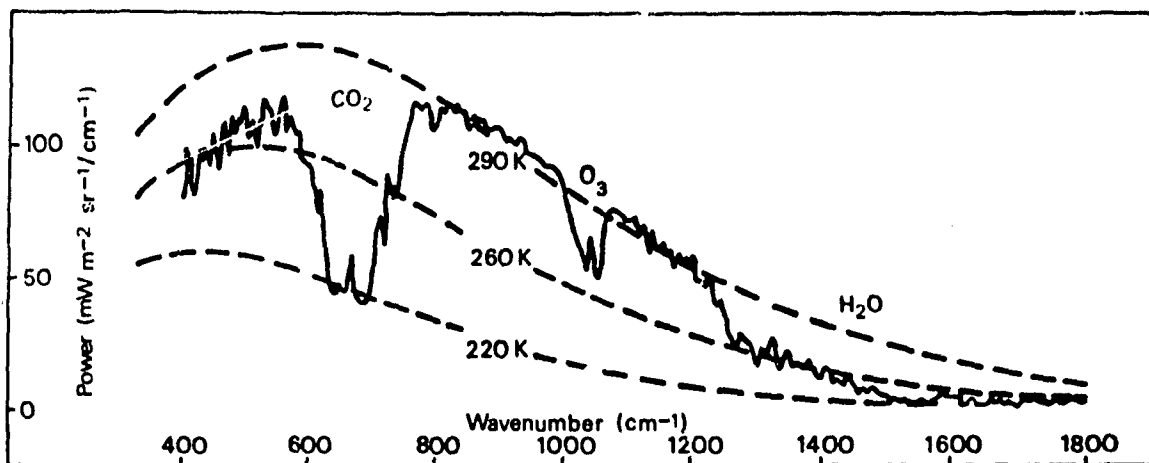


Figure 6. Power spectral density plot from Nimbus 3 Iris data (full line) compared with black body spectrum (broken line). (From Nimbus 4 users handbook, NASA and General Electric).

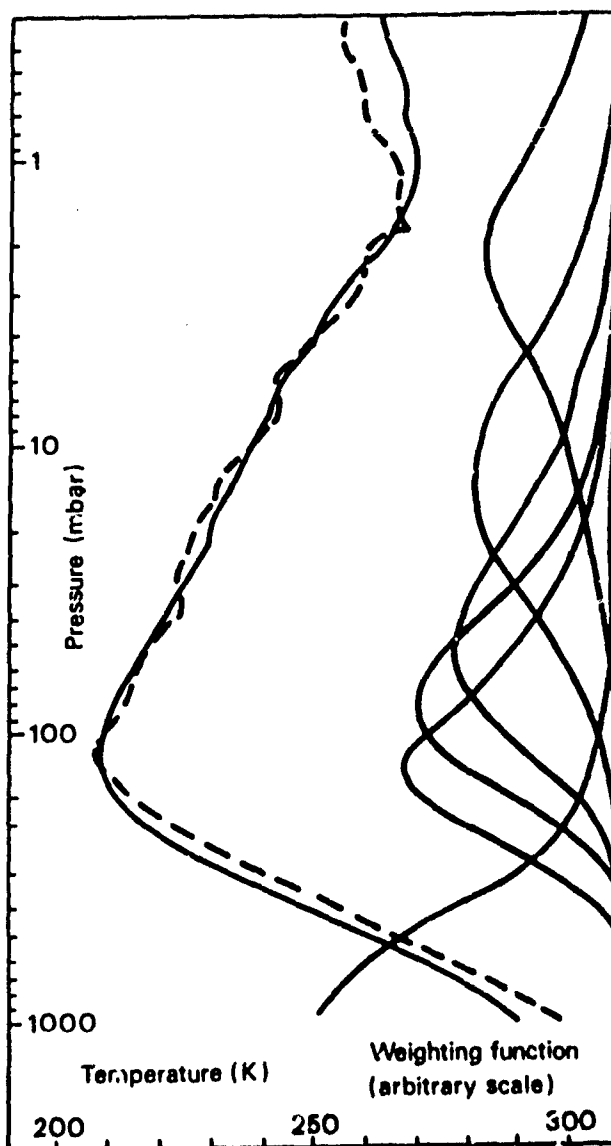


Figure 7. Comparison between a profile computed from Nimbus 4 SCR data (full line) and radio and rocket sonde (broken line) over Wallops Island, 27th August, 1970. The weighting functions for the six channels of this instrument are also shown.

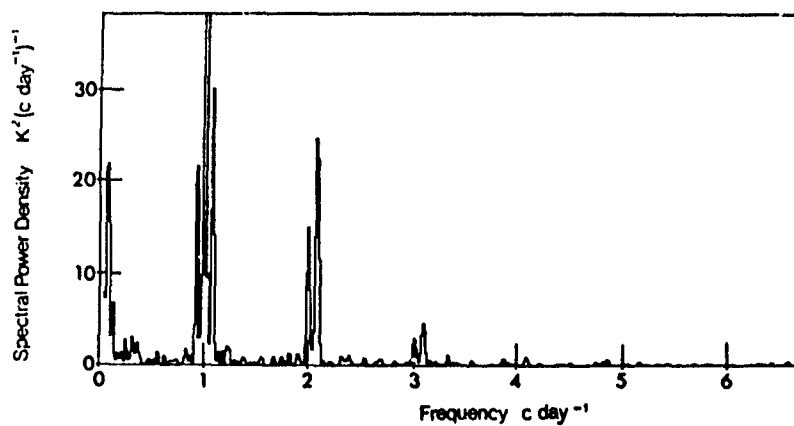


Figure 8. Power spectrum of atmospheric temperatures at 45 km altitude, latitude 60S as observed by the SCR on Nimbus 4.

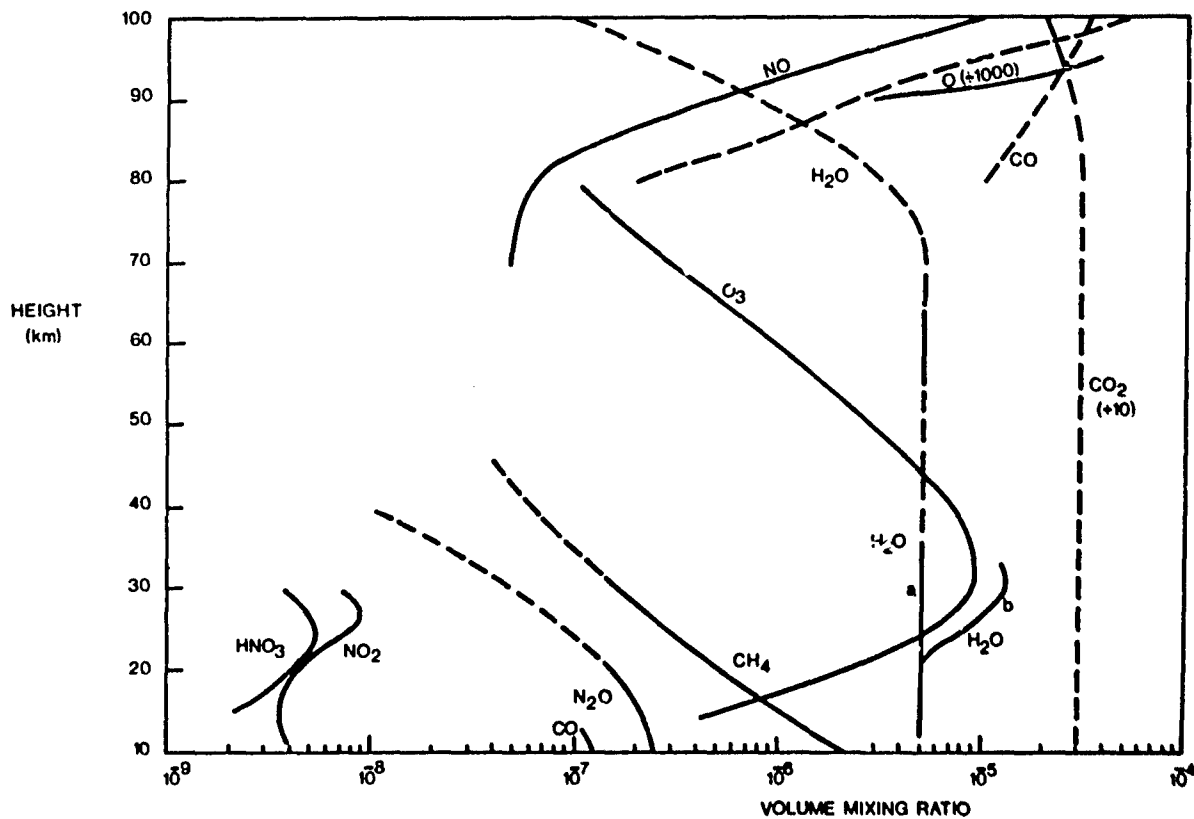


Figure 9. Distribution of minor constituents in the stratosphere and mesosphere. (Full lines represent measurements, dotted lines calculations).

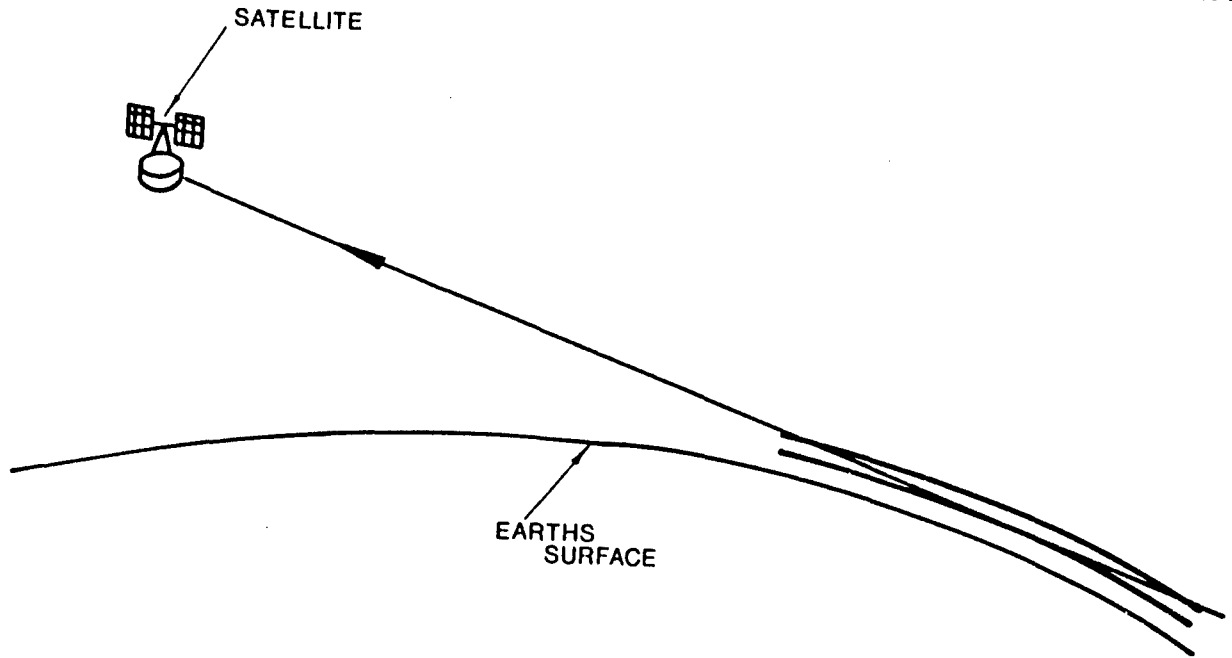


Figure 10. Limb sounding.

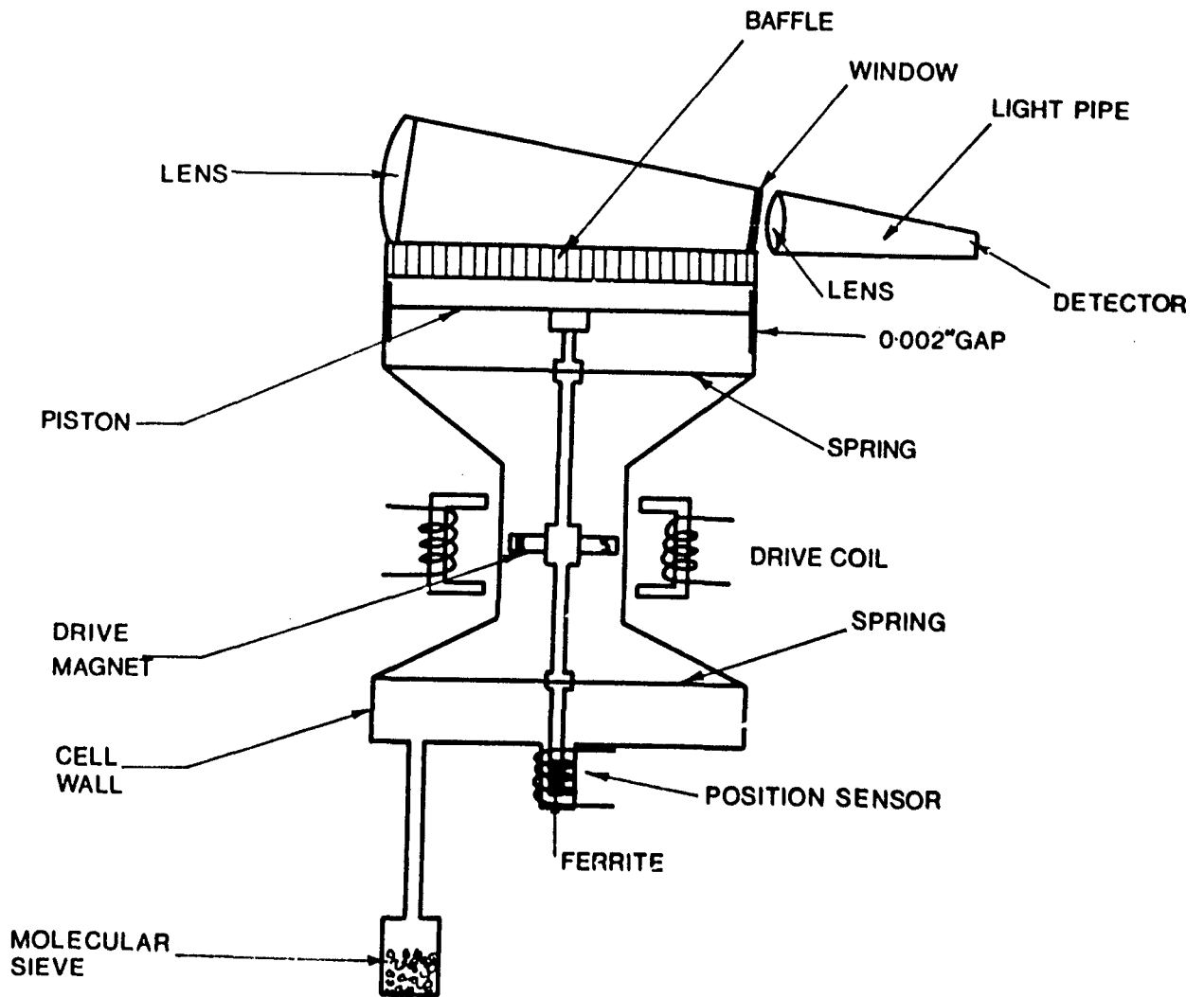


Figure 11. 60 mm pressure modulator cell for the Nimbus 6 PAR.

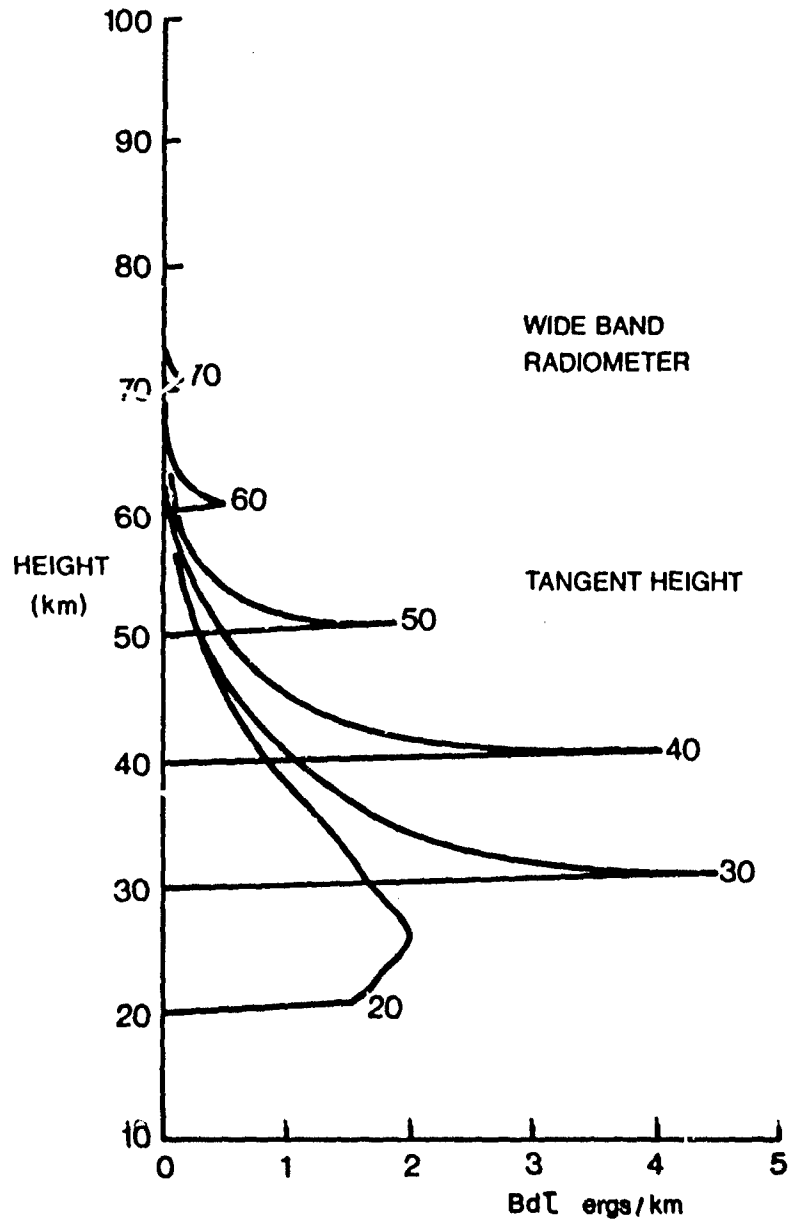


Figure 12. Plots of the product of the Planck function for a standard atmosphere and dt/ds for a limb sounding radiometer with a spectral interval 640 cm^{-1} to 700 cm^{-1} , and an angular field of 0.05° corresponding to 3.5 km at the limb.

TARGET DETECTION AND IDENTIFICATION METHODS BASED ON RADIO- AND OPTICAL WAVES

by
Dag T Gjessing
Chief Scientist

Royal Norwegian Council for Scientific and Industrial Research
Remote Sensing Technology Programme
P O Box 25 - N-2007 Kjeller, Norway

ABSTRACT

Based on technology that is in the process of being developed (tunable lasers, IR heterodyne receivers etc) a sensor system which has an optimum detection/identification capability can be designed when the basic signature of the target is known (geometric shape, chemical composition of surface material etc).

The lecture will derive most of the essential relationships from first principles so as to ensure a physical understanding of the interaction of electromagnetic waves with geometrical surfaces and molecular structures.

The first chapter on fundamentals forms the basis for a section on methodology for the design of optimum systems.

1 INTRODUCTION

The last decade has been characterized by substantial progress in the field of target detection. New sophisticated radar systems incorporating powerful computing systems for the retrieval of the radar signals in a background of noise have been developed. By the aid of such systems, the detection and acquisition potential of the radar system has been improved substantially.

Similarly, new systems involving optical waves have been developed, increasing the *detection* capability still further.

What is needed, however, is an improvement in our capability in regard to target *identification*. Whereas one in many cases can detect the target at large distances, one has often to move up very close before a definite identification is possible.

It is one of the objectives of this contribution to discuss methods by which, based on new technology, the identification potential of our systems can be improved. Specifically, we shall discuss detection/identification systems which are harmonised to the modern command and control systems where the electronic computer possessing storage as well as computing capabilities is an integral part. With such systems it is possible, as we shall see, to match the detection/identification system to the perception capability of the electronic computer and not only, which often is the case today, to the limited perception capability of the human observer. Similarly, as in the case of matching the radar receiver to the computer, we can, by the aid of processors, match the radar illuminator to the target of interest. With such "matched illumination, matched reception" systems based on modern information theory (cybernetics) we can design an optimum system with regard to both detection *and* identification.

Before leaving this point, it may be worth noting the following: If our target were "suspended in mid air" viewed through a homogeneous and transparent atmosphere (viewed through vacuum) and viewed against a cold background with no reflection capability, there would exist a unique relationship between the optimum illumination function and the characteristics of the object to be identified. Similarly, there would exist a unique relationship between the optimum receiving system and the characteristics of the target.

In the realistic situation, however, the target is viewed against a background causing reflections which add noise to our system. Similarly, the propagation medium between the observer and the target is not transparent, nor is it homogeneous. This gives rise to both additive noise (attenuation) and to multiplicative noise (distortion). Thus, in order to have the basis for the design of an optimum system, we shall need information about the signature of the target as well as of that of the atmosphere and of the background. Before presenting a set of potential detection/identification criteria, we shall give a brief sketch of the state-of-the-art as regards the methods and the technology on which the future detection/identification methods can be based.

2 NEW TECHNOLOGY AND NEW METHODS IN RELATION TO THE DETECTION/IDENTIFICATION PROBLEM

Significant technological advances during the last few years in the fields of microwave technique, electrooptics and computer technology open new avenues with regard to detection and identification of objects and of chemical agents with previously unidentifiable properties in our environment.

- *Wide range tunable microwave sources* make it possible to illuminate the object under investigation over a frequency band in a prescribed manner for the particular target "fingerprint" to be revealed with optimum contrast and sensitivity.
- *Microwave receiver elements* will soon exist from which it is possible to determine the wavefront (amplitude and phase) resulting from scattering from an object under investigation over a large spatial area such that the geometrical shape of the object can be determined.
- Similarly, in the infrared and visible region, *tunable lasers* are available over a large range of wavelengths. Thus an illumination can be chosen so as to:
 - i) Penetrate the medium (e.g. the atmosphere) between the observer and the object of interest
 - ii) Give maximum information about the molecular structure (the chemical compounds) of the object surface and of the agents emitted from the object (exhaust gases, oil spills, fragrance etc)
- *Electrooptical receiving systems*, specifically superheterodyne receivers, will soon, as was the case with microwaves 30 years ago, give a dramatic improvement in sensitivity (typically 4-6 orders of magnitude in the infrared region) and wavelength

resolution. By means of such a receiving system and a coherent tunable source, the signal-to-noise ratio of the signals scattered back from the object under investigation is such that the scattered (reflected) signal may be analyzed in great detail and very specific information about target molecular structure can be obtained.

- *Low cost electronic data processors* (micro processors) make it possible to perform the intricate and previously time-consuming computations necessary in real time (parallel processing).
- *Methods in electromagnetic field theory* have been developed from which the shape of the reflecting body (target in a background of interfering bodies) can be determined from measurements of the scattered EM field in space, time and frequency.
- Finally, *statistical estimation methods* such as Kalman filtering and pattern recognition methods have been developed. From these it is possible to make optimum use of a complex set of information (multisensor information about a target) so as to increase the overall sensitivity and the confidence level of the observations.

The preceding decade has been characterized by an endeavour to explore target imaging methods over a large spectral range (sidelooking microwave radars, optical and IR scanners). This is not likely to be the optimum approach when the task is to detect, identify and provide quantitative information about specific objects.

The next decade is expected to be characterized by dedicated detection and recognition methods which make optimum use of available components and techniques.

3 POTENTIAL CRITERIA FOR DETECTION AND IDENTIFICATION OF TARGETS

As we have seen, new technology and new methods open very interesting possibilities in regard to the detection/identification problem. Our task now is one of matching new technological achievements to our particular application. In exploring new detection criteria in relation to potential techniques, the relative merits of these criteria should be assessed.

Potentially, there are numerous such criteria. However, employing a phenomenological classification rather than an application oriented one, a limited number emerges. A set of such are:

- Detection/identification on the basis of shape and size of the target (target macrostructure)
- Detection/identification on the basis of the chemical composition of the target surface (molecular microstructure of target).
- Detection/identification on the basis of the gases which the target may emit (scent from plants, odours from organic substances including human beings, exhaust gases from vehicles etc).
- Detection/identification on the basis of the footprints, tracks or traces which a moving object leaves behind.
- Detection/identification on the basis of the motion pattern of the object (Doppler spectrum).

The target will in general possess useful fingerprints in various spectral ranges. Some of these are weak and some are pronounced. When it comes to determining which of these fingerprints to utilize, we shall also have to consider the *fingerprints of the background*, the noise, and the properties of the medium through which the illuminating waves must pass in order to illuminate the object. Thus, consideration will have to be given to the following:

- Characteristics (fingerprints) of the target (deterministic or statistical).
- Characteristics (statistics) of the background (additive noise).
- Characteristics (structure) of the propagation medium between the platform of observation and the target (distortion, attenuation, multiplicative and additive noise).

Since at least the two latter factors vary in time and space, it is not likely that there exists a unique frequency band within which optimum detection and identification capability is achieved at all times. One would therefore wish to have observations in multiple fingerprint regions and sort out the best set of data under any given condition.

We shall now proceed to discuss the three main aspects of the general complex of problems briefly mentioned above. These are:

- a) Detection and identification based on chemical properties of the object surface or of the chemicals which the object emits or leave behind.
- b) Detection and identification based on object shape and structure or on the geometrical footprints left behind.
- c) Detection and identification on the basis of the motion pattern of the object.

What we then in essence ultimately are aiming at is a multisensor system which through an appropriate weighting procedure injects the information from the various sensors into a computer system which through a Kalman filtering process provides the basis for a decision on position and identity of the target.

4 FUNDAMENTAL RADIO-SCIENCE PRINCIPLES IN THE STUDY OF GEOMETRIC, MOLECULAR AND MOTION SIGNATURES

The list of potential signatures rely on three basic physical principles. The interaction between electromagnetic waves and geometrical objects, the interaction with molecules and the influence of the motion pattern of the object on the frequency of the scattered electromagnetic wave. Let us start with the molecule.

4.1 Fundamental principles in the study of the molecular microstructure

In this section we shall focus our attention on the molecule. Through a study of the molecular structure, we will gain information about the chemical composition of solids, liquids or gases in our environment. Our intention is to lay the foundation for microstructure investigations from remote platforms.

The tool at our disposal are the electromagnetic waves. In the study of liquid or solid surfaces, we illuminate the surface with electromagnetic waves and we detect and analyse the reflected (scattered) signal. From this, it is possible to extract information about the molecular structure. Similarly, in the study of gases, we observe the electromagnetic waves which are subjected to absorption by the gas.

Fundamentally there are three physical principles on the basis of which spectroscopic investigations of the molecular structure can be performed.

Absorption spectroscopy is based on absorption of electromagnetic energy by the molecules at specific electromagnetic wavelengths. In the case of a gas, this absorption phenomenon is covered by the Beer-Lambert law which states

$$P = P_i e^{-\alpha_\lambda L}$$

Here

P = intensity of electromagnetic wave after an absorption path of length L

P_i = incident intensity

c = gas concentration

α_λ = absorption coefficient for the wavelength λ

In the case of solid or liquid surfaces, the phenomenological problem is the same. When electromagnetic waves strike a surface, part of the energy is absorbed. The remaining energy is reflected back and is thus observable. Measuring the absorbed energy as a function of electromagnetic frequency, we obtain information about the molecular structure, as we shall see shortly.

Figure 4.1 illustrates the basic principles of absorption, reflection and emission spectroscopy. Note that the reflection and absorption modes of operation imply an active source of illumination, whereas in the emission case the generator of electromagnetic waves is the body itself.

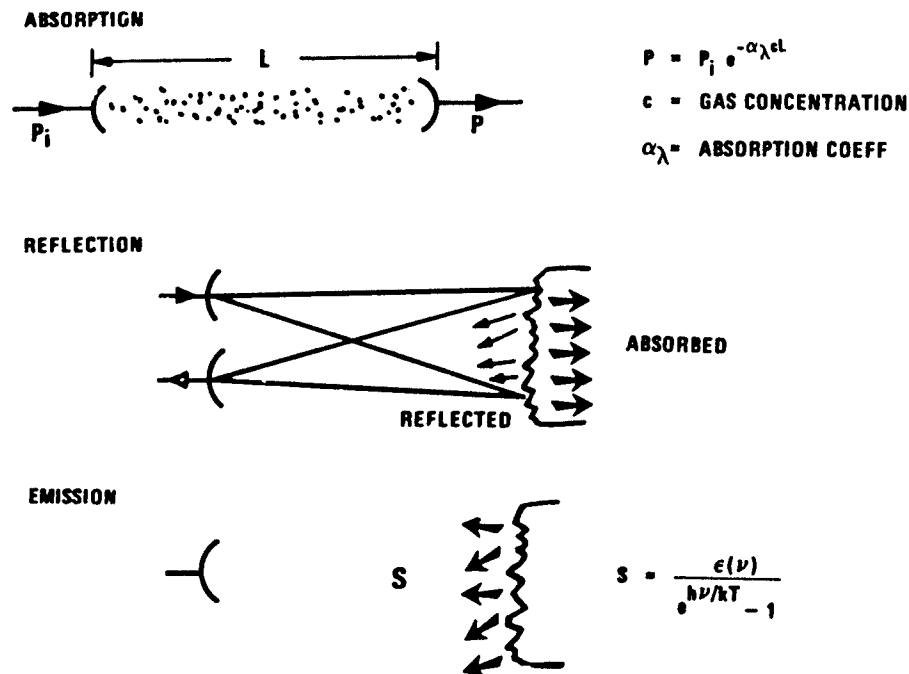


Figure 4.1 Study of molecular structure by absorption, reflection or emission spectroscopy

Fluorescence spectroscopy is another technique of considerable potential. When molecules absorb electromagnetic energy as described above, part of the absorbed energy is reemitted at different frequencies. The frequency spectrum of the emitted fluorescent energy relative to that which stimulated the emission gives information about the molecular structure. Additional information for identification is obtained by measuring the rate at which the reemitted energy decays with time.

Raman scattering can under certain conditions provide significant detailed information about the molecular microstructure. If certain molecules (gases) are stimulated by a laser pulse of large intensity and short wavelength (ultraviolet radiation) each type of molecule will scatter light energy in all directions, the frequency of this reemitted light being frequency shifted relative to the stimulating wave. Measuring this frequency shifted spectrum, information about the density of a large number of gases can be obtained simultaneously.

Having introduced the topic of molecular spectroscopy, we shall proceed to consider the basic absorption mechanisms (1).

There are several such absorption mechanisms: pure rotational spectra, inversion spectra, paramagnetic spectra, vibrational spectra and electronic spectra. In this presentation we shall, for the purpose of illustrating the basic principles involved, restrict ourselves to mentioning rotational and vibrational spectra only.

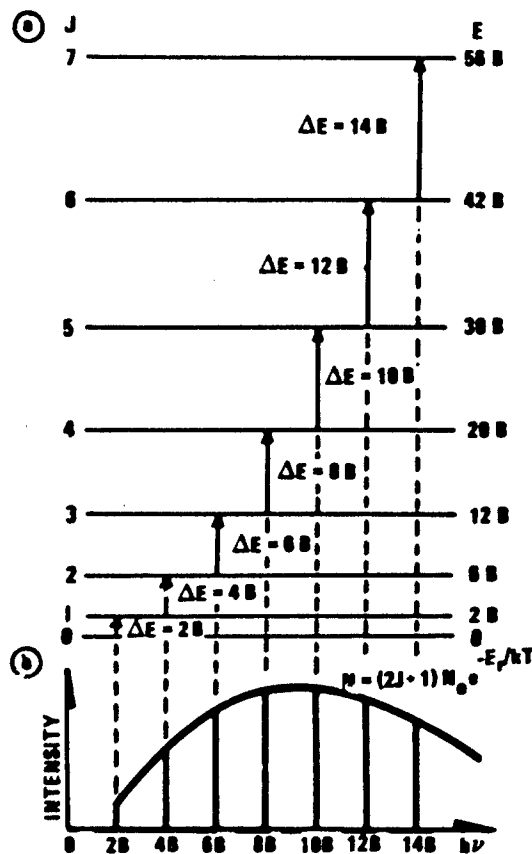


Figure 4.2 a) Structure of rotational levels, with $B = \frac{h^2}{8\pi^2 I}$
 b) Resulting absorption spectrum for a molecular species
 Intensity of line is determined by product of degeneracy and occupation probability.

a) Pure rotational spectra

This category constitutes one of the principal classes of microwave molecular spectra. The spectra arise from the transitions between quantized rotational energies of molecules in single electronic ground states. If the molecule is excited by an electromagnetic field of a frequency ν corresponding to the energy difference between the ground state and the next level ($h\nu = E_1 - E_0$), the molecule will absorb this energy difference from the electromagnetic field, resulting in an absorption line at this frequency.

Consider a molecule as a rigid body rotating round an axis through the centre of gravity. If the angular momentum round the axis of interest is I and the frequency of rotation is ω , the corresponding rotational energy will be given by

$$E_R = \frac{1}{2} I \omega^2$$

The quantum theory, however, requires the angular impulse $I\omega$ to be quantized in units of $h/2\pi$, where h is Planck's constant.

This means that we can only have energies that are integral multiples of $h\nu$. This leads to the following expression for the rotational energy E_R

$$E_R = \frac{h^2}{8\pi^2 I} J(J+1) \quad (4.1)$$

where J is the rotational quantum number.

The selection rule for allowed transitions is that $\Delta J = \pm 1$. The absorption lines are therefore equally spaced, with a spacing $\frac{h^2}{4\pi^2 I}$. The structure of rotational energy levels is shown in Figure 4.2, with the corresponding absorption spectrum.

The main group of molecules giving rise to absorption lines within the range of microwave frequencies are the hydrogen halides.

The only atmospheric gases offering absorption through the mechanism under consideration are SO_2 , O_3 and H_2O .

Let us now consider another important mechanism for absorption, the mechanism of the vibrational spectra.

b) Vibrational spectra

Consider a molecule within which potential forces are acting; the atoms are thus bound together by elastic forces. If these atoms, having a finite mass, are excited by an alternating electromagnetic field, resonance will occur when the stimulating frequency equals that corresponding to the difference between two quantized vibrational energy levels.

Consider again two rigid atoms with masses m_1 and m_2 respectively. These two are tied together by forces which can be represented by springs. We have a ball-and-spring system where the restoring force obeys Hooke's law. The frequency of this simple, harmonic motion, oscillating ball-and-spring system is given by

$$\nu_0 = \frac{1}{2\pi} \left(\frac{K}{\mu} \right)^{1/2} \quad (4.2)$$

where K = spring constant (Hooke's law)

μ = the reduced mass:

$$\mu = \frac{m_1 m_2}{m_1 + m_2}$$

In a way analogous to the case of rotational energies, we have that the energy at frequency ν is given by

$$E_\nu = \left(\nu + \frac{1}{2} \right) \frac{h}{2\pi} \left(\frac{K}{\mu} \right)^{1/2} = \left(\nu + \frac{1}{2} \right) h\nu_0 \quad (4.3)$$

where $\nu = 0, 1, 2, 3$ etc, is the vibrational quantum number, and ν_0 can be thought of as the "ground harmonic" of the oscillating mode.

The above example was given for two atoms. A complex molecule will have a large number of oscillating modes leading to numerous energy levels. However, Equation (4.3) still applies, with appropriate values of ν_0 . It is possible to find the discrete energy levels, and thus the frequencies corresponding to maximum absorption, from knowledge about the molecular composition. From Equation (4.3), any particular mode will give a set of equally spaced energy levels. The vibrational spectra of importance all lie in the infrared range of frequencies.

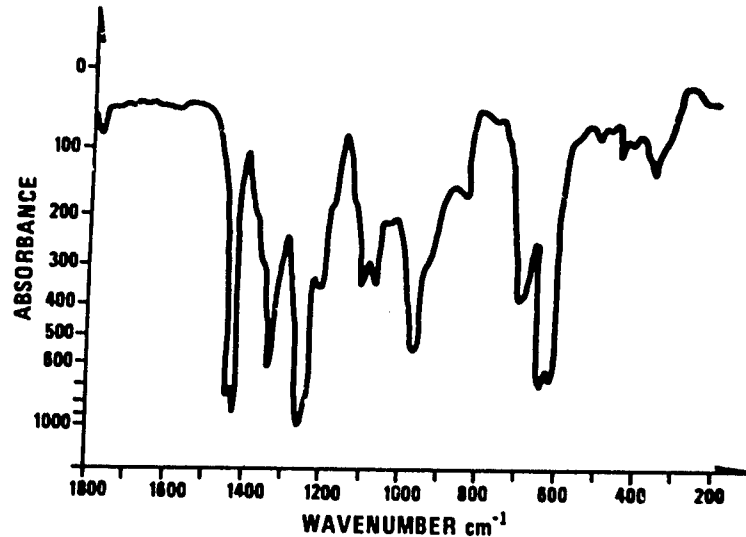


Figure 4.3 Infrared absorption spectrum for vinyl

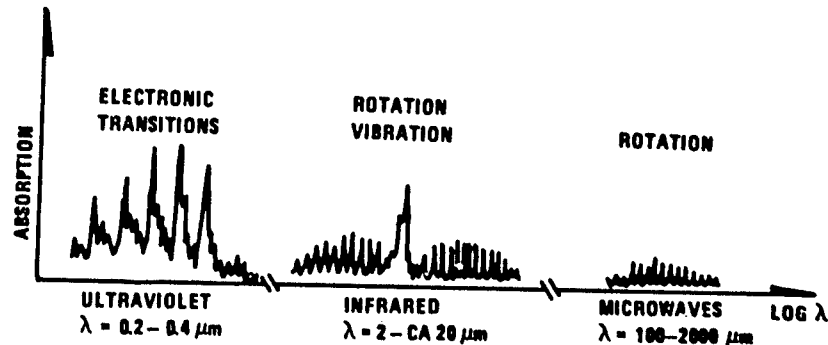


Figure 4.4 Typical form of molecular absorption spectra
Note that the vibrational transitions are split up by the rotational transitions.

Figure 4.3 (2) show a theoretical absorption spectrum for the most typical atmospheric gases at radio frequencies.

Figure 4.4 shows the typical form of molecular absorption spectra arising from the different effects discussed.

To conclude the chapter on fundamental principles in the study of molecular structures, we note that from knowledge about the basic molecular structure, the absorption spectrum of a gas or the reflection spectrum of a liquid or solid surface can be computed, at least in principle. If, however, we are dealing with a mixture of many different molecules the resulting spectra will be very complex. In practice, the composite spectrum can often be synthesized directly from knowledge about the absorption spectra (or reflection spectra as the case may be) of the individual constituents. Knowing for each constituent the position of the individual absorption lines, the linewidth and the intensities, the composite spectrum is obtained.

Using this approach, contributions from all the lines are added, taking into account factors such as line broadening and shifts in a gas due to thermal motion of and collision between molecules and local field effects in solids and liquids.

4.2 Remote probing of the surface macrostructure; Roughness of the earth surface

We have been concerned with the microstructure molecular scale of absorbing, reflecting and emitting surfaces. We shall now concern ourselves with the macrostructure, the surface geometry, as revealed through surface irregularities, from the smallest due to vegetation or fine-scale structured rock and sand, to those on a larger scale due to topographic effects.

The question which arises is the following: Having at our disposal an illuminator (transmitter of electromagnetic waves) and a set of receivers capable of determining the properties of the wave reflected back from the object under investigation (ground surface, rock structure, vegetation, etc) how should we proceed in order to obtain maximum information about the object's macrostructure? In practice, there are many ways of modulating a transmitter, and there are many specific antenna arrangements on the basis of which spatial resolution can be achieved. In this chapter on basic principles we shall discuss the general properties of a wave scattered (reflected) from a rough surface. These are:

- correlation properties in space of the scattered wave (properties of the wavefront)
- correlation properties in the frequency domain of the scattered wave (bandwidth of the reflecting surface)

In the following sections these characteristic properties of a scattered electromagnetic wave will be discussed in turn. The purpose of this discussion is to form the basis for an understanding of the physical basic principles in remote probing to enable maximum information to be obtained about the reflecting surface from observations making use of electromagnetic waves (radio- to optical wavelengths).

4.2.1 Scattering/diffraction from irregular targets – Basic relations

Our objective is firstly to derive the basic expressions to be used in remote investigations of the target macrostructure. But before doing this, before we attempt to synthesize the surface signature, we shall lay the basis for a detailed understanding of the physical principles involved by deriving the general equation governing diffraction and scattering processes.

When dealing with the problem of scattering (reflection) from objects (scattering elements) which are distributed within a volume in space in a random or semi-random fashion, it is a matter of personal taste whether we base the discussion on a scattering process or consider it as being a diffraction problem.

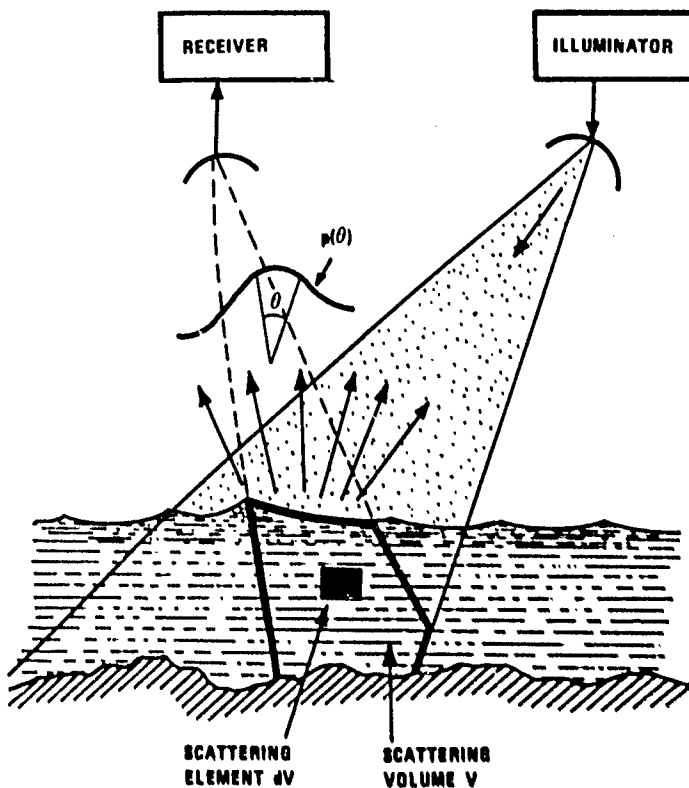
Radio propagation over natural obstructions has long been a subject of considerable interest. Classical knife-edge diffraction theory is used as an idealization of the physical problem. However, due to difficulties in obtaining an analytical solution, particularly when complex ground reflections are considered, most of the previous work has been restricted to compilations of results from theory and measurements, i.e. magnitude considerations only. These are probably of limited general interest in a presentation such as this. The knife-edge diffraction problem has been formally solved by several techniques. The early work by Sommerfeld, who based his analysis on the wave equation with appropriate boundary conditions, is perfectly rigorous and not restricted to small diffracting angles, but generalization to the multiple-reflection problem is not readily accomplished.

Fresnel and Kirchoff based their work on an analytic formulation of Huygens' principle. The Fresnel-Kirchoff method has the advantage of the simplicity of the ray-path concept, and is used almost exclusively in radio propagation literature. However, the method suffers from lack of rigour and from the appearance of the Fresnel integrals, which tend to obscure physical interpretations. In order to obtain practical solutions to the problem of diffraction in the presence of multiple reflections, a phasor summation of the Fresnel-Kirchoff results is therefore normally performed for the single-ray problem.

In a paper by Ratcliffe (3) a very ingenious and general method for solving complex diffraction problems is sketched. Ratcliffe shows that if, in particular, a one-dimensional diffracting screen is illuminated by a wave (wavelength λ), then the angular power spectrum $P(\theta)$ produced, expressed in terms of $\sin \theta$, is the Fourier transform of the spatial distribution $E(z)$ of the wavefront just as it leaves the screen, provided z is expressed in terms of λ .

Now let us derive the expression for the scattered/reflected/diffracted field from knowledge about the spatial distribution of the scattering elements and from knowledge about the geometry. Note that we are considering the general case of three dimensions, not limiting ourselves to scattering from a surface only.

Referring to Figure 4.5, consider a volume element $dv = dx dy dz = d^3\vec{r}$, within the scattering volume V , this scattering volume being confined to the spatial region in the scattering strata illuminated by the transmitting antenna and "seen" by the receiving antenna.



If the permittivity (refractive index squared) within the elementary volume differs by a small amount $\Delta\epsilon$ from the average value of the permittivity ϵ_0 , the element of dielectric becomes polarised, giving rise to a dipole moment ($d\vec{P} = \Delta\epsilon dv \vec{E}_0$) when under the influence of an electric field E_0 . At a distance R from the scattering element, the dipole moment results in a polarisation potential $d\vec{r}$ and, provided $k^2 \vec{r} \gg \nabla \nabla \cdot \vec{r}$ (which requires $R \gg V^{1/3}$), the scattered field strength $\vec{E}_s \approx k^2 \vec{r}$, where k is the wavenumber of the electric field. The scattered field resulting from the integral of elementary scattering elements is then given by

$$\vec{E}_s = \frac{k^2}{4\pi} \int \frac{1}{R} \vec{E}_0(\vec{r}) \epsilon(\vec{r}) e^{-j\vec{k} \cdot \vec{r}} d^3\vec{r} \quad (4.4)$$

omitting the time factor $e^{j\omega t}$.

Here

- $\vec{k} = \vec{k}_0 - \vec{k}_s$
- \vec{k}_0 = wavenumber of incident field
- \vec{k}_s = wavenumber of scattered field
- $|\vec{k}_0| = |\vec{k}_s| = 2\pi/\lambda$
- λ = radio wavelength

Thus

$$|\vec{k}| = \frac{4\pi}{\lambda} \sin \theta/2$$

where θ , the scattering angle, is the angle between \vec{k}_0 and \vec{k}_s . The vector \vec{r} is the position vector of the scattering element, $\epsilon(\vec{r})$ is the space function of the normalised permittivity fluctuation $\Delta\epsilon/\epsilon_0$, and $E_0(\vec{r})$ is the corresponding space function for the electric field.

Figure 4.5 Scattering from irregularities distributed in depth

Note that Equation (3.1), which is derived from Maxwell's equations, is general and does not consider the nature of the refractive index irregularities described by the function $\epsilon(\vec{r})$ or the irregularities in the electric field described by the $E_0(\vec{r})$ function. The functions may be stochastic, in which case the refractive index field is conveniently described by the spatial autocorrelation function of the refractive index in the same way as the electric field E_0 is described by its spatial autocorrelation function, or they may be ordered variations, say a horizontal layer through which the pertinent parameters vary in a systematic fashion as well-behaved functions.

From the basic equation (4.4) for scattered field strength we see that there are two limiting cases:

- a) If the field $\vec{E}_0(\vec{r})$ is constant within the scattering volume and the scattering volume is limited in extent (or varies slowly in space in comparison with the $\epsilon(\vec{r})$ function) then

$$\vec{E}_s = \frac{k^2 \vec{E}_0}{4\pi R} \int_V \epsilon(\vec{r}) e^{-j\vec{k}\cdot\vec{r}} d^3\vec{r}$$

which states that the scattered field \vec{E}_s is proportional to the three-dimensional Fourier transform of the spatial variation in refractive index within the scattering volume V .

- b) If the $\epsilon(\vec{r})$ function is constant within the scattering volume and the field strength \vec{E}_0 varies, then the diffraction field \vec{E}_D is the Fourier transform of the spatial variation in field strength within the scattering volume V .

$$\vec{E}_D = \frac{k^2 \epsilon}{4\pi R} \int_V \vec{E}(\vec{r}) e^{-j\vec{k}\cdot\vec{r}} d^3\vec{r}$$

This is the same expression as that developed by Ratcliffe, referred to above (3). See also (4,5,6).

It then only remains, on the basis of the expressions above for scattered field strength \vec{E}_s , to calculate the angular distribution of scattered power.

The desired expression for the received power is obtained by multiplying \vec{E}_s by its complex conjugate \vec{E}_s^* , this obtaining an expression for the scattered angular power spectrum $P(\theta)$ of the form

$$P(\theta) \sim \Phi(K) \sim \int R_E(\vec{x}) e^{-j\vec{k}\cdot\vec{x}} d^3\vec{x}$$

Hence, the angular power spectrum $P(\theta)$ is the Fourier transform of the spatial autocorrelation of the electric field over the scattering volume (7).

This important result will be used in the following sections.

4.2.2 Spatial correlation properties of electromagnetic wave reflected from the earth surface; measurement of transverse distribution of scattering surface elements by remote probing techniques

Our attention is now focused on the transverse distribution of the scattering elements constituting the scattering object. In order to reveal this structure we shall use another characteristic of an electromagnetic wave, namely its spatial correlation properties.

Classically, we know that there are three classes of antenna systems that have a spatial resolution potential. These are:

- *Aperture antenna* where the angular resolution $\beta = \lambda/D$, D being the aperture diameter and λ the radio wavelength. If R is the distance between the observation platform and the object to be analysed, then the aperture antenna system has a resolution capability δx given by

$$\delta x = R \frac{\lambda}{D}$$

- *Array antenna* which makes use of a set of antenna elements distributed along a baseline or in a plane. Each element is capable of measuring amplitude and phase of the wavefront at a point. On the basis of these point-observations of field strength, information about the target can be extracted. This will be the subject of the current section.

- *Synthetic aperture antenna* which makes use of measurements of amplitude and phase over a baseline by shifting one sensor from one point to another, probing the wavefront sequentially in time (in series and not in parallel). In principle there is little difference between the linear array antenna and the synthetic aperture antenna (8). See Figure 4.6.

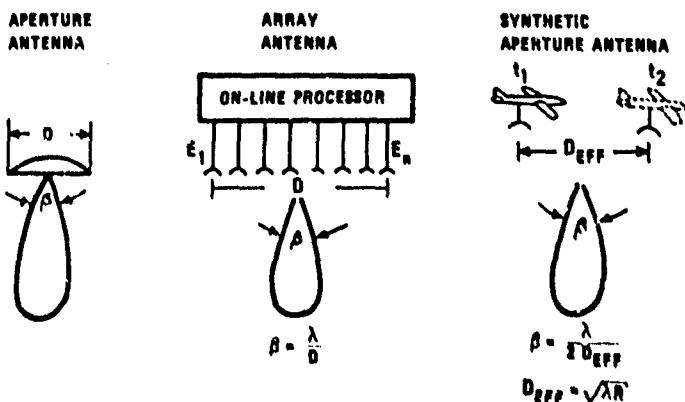


Figure 4.6 Basic principle related to three classes of high resolution antenna system

If the object to be investigated is at rest and if atmospheric effects can be neglected, there is no difference in principle between the synthetic aperture antenna and the array antenna.

However, as we shall see in the following chapter where we discuss the propagation limitations, irregularities in the atmospheric refractive index structure caused by turbulence impose particular limitations on the resolving power of a synthetic aperture antenna system. These aspects will be considered in Chapter 4.

We shall now analyse the phased array concept with a view to obtaining information about the transverse geometrical shape of the object by means of field strength measurements at n points along the baseline.

There are several approaches at our disposal. In view of the fact that many of the derivations later are essentially hinged on the relationship between the angle of arrival spectrum (angular

power distribution) and the spatial correlation properties of field strength, it is probably justifiable to present two different approaches here.

First let us present an approach which is a direct consequence of the basic equations derived above. Referring specifically to Equation (4.5), this states that the angular power spectrum (the radiation pattern) emitted from a scattering/diffracting/reflecting area is the Fourier transform of the spatial autocorrelation function of field strength over this area. We see that this relationship refers to the case where the area is considered as a radiator, i.e. as a transmitting antenna.

Now let us consider the case of a receiving antenna. The power reaching this array antenna is distributed as $P(\theta)$ over an angular region.

Applying the inverse Fourier transform, it is self-evident that the $P(\theta)$ angle of arrival spectrum will give a spatial field strength autocorrelation over the array antenna which is the Fourier transform of the $P(\theta)$ angular power spectrum.

Thus, when our task is to measure the transverse distribution of the scatterers constituting the object of interest, we obtain information about this directly by using an array antenna measuring the autocorrelation function of field strength over the array. As is the case with any receiving antenna, the greater the required space resolution, the longer should the antenna be.

We shall return to this discussion shortly. Now let us present another approach adopted by Hagfors (9). Suppose that the scattered field-wave impinging on the receiver is sensed by two small antennas displaced a distance ξ wavelengths along a direction perpendicular to the line joining the "transmitter", i.e. the scatterers, and the receiver.

At an instant t the complex field strength from the direction θ (where θ is measured in a plane containing the two receiving antennas and the target from which the backscattered field originates); is taken to be $\hat{E}(S,t)dS$ at the midpoint of the receiving antenna baseline. Here $S = \sin \theta$.

The complex electromagnetic field induced in the two antenna elements from this direction is thus given by

$$de_1 \cong E(S,t) e^{-j\pi\xi S} dS \quad (4.6)$$

$$de_2 \cong E(S,t) e^{+j\pi\xi S} dS \quad (4.7)$$

provided the two antennas are identical so that the effective angular spectra can be assumed to be very nearly equal.

Integrating over all directions S , we obtain the total electromagnetic field in the two antennas

$$e_1 \cong \int E(S,t) e^{-j\pi\xi S} dS \quad (4.8)$$

$$e_2 \cong \int E(S,t) e^{+j\pi\xi S} dS \quad (4.9)$$

Note that the carrier frequency time variation is neglected and only the slow variation with time of the angular spectrum $E(S,t)$ retained.

The normalized complex correlation of these two voltages is then

$$R(\xi) = \frac{e_1 \cdot e_2^*}{e_1^2} = \frac{\int |E(S)|^2 e^{-j2\pi\xi S} dS}{\int |E(S)|^2 dS} \quad (4.10)$$

The above equation states that the spatial autocorrelation function $R(\xi)$ of field strength is the Fourier transform of the angular power spectrum (see (3,4,5,6)).

Knowledge about $R(\xi)$ is thus a sufficient condition for determining the angular power spectrum $|E(S)|^2$. This is the same result as that obtained above.

Note that if ξ is measured along a horizontal direction, the angle of arrival spectrum is measured in the horizontal plane. If ξ is measured vertically, the angle of arrival spectrum of power $(|E(S)|^2 = P(\theta))$ is measured in the vertical plane. This angular distribution in the vertical plane $P(\theta)$ is proportional to the transverse vertical distribution $\sigma(x)$ of the scatterers constituting the target of interest. Without going into detail about this transverse distribution as measured through the angle of arrival spectrum and effects of virtual scattering centres (giving effects such as glint), the first order relationship between the transverse distribution $\sigma(x)$ of the target scattering cross-section and the angular power spectrum (angle of arrival spectrum) a distance R from the target is given by

$$P(\theta) \sim \sigma\left(\frac{x}{R}\right)$$

Thus, using as an example an object which gives constant scattering between certain limits Δx apart, the angular power spectrum $P(x/R)$ is rectangular. The width is $\Delta x/R$, where Δx is the width of the object.

The Fourier transform of this rectangular angle of arrival spectrum is a $(\sin x)/x$ function, the width of which is given by

$$L \sim \frac{\lambda R}{\Delta x} \quad (4.11)$$

where λ is the wavelength of the radio wave.

This relationship is well known from antenna theory. From antenna theory we know that if L is the width of the illuminating field strength distribution (antenna aperture), the half power width of the resulting angular power spectrum is given by

$$\beta \sim \frac{\lambda}{L}$$

and since in the case of our "rectangular" target

$$\beta \sim \frac{\Delta x}{R} \quad (4.12)$$

the expression for L above follows directly.

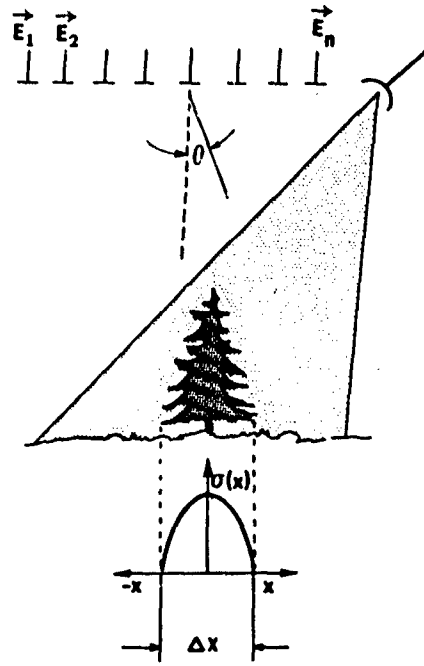


Figure 4.7 Basic principle for the measurement of transverse distribution of scatterers by spatial correlation measurement of field strength

Figure 4.7 illustrates the basic principles related to the determination of angular power spectrum on the basis of spatial field strength correlation measurements.

By measuring amplitude and phase of the wave scattered back from the object of interest at a number of points in a plane normal to the direction to the object, information about the transverse distribution of the scatterers constituting the object is obtained.

In Chapter 6 on general remote sensing methodology, some examples illustrating the potential of the technique will be given.

4.2.3 Bandwidth properties of electromagnetic waves reflected from a surface (correlation properties in the frequency domain); distribution in depth of scattering surface

We shall now focus our attention on the bandwidth problem (7).

We have seen in the first chapter that in order to determine the molecular structure of the absorbing or reflecting material by measuring the absorption or reflection spectrum, we have to change the frequency of our transmitter (illuminator) in some manner.

There are thus two factors that influence the signal reflected back from the rough surface:

- a) the molecular structure of the surface material
- b) the geometrical shape (the roughness) of the surface

In order to distinguish between the two effects, we must know both processes in some detail. There are three practical situations which warrant information about the correlation properties in the frequency domain of the reflecting surface:

- When the aim is to measure atmospheric gases by spectroscopic methods, it is practical to use the ground or the sea surface as the reflector, thus obtaining a monostatic measuring situation. Information about both the spectral and the geometrical effects of the reflector is then imperative.
- When information about the molecular surface structure is required, information about the influence of the surface roughness is imperative.
- Finally, as we shall see in the following, by measuring the correlation properties in the frequency domain resulting from a multifrequency illumination of (or emission from) the surface under investigation, information about the roughness of the surface is obtained (distribution in depth of the scattering surface).

Consider the case of diffuse (not specular) reflection (scattering) from a rough surface. The surface consists of a collection of scattering elements distributed in depth z from which a set of waves is reflected back to the receiver. These waves will interfere (multipath fading) and the result is a signal with limited bandwidth, i.e. with limited correlation properties in the frequency domain. We shall now calculate this correlation function (bandwidth of reflector).

To avoid the confusion which often arises when the term "bandwidth" is used in relation to scattering processes, let us define what we mean by bandwidth.

Consider the case where several radio waves having different frequencies are transmitted simultaneously. At the receiver, the power at each of these frequencies is measured as a function of time (i.e. we measure $P_{F_1}(t)$, $P_{F_2}(t)$ etc). If we take the instantaneous ratio of power at the various frequencies and integrate the ratio (i.e. we form $\int \frac{P_{F_1}(t)}{P_{F_2}(t)} dt$) then we obtain information about bandwidth.

On the other hand, if we integrate the signal at either frequency over the appropriate time interval by forming $\frac{\int P_{F_1}(t) dt}{\int P_{F_2}(t) dt}$ we do not obtain information about bandwidth but something which is often referred to in radioscience literature as "the wavelength dependence of the scatter circuit".

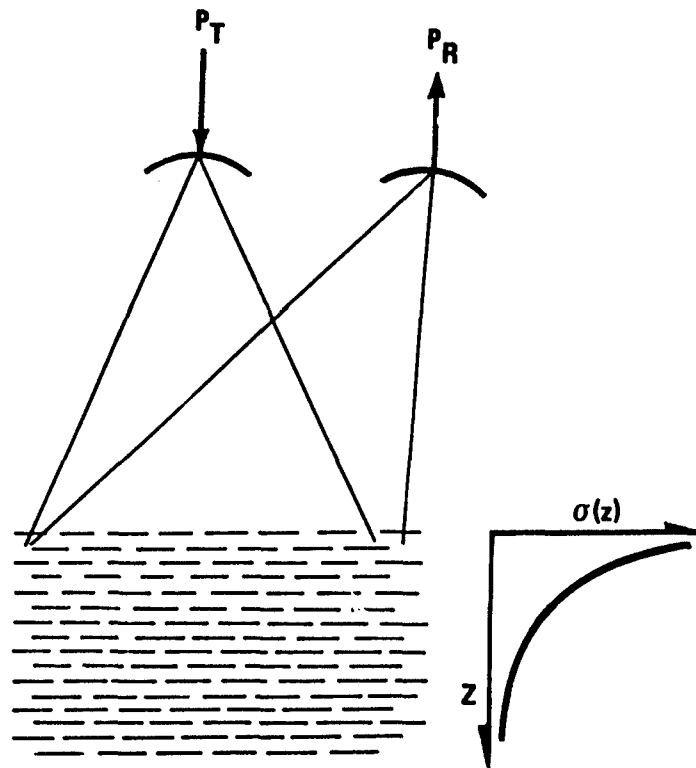


Figure 4.8 Geometry of the scattering in depth process (correlation properties in the frequency domain)

Forming the $\int \frac{P_{F_1}(t)}{P_{F_2}(t)} dt$ is one way of obtaining information about bandwidth. Another is the following:

As in the case above, we transmit a set of radio waves having different frequencies. We now make sure that all these frequencies are correlated in amplitude and phase. This is, as an example, achieved by amplitude modulating a carrier, thus obtaining two sidebands $2F_{AM}$ apart, F_{AM} being the frequency of the modulating wave. These sidebands, obviously, are correlated in amplitude and phase. At the receiving end we pick up the two sidebands and correlate one with the other (i.e. we form the cross-correlation function $R_{12}(\tau)$). The more narrow-banded the transmission channel, the poorer is the correlation. (Transmitting many correlated waves spread over a frequency band, we can find the complete autocorrelation function $R(\Delta F)$ in the frequency domain.)

If the scattering cross-section σ associated with a scattering element distance z from the receiver is denoted $\sigma(z)$, the associated delay function of the received field is $P(\tau) \cong \sigma(z/c)$, where c is the velocity of light.

Using analogous results from network theory, we have the following relationships:

The Fourier transform (FT) of the delay function is known as the impulse response $F(\omega)$. Impulse response is thus

$$F(\omega) = \text{FT}(P(\tau))$$

Furthermore, the resulting power spectrum $W(\omega)$ is given by

$$W(\omega) = F(\omega) F^*(\omega) \quad (4.13)$$

Thus, knowing the distribution in depth of the scattering elements $\sigma(z)$, the bandwidth of the reflecting surface ($\Delta\omega$) given by $W(\Delta\omega)/W(0) = 1/2$ is obtained by a simple Fourier transformation of the $\sigma(z/c)$ function.

For the purpose of illustrating the essential points, let us discuss as an example the scattering process from vegetation.

We shall assume that the ground surface being illuminated consists essentially of coniferous trees having needles distributed evenly in depth in such a way that the shadowing effect becomes progressively more dominant as the wave progresses. Let us, for the sake of simplicity, assume an exponential shadowing effect such that the illuminated scattering facets are distributed in an exponential manner in depth. This leads to a set of waves arriving at the receiver. These waves will interfere and the result is a limited correlation bandwidth of the reflecting surface. We shall now calculate this bandwidth.

The delay function of these reflected waves is given by

$$P(\tau) = e^{-\alpha\tau}$$

since the distribution in depth of scattering cross-section is assumed to be exponential.

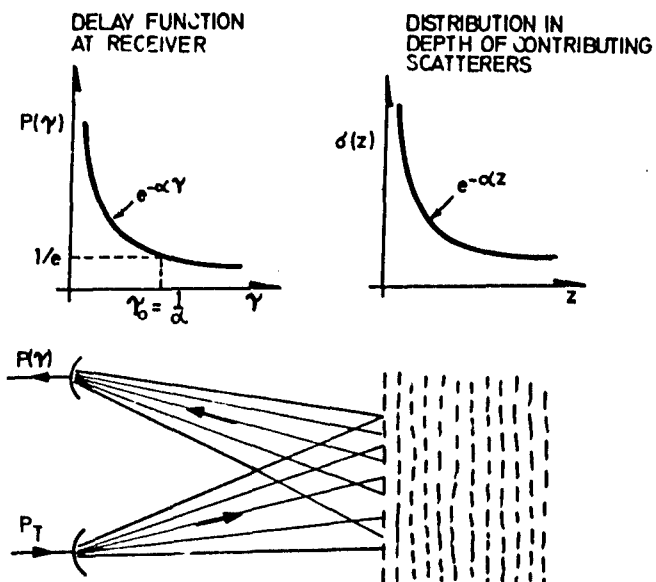


Figure 4.9 Geometry of the scattering process (correlation properties in the frequency domain)

The 1/e width of this delay function is given by

$$\tau_0 = \frac{1}{\alpha}$$

The Fourier transform (FT) of the delay function is given by

$$\begin{aligned} \text{Impulse response} \\ F(\omega) &= \text{FT}(\text{delay function}) \\ &= \text{FT}(e^{-\alpha\tau}) \\ &= (\alpha + j\omega)^{-1} \end{aligned}$$

The resulting power spectrum is thus (7)

$$W(\omega) = F(\omega)F^*(\omega) = (\alpha^2 + \omega^2)^{-1} \tag{4.14}$$

The half power width $\Delta\omega$ of this spectrum is given by

$$\frac{W(\omega)}{W(0)} = \frac{1}{2} = \frac{\alpha^2}{\alpha^2 + \Delta\omega^2} \tag{4.15}$$

ie

$$\Delta\omega = \alpha = 1/\tau_0$$

Hence, if the 1/e penetration depth of the electromagnetic wave is $c\tau_0 = \Delta z$ metres, the "bandwidth" (width of power spectrum) is given by

$$\Delta F = \frac{c}{2\pi\Delta z}$$

The "bandwidth" discussion above may appeal to the radio engineer. However, to the scientist familiar with statistics and signal analysis it may be more meaningful to express the results in terms of the correlation properties of the signal scattered back from the rough terrain surface.

Specifically, we shall now calculate the autocorrelation function in the frequency domain $R(\Delta\omega)$. The voltage V_1 of the signal scattered back at frequency ω is given by

$$V_1 = F(\omega) = (\alpha + j\omega)^{-1} \tag{4.16}$$

Similarly, the voltage V_2 at frequency $(\omega + \Delta\omega)$ is given by

$$V_2 = F(\omega + \Delta\omega) = [\alpha + j(\omega + \Delta\omega)]^{-1} \tag{4.17}$$

The normalized complex autocorrelation of these two voltages is then given by

$$R(\Delta\omega) = \frac{\int_{-\infty}^{\infty} (\alpha + j\omega)^{-1} [\alpha - j(\omega + \Delta\omega)]^{-1} d\omega}{\int_{-\infty}^{\infty} (\alpha^2 + \omega^2)^{-1} d\omega} \tag{4.18}$$

Solving this integral we derive the following expression for the modulus of the autocorrelation function

$$R(\Delta\omega) = \left[1 + \left(\frac{\Delta\omega}{2\alpha} \right)^2 \right]^{-1/2} \tag{4.19}$$

Defining now the correlation distance in the frequency domain to be the halfwidth of the autocorrelation function, we have

$$\begin{aligned} \Delta\omega_{1/2} &= 2\alpha\sqrt{3} \\ \Delta F &= \frac{\sqrt{3}}{\pi} \frac{c}{\Delta z} \text{ Hz} \end{aligned} \tag{4.20}$$

4.2.4 Temporal correlation properties of the scattered waves; studies of the target's motion pattern

There are several factors which determine the temporal correlation properties of the scattered signal. These have been studied extensively over many years (4,7,10,11,12). We shall present the main results.

In order to ensure an understanding of the physical principles involved, we shall derive the results from first principles. Consider a scattering element within the spatial region (the scattering volume) contributing to the scattered signal. The wave incident on this has wavevector k_1 , whereas that of the scattered wave is k_2 .

If this scattering element is in motion relative to the observation platform -- the transmitter/receiver -- then the wave scattered back by the scattering element with velocity \dot{V} is subjected to a Doppler shift F . This frequency shift is given by the familiar relationship

$$\begin{aligned} F &= \frac{1}{2\pi} (k_1 - k_2) \cdot \dot{V} \\ &= \frac{1}{2\pi} k \cdot \dot{V} \end{aligned} \tag{4.21}$$

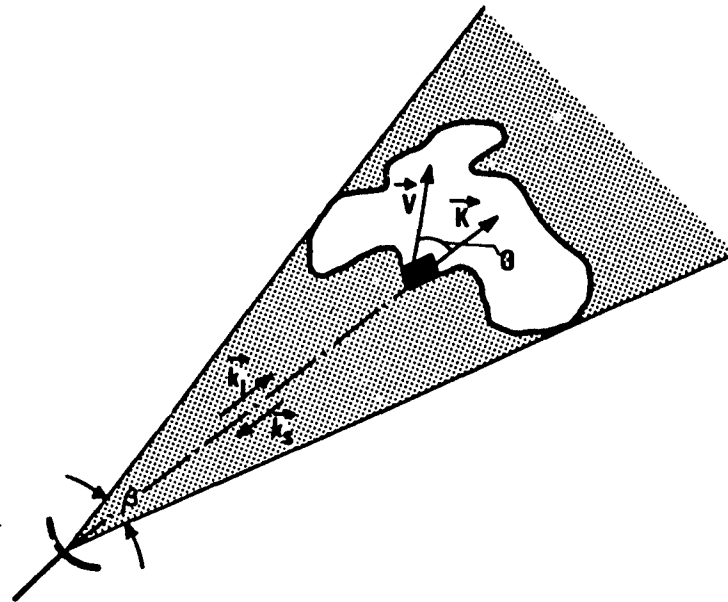


Figure 4.10 The scattered signal is Doppler shifted as a consequence of the motion of the scattering element relative to the radar

Assuming a monostatic radar situation as depicted in Figure 4.10 we measure pure backscatter such that the angle between \hat{k}_1 and \hat{k}_2 is 180° and the vector difference \hat{K} is directed along the direction of propagation. The magnitude of the vector difference \hat{K} is then $4\pi/\lambda$. Thus, from one single scattering element we have a Doppler shift F given by (16,17)

$$\begin{aligned} F &= \frac{1}{2\pi} \cdot \frac{4\pi}{\lambda} V \cos \theta \\ &= \frac{2V}{\lambda} \cos \theta \end{aligned} \quad (4.22)$$

where θ is the angle between \hat{K} and \hat{V} .

However, we have many scattering elements contributing at any one given time. The result is that a set of waves reaches the receiver. These will have different Doppler shift, different phase and different amplitude. This situation leads to amplitude scintillations, i.e. to fading. Let us now consider two limiting cases:

a) Influence on the scintillation spectrum of the velocity distribution of the scattering elements

Let us assume that the beamwidth β (angle subtended by the object) is small such that the difference vector \hat{K} is constant within the scattering volume. The width ΔF of the Doppler spectrum causing scintillation is then

$$\begin{aligned} \Delta F_V &= \frac{1}{2\pi} \hat{K} \cdot \delta \hat{V} \\ &= \frac{2\delta V}{\lambda} \cos \theta \end{aligned} \quad (4.23)$$

when the width of the velocity distribution is δV .

The correlation time τ is inversely proportional to ΔF . As an example, let us consider the scattered signal from a patch of the ocean surface, using a 3 cm (X-band) stationary radar. The radar senses the ripples (capillary waves) that have an oscillation frequency around 20 Hz. Decorrelation will be even faster, since each ripple oscillation only has to proceed a fraction of 2π in phase before the total backscattered signal from all ripples has changed. In fact, a scintillation frequency of about 100 Hz is observed. Thus, every 10 ms the radar sees essentially a "new" patch of ocean, uncorrelated to the previous one. In the presence of swell, the signal is also modulated by the much longer gravity waves, and a second correlation time of several seconds appears.

b) Influence on scintillation spectrum of the spatial distribution of the scatterers; constant speed of the scattering elements

Let us now consider the case where all the scattering elements are moving at the same velocity \hat{V} . If, in addition, the difference wavevector \hat{K} is also constant, there will be no Doppler broadening, but merely a constant Doppler shift causing no scintillation. Using a finite beamwidth β on our radar antenna, however, the direction of the wavevector \hat{K} will vary within the limits of β . The corresponding Doppler broadening is then

$$\begin{aligned} \Delta F_K &= \frac{1}{2\pi} \Delta \hat{K} \cdot \hat{V} \\ &= \frac{2V}{\lambda} (\cos \theta - \cos(\theta + \beta)) \end{aligned}$$

which by expansion and approximation yields

$$\Delta F_K = \frac{2V}{\lambda} \sin \beta \sin \theta \quad (4.24)$$

We see thus, that the spatial distribution and relative velocities of scatterers constituting the object to be detected and identified, determine the scintillation spectrum of the scattered electromagnetic wave.

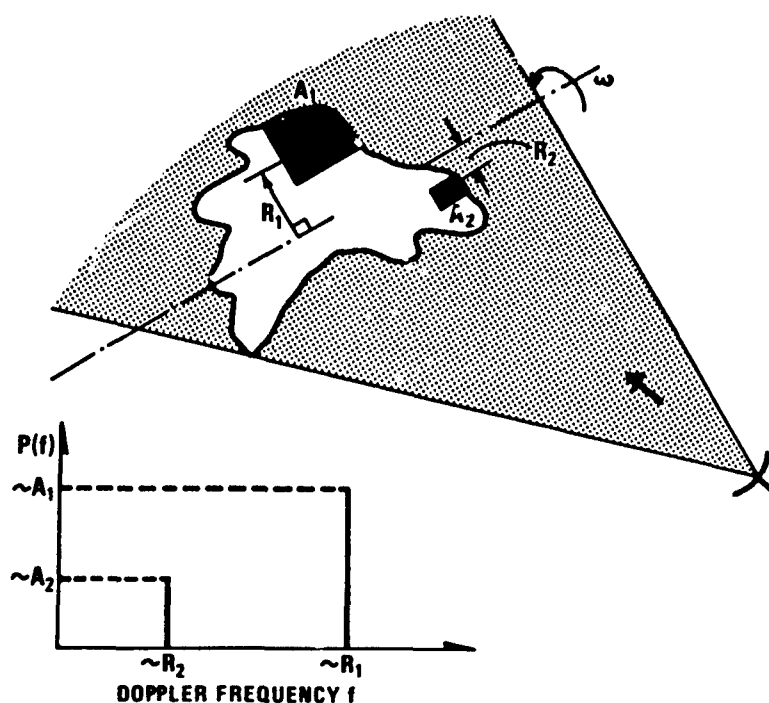


Figure 4.11 Example illustrating the relationship between Doppler spectrum and motion pattern of an object

The merits of the Doppler technique as a means of identifying an object through its motion pattern are illustrated in Figure 4.11.

5 PROPAGATION LIMITATIONS IN THE DETECTION AND IDENTIFICATION OF OBJECTS

When discussing this subject one should make two distinctions:

- The absorbing effect of the atmosphere (as discussed in Section 4.1) giving rise to transmission windows in the frequency band as illustrated in Figure 4.3. Outside these windows, the radio wave suffers attenuation. These attenuation bands may be very sharp when we are dealing with gases; when the absorption is caused by liquid or solid particles the loss mechanism (e.g. Mie scattering) may be such that we get wide, continuous absorption bands.
- The refraction/diffraction/scattering effect of inhomogeneities in the atmospheric refractive index structure causes a loss in the spatial resolution capability of the detection/identification system. This effect is often referred to as "blurring", "contrast loss" or "distortion".

The absorption phenomena are covered extensively in the literature (see e.g. (13)) and are presented in review form in Section 4.1 above.

In this chapter on propagation limitations we shall therefore limit ourselves to providing the basis for an understanding of the effects of refractive index inhomogeneities. The approach will be to give the basic semi-intuitive results so as to ensure a physical understanding of the phenomena rather than presenting detailed mathematics. Readers who are interested in further details are referred to (14).

In this context it should be mentioned that radiometeorologists over more than two decades have used radio waves to study the detailed atmospheric structure. They have even used much the same general techniques as the ones treated here. This suggests that the influence of atmospheric factors on the electromagnetic wave is an important one and must be taken into consideration when we study detection/identification methods. It also suggests, however, that a substantial amount of work has already been completed in this field and, as a consequence, solutions to many of our problems already exist. We shall now, with reference to this work, give some of the more important results.

5.1 Influence of atmospheric effects on the spatial correlation properties of an electromagnetic wave

As a consequence of the fact that irregularities in the atmospheric refractive index structure lead to multipath phenomena and delay variations and a spread in the angle of arrival when an electromagnetic wave passes through the irregular transmission medium, we suffer a loss in bandwidth and reduced spatial correlation of waves. We shall now give some theoretical results, which are well confirmed experimentally, giving information about the amplitude covariance of field strength at points separated in a plane normal to the direction of propagation.

Before presenting the accurate results of comprehensive calculations, we shall, as in the case of scattering mechanisms above, give some quantitative results for the purpose of ensuring an understanding of the basic physics involved.

Referring to the simple geometrical sketch of Figure 5.1, we see that there are two extreme paths through which the electromagnetic waves can travel from the transmitter T to the receiver R. One is the shortest direct way from T to R, the other is via a path which is $\lambda/2$ wavelength longer than the direct route. The result of these two waves is the vector sum of two signals with a 180° difference in phase causing destructive interferences.

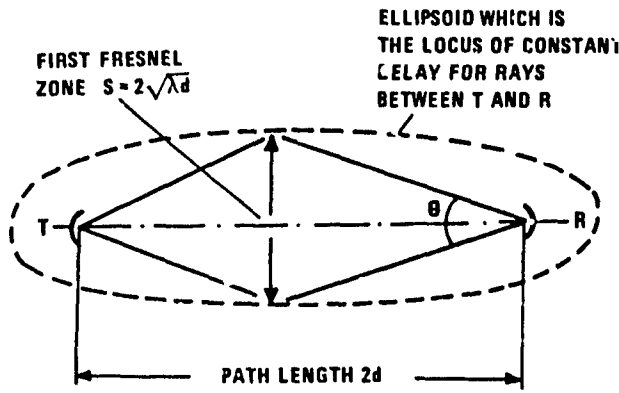


Figure 5.1 The geometry of line-of-sight propagation

To the first order, therefore, we would expect the width θ of the angle of arrival spectrum at the receiving point to be given by

$$\tan^{-1} \theta/2 = \frac{\sqrt{\lambda d}}{d}$$

$$\theta \approx 2 \cdot \sqrt{\lambda/d} \tag{5.1}$$

Knowing the angular power spectrum, i.e. the beamwidth, the correlation distance in a plane through the point of the receiver normal to the line T-R can be calculated. We have shown in Chapter 4 that this spatial correlation of field strength is the Fourier transform of this angular power spectrum.

If this power spectrum is a $(\sin x)/x$ function, then the Fourier transform is a rectangular function. If the width of this correlation distance of field strength is L , then we have the following relationship between the half-power width of the beam $\theta_{1/2}$ and the correlation distance L .

$$\theta_{1/2} = \frac{0.88\lambda}{L} \tag{5.2}$$

where λ is the wavelength of the electromagnetic wave.

In passing, note that this is the same expression as that relating antenna beamwidth $\theta_{1/2}$ to the antenna aperture diameter L . This is not surprising since the antenna radiation pattern (the $P(\theta)$ function) is the Fourier transform of the illuminating field strength distribution over the antenna aperture.

From Equations (5.1) and (5.2) above, therefore, we have

$$\frac{0.88\lambda}{L} = \frac{2\sqrt{\lambda d}}{d}$$

i.e. correlation distance $L = 0.44 \sqrt{\lambda d}$

Thus, the correlation distance of field strength transverse to the line of propagation is comparable with the first Fresnel zone. This is shown in Figure 5.2. Note that in this figure the normalization factor is $\sqrt{\lambda d}$, where d is the path length, not half path length as in Figure 5.1. Hence we shall have to multiply our approximate correlation distance by $\sqrt{2}$ when referring to Figure 5.2.

This figure gives the correlation between the amplitude scintillation at two small receiving antennas spaced L meters apart in a plane normal to the direction of propagation.

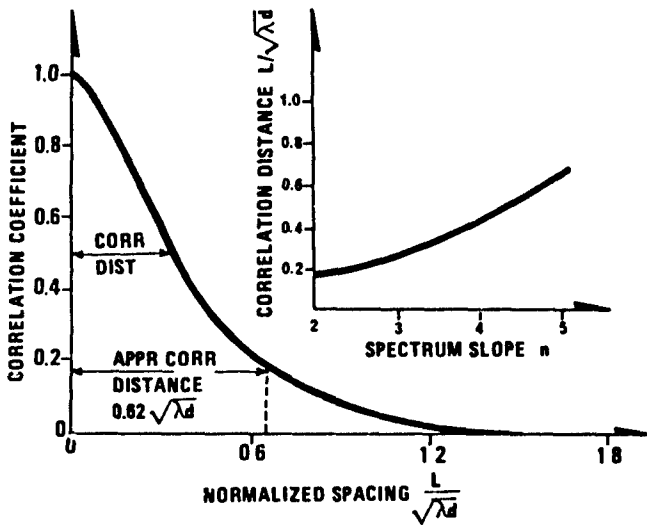


Figure 5.2 Spatial correlation of the field
Normalization factor $\sqrt{\lambda d}$ refers to path length d (from Lee and Harp (15), Kjelaas (17)).

The correlation function is calculated for a Kolmogorov spectrum where the refractive index irregularity spectrum $\Phi(K)$ is of the form $\Phi(K) \approx K^{-11/3}$.

The inserted figure shows how the correlation distance (the halfwidth of the covariance function) varies with spectrum slope n (where n is given by $\Phi(K) \approx K^{-n}$).

Note that the approximate results agree well with the curve obtained for rigorous computations.

Then let us investigate what happens if we transmit two frequencies simultaneously and correlate the signals at the two frequencies in one point at the receiving end.

5.2 Influence of atmospheric effects on the frequency correlation properties of an electromagnetic wave

Let us first calculate the correlation distance in the frequency domain (the bandwidth) using a simple, approximate approach.

From Chapter 4 above, we have learnt that the bandwidth function (autocorrelation function in the frequency domain) is obtained by Fourier transforming the delay function.

For simplicity, let us again assume that the delay function is of the $(\sin x)/x$ form with a half-power width $\Delta\tau = (\lambda/2)/C$. The bandwidth function, i.e. the frequency transfer function $P(\Delta F)$ or the correlation function in the frequency domain $R(\Delta F)$, would then be a rectangular function, the width of which is

$$\Delta F = \frac{1}{\Delta\tau} = \frac{2C}{\lambda}$$

= half-frequency of the electromagnetic wave

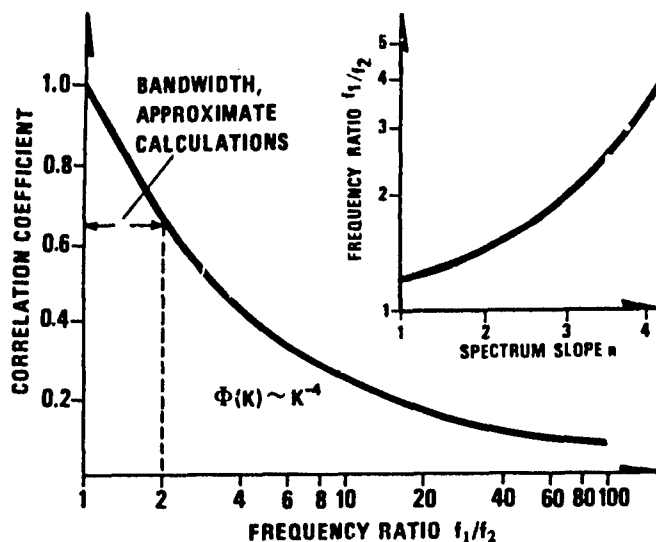


Figure 5.3 Amplitude covariance vs frequency separation f_1/f_2 (after Lee and Harp (15))

The insertion shows the influence on bandwidth of the slope n of the refractive index spectrum ($\Phi(k) \cong k^{-n}$). Bandwidth is defined as λ_1/λ_2 for correlation coefficient = 1/2.

These were the approximate results.

We see that these too fit well on the curve giving the comprehensive results based on the work by Lee and Harp.

5.3 Implications of an irregular atmospheric refractivity structure; the influence of atmospheric refractive index irregularities on the resolution performance of a radar

In the example to follow, we shall focus our attention on the resolving power of a sidelooking radar under conditions of atmospheric limitations. There are several schemes by which a synthetic aperture antenna can be made to give optimum resolution. Let us discuss the case where the phase curvature departs less than $\lambda/8$ from the plane over the observation baseline. For this case the effective (synthetic) aperture is given by

$$D_{\text{eff}} = 2\sqrt{\lambda R} \quad (5.3)$$

such that the width of the synthetic "antenna diagram" is given by

$$\beta = \frac{x}{2\sqrt{\lambda R}} \quad (5.4)$$

and the corresponding target resolution Δ at the distance R is given by

$$\Delta = R\beta = \frac{\sqrt{\lambda R}}{2} \quad (5.5)$$

If the field strength of the arriving wave is not correlated over the synthetic aperture $2\sqrt{\lambda R}$, a loss in resolving power is suffered.

In the preceding section, we developed expressions for the spatial covariance function of amplitude fluctuations in terms of the pertinent atmospheric parameters.

Referring to Figure 5.2, we see that when the slope n of the refractivity spectrum $\Phi(k) \cong k^{-n}$ varies, so does the spatial correlation distance of the amplitude fluctuations.

Therefore, in order to obtain information about the variability (the frequency of occurrence) of the "blurring", we shall need information about the variability of the refractive index structure parameter n ($\Phi(k) \cong k^{-n}$). Earlier investigation by the author (see e.g. (18)) shows that the probability distribution of n is very close to being a normal distribution (Gaussian). $n = 7$ is exceeded in 1% of the time whereas $n = 1.5$ is exceeded in some 90% of the time.

Using this probability distribution, we find the corresponding distribution for field strength correlation distance from Figure 5.2.

From antenna theory, we know that only if the field strength is correlated in amplitude and phase over the antenna aperture D will the resolving power Δ of the antenna a distance R from the object be given by

$$\Delta = \frac{\lambda}{D} R$$

If the correlation distance of the field strength is less than the antenna aperture D , then the resolving power will be reduced. The degree to which the resolution is reduced by atmospheric effects depends in practice on the signal processing capability of our receiving system.

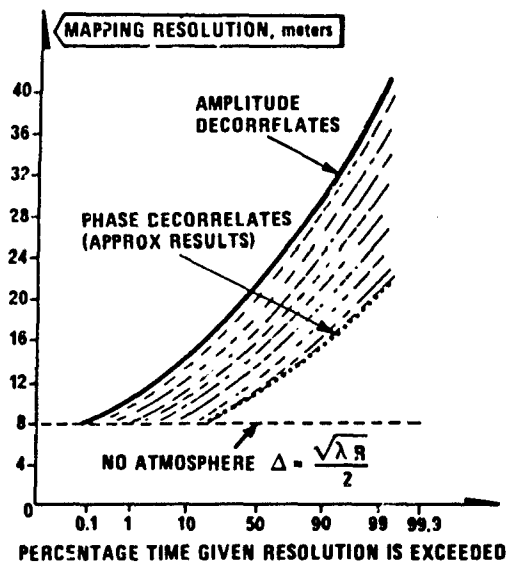


Figure 5.4 Probability distribution of target resolution calculated from radiosonde data and compared with the resolution that would have been obtained with a synthetic aperture antenna under conditions of no refractive index irregularities
Note that the curve for phase is approximate only.

ever, the correlation distance of phase is determined not only by the slope n of the refractive index fluctuations, but also by the scale length L_0 . The outer scale of turbulence L_0 is the scale size at which energy is fed into the turbulence field. Therefore, in order to compute the probability distribution of the correlation distance of phase fluctuations, we need information about the variability of the scale L_0 . This is not readily obtainable.

From the theoretical and experimental data of Janes and Thompson (19), the correlation distance of phase for a refractivity spectrum of the form $\Phi(K) \cong K^{-11/3}$ can be inferred. Based on these results an approximate curve for the effect of the phase fluctuations is shown in Figure 5.4.

In order to overcome these atmospheric limitations, there are several methods at our disposal.

One, obviously, involves selecting the right atmospheric conditions, when the adverse effects are at a minimum.

Another method involves a sidelooking radar system consisting of more than one antenna. If a synthetic aperture system of two antennas is arranged in such a way that the spacing between the antenna is longer than the correlation distance of field strength, then the second antenna can be used to assess the extent of the atmospheric influences, by checking the result of antenna number one at the same point in space but at a different point in time. In this manner the atmospheric effects can be reduced.

6 METHODOLOGY FOR DESIGN OF OPTIMUM SYSTEMS

The objective of this chapter is to provide the basis for an optimum design of specific remote sensing systems. The design philosophy is based on the following:

We have to our disposal:

- A set of sensors (see above)
- Knowledge about the basic principles on which the action of these sensors are based, knowledge about the interaction between the electromagnetic waves to which these sensors are coupled and the target that we seek information about (Chapter 4 above)
- Information about the limitations which the propagation medium between the observation platform and the object of interest impose
- Knowledge about the shape, size and chemical composition of the object of interest (i.e. signature information), and, in some cases, about other possible objects (interferents)

We shall be concerned with the design of remote sensing systems which in an optimum way make use of available knowledge and of available sensors.

We seek a system where the illumination, i.e. the electromagnetic waves, are matched to the parameter to be measured in an optimum manner in an environment of "noise" (matched illumination) and we seek a set of detecting sensors which are matched to the waves which are reflected, emitted or absorbed by the object of interest (matched reception) (14,15).

In this example we shall define the resolution capability as

$$\Delta' = \frac{\lambda R}{\text{correlation distance}}$$

In the preceding section we gave the relationship between the correlation distance and the slope n of the refractive index spectrum. This correlation distance is defined as the antenna spacing required for the correlation coefficient of amplitude fluctuations at the two antennas to drop to 1/2.

In Figure 5.4 the probability distribution of the resolution capability Δ' is plotted for a 10 km path and compared with that which would have been achieved in the case of no refractive index irregularities in the transmission medium (8).

Note that these results are based on the correlation distance of amplitude only. To complete the picture, we have also to consider the fluctuations in phase and the spatial correlation properties of these.

Obviously, if the phase variations caused by atmospheric effects are comparable with the wavelength and not correlated over the aperture of the synthetic antenna, we shall suffer a really dramatic loss in resolution capability. Thus, in the probability distribution of spatial resolution capability given in Figure 5.4 we shall need a second curve, namely that determined by the correlation distance of the phase fluctuations. Between the resolution determined by a limited correlation distance of amplitude and that determined by phase, there will be a "grey zone".

Increasing the baseline of our synthetic aperture antenna, the amplitude scintillations will first play a role and introduce some blurring effects. Increasing the baseline still further, the lack of phase coherence will be noticed. This will greatly influence the resolution capability of our synthetic aperture radar system. How-

6.1 Statement of the problem

In brief, the problem is the following:

A method of optimum sensitivity for the detection, identification and quantitative evaluation of an object or a chemical agent is sought. It is assumed that all the pertinent data pertaining to the target are known. These target "fingerprints", are typically:

- The shape, size and texture of the object, i.e. the distribution of scattering elements in height, width and depth (the macrostructure).
- The chemical composition of the surface or surface layers.
- The chemical composition of the gases (or liquids) which the object of interest may emit (scent from plants, odours from fermenting organic substances, gases from soil, exhaust gases from vehicles etc).
- The footprints, tracks or traces which a moving object leaves behind it.

6.2 Detection and identification of an object on the basis of knowledge about the chemical composition of the surface

The objective of this section is to discuss methods by which a target of interest can be detected and identified, based on knowledge about the molecular surface structure (composition of paint, type of rubber, plastics, canvas etc).

In order to reveal these fingerprints of chemical structures, we illuminate the object on which this agent may be present with electromagnetic waves, and we change the frequency over the frequency band of interest in some prescribed manner which is optimum with regard to the detection and identification of the particular chemical compound of interest. The situation is assumed to be the following:

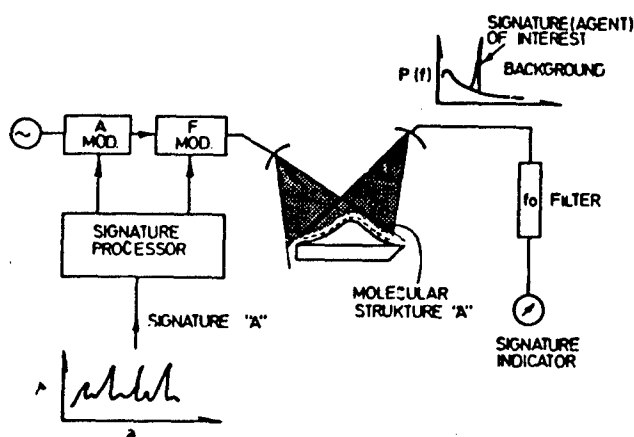


Figure 6.1 The basic principles for matched illumination as a mean of detecting and identifying an object

- We are looking solely for a specific chemical compound
- We know the absorption spectrum or reflectance spectrum of this compound
- We know nothing about any of the other agents (interferents) which may be present
- We have very meager information about the vegetation (topography) on which the agents may be deposited, but we have some general idea about the roughness of the structure (grass, coniferous trees, rocky ground etc).

then, as depicted in Figure 6.1, assume that we have an illuminator in the form of a laser system which can be amplitude- as well as frequency-modulated. We now want to structure the illumination so as to match the signature of the object. This matched illumination concept is one which is known under different names for other applications. In communications theory it is known as preemphasis, in signal analysis it is known as prewhitening, etc.

For the sake of illustrating this point, let us look at Figure 6.2. At the top of this figure we have shown a simplified reflection spectrum signature of an absorbing surface.

If the laser generator shown in Figure 6.1 is frequency modulated (tuned) with a linear saw-tooth modulation, the top curve of Figure 6.2 would be the waveform (voltage as a function of time) reflected back from the target.

Amplitude modulating the illuminator in a manner illustrated in Figure 6.2, second curve from above, seeking the same strength of all the lines in the reflectance spectrum, the results shown are obtained.

Referring now to the fourth curve from above, we change the relative position of the maxima and of the minima of the spectrum so as to get a periodic function as shown in the fifth graphical representation. This is achieved by changing the rate dF/dt at which the frequency is changed. It is then obvious that if a more detailed A and ϕ operation is applied, the result is a sinusoidal variation, shown at the bottom of Figure 6.2. To detect this requires only a very small bandwidth, as shown in Figure 6.1.

For the purpose of emphasizing the merits of the technique, some illustrative examples are given in Figure 6.3. Two different absorption spectra are considered. Type "A" is characterized by 8 absorption lines, whereas type "B" has 10 absorption lines. Each absorption line is Lorentz shaped. In the interval between the lines the absorption/reflection is assumed to be zero.

Adopting the amplitude- and frequency- modulation scheme illustrated in Figure 6.2 above, the illumination is structured for type "A" molecules. Figure 6.3 shows the result of this optimization process. Note that the spectrum density function associated with optimized illumination is narrow, whereas the spectrum resulting from conventional illumination is wide. Note also that if an extensive structuring of the illumination had been accomplished, the resulting signal spectrum would have been a delta function.

Figure 6.3 also shows the discriminating power of the technique (right-hand figure). Here an illumination which has been structured for type "A" molecules is applied to structure "B". Note the marked difference in maximum spectral intensity and the shift in frequency of the peaks.

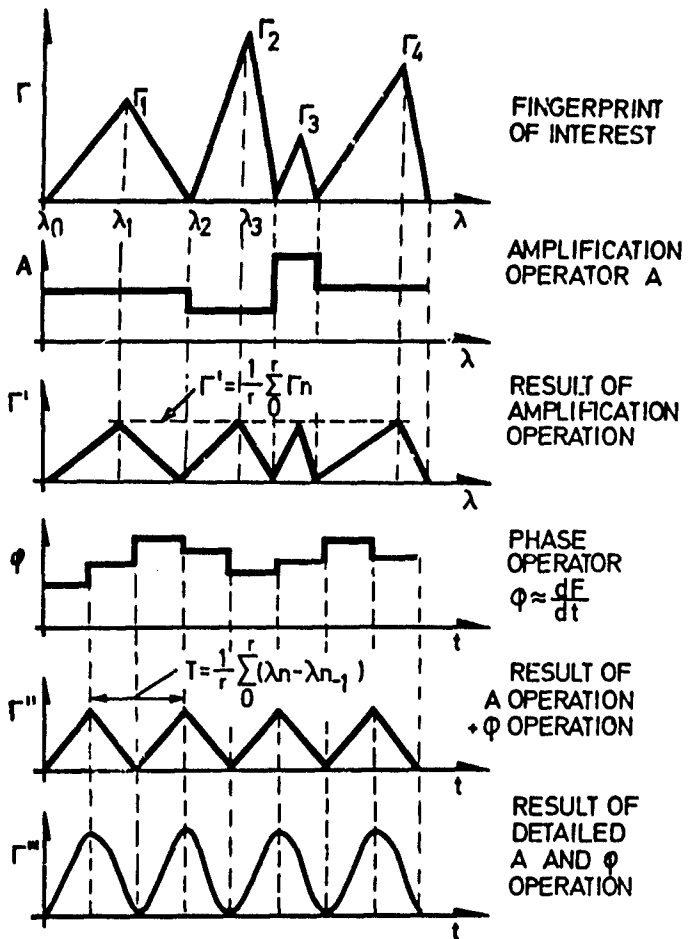


Figure 6.2 Example of an optimum structuring of the illumination function for the purpose of detecting/identifying a particular molecular structure

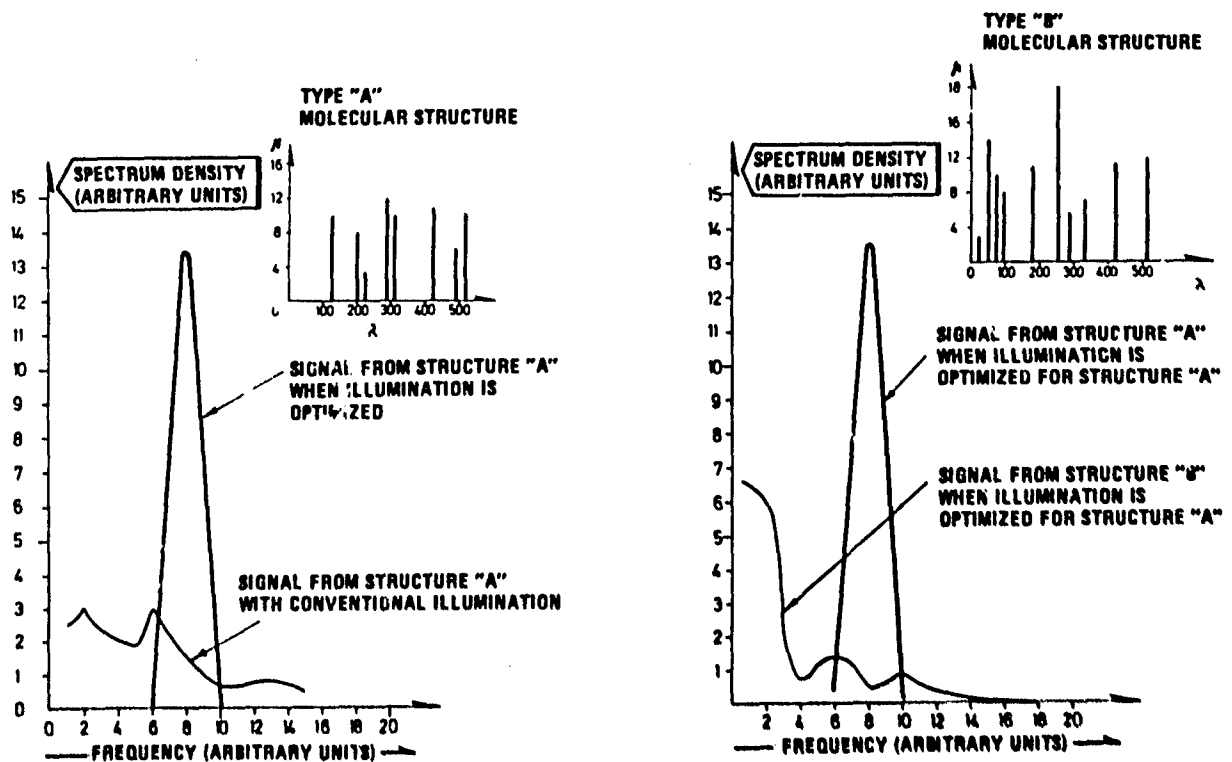


Figure 6.3 The effect of optimized illumination - theoretical results

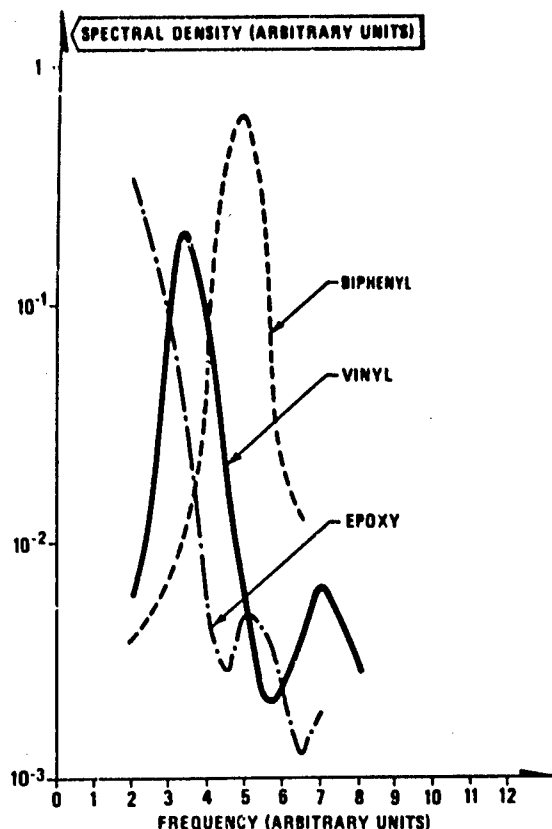


Figure 6.4 The effect of matched illumination for epoxy, vinyl and biphenyl

The illumination which has been structured for vinyl is applied to epoxy. Similarly, the curve for biphenyl is obtained by structuring the illumination for biphenyl. Computer simulations.

Using a computer simulation program implementing this crude technique involving "first order matching" only for three frequently encountered compounds, namely epoxy, vinyl and biphenyl, Figure 6.4 results. Note that by the use of narrow filters as depicted in Figure 6.1 above, the particular agent of interest can be selected when its absorption spectrum is known.

Having given the general expression for the matched illumination function in terms of functions describing the material of interest, we shall go on to consider the effect of the geometry (the surface roughness) in relation to that of surface chemistry.

The question we now ask is: how should the transmitting/receiving system be structured in order to give maximum information about the geometrical shape of an object. Or, how should the system be structured to have optimum sensitivity in relation to a given object of known size and shape.

6.3 Optimum detection and identification on the basis of geometrical shape of object

When making use of the geometrical shape of the object for detection purposes, we shall, contrary to the above, choose frequencies which are not affected by the detailed molecular structure of the scattering surface. In the absence of this effects, there are three remaining effects which are of importance:

- The multiplicative effect of atmospheric irregularities (turbulence) and of particulate matter (rain, snow, dust etc).
- The additive effect of the background scatterers.

The first effect determines the frequency band to be employed. The higher the frequency of the illuminator, the more severe is the impact of atmospheric irregularities. The shape of the background elements relative to that of the target determines the detailed structuring of the illumination function. To establish an illumination function we have four degrees of freedom, space and time of frequency. We can structure the illuminating wave in the frequency domain and we can structure the wave in space (shape the wavefront) so as to match the target of interest. First let us consider the frequency domain.

6.3.1 Optimum frequency distribution of an illuminating wave with regard to a target of known geometrical form

We shall in this chapter investigate the information obtainable by modulating the illumination of the target in time. There are, as we well know, several ways of doing this. We will discuss one powerful method.

Knowing the distribution in depth of the scatterers, we have shown in Section 4.3 above that we can calculate the correlation properties in the frequency domain (bandwidth) of the signal reflected (scattered) back from the target (21). We shall use the results of this reference for the purpose of establishing the optimum frequency distribution of the illuminating wave to determine the distribution in depth (longitudinal) of the scatterers constituting the target.

To illustrate the principle employed, two figures will be presented. In Figure 6.5 a target with the shape of a pyramid is illuminated by a set of waves whose frequency spectrum is rectangular, i.e. the correlation properties of the illuminator in the frequency domain is a rectangular function.

The delay spectrum of the pyramid, having a rough surface (so as to give diffuse reflection) is also a rectangular function. We have shown (Section 4.2 above and (20)) that the effect of a target having a finite depth is to decorrelate the frequency properties of the waves scattered back from the target.

Specifically, if a set of waves correlated in amplitude and phase impinges on a target having a given distribution in depth of the scatterers $P(z/c)$, then the correlation properties of the reflected waves are limited to some function of the Fourier transform of $P(z/c)$. Accordingly, as depicted in Figure 6.5, the transmitted rectangular correlation function is reduced to a $(\sin x)/x$ function upon reception if the target delay spectrum is rectangular.

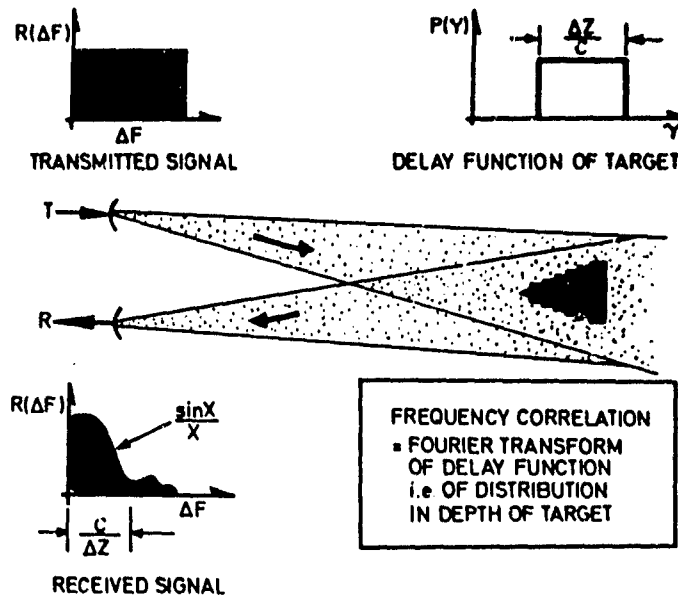


Figure 6.5 The basic principle - distribution in depth of target

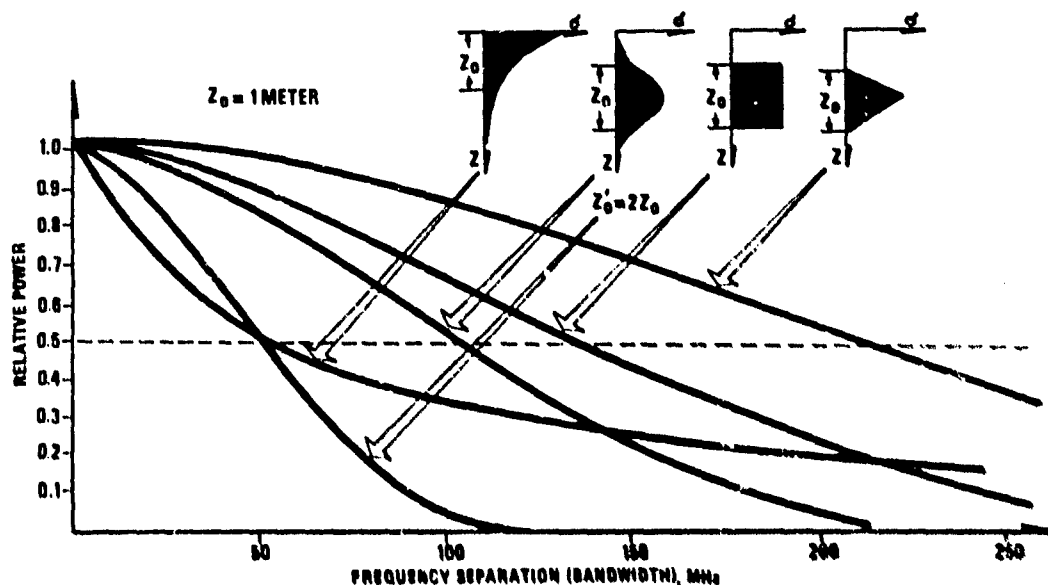
The identification potential of this multifrequency system is illustrated in Figures 6.6 and 6.7. Here the frequency properties of the scattered signal are calculated for a set of scattering objects having different shape and size. Note the very marked influence of object shape and the dramatic size dependence. Note also that the peak of the $w(f)$ spectrum in Figure 6.7 is determined by the spacing of the branches, whereas the width of the curve, as before, is determined by the height of the tree. Table 6.1 gives the mathematical expression for the bandwidth. Note that there is a simple and direct relationship between bandwidth and correlation distance in the frequency domain, see Section 4.2 above.

It should be noted that Figures 6.6 and 6.7 together with Table 6.1 refer to the monostatic backscatter situation where both the transmitter (the illuminator) and the receiver are located at the same spot. In practice this causes some difficulties since we shall have to ensure good isolation between the transmitting and the receiving antenna so as to prevent direct transmission from one to the other (21).

In conclusion it should therefore be noted that when measuring the correlation properties in the frequency domain of the signal scattered back from the target, information about its distribution in depth is obtained by Fourier transformation of the received signal.

This simple, direct method would have been effective if the target were suspended in the air with no interfering background. In the more realistic case of an interfering background, one has to use a *selective detection method*. The procedure is analogous to that discussed in some detail in connection with the study of molecular structures above.

We should match the illuminating wave to the target of interest so as to get a narrow band signal of known frequency back from the target of interest, and a signal distributed in frequency from all the interferences, the background.



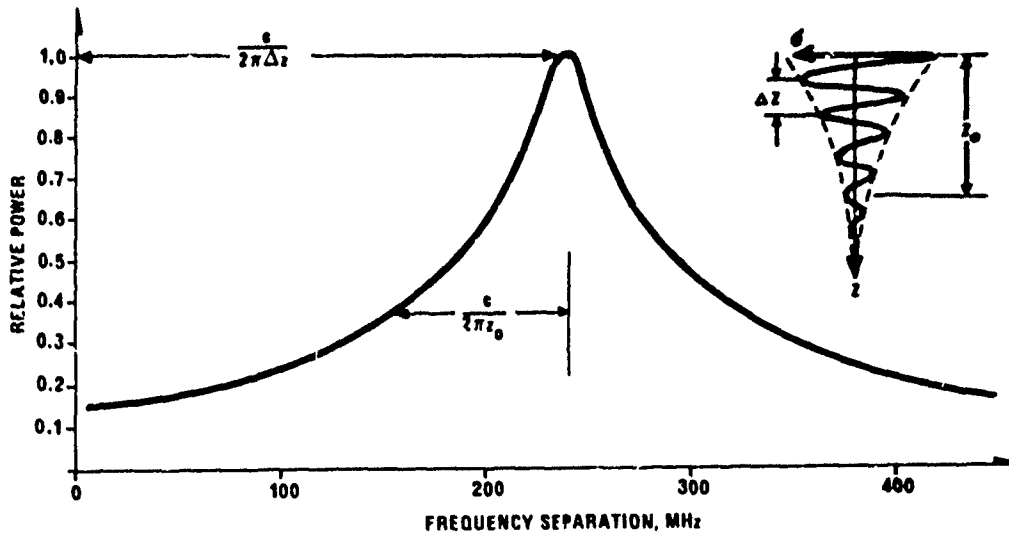


Figure 6.7 Bandwidth properties of a scattering surface in which there is a periodic structure such as evenly spaced branches of a tree
 In the example z_0 is 1 m and Δz is 20 cm.

DISTRIBUTION IN DEPTH OF SCATTERERS	FREQUENCY DEPENDENCE OF REFLECTING SURFACE	HALF POWER BANDWIDTH
<p>EXPONENTIAL</p>	$W(\omega) = \frac{\sigma_0^2}{\left(\frac{c}{z_0}\right)^2 + \omega^2}$	$\Delta F_{1/2} = 0.16 \frac{c}{z_0} \text{ Hz}$
<p>GAUSSIAN</p>	$W(\omega) = \frac{\pi}{4} \frac{\sigma_0^2}{\left(\frac{c}{z_0}\right)^2} e^{-\frac{\omega^2 z_0^2}{8 c^2}}$	$\Delta F_{1/2} = 0.37 \frac{c}{z_0} \text{ Hz}$
<p>RECTANGULAR</p>	$W(\omega) = 4\sigma_0^2 \left(\frac{\sin \frac{z_0}{2c} \omega}{\omega}\right)^2$	$\Delta F_{1/2} = 0.44 \frac{c}{z_0} \text{ Hz}$
<p>TRIANGULAR</p>	$W(\omega) = \frac{64 \sigma_0^2}{\left(\frac{z_0}{c}\right)^2} \left(\frac{\sin \frac{z_0}{4c} \omega}{\omega}\right)^4$	$\Delta F_{1/2} = 0.64 \frac{c}{z_0} \text{ Hz}$
	$W(\omega) = 4\sigma_0^2 \left(\cos \frac{z_0}{2c} \omega\right)^2$	$\Delta F_{1/2} = 0.25 \frac{c}{z_0} \text{ Hz}$

Table 6.1 Bandwidth properties of some geometry surfaces

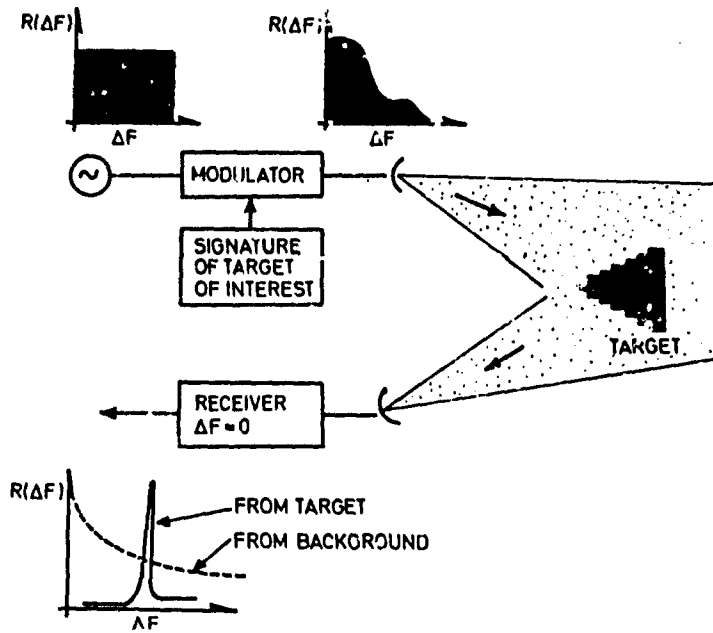


Figure 6.8 *Illumination function for optimum detection sensitivity*
 - Our system has optimum sensitivity for objects of interest
 - Minimum sensitivity for other objects (background)

Figure 6.8 illustrates the principle of operation.

On the basis of the principles discussed in section 6.2 above, we have structured the correlation properties of the illuminating waves so as to be matched to the object of interest (see Figure 6.9). In our example, the illumination is matched to an object 50 cm deep having a gaussian distribution of the scattering surface. We see that this gives rise to a narrow-band signal from the object of interest whereas the returns from targets to which the illumination is not optimized are relatively broadbanded.

Note that there is no unique relationship between the delay function $\sigma(\frac{z}{c})$ and the shape of the object. Obviously, the variation in z has to be restricted to the boundary of the object, but there are a large number of geometrical shapes that give the same delay function.

Finally, let us now investigate what information we can obtain about an object by measuring the spatial correlation properties of the waves scattered from an object of a given shape.

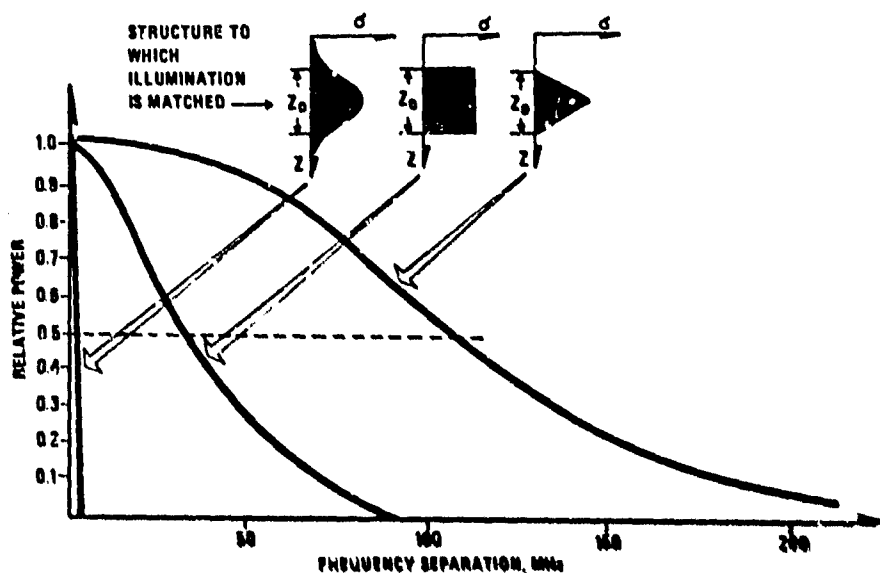
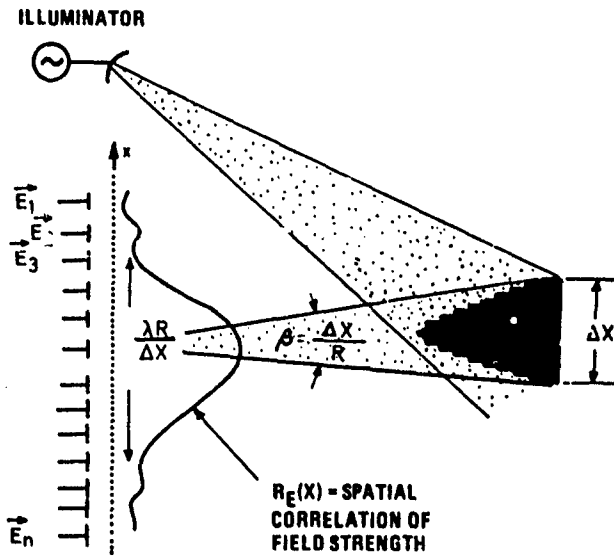


Figure 6.9 *Theoretical results of matched illumination*
 The illumination is matched to the "gaussian object".

6.3.2 Determination of target distribution in space by spatial correlation measurements of field strength

We have just completed a discussion about an experimental determination of the distribution in depth (in the direction of propagation) of the scattering elements constituting a scattering object. We have shown that if we illuminate an object by a set of EM waves with mutually correlated amplitudes and phases, this set of correlated waves is subjected to a decorrelation process. The degree to which the waves are decorrelated depends on the distribution in depth of the scattering elements constituting the object. Specifically, the correlation function in the frequency domain (covariance function for waves having separate frequencies) is the Fourier transform of the distribution in depth of the scatterers (Fourier transform of delay spectrum).



We will now focus our attention on the spatial correlation properties of a scattered wave in relation to the spatial distribution of scatterers over the object. In exactly the same way as for spaced frequencies, we have shown in Section 4.2 that the transverse (normal to direction of propagation) spatial correlation of the complex field strength is the Fourier transform of the angle of arrival spectrum, i.e. the Fourier transform of some function which is determined by the transverse distribution of the scatterers constituting the target of interest. Thus, if X be a distance coordinate orthogonal to the Z -direction of propagation, then if $\sigma(X)$ be the distribution of scattering elements over the scattering object under investigation, the spatial correlation of field strength in the X -direction is given by

$$R_E(x) = \text{Fourier transform of } \sigma(X/R)$$

R being the distance between the point of observation and the target. Note that $\sigma(X/R)$ is the angular power spectrum of the scattered wave.

Figure 6.10 illustrates the basic principle related to the determination of angular power spectrum on the basis of field strength correlation measurements.

By measuring the amplitude and phase of the wave scattered back from the target of interest at a number of points in a plane normal to the direction to the target (direction of propagation) information about the transverse distribution of the scatterers constituting the target is obtained.

Figure 6.10 Wavefront analysis by array matrix
Spatial correlation of field $R_E(x)$ = Fourier transform of angular distribution of scattered power $P(\theta)$

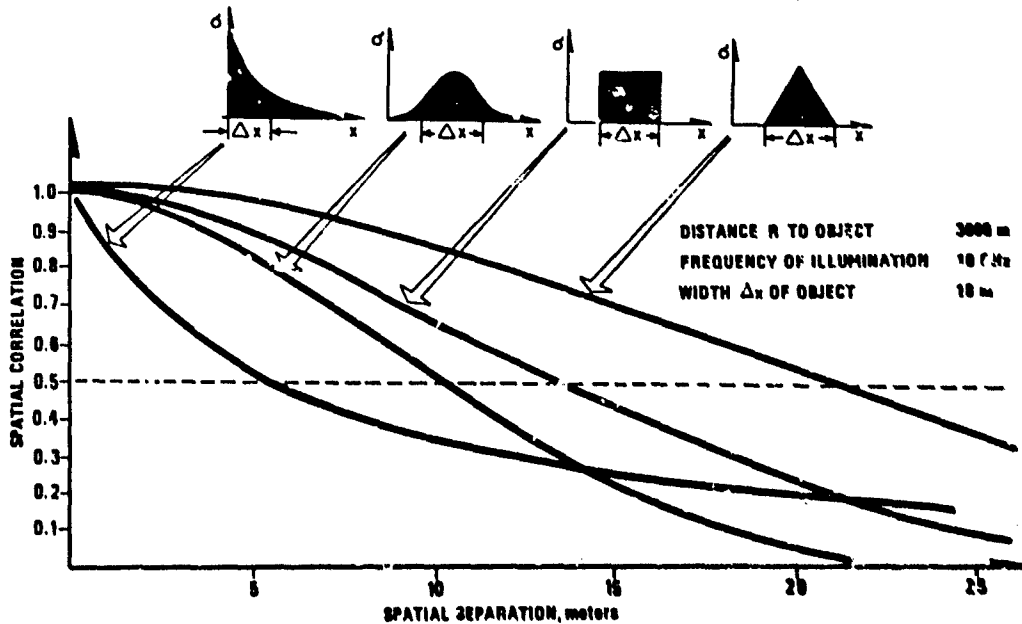


Figure 6.11 Theoretical results illustrating the identification potential of a single frequency illuminator and a multi-element receiving antenna system

The results of a simulated calculation are shown in Figure 6.11. Here we illuminate the object 3000 m away by one single 10 GHz radio wave (wavelength is 3 cm). We measure the transverse spatial correlation of the received field. Note the marked effect of object shape and the dramatic effect of size even at a distance as great as 3000 m and for radio frequencies as low as 10 GHz.

In an operational system, the target illuminator will shine a small fraction of its power on the array antenna. In practice it may be more practical to shift the frequency of the wave illuminating the array slightly relative to the frequency of the wave

illuminating the target so as to obtain a suitable intermediate frequency for efficient amplification and subsequent quantization and storage in the receiving system. By this system the amplitude and relative phase are measured in each antenna element. An on-line computer processing system (parallel processing) reads the information about amplitude and phase stored at each antenna element and performs the appropriate computations.

The reader who is familiar with the principle of holography will immediately recognize this as basic microwave holography.

7 CONCLUSIONS

Significant advances during the last few years in the fields of microwave techniques, electrooptics and computer technology open new avenues with regard to detection and identification of objects, of gases, of tracks and footprints, etc.

Possessing the basic information about the target signature (geometrical form, surface molecular structures, motion pattern etc) a system of optimum detection and identification potential can be designed when we know the mechanisms governing the interaction of electromagnetic waves with solids, gases or liquids constituting the target of interest and its environment.

Acknowledgements

The author would like to acknowledge the very capable assistance of Anton G Kjelaas in particular, in connection with the computer calculations.

Likewise, I wish to express my sincere thanks to Ruth Sand, Britt Tronvold and Rannveig Løken for typing the manuscript and to Marit Støversten and Hans Olaf Stensrud for doing the artwork for all the figures.

References

- (1) Gordy W: Microwave Spectroscopy, *Handbuch der Physik*, p 28, Springer-Verlag, Berlin (1957)
- (2) Ghosh S H, Malaviya V: Microwave absorption in the earth's atmosphere *J Atmosph Terr Phys* 21, 4 (1961)
- (3) Ratcliffe J A: Some aspects of diffraction theory and their application to the ionosphere. *Rep Progr Phys* 19, 188 (1956)
- (4) Gjessing D T: Determination of permittivity variations in the troposphere by scatter-propagation methods. *Proc IEE Monogr* 510E, Apr 1962. *Proc IEE Part C* 109, 16 (1962)
- (5) Batchelor G K: The scattering of radio waves in the atmosphere by turbulent fluctuations in refractive index. Research Report EE262, School of Electrical Engineering, Cornell University (1955)
- (6) Balser M: Some observations on scattering by turbulent inhomogeneities. *Trans IRE AP-5*, 4, 383 (1957)
- (7) Gjessing D T: Atmospheric structure deduced from the forward scatter wave propagation experiments. *Radio Sci* 4, 12, 1195-1210 (1969)
- (8) Gjessing D T: On the influence of atmospheric refractive index irregularities on the resolution performance of a radar. *Atmospheric Effects on Radar Target Identification and Imaging*, Ed: H Jeske, D Reidel Publishing Company (1975)
- (9) Hagfors T: Investigation of the scattering of radio waves at metric wavelengths in the lower ionosphere. *Geophys Norwegia* 21, 2 (1959)
- (10) Rice S O: Mathematical analysis of random noise. *Bell Syst Tech J* 23, 282 (1944)
- (11) Gjessing D T, Irgens R: On the scattering of electromagnetic waves by a moving tropospheric layer having sinusoidal boundaries. *IEEE Trans PTGAP AP-12*, 1 (1964)
- (12) Gjessing D T, Irgens F: Scattering of radio waves by a moving atmospheric rippled layer: A simple model experiment. *IEEE Trans PTGAP AP-12*, 6 (1964)
- (13) McClatchey R A et al: AFCRL atmospheric absorption line parameters compilation, Rapport ERP 434, TR-73-0096, Air Force Cambridge Research Laboratories (1973)
- (14) Gjessing D T: *Remote surveillance by electromagnetic waves for Air - Water - Land*. Ann arbor Science Publishers Inc. USA (1978)
- (15) Lee R W, Harp J C: Weak scattering in random media. *Proc IEEE* 57, 375 (1969)
- (16) Gjessing D T, Kjelaas A G, Nordø J: Spectral measurements and atmospheric stability. *J Atmosph Sci* 26, 3, 462-468 (1969)
- (17) Kjelaas A: *Private communication*
- (18) Gjessing D T, McCormick K S: On the prediction of the characteristic parameters of long distance tropospheric communication links. *IEEE Trans COM-22*, 9 (1974)
- (19) Jones H B, Thompson M C: Comparison of observed and predicted phase-front distortion in line-of-sight microwave signals. *Trans IEEE AP-21*, 2, 263-311 (1973)
- (20) Gjessing D T: A generalized method for environmental surveillance by remote probing. *J Radio Sci*, Jan (1978)
- (21) Gjessing D T: Scattering mechanisms and channel characterization in relation to broadband radio communication systems. ACARD Conf Proc *Aspects of Electromagnetic Scattering in Radio Communications*, Cambridge USA, October 1977

BIBLIOGRAPHY

CONTENTS

	Page
1. Atmospheric Transmission – Radio and Optical Tropospheric Scattering Weather Multipath – Ground Effects	B-1
2. Optical Sensing Problems Coherent and Incoherent Propagation Laser Transmission	B-8
3. Remote Sensing (IR, UV, Microwaves)	B-9
4. Radio Wave Scintillation Tracking and Communication Navigation and Positioning Systems Radar and Navigation Correction Techniques	B-9
5. Low Frequency Propagation and Systems – Omega and Loran "C" Systems	B-12
6. HF Transmissions Back and Forward Scatter Radar Ray Tracing	B-16
7. Forecasting and Predicting Ionospheric Parameters – Artificial Modification of the Ionosphere	B-19

**1. Atmospheric Transmission – Radio and Optical
Tropospheric Scattering
Weather
Multipath – Ground Effects**

76A41090 76/08/00 19 pages

DESIGN OF CHAFF AND CHAFF-SUPPORTED COMMUNICATION SYSTEMS

Ince, A.N.; Goessl, H.; Vogt, I.M.

(SHAPE Technical Center, The Hague, Netherlands); (Deutsche Versuchsanstalt Fuer Luft- und Raumfahrt, Oberpfaffenhofen, West Germany)

The use of chaff for establishing communications of limited duration between non-adjacent troposcatter stations is investigated. The optimum location for the release of chaff is determined theoretically considering the path geometry, the antenna elevation and directivity, and the weather and atmospheric effects. Amplitude, polarization, and fading characteristics of the signal energy scattered by chaff are calculated and the type and weight of chaff required to provide a given signal-to-noise ratio is estimated. Experiments which were conducted to check the validity of the theoretical calculation are then described. Finally, a practical scheme for overpassing troposcatter stations and for communications between mobile users which are not in line of sight is considered.

76A28581 76/00/00 9 pages

REQUIREMENTS FOR PROPAGATION RESEARCH AT FREQUENCIES ABOVE 15 GHZ

Brussaard, G.

(ESA, European Space Research and Technology Center, Noordwijk, Netherlands)

After indicating future requirements for use of the 20 and 30 GHz bands for satellite communication systems, the paper describes the atmospheric effects on radiowave propagation in the 15–40 GHz range. Present knowledge regarding the different phenomena is reviewed and gaps and inaccuracies in available prediction methods are indicated. Using this information as a basis, the requirements for future propagation research by the agency are outlined.

76A15970 75/12/00 5 pages

ATMOSPHERIC EFFECTS ON TERRESTRIAL MM-WAVE COMMUNICATIONS

Dudzinsky, S.J., Jr

(Rand Corp., Santa Monica, Calif.)

This paper surveys available data on the transmission properties of millimeter waves and available meteorological data. These data are then combined to provide the design engineer with a methodology for quantitatively estimating the performance of millimeter-wave systems operating in the atmosphere and in the presence of rainfall. Emphasis is on high-reliability communications in which outages due to rainfall are 0.1 percent or less, but the methodology described applies to lower availability systems as well.

75A41750 75/05/00 6 pages

NORTH SEA COMMUNICATIONS

Willett, R.R.

(Marconi Communication Systems, Ltd., Chelmsford, Essex, England)

Outlines of the requirements of a communications system for North Sea Oil operations and a summary of the principal features of a tropospheric scatter system and of the Intelsat 4 system. It is shown by means of a simple cost comparison that the tropo system now being implemented will have a running cost per telephony channel which is about half that of an equivalent Intelsat 4 system using a half-transponder on an interruptible lease basis. The article concludes that a more specialized satellite system than Intelsat 4 could provide North Sea telephony and data channels at a lower cost than the tropo system from about 1978 onwards.

75A37292 75/00/00 8 pages

DUAL POLARISATION FREQUENCY RE-USE IN SATELLITE COMMUNICATIONS SYSTEMS AT 11 GHZ

Watson, P.A.; Soutter, C.J.

(Bradford University, Bradford, Yorks., England)

75A33203 75/00/00 8 pages

MEASUREMENT OF PROPAGATION-DEPENDENT MODULATION DISTORTION ON WIDEBAND DIRECTIONAL RADIO PATHS

Giloi, H.G.

(Deutsche Bundespost, Fernmeldetechnisches Zentralamt, Darmstadt, West Germany)

The time delay between waves arriving at a receiving antenna via different pathways is determined by evaluating pilot level and noise records. This investigation is relevant to the fact that multipath propagation that often occurs on line-of-sight radio links is frequency-selective, and that it causes level deviations and intermodulation noise in the broad base band of high-capacity FM-FDM systems.

75A19777 74/00/00 5 pages
ATMOSPHERIC EFFECTS ON TERRESTRIAL MILLIMETER-WAVE COMMUNICATIONS
Dudzinsky, S.J., Jr
(Rand Corp., Santa Monica, Calif.)

Proper design of reliable millimeter-wave communications links that operate on paths through the atmosphere requires an understanding of atmospheric transmission losses, especially losses due to rainfall attenuation. This paper combines information on transmission properties of millimeter waves with meteorological data to derive a methodology useful to the design engineer. Emphasis is on high-reliability communications in which outages are 0.1 per cent or less.

75A18085 74/00/00 6 pages
PROPAGATION MODELS FOR OPTICAL COMMUNICATION THROUGH FOG AND CLOUDS
Bucher, E.A.
(MIT, Lexington, Mass.)

This paper discusses three models of light propagation through clouds and fogs. First, the simple single scatter attenuated beam model is reviewed. Second, a diffusion model is presented which adequately describes light transmission through thick clouds. Third, a model based on the strong forward scatter observed with particles large compared to a wavelength shows a 'spreading beam' mode of multiple forward scatter transmission. This multiple forward scatter mode predicts the possibility of optical communication where simple attenuated beam models predict a loss in communication capability.

75A17695 74/06/00 12 pages
THE MEASUREMENT OF SLANT PATH ATTENUATION USING RADAR, RADIOMETERS AND A SATELLITE BEACON
Strickland, J.I.
(Department of Communications, Communications Research Centre, Ottawa, Canada)

In the investigation conducted, attenuations measured directly and attenuations calculated from sky noise temperature measurements have been compared for many rain attenuation events. It was found that radar measurements, after calibration with attenuations measured directly at the frequency of interest, provide detailed information on the intensity and the spatial and temporal distribution of precipitation which cannot be obtained by other methods.

74A44839 74/00/00 348 pages
RADIO WAVE PROPAGATION
Picquenard, A.
(Instituto Tecnológico de Aeronautica, Sao Jose Dos Campos, Sao Paulo, Brazil)

The propagation characteristics of radio waves in a dielectric are investigated, giving attention to plane waves and spherical waves. Questions of tropospheric propagation are considered along with wave propagation in the ground, wave propagation close to the earth's surface, wave propagation in ionized media, and ionospheric propagation. Principles and practical approaches involved in the calculation of radio links are examined. Subjects discussed in an Appendix include the properties of electromagnetic fields, Maxwell's equations, retarded potentials, Hertzian vectors, statistical distributions, Fourier transformations, Fresnel zones, the Doppler effect, and a calculation of the signal-to-noise ratio.

74A39708 74/00/00 6 pages
ESTIMATION OF TROPOSPHERIC PROPAGATION LOSS ON TERRESTRIAL INTERFERENCE PATHS
Weiss, H.J.
(Communications Satellite Corp., Washington, D.C.)

Propagation mechanisms accountable for the attenuation between two points on the earth's surface may be classed into those supporting 'surface propagation' and 'volume propagation'. Methods for estimating the transmission loss for each propagation mechanism and mode differ and require input data regarding path geometry, general or specific earth surface characteristics, general or specific climatic conditions, and certain station characteristics; however, the modes are not equally sensitive to these input data nor do they show the same variation in time. It is therefore necessary to determine the transmission loss for each mode and isolate those predicting the highest field strengths.

74A39653 74/00/00 5 pages
THE EFFECTS OF ATMOSPHERIC FADING ON A SECOND-ORDER PHASE-LOCKED LOOP PRECEDED BY A BANDPASS LIMITER
Korgel, C.C.
(Martin Marietta Aerospace, Denver, Colo.)

74A32916 74/05/00 4 pages
RAIN DEPOLARIZATION - THEORY AND EXPERIMENT
Taur, R.R.
(COMSAT Transmission Systems Laboratory, Clarksburg, Md.)

Experimental measurement data of the one-year-long monitored rain depolarization of a satellite-earth propagation path

have been found to agree generally with theoretical predictions. However, theory is shown to yield higher values of cross-polarization discrimination. This difference is believed to be attributable to near-field effects and to errors introduced by the assumption of ellipsoidal raindrops.

74A18012 73/00/00 6 pages
 INTERLEAVED VITERBI DECODING APPLIED TO TROPOSCATTER CHANNELS
 Goldberg, B.; Moyes, E.D; Quigley, J.E.
 (US Army, Electronics Command, Fort Monmouth, N.J.)

During the past several years, an extensive amount of digital error data has been collected on a bit-by-bit basis over troposcatter communications channels. Based upon a thorough computer analysis of many simulated error control coding schemes, it was determined that the optimum performance improvement would be achieved through the use of an interleaved convolutional encoder/viterbi decoder concept. This paper describes the search effort including the channel error behavior properties and the various coding concepts which led to the development of an interleaved convolutional encoder/viterbi decoder which is currently being built.

73A43156 AD-771827 ESD-TR-73-307 73/10/00 10 pages
 COMPUTER SIMULATION OF LIGHT PULSE PROPAGATION FOR COMMUNICATION THROUGH THICK CLOUDS
 Bucher, E.A.
 (MIT, Lexington, Mass.)

This paper reports computer simulations of light pulse propagation through clouds. The amount and distribution of multipath time spreading was found to be independent of the detailed shape of the scattering function for sufficiently thick clouds. Moreover, the amount of multipath spreading for many scattering functions and cloud thicknesses can be predicted from a common set of data. Spatial spreading of the exit-spot diameter was found to saturate as a cloud of a given physical thickness became optically thicker and thicker. We observed that the propagation parameters for sufficiently thin clouds were dependent both on the cloud parameters and on the scattering function.

75A33703 73/00/00 7 pages
 SINGLE AND DUAL PATH PROPAGATION AT 18 GHZ WITH APPLICATION TO THE DESIGN OF DIGITAL RADIO RELAY SYSTEMS
 Chamberlain, J.K.; Rees, H.W.; Stagg, L.J.
 (General Electric Co. Ltd., Hirst Research Centre, Wembley, Middx., England)

The review of the results of the latest of a series of single and dual path propagation experiments at 18 GHz obtained over West London, UK, is brought up to date. The application of these results to the design of digital radio-relay systems for operation in the 17.7 to 19.9 GHz band is described.

73A18712 72/12/00 6 pages
 ON THE REDUCTION OF RAINFALL OUTAGES BY SPACE DIVERSITY FOR MILLIMETER-WAVE EARTH-SATELLITE COMMUNICATIONS SYSTEMS
 Reber, E.E.; McDonald, D.V.
 (Aerospace Corp., Los Angeles, Calif.); (USAF, Washington, D.C.)

Space diversity – i.e. judicious placement of several ground terminals within a predetermined area – is examined as a means of avoiding rainfall-induced blackouts of millimeter-wave earth-satellite communications systems. The concept of space diversity implemented by a primary station and four secondary stations within an 80-km radius is examined on the basis of hourly rainfall data for the ten-year period from January 1, 1961, to December 31, 1970. The accumulated hours of simultaneous rainfall in several rainfall rate categories are determined for three climatologically different regions of the United States. The minimum simultaneous rainfall in each space diversity system was obtained by selecting the lowest value of rainfall, including no rainfall, at any of the five stations for each clock-hour of rainfall at the primary station. Results show that a space-diversity system with five stations in an 80-km radius will have at least one station free of rainfall at rates greater than 5 mm/hr 99.99% of the time.

73A12775 72/00/00 336 pages
 PROPAGATION OF RADIO WAVES (4th Edition)
 Dolukhanov, M.P.

Ground, ionospheric, and tropospheric wave propagation throughout the entire spectrum from 0.001 Hz to 1000 GHz is examined in a systematic manner designed as a teaching course in colleges and universities. Electrical parameters of the main forms of the earth's surface are defined, and propagation characteristics are examined for cases of locally uneven terrain and for flat and spherical smooth surfaces. Absorption, scattering, and reflection in the ionospheric and tropospheric layers are studied along with multiple-beam effects and features characteristic of specific frequency bands.

76N75637 AD-A018198 74/12/00 73 pages
 SYNOPTIC WEATHER IN RELATION TO ANOMALOUS PROPAGATION OVER BASS STRAIT
 Whitting, B.F.; Bourne, I.A.; Unthank, E.L.; Hopper, V.
 Melbourne Univ., Parkville, Australia

77N27301 AD-A038870 RADC-TR-77-73 77/02/00 90 pages
 MULTIPATH DISPERSION IN LOW VISIBILITY OPTICAL COMMUNICATION CHANNELS -- FINAL REPORT,
 1 JULY 1975 - 30 SEPTEMBER 1976
 Kennedy, R.S.; Shapiro, J.H.
 Massachusetts Inst. of Tech., Cambridge

The potential for optical communication through low-visibility scattering atmospheres is the underlying concern of this investigation. To access that potential, the effects of the channel upon the optical signal propagating through it must be determined. The work reported here is primarily concerned with one of those effects, the time dispersion, or multipath spread, of the transmitted signal. The investigation was primarily an experimental one, utilizing the existing propagation facility operating over a thirteen kilometer experimental path between the MIT campus and a field station located at an air force site in suburban Boston. Experiments were performed at visible and near infrared wavelengths, with highly collimated transmitting beams. Measurements of the multipath spread for various receiver fields of view, and at various off-axis angles were made. Little multipath and angular spread were observed within the realm of atmospheric conditions for which a detectable signal could be obtained. For optical thicknesses less than ten, the on-axis measurements are consistent with the hypothesis that the received signal is dominated by unscattered radiation; however, the off-axis measurements suggest that the scattered field itself may be only slightly spread in time and angle. Guided by the observed narrowness of the angular spectrum, an approximation to the linear transport equation was developed. The resulting equation is more amenable to solution than is the full transport equation. Here it is solved for isotropic scatter. For such scattering it is found that substantial spreading in both time and angle will occur when the optical thickness becomes appreciably greater than one.

77N24365 AD-A034073 TACMEMO-280-1-76 76/09/22 66 pages
 REFRACTIVE EFFECTS GUIDEBOOK (REG)
 Pacific Fleet, FPO San Francisco, 96610. Third Fleet.

The Refractive Effects Guidebook (REG) is designed to provide the fleet with an initial capability to tactically exploit large scale atmospheric refractive conditions. Using routine weather information available to fleet units. The REG presents guidelines for planning the employment of radar, sensor and communications systems according to existing and predicted refractive conditions that frequently cause unusual performance (termed anomalous propagation).

77N21291 AD-A032000 RADC-TR-76-250 76/08/00 233 pages
 HYBRID TROPO TRANSMISSION SYSTEM -- FINAL TECHNICAL REPORT, 15 MAY 1973 - 29 DECEMBER 1975
 Unkauf, M.; Dagnell, R.
 Raytheon Co., Sudbury, Mass.

This document describes the design, development, laboratory testing, and over-the-air testing of digital data tropo transmission system and hybrid tropo transmission system (HTTS). Digital transmission was accomplished at data rates of 1.75, 3.5 and 7.0 MBPS by using the Raytheon distortion adaptive receiver (DAR-IV) modulation/demodulation (modem) technique. Testing of the DAR-IV was performed using the RADC troposcatter media simulator and confirmed by actual over-the-air tests on the AN/MRC-98, AN/TRC-97 and AN/TRC-132 radio equipments in both modes. The test results showed that the DAR-IV technique has the potential to provide quality digital data transmission on both tactical and DCS troposcatter links. Within its multipath spread capabilities, the DAR-IV was shown to typically operate within 3 db of theoretical. The extent of multipath spread accommodated was found to be approximately equal to the inverse of the transmission bit rate. Design improvements are identified to achieve greater multipath spread capacity at the higher data rates. Hybrid transmission was accomplished by using separate analog and digital subcarriers with conventional FDM/FM modulation for analog traffic of up to 60 voice channels. Testing in the hybrid transmission mode revealed that a dual subcarrier approach was feasible but somewhat inefficient in power utilization.

77N18898 AD-A030863 NELC-TN-3233 76/10/01 56 pages
 EXPERIMENTAL TEST PLAN TO INVESTIGATE THE PROPAGATION OF BLUE/GREEN RADIATION THROUGH CLOUDS
 Mooradian, G.C.; Geller, M.; Stotts, L.B.; Hughes, H.G.
 Naval Electronics Lab. Center, San Diego, Calif.

It is the purpose of this test plan to define an experiment to measure the peak power losses and temporal characteristics as a function of the field-of-view of optical pulses propagating through clouds (marine fogs). In addition to the propagation measurements the meteorological parameters describing the propagation path will be measured and used as inputs to computer codes to assess the measured results and for propagation prediction purposes. Of primary interest here are those frequencies in the blue-green portion of the spectrum which after propagating through a cloud, can penetrate sea water and be of use as a submarine-to-aircraft satellite communications system.

76N26375 AD-A019114 NRL-MR-3163 75/11/00 34 pages
 DETECTION RANGES OF LOW ALTITUDE TARGETS OVER THE SEA SURFACE
 Hsiao, J.K.
 Naval Research Lab., Washington, D.C.

In this report the computation of the detection range of a low altitude target over a reflecting sea surface is presented. This detection range usually lies within the intermediate region between the interference and diffraction regions. Since

computations of signal strength in this region are estimated by interpolation, the results are an approximation. It is recommended that a rigorous solution be pursued. Furthermore, ducting and other anomalous atmospheric conditions are not taken into account. Work along these lines is also recommended.

75N25738 AD-A019269 ECCM-5578 75/10/00 55 pages
 ENHANCEMENT OF POINT SOURCE THERMAL RADIATION USER CLOUDS IN A NONATTENUATING MEDIUM
 Cantor, I.

Army Electronics Command, Fort Monmouth, N.J.

A detailed series of graphs is provided along with accompanying analyses to show cloud overcast effects upon the visible radiation emanating from a point source to a target at the ground. The appendix graphs apply to the following set of hypothetical conditions. The medium of propagation is a nonattenuating (no scattering or absorbing) atmosphere. The overlying cloud acts as a 100% diffusely reflecting surface, the ground surface is nonreflecting and the target acts as a Lambert-type receiver. Total atmospheric radiation transmission maxima are about 300% of the direct transmission in a nonattenuating atmosphere. This occurs, for example, when a high-altitude source is close to an overcast with the target parallel to the ground and clouds and its horizontal distance is close to ground zero.

76N21373 AD-A017085 DOT-TSC-FAA-75-13 FAA-RD-75-150 75/09/00 41 pages
 PERFORMANCE EVALUATION OF DATA MODEMS FOR THE AERONAUTICAL SATELLITE CHANNEL -
 INTERIM REPORT, AUGUST 1974 - JUNE 1975

Duncombe, C.B.; Salwen, H.

(Proteon Associates, Inc.)

Transportation Systems Center, Cambridge, Mass.

The modems tested included a high performance DPSK modem, a high performance CPSK modem, two hybrid voice/data modems, and a lower performance CPSK modem. Data performance results are presented in the form of probability of bit error versus signal to noise density and signal to multipath ratios with doppler spread as a parameter. Some tests were conducted with a hard limiting IF processor in cascade with the channel simulator to simulate satellite characteristics. The characteristics of the aeronautical satellite channel simulator are also described.

76N20190 AD-A016171 TSC-FAA-75-18 75/06/00 170 pages
 US AERONAUTICAL L-BAND SATELLITE TECHNOLOGY TEST PROGRAM - INTERIM REPORT, 1 DECEMBER
 1974 - 1 JUNE 1975

Schroeder, E.H.; Sutton, R.W.; Thompson, A.D.; Paulson, C.V.; Wilson, S.G.

Boeing Commercial Airplane Co., Seattle, Wash.

The US aeronautical L-band satellite test program was performed between September 1974 and April 1975 as part of an international ATS-6 L-band satellite test program. The US program consisted of both technology and ATC communications demonstration tests. The technology tests were comprised of multipath channel characterization tests; modem tests of voice, data, and ranging; and aircraft antenna tests. Multipath results include delay-doppler scatter function characteristics and calculations of spectra, spreads and auto correlations for both over-ocean and conus multipath. Comparison of sample results with model prediction is given. Voice modem intelligibility scores, digital data bit error rates and ranging modem performance are presented parametrically as functions of C/N_0 and S/I . Experimentally derived gain and multipath rejection performance data are given for the slot-dipoles, phased array, patch, and crossed-slot antennas for various aircraft/satellite geometries.

75N31200 AD-A009736 75/04/00 77 pages
 JOINT NRL/NELC OPTICAL-SATELLITE-COMMUNICATION ATMOSPHERIC-PROPAGATION TEST PLAN

Livingston, P.M.; Trusty, G.L.; Ruhnke, L.H.; Mooradian, G.

Naval Research Lab., Washington, D.C.

An experimental program has been planned to test the hypothesis that optical communication systems based on the heterodyne principle can be used for practical navy ship/satellite communications through clouds of moderate thickness. The island of Hawaii has been chosen as the site of a major field effort by NRL and NELC because the trade winds drive typical marine orographic clouds through an elevated mountain pass reproducibly on a daily basis, the mountain pass is accessible by road, and (as is summarized herein) the clouds there have already been well studied. A theoretical formulation based on radiation transport theory shows that the reliability of an optical heterodyne communication system can be expressed as a function of the cloud properties. The experiments will test the relationship between a system carrier-to-noise ratio (C/N) and cloud properties. They will establish the averaging times necessary for a meaningful C/N , determine the relationship between C/N and the optical-thickness and droplet-size parameters of the cloud, relate reproduction of clear-path C/N values, averaged mean-square wavefront tilt received, and optical turbulence, and measure the reduction of C/N in a cloud as the receiver (or transmitter) is pointed off-axis (thus examining the security of a system).

75N22308 AD-A006268 FAA-74-75-VOL-2 74/07/00 471 pages
MULTIPATH IN AIR TRAFFIC CONTROL FREQUENCY BANDS, VOLUME 2, CHAPTERS C3--G4, GENERAL BIBLIOGRAPHY

Hartman, W.J.

Institute for Telecommunication Sciences, Boulder, Colo.

Theories and techniques dealing with multipath problems are presented with emphasis placed on air traffic control frequencies. The material presented is oriented toward frequencies above VHF, and toward line-of-sight paths. The following factors are included: causes of multipath, doppler effects, methods for reducing the effects of multipath, and specific system considerations.

75N22080 75/02/00 26 pages

INFLUENCE OF TOPOGRAPHY AND ATMOSPHERIC REFRACTION IN UHF GROUND-AIR COMMUNICATIONS

Ince, A.N.; Williams, H.P.

SHAPE Air Defense Technical Center, The Hague, Netherlands

The results of field strength measurements in UHF ground-air communication using four different ground terminals are presented. The local conditions at the ground terminals varied considerably. In one case the site was flat and clear over a distance of 2 km, in another the site was the highest in the district, a third site had nearby buildings, while the fourth site had marked local undulations and a nearby valley. In all four cases the field strength at the optical horizon was very close to the theoretical value for a smooth earth. The field strength at this point was virtually unaffected by the local ground conditions. Using this fact, and taking into account the statistics of atmospheric refraction it is possible to predict the reliability of UHF ground-to-air communication for high-flying aircraft.

75N22054 75/02/00 12 pages

PROPAGATION IN DUCTS AND WAVEGUIDES POSSESSING IRREGULAR FEATURES. FULL WAVE SOLUTIONS

Bahar, E.

Nebraska Univ., Lincoln

The impetus to produce rigorous solutions to more realistic models of pertinent propagation problems over a wide frequency range has generated the need to derive full wave solutions to problems of radio wave propagation in non-uniform multilayered structures. The considerable growth in civil and military interest in the development of more reliable communication and detection systems, the potential for developing radio wave methods for remote sensing and the need to develop hardened communication systems have contributed much to this renewed interest. These developments have been paralleled by remarkable advances that have been made in the availability of high powered, very low frequency electromagnetic sources that are capable of radiating deeper into the earth's crust as well as the availability of transmitters operating at optical frequencies. The ready access to large, versatile digital computers has made it possible to employ the full wave approach to obtain numerical solutions to a wide class of important problems which have hitherto been either ignored or over-idealized in order to reduce them to tractable problems.

75N21506 AD-A002929 NRL-MR-2903 74/10/00 56 pages

ATMOSPHERIC TURBULENCE AND THE EXTENSION OF THE RADIO HORIZON

Skolnik, M.I.

Naval Research Lab., Washington, D.C.

The possibility that atmospheric turbulence (clear air turbulence) can cause extended propagation beyond the optical line of sight is examined. It is possible for a distant transmitter to interfere with a receiver via scattering from atmospheric turbulence, but it is not likely that a radar will receive distant ground echo via scattering from turbulence. From a compilation of published data it is shown that the structure constant of the atmosphere (a measure of scattering) is a function of altitude with an apparent maximum in the vicinity of 500 to 1000 m.

75N14956 AD-787453 DOT-TSC-FAA-74-8 FAA-RD-74-151 74/08/00 77 pages

MULTIPATH CHANNEL SIMULATION AND MODEM EVALUATION PROGRAM - INTERIM REPORT, OCTOBER 1973 - APRIL 1974

Duncombe, C.B.

Transportation Systems Center, Cambridge, Mass.

The Department of Transportation, Transportation Systems Centre has developed a laboratory communications test facility. To evaluate in a laboratory controlled simulated environment, alternative modulation techniques having potential application in aeronautical and maritime satellite communications and surveillance systems. The main feature of the communication test facility is the hardware for simulating, by means of laboratory equipment, the narrowband (50 KHz) aerosat satellite-to-aircraft propagation channel. The simulator also simulates the maritime satellite-to-ship propagation channel and is expandable to wideband (10 MHz) systems; e.g., future conus ATC systems. The simulator includes provisions for duplicating multipath phenomena over the satellite links and includes provisions for adjustment and programming of channel parameters covering a wide range of environmental conditions. (Modified author abstract.)

74N34160 AD-778390/5 TSC-FAA-74-1 FAA-RD-74-54 74/03/00 298 pages
 IMPACT OF SATELLITE AERONAUTICAL CHANNEL ON MODEM SPECIFICATIONS – FINAL REPORT, AUGUST 1972 – MARCH 1973

Bello, P.A.; Boardman, C.J.; Chase, D.; Derosa, J.K.
 Transportation Systems Center, Cambridge, Mass.; CNR, Inc., Newton, Upper Falls, Mass.

The report analyzes the effects of surface-scattered multipath on the performance of ranging and data modems such as might be used on the aircraft-satellite channel of an air-traffic control system. An exact analysis is carried out on the effects of noise and multipath on the one-way ranging errors of a single-sideband tone ranging modem. These results are shown to be applicable at high SNR and direct path/multipath ratios to a double-sideband tone ranging modem whose side-band separation equals the tone separation in the single sideband system. The conventional practice of calculating ambiguity error probabilities with an assumption of Gaussian ranging error distribution is shown to be inapplicable for many situations of practical interest. (Modified author abstract.)

74N15397 73/00/00 132 pages
 A STUDY OF IRRADIANCE SCINTILLATION EFFECTS OF AN OPTICAL WAVE PROPAGATING THROUGH A TURBULENT ATMOSPHERE – PH.D. THESIS

Wang, T.I.
 Dartmouth Coll., Hanover, N.H.

Amplitude or irradiance scintillations of an optical wave propagating in a clear turbulent atmosphere are studied. The probability distribution of the irradiance is specified by a log-normal distribution or a Rice-Nakagami distribution. A simple set of equations is derived to describe the variance and covariance functions of log-amplitude fluctuations and also the log-irradiance fluctuations in order to show whether the variance of the log-irradiance fluctuations saturates and even decreases with increasing path length and turbulence. Results show that irradiance fluctuations cannot be strictly log-normal in the saturation region and that this assumption is not useful in calculating the log-irradiance variances and covariances.

74N13871 73/09/00 11 pages
 THE INTERRELATION OF PROPAGATION EFFECTS AND DESIGN FACTORS FOR FIXED SERVICE COMMUNICATION SATELLITE SYSTEMS

Fansler, B.J.; Segner, S.M.
 Army Satellite Communications Agency, Fort Monmouth, N.J.; Army Electronics Command, Fort Monmouth, N.J.

The problems of frequency sharing between multichannel transmission using satellites and multichannel transmission using radio relay are reviewed. Two cases of potential interference involve determination of coordination distance based on normalized basic transmission in the absence and in the presence of precipitation. One case is for the earth station received signal being interfered with by terrestrial station transmitters. The second is for earth station transmitted signal interfering with terrestrial station receivers. Taking advantage of a newly written computer program, the effects of varying propagation factors, radio climatic regions, rain climatic zones and interference duration is investigated.

73N31099 FTZ-A-455-TBR-34 72/01/00 29 pages
 OBSERVATIONS OF A 210 KM LONG 12 GHZ LINK

Abel, N.
 Fernmeldetechnisches Zentralamt, Darmstadt, West Germany

An experimental trans-horizon radio link of 210 km path length at 12 GHz was established in southwestern Germany, and the received signal was observed for 18 months. Cumulative probability distributions of the transmission loss relative to free space are presented. The behavior of the signal revealed different propagation mechanisms: tropospheric scatter propagation, reflection by layer-like structures, and attenuation and scattering by precipitation. The annual median value of field strength was considered in conjunction with existing propagation curves.

73N28019 OT/TRER-34 72/08/00 81 pages
 A REVIEW OF PROPAGATION FACTORS IN TELECOMMUNICATIONS APPLICATIONS OF THE 10 TO 100-GHZ RADIO SPECTRUM

Thompson, M.C., Jr; Vogler, L.E.; Janes, H.B.; Wood, L.E.
 Institute for Telecommunication Sciences, Boulder, Colo.

Systems applications in the 10- to 100-GHz frequency band, propagation factors pertinent to the design of these systems, and recommendations for future action are discussed. Consideration is given to the complementary roles of experiment and analysis in providing the information necessary for optimum utilization of EHF frequencies.

73N23256 AD-757553 SIG-A-125 RADC-TR-72-350 73/01/00 172 pages
 DIGITAL TROPOSCATTER EXPERIMENTS – FINAL REPORT, MARCH 1971 – JULY 1972

Ehrman, L.; Graham, J.W.
 Signatron, Inc., Lexington, Mass.

Extensive measurements and predictions were made at 900 MHz to characterize the loss and multipath variations over the 168 mile Youngstown N.Y. to Verona N.Y. troposcatter link. Cumulative distributions of loss and multipath

spread are in good agreement with predictions. Dual space and frequency diversity multipath analyses demonstrate that diversity receivers can use common timing provided the mean delays between paths are equalized. Time synchronization improvements made to a time-gated 3 MBPS coherent MODEM demonstrate that bit sync can be maintained reliably at signal levels well below those levels required for acceptable error rate and demultiplexer performance. (Author modified abstract.)

73N17178 AD-752249 TN-1972-27 ESD-TR-72-216 72/09/00 151 pages
DIVERSITY TECHNIQUES FOR AIRBORNE COMMUNICATIONS IN THE PRESENCE OF GROUND REFLECTION MULTIPATH

Berger, H.; Evans, J.E.
Lincoln Lab., Mass. Inst. of Tech., Lexington

The signal power reduction due to multipath fading is an important design consideration in the development of air-air and ground-air communications links at L-band. A first order mathematical model of ground reflection multipath is used to predict the relationship between the depth of fading and environmental parameters such as surface roughness and the terminal positions relative to earth. The model is then used to investigate two techniques for reducing the loss in received signal power - frequency diversity and antenna height diversity. A measurement program to experimentally evaluate the applicability of antenna height diversity is outlined.

2. Optical Sensing Problems Coherent and Incoherent Propagation Laser Transmission

74A41017 74/08/23 3 pages
INTERACTION OF COHERENT ELECTROMAGNETIC WAVES WITH RELATIVISTIC ELECTRONS IN A MEDIUM
Schneider, S.; Spitzer, R.
(Stanford University, Stanford, Calif.)

Considerations of Milburn (1963) and Arutyunian et al. (1964) in discussions of the vacuum effect involving the conversion of optical photons are extended by taking into account the coherence of the field driving the charged particle. Aspects of possible constructive interference from many-electron effects are also examined. The investigation involves scattered radiation at energies below those at which atomic resonances occur, for which the assumption of slowly varying electric susceptibility is expected to be valid. The qualitative features of the effect, however, are expected to persist in the region of anomalous dispersion corresponding to X-ray and gamma-ray frequencies.

78N15889 AD-A046796 NRL-MR-3532 ECTPC-37 77/07/00 92 pages
MUTUAL INTERFERENCE OF OPTICAL COMMUNICATION LINKS - INTERIM REPORT
Kershenstein, J.C.; Horrigan, F.A.
Naval Research Lab., Washington, D.C.

The problem of interference in optical communications systems caused by such communication systems is discussed together with suggestions to reduce this interference. The propagation of optical signals is studied to determine which propagation modes can contribute to interference. Twenty-four modes of possible interference are identified and analyzed. Conclusions are drawn which indicate that in 21 of the 24 modes interference can be eliminated by simple geometric and modulation coordination restrictions. In the three remaining modes, which are scatter links, geometric coordination can resolve the conflicts, but it is definitely more restrictive and difficult to implement than for other modes.

77N30471 AD-A036503 RADC-TR-77-18 77/01/00 73 pages
PROPAGATION OF MULTIWAVELENGTH LASER RADIATION THROUGH ATMOSPHERIC TURBULENCE -
FINAL REPORT, 1 FEBRUARY - 30 NOVEMBER 1976
Kerr, J.R.; Elliot, R.A.; Fossey, M.E.; Holmes, J.F.; Lee, M.H.
Oregon Graduate Center for Study and Research, Beaverton

A complete theory is presented for the statistical effects of atmospheric turbulence on coherent radiation reflected from a diffuse target. This study, which is motivated by the need to understand speckle and scintillation effects on the operation of coherent adaptive optical transmitter (COAT) systems, constitutes a significant advance in the field of turbulence scattering phenomena. Both phase and amplitude perturbations are taken into account, and the analysis includes multiple scattering (saturation) conditions and finite receiver apertures. The development is free from certain restrictive assumptions employed in previous work, and yields results for the variance and covariance of irradiance which lead to clear physical insight. It is found that the covariance comprises two additive terms which represent respectively (1) the incoherent scattering mechanism which is independent of source spectral width, and (2) the coherent mechanism related to 'speckles'. A technique is also developed for quantitative numerical predictions using reasonable computer time. Results from an ongoing program of experimental verification are given which support the theory.

77N12389 AD-A074863 RADC-TR-76-11 76/04/00 73 pages
 PROPAGATION OF MULTIWAVELENGTH LASER RADIATION THROUGH ATMOSPHERIC TURBULENCE -
 INTERIM TECHNICAL REPORT, 1 AUGUST 1975 - 31 JANUARY 1976
 Kerr, J.R.; Holmes, J.F.; Lee, M.; Pincus, P.A.
 Oregon Graduate Center for Study and Research, Beaverton

This report reviews initial progress on a new program of investigation of scintillation and coherence effects for a laser-illuminated, noncooperative target as viewed through atmospheric turbulence. The application of the effort is in the prediction of turbulence effects on the operation of coherent optical adaptive transmitter (COAT) systems. Significant analytical progress is reviewed, including results for the mutual coherence function, variance and covariance of irradiance, spectra, and statistics for a coherently illuminated diffuse target. It is found that there are three pertinent covariance scales and six possible parameter realms, and that the normalized variance will be unity except in those cases when the target spot is sufficiently small as to constitute a quasi-point-source. The analysis is partially extended to a more complex target and to the incoherent case, and future analytical tasks and applications to real adaptive systems are outlined. The establishment of an experimental field facility is also described, which will be capable of measuring all pertinent quantities at both visible and middle-infrared wavelengths.

77N11856 AD-A025338 ESD-TR-76-34 75/12/00 29 pages
 OPTICS RESEARCH - SEMI ANNUAL TECHNICAL REPORT, 1 JULY - 31 DECEMBER 1975
 Rediker, R.H.
 Lincoln Lab., Mass. Inst. of Tech., Lexington

Contents: laser technology and propagation - A. propagation - (laboratory experiment on phase correction for thermal blooming, phase compensation for multiple-pulse thermal blooming, phase compensation for turbulence, fog hole boring and propagation study), B. pollution studies - atmospheric CO monitoring over long paths in the 1975 regional air pollution study (RAPS) in St Louis - (introduction, site 108 - Granite City, Illinois, site 105 - Downtown, St Louis, Missouri).

3. Remote Sensing (IR, UV, Microwaves)

78N14757 AD-A046275 FAA-RC-77-54 77/03/00 33 pages
 REMOTE SENSING WIND AND WIND SHEAR SYSTEM - INTERIM REPORT, JANUARY 1974 - SEPTEMBER 1976
 Mandics, P.A.
 National Oceanic and Atmospheric Administration, Boulder, Colo.

The prototype development of an acoustic doppler remote sensing system to detect low level wind shear generated by synoptic scale features such as frontal surfaces is described. The detector system measures the vertical profile of wind by determining the doppler frequency shift of vertically transmitted acoustic signals that are scattered by small scale atmospheric inhomogeneities. Significant improvements were accomplished on the acoustic transmitter and receiver antennas, and signal processing. A conical horn reflector antenna with a 2-m diameter aperture fed by 12 high power acoustic drivers through a manifold increased the transmitted power by more than 100%. Substantial improvements were achieved in received signal to noise ratio by developing a narrow beam, off focus steered receiver antenna that is capable of tracking the upward propagating acoustic pulse. Development of new system software made all digital signal processing and computerized system control possible. Tests of one leg of the prototype revealed that the system measured winds reliably up to a height of 600 m when surface winds did not exceed 10 m/s.

4. Radio Wave Scintillation Tracking and Communication Navigation and Positioning Systems Radar and Navigation Correction Techniques

76A42122 76/09/00 10 pages
 USE OF THE SPACELAB FOR TECHNOLOGICAL TASKS, ESPECIALLY COMMUNICATIONS AND NAVIGATION
 Rother, D.
 (Standard Elektrik Lorenz AG, Stuttgart, West Germany)

This report is concerned with experiments to be carried out in the European Spacelab in order to improve existing communications, monitoring and navigation systems or to facilitate the development of new methods. The experiments are based on proposals from industry and scientific institutes which had been sent to the Ministry of Technology of the Federal Republic of Germany. Standard Elektrik Lorenz AG in Stuttgart (Germany) was given the task of undertaking a survey study in the field of communications and navigation. A short survey of experiment suggestions which were given special attention in the study are described in this report in more detail. The experiments are mainly in the field of (1) wave propagation, (2) environmental control, (3) navigation and position finding, and (4) communications. Spacelab is not, basically, intended for operational use, but to test systems and installations and to undertake special research.

76A33303 76/04/15 3 pages

LABORATORY MICROWAVE SPECTRUM AND REST FREQUENCIES OF THE N2H+/ION

Saykally, R.J.; Dixon, T.A.; Anderson, T.G.; Szanto, P.G.; Woods, R.C.

(Wisconsin University, Madison, Wis.)

76A12092 75/11/00 4 pages

THE RELATION BETWEEN THE SPECULAR-TO-INTERFERENCE RATIO AND THE SCINTILLATION INDEX

Valley, G.C.

(Calspan Corp., Buffalo, N.Y.)

This paper points out evidence that in many cases the fluctuations in a signal transmitted through ionospheric irregularities do not obey Rician statistics and that therefore, the Rician relation between the specular-to-interference ratio and the scintillation index, recently discussed by Shaft, may not apply to ionospheric communications studies in these cases.

75A27065 75/04/00 6 pages

COMPUTER MODELING OF THE STATISTICAL PROPERTIES OF TRANSIONOSPHERIC SCINTILLATION CHANNELS

Deckelman, W.F.; Ziemer, R.E.

(McDonnell Douglas Corp., St Louis, Mo.); (Missouri University, Rolla, Mo.)

This concise paper shows that a band-limited bivariate-normal time series is a useful model for the envelope of scintillating radio signals traversing the ionosphere. A software model is presented whose generated time series is compared to an actual block of scintillation data. A comparison of computer-generated and actual scintillation data shows that the fade-duration distribution of the simulated data fits that of the actual data closely through proper choice of model parameters.

75A15115 74/11/00 4 pages

GEOMETRIC CONSIDERATIONS IN THE DESIGN OF COMMUNICATIONS CIRCUITS USING FIELD-ALIGNED IONOSPHERIC SCATTER

Stathacopoulos, A.C.; Barry, G.H.

(General Research Corp., Santa Barbara, Calif.); (Barry Research Corp., Palo Alto, Calif.)

The aspect sensitivity of man-made, field-aligned ionospheric irregularities implies that the geometry of VHF communications circuits using these scatterers must be carefully designed. The design problem is sufficiently complex that it is best approached with the aid of a computerized model. Examples are presented showing the results of path modeling for man-made clouds located in Colorado and in Italy. The effects of variations in cloud height and communications circuit frequency are evident from these examples. It is concluded that geometric restrictions are sufficiently strong as to limit the application of the technique to certain specialized point-to-point or point-to-zone uses.

74A40389 73/09/00 4 pages

EFFECT OF PROPAGATION TIME OF SIGNALS ON THE ACCURACY OF MEASUREMENTS WITH FREQUENCY AND PHASE TYPE RADIO ENGINEERING SYSTEMS

Vasilev, M.B.; Savich, N.A.

The causes of the errors which appear in frequency and phase type radio systems of the interrogation type due to changes in the plasma parameters during the time of propagation of the signals are analyzed, and the magnitude of these errors is estimated. The rate of change of the integrated electron density can differ for the interrogation and reply signals over the different segments of the path because of ionospheric inhomogeneities, solar plasma streams, and similar effects.

74A34869 73/00/00 51 pages

METHODS OF VISUALIZING ULTRASOUND

Marsh, D.M.

(Tube Investments Ltd., Saffron Walden, Essex, England)

The present work first reviews the operating principles and main features of present techniques for the visualization of ultrasound, including Schlieren methods, photoelastic methods, and scanning detector methods. The performances of these various methods and of combined methods are compared. The second section discusses computer simulation of ultrasonic fields based on theories of ultrasonic propagation and interaction.

74A34083 73/00/00 4 pages

DIURNAL AND SEASONAL VARIATIONS IN ATMOSPHERIC TIME DELAY

Lovine, D.M.

(Maryland University, College Park, Md.)

Calculations of the diurnal variations of the propagation delay introduced by the atmosphere in satellite-to-earth communications are reported and discussed in the context of a one-way satellite-borne system for time dissemination. A spherically symmetric model for the atmosphere is assumed and the techniques of geometrical optics are employed. Attention is restricted to frequencies below about 15 GHz for which the atmosphere is non-dispersive and data are presented in terms of the difference between free space delay and actual delay.

76N20331 76/00/00 15 pages

HIGH RESOLUTION MEASUREMENTS OF TIME DELAY AND ANGLE OF ARRIVAL OVER A 911 KM HF PATH
Rice, C.W.

Communications Research Centre, Ottawa, Ontario

The results of some 40 hours of afternoon and evening measurements of HF propagation over a 911 km path are presented. An FMCW sounding technique was employed with a linear receiving array of 1.2 km aperture. These arrangements made it possible to resolve modes differing in time of arrival by as little as 20 microseconds, and to determine the angle of arrival of each mode. The results show that markedly nonlinear phase fronts can occur even for apparently single modes of propagation, as a result of the irregular structure of the ionosphere which splits the signal into a number of sub-modes. This finding presents a possible limitation to the accuracy of HF direction-finding, which applies even to systems capable of resolving the modes.

76N20308 76/00/00 15 pages

PLASMASPHERIC CONTRIBUTION TO GROUP-PATH-DELAY OF TRANSIONOSPHERIC SATELLITE NAVIGATION SIGNALS

Soicher, H.

Army Electronics Command, Fort Monmouth, N.J.

A satellite navigation concept requires measurement of the time delay that satellite-emitted signals experience when traversing the distance between satellite and user. A pulse propagating this distance is slowed somewhat by an amount which is directly proportional to the total number of free electrons (TEC) along its path. For high orbit satellites, TEC includes the ionospheric as well as the plasmaspheric electron contents. The radio beacon experiment (RBE) aboard the ATS-6 satellite examined the ionospheric content, N_I (by the Faraday technique), the total ionospheric and plasmaspheric contents, N_T (by the group delay technique), and the plasmaspheric content ($N_T - N_I$) = N_p . Although diurnal, day-to-day, and seasonal variations of N_p were observed, they were much smaller than corresponding variations of N_I and N_T . The ratio of plasmaspheric to ionospheric contents varied diurnally, seasonally, and from day-to-day. The diurnal variations exhibits basically a nearly constant night behavior and a much lower day behavior with rapid changes just after local sunrise and just after local sunset.

76N20306 76/00/00 9 pages

CHANNEL FADING ON AIR MOBILE SATELLITE COMMUNICATIONS LINKS

Maynard, L.A.

Communications Research Centre, Ottawa, Ontario

Statistical measurements of the fading and time dispersion of the earth-space path have been made at locations varying in geomagnetic latitude. These measurements have demonstrated that the required system margins for a given grade of service vary strongly with frequency, geomagnetic latitude, and the way in which system reliability is specified. Preliminary measurements of the multipath characteristics of the North Atlantic show that the reflection process is diffuse.

76N20304 76/00/00 16 pages

AMPLITUDE SCINTILLATION OBSERVATIONS AND SYSTEMS APPLICATION

Whitney, H.E.; Aarons, J.

Air Force Cambridge Research Labs., L.G.Hanscom Field, Mass.

For the design of a transionospheric communications link, scintillation data are to be reduced to statistical descriptions during those intervals for which there is stationariness of the rms fluctuations of the signal. The fade statistics are useful in choosing coding and/or time diversity techniques to overcome this fading. Signal statistics of this type are illustrated using data recorded at equatorial, sub-auroral, and auroral latitudes. These signal statistics are folded into a morphological pattern which contains statistics of scintillation fading as a function of geomagnetic latitude, instantaneous magnetic excursion, and local time. Recent data taken at auroral and sub-auroral latitudes have shown the effects on F layer irregularities of magnetic storms. In particular, the magnetic storms of August 1972 illustrate worst case scintillation levels. Data during the storm of October 31–November 1, 1973 are used to show the correlation of scintillation with local magnetic variations.

76N20302 AGARD-CP-173 76/00/00 424 pages

RADIO SYSTEMS AND THE IONOSPHERE

Advisory Group for Aerospace Research and Development, Paris, France

75N25377 AD-A006657 ONRL-C-1-75 75/02/03 10 pages

MEETING FOR DISCUSSION. THE THEORY OF ELECTRIC AND MAGNETIC WAVES IN THE IONOSPHERE AND THE MAGNETOSPHERE

Harris, M.S.

Office of Naval Research, London, England

A two-day meeting for discussion to mark the fiftieth anniversary of radio investigations of the ionosphere was sponsored by the Royal Society and URSI in London on 5–6 December 1974. Abstracts of papers presented on the early history of ionospheric investigations as well as those on the theory of electric and magnetic waves in the ionosphere and magnetosphere are given.

75N21495 NASA-CR-120737 BER-186-70 75/01/00 158 pages
 THRESHOLD DETECTION IN AN ON-OFF BINARY COMMUNICATIONS CHANNEL WITH ATMOSPHERIC
 SCINTILLATION - FINAL REPORT
 Webb, W.E.
 Alabama Univ., University

The optimum detection threshold in an on-off binary optical communications system operating in the presence of atmospheric turbulence was investigated assuming a Poisson detection process and log normal scintillation. The dependence of the probability of bit error on log amplitude variance and received signal strength was analyzed and semi-empirical relationships to predict the optimum detection threshold derived. On the basis of this analysis a piecewise linear model for an adaptive threshold detection system is presented. The bit error probabilities for nonoptimum threshold detection systems were also investigated.

74N28273 74/05/00 28 pages
 LONG-TERM INTEGRATED RADIOPHYSICAL STUDIES OF THE IONOSPHERE, NEAR SPACE, AND THE
 PROPAGATION OF RADIO WAVES FROM SPACE OBJECTS
 Misyura, V.A.
 Kanner (LEO) Associates, Redwood City, Calif.

The radiophysical studies reported consist of direct measurements of certain effects induced in the propagation of radio waves from space objects. From measured effects and from data on the motion and position of space objects, physical parameters of the medium and bodies are determined.

5. Low Frequency Propagation and Systems - Omega and Loran "C" Systems

75A34751 74/00/00 439 pages
 ELF-VLF RADIO WAVE PROPAGATION; PROCEEDINGS OF THE ADVANCED STUDY INSTITUTE, SPATIND,
 NORWAY, APRIL 17-27, 1974
 Holtet, J.A.
 (Norske Institutt for Kosmisk Fysikk, Oslo, Norway)

Papers are presented which review the properties of the lower ionosphere, set forth the basic principles in the theory of ELF-VLF wave propagation, and describe experiments on this propagation in the earth-ionosphere duct. Some of the topics covered include the photochemistry of the mesosphere, coupling between the neutral and the ionized atmosphere, the coalescence of coupling points and 'cross-over' for ion cyclotron whistlers, the effect of ground conductivity on VLF propagation, VLF phase perturbations associated with geomagnetic activity, the measurement of electron density below 70 km, ELF noise measurements, multipath doppler shifts in man-made VLF signals, and ELF-VLF applications in navigation and communications. Individual items are announced in this issue.

75A16361 74/10/00 4 pages
 PROPAGATION ANOMALIES THAT MIGHT AFFECT THE RELIABILITY OF THE OMEGA NAVIGATION SYSTEM
 Rumi, G.C.
 (Istituto Elettrotecnico Nazionale Galileo Ferraris, Turin, Italy)

It is shown that, under specific ionospheric conditions, the VLF sky signals of the Omega navigation system might undergo an extra phase delay that depends on their frequency and on their azimuth of propagation. Even under quiet ionospheric situations could such an anomaly arise, and be strong enough to upset the normal Omega operation. As an application, the signals from the Omega transmitter in Trinidad are considered and the geographical points where their reception may be affected by the discussion anomalous phase delay, are tabulated.

75A15368 74/00/00 4 pages
 A NEW EVIDENCE OF SUNRISE LAYER FOR TRANSEQUATORIAL NWC /22.3 KHZ/ LONG PATH PROPAGATION
 Shibata, T.
 (University of Electro-Communications, Chofu, Tokyo, Japan)

74A36888 73/07/00 8 pages
 SOLAR-TERRESTRIAL DISTURBANCES OF AUGUST 1972. XIV - LF/MF/HF RADIO WAVE PROPAGATION
 DISTURBANCES
 Wakai, N.; Ouchi, C.; Nemoto, C.; Kogaku, T.

Review of the variations observed in the field intensities of signals at 5, 2.5, 1.85, and 0.75 MHz and in the intensity and phase of 100 KHz signals during the solar-ionospheric disturbances early in August 1972. Ionograms recorded in the night from August 5th to 6th showed the occurrence of a nighttime E (intermediate) layer in association with an increase in the absorption of HF and MF waves and a phase advance of LF signals.

74A32315 74/05/00 7 pages
GENERATION OF ULF BY A HORIZONTAL ELECTRIC DIPOLE
 Greifinger, C.; Greifinger, P.
 (R & D Associates, Santa Monica, Calif.)

A horizontal electric dipole antenna at the ground operating at ULF can excite hydromagnetic TE waves in the hydromagnetic waveguide centered at the F2 ionization maximum. Propagation in the waveguide accompanied by leakage into the earth-ionosphere cavity provides a mechanism by which magnetic fluctuations may be transmitted to ground receivers some thousands of kilometers from the transmitter. At ULF, the optimum direction for this mode of operation is broadside to the dipole. Under favorable ionospheric conditions, a dipole 30 km in length and driven at a peak current of 500 amp could produce a ground signal of the order of a milligamma at a distance of 2000 km.

74A23389 73/00/00 4 pages
ON SUNRISE FADING OF VLF /NWC, 22.3 KHZ/ SIGNALS OBSERVED AT SUGADAIRA
 Shibata, T.
 (University of Electro-Communications, Tokyo, Japan)

Continuous observations of the field strength and the relative phase-shift of frequency-stabilized VLF (NWC, 22.3 KHz) signals transmitted from Northwest Cape, Australia, were started in January, 1972 at Sugadaira, Nagano, Japan. The great circle path between NWC and Sugadaira is about 6970 km. The seasonal variation in time of fading, of the solar zenith angle, and of the spacing distance is described, emphasizing that a solar zenith angle $\chi =$ about 94 to 95 deg is most proper for the summer season. The spacing distances are calculated by using the newly defined χ , whose anomalous characteristics seem to be reflected from some unknown effects of transequatorial propagation.

73A34673 SAE Paper 730313 73/04/00 8 pages
VLF RADIO NAVIGATION
 Wilson, J.A.

The fundamentals of radio navigation are reviewed together with the propagation characteristics of the VLF portion of the radio spectrum and the historical background of present-day VLF navigation systems. Features and performance of the Omega system and the global navigation system are compared to illustrate the current state of the art, and developments which can be reasonably expected in the future are discussed.

73A28651 72/07/00 8 pages
NUMERICAL SOLUTION OF THE PROBLEM OF TRANSMISSION OF ELF WAVES THROUGH THE LOWER IONOSPHERE
 Aksenov, V.I.; Nazarova, M.V.

(Previously cited in Issue 19, p.2767, accession No. A72-38651.)

73A15060 72/00/00 5 pages
PROPERTIES OF VLF SIGNALS
 Reder, F.H.
 (US Army, Electronics Command, Fort Monmouth, N.J.)

The basic facts of VLF wave propagation in the waveguide formed by the ground and the ionospheric shell are reviewed, and the phase and amplitude anomalies caused by ionospheric disturbances are examined. Typical equipment problems are discussed, showing that selection of the most suitable VLF signal for timing and navigation purposes requires consideration of the signal frequency, path length, path orientation and path location. Guidelines for the selection of reliable equipment are proposed.

73A10904 72/00/00 13 pages
SYNOPTIC STUDIES OF D-REGION IONIZATION CHANGES AND ELECTRON DENSITIES BY THE PARTIAL REFLECTION DIFFERENTIAL ABSORPTION EXPERIMENT.
 Belrose, J.S.
 (Department of Communications, Communications Research Centre, Ottawa, Canada)

77N81499 AD-A032597 GUUS-10766 TR-6 75/12/00 6 pages
ULTRASONIC BOUNDED BEAM REFLECTION AND TRANSMISSION EFFECTS AT A LIQUID SOLID-PLATE LIQUID INTERFACE - TECHNICAL REPORT, 1 JANUARY - 31 OCTOBER 1976
 Plona, T.J.; Pitts, L.E.; Plona, T.J.; Mayer, W.G.
 Georgetown University, Washington, D.C.

78N14223 AD-A046237 RDA-TR-2005-002 DNA-4339T 77/06/10 43 pages
 EFFECT OF A CYLINDRICALLY-SYMMETRIC IONOSPHERIC DISTURBANCE ON ELF PROPAGATION IN THE
 EARTH-IONOSPHERE WAVEGUIDE
 Greifinger, C.; Griefinger, P.
 R & D Associates, Marina del Rey, Calif.

A nuclear explosion in the earth's ionosphere produces a depression in the ionosphere that is approximately cylindrically symmetric. In this paper, a method is developed for calculating the change in amplitude and phase at a receiver of an ELF (extremely low frequency) radio wave in the presence of such a localized, cylindrically-symmetric disturbance. Numerical results are obtained for the particular configuration where the center of the disturbance is directly above the transmitter-receiver path. The attenuation from one edge of the disturbance to the opposite edge is found to be only about half of that calculated by the two-dimensional WKB approximation usually employed in such problems.

78N13300 AD-A045606 LMSC-D560323 77/06/30 124 pages
 ANALYSIS OF SATELLITE DATA ON PRECIPITATING PARTICLES IN COORDINATION WITH ELF
 PROPAGATION ANOMALIES - ANNUAL REPORT, PERIOD ENDING 14 JUNE, 1977
 Imhof, W.L.; Larsen, T.R.; Reagan, J.B.; Gaines, E.E.
 Lockheed Missiles and Space Co., Palo Alto, Calif.

Based on energetic particle measurements from a satellite, a study has been made of the effects of particle precipitation into the atmosphere on the transmission of ELF signals. Coordinated exercises were conducted between satellite measurements of the precipitating particles and ELF transmissions between the US Navy Wisconsin test facility and receiving stations in Maryland, Greenland, Norway, and Italy. Significant fluxes of precipitating electrons were often measured with the Lockheed payload on the polar-orbiting satellite 1972-076B. Based on the fluxes, energy spectra, and pitch-angle distributions of the particle, ion-pair production profiles were calculated and electron density profiles subsequently obtained with application of known effective electron loss rates. From the coordinated data, correlative studies between signal strengths and electron density profiles were performed with use of an ELF wave-guide-mode computer program developed at the Naval Ocean Systems Center. With the inclusion of data from several stations, the transmission signal strength could be studied simultaneously under a variety of ionospheric conditions. The wave-guide computer program calculations indicated that energetic particle precipitation events may cause a signal enhancement or degradation, depending upon where the disturbance is occurring along the path. The consistent occurrence during electron precipitation events of signal strength anomalies in either direction is supported by the coordinated satellite/ELF station measurements.

78N11288 AD-A043501 DNA-4250F 77/01/00 48 pages
 VLF/LF PROPAGATION BENEATH IRREGULARLY PERTURBED IONOSPHERES - FINAL REPORT,
 29 MARCH - 30 NOVEMBER 1976
 Price, G.H.; Hatfield, V.E.
 Stanford Research Inst., Menlo Park, Calif.

The disturbance to very-low-frequency and low-frequency propagation produced by numbers of large-yield, low-altitude nuclear detonations is considered. The consequent lower-ionospheric irregularity both reduces the coherent reflection and produces an incoherently scattered component of the signal. These effects are found to be appreciable at detonation densities in the range of those considered in conjunction with large-scale attack scenarios.

77N30352 AD-A039777 TRW-26766-6001-RU-00 77/01/31 35 pages
 ULF GENERATED BY A SATELLITE-EMITTED BEAM - FINAL REPORT
 Fredricks, R.W.
 TRW Defense and Space Systems Group, Redondo Beach, Calif.

The work reported under this contract was motivated by the need to investigate possible LF systems that are capable of providing means to communicate with submerged submarines. Since ULF waves have a large skin depth in sea water, it seems natural to consider them for the stated purpose. A basis for the present work was formed in 1974 when TRW personnel performed preliminary calculations of generation of ULF signals by satellite-launched ion beams. The model used in the earlier calculations was a 'broad' ion beam. The term 'broad' means that finite beam radius effects were ignored. Thus, such an idealization, which is mathematically convenient, must lead to larger signals and higher efficiency than the realistic case of a beam of finite radial extent. Since the broad-beam calculation gave encouraging results, it was considered worthwhile to examine the finite-cross-section, or 'pencil' beam. The results of this analysis of a finite-radius beam of ions are presented.

77N29135 AD-A040320 APL/JHU-TG-12980 77/01/00 404 pages
 EXPERIMENTAL RESEARCH ON THE PROPAGATION OF LORAN-C SIGNALS. VOLUME D. DATA AND
 ANALYSIS
 Fehner, L.F.; Jerarji, T.W.; McCarty, T.A.; Roll, R.; Smith, R.R.
 Applied Physics Lab., John Hopkins Univ., Laurel, Md.

This report (Volume D of TG 1298) documents the data that were recorded and the analyses that were performed in conjunction with an experiment conducted by the John Hopkins University applied physics laboratory for the US Air Force and the defense advanced research projects agency to determine the validity of one facet of the theory of

groundwave propagation at 100 KHz. Volume A is the summary report, Volume B describes test operations, and Volume C describes the measurement system. The goal of the experiment was to determine if an analytic function could be developed for operational use that relates secondary phase factor to envelope to cycle difference so that geodetic position can be computed, accurately and in real time, from Loran-C coordinates. Field test data were collected and analyzed. They show trends that tend to support the hypothesis that the desired functional relationship exists, at least under certain conditions. Additional analysis and perhaps tests will be necessary to define these conditions or to prove conclusively the existence of such a relationship.

76N20346 AD-A016527 PSR-504 AFCRL-TR-75-0382 75/07/00 59 pages
 VLF/LF TE-MODE PROPAGATION UNDER DISTURBED IONOSPHERIC CONDITIONS - FINAL REPORT, 1 MAY-30 JUNE, 1975
 Field, E.C.; Dore, M.A.
 Pacific-Sierra Research Corp., Santa Monica, Calif.

The report compares calculated attenuation rates for transverse magnetic (TM) and transverse electric (TE) modes propagating in the earth-ionosphere waveguide. Frequencies from 10 to 50 KHz are considered, and attention is restricted to situations where the field can be represented in terms of the least-attenuated TM or TE mode. Nine model ionospheres corresponding to conditions caused by widespread high-altitude fission debris are used as inputs to the calculations. Certain of these models are also representative of polar-cap-absorption (PCA) events. The calculations utilize full-wave methods, and account for the vertical inhomogeneity of the ionosphere, the effects of heavy ions, and the curvature of the earth. In addition to the modal attenuation rates, results are given for field-strength, height-profiles, plane-wave ionospheric reflection coefficients, and the relative importance of heavy ions vis-a-vis electrons.

75N14954 PB-234669/0 R-7103 74/05/10 39 pages
 LONG TERM SKYWAVE FIELD STRENGTH MEASUREMENTS IN THE 550-1600 KHZ FREQUENCY BAND
 Damelin, J.
 Federal Communications Commission, Washington, D.C.

The report presents a compilation of ionospheric field strength data in the 550-1600 KHz frequency band accumulated by the Commission in the course of skywave recording at its field monitoring stations. These data were recorded over some 26 different transmission paths within the continental United States, usually over a period of an eleven year sunspot cycle. The actual recording paths are shown on a map.

75N10747 AD-784378 APL-TG-1243 74/05/00 41 pages
 PROPAGATION EFFECTS AT RADIO FREQUENCIES ON SATELLITE NAVIGATION SYSTEMS
 Pisacane, V.L.; Feen, M.M.
 Applied Physics Lab., John Hopkins Univ., Silver Spring, Md.

The report discusses the effects of the neutral and ionized atmosphere on radio frequency signals used in satellite navigation systems. Knowledge of the signal velocity along the transmission path is necessary to properly interpret the navigation measurements. A technique for taking into account the influence of the neutral atmosphere on radio frequency signals is discussed. The algorithm is based on modeling of the refractive index as a function of surface temperature, pressure, and humidity. Several techniques for accounting for the effects of the ionized atmosphere at VHF and UHF are considered. Recent results are presented on the development of corrective algorithms that could be used operationally by navigators. The techniques developed are based on real-time prediction of the atmospheric electron density distribution.

74N32103 AD-780159 SRI-JSR-73-7 74/04/00 23 pages
 LORAN PROPAGATION
 Berman, S.M.
 Stanford Research Inst., Menlo Park, Calif.

The possibility of using position independent weighted averages of phase and signal arrival times to eliminate the corrections in these times caused by intervening media is examined for the case of Loran C ground waves. Three analytically simple examples are considered - short, longitudinal, homogeneous paths; longitudinal paths with one inhomogeneity, and first-order corrections to longitudinally homogeneous paths taking into account the sphericity of the earth. In each of these cases suitable weighted averages can be made in which one unknown such as the media conductivity can be eliminated.

73N11131 FOA-3-C-3673-6C REPT-18 71/04/00 47 pages
 THE INFLUENCE OF THE LOWER IONOSPHERE ON WAVE PROPAGATION IN THE LF RANGE UP TO A DISTANCE OF 300 KM
 Ladell, L.
 Research Inst. of National Defence, Stockholm, Sweden

Calculations of the electric field strength of ionospheric waves are presented, assuming realistic ionospheric models. The earth magnetic field is neglected and the ionosphere is considered to be horizontally stratified. The calculations are made by a multislab approximation method, using a computer. It is determined that of the three different ionospheric profiles considered, only the night profile gives a seriously disturbing ionospheric wave.

**6. HF Transmissions
Back and Forward Scatter Radar
Ray Tracing**

77A15862 76/07/00 5 pages

COMPUTERIZED METHODS FOR THREE-DIMENSIONAL RAY TRACING IN THE IONOSPHERE

Singh, S.; Mathur, N.C.

(Indian Army, New Delhi, India); (Indian Institute of Technology, Kanpur, India)

A three-dimensional ray-tracing computer program has been developed to study ionospheric effects on the propagation of HF, VHF, and microwave frequencies. The program is quite general and can be used with any model of electron density, earth's magnetic field, and electron collision frequency. The program has been employed to study effects of the ionosphere on skip distance, maximum height of reflection, various path lengths, elevation error, and differential phase path.

76A46801 76/08/00 7 pages

RAY-TRACING IN THE IONOSPHERE FOR LONG RANGE PROPAGATION STUDIES

Bertini, F.; De Giorgio, M.T.; Pellegrini, P.F.

(CNR, Istituto di Ricerca sulle Onde Elettromagnetiche, Florence, Italy)

An ionospheric three-dimensional ray-tracing procedure on a world-wide scale is described which was applied at IROE for long-range propagation studies. This procedure is based on the numerical integration of the ray canonical equations originating from geometric optics and uses a three-dimensional model of the ionospheric electron density constructed from experimental data. The theoretical formulation of the problem is summarized; a description is given of the model assumed for the earth's magnetic field and of the procedure followed for modelling the electron density distribution. This procedure has the advantage that the world-wide behaviour is accurately represented with minimum memory requirement of the computer. The method for integrating the ray equations is outlined; particular attention was paid to the minimization of the machine time. Some ray-tracing results are presented displaying typical propagation modes.

75A29338 75/02/00 3 pages

PROPAGATION MODES OF DECAMETER-RANGE RADIO WAVES FROM OBSERVATIONS USING THE METHOD OF ROTARY OBLIQUE PROBING ALONG PATHS BETWEEN CUBA AND THE SOVIET UNION

Berdeians, D.; Bocharov, V.I.; Lobachevskii, L.A.; Martines, R.; Soares, K.H.; Tushentsova, I.A.

(Akademiia Nuak SSSR, Institut Zemnogo Magnetizma, Ionosfery i Rasprostraneniia Radiovoln, Krasnaya Pakhra, USSR; Academia de Ciencias de Cuba, Havana, Cuba)

75A28063 74/08/00 3 pages

COMPUTERISED METHODS FOR TWO DIMENSIONAL RAY TRACING IN THE IONOSPHERE

Singh, S.

(Indian Army, New Delhi, India)

Computerized ray tracing in two dimensions is studied using a quasi-parabolic layer as an analytic ionospheric model. The theory of ray tracing for an isotropic medium without electron collision is outlined, and equations for the parameters of a ray traveling through a quasi-parabolic layer are derived. Results of computer calculation of these parameters for a set of 10 frequencies (2 to 30 MHz) transmitted at elevation angles from 0 deg to 90 deg are discussed, and they show that ground range is dependent on both the angle of elevation and the transmission frequency, while the maximum reflection height for a quasi-parabolic ionosphere is a function of the transmission frequency.

75A26594 74/09/00 35 pages

HF AND UHF PROPAGATION STUDIES OF THE MID-LATITUDE IONOSPHERE

Hartmann, G.K.

(Max-Planck-Institut fuer Aeronomie, Lindau ueber Northeim, West Germany)

Attention is concentrated on the main trough region of the mid-latitude ionosphere. Examples are given of particularly interesting results obtained by different ground based techniques, including bottomside ionosondes. Swept frequency backscatter systems and incoherent scatter radars. Satellite-to-ground propagation experiments are then reviewed; these include scintillation and radio holography studies, together with total electron content studies by Faraday rotation, differential phase (dispersive doppler) and differential group delay methods. HF propagation studies provide a good way of investigating the motion of the trough (and hence of studying the plasmopause), the interchange of ionization between the ionosphere and the plasmasphere, magnetic storm effects, gravity waves, and effects of practical importance in radio communications and navigation systems.

75A25563 75/03/00 7 pages

THE EFFECT OF FREQUENCY SEPARATION ON THE CORRELATION OF BEARING ERRORS MEASURED ON IONOSPHERICALLY PROPAGATED HF SIGNALS FROM COLOCATED TRANSMITTERS

Reynolds, J.S.B.; Morgan, A.D.

(Government Communications Headquarters, Cheltenham, Glos., England)

75A15116 74/11/00 8 pages

HF-VHF COMMUNICATIONS EXPERIMENT USING MAN-MADE FIELD-ALIGNED IONOSPHERIC SCATTERERS

Barry, G.H.

(Barry Research Corp., Palo Alto, Calif.)

Scatter from man-made, field-aligned, F-layer irregularities offers a means of over-the-horizon communication at VHF frequencies. Experimental data collected in 44 days of field operation in the Autumns of 1972 and 1973 define representative characteristics of signals transmitted over such a scatter circuit. A cloud of field-aligned scatterers was created by the Platteville, Colorado, ionospheric modification facility; test transmitting sites were established in Texas and receiving sites in California. The data describe means and peak cloud radar cross section; the dependence of cross section on heater power, heater modulation, time of day, and signal frequency; the circuit coherent and incoherent bandwidths; the signal amplitude statistics and spatial correlation; and the signal spectral spreading.

75A11815 74/10/00 7 pages

A QUALITATIVE EXAMINATION OF THE EFFECT OF SYSTEMATIC TILTS, IN THE IONOSPHERE, ON HF BEARING MEASUREMENTS

Morgan, A.D.

(Government Communications, Cheltenham, Glos., England)

Qualitative investigation of the effect of systematic tilts in the ionosphere on high-frequency bearing measurements taken over a three-week period in both Spring and Summer. The results obtained suggest that bearing measurements can be used to examine systematic tilt effects in the ionosphere.

74A10414 73/00/00 6 pages

CONTRIBUTION TO THE THEORY OF ULTRALONG PROPAGATION OF SHORT RADIO WAVES

Guverich, A.V.; Tsedilina, E.E.

(Akademiia Nauk SSSR, Fizicheskii Institut, Moscow, USSR); (Akademiia nauk SSSR, Institut Zemnogo Magnetizma, Ionosfery i Rasprostraneniia Radiovoln, Krasnaya Pakhra, USSR)

(For abstract see issue 15, p.1844, accession No.A73-31888.)

73A33726 73/00/00 5 pages

MEASUREMENTS OF WIND-INDUCED DOPPLER SHIFTS AT 16 GHZ OVER A LONG RANGE BISTATIC SCATTER LINK.

Olsen, R.L.; Lammers, U.H.W.

(Department of Communications, Communications Research Centre, Ottawa, Canada); (USAF, Cambridge Research Laboratories, Bedford, Mass.)

The results of measurements of wind-induced doppler shifts performed at 15.7 GHz over a 500 km bistatic scatter link are used to estimate average wind velocities in the upper troposphere. The advantages of this remote sensing technique are discussed, and the difficulties encountered during abnormal propagation conditions are examined.

73A31888 73/04/00 6 pages

THEORY OF SHORT RADIO WAVE PROPAGATION OVER VERY GREAT DISTANCES

Gurevich, A.V.; Tsedilina, E.E.

(Akademiia nauk SSSR, Fizicheskii Institut, Moscow, USSR); (Akademiia nauk SSSR, Institut Zemnogo Magnetizma, Ionosfery i Rasprostraneniia Rodiovoln, Krasnaya Pakhra, USSR)

Equations are derived to describe the propagation of short radio waves over very large distances about the globe in an adiabatic approximation. Conditions of capture in an ionospheric wave channel are studied for radio waves transmitted from the earth surface.

77N73674 AD-A027429 CNR-14 74/05/14 90 pages

HF CHANNEL SIMULATION - FINAL REPORT, 15 OCTOBER 1973 - 14 APRIL 1974

Pinto, R.W.; Bello, P.A.

CNR, Inc., Newton Upper Falls, Mass.

78N13288 AD-A044004 ECAC-PR-75-071-VOL-1 FAA-RD-77-56-1 77/05/00 111 pages

EMC ANALYSIS OF THE PROPOSED AEROSAT VHF SUBSYSTEM WITH CURRENT INBAND COMMUNICATIONS SYSTEMS. VOLUME 1 - USA AND CANADA - FINAL REPORT

Slay, F.M.

IIT Research Inst., Annapolis, Md.

Information and guidelines are presented pertaining to the electromagnetic compatibility (EMC) of ground and airborne equipments in the aeronautical mobile VHF service with the proposed aerosat VHF avionics. Volume I provides general guidelines for aerosat avionics compatibility with the VHF environment and predicted interactions with aeronautical mobile VHF equipments in the United States and Canada. Volume II addresses the worldwide VHF environment. The frequency bands considered are 125.4-126.0 MHz and 131.4-132.0 MHz. The analysis is based on the VHF frequency

assignments in use when the study was performed (1975); co-channel operation of aerosat and air traffic control (ATC) stations is not considered.

76N20323 76/00/00 14 pages

ADAPTIVE SIGNAL SELECTION FOR DISPERSIVE CHANNELS AND ITS PRACTICAL IMPLICATIONS IN COMMUNICATIONS SYSTEM DESIGN

Darnell, M.

Admiralty Surface Weapons Establishment, Portsmouth, England

Possible techniques are considered whereby the operation of an HF communications system could be made adaptive in response to the state of the channel. Adaptive RF equipment, source encoding/decoding and channel encoding/decoding procedures are described and their interactions discussed. Adaptive signal selection implies adaptive signal generation and processing equipment. Possible formats for such units are outlined, together with the inputs required for their operation and the advantages accruing from their use.

76N20312 76/00/00 18 pages

A COMPARISON BETWEEN THE DEUTSCHE BUNDESPOST IONOSPHERIC HF RADIO PROPAGATION PREDICTIONS AND MEASURED FIELD-STRENGTHS

Damboldt, T.

Forschungsinstitut der Deutschen Bundespost, Darmstadt, West Germany

The Deutsche Bundespost makes long term propagation predictions for use by its own frequency planning department and for various other users. The forecast computer program is reported, followed by an outline of field strength measurements. Afterwards the measurements are compared with the forecasts. Some of the deviations between forecasts and measurements are analyzed.

76N14353 AD-A013648 ITT-EPL-278 CB-115 75/06/00 145 pages

TRACKER STUDIES - FINAL REPORT, FEBRUARY - DECEMBER 1974

Dewitt, R.N.

ITT Electro-Physics Labs., Inc., Columbia, Md.

The existence of multi-mode propagation can have two deleterious effects on an OTH radar tracker; it can lead to ambiguity in the interpretation of the range of detected targets, and it can lead to difficulties in determining from a single detection sample; any testing to determine mode identity must be performed at or beyond the tracker. Three methods are considered for identifying propagation modes; one based on testing for the occurrences of echoes in regions or combinations of regions of the radar-observable space accessible to only a single propagation mode, another based on the amplitude fluctuations observed on echoes, and a third in which mode separations are tracked and taken into account. Predictive filters are given general treatment. The Kalman filter tracking algorithm is discussed with the modifications required to implement the first and third (above) mode-identification techniques. The use of signal strength fluctuations as a mode-identification criterion is examined and dismissed as being insufficiently predictable to provide a reliable means for identifying propagation modes.

76N12571 AD-A011719 LTIRF-368/IP AFCRL-TR-74-0563 74/10/00 59 pages

AIRBORNE AND GROUND BASED ARCTIC DIGITAL IONOSPHERIC SOUNDINGS - FINAL REPORT, 1 OCTOBER 1973 - 30 JUNE 1974

Bibl, K.; Reinisch, B.W.

Lowell Technological Inst. Research Foundation, Mass.

High frequency radio wave propagation studies at Goose Bay, Labrador and between Goose Bay and an instrumented KC-135 aircraft are discussed. Both power and phase-coherent detection schemes were applied to investigate the coherence of the ionospheric echoes. Backscatter ionograms were recorded in this dynamic environment using digital power-integration techniques. Stable synchronization between the ground station and the aircraft enabled the recording of swept frequency oblique ionograms over distances of up to 3000 km. Alternating with vertical and oblique incidence ionograms, doppler and angle of arrival measurements were carried out at the ground on multiple fixed frequencies transmitted with the aircraft's digisonde-drift system.

76N11336 AD-A011924 TR-PL-10132 RADC-TR-75-116 75/05/00 318 pages

LONG RANGE SENSOR COMMUNICATION - FINAL TECHNICAL REPORT

Sykes, C.B.; Robertson, R.G.

Atlantic Research Corp., Alexandria, Va.

A performance study was conducted to determine the feasibility of direct long-range remote sensor communications without the use of relays. Of the propagation modes analyzed, HF ionospheric, MF, HF ground-wave, and forward meteor scatter, the HF ionospheric propagation mode is favored and performance predictions using this mode for digital message transmission are presented. The performance is given in terms of predicted message error rate and circuit outage under various conditions of range, frequency, hour, season, sunspot number and geographic location.

assignments in use when the study was performed (1975); co-channel operation of aerosat and air traffic control (ATC) stations is not considered.

76N20323 76/00/00 14 pages

ADAPTIVE SIGNAL SELECTION FOR DISPERSIVE CHANNELS AND ITS PRACTICAL IMPLICATIONS IN COMMUNICATIONS SYSTEM DESIGN

Darnell, M.

Admiralty Surface Weapons Establishment, Portsmouth, England

Possible techniques are considered whereby the operation of an HF communications system could be made adaptive in response to the state of the channel. Adaptive RF equipment, source encoding/decoding and channel encoding/decoding procedures are described and their interactions discussed. Adaptive signal selection implies adaptive signal generation and processing equipment. Possible formats for such units are outlined, together with the inputs required for their operation and the advantages accruing from their use.

76N20312 76/00/00 18 pages

A COMPARISON BETWEEN THE DEUTSCHE BUNDESPOST IONOSPHERIC HF RADIO PROPAGATION PREDICTIONS AND MEASURED FIELD-STRENGTHS

Damboldt, T.

Forschungsinstitut der Deutschen Bundespost, Darmstadt, West Germany

The Deutsche Bundespost makes long term propagation predictions for use by its own frequency planning department and for various other users. The forecast computer program is reported, followed by an outline of field strength measurements. Afterwards the measurements are compared with the forecasts. Some of the deviations between forecasts and measurements are analyzed.

76N14353 AD-A013648 ITT-EPL-278 CB-115 75/06/00 145 pages

TRACKER STUDIES - FINAL REPORT, FEBRUARY - DECEMBER 1974

Dewitt, R.N.

ITT Electro-Physics Labs., Inc., Columbia, Md.

The existence of multi-mode propagation can have two deleterious effects on an OTH radar tracker; it can lead to ambiguity in the interpretation of the range of detected targets, and it can lead to difficulties in determining from a single detection sample; any testing to determine mode identity must be performed at or beyond the tracker. Three methods are considered for identifying propagation modes; one based on testing for the occurrences of echoes in regions or combinations of regions of the radar-observable space accessible to only a single propagation mode, another based on the amplitude fluctuations observed on echoes, and a third in which mode separations are tracked and taken into account. Predictive filters are given general treatment. The Kalman filter tracking algorithm is discussed with the modifications required to implement the first and third (above) mode-identification techniques. The use of signal strength fluctuations as a mode-identification criterion is examined and dismissed as being insufficiently predictable to provide a reliable means for identifying propagation modes.

76N12571 AD-A011719 LTIRF-368/IP AFCRL-TR-74-0563 74/10/00 59 pages

AIRBORNE AND GROUND BASED ARCTIC DIGITAL IONOSPHERIC SOUNDINGS - FINAL REPORT, 1 OCTOBER 1973 - 30 JUNE 1974

Bibl, K.; Reinisch, B.W.

Lowell Technological Inst. Research Foundation, Mass.

High frequency radio wave propagation studies at Goose Bay, Labrador and between Goose Bay and an instrumented KC-135 aircraft are discussed. Both power and phase-coherent detection schemes were applied to investigate the coherence of the ionospheric echoes. Backscatter ionograms were recorded in this dynamic environment using digital power-integration techniques. Stable synchronization between the ground station and the aircraft enabled the recording of swept frequency oblique ionograms over distances of up to 3000 km. Alternating with vertical and oblique incidence ionograms, doppler and angle of arrival measurements were carried out at the ground on multiple fixed frequencies transmitted with the aircraft's digisonde-drift system.

76N11336 AD-A011924 TR-PL-10132 RADC-TR-75-116 75/05/00 318 pages

LONG RANGE SENSOR COMMUNICATION - FINAL TECHNICAL REPORT

Sykes, C.B.; Robertson, R.G.

Atlantic Research Corp., Alexandria, Va.

A performance study was conducted to determine the feasibility of direct long-range remote sensor communications without the use of relays. Of the propagation modes analyzed, HF ionospheric, MF, HF ground-wave, and forward meteor scatter, the HF ionospheric propagation mode is favored and performance predictions using this mode for digital message transmission are presented. The performance is given in terms of predicted message error rate and circuit outage under various conditions of range, frequency, hour, season, sunspot number and geographic location.

75N26322 AD-A003641 RADC-TR-74-316 74/12/00 82 pages
 BEYOND-THE-HORIZON VHF COMMUNICATION USING MAN-MADE IONOSPHERIC SCATTERERS – FINAL
 TECHNICAL REPORT, MAY 1973 – JULY 1974
 Sasselli, R.A.; McLaughlin, J.F.
 Barry Research Corp., Palo Alto, Calif.

The report summarizes the design of a communications circuit using the man-made ionospheric scatterers and the characteristics of VHF signals propagated over such a circuit. It represents a compilation of experimental data obtained during field exercises in which communications were established between terminals separated 1400 km and 2200 km. The scattering cloud was located 1000–1200 km from both transmitter and receiver terminals. The report summarizes the requirements of an ionospheric heater and describes the characteristics of the disturbance itself. These characteristics include observed radar cross section as a function of time of day, amount of heater radiated power, and heater modulation.

75N26215 AD-A03862 NELC/TD-379 74/01/01 11 pages
 SHIP-TO-SHIP TACTICAL (GROUNDWAVE RANGE) HF COMMUNICATIONS. (PERFORMANCE PREDICTIONS
 IN GRAPHICAL FORM)
 Kelly, W.H.
 Naval Electronics Lab. Center, San Diego, Calif.

The document addresses ship-to-ship tactical HF communications (groundwave distances over seawater). It provides performance predictions in ready-to-use graphical form, and discusses transmission system factors that influence system performance. It suggests a deviation from the traditional procedure of tactical HF frequency assignment (static assignment in the 2–6-MHz band) to a more dynamic assignment procedure by making assignments based upon the tactical situation and performance predictions covering the entire HF band. The predictions show that under certain conditions expected HF groundwave ranges will be greater in the 10–20-MHz band than at 2 MHz. Further, they indicate that atmospheric noise has considerable influence over performance and that shipboard HF antenna system improvement can provide significant improvement in system performance.

75N14951 AD-786977 APL-TG-1253 74/07/00 25 pages
 AN ANALYSIS OF TWO PROBLEMS RELATED TO OVER-THE-HORIZON DETECTION IN THE HF BAND
 Shotland, E.
 Applied Physics Lab., John Hopkins Univ., Silver Spring, Md.

A 21-db discrepancy between theory and experiment concerning Bragg scattering of HF ground waves by a rough sea is analyzed and resolved. In addition, a new and more efficient method of non-dimensionalization is proposed for the quantities of radio propagation in the HF band that could be adopted by all electromagnetic and acoustical wave bands of propagation. It is especially useful in the application of the Norton-Barrick concept of basic transmission loss.

7. Forecasting and Predicting Ionospheric Parameters – Artificial Modification of the Ionosphere

75A36062 75/02/00 20 pages
 SOLAR-TERRESTRIAL RELATIONS AND SHORT-TERM IONOSPHERIC FORECASTING
 Cook, F.E.; McCue, C.G.
 (Department of Science, Ionospheric Prediction Service, Darlinghurst, New South Wales, Australia)

Since the ionosphere is produced by the quiet sun and disturbed by the active sun, short-term ionospheric forecasting is discussed in three stages (1) forecasting the solar activity; (2) the relations between the solar activity and geophysical disturbances, particularly magnetic storms, daylight fadeouts and polar cap absorption; (3) the effects of these geophysical disturbances on the ionosphere and on ionospheric radio communications. A short history of the subject is given, the international arrangements for collecting and rapidly exchanging the required solar and geophysical data are outlined, and short-term forecasting services at present operating are described briefly.

(e-10)

REPORT DOCUMENTATION PAGE			
1. Recipient's Reference	2. Originator's Reference AGARD-LS-93✓	3. Further Reference ISBN 92-835-1280-4	4. Security Classification of Document UNCLASSIFIED
5. Originator	Advisory Group for Aerospace Research and Development North Atlantic Treaty Organization 7 rue Ancelle, 92200 Neuilly sur Seine, France		
6. Title	RECENT ADVANCES IN RADIO AND OPTICAL PROPAGATION FOR MODERN COMMUNICATIONS, NAVIGATION AND DETECTION SYSTEMS		
7. Presented	on 8-9 May 1978 in Oslo, Norway, 11-12 May 1978 in London, England and 15-16 May 1978 in Rome, Italy.		
8. Author(s)	Various	9. Date	April 1978
10. Author's Address	Various	11. Pages	274 pages including Bibliography
12. Distribution Statement	This document is distributed in accordance with AGARD policies and regulations, which are outlined on the Outside Back Covers of all AGARD publications.		
13. Keywords/Descriptors	Electromagnetic wave transmission Light transmission Radio transmission	Ionospheric propagation Ionospheric disturbances Lasers	Remote sensing Navigation Telecommunication
14. Abstract	<p>After an introduction to optical problems of systems the following are presented: physics of incoherent optical propagation, problems relative to laser transmission, remote sensing (IR, UV Microwave).</p> <p>The radio wave propagation lectures include high-frequency transmissions forecasting the prediction of ionospheric parameters, ionospheric time delay, ionospheric scintillation, artificial modification of the propagation medium, low and very low frequency propagation.</p> <p>The material in this book has been assembled to support a Lecture Series presented in Oslo (8, 9 May 1978), London (11, 12 May 1978) and Rome (15, 16 May 1978), under the joint sponsorship of the Electromagnetic Wave Propagation Panel and Consultant and Exchange Programme of AGARD.</p>		

<p>AGARD Lecture Series No.93 Advisory Group for Aerospace Research and Development, NATO</p> <p>RECENT ADVANCES IN RADIO AND OPTICAL PROPAGATION FOR MODERN COMMUNICATIONS, NAVIGATION AND DETECTION SYSTEMS</p> <p>Published April 1978</p> <p>274 pages including Bibliography of 104 items</p> <p>After an introduction to optical problems of systems the following are presented: physics of incoherent optical propagation, problems relative to laser transmission, remote sensing (IR, UV Microwave).</p> <p>The radio wave propagation lectures include high-frequency transmissions forecasting and prediction of</p> <p>P.T.O.</p>	<p>AGARD-LS-93</p> <p>Electromagnetic wave transmission Light transmission Radio transmission Ionospheric propagation Ionospheric disturbances Lasers Remote sensing Navigation Telecommunication</p>	<p>AGARD Lecture Series No.93 Advisory Group for Aerospace Research and Development, NATO</p> <p>RECENT ADVANCES IN RADIO AND OPTICAL PROPAGATION FOR MODERN COMMUNICATIONS, NAVIGATION AND DETECTION SYSTEMS</p> <p>Published April 1978</p> <p>274 pages including Bibliography of 104 items</p> <p>After an introduction to optical problems of systems the following are presented: physics of incoherent optical propagation, problems relative to laser transmission, remote sensing (IR, UV Microwave).</p> <p>The radio wave propagation lectures include high-frequency transmissions forecasting and prediction of</p> <p>P.T.O.</p>	<p>AGARD-LS-93</p> <p>Electromagnetic wave transmission Light transmission Radio transmission Ionospheric propagation Ionospheric disturbances Lasers Remote sensing Navigation Telecommunication</p>
<p>AGARD Lecture Series No.93 Advisory Group for Aerospace Research and Development, NATO</p> <p>RECENT ADVANCES IN RADIO AND OPTICAL PROPAGATION FOR MODERN COMMUNICATIONS, NAVIGATION AND DETECTION SYSTEMS</p> <p>Published April 1978</p> <p>274 pages including Bibliography of 104 items</p> <p>After an introduction to optical problems of systems the following are presented: physics of incoherent optical propagation, problems relative to laser transmission, remote sensing (IR, UV Microwave).</p> <p>The radio wave propagation lectures include high-frequency transmissions forecasting and prediction of</p> <p>P.T.O.</p>	<p>AGARD-LS-93</p> <p>Electromagnetic wave transmission Light transmission Radio transmission Ionospheric propagation Ionospheric disturbances Lasers Remote sensing Navigation Telecommunication</p>	<p>AGARD Lecture Series No.93 Advisory Group for Aerospace Research and Development, NATO</p> <p>RECENT ADVANCES IN RADIO AND OPTICAL PROPAGATION FOR MODERN COMMUNICATIONS, NAVIGATION AND DETECTION SYSTEMS</p> <p>Published April 1978</p> <p>274 pages including Bibliography of 104 items</p> <p>After an introduction to optical problems of systems the following are presented: physics of incoherent optical propagation, problems relative to laser transmission, remote sensing (IR, UV Microwave).</p> <p>The radio wave propagation lectures include high-frequency transmissions forecasting and prediction of</p> <p>P.T.O.</p>	<p>AGARD-LS-93</p> <p>Electromagnetic wave transmission Light transmission Radio transmission Ionospheric propagation Ionospheric disturbances Lasers Remote sensing Navigation Telecommunication</p>

<p>ionospheric parameters, ionospheric time delay, ionospheric scintillation, artificial modification of the propagation medium, low and very low frequency propagation.</p> <p>The material in this book has been assembled to support a Lecture Series presented in Oslo (8, 9 May 1978), London (11, 12 May 1978) and Rome (15, 16 May 1978), under the joint sponsorship of the Electromagnetic Wave Propagation Panel and Consultant and Exchange Programme of AGARD.</p>	<p>ionospheric parameters, ionospheric time delay, ionospheric scintillation, artificial modification of the propagation medium, low and very low frequency propagation.</p> <p>The material in this book has been assembled to support a Lecture Series presented in Oslo (8, 9 May 1978), London (11, 12 May 1978) and Rome (15, 16 May 1978), under the joint sponsorship of the Electromagnetic Wave Propagation Panel and Consultant and Exchange Programme of AGARD.</p>
<p>ISBN 92-835-1280-4</p>	<p>ISBN 92-835-1280-4</p>